

THIS WEEK

EDITORIALS

FUNDING The perils and pitfalls of grants that are renewed annually **p.8**

WORLD VIEW Biotechnology is the way to save Indian species **p.9**

PARASITES Plant defence chemicals score an own goal **p.10**



An unhealthy obsession

The energy expended by US biomedical scientists on complaining about grant-application limits would be better directed at the real problem: stagnant funding.

The US National Institutes of Health (NIH) announced last week that it plans to hold firm on an unpopular three-year-old policy limiting grant applicants to one resubmission if a proposal is rejected the first time. The world's largest biomedical research funder is pushing back against a powerful current of unhappiness among its grant recipients. Last year, more than 2,300 of them signed a letter to the US\$31-billion agency condemning the policy as irrational and damaging in an era of historically low grant-application success rates. The 'two strikes and you're out' rule, the letter-writers argued correctly, makes it more likely that some highly meritorious applications will fail to win funding. The policy is particularly hard on the youngest scientists, who suffer both from a dearth of grant-writing experience and the lack of a large body of work to build on in crafting a new proposal. Senior scientists with narrowly focused research programmes are also hurt, as they may have trouble developing a "substantially" different proposal after they have failed twice, as the NIH requires.

But the fact that the critics are correct is beside the point. Other countries have already instituted much more draconian schemes. In the United Kingdom, for instance, applicants to the Medical Research Council who have failed to win funding on their first bid must wait a year before even trying a second time. In the case of the NIH, the bottom line is that, even if the agency were to reintroduce a rule allowing third submissions of twice-failed grants, the same absolute number of applicants would end up getting funded. Indeed, some excellent applications would probably fail to pass muster under any submission regime, as the Comment on page 34 makes clear. With application success rates at historic lows largely because the number of applicants is at historic highs, many first-rate proposals would still go begging.

The crucial problem is not that applicants are limited to two tries; it is that too many aspiring applicants are chasing a stagnant pool of funds that is, in real terms, being eroded further by inflation each year. The latest figures from the National Institute of Allergy and Infectious Diseases, the NIH's second-largest institute, highlight the problem. It is currently funding 6% of the applications for mainstay 'R01' grants that it receives from established scientists, and 10% of those from early-career investigators.

Yet the two-versus-three-chances issue continues to generate heat in the community. One online discussion, at the DrugMonkey blog, generated more than 46 comments totalling some 5,000 words in less than one week in October, after *Nature's* News blog noted that the NIH was considering returning to the three-strikes system.

All the time and energy that these and other angst-ridden scientists are devoting to complaints about how a finite pie is being sliced would be far better directed at trying to enlarge it. Only a bigger funding pie — or a dramatic exodus of aspiring grant-winners from the ranks of US biomedical science, surely a less desirable outcome — will give grant applicants a decent chance of winning funding.

Before US readers roll their eyes at the suggestion that lobbying

for more money could succeed in a dire fiscal climate, they might cast those eyes northwards to Canada, where, last summer, some 2,000 white-coated scientists and graduate students marched on the parliament in Ottawa to protest at what they described as anti-science policies and funding cuts being enacted by the government of Prime Minister Stephen Harper. The photogenic Parliament Hill protest generated around 40 items of news coverage — no mean feat

"Only a bigger funding pie will give grant applicants a decent chance of winning funding."

in a country with one-tenth the population of the United States. The march clearly got the Harper government's attention: the same day, Gary Goodyear, the minister for science and technology, issued an animated defence of his government's record on science.

But with few exceptions, US scientists, like scientists everywhere, have been loath to take to the streets with placards — to be visibly, outspokenly political in defence of their own best interests. Clearly, in the current US context, that strategy, or lack of one, is failing. And things could get much worse. The across-the-board cuts that will take effect in early January if Congress and the White House fail to agree on a deficit-reduction plan would slice 8% from the NIH's budget, making the current situation look comparatively comfortable. That threat should be enough to galvanize researchers into action.

One thing is certain. If each signatory of last year's letter blasting the NIH were to recruit four colleagues, and if all donned white coats in a coordinated march on Capitol Hill, the media would take notice. The sight of 12,000 biomedical scientists alarmed about the present and future of their enterprise would capture politicians' attention in a way that no number of letters and e-mails from advocacy groups will ever do. Such a dramatic call to action may seem — well — dramatic, but if it is not warranted now, then when? ■

Suspend disbelief

Wrangling over scientific misconduct could influence Romania's general election.

One of Romania's best known cultural figures is playwright Eugène Ionesco, who co-founded the twentieth-century movement known as the theatre of the absurd. Had he been alive today, he might have written an absurdist play about his native country — with science taking a strong supporting role.

Romania remains one of the problem children in the European Union (EU). It has stacked up debilitating debt in the past decade,

and in recent months has worryingly veered away from democratic principles. However, ahead of joining the EU in 2007, the country started to develop the framework for a serious scientific base, something that its leaders considered important to make good the damage caused by 40 years of communist dictatorship. Most of the best scientists had left the country, and an appropriately funded, meritocratic system was needed to tempt them back.

The present government of Social Democrat Victor Ponta has been in office for less than a year but it has reversed many of the positive steps taken. Should his Social Liberal Union (USL) coalition gain the absolute majority predicted by some in the general election to be held on 9 December, it is likely to dismantle even more of the institutions set up to ensure meritocracy in academic appointment and funding, and will probably strip away the remaining checks against academic corruption.

Those checks are essential, not least to scrub clean Ponta's government. In the past week, the watchdog website Integru.org has highlighted two cases of alleged plagiarism and one case of alleged data manipulation involving the research minister Ecaterina Andronescu, then a chemist at the Polytechnic University of Bucharest. She denies them. In accordance with Integru's methods, each of the allegations was confirmed by several independent scientific experts from other countries in Europe and North America.

Unlikely as it sounds given the briefness of Ponta's tenure, Andronescu was his third appointment as research minister, and the third to be accused of misconduct. Ponta's first choice, Corina Dumitrescu, was withdrawn before she was confirmed by parliament. She stood accused of plagiarism and falsely claiming that she attended Stanford University. Ioan Mang was appointed in her place on 7 May but was forced to resign just a week later after *Nature* exposed extensive plagiarism in his academic papers in computer science (see *Nature* **485**, 289, 2012). Absurdity peaked in June, when *Nature* revealed that Ponta himself had plagiarized in his 2003 PhD thesis (see *Nature* **486**, 305, 2012).

The accused all dismiss the charges as politically motivated. Ponta promptly ditched the committees responsible for considering the allegations, replaced them with sympathizers, and insisted that the wrong

committee had judged him guilty. In a televised electoral debate on 2 December, which heavily featured Integru's evidence against her, Andronescu responded by emotionally repeating her unlikely election slogan: 'justice all the way'. A press release from her ministry attempted to dismiss the authority of Integru.org.

On 30 November, Andronescu announced her decision not to withdraw Ponta's PhD, even though a report from the awarding University of Bucharest confirmed plagiarism.

"Could the issue of scientific integrity influence a general election?"

Only the research minister can order such revocation. Yet she claimed, absurdly, that it was not in her legislative power to do so. She similarly failed to take responsibility for plagiarism and other scientific misconduct allegedly perpetrated by leading figures in other universities. She has also announced her intention to eliminate rules that require grant applications to be sent to reviewers outside Romania, claiming that the process costs too much.

Those who are struggling to absorb the scale on which Romania's scientific system is failing must do as they would in the theatre — suspend their disbelief. But they might also reflect on the challenge of building a strong democratic state on the ashes of a corrupted dictatorship. Ponta's attempt in July to impeach President Traian Băsescu, a Democratic Liberal, drew a formal rebuke from the EU as undemocratic.

The second largest contender in the elections is a coalition led by the Democratic Liberals. The Democratic Liberals were responsible for bringing in the exemplary laws and structures for science that Ponta is now dismantling. But their governing coalition was also responsible for carrying out an austerity programme that, among other things, cut public-sector wages by 25% in 2010. The coalition collapsed in February this year and is still struggling to recover. But thanks in good part to the very public war on academic corruption in government, it may yet prevent the USL from winning an absolute majority. Could the issue of scientific integrity influence a general election? That would be astonishing perhaps, but not absurd. ■

The second largest contender in the elections is a coalition led by the Democratic Liberals. The Democratic Liberals were responsible for bringing in the exemplary laws and structures for science that Ponta is now dismantling. But their governing coalition was also responsible for carrying out an austerity programme that, among other things, cut public-sector wages by 25% in 2010. The coalition collapsed in February this year and is still struggling to recover. But thanks in good part to the very public war on academic corruption in government, it may yet prevent the USL from winning an absolute majority. Could the issue of scientific integrity influence a general election? That would be astonishing perhaps, but not absurd. ■

Haste not speed

US science would benefit if Congress improved the predictability and stability of funding.

The sad saga of the US Superconducting Super Collider is well known: after spending nearly US\$2 billion digging tunnels under the plains of Texas, the US Congress in 1993 cancelled the proton smasher at a stroke. Compare that to the stately funding stream that CERN, Europe's particle-physics facility near Geneva, Switzerland, used to build the Large Hadron Collider. Each of CERN's 20 member states contributes a specific amount of money, governed by treaty, towards a fixed five-year budget.

A report from a panel of US presidential science advisers (see page 18) points out this obvious difference: European funding is slow and steady, whereas US funding, disbursed by congressional appropriators on an annual basis, is fickle.

It is not just large facilities that struggle. The top-line budgets of US science agencies can vacillate in destructive ways. For instance, the doubling of the budgets at the National Institutes of Health (NIH) from 1998 to 2003 induced many universities to open departments, take on postdoctoral students and construct new buildings. When the cash from the NIH suddenly dried up, the biomedical boomtown went bust.

Appropriators in Congress are unlikely ever to commit to multi-year budgets. But the advisory report makes some good suggestions

for reining in the worst aspects of the US budget cycle. First, it proposes that science agencies should start planning budgets into the future, even though appropriators might well ignore them. There is a belief in Washington DC that, in being planned, a programme is put out in the open and is therefore vulnerable to the budget-cutter's axe. That idea is incorrect. For years, the Department of Defense has been laying out budget plans in five- or six-year increments. Although appropriators do not have to abide by the plan, they are able to see the agency's rationale. NASA also plans notional five-year budgets (although its costings for large missions are sometimes off target). The NIH, the National Science Foundation (NSF) and the Department of Energy should follow suit.

A second recommendation is for appropriators to match the funding levels set by authorization committees more closely. The congressional representatives on authorization committees know their agencies well, and often plan budgets in two- or three-year increments. But the exercise is largely a fiction. For instance, the most recent NSF reauthorization called for \$7.8 billion in 2012, but appropriators ended up giving the agency only \$7 billion.

The US way of doing things is not all wrong. There can be some advantages: an agency can pick up on a new scientific idea, propose a visionary programme and get it funded all in the space of a year — something that rarely happens in Europe, where some programmes end up being supported way past their prime. But when it comes

to funding science, predictability is more of a virtue than speed, and stability better than surprise. The US scientific enterprise, dynamic as it is, could benefit if its budgets became a little more plodding. ■

➔ **NATURE.COM**

To comment online,
click on Editorials at:
go.nature.com/xhunqv



Extinction need not be forever

Biotechnology can help to save endangered species and revive vanished ones. Conservationists should not hesitate to use it, says Subrat Kumar.

Charismatic mammals such as cheetahs and tigers are important for wildlife tourism. Yet in India, these and other species are in trouble — or worse. Cheetahs are already extinct here and the country's tiger population was put at just 1,706 in a census last year, down from an estimated 40,000 at the start of the twentieth century. The plight of the tiger is so dire that in July, India took the serious step of banning tourism in core areas of tiger reserves. The ban, which affected 41 tiger parks across the country and drew protests from tour operators and conservationists alike, was not lifted until October, when the government announced tighter regulations for visitors.

Pressures such as habitat loss have led to progressive decline in tiger numbers. Poachers are a bigger threat, and India lacks the funds, manpower and infrastructure necessary to curb the killing of these magnificent mammals. Efforts to protect surviving populations need to be stepped up. But it is high time that we, as a modern society, took on the problem of conservation with greater use of the advanced tools given to us by the tremendous scientific developments of the past few years.

People work hard at zoological parks around the world to breed endangered animals in captivity, but reliable repopulation strategies still evade us. Captive breeding has been successful in some cases, but it remains difficult to breed migratory birds and fish and large species, especially whales and dolphins. Even when such efforts are successful, there are often problems such as extensive inbreeding owing to small population sizes, a lack of immunity against disease in the inbred populations, induced behavioural changes (which can impair the hunting abilities of the released animals) and loss of habitat during the time animals are held in captivity.

Given the urgent need, it seems wise to pursue other approaches. We now have the technology to generate genetically modified organisms for research purposes or for use as biological-product factories. These advances in molecular biology can, and should, be used to revive lost species from their stored genetic material or to add genetic diversity to remnant populations. We must collect as many DNA samples from endangered, threatened and extinct species as we can, so that if the human population ever reduces its footprint on Earth, these species can be reintroduced.

Cloning and interspecies nuclear transfer are two possibilities, and there are others. Scientists in California, for example, have already produced stem cells similar to those found in early embryos using cryopreserved cells collected from critically endangered rhinos and monkeys. Researchers

in Australia have done the same for the snow leopard. The ultimate goal is to convert stem cells from these threatened species into germ cells that could diversify the gene pools of dwindling populations. To be sure, technological gaps prevent this approach from being widely applied, but they can be filled.

All these efforts require genetic material from the endangered or extinct species. The 'frozen zoo' at San Diego Zoo in California has been maintained since 1976 and holds some 8,400 samples from more than 800 species and subspecies, including DNA, sperm, eggs and embryos, stored in liquid nitrogen. An Indian government laboratory in Hyderabad has started to bank blood samples from the country's endangered animals, but there are fewer than a dozen such facilities around the world. We need to establish more frozen zoos worldwide.

Could the technology also be used to attempt to revive extinct species from which we have already collected biological samples? Why not? I hope that at least one responsible government will be able to see the advantage that it can get from such a revival in terms of both tourism and science. If the species has unusual characteristics, scientists would be able to study its behaviour and capabilities. We could collect information on the animal's origins and evolutionary patterns, as well as bioactive compounds that could be useful for treating human diseases. Species revival is justified on scientific grounds, but we need strong political backing and long-term commitment for it to happen.

Some conservationists fear that a lost species revived in this way would cause ecological disturbances and compete with other species. The once-extinct species might even spread so successfully that it would wipe out other species. However, any species that we bring back could be engineered to be eliminated easily should it pose a problem. And the risk of disturbance from a single, previously native revived species is no greater than those we already face from the large numbers of invasive species introduced by human trade and travel. These risks, I argue, are negligible compared with the scientific and social benefits of reviving the lost species.

There was a time when travellers on a safari in the Indian countryside could expect to see Asiatic lions, Bengal tigers, Asiatic cheetahs and South China tigers, to name but a few species that are now extinct or on the verge of extinction. Biotechnology cannot address the poaching and habitat loss that are driving these animals out, but it can act as insurance to protect their future. ■

Subrat Kumar is assistant professor in the School of Biotechnology at KIIT University in Bhubaneswar, India.
e-mail: subrat_kumar@yahoo.com

IT IS
HIGH TIME
THAT WE TOOK ON THE
PROBLEM OF
CONSERVATION
USING
ADVANCED
TOOLS.

➔ **NATURE.COM**
Discuss this article
online at:
go.nature.com/8e9ad1

RESEARCH HIGHLIGHTS

Selections from the scientific literature

HUMAN EVOLUTION

New Neanderthal extinction time

Whether modern humans and Neanderthals co-existed and interacted thousands of years ago has been the subject of much debate. A fossil analysis suggests that Neanderthals had already become extinct in the Caucasus region — thought to be one of their final refuges — by the time modern humans arose.

Ron Pinhasi at University College Dublin and his colleagues radiocarbon-dated Neanderthal fossils that they found in caves in the Caucasus region, which served as a corridor for hominids passing from Asia to Europe. The team suggests that Neanderthals vacated the northern Caucasus about 39,000 years ago and the southern Caucasus about 37,000 years ago. Modern humans arose elsewhere between 45,000 and 40,000 years ago, suggesting that the two groups did not co-exist in that part of the world.

J. Hum. Evol. 63, 770–780 (2012)

ECOLOGY

Beware the parasite's parasite

Plants besieged by caterpillars release a chemical alarm that summons an army of defenders, such as parasitoid wasps whose voracious larvae devour caterpillars from within. But this plant-defence system is open to sabotage from the parasite's parasites.

Erik Poelman of Wageningen University in the Netherlands and his colleagues found that, in some cases, volatile compounds released by plants damaged by infected caterpillars also attract another set of wasps, called hyperparasitoids, that attack the cocoons of the caterpillar-eating wasp larvae. Infection with *Cotesia glomerata* wasps affects caterpillars' oral secretions, causing the plants they eat to give off a different blend of chemicals from those colonized by unaffected caterpillars. These chemicals seem to call in the hyperparasitoids. In the lab,

the hyperparasitoid *Lysibia nana* (pictured) preferred plants munched by caterpillars infected with *C. glomerata* to those eaten by their uninfected counterparts.

PLoS Biol. 10, e1001435 (2012)

CLIMATE MODELLING

Climate fingerprints

The latest global climate models produce a 'fingerprint' that aligns well with actual temperature observations, and underscores the human influence on climate through the release of greenhouse

gases and ozone-depleting chemicals.

Ben Santer of the Lawrence Livermore National Laboratory in Livermore, California, and his group analysed simulations from 20 climate models at the core of the Intergovernmental Panel on Climate Change's fifth assessment, and compared the results with satellite temperature records dating back to 1979. The team found general agreement with observed global-warming patterns, although the models typically overestimate warming in the lower atmosphere while underestimating cooling trends higher up, in the stratosphere.



ANTHROPOLOGY

Nomadic group of Irish descent

The Irish Travellers, an itinerant, socially isolated group in Ireland, are probably descended from a small group of Irish founders, rather than from the more widespread European Roma population, who have a similar lifestyle.

John Relethford of the State University of New York College at Oneonta and Michael Crawford at the University of Kansas in Lawrence compared genes from 119 of the Travellers with those of Irish, Roma, English, Hungarian and Indian populations. On the basis of population variations in 12 of the genes, the authors report

that the Travellers, who make up less than 0.2% of the Irish population, are genetically more similar to Irish people than to the other groups.

The researchers went on to do a genetic comparison between the Travellers and residents of four Irish provinces. They found that although the Travellers were still distinct genetically, the differences could be accounted for by the effect of random genetic variations in the historically small group, according to a mathematical model.

Am. J. Phys. Anthropol. <http://dx.doi.org/10.1002/ajpa.22191> (2012)

The analysis suggests that climate modellers could improve model performance by incorporating more realistic treatments of ozone chemistry and aerosols.

Proc. Natl Acad. Sci. USA
<http://dx.doi.org/10.1073/pnas.1210514109> (2012)

NEUROSCIENCE

Simulated brain solves problems

A computer model of the brain containing 2.5 million virtual neurons exhibits complex behaviours such as recognizing numerical patterns and doing simple arithmetic.

Chris Eliasmith and his team at the University of Waterloo, Canada, have developed a brain model that can 'see' images and perform tasks, writing out answers with a robotic arm. The model simulates the physiology of each of its 'neurons', such as the spikes of electricity that flow through them. The cells are divided into groups corresponding to specific parts of the brain that process images, control movements and store short-term memories. These regions are wired together, allowing the 'brain' to perform at least eight different tasks.

However, the model is limited: it is slow, simulates only a small fraction of the human brain and cannot learn completely new tasks or deal with inputs beyond the ten numerals.

Science 338, 1202–1205 (2012)
For a longer story on this research, see go.nature.com/edkkvr

GEOLOGY

Tohoku quake's predecessor

Japan's Sendai region, which was devastated by a magnitude-9 earthquake and a tsunami in 2011, experienced similar events in AD 869 — and such disasters could occur in the area more often than previously thought.

Seismic assessments have typically underestimated the

earthquake hazard for the Sendai area, in part because of uncertainty surrounding the size of the 869 Jogan earthquake and the frequency of large earthquakes in the region. Yuki Sawai and his colleagues at the Geological Survey of Japan in Tsukuba studied sediment samples from 399 locations along the coast near Sendai, looking for tsunami deposits and signs of seismic activity. They found deposits associated with the Jogan earthquake stretching at least 1.5 kilometres inland — farther than deposits from tsunamis that occurred between 869 and 2011. Earthquake modelling suggests that the Jogan event had a magnitude of 8.4 or higher. Moreover, the authors estimate that such an event could occur every 500–800 years.

The findings, which were reported in preliminary form before 2011, might have improved earthquake hazard assessment for the Sendai region, the authors say. *Geophys. Res. Lett.* <http://dx.doi.org/10.1029/2012GL053692> (2012)

CLIMATE CHANGE

Ever faster polar ice loss

An analysis of dozens of studies on polar ice has yielded the most accurate estimate yet of ice-sheet melting. Between them, Antarctica and Greenland are now losing mass three times faster than they were 20 years ago, and Greenland alone is shedding ice at about five times the rate it was in the mid-1990s.

Previous melting estimates have been inconsistent. To address this uncertainty, Andrew Shepherd at the University of Leeds, UK, Erik Ivins at NASA's Jet Propulsion Laboratory in Pasadena, California, and their colleagues compared and combined four types of satellite data on ice-sheet mass. They found that, since 1992, the ice sheets have contributed more than 11 millimetres to

COMMUNITY CHOICE

The most viewed papers in science

MICROBIOLOGY

Cheaters are bad for biofilms

HIGHLY READ
on royalsociety-publishing.org
in October

Just as self-interest can hamper cooperation and fitness in human societies, the presence of 'cheater' microorganisms decreases the population fitness of tight-knit bacterial communities.

Certain bacteria form organized assemblies known as biofilms by releasing small-molecule signals that trigger cellular aggregation. The films offer survival advantages, helping the microbes to resist antibiotics, for example. Researchers led by Stephen Diggel at the University of Nottingham, UK, created biofilms consisting of varying proportions of cooperative *Pseudomonas aeruginosa* — a human pathogen — and a 'cheating' mutant that cannot respond to the aggregation signal but still benefits from being part of the biofilm. Biofilms containing more 'cheaters' grew more slowly and were less resistant to antibiotics than films with few or no cheaters.

Strategies that take advantage of the evolution of cheating pathogens may be useful in combating biofilms, which can cause persistent infections, the authors suggest.

Proc. R. Soc. B. 279, 4765–4771 (2012)

sea-level rise — one-fifth of the total for that period.

The authors say that their estimates are two to three times more accurate than those from the latest report of the Intergovernmental Panel on Climate Change.

Science 338, 1183–1189 (2012)
For a longer story on this research, see go.nature.com/ydpp6a

ECOLOGY

Night light helps shorebird

Artificial lighting can harm wild creatures by disorientating them, but for some — such as the common redshank, a migratory shorebird — it can help.

Ross Dwyer at the University of Exeter in Penryn, UK, and his colleagues studied the bird (*Tringa totanus*; pictured) in an estuary near industrial sites in eastern Scotland. The researchers tagged the redshanks with posture-sensitive radio transmitters, making it possible to measure how much time the birds spent with their heads down



— sweeping through mud or sand to search for food — and up, stalking prey visually. The authors found that redshanks near artificial light spent more time visually stalking — which is more efficient than searching by touch — than those in darker areas, suggesting that the light improves the animal's foraging opportunities.

J. Anim. Ecol. <http://dx.doi.org/10.1111/1365-2656.12012> (2012)

NATURE.COM

For the latest research published by Nature visit:
www.nature.com/latestresearch

TIM MASON/BES

SEVEN DAYS

The news in brief

BUSINESS

Gene-patent justice

The US Supreme Court said on 30 November that it would re-examine the question of whether human genes are patentable. The move is the latest in a three-year legal battle between Myriad Genetics, a diagnostics company in Salt Lake City, Utah, and a coalition of medical associations and physicians that has challenged the validity of the company's patents on the *BRCA1* and *BRCA2* gene variants — linked to inherited breast and ovarian cancer. See go.nature.com/jbqdxl for more.

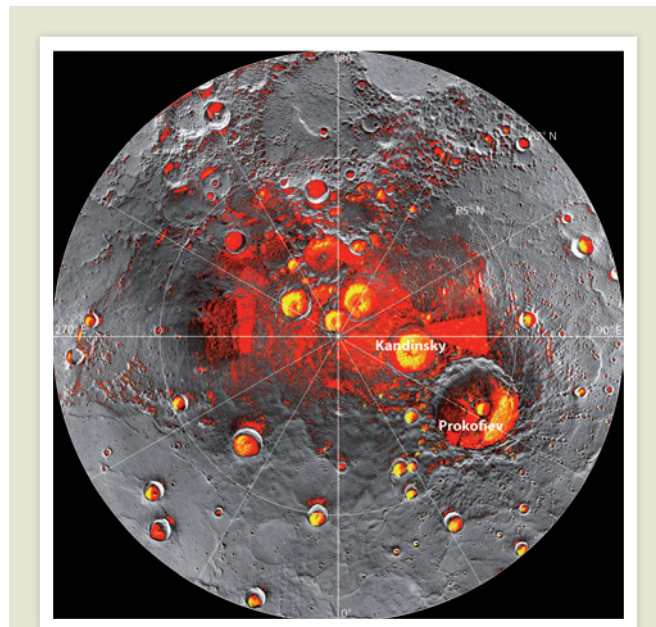
Stem-cell ruling

In a landmark decision, the German Federal Court of Justice ruled on 27 November that patents may be granted on human embryonic stem cells if claims are restricted to the use of cells that are obtained without destroying a viable embryo. A European Court of Justice ruling had said last year that research patents depending even indirectly on human embryonic stem cells should be outlawed on moral grounds. The European court also equated human embryonic stem-cell lines with embryos, but the German court explicitly stated that they are not equivalent.

RESEARCH

Collider cuts

SuperB, a particle accelerator that was to be built in southeast Rome to produce B mesons by smashing together electrons and positrons, may have to be scaled back or cancelled altogether. The project was officially launched in October 2011 (see go.nature.com/xt0000), but the Italian government said on



Water ice on Mercury

Craters on Mercury may hold as much as one trillion tonnes of water ice, according to results from NASA's MESSENGER probe, published on 29 November in *Science*. Although the surface of the planet reaches temperatures of 400 °C, the depths of many polar craters never see the Sun and are thought to remain below –170 °C. The suspected ice (pictured in red) may have been deposited by comet or asteroid impacts. See go.nature.com/mhxe15 for more.

27 November that it would not contribute more than its initial investment of €250 million (US\$326 million) after the project's estimated costs increased to €1 billion and it failed to secure enough investment from international partners. See go.nature.com/u5g4ey for more.

GM study rebutted

A final review by the European Food Safety Authority (EFSA), published on 28 November, has rejected the findings of a controversial paper published in September (see go.nature.com/3slkys) claiming that rats fed genetically modified maize (corn) showed adverse health effects, including higher incidence of tumours and

earlier mortality than controls. The review's conclusion that the study was "inadequately designed, analysed and reported" and "does not meet acceptable scientific standards" is in line with both the EFSA's initial review published in October (see go.nature.com/rypoy5) and assessments by six European Union member states.

Mental-health guide

The upcoming revision of the *Diagnostic and Statistical Manual of Mental Disorders (DSM-5)* has passed the final hurdle before it heads to the presses. On 1 December, the American Psychiatric Association's board of trustees approved the revised text,

which includes controversial changes to the definitions of autism and major depression (see *Nature* **482**, 14–15; 2012). The manual is slated to be published by May 2013.

Mess in Texas

The Cancer Prevention and Research Institute of Texas (CPRIT) announced the freezing of an US\$11-million commercialization grant to Peloton Therapeutics in Dallas on 29 November, after an audit revealed that the 2010 award was made without commercial or scientific review (see go.nature.com/ctjei4). The finding comes on the heels of months of controversy about an \$18-million unreviewed CPRIT grant to the University of Texas MD Anderson Cancer Center in Houston (see *Nature* **486**, 169–171; 2012).

'Two strikes' rule

The US National Institutes of Health has said that it will continue an unpopular policy that prevents grant applicants from resubmitting rejected proposals more than once. Before January 2009, when the policy was introduced, applicants were allowed to resubmit unsuccessful grants twice. See page 7 and go.nature.com/pkskun for more.

POLICY

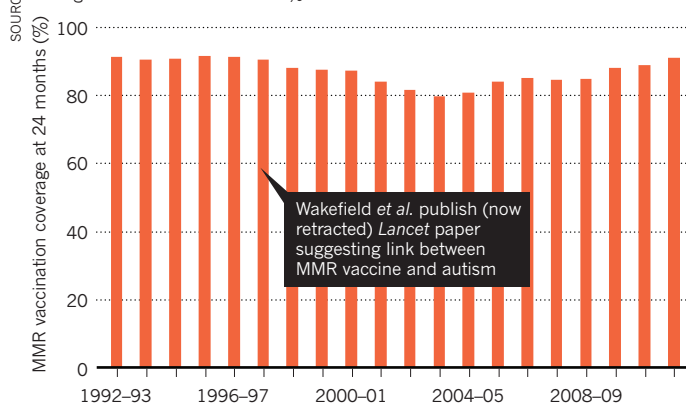
Tree felling drops

The rate at which trees are being cut down in the Brazilian Amazon has fallen by 27% in the past year, to a record low. Preliminary work by the National Institute for Space Research (INPE), published on 27 November, suggests that 4,656 square kilometres of forest were clear-cut between August 2011 and July 2012, compared with 6,418 km² in the previous 12 months. See go.nature.com/ttnvqa for more.

NASA/JHUAPL/CARNegie INST. WASHINGTON/NAIC, ARCI/BO OBSERV.

MMR VACCINES REVIVED

Childhood immunization against measles, mumps and rubella (MMR) in England is now more than 90%.



MMR vaccination

The immunization of children in England against measles, mumps and rubella (MMR) by 24 months of age has now reached more than 90%, its highest level since 1997-98 (see **graph**). Vaccinations dipped to as low as 79% after authors led by Andrew Wakefield published a now-retracted paper in *The Lancet* suggesting a link between the MMR vaccine and autism. The World Health Organization's recommended target is 95%.

Funder concessions

The Engineering and Physical Sciences Research Council (EPSRC), Britain's biggest public funder of physics, mathematics and engineering, has agreed to remove controversial wording that asked grant applicants to

outline the national importance of their work "over a 10-50 year time-frame". In an article in *Times Higher Education* on 29 November, EPSRC chairman Paul Golby wrote that the research council would commission independent reviews to examine its peer-review processes and how it seeks strategic advice. The announcement follows protests by scientists in May (see *Nature* **488**, 20-22; 2012).

Science down under

The Australian government published its National Research Investment Plan on 28 November. The plan identifies eight 'key challenges' for the country, including the production of energy and food, that will guide public spending on research during 2013-16. It also highlights

areas in need of further action by the government and research funders, such as developing better links between universities and industry and more support for international collaboration.

PEOPLE

Fraud verdict

A culture of "flawed science" in social psychology owing to weak peer review allowed Diederik Stapel, formerly based at Tilburg University in the Netherlands, to commit extensive research fraud that spanned more than a decade, says a 28 November report issued by the committees investigating him (see *Nature* **479**, 15; 2011). The committees identified 55 publications in which fraud was certain, 11 papers with indications of fraud, and 10 tainted doctoral dissertations.

Confucius prize

Agricultural scientist Yuan Longping is to share US\$1.5 million in prize money with former United Nations secretary-general Kofi Annan, it emerged last week. The pair were awarded the Confucius Peace Prize in early November but the amount of the prize, which varies each year, had not been confirmed. The Chinese prize was set up in 2010 after the Nobel Peace Prize was

COMING UP

7 DECEMBER

Climate negotiators end a fortnight of debate at the United Nations Framework Convention on Climate Change in Doha.

go.nature.com/wnhovv

12 DECEMBER

British scientists start 100 hours of drilling to reach Antarctica's subglacial Lake Ellsworth, buried under more than 3 kilometres of ice (see *Nature* **491**, 506-507; 2012).

www.ellsworth.org.uk

awarded to dissident Chinese writer Liu Xiaobo. Last year's winner was Russian president Vladimir Putin.

Committee head

Republican Congressman Lamar Smith was selected as the next chairman of the House Committee on Science, Space, and Technology on 28 November. In 2009, Smith criticized parts of the US media for coverage that was "slanted in favour of global warming alarmists". He replaces Ralph Hall, who is stepping down at the end of this year. See page 17 and go.nature.com/6z6u1a for more.

Neurologist leaves

Sidney Gilman, a neurologist at the University of Michigan in Ann Arbor implicated in insider trading, has retired, a university spokesman confirmed on 28 November. Gilman tipped off CR Intrinsic Investors, a hedge fund in Stamford, Connecticut, about safety data from clinical trials of a drug for Alzheimer's disease before the results were made public. See go.nature.com/n8tnbi for more.

➔ NATURE.COM

For daily news updates see:

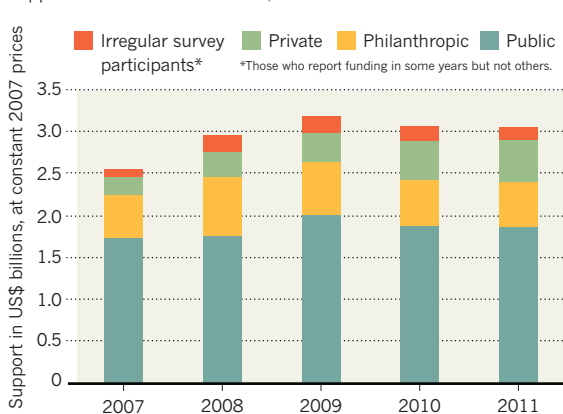
www.nature.com/news

TREND WATCH

Global funding for work on neglected diseases totalled US\$3.32 billion in 2011, essentially stable in real terms compared with 2010, according to the *G-FINDER* investment survey by Policy Cures, a health-policy analysis firm based in London and Sydney, Australia. Over the past three years, public and philanthropic funding has declined as some government aid budgets have been cut, whereas industry funding has grown (mostly owing to investments in trials for dengue vaccines).

FLAT FUNDING FOR NEGLECTED DISEASES

Public funding still supplies more than 60% of financial support for diseases such as HIV, malaria and tuberculosis.



NEWS IN FOCUS

MATERIALS New technique for making nanoparticles blasts off **p.16**

DRUGS US regulators vow to unclog the antibiotics pipeline **p.19**

CLIMATE Tracking greenhouse gases, city by city **p.20**



ENERGY Radical reactor designs fire hopes of a nuclear revival **p.26**

DIPTENDU DUTTA/AFP/GETTY IMAGES



India's hydroelectric projects, such as this dam on the River Teesta, are raising environmental concerns.

ENVIRONMENT

Flood of protest hits Indian dams

Himalayan plans pose ecological threat, researchers warn.

BY JANE QIU

The days when the gigantic Indian rivers — the Ganges, Indus and Brahmaputra — roar freely down the steep slopes of the Himalayas may be numbered.

Roughly 300 dams are proposed or under construction in the deeply cut valleys of India's mountainous north, part of a massive effort to meet the country's spiralling energy demands. But the projects are facing fierce resistance from local communities, as well as from scientists who predict that the dams' ecological impacts will be much greater than official environmental assessments suggest. "The magnitude of dam building in the Himalayas is overwhelming,"

says Kamaljit Bawa, a conservation biologist at the University of Massachusetts, Boston. "They are moving too fast without properly assessing the risks and alternatives."

Last week, the battle flared up once more in the Indian state of Sikkim, where the 520-megawatt Teesta IV hydroelectric project would block a tributary of the Brahmaputra (see 'A deluge of dams'). As the Indian government's Ministry of Environment and Forests started to review the environmental impact assessment (EIA) for the project, indigenous Lepcha and Bhutia communities redoubled their protest, saying that the dam would take away the last stretch of free-flowing river in the heart of their sacred land. Following previous

demonstrations, a petition objecting to the construction has now attracted more than 1,300 signatures.

Advocates say that the projects are a vital part of the drive to double India's electricity-generating capacity to 300,000 megawatts by 2022, a goal that is said to be essential for the country's economic growth. Electricity shortages are already wreaking havoc: in July, for example, a massive blackout across the country left 600 million people without electricity. Yet India is also the world's third-largest emitter of carbon dioxide, mainly due to the burning of coal for electricity, and its emissions are expected to double by 2030 if the country's energy mix does not change substantially. The government sees the largely untapped hydropower in the Himalayas as a panacea for both problems, and it plans to add another 110,000 megawatts of hydroelectric capacity by 2025, an eightfold increase¹.

According to a study published this month², that would create a dam for every 3,000 square kilometres of valleys in the Indian Himalayas, 62 times the global average density for hydroelectric stations. "The consequences would be dire," says Maharaj Pandit, an ecologist at the University of Delhi, who led the study. Most of the dams would be in regions of high biodiversity, and about 1,700 km² of forests would be either submerged or damaged by new infrastructure and other dam-related activities. Pandit's ecological modelling suggests that, by 2025, this would reduce tree biodiversity in the region by more than one-third, and lead to the extinction of 22 flowering plants and 7 vertebrate taxa.

Although hydroelectric projects in flatter terrain create huge reservoirs, providing a substantial head of water to generate power, most of those in the Indian Himalayas would use run-of-the-river dams, which require smaller reservoirs. Such dams divert water through tunnels to the turbines, and return it to the river downstream. Developers argue that the approach reduces a dam's environmental footprint — but ecologists say that a series of barriers along the rivers would seriously fragment both terrestrial and aquatic ecosystems.

"The blow would be fatal to fish biodiversity," says Pandit, whose studies show that the volume of water in a river is the key determinant of the ►

► **NATURE.COM**
Read more about
damming the
Mekong River:
go.nature.com/ymuzel

► richness of fish species³.

Dulal Goswami, an environmental scientist at Gauhati University in Guwahati, Assam, worries that the geological hazards of the region have not been properly considered. “The Himalayas are fragile and dynamic,” he says. Earthquakes of magnitude 7 or 8 are not uncommon, and increasing glacial melts due to climate change are causing more floods, both of which can damage dams and tunnels.

And the rivers’ heavy sediment loads could clog the dams. According to Goswami, the Brahmaputra carries 400 million tonnes of sediment each year, peaking at 25 million tonnes a day during extreme monsoon events.

The Indian government has required EIAs for the projects, but these are lax, says Neeraj Vagholikar, a conservationist at the non-governmental organization Kalpavriksh in Pune. For example, he says, the EIA of a dam project on the Siyom River lists just five bird species in an area that ecologists say has more than 300; similarly, the EIA for the Lower Subansiri dam lists 55 fish species in a river that has at least 156.

The assessments usually cover a radius of only 10 kilometres from the dam and reservoir, and do not consider downstream effects or secondary impacts caused by the influx of labour and infrastructure such as power lines. And the cumulative impact of multiple dams along the

A DELUGE OF DAMS

The Indian state of Sikkim, deep in the Himalayas, plans dozens of hydropower projects, and hundreds more are springing up across the country’s mountainous north.



same river is not assessed before individual projects are approved. “This is particularly important for areas with densely clustered dams,” says Bawa. Even if the impacts of individual projects are acceptable, the cascading effects on ecosystems and the geological hazards of dams stacking on top of one another along the same

river may be serious, he says. “It’s based on such poor assessments that 99% of the projects get approved,” adds conservationist Samir Mehta, south Asia programme director of International Rivers, a non-governmental organization based in Berkeley, California.

Some also argue that the assessments are not sufficiently independent. “Agencies that conduct the EIAs are selected and paid for by dam developers and deliver favourable assessments in order to be invited back,” says Mehta. The Ministry of Environment and Forests did not respond to *Nature’s* questions about the allegations.

India is not alone in its rush to build dams in the Himalayas. Other countries, especially China, Pakistan, Nepal and Bhutan, plan to add hundreds more dams along the rivers, prompting similar concerns about their EIAs. Damming rivers upstream could have significant impacts on downstream nations, but “every country behaves as if the river is 100% theirs”, says Edward Grumbine, an environmental-policy researcher at the Chinese Academy of Sciences’ Kunming Institute of Botany. “This is a recipe for disaster.” ■

1. Bawa, K. *et al. Science* **327**, 1457–1478 (2010).
2. Pandit, M. K. & Grumbine, E. *Conserv. Biol.* **26**, 1061–1071 (2012).
3. Bhatt, J. P., Manish, K. & Pandit, M. K. *PLoS ONE* **7**, e46237 (2012).

MATERIALS

Nanoparticle blast caught on film

Combustion could help to make minuscule matter.

BY EUGENIE SAMUEL REICH IN BOSTON

It was a pretty explosive premiere for a movie about a chemical reaction. A microscopic droplet drifted across the screen — almost in homage to the panning gun barrel of the James Bond movies — and then: bang!

Scientists watching the scene last week at a meeting of the Materials Research Society (MRS) in Boston, Massachusetts, were gripped, because the death of the droplet was also an act of creation. Lutz Mädler, a process engineer at the University of Bremen in Germany, had, for the first time, captured on camera a process that makes beautifully

homogeneous metal oxide nanoparticles (see ‘Blow up’). His goal is to pave the way for faster, cheaper ways to make these fragments of matter, measuring just billionths of a metre across, which are finding uses as catalysts, medical imaging probes and more.

Mädler’s presentation was part of the first MRS session ever to be dedicated to the combustion synthesis of nanoparticles. The technique aims to improve the process of making nanoparticles, which generally requires multiple, complex steps from expensive precursors. The solution, say Mädler and others, is to create the particles in bulk by simply igniting tiny droplets of precursor

materials — a strategy that industry has used for decades to make carbon black for tyres and silica for optic fibres.

“This is a field that mushroomed out of industry, and didn’t have an academic following,” says Sotiris Pratsinis, a process engineer at the Swiss Federal Institute of Technology (ETH) Zurich. “These are beautiful fundamental studies.”

Mädler’s work aims to overcome a key drawback of combustion synthesis: the process is little understood and tends to be poorly controlled. In 2002, and working with Pratsinis, Mädler developed a way to make metal oxide nanoparticles by burning organometallic complexes dissolved in organic solvents (L. Mädler *et al. J. Aerosol Sci.* **33**, 369–389; 2002). The approach worked well in the lab, but the ingredients were too expensive for most commercial applications. Mädler resolved to pick apart the process so that he could replicate it with cheaper precursors, such as metal nitrates, which can be produced directly from ores.

At present, metal nitrates yield nanoparticles that are inhomogeneous — often with hollow areas inside — but Mädler says that his high-speed videos reveal how mixing processes in the combustion of organic

► richness of fish species³.

Dulal Goswami, an environmental scientist at Gauhati University in Guwahati, Assam, worries that the geological hazards of the region have not been properly considered. “The Himalayas are fragile and dynamic,” he says. Earthquakes of magnitude 7 or 8 are not uncommon, and increasing glacial melts due to climate change are causing more floods, both of which can damage dams and tunnels.

And the rivers’ heavy sediment loads could clog the dams. According to Goswami, the Brahmaputra carries 400 million tonnes of sediment each year, peaking at 25 million tonnes a day during extreme monsoon events.

The Indian government has required EIAs for the projects, but these are lax, says Neeraj Vagholikar, a conservationist at the non-governmental organization Kalpavriksh in Pune. For example, he says, the EIA of a dam project on the Siyom River lists just five bird species in an area that ecologists say has more than 300; similarly, the EIA for the Lower Subansiri dam lists 55 fish species in a river that has at least 156.

The assessments usually cover a radius of only 10 kilometres from the dam and reservoir, and do not consider downstream effects or secondary impacts caused by the influx of labour and infrastructure such as power lines. And the cumulative impact of multiple dams along the

A DELUGE OF DAMS

The Indian state of Sikkim, deep in the Himalayas, plans dozens of hydropower projects, and hundreds more are springing up across the country’s mountainous north.



same river is not assessed before individual projects are approved. “This is particularly important for areas with densely clustered dams,” says Bawa. Even if the impacts of individual projects are acceptable, the cascading effects on ecosystems and the geological hazards of dams stacking on top of one another along the same

river may be serious, he says. “It’s based on such poor assessments that 99% of the projects get approved,” adds conservationist Samir Mehta, south Asia programme director of International Rivers, a non-governmental organization based in Berkeley, California.

Some also argue that the assessments are not sufficiently independent. “Agencies that conduct the EIAs are selected and paid for by dam developers and deliver favourable assessments in order to be invited back,” says Mehta. The Ministry of Environment and Forests did not respond to *Nature’s* questions about the allegations.

India is not alone in its rush to build dams in the Himalayas. Other countries, especially China, Pakistan, Nepal and Bhutan, plan to add hundreds more dams along the rivers, prompting similar concerns about their EIAs. Damming rivers upstream could have significant impacts on downstream nations, but “every country behaves as if the river is 100% theirs”, says Edward Grumbine, an environmental-policy researcher at the Chinese Academy of Sciences’ Kunming Institute of Botany. “This is a recipe for disaster.” ■

1. Bawa, K. *et al. Science* **327**, 1457–1478 (2010).
2. Pandit, M. K. & Grumbine, E. *Conserv. Biol.* **26**, 1061–1071 (2012).
3. Bhatt, J. P., Manish, K. & Pandit, M. K. *PLoS ONE* **7**, e46237 (2012).

MATERIALS

Nanoparticle blast caught on film

Combustion could help to make minuscule matter.

BY EUGENIE SAMUEL REICH IN BOSTON

It was a pretty explosive premiere for a movie about a chemical reaction. A microscopic droplet drifted across the screen — almost in homage to the panning gun barrel of the James Bond movies — and then: bang!

Scientists watching the scene last week at a meeting of the Materials Research Society (MRS) in Boston, Massachusetts, were gripped, because the death of the droplet was also an act of creation. Lutz Mädler, a process engineer at the University of Bremen in Germany, had, for the first time, captured on camera a process that makes beautifully

homogeneous metal oxide nanoparticles (see ‘Blow up’). His goal is to pave the way for faster, cheaper ways to make these fragments of matter, measuring just billionths of a metre across, which are finding uses as catalysts, medical imaging probes and more.

Mädler’s presentation was part of the first MRS session ever to be dedicated to the combustion synthesis of nanoparticles. The technique aims to improve the process of making nanoparticles, which generally requires multiple, complex steps from expensive precursors. The solution, say Mädler and others, is to create the particles in bulk by simply igniting tiny droplets of precursor

materials — a strategy that industry has used for decades to make carbon black for tyres and silica for optic fibres.

“This is a field that mushroomed out of industry, and didn’t have an academic following,” says Sotiris Pratsinis, a process engineer at the Swiss Federal Institute of Technology (ETH) Zurich. “These are beautiful fundamental studies.”

Mädler’s work aims to overcome a key drawback of combustion synthesis: the process is little understood and tends to be poorly controlled. In 2002, and working with Pratsinis, Mädler developed a way to make metal oxide nanoparticles by burning organometallic complexes dissolved in organic solvents (L. Mädler *et al. J. Aerosol Sci.* **33**, 369–389; 2002). The approach worked well in the lab, but the ingredients were too expensive for most commercial applications. Mädler resolved to pick apart the process so that he could replicate it with cheaper precursors, such as metal nitrates, which can be produced directly from ores.

At present, metal nitrates yield nanoparticles that are inhomogeneous — often with hollow areas inside — but Mädler says that his high-speed videos reveal how mixing processes in the combustion of organic

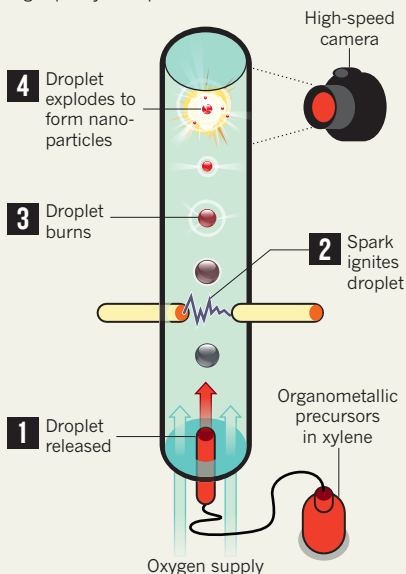
droplets help to make the particles more homogeneous. That should enable researchers to choose better precursors and additives that could improve combustion, and yield better-quality end products, says Karsten Wegner, a process engineer and consultant also at ETH Zurich. More and more chemicals companies are asking Wegner for advice on ways to scale up nanoparticle combustion-synthesis processes, he says, and the range of nanomaterials they want to make in large quantities is growing exponentially.

As industry explores the commercial appeal of the technique, researchers are turning to it to create specialized nanoparticles that can be tailored to medical imaging, sensing or toxicity studies. Ian Kennedy, a mechanical engineer at the University of California, Davis, is using combustion to make nanoparticles that contain europium, an exotic and expensive element that phosphoresces strongly. At the MRS meeting, Kennedy described how attaching an antibody to the particles can turn them into detectors that flag up environmental and biological toxicity. "These are exotic materials that haven't been made this way before," says Margaret Wooldridge, a mechanical engineer working on combustion synthesis at the University of Michigan, Ann Arbor.

Exploding droplets are themselves nothing new, says Kennedy — he was studying them in diesel fuel in the 1970s. But imaging techniques like Mädlar's will give materials scientists a better understanding of how the explosions affect the properties of the materials produced. "This field is a bridge between combustion research and materials science," says Wooldridge. "It's growing, and you see a lot of younger people coming in." ■

BLOW UP

Exploding droplets can produce high-quality nanoparticles.



POLICY

Quiet Texan to head science committee

Innovation promoter wins key role in US Congress.

BY HELEN SHEN

Science advocates are cautiously hopeful after Lamar Smith, a quiet Texan who is known to be a strong supporter of US innovation, was named as the next chair of the Committee on Science, Space, and Technology in the US House of Representatives. Republican congressional leaders confirmed on 28 November that, in January, Smith will replace Ralph Hall, another Texas Republican, who is stepping down because of a party rule that limits a ranking member's tenure on a House committee to six years.

Smith will become the gatekeeper for much of the science-related legislation that reaches the House floor during the next Congress. Although successful House bills must also pass the Senate before becoming law, Smith — who has served on the committee for 26 years — will be "a key player in setting the agenda," says Scott Pace, director of the Space Policy Institute in Washington DC.

The choice was welcomed by technology advocates such as Keith Grzelak, vice-president for government relations for the US arm of the Institute of Electrical and Electronics Engineers, based in Washington DC. "He understands the role that science, technology and engineering can play in boosting the economy," says Grzelak.

Smith spearheaded the America Invents Act of 2011, which aimed to simplify patent applications (see *Nature* 472, 149; 2011). He has also championed legislation to make immigration easier for foreign graduates with science, technology, engineering and mathematics degrees. "We can't have innovation without research and development," Smith said in a statement after his new role was announced.

Like many of his Republican colleagues, Smith has expressed doubts about the reality of anthropogenic global warming and has criticized the media for "a steady pattern of bias on climate change". But his tone has been more moderate than that of his challengers for the chairmanship, Dana

Rohrabacher (Republican, California) and committee vice-chairman Jim Sensenbrenner (Republican, Wisconsin). He is also less outspoken than Hall, who invited several staunch climate-change sceptics to testify before the committee last year.



Lamar Smith will be Republicans' gatekeeper on science legislation.

The committee faces a number of pressing tasks next year, such as reauthorizing NASA — which includes setting the space agency's objectives and also the amount of money the government can appropriate for its operations. Also in need of reauthorization in 2013 will be the America COMPETES act, first passed in 2007. This seeks to enhance US competitiveness in the physical sciences with funding increases to key agencies

such as the National Science Foundation and the Department of Energy's Office of Science.

The fate of America COMPETES will send a statement to the rest of the world about US research and development priorities, says Michael Lubell, director of public affairs at the American Physical Society in Washington DC. "If the signal is going to be the US cannot afford to do this," says Lubell, "I think that's going to be a big mistake." He hopes that Smith, who ultimately voted against reauthorization of America COMPETES in 2010, will support the measure this time and bring on board other Republicans — only 16 of whom supported the final version of the reauthorized act two years ago.

Eddie Bernice Johnson, a Texas representative who is the committee's top-ranking Democrat, hopes that Smith will quiet the partisan posturing on issues such as climate change and the role of the Environmental Protection Agency that marked Hall's chairmanship. "The selection of witnesses has been pretty one-sided," she says.

But fiscal concerns may play the biggest part in shaping Smith's decisions. The country is bracing itself for sweeping federal budget cuts in January unless Republicans and Democrats can reach a compromise on measures to reduce the deficit, and science would not escape the axe. ■

DREW ANGERER/AP PHOTO

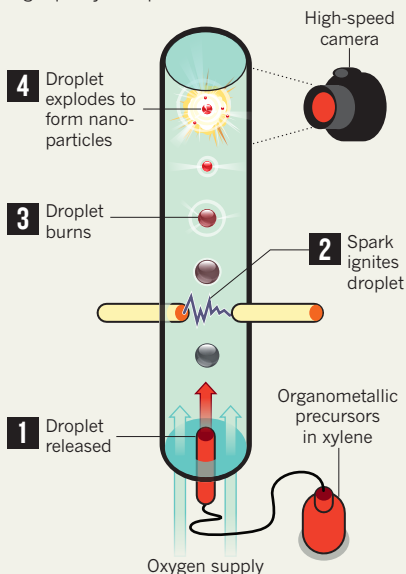
droplets help to make the particles more homogeneous. That should enable researchers to choose better precursors and additives that could improve combustion, and yield better-quality end products, says Karsten Wegner, a process engineer and consultant also at ETH Zurich. More and more chemicals companies are asking Wegner for advice on ways to scale up nanoparticle combustion-synthesis processes, he says, and the range of nanomaterials they want to make in large quantities is growing exponentially.

As industry explores the commercial appeal of the technique, researchers are turning to it to create specialized nanoparticles that can be tailored to medical imaging, sensing or toxicity studies. Ian Kennedy, a mechanical engineer at the University of California, Davis, is using combustion to make nanoparticles that contain europium, an exotic and expensive element that phosphoresces strongly. At the MRS meeting, Kennedy described how attaching an antibody to the particles can turn them into detectors that flag up environmental and biological toxicity. "These are exotic materials that haven't been made this way before," says Margaret Wooldridge, a mechanical engineer working on combustion synthesis at the University of Michigan, Ann Arbor.

Exploding droplets are themselves nothing new, says Kennedy — he was studying them in diesel fuel in the 1970s. But imaging techniques like Mädlar's will give materials scientists a better understanding of how the explosions affect the properties of the materials produced. "This field is a bridge between combustion research and materials science," says Wooldridge. "It's growing, and you see a lot of younger people coming in." ■

BLOW UP

Exploding droplets can produce high-quality nanoparticles.



POLICY

Quiet Texan to head science committee

Innovation promoter wins key role in US Congress.

BY HELEN SHEN

Science advocates are cautiously hopeful after Lamar Smith, a quiet Texan who is known to be a strong supporter of US innovation, was named as the next chair of the Committee on Science, Space, and Technology in the US House of Representatives. Republican congressional leaders confirmed on 28 November that, in January, Smith will replace Ralph Hall, another Texas Republican, who is stepping down because of a party rule that limits a ranking member's tenure on a House committee to six years.

Smith will become the gatekeeper for much of the science-related legislation that reaches the House floor during the next Congress. Although successful House bills must also pass the Senate before becoming law, Smith — who has served on the committee for 26 years — will be "a key player in setting the agenda," says Scott Pace, director of the Space Policy Institute in Washington DC.

The choice was welcomed by technology advocates such as Keith Grzelak, vice-president for government relations for the US arm of the Institute of Electrical and Electronics Engineers, based in Washington DC. "He understands the role that science, technology and engineering can play in boosting the economy," says Grzelak.

Smith spearheaded the America Invents Act of 2011, which aimed to simplify patent applications (see *Nature* 472, 149; 2011). He has also championed legislation to make immigration easier for foreign graduates with science, technology, engineering and mathematics degrees. "We can't have innovation without research and development," Smith said in a statement after his new role was announced.

Like many of his Republican colleagues, Smith has expressed doubts about the reality of anthropogenic global warming and has criticized the media for "a steady pattern of bias on climate change". But his tone has been more moderate than that of his challengers for the chairmanship, Dana

Rohrabacher (Republican, California) and committee vice-chairman Jim Sensenbrenner (Republican, Wisconsin). He is also less outspoken than Hall, who invited several staunch climate-change sceptics to testify before the committee last year.



Lamar Smith will be Republicans' gatekeeper on science legislation.

The committee faces a number of pressing tasks next year, such as reauthorizing NASA — which includes setting the space agency's objectives and also the amount of money the government can appropriate for its operations. Also in need of reauthorization in 2013 will be the America COMPETES act, first passed in 2007. This seeks to enhance US competitiveness in the physical sciences with funding increases to key agencies

such as the National Science Foundation and the Department of Energy's Office of Science.

The fate of America COMPETES will send a statement to the rest of the world about US research and development priorities, says Michael Lubell, director of public affairs at the American Physical Society in Washington DC. "If the signal is going to be the US cannot afford to do this," says Lubell, "I think that's going to be a big mistake." He hopes that Smith, who ultimately voted against reauthorization of America COMPETES in 2010, will support the measure this time and bring on board other Republicans — only 16 of whom supported the final version of the reauthorized act two years ago.

Eddie Bernice Johnson, a Texas representative who is the committee's top-ranking Democrat, hopes that Smith will quiet the partisan posturing on issues such as climate change and the role of the Environmental Protection Agency that marked Hall's chairmanship. "The selection of witnesses has been pretty one-sided," she says.

But fiscal concerns may play the biggest part in shaping Smith's decisions. The country is bracing itself for sweeping federal budget cuts in January unless Republicans and Democrats can reach a compromise on measures to reduce the deficit, and science would not escape the axe. ■

DREW ANGERER/AP PHOTO

POLICY

US advisers seek research overhaul

Report calls for stable funding and industry collaborations.

BY ERIC HAND

Eric Isaacs got some high-level validation last week. The director of Argonne National Laboratory in Chicago, Illinois, Isaacs had enlisted two industrial giants — Dow Chemical and Johnson Controls — to help with the basic research for a lithium-air battery that could one day match the energy density of petrol. “You have to have everyone working together very early on,” he says.

On 30 November, the same day that Argonne received US\$120 million from the Department of Energy to lead a national energy-storage research centre, science advisers to US President Barack Obama were praising the idea of national labs partnering more often with industry. In a report, the President’s Council of Advisors on Science and Technology (PCAST) said that industry ties with universities and national labs such as Argonne are crucial for maintaining international competitiveness in research (PCAST *Transformation and Opportunity* Executive Office of the President, 2012). The panel also recommended that the US Congress find ways to make research funding for long-term initiatives more stable, and said that foreign graduate students in science should be given fast-tracked, long-term visas.

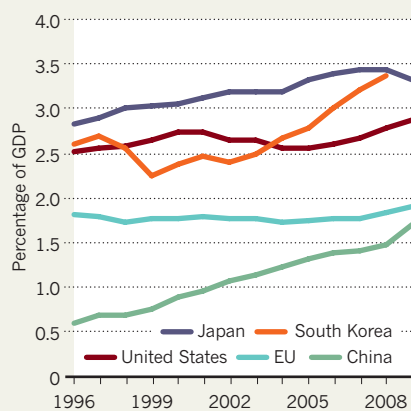
PCAST’s calls to action echo those made in a June study from the National Academies, which also underscored the need for heightened industry involvement in research (Committee on Research Universities *Research Universities and the Future of America* National Academies Press, 2012). But Michael Turner, an astrophysicist at the University of Chicago and a consultant on the PCAST report, says that the latest publication may carry extra weight in Washington DC because of its authors. “These

are people who speak directly to the president and his closest advisers,” he says.

Like earlier studies, the PCAST report says that US research pre-eminence is under threat as industry support for basic research shrivels and other nations ramp up spending. “We

BIG SPENDERS

Presidential advisers say that US research spending should increase to 3% of gross domestic product (GDP) to stay competitive.



do have rivals, more and more of them, all the time,” says John Holdren, director of the White House Office of Science and Technology Policy and co-chairman of PCAST. Despite a challenging fiscal climate, the PCAST report says, US spending on research and development should rise to 3% of gross domestic product — roughly \$450 billion — compared with 2.9% in 2009 (see ‘Big spenders’).

David Goldston, director of governmental affairs at the Natural Resources Defense Council in Washington DC, says that such a sum may be unrealistic. Universities cannot simply

continue to clamour for more money, he adds. “If we thoughtfully shrank the system, what would that entail and in what ways would we really be worse off?” He notes that the 2012 National Academies study recommended that research universities try to stretch the funding that they already have by rooting out inefficiencies in research management.

Another recommendation, for greater funding stability, clearly faces an uphill battle. With the US Congress setting agency funding levels on a yearly basis, budgetary uncertainties can not only hamper research in the United States but also interfere with long-term collaborations with sister agencies abroad, says Subra Suresh, director of the US National Science Foundation in Arlington, Virginia. Suresh has noted how much easier his life would be if funding were more predictable, as it is in Europe. There, the European Commission and European Parliament are planning the next seven-year budget, and the German Research Foundation (DFG), for example, works with five-year guaranteed budgets.

But Bart Gordon, a former Democratic congressman from Tennessee and chairman of the House science committee until 2011, says that congressional appropriators are likely to want to continue to wield power over annual budgets. PCAST vice-chairman William Press, a computational biologist at the University of Texas at Austin, says that he would be content if the science advisers’ report convinced appropriators to stick more closely to funding levels decided by authorizing committees, which plan agency budgets with an eye on longer-term goals.

William Banholzer, chief technology officer for Dow, which is based in Midland, Michigan, says that interactions between federal researchers and industry could also be improved. For instance, he says, if Dow wants to change the direction of the research that it sponsors at Argonne, it has to seek approval at three levels: Argonne, the University of Chicago (which leads a consortium that manages the lab) and the Department of Energy. “At least one of those is redundant,” he says.

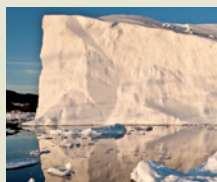
Isaacs doesn’t deny that national labs need to become more welcoming to industrial partners. The benefits are clear, he says. “You can have impact by winning a Nobel prize. But you can also have impact by inventing a way to produce biofuels [or by] working with Dow.” ■ SEE EDITORIAL P.8

SOURCE: NSF



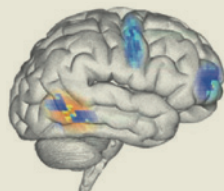
MORE
ONLINE

TOP STORY



Polar ice sheets melting at quickening pace
go.nature.com/ydpp6a

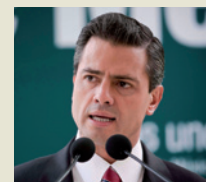
WATCH



Virtual brain mimics human behaviour
go.nature.com/edkkvr

POLICY

Mexican scientists pin hopes on incoming president
go.nature.com/qds1ea



RODRIGO OROPEZA/XINHUA PRESS/CORBIS

DRUG DEVELOPMENT

FDA under pressure to relax drug rules

Industry says antibiotic pipeline is being blocked by overly stringent clinical-trial requirements for new treatments.

BY HEIDI LEDFORD

The latest skirmish in the battle between human and microbe played out on 29 November in a hotel conference room in Silver Spring, Maryland. There, an assembly of scientists and clinicians debated the merits of an experimental antibiotic. For some, the coveted prize was not just an endorsement of the drug itself, but a sign that the US Food and Drug Administration (FDA) is finally ready to rethink its clinical-trial requirements for antibiotics — requirements that the drug industry says are unrealistic.

The number of FDA approvals of new antibiotics has dropped even as multi-drug-resistant strains of bacteria have proliferated. FDA advisers at last week's meeting did recommend approval of telavancin (Vibativ) — a derivative of vancomycin — for the treatment of hospital-acquired pneumonia when alternative drugs are not suitable. But that vote came nearly two years after the FDA had rejected the drug for a second time because clinical data did not measure up to the agency's guidelines.

"The agency has painted itself into a statistical corner," says Scott Hopkins, chief medical officer of Rib-X, a drug company in New Haven, Connecticut, focused on antibiotics. "While the infectious-disease community was crying out for new antibiotics, the FDA seemed to be going in the opposite direction."

Many trace the agency's tougher stance to the scandal surrounding telithromycin (Ketek), an antibiotic approved by the FDA in 2004 and later linked to liver failure (see 'Long and winding road'). In 2007, the US Congress launched an investigation into whether the FDA had ignored staff concerns about Ketek's safety. The following year, the agency convened its advisers to discuss antibiotics then under review. "Four drugs representing over a billion dollars of investment went into that week and only one came out alive," recalls Mark Leuchtenberger, president of Rib-X.

Telavancin was caught in the changing tides. When Theravance, the company in South San Francisco, California, that developed the drug, designed the large phase III clinical trials needed for approval, the FDA simply required a demonstration that the drug eliminated symptoms of infection as reliably as the

approved antibiotic vancomycin. But, after Theravance submitted its second application on 30 June 2010, the FDA decided instead that applicants needed to show that patients were no more likely to die — of any cause — within 28 days of treatment with a new drug.

Theravance scrambled to gather the data, hunting down medical records for 1,419 out of the 1,503 patients scattered across dozens of countries that were enrolled in the telavancin trials. But the FDA determined that the study lacked statistical power and asked for new clinical studies. Theravance refused, and a stalemate followed.

Strict clinical guidelines for antibiotics have dogged the industry ever since, with pneumonia providing a good illustration. Patients who contract pneumonia in hospital are already ill, making it hard to know if the treatment under review played a part in their death. That means trials have to be larger to capture enough deaths to have any statistical meaning. This, combined with the relative rarity of infections that warrant the use of new antibiotics and the further FDA requirement that patients not receive other antibiotics before they get the experimental drug, has set the goal out of reach, argues David Shlaes, who runs Anti-Infectives Consulting in Stonington, Connecticut. Not a single new antibiotic for hospital-acquired pneumonia has been submitted for approval since the new guidelines were put in place. "The trial simply cannot be done," says Shlaes. "Whoever was writing these guidance documents doesn't live on the same planet that I do."

However, since the Ketek scandal, the political winds have reversed. This summer, Congress passed a set of measures to encourage antibiotic development. In May, Janet Woodcock, head of the FDA's Center for Drug Evaluation and Research, pledged to "reboot" the antibiotic-approval process. And in September, the FDA told Theravance that its advisers would take another look at telavancin, resulting in last week's vote.

Investors have also noticed these changes, says Leuchtenberger. Last week, Rib-X announced that it had raised US\$18.7 million to help the company start phase III trials of an antibiotic that could target skin infections. "Without some of these positive developments this year, you're looking at a number of companies that



The FDA's Janet Woodcock.

LONG AND WINDING ROAD

US Food and Drug Administration (FDA) rules have hampered the approval of antibiotics.

12 FEBRUARY 2007 The FDA changes the label for the antibiotic Ketek to note risk of serious liver damage.

13 FEBRUARY 2007 Congress investigates the FDA's approval of Ketek.

19–20 NOVEMBER 2008 FDA advisers reject three antibiotic applications.

30 JUNE 2010 Drug firm Theravance resubmits trial data to the FDA for approval of telavancin in hospital-acquired pneumonia.

23 NOVEMBER 2010 The FDA proposes changes to guidance for approval of antibiotics to treat hospital-acquired pneumonia.

21 DECEMBER 2010 The FDA rejects telavancin for pneumonia and asks for additional clinical trials.

9 MAY 2012 Janet Woodcock, head of the FDA's Center for Drug Evaluation and Research, calls for a "reboot" of antibiotic evaluation.

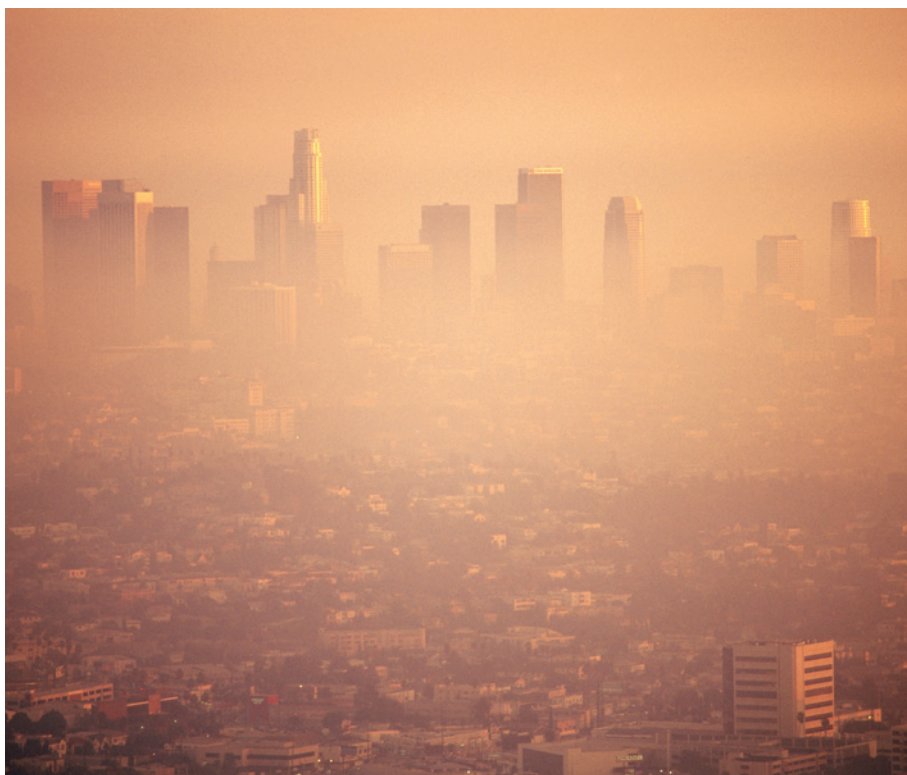
26 JUNE 2012 Congress approves incentives for antibiotic development.

29 NOVEMBER 2012 Telavancin wins approval for the treatment of certain pneumonias.

might not be around any more," he says.

Shlaes, however, emerged from the telavancin meeting still doubtful, noting a continued focus on all-cause mortality. He says that, for now, he will continue to advise his clients to apply for approval in Europe first, where regulators have not been as demanding as the FDA. "I've been very optimistic about the whole thing," he says. "But the FDA has to do something to show that it is actually rebooting." ■

BRENDAN SMIALOWSKI/BLOOMBERG VIA GETTY



Cities such as Los Angeles produce plumes of pollution that contain greenhouse gases.

CLIMATE CHANGE

Megacities move to track emissions

Scientists monitor greenhouse gases in urban areas as a first step to gauging success of climate initiatives worldwide.

BY JEFF TOLLEFSON

At the top of Mount Wilson in southern California, an infrared sensor scans the horizon, silently mapping carbon dioxide levels across Los Angeles. In the city below, scientists fire lasers into the sky to measure the daily rise and fall of a dome of pollution that caps the valley. Other instruments perched on towers are set to track air as it flows into the city and out again, laden with emissions. Eventually, instrumented aircraft will join the effort. Once the operation is fully under way in 2013, the CO₂ that Los Angeles exhales will be monitored and quantified to a degree well beyond that of any other major city.

United Nations data suggest that cities are responsible for some 70% of global greenhouse-gas emissions and that countries with high urbanization rates emit more CO₂ per capita (see 'Urban emitters'). By

closely tracking emissions in Los Angeles and other megacities, researchers hope to test greenhouse-gas monitoring systems that may one day allow scientists to gauge the success of local — and, ultimately, national — climate initiatives. Early results presented this week at the American Geophysical Union meeting in San Francisco, California, offer promising signs that such independent verification is possible through a combination of atmospheric measurements and modelling.

"Megacity emissions are both important and scientifically tractable," says Riley Duren, a systems engineer who is spearheading the monitoring initiative at NASA's Jet Propulsion Laboratory (JPL) in Pasadena, California. Scientists might be a couple of decades away from being able to track all anthropogenic greenhouse-gas emissions at high resolution from space, Duren says, "but the technology exists today to go after the emissions of cities".

Duren and his partners have linked up with French researchers who are monitoring emissions in Paris, and the team is also discussing a similar project in São Paulo, Brazil. In Indianapolis, a monitoring programme has been up and running since 2010. These projects arose when mandatory climate regulations seemed likely for many countries; that expectation has since faded, but scientific interest in monitoring and verification has only increased.

Turning to the atmosphere to verify emissions estimates — which are typically based on industry reports of energy consumption — is far from trivial. Cities produce plumes of pollution that scientists must characterize as the plumes evolve and disperse downwind. To convert atmospheric concentrations of greenhouse gases into emissions, researchers must understand local meteorology and trace emissions back to their sources.

TOWER POWER

Working with state, academic and private partners, the Los Angeles team aims to have 13 monitoring stations on towers within six months. These will track air moving through the basin while balloons and lasers measure the boundary between the pollution that sits over the city and the cleaner air above. This boundary determines the volume of air that scientists are investigating, and thus the relationship between measured concentrations of CO₂ and overall emissions. At sunrise each day, the polluted air warms and rises, mixing with cleaner air and escaping over the mountains that ring the city. All of this information will be plugged into a high-resolution model that can be used essentially to track these atmospheric processes backwards and forwards through time to understand the greenhouse-gas measurements.

The approach builds on the Indianapolis project. Paul Shepson, an atmospheric chemist at Purdue University in West Lafayette, Indiana, led a team that received about US\$1.5 million from the National Institute of Standards and Technology (NIST) in 2009 to set up the experiment. The team deployed a pair of towers to measure air as it entered and exited Indianapolis, and Shepson augmented those measurements with detailed assessments from aircraft. With further funding, the team expects eventually to encircle Indianapolis with a dozen towers to measure CO₂ and methane.

"It's a great city for a test case, isolated and flat as a pancake," says Shepson.

He reckons that his initial calculations come within 30–40% of the city's stated CO₂ emissions. He expects to reduce that uncertainty

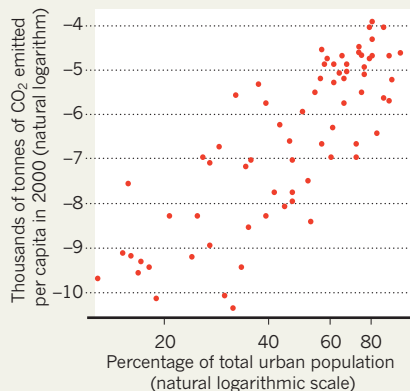
to 20% by incorporating data from the towers in a high-resolution emissions model developed by atmospheric scientist Kevin Gurney, a

➔ NATURE.COM
Read more about
science and
urbanization:
go.nature.com/9233vu

ROBERT LANDAU/CORBIS

URBAN EMITTERS

A plot of 71 countries shows that urbanization correlates with higher carbon dioxide emissions.



co-investigator on the project who is based at Arizona State University in Tempe. Team members are due to present initial results at the San Francisco meeting this week.

Gurney's model incorporates real data about energy use: industrial activities at the level of individual buildings together with traffic patterns. Vehicles are classified by the type of fuel used and emissions produced, and are simulated moving throughout the city much as normal vehicles would. Gurney

foresees a day when the combined results of the greenhouse-gas measurements and modelling will enable cities to pinpoint methane emissions from natural-gas leaks, for example, or identify neighbourhoods that would benefit from traffic initiatives or projects to make existing buildings more energy efficient.

"I've had mayors calling me, and they all pretty much say the same thing: where do we start?" says Gurney, who has already applied the model to Phoenix in Arizona and is now adapting it to Los Angeles. "If you are going to spend money," Gurney adds, "you need to know where to do it."

This is why Los Angeles has bought into the monitoring programme. Committed to reducing its emissions to 35% below 1990 levels by 2030, the city has pursued a range of initiatives, from cracking down on shipping emissions and ramping up renewable energy to installing more-efficient streetlights and synchronizing traffic lights. "We're doing what we can, but we want to make sure that what we are doing is actually working," says Romel Pascual, Los Angeles' deputy mayor for the environment.

NIST has invested about \$1.1 million in the Los Angeles initiative in the hope of advancing the science and making it more applicable to other cities. The goal is to reduce the overall uncertainty in calculating emissions to 10%.

The final phase will extend this effort into

space. The sensor currently installed on Mount Wilson is a prototype of a next-generation instrument that could eventually be launched on a satellite, says Charles Miller, a colleague of Duren's at the JPL. Tuned to near-infrared wavelengths, the sensor measures the proportion of the heat being absorbed by CO₂, and thus the CO₂ concentration in the atmosphere. Ultimately, Miller and Duren envisage a trio of geostationary satellites that would allow constant surveillance of greenhouse-gas emissions — not just over Los Angeles, but around the planet. "This is a completely wide open and untested area," Miller says, "but one with great promise." ■

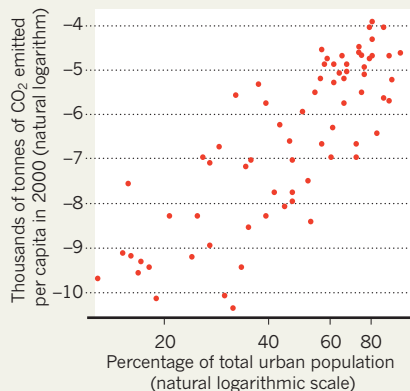
CORRECTIONS

The News story 'Drug-pollution law all washed up' (*Nature* **491**, 503–504; 2012) incorrectly said that Axel Singhofen is a Member of the European Parliament (MEP). In fact, he is an adviser to Green MEPs who sit on the environment committee.

The World View 'Science should be ready to jump off 'the cliff'' (*Nature* **491**, 639; 2012) stated that the United States would raise only \$2.2 billion in taxes this year. In fact, it will raise \$2.2 trillion.

URBAN EMITTERS

A plot of 71 countries shows that urbanization correlates with higher carbon dioxide emissions.



co-investigator on the project who is based at Arizona State University in Tempe. Team members are due to present initial results at the San Francisco meeting this week.

Gurney's model incorporates real data about energy use: industrial activities at the level of individual buildings together with traffic patterns. Vehicles are classified by the type of fuel used and emissions produced, and are simulated moving throughout the city much as normal vehicles would. Gurney

foresees a day when the combined results of the greenhouse-gas measurements and modelling will enable cities to pinpoint methane emissions from natural-gas leaks, for example, or identify neighbourhoods that would benefit from traffic initiatives or projects to make existing buildings more energy efficient.

"I've had mayors calling me, and they all pretty much say the same thing: where do we start?" says Gurney, who has already applied the model to Phoenix in Arizona and is now adapting it to Los Angeles. "If you are going to spend money," Gurney adds, "you need to know where to do it."

This is why Los Angeles has bought into the monitoring programme. Committed to reducing its emissions to 35% below 1990 levels by 2030, the city has pursued a range of initiatives, from cracking down on shipping emissions and ramping up renewable energy to installing more-efficient streetlights and synchronizing traffic lights. "We're doing what we can, but we want to make sure that what we are doing is actually working," says Romel Pascual, Los Angeles' deputy mayor for the environment.

NIST has invested about \$1.1 million in the Los Angeles initiative in the hope of advancing the science and making it more applicable to other cities. The goal is to reduce the overall uncertainty in calculating emissions to 10%.

The final phase will extend this effort into

space. The sensor currently installed on Mount Wilson is a prototype of a next-generation instrument that could eventually be launched on a satellite, says Charles Miller, a colleague of Duren's at the JPL. Tuned to near-infrared wavelengths, the sensor measures the proportion of the heat being absorbed by CO₂, and thus the CO₂ concentration in the atmosphere. Ultimately, Miller and Duren envisage a trio of geostationary satellites that would allow constant surveillance of greenhouse-gas emissions — not just over Los Angeles, but around the planet. "This is a completely wide open and untested area," Miller says, "but one with great promise." ■

CORRECTIONS

The News story 'Drug-pollution law all washed up' (*Nature* **491**, 503–504; 2012) incorrectly said that Axel Singhofen is a Member of the European Parliament (MEP). In fact, he is an adviser to Green MEPs who sit on the environment committee.

The World View 'Science should be ready to jump off 'the cliff'' (*Nature* **491**, 639; 2012) stated that the United States would raise only \$2.2 billion in taxes this year. In fact, it will raise \$2.2 trillion.



THE QUANTUM SPACE RACE

Fierce rivals have joined forces in the race to teleport information to and from space.

BY ZEEYA MERALI

Three years ago, Jian-Wei Pan brought a bit of *Star Trek* to the Great Wall of China. From a site near the base of the wall in the hills north of Beijing, he and his team of physicists from the University of Science and Technology of China (USTC) in Hefei aimed a laser at a detector on a rooftop 16 kilometres away, then used the quantum properties of the laser's photons to 'teleport' information across the intervening space¹. At the time, it was a world distance record for quantum teleportation, and a major step towards the team's ultimate aim of teleporting photons to a satellite.

If that goal is achieved, it will establish the first links of a 'quantum Internet' that harnesses the powers of subatomic physics to create a super-secure global communication network. It will confirm China's ascent in the field, from a bit-player a little more than a decade ago to a global powerhouse: in 2016, ahead of Europe and North America, China plans to launch a satellite dedicated to quantum-science experiments. It will offer physicists a new arena in which to test

NATURE.COM

To read a News
Feature on quantum
simulation, see:
go.nature.com/9t1zrs

the foundations of quantum theory, and explore how they fit together with the general theory of relativity — Einstein's very different theory of space, time and gravity.

It will also mark the culmination of Pan's long, yet fiercely competitive, friendship with Anton Zeilinger, a physicist at the University of Vienna. Zeilinger was Pan's PhD adviser, then for seven years his rival in the long-distance quantum-teleportation race, and now his collaborator. Once the satellite launches, the two physicists plan to create the first intercontinental quantum-secured network, connecting Asia to Europe by satellite. "There's an old Chinese saying, 'He who teaches me for one day is my father for life,'" says Pan. "In scientific research, Zeilinger and I collaborate equally, but emotionally I always regard him as my respected elder."

FAST MOVER

Pan was only in his early thirties when he set up China's first lab for manipulating the quantum properties of photons in 2001, and when he proposed the satellite mission in 2003. And he was 41 in 2011, when he became the youngest researcher ever to be inducted into the Chinese Academy of Sciences. "He almost single-handedly pushed this project through and put China on the quantum map," says team member Yu-Ao Chen, also at the USTC.

Pan's drive dates back to his undergraduate years at the USTC in the late 1980s, when he first encountered the paradoxes at play in the atomic realm. Quantum objects can exist in a superposition of many states: a particle can spin both clockwise and anticlockwise at the same time, for instance, and it can simultaneously be both here and over there. This multiple personality is described mathematically by the particle's wavefunction, which gives the probability that it is in each of those states. Only when the particle's properties are measured does the wavefunction collapse, choosing a definite state in a single location. Crucially, there is no way, even in principle, to predict the result of a single experiment; the probabilities show up only as a statistical distribution and only when the experiment is repeated many times.

Things get even weirder when two or more particles are involved, thanks to the quantum property of entanglement. Multiple particles can be prepared in such a way that measurements on one are correlated with measurements made on the others, even if the particles are separated by huge distances — and even though the phenomenon of superposition demands that these properties cannot be fixed until the instant they are probed. It is as strange as a physicist in Beijing and another in Vienna flipping coins in unison, and finding that they always either both throw heads or both throw tails. "I was obsessed with these quantum paradoxes," says Pan. "They distracted me so much that I couldn't even study other things." He wanted to test the veracity of these almost inconceivable claims, but he could not find a suitable experimental quantum physics lab in China.

The natural progression for budding Chinese physicists in Pan's position was to study in the United States — so natural, in fact, that fellow students joked that their university's acronym, USTC, actually stood for 'United States Training Centre'. But Pan wanted to learn from a quantum experimental master. And for him, one physicist stood out: Zeilinger.

In 1989, Zeilinger had collaborated with physicists Daniel Greenberger, now at the City University of New York, and Michael Horne, now at Stonehill College in Easton, Massachusetts, on a key theorem governing the entanglement of three or more particles². The work was a turning point for the field — and for Zeilinger. "At conferences, I realized that very important older physicists had started to regard me as the

quantum expert," he says. By the mid-1990s, Zeilinger had set up his own quantum lab at the University of Innsbruck in Austria and needed a student to test some of his ideas. Pan seemed the perfect fit. So, in a rare move for a Chinese student, Pan relocated to Austria, beginning a relationship with Zeilinger that would see their careers develop in tandem over the next two decades.

Even as a graduate student, Pan had big ambitions for his home country. At their first meeting, Zeilinger asked Pan what his dream was. "To build in China a world-leading lab like yours," Pan replied. Zeilinger was impressed. "When he first came, he knew nothing about working in a lab, but he quickly picked up the rules of the game and was soon inventing his own experiments," he says. "I always knew he would have a wonderful career — but the incredible success that he has had, I don't think anyone could have foreseen. I am very proud of him."

While Pan was mastering his craft in Zeilinger's lab, physicists around the world were slowly embracing the notion that the esoteric quantum features that so enchanted Pan could be harnessed to create, say, ultra-powerful quantum computers. Standard computers chug slowly through information coded in binary digits — strings of zeros and ones. But as early as 1981, the physicist Richard Feynman had pointed out that quantum bits, known as 'qubits', need not be so encumbered. Because a qubit can simultaneously exist in superpositions of 0 and 1, it should be possible to build faster, more powerful quantum computers that would entangle multiple qubits together and perform certain calculations in parallel, and at breathtaking speed.

Another emerging idea was ultra-secure quantum encryption for applications such as bank transactions. The key idea is that measuring a quantum system irrevocably disrupts it. So two people, Alice and Bob, could generate and share a quantum key, safe in the knowledge that any meddling by an eavesdropper would leave a trace.

By the time Pan returned to China in 2001, the potential for quantum-based technologies was recognized enough to attract financial support from the Chinese Academy of Sciences and the National Natural Science Foundation of China. "The lucky thing was that in 2000 the economy of China started to grow, so the timing was suddenly right to do good science," Pan says. He plunged into building his dream lab.

Back in Austria, meanwhile, Zeilinger had moved to the University of Vienna, where he continued to set quantum records thanks to his penchant for thinking big. One of his most celebrated experiments showed that buckyballs, fullerene molecules containing 60 carbon atoms, can exhibit both wave and particle behaviour³ — a peculiar quantum effect that many thought could not survive in such large molecules. "Everyone had been talking about maybe trying this experiment with small, diatomic molecules," recalls Zeilinger. "I said, 'no guys, don't just think of the next one or two steps ahead, think about how to make a huge unexpected leap beyond everyone's thinking'."

That was a lesson that Pan heeded well. Physicists around the world were beginning to imagine the futuristic quantum Internet, based on links between quantum computers that had yet to be built. At a time when most practitioners were still happy to get quantum information safely across a lab bench, Pan was already starting to think about how to teleport it across the planet.

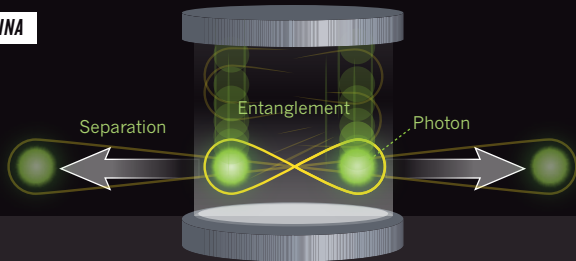
First proposed in 1993 by computer scientist Charles Bennett of IBM in New York and his colleagues⁴, quantum teleportation earned its sensational name because, "like something out of *Star Trek*", says Chen, it allows all

Experiments in the Canary Islands hold the distance record for quantum teleportation.

QUANTUM AT A DISTANCE

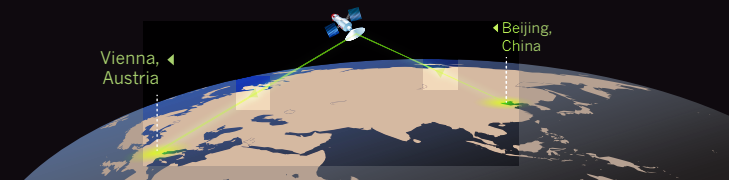
The subtleties of quantum measurement allow for a unique kind of communication.

IN CHINA

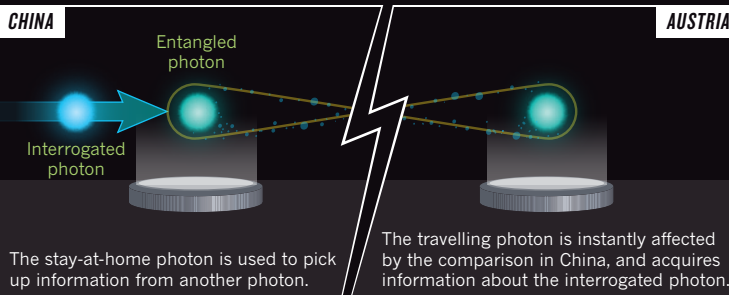


Two photons are 'entangled' in the lab. Although their individual polarizations are not yet set, the entanglement ensures that any measurement will find both polarizations to be identical — no matter how widely the particles are separated.

One entangled photon is then beamed from Beijing to Vienna.



CHINA

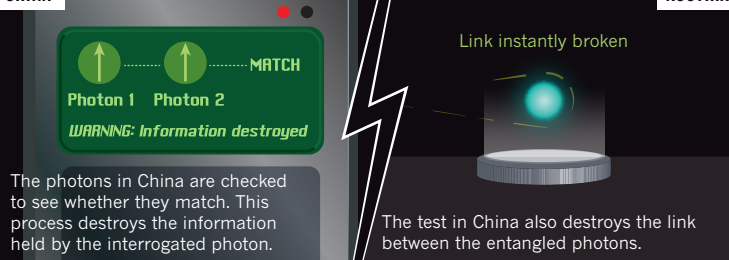


The stay-at-home photon is used to pick up information from another photon.

AUSTRIA

The travelling photon is instantly affected by the comparison in China, and acquires information about the interrogated photon.

CHINA



The photons in China are checked to see whether they match. This process destroys the information held by the interrogated photon.

AUSTRIA

Link instantly broken

The test in China also destroys the link between the entangled photons.

The result of the test in China is communicated through conventional means. It tells the experimenters in Austria how to put their photon into a state identical to that of the interrogated photon — which has thus been 'teleported'.



information about a quantum object to be scanned in one location and then recreated in a new place. The key is entanglement (see 'Quantum at a distance'): because operations carried out on one of the entangled particles affect the state of its partner, no matter how far away it is, the two objects can be manipulated to act like two ends of a quantum telephone line, transmitting quantum information between two widely separated locations.

The challenge arises when entangled particles, which must be produced together, are transmitted to their respective ends of the phone connection. Such a journey is fraught with noise, scattering interactions and all manner of other disruptions, any of which can destroy the delicate quantum correlations required to make teleportation work. Currently, for example, entangled photons are transported through optical fibres. But fibres absorb light, which keeps the photons from travelling more than a few hundred kilometres. Standard amplifiers can't help, because the amplification process will destroy the quantum information. "For teleporting to distances beyond the range of a city, we need to teleport through a satellite," says Chen.

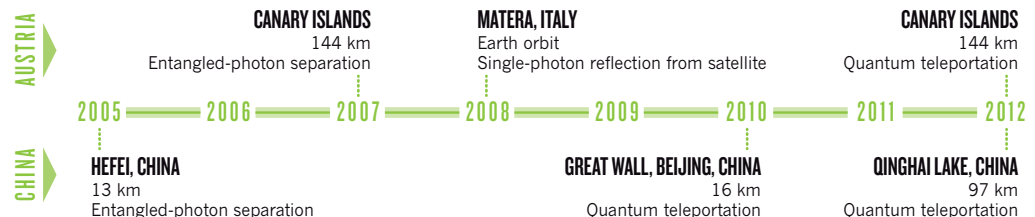
But would entanglement survive the upward trip through Earth's turbulent atmosphere to a satellite hundreds of kilometres overhead? To find out, Pan's team, including Chen, began in 2005 to carry out ground-based feasibility tests across ever-increasing expanses of clear air to find out whether photons lose their entanglement when they bump into air molecules. But they also needed to build a target detector that was both small enough to fit on a satellite and sensitive enough to pick out the teleported photons from background light. And then they had to show that they could focus their photon beam tightly enough to hit the detector.

The work aroused Zeilinger's competitive instincts. "The Chinese were doing it, so we thought, why not try it?" he says with a laugh. "Some friendly competition is always good." The race began to push the distance record farther and farther (see 'Duelling records'). Over the next seven years, through a series of experiments carried out in Hefei, then by the Great Wall in Beijing and finally in Qinghai, the Chinese team teleported over ever-greater distances, until it passed 97 kilometres⁵. The researchers announced their results in May, posting a paper on the physics preprint server, arXiv — much to the chagrin of the Austrian team, which was writing up the results of its own effort to teleport photons between two of the Canary Islands. The Austrian group posted its paper on arXiv eight days later, reporting a new distance record of 143 kilometres⁶. The papers were eventually published, in quick succession, in *Nature*^{5,6}. "I think that was in recognition of the fact that each experiment has different and complementary merits," says Xiao-song Ma, a physicist at the University of Vienna and a member of the Austrian team.

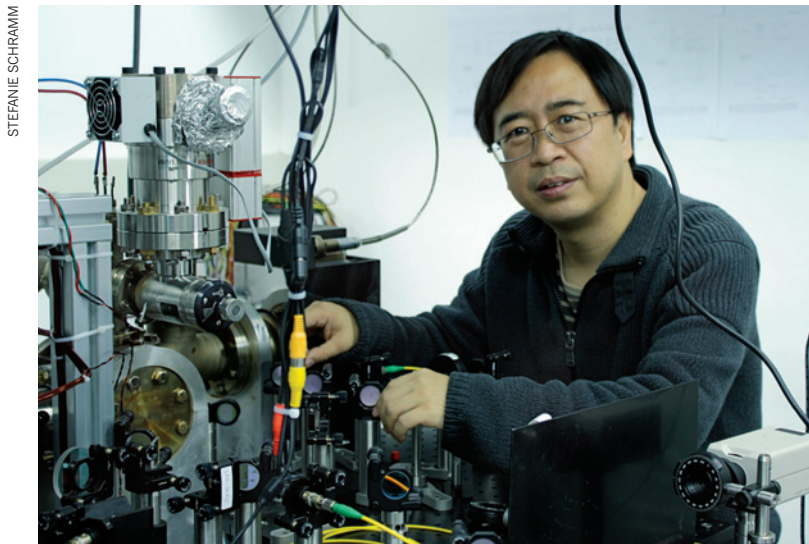
Both teams agree that any scientific concerns about teleporting to a satellite have been defused. Now they just need a satellite to host the tests and a functioning payload to put on board. Zeilinger's team had been discussing a possible quantum satellite mission with the European Space Agency

DUELLING RECORDS

Teams based in China and Austria have competed for seven years to establish milestones — first for the separation of entangled particles, which define the ends of a quantum telephone line, and then for the teleportation of information along the line.



"I WAS OBSESSED WITH THESE QUANTUM PARADOXES."



STEFANIE SCHRAMM

Jian-Wei Pan is working on ways to teleport photons between Earth and space.

(ESA), but those talks gradually fizzled out. "Its mechanisms are so slow that no decision was made," says Zeilinger. ESA's hesitation opened up a gap for the China National Space Administration to swoop in. Pan has been instrumental in pushing through the mission, which should see a quantum-physics satellite launched in 2016. This places Pan ahead in the quantum space race, and his team will handle the bulk of the scientific tests.

KEY TO SUCCESS

But there is no point in developing the first global quantum communication network if you do not have anybody to talk with. So Pan has invited his one-time rival to join him on the project. Their first joint goal will be to generate and share a secure quantum key between Beijing and Vienna. "Ultimately, teleporting to a satellite is too big a task for any single group to do alone," says Ma.

Although the promise to push forward the technological frontier has been the main attraction for the Chinese government, many physicists find the satellite project tantalizing for other reasons. "As a scientist, what drives me is learning more about the foundational side of physics," says Chen. So far, quantum theory's weirdness has been replicated time and again in labs, but it has never before been tested across distances that stretch into space — and there is reason to think that if it is going to break down anywhere, it will be there. At these larger scales, another fundamental theory of physics holds sway: general relativity. Relativity portrays time as another dimension interwoven with the three dimensions of space, thereby creating a four-dimensional space-time fabric that comprises the Universe. Gravity manifests because this malleable fabric bends around massive objects such as the Sun and it pulls less-massive objects, such as planets, towards them.

The challenge is that quantum theory and general relativity present fundamentally different conceptions of space and time, and physicists have struggled to meld them into

one unifying framework of quantum gravity. In Einstein's picture, space-time is perfectly smooth, even when examined at infinitesimal scales. Quantum uncertainty, however, implies that it is impossible to examine space at such small distances. Somewhere along the line either quantum theory or general relativity, if not both, must give way, but it is not yet clear which. The satellite experiments could help by testing whether the rules of quantum theory still apply over scales across which gravity's pull cannot be ignored.

An obvious question is whether entanglement can stretch between Earth and a satellite. The team plans to answer it by producing a series of entangled particles on the satellite, firing one of each pair down to a ground station and then measuring its properties to verify that the pairs are correlated — and that the equipment is working properly. "If entanglement doesn't survive we'd have to look for an alternative theory to quantum mechanics," says Nicolas Brunner, a theoretical physicist at the University of Geneva, Switzerland, who works on protocols for teleportation to a satellite.

The satellite could also go a step further and probe some of the predictions about the structure of space-time made by candidate quantum-gravity theories. For instance, all such theories predict that space-time would become grainy if scientists could somehow see it at scales of 10^{-35} metres, a characteristic distance known as the Planck length. If that is indeed the case, then photons travelling from the satellite along this grainy road would be very slightly slowed⁷ and their polarizations would undergo a tiny, random rotation⁸ — effects that could be large enough to be picked up at the ground station. "A satellite will open a truly novel window into a regime that experimenters haven't had access to before — and that is fantastic," says Giovanni Amelino-Camelia, a physicist at the Sapienza University of Rome, Italy.

Pan, Zeilinger and their teams are currently scrutinizing the ideas generated in a recent series of workshops at the Perimeter Institute for Theoretical Physics in Waterloo, Canada, where physicists were asked to come up with other foundational questions that could be tested by satellites⁹. The questions that arose included: how does an entangled particle always know the result of a measurement made on its far-distant partner? Do the pairs somehow communicate through some still-unknown information channel? What causes the quantum wavefunction to collapse when it is measured? Is gravity somehow involved? And is time a precisely defined quantity, as described in general relativity — or is it fuzzy, as might be expected from quantum mechanics?

Answering such questions will require apparatus of extraordinary sensitivity, says Pan. But meeting the technical challenges they raise will be easier now that the teams have joined forces, he says. The Austrian group, too, is seizing the new collaboration with enthusiasm. As Zeilinger says, "One of my students has just started learning Chinese." ■

Zeeya Merali is a freelance writer based in London.

1. Jin, X.-M. *et al. Nature Photon.* **4**, 376–381 (2010).
2. Greenberger, D., Horne, M. A. & Zeilinger, A. in *Bell's Theorem, Quantum Theory and Conceptions of the Universe* (ed. Kafatos, M.) 69–72 (Kluwer, 1989).
3. Arndt, M. *et al. Nature* **401**, 680–682 (1999).
4. Bennett, C. H. *et al. Phys. Rev. Lett.* **70**, 1895–1899 (1993).
5. Yin, J. *et al. Nature* **488**, 185–188 (2012).
6. Ma, X.-S. *et al. Nature* **489**, 269–273 (2012).
7. Amelino-Camelia, G., Ellis, J., Mavromatos, N. E., Nanopoulos, D. V. & Sarkar, S. *Nature* **393**, 763–765 (1998).
8. Contaldi, C. R., Dowker, F. & Philpott, L. *Class. Quant. Grav.* **27**, 172001 (2010).
9. Rideout, D. *et al. Class. Quant. Grav.* **29**, 224011 (2012).



RADICAL REACTORS

For decades, one design has dominated nuclear reactors while potentially better options were left by the wayside. Now, the alternatives might finally have their day.

Back in 2000, when Kirk Sorensen was a NASA engineer looking at nuclear-power options for future colonies on the Moon, he came across a book that described the molten-salt reactor: an energy source in which the nuclear fuel was liquid.

It sounded bizarre, says Sorensen. Every reactor he had ever heard of used some form of solid uranium fuel — starting with the 'light-water'

reactors that currently dominate the nuclear-power industry. But the book explained that the molten-salt technology had been demonstrated some three decades earlier at the Oak Ridge National Laboratory in Tennessee — and that the fluid uranium- or thorium-containing fuel offered major advantages. Molten-salt reactors would be impervious to catastrophic meltdown, for example, and instead of producing nuclear waste laced with plutonium and other long-lived radioisotopes, they could destroy those isotopes almost completely.

The list of advantages went on and on, says Sorensen: the molten-salt idea “had the potential to solve almost all the problems of nuclear energy in a far, far more elegant way” than light-water reactors. “So why didn’t we do it this way in the first place?”

A lot of people have been asking that question in the past decade — and not just about the molten-salt reactor. That particular technology was abandoned in 1976 because of warring agendas within the US research programme. But it was just one of several alternative technologies to be sidelined during the first rush to commercialize nuclear power. Others include ‘fast’ reactors that would also burn up nuclear waste, and high-temperature reactors that could take a huge bite out of greenhouse-gas emissions by generating zero-carbon heat for industry. Taken together, these alternative technologies could eliminate most or all of nuclear energy’s drawbacks. But they have received only fitful attention from researchers over the decades, thanks to constantly shifting agendas and funding levels.

Now, change may be coming. Over the past decade, the need for safe, carbon-free energy — especially in fast-developing nations such as China — has sparked government interest in alternative nuclear technologies, along with commercial efforts to revive and market some designs. Optimists think that even the nuclear disaster at the Fukushima Daiichi power plant in Japan last year will ultimately boost the market for safer alternative reactors. From start-ups such as Flibe Energy, which Sorensen founded last year in Huntsville, Alabama, to commercialize the molten-salt reactor, to industry giants such as General Electric-Hitachi Nuclear Energy, which is developing a commercial fast reactor, companies hope to be ready.

Reviving the technologies will not be quick or easy. Although the basic designs were worked out decades ago, engineers hoping to put them into practice must develop things such as radiation-resistant materials, more-efficient heat exchangers and improved safety systems — and must then prove to regulators that all these systems will work. “Nuclear

is hard,” says Edwin Lyman, senior global-security analyst for the Union of Concerned Scientists in Cambridge, Massachusetts. “It’s

expensive. It’s slow. And the stakes are very high, because safety has to be a factor.”

But those involved share a conviction that the best hope for the nuclear industry’s future is to reclaim its past. As Sorensen points out about the cancellation of the molten-salt programme: “Nobody ever said, ‘Maybe we made a mistake. Maybe we should go back and revisit that decision.’”

FIRST, NOT BEST

Light-water reactors achieved their dominance not because they were best, but because they were first. Originally developed in the late 1940s as a compact power source for nuclear ships and submarines, the light-water design was adapted and scaled up during the 1950s, when the United States sought to put a peaceful face on atomic energy by creating a commercial nuclear-power industry. ‘Light water’ is ordinary H₂O, which flows through the reactor core, absorbs its heat and circulates it to a conventional steam turbine that turns the heat into electricity (see ‘The nuts and bolts of nuclear’).

Eventually, such reactors were meant to be part of a larger system that would make up for a basic inefficiency: left alone, any nuclear reactor will quickly poison itself. As the chain reaction proceeds, the fuel accumulates more and more of the fragments left over after the uranium atoms split, which in turn absorb more and more of the neutrons required to keep the reaction going. After perhaps 18 months, the fuel is ‘spent’ and has to be removed — even though it still contains much of its original energy.

“So there was always this vision that there would be a recycled-spent-fuel infrastructure that would allow you to recover more of the fuel’s energy,” says William Magwood, a former director of the Office of Nuclear Energy at the US Department of Energy (DOE) and now a member of the US Nuclear Regulatory Commission. A worldwide network of reprocessing plants would take the spent fuel, chemically extract the still-usable components — mostly uranium-235, plus the fissionable plutonium-239 formed when neutrons are captured by non-fissile uranium-238 — and then turn them into fresh reactor fuel. Ultimately, the plan was to transition to a new generation of ‘breeder’ reactors designed to maximize plutonium production. The only waste would be a comparatively small residue of intensely radioactive fission products that would decay within a few centuries, and could be disposed of in, say, a well-designed concrete bunker.

This vision became the dominant US strategy in the 1960s and early 1970s, says Magwood, to the point at which authorities terminated much of the research funding for non-breeder reactor designs — including the molten-salt reactor. And the scheme took off: of the 437 nuclear-power reactors currently operating around the world, 356 are light-water reactors.

But then, in May 1974, India tested a nuclear bomb made with plutonium extracted from

reactor fuel. Governments around the world suddenly had to face the geopolitical realities: large-scale commercial reprocessing would invite rampant nuclear-weapons proliferation. Because each reprocessing plant would be working with bomb-grade plutonium by the tonne, how could inspectors ever be sure that no one had diverted the 4–6 kilograms required for a weapon?

So in April 1977, US President Jimmy Carter banned commercial reprocessing. President Ronald Reagan lifted that ban a few years later, but the costs of the facilities were so high that only two commercial reprocessing plants have been opened for reactor fuel since then, both in France. Research on breeder reactors largely ceased, because they seemed to make little sense without reprocessing. And engineers found themselves left with a complicated disposal problem: they would now have to isolate tens of thousands of tonnes of spent fuel for hundreds of centuries, thanks to the 24,100-year half-life of plutonium-239. No one has yet worked out how to guarantee isolation on that timescale (see *Nature* **473**, 266–267; 2011).

Meanwhile, the 1970s also brought an increasing outcry over safety. If the flow of water through a light-water reactor is interrupted for any reason, then heat becomes trapped in the core. Even if the reactor is technically shut down, the fission products can still produce enough heat from radioactive decay to melt the fuel and escape into the environment. All light-water reactors have emergency back-up cooling systems — but what if those systems fail? That fear was realized in March 1979, when an accidental loss of coolant triggered a partial meltdown at the Three Mile Island nuclear power plant near Harrisburg, Pennsylvania — and dramatically confirmed at Fukushima Daiichi, which saw a complete meltdown in March 2011 (see *Nature* **483**, 138–140; 2012).

A SECOND CHANCE

The public and political backlash after the Three Mile Island incident created a worldwide ‘nuclear brown-out’ that lasted for a quarter of a century. Power companies scrapped their nuclear expansion plans and cancelled almost all of their reactor orders. And the industry became even more reluctant to explore new technologies. “The industry is risk-averse to moving beyond technology and materials they have lots of experience with” and that they know can get regulatory approval, says Per Peterson, a nuclear engineer at the University of California, Berkeley.

With little interest from industry and no practical hope for deployment, advanced-reactor research struggled with inconsistent direction and support. “It’s very hard to do planning and advanced engineering R&D if you’re up and down, up and down,” says Michael Corradini, a nuclear engineer at the University of Wisconsin-Madison.

This picture didn’t begin to change ►

► **NATURE.COM**
Hear more about
radical reactors on
Nature’s podcast:
go.nature.com/jqcno5

► until around the turn of the millennium. “Nuclear construction had taken off in China and south Asia — any place that doesn’t have oil and gas,” recalls Charles Forsberg, a nuclear engineer at the Massachusetts Institute of Technology (MIT) in Cambridge. (There are currently 64 reactors under construction around the world, with hundreds more planned.) In the United States, he says, “the feds realized that, if we’re not doing anything on nuclear, we won’t be at the table”. Climate change, too, drove renewed interest in nuclear technology in the United States and Europe. Given the erratic output of both wind and solar generators, says Forsberg, “if you’re going to get off fossil fuel, you have to have a serious nuclear programme”.

RADICAL INVESTMENT

One result of this renewed focus was the US Nuclear Power 2010 programme. Announced by the DOE in February 2002, this government–industry cost-sharing plan was designed to help manufacturers to develop and license light-water reactors with advanced safety features, such as the ability to keep the coolant moving during an accident, using gravity and natural convection. Several such reactors are now being planned around the world, including four under construction in the United States — the first new reactors there in a generation.

Even more radical designs might find an opening with the DOE’s cost-sharing programme for Small Modular Reactor development, launched this year. That scheme’s goal is to move away from the current multi-gigawatt nuclear plants, which can cost between US\$10 billion and \$15 billion to build, towards plants of 250 megawatts or less — small enough to mass-produce in a factory and ship to the intended site. Four reactor vendors, all with advanced light-water designs, competed for

what the name implies: they generate steam at up to 1,000 °C, much hotter than the roughly 300 °C available from light-water reactors. This requires some radically different design choices, such as the use of helium gas instead of water to extract heat, and the use of a heat-resistant fuel made from oxides and carbides of uranium.

Such reactors cannot melt down: the fuel is stable up to 1,600 °C, hundreds of degrees hotter than the core would become even if all power and coolant were lost. The high temperatures would make the reactors more efficient at producing electricity. And they could slash carbon emissions by supplying heat for industrial processes. In the United States, roughly 23% of all energy is used in industrial applications such as petroleum cracking and plastics manufacture, many of which need temperatures of at least 700 °C. Currently, those temperatures tend to be generated by burning natural gas; high-temperature reactors could provide a zero-carbon alternative.

A number of commercial high-temperature reactors are under development around the world. But this year, a consortium of petrochemical companies and reactor manufacturers agreed to back the Antares high-temperature reactor design from the French company AREVA, based in Paris. “All that’s left is about \$800 million of work design and licensing effort required to get the technology to the point where the Nuclear Regulatory Commission could approve it,” says Fred Moore, head of the division that provides power and steam for the Dow Chemical Company, headquartered in Midland, Michigan. He estimates that this should take 5–7 years. If all goes to plan, high-temperature systems will be among the first advanced reactors to be deployed, starting in the 2020s.

Not far behind would be fast reactors, which tackle a problem that high-temperature reactors cannot: spent nuclear fuel. Fast reactors

that collectively make disposal of spent fuel a nightmare. Fast neutrons, by contrast, rarely get absorbed. They don’t hit their targets often, but when they do, that target almost always splits. As a result, fast reactors not only avoid the problem of producing long-lived isotopes, but can even destroy them in spent fuel.

Building a fast reactor is tricky, says Peterson, not least because it has to be cooled by liquid sodium or some other substance that won’t slow the neutrons down as water does. This can make for a bulky design. “And it’s very challenging to build heat exchangers” to make steam for the power turbines, he says, because sodium reacts violently with moisture to produce explosive hydrogen gas. Researchers are actively studying other, less reactive options for cooling, such as lead and supercritical carbon dioxide, he says.

Nevertheless, some 20 fast reactors have been operated over the years — many of them following the 1970s breeder design that was built to maximize plutonium production instead of consuming it — and at least four manufacturers are developing small fast reactors for spent-fuel consumption. A leading example is the Super Power Reactor Innovative Small Module (S-PRISM) from General Electric–Hitachi in Wilmington, North Carolina. It calls for a compact sodium-cooled fast reactor, integrated with a recycling unit that would take the reactor’s spent fuel, remove the fission products that poison the nuclear reaction, and put the rejuvenated fuel back into the reactor. At no point would it isolate bomb-ready plutonium.

The potential market is substantial, says Eric Loewen, head of advanced-reactor development for General Electric–Hitachi. “We have a usability study going on with the United Kingdom, where we would take the 100 tonnes of plutonium from their reprocessing plants and turn it into an energy resource,” he says. And in the United States and elsewhere, he says, “our vision is a network of advanced recycling centres”, each with six S-PRISM reactors and one recycling centre that could keep up with the waste from between one and three light-water reactors, and get rid of the backlog currently sitting in storage.

That network will not be cheap. But the fundamental challenge is political, says Loewen, echoing Forsberg and many other experts: what is needed is “a policy framework that lets people see spent fuel as an asset, rather than something to be thrown away.”

MOLTEN-SALT REACTORS

The great virtue of solid reactor fuel is its predictable geometry. The great drawback is its complexity. The intensity of neutron bombardment, the distribution of fission products, the radiation damage to the fuel’s crystalline structure: everything varies from point to point. This is a constant headache for designers trying to ensure that the reactor operation

“IF YOU’RE GOING TO GET OFF FOSSIL FUEL, YOU HAVE TO HAVE A SERIOUS NUCLEAR PROGRAMME.”

the award, which on 20 November went to a consortium headed by the Babcock and Wilcox Company of Charlotte, North Carolina.

But other designs could also benefit, says Peterson. “If we can generate a market for light-water small modular reactors,” he says, “that makes it much easier to develop a market for prototype advanced reactors.” Power companies could experiment with the new technology by simply sliding in another module. If it works, great, says Peterson. If it doesn’t, not much has been lost. “This lowers their whole risk threshold,” he says.

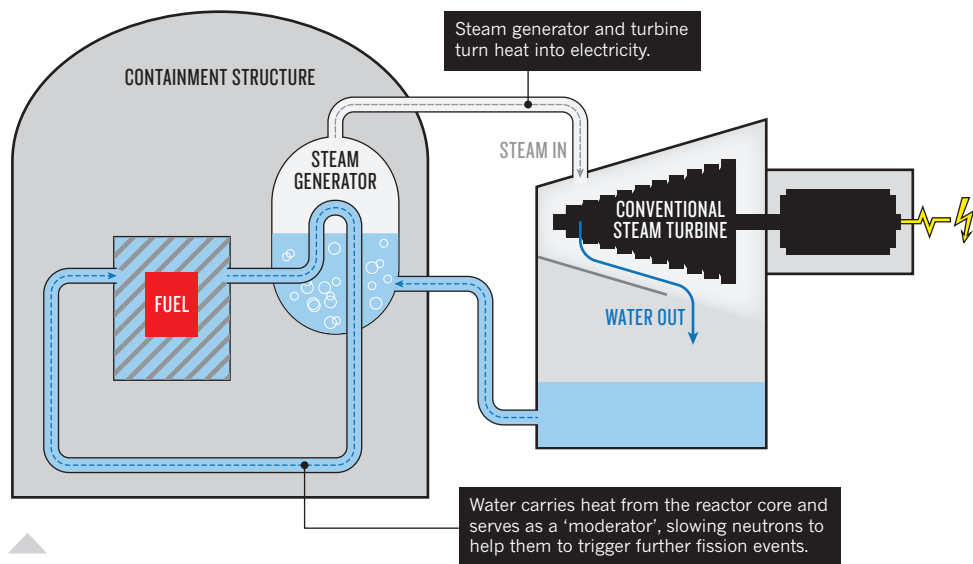
Prime candidates for slide-in modules are high-temperature reactors, which do exactly

could consume the stuff, turning waste into energy and easing the disposal problem.

Fission neutrons are ‘fast’ when they have just emerged from newly split nuclei at a mean energy of roughly 2 million electronvolts. In light-water reactors, collisions with the hydrogen nuclei in the coolant water quickly slow the neutrons to just a fraction of an electron volt, which makes them more likely to trigger another fission reaction. But slow neutrons have a drawback: instead of splitting the target uranium nuclei, they often get absorbed, transforming the nuclei into long-lived isotopes of plutonium, neptunium, americium, curium or other heavy elements — the ones

THE NUTS AND BOLTS OF NUCLEAR

All nuclear reactors rely on fission to make heat, which can be used for generating electricity. But engineers have come up with many alternatives to the commonly used light-water reactor.



LIGHT-WATER NUCLEAR REACTORS

This design, dating from the 1940s–50s, currently dominates the nuclear industry.

- **FUEL:** URANIUM OXIDE ENCASED IN ZIRCONIUM METAL
- **COOLANT:** ORDINARY WATER
- **MODERATOR:** WATER

is stable — and trying to convince regulators that even the worst meltdown won't allow any part of the fuel to collapse into a critical mass.

But all these concerns go away when the fuel is already a liquid — one major reason why Oak Ridge wanted to develop the molten-salt reactor back in the 1960s. 'Molten-salt' refers to the fuel, usually uranium tetrafluoride, which is liquid at operating temperatures when blended with 'FLiBe': a mixture of lithium fluoride and beryllium fluoride that serves as a coolant. "It's a pot — a big, dumb, pot," says Forsberg. "You throw fuel in, it's mixed, and the overall composition changes not at all."

Liquid fuel has another big advantage, says Sorensen: "You don't have to remove it from the reactor until it's completely consumed." Instead, the fuel is circulated through an external recycling unit that extracts the fission products continuously, keeping the fuel from being poisoned. The design also allows for an elegant approach to safety, says Sorensen: at the bottom of the reactor is a hole, plugged with a chunk of fuel that is kept solid by a refrigeration unit. If the reactor loses power in an emergency, the refrigeration will cease, the plug will melt and the fuel will safely drain into underground holding tanks. Finally, the molten-salt design can accommodate a variety of fuels, ranging from conventional uranium to raw nuclear waste or thorium — an element that is roughly three times more abundant than uranium.

For all of that, reviving the molten-salt

reactor after a four-decade hiatus is a daunting task. "We have to rebuild a knowledge base that has largely gone away," says Sorensen. He founded FLiBe Energy to try, though. The company is developing a 40-megawatt reactor that might be used on military bases so that they can operate independently of the grid.

SOLID CHANCE

In September 2011, Forsberg, Peterson, MIT's Lin-wen Hu and Todd Allen, a nuclear engineer at the University of Wisconsin-Madison, became principal investigators on a 3-year, DOE-funded project that could be a step on the way to the molten-salt reactor: a FLiBe-cooled high-temperature reactor. "No one has ever built a salt-cooled solid-fuel reactor," says Peterson. But if the project works, the reactor core could be four to five times smaller than those in other designs and, because of the stability of the FLiBe salt, it would "always be hundreds of degrees below the failure limits," he says.

Peterson says that the company could have a test reactor within a decade, although "that assumes abundant resources". That is a big assumption: the global economic crisis has made financing for all advanced reactors much harder to come by. Furthermore, notes Corradini, pointing to the sudden abundance of shale gas in the United States, "cheap fossil fuels have postponed many of the clean-energy projects in the United States, not just nuclear".

Paul Genoa, director of policy development

ADVANCED REACTORS

These decades-old reactor designs have been revived and modernized in recent years.

HIGH-TEMPERATURE REACTORS

Deliver heat at up to 950 °C for industry, cutting carbon emissions.

- URANIUM OXIDE/CARBIDE MIX COATED WITH SILICON CARBIDE; STABLE TO 1,600 °C
- HELIUM GAS OR FLIBE (MIXTURE OF LITHIUM FLUORIDE AND BERYLLIUM FLUORIDE)
- GRAPHITE

FAST REACTORS

Use unmoderated 'fast' neutrons to burn up heavy elements in spent nuclear fuel.

- METALLIC OR CERAMIC-CLAD URANIUM
- HELIUM GAS; LIQUID SODIUM METAL; MOLTEN LEAD; OR MOLTEN LEAD-BISMUTH MIX
- NONE

MOLTEN-SALT REACTORS

Use liquid fuel to increase safety and minimize long-term nuclear wastes.

- URANIUM OR THORIUM FLUORIDE
- FLIBE
- GRAPHITE

for the Nuclear Energy Institute trade group in Washington DC, takes the long view. "We did the light-water reactors first, to get going," he says. Next, in the 2020s, will come advanced light-water reactors for increased safety, followed closely by high-temperature reactors that expand the attack on carbon emissions. "And then we build fast reactors to consume the waste."

Molten-salt reactors are something of a wild card, says Genoa, but are worth developing. Some even wilder cards are under investigation: one notable example is the accelerator-driven reactor, which would drive fission reactions using neutrons from a high-energy particle accelerator. It could be fuelled with thorium, and shut down instantly by switching off the accelerator.

But will nuclear energy really evolve? Those in the field see reason for optimism, particularly if the increasingly tangible consequences of climate change force governments to put a price on carbon. Even the Fukushima disaster could ultimately spur new nuclear technologies, says Genoa. "It scared people and made them concerned about nuclear energy," he says. But as people looked more closely, "they said, 'Hey, those were 30-year-old plants'". In time, he says, smart, new reactors will look a whole lot more appealing. ■ [SEE COMMENT P.31](#)

M. Mitchell Waldrop is a features editor for *Nature* in Washington DC.

COMMENT

GRANTS Analysis probes whether NIH is funding the most-cited work **p.34**

BIOGRAPHY A life of Dorothy Winch, the fourth woman of crystallography **p.37**

Q&A Photographer who chronicles vanishing ice **p.40**



OBITUARY Farish A. Jenkins Jr, palaeontologist, explorer and artist, remembered **p.42**

PALLAVA BAGLA/CORBIS



Thorium dioxide pellets could be the nuclear fuel of the future if proliferation concerns can be addressed.

Thorium fuel has risks

Simple chemical pathways open up proliferation possibilities for the proposed nuclear ‘wonder fuel’, warn **Stephen F. Ashley** and colleagues.

Thorium is being touted as a potential wonder fuel. Proponents believe that this element could be used in a new generation of nuclear-power plants to produce relatively safe, low-carbon energy with more resistance against potential nuclear-weapons proliferation than uranium. Although thorium offers some benefits, we contend that the public debate is too one-sided: small-scale chemical reprocessing of irradiated thorium can create an isotope of uranium that could be used in nuclear weapons, raising proliferation concerns.

Global stocks of thorium are uncertain, but the element is thought to be three to four times more naturally abundant than uranium

(see ‘World thorium deposits’). The silver-white metal is often encountered as oxide waste from the mining of rare-earth elements, and substantial thorium deposits are found in Australia, Brazil, Turkey, Norway, China, India and the United States. The last three of these, together with the United Kingdom, are exploring the potential use of thorium in civil nuclear-energy programmes.

One of many voices proposing the deployment of new thorium-based molten salt reactors (see page 26) is the Weinberg Foundation, a non-profit organization based in London that promotes thorium-fuelled technologies to combat climate change. Molten salt reactors were developed in the 1960s and

use liquid nuclear fuels, that can incorporate thorium, rather than solid fuel rods. They are claimed to be more efficient and less susceptible to meltdown-related accidents than existing technologies. Small modular reactors, such as high-temperature gas-cooled reactors that use solid thorium-based fuels, are also being pursued, most notably by China.

Naturally-occurring thorium is made up almost entirely of thorium-232, an isotope that is unable to sustain nuclear fission. When bombarded with neutrons, thorium is converted through a series of decays into uranium-233, which is fissile and long-lived — its half-life is 160,000 years. A side product is uranium-232, which decays into other

► isotopes that give off intense γ -radiation that is difficult to shield against. Spent thorium fuel is typically difficult to handle and thus resistant to proliferation.

We are concerned, however, that other processes, which might be conducted in smaller facilities, could be used to convert ^{232}Th into ^{233}U while minimizing contamination by ^{232}U , thus posing a proliferation threat. Notably, the chemical separation of an intermediate isotope — protactinium-233 — that decays into ^{233}U is a cause for concern.

Thorium is not a route to a nuclear future that is free from proliferation risks. Policies should be strengthened around thorium's use in declared nuclear activities, and greater vigilance is needed to protect against surreptitious activities involving this element.

PROTACTINIUM PATHWAY

The decay path of thorium is well understood. If bombarded with neutrons, isotopically pure ^{232}Th forms ^{233}Th , which has a half-life of 22 minutes and β -decays to ^{233}Pa . That isotope has a half-life of 27 days and β -decays to ^{233}U , which can undergo fission. The International Atomic Energy Agency (IAEA) considers 8 kilograms of ^{233}U to be enough to construct a nuclear weapon¹. Thus, ^{233}U poses proliferation risks.

Although ^{233}U is not used today in commercial reactors, the United States accumulated two tonnes of it during the cold war. Plans to dispose of much of it by burial are controversial and pose security and safety risks, according to a 2012 report².

The chemical reprocessing needed to separate ^{233}U from spent nuclear fuel requires major infrastructure, such as large

reprocessing plants, which are difficult to hide. With thorium fuel, the presence of highly radiotoxic ^{232}U means that the spent fuel must be handled using remote techniques in heavily-shielded containment chambers.

After irradiating thorium with neutrons for around one month, chemical separation of ^{233}Pa could yield minimal ^{232}U contamination, making the ^{233}U -rich product easier to handle. If pure ^{233}Pa can be extracted, then it merely needs to be left to decay to produce pure ^{233}U . The problem is that neutron irradiation of ^{232}Th could take place in a small facility, such as a research reactor, of which around 500 exist worldwide. The ^{232}Th need not be part of a nuclear-fuel assembly nor be involved in energy generation.

It has been demonstrated that around 200 g of thorium metal could produce 1 g of ^{233}Pa — and hence 1 g of ^{233}U — if exposed to neutrons at levels typically found in power reactors and some research reactors for a month, followed by protactinium separation³. Thus, only 1.6 tonnes of thorium metal would be required to produce the 8 kg of ^{233}U required for a weapon. This amount of ^{233}U could feasibly be obtained by this process in less than a year.

The separation of protactinium from thorium is not new. We highlight two well-known chemical processes — acid-media techniques^{3,4} and liquid bismuth reductive extraction^{5–7} (see 'Ways to obtain pure protactinium') — that are causes for concern, although there may be others. Both methods use standard nuclear-lab equipment and hot cells — containment chambers in which highly radioactive materials can be manipulated safely. Such apparatus is not

necessarily subject to IAEA safeguards.

The most common acid-media technique uses manganese dioxide to precipitate the protactinium as protactinium oxide⁴. Any radiotoxic uranium by-products are dissolved in acid and removed during the precipitation. This method was used in the 1960s by researchers at Oak Ridge National Laboratory in Tennessee to extract 1 g of ^{233}Pa from 200 g of an irradiated thorium compound³.

The main difficulty is that β -decay from each gram of ^{233}Pa produces 50 watts of heat³, which complicates the handling. Scaling up the production of ^{233}Pa would not be easy, but given the possibility of parallel processing of small quantities, our concerns over this technique remain.

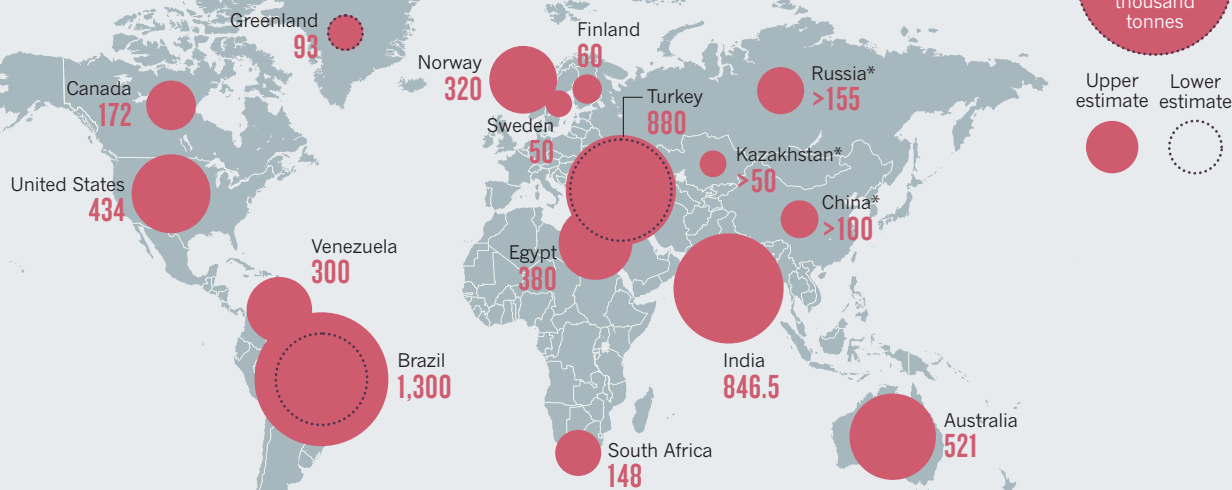
A second chemical method, suggested in the 1970s (refs 5,7), is being revisited for next-generation molten salt reactors (see, for example, ref. 8). These use thorium-based liquid fuels containing a fluoride-based salt with the typical composition $^7\text{LiF}-\text{BeF}_2-\text{ThF}_4-\text{UF}_4$. The process is pyrochemically based, using high temperature oxidation-reduction reactions. It involves first fluorination and then extraction using molten bismuth to obtain protactinium.

The infrastructure for pyrochemistry is more complex than for acid-media techniques, and scaling it up is even more challenging. Pyrochemical reprocessing technologies are in their infancy. But we are concerned that such a technique could be used in small batches⁹ to slowly accumulate protactinium.

Given the need for access to a research or power reactor to irradiate thorium, the most likely security threat stems not from terrorist

WORLD THORIUM DEPOSITS

Thorium oxides, silicates and phosphates are found worldwide, often alongside rare-earth elements. Thorium is not yet mined commercially, and abundances are only approximately known in most countries. Numbers show upper estimates of identified thorium reserves (in thousand tonnes).



*Upper estimate not known.

SOURCE: URANIUM 2011: RESOURCES, PRODUCTION AND DEMAND (OECD NEA/IAEA, 2012).

THORIUM CHEMISTRY

Ways to obtain pure protactinium

Acid-media techniques

After irradiating thorium-based materials for one month, the canisters are removed and dissolved in nitric acid^{3,4}. The resultant sludge goes through three stages of filtration. Protactinium is separated during the second stage, by co-precipitation with MnO₂ (ref. 3). It is separated further in the third stage using iodic acid and combustion to form protactinium oxide, containing only ²³³Pa. Any traces of ²³²Pa (half-life of 1.3 days) and ²³⁴Pa (half-life of 6.7 hours), formed by competing reactions, decay to ²³²U and ²³⁴U during the dissolution stage, in which they are removed. Left to decay, ²³³Pa becomes ultra-pure (>99%) ²³³U.

Liquid bismuth reductive extraction

Fluorine is passed over the irradiated molten-salt fuel⁶ to convert approximately 99% of the uranium to UF₆, which can then be removed⁵⁻⁷. The remaining protactinium, fission products and unreacted uranium are fed into a column containing liquid bismuth, lithium and thorium. The fission products are retained in the salt, and the protactinium and uranium are extracted in the liquid bismuth. Further fluorination of the bismuth removes the remaining uranium, including ²³²U, ²³⁴U and other isotopes. The ²³³Pa left behind is highly pure and decays into ²³³U.

organizations but from wilful proliferating nation states. We have three main concerns:

First, nuclear-energy technologies that involve irradiation of thorium fuels for short periods could be used covertly to accumulate quantities of ²³³U by parallel or batch means, perhaps without raising IAEA proliferation flags.

Second, the infrastructure required to undertake the chemical partitioning of protactinium could be acquired and established surreptitiously in a small laboratory.

Third, state proliferators could seek to use thorium to acquire ²³³U for weapons production. These three points should be included in debates on the proliferation attributes of thorium.

MONITORING THORIUM

The emergence of thorium technologies will bring problems as well as benefits. There is a need for appropriate monitoring of thorium-related nuclear technologies within declared and undeclared facilities. The IAEA and the Nuclear Suppliers Group, the group of countries that controls nuclear exports, have a role to play in observing such developments.

Steps are needed to control the short-term irradiation of thorium-based materials with neutrons. Similarly, civil nuclear-fuel cycles involving in-plant reprocessing of thorium-based fuels should be avoided.

Hot cells are a key technology in protactinium separation. The Additional Protocol of the Nuclear Non-Proliferation Treaty¹⁰ requires disclosure of large hot-cell facilities. The associated size cut-off is potentially important with protactinium pathways in mind. We are comforted that large hot-cell facilities are treated by the IAEA as nuclear technologies that can be 'dual use' for military or peaceful purposes, but concerns will always remain about hidden undeclared facilities.

Thorium is not as benign as has been suggested and we call for greater debate on its associated risks. In this way, a safer nuclear future can be assured. ■

Stephen F. Ashley is a research associate and **Geoffrey T. Parks** is a senior lecturer in nuclear engineering in the Department of Engineering, University of Cambridge, Cambridge, UK. **William J. Nuttall** is professor of energy in the Department of Design, Development, Environment and Materials, The Open University, Milton Keynes, UK. **Colin Boxall** is director of Energy Lancaster, Engineering Department, Lancaster University, Lancaster, UK. **Robin W. Grimes** is director of materials physics at the Centre for Nuclear Engineering, Imperial College London, London, UK.
e-mail: sfa24@cam.ac.uk

1. International Atomic Energy Agency. *IAEA Safeguards Glossary 2001 Edition* (IAEA, 2002)
2. Alvarez, R. *Managing the Uranium-233 Stockpile of the United States* (Institute for Policy Studies, 2012); available at <http://go.nature.com/6exukv>.
3. Coddling, J. W., Berreth, J. R., Schuman, R. P., Burgus, W. H. & Deal, R. A. *Separation and Purification of a Gram of Protactinium-233* Atomic Energy Commission Report IDO 17007 (1964).
4. Katzin, L. I. & Stoughton, R. W. J. *Inorg. Nucl. Chem.* **3**, 229–232 (1956).
5. McNeese, L. E., Ferris, L. M. & Nicholson, E. L. *Molten-Salt Breeder Reactor Fuel Processing* Oak Ridge National Laboratory Technical Report No. CONF-720522-3 (1972).
6. Whatley, M. E., McNeese, L. E., Carter, W. L., Ferris, L. M. & Nicholson, E. L. *Nucl. Appl. Technol.* **8**, 170–178 (1970).
7. Shaffer, J. H., Moulton, D. M. & Grimes, W. R. US Patent 3,577,225 (1971).
8. Delpech, S. *et al. J. Fluorine Chem.* **130**, 11–17 (2009).
9. Grimes, W. R., Moulton, D. M. & Shaffer, J. H. US Patent 3,495,975 (1970).
10. International Atomic Energy Agency. *Model Protocol Additional to the Agreement(s) between State(s) and the International Atomic Energy Agency for the Application of Safeguards* INFCIRC/540/Corr (IAEA, 1997).



ILLUSTRATION BY PHIL DISLEY

Conform and be funded

Too many US authors of the most innovative and influential papers in the life sciences do not receive NIH funding, contend **Joshua M. Nicholson** and **John P. A. Ioannidis**.

The US National Institutes of Health (NIH) is the largest funder of biomedical research in the world. Between 2002 and 2011, it issued around 460,000 research grants totalling almost US\$200 billion. The NIH has unquestionably propelled numerous medical advances and scientific breakthroughs, and its funding makes much of today's scientific research possible¹.

However, concern is growing in the scientific community that funding systems based on peer review, such as those currently used by the NIH, encourage conformity if not mediocrity, and that such systems may ignore truly innovative thinkers^{2–4}. One tantalizing question is whether biomedical researchers who do the most influential scientific work get funded by the NIH.

The influence of scientific work is difficult to measure, and one might have

to wait a long time to understand it⁵. One proxy measurement is the number of citations that scientific publications receive⁶. Using citation metrics to appraise scientists and their work has many pitfalls⁷, and ranking people on the basis of modest differences in metrics is precarious. However, one uncontested fact is that highly cited papers (and thus their authors) have had a major influence, for whatever reason, on the evolution of scientific debate and on the practice of science.

To explore the link between highly cited research and NIH funding, we evaluated scientists who have published papers since 2001 — as first, last or single authors — that have so far received 1,000 citations or

more. We found that three out of five authors of these influential papers do not currently have NIH funding as principal investigators. Conversely, we found that a large majority of the current members of NIH study sections — the people who recommend which grants to fund — do have NIH funding for their work irrespective of their citation impact, which is typically modest.

There are probably many reasons why highly cited scientists do not have current funding. They might have changed careers or moved to industry, for instance. Perhaps they are receiving some funding as co-investigators, or are still young and have just started their own lab. But the NIH's mandate is to fund "the best science, by the best scientists" — regardless of age or employment sector. We think our findings suggest that this aim is not being met.

NATURE.COM

For more on
NIH research
funding, see:
go.nature.com/vv52yf

To ensure that we captured people who were eligible for NIH funding, we focused on scientists in the life and health sciences whose affiliation address was in the United States. We aimed to assess whether these scientists currently receive NIH funding as principal investigators using information from the NIH RePORTER website. (For detailed methods, see Supplementary Information at go.nature.com/uo8jbp.)

Of the more than 20 million papers published worldwide between 2001 and 2012 and catalogued by the Scopus database, 1,380 had received 1,000 citations or more as of April 2012. Of those 1,380 papers, 700 were catalogued in the life or health sciences and had an author affiliation in the United States. These 700 papers had a total of 1,172 discrete single, first or last authors.

SELECTION CRITERIA

We stratified eligible authors of extremely highly cited papers according to whether or not they were current members of NIH study sections. This was because the NIH policy is to invite principal investigators of funded projects to become members of study sections (see go.nature.com/kgtrlm).

We also wanted to look closely at members of NIH study sections because these scientists are arguably the most influential group in the grant-funding process. Studying their track records and impact could reveal problems or discrepancies in that process.

We discovered that serving on a study section is not necessarily tied to impact in the scientific literature. (see 'Is funding tied to impact?'). When we cross-checked the NIH study-section rosters against the list of 1,172 authors of highly cited papers, we found only 72 US-based authors who between them had published 84 eligible articles with 1,000 or more citations each and who were current members of an NIH study section. These 72 authors comprised 0.8%

of the 8,517 study-section members. Most of the 72 ($n=64$, 88.9%) currently received NIH funding.

We then randomly selected 200 eligible life- and health-science papers with 1,000 or more citations (analysing all 700 would have required intensive effort and yielded no extra information in terms of statistical efficiency). We excluded those in which the single, first or last author was a member of an NIH study section, and those in which the single or both the first and last author were not located in the United States on the basis of their affiliations at the time of publication. This generated a group of 158 articles with 262 eligible US authors who did not participate in NIH study sections. Only the minority ($n=104$, 39.7%) of these 262 authors received current NIH funding.

The rate of NIH funding among highly cited researchers is not much better and may be worse than that of biomedical scientists in general. Annual data for the years 2001–11 suggest that 24–37% of biomedical scientists who applied for grants were funded as principal investigators (these rates even exclude some types of grants; see go.nature.com/gohji3). The acceptance rates for individual grants are substantially lower, but if one allows for several grants submitted and for several years of submissions, a sizeable portion of general applicants — if not the majority — probably end up being awarded at least one grant.

Among authors of extremely highly cited papers, study-section members and non-members showed no significant difference in their total number of highly cited papers, despite the fact that members of study sections were significantly more likely than

non-members to have current NIH funding. This was true both for authors with multiple highly cited papers (13/13 versus 13/19, $p=0.024$) and for those with a single eligible highly cited paper (51/59 versus 91/243, $p<0.0001$) and overall in a stratified analysis ($p<0.0001$).

FAMILIAR STORY

One can also examine the similarity between different grants by using a similarity ('match') score provided by NIH RePORTER. To calculate the match score, a fingerprint is created of each grant that contains its key terms, weighted by how frequently they appear in the grant. That fingerprint can then be compared against the fingerprints of other grants.

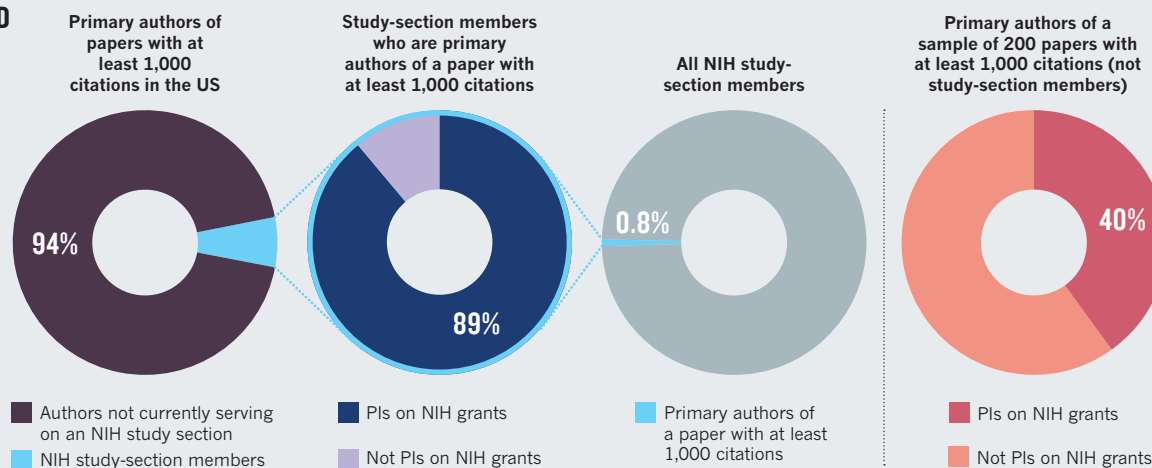
We found that the grants of study-section members were more similar to other currently funded NIH grants than were non-members' grants (median score 421.9 versus 387.6, $p=0.039$). This could suggest that study-section members fund work that is more similar to their own, or that they are chosen to serve as study-section members because of similarities between their own and funded grants.

If NIH study-section members are well-funded but not substantially cited, this could suggest a double problem: not only do the most highly cited authors not get funded, but worse, those who influence the funding process are not among those who drive the scientific literature. We thus examined a random sample of 100 NIH study-section members. Not surprisingly, 83% were currently funded by the NIH. The citation impact of the 100 NIH study-section members was usually good or very good, but not exceptional: the most highly cited paper they had ever published as single, first or last author had received a median of 136 (90–229) citations and most were already mid- or late-career researchers (80% were associate or full

"There are probably many reasons why highly cited scientists do not have current funding."

IS FUNDING TIED TO IMPACT?

Most single or first or last (primary) authors of papers with at least 1,000 citations were not current principal investigators (PIs) on NIH grants. NIH study-section members largely had funding, yet few seem to have authored an extremely highly cited paper.



professors). Only 1 of the 100 had ever published a paper with 1,000 or more citations as single, first or last author (see Appendix 1 of Supplementary Information for additional citation metrics).

This overall picture (see 'Is funding tied to impact?') might, in part, be explained by the NIH policy to try to recruit reviewers who are successful in securing grants (see go.nature.com/kgtrlm). Even so, it is worrying that the majority of highly cited investigators do not have current NIH funding as principal investigators.

This does not mean that these investigators are not funded at all. Moreover, it is impossible to tell whether these investigators have chosen not to seek funding from the NIH (for example, if they did not like the agency's funding process or had left science) or if they have sought funding and been repeatedly rejected.

FUNDING PROBE

To investigate a little, a *Nature* editor contacted a sample of highly cited investigators who are not currently listed as principal investigators on NIH grants. She found that there were many reasons why these scientists were not currently funded by the NIH. In some cases, they had applied for NIH grants but had been unsuccessful. In others, the researchers were graduate students at the time of the high-impact publication, so had just started their own labs (the average age for being awarded a first NIH grant as primary investigator is 44 years).

Some had moved into industry or changed fields entirely (becoming a venture capitalist, for instance). One had retired; another was receiving some NIH funding as a co-investigator but was not listed as a principal investigator, so did not appear in our search. Future samples might also have to account for an increasing number of highly collaborative papers for which the first and last authors are not principal investigators, but this was not a prominent issue in this sample.

Although it might seem as if these explanations suggest that highly cited researchers are not lacking support, we maintain our concerns. The mission of the NIH is to support the best scientists, regardless of whether they are young, old or in industry. If they have left academia — or moved out of research entirely — it could suggest that these authors of high-impact work did not want to continue the struggle for federal funding. Such innovative thinkers should not have so much trouble obtaining funding as principal investigators. One cannot assume that investigators who have authored highly cited papers will continue to do equally influential work in the future. However, a record of excellence may be the best predictor of future quality, and it would seem appropriate to give these scientists the

opportunity of funding for their projects.

We feel that by allowing grant holders to serve as grant reviewers, a conflict of interest becomes inescapable. Exceptional creative ideas may have difficulty surviving in such a networked system. Scientists who think creatively may be discouraged by the funding process and outcomes, or might not have time to contribute as reviewers to a process that is arduous and not perfectly meritocratic. Not surprisingly, although NIH funding has been instrumental in maintaining and expanding the biomedical research endeavour, there are many examples of major scientific discoveries, including Nobel prizes, that emerged from unfunded work¹.

More alternative funding modes should be tested in pilot schemes and in experimental controlled studies of optimizing funding processes. For example, the American Cancer Society uses impartial laymen known as stakeholders in their grant reviews to limit bias, which may reduce the influence of strongly opinionated group members⁸ (see go.nature.com/iosnre). Using non-experts or experts from different scientific fields in the study sections could also help to reduce the impact of a vocal minority^{4,9}.

Serious consideration should be given to increasing funding for investigators of outstanding ability who have already proved that they can accomplish something major; for example, as judged by extreme citation impact. Such investigators could be funded by processes analogous to those of the Howard Hughes Medical Institute or the NIH MERIT awards, without having to submit grant proposals or, as is currently done, by calling for proposals that present only broad goals.

Funding all scientists who are key authors of unrefuted papers that have 1,000 or more citations would be a negligible amount in the big picture of the NIH budget, simply because there are very few such people. This could foster further important discoveries that would otherwise remain unfunded in the current system. ■

Joshua M. Nicholson is in the Department of Biological Sciences, Virginia Tech, Blacksburg, Virginia, USA. **John P. A. Ioannidis** is at the Stanford Prevention Research Center, Stanford, California, USA. e-mail: jioannid@stanford.edu

1. Tatsioni, A., Vavva, E. & Ioannidis, J. P. *FASEB J.* **24**, 1335–1339 (2010).
2. Horrobin, D. F. *Lancet* **348**, 1293–1295 (1996).
3. Ioannidis, J. P. *Nature* **477**, 529–531 (2011).
4. Nicholson, J. M. *BioEssays* **34**, 448–450 (2012).
5. Young, N. S., Ioannidis, J. P. A. & Al-Ubaydli, O. *PLoS Med.* **5**, e201 (2008).
6. Garfield, E. *Citation Indexing: Its Theory and Application in Science, Technology, and Humanities* (Wiley, 1979).
7. Kelly, C. D. & Jennions, M. D. *Trends Ecol. Evol.* **21**, 167–170 (2006).
8. Couzin, I. D. et al. *Science* **334**, 1578–1580 (2011).
9. Horrobin, D. F. *New Sci.* **94**, 842–844 (1982).



Dorothy Wrinch (right) with her model of protein structure in 1938.

X-RAY CRYSTALLOGRAPHY

Symmetry wars

Philip Ball is gripped by the life of a remarkable scientist whose flawed theory dented her reputation.

X-ray crystallography and the study of biomolecular structure was one of the first fields of modern science in which women scientists came to the fore. Dorothy Crowfoot Hodgkin, Rosalind Franklin and Kathleen Lonsdale are the best known of the women who made major contributions in the face of casual discrimination and condescension. In *I Died for Beauty*, Marjorie Senechal suggests that there was nearly a fourth: Dorothy Wrinch, a name that few now recognize and that is often derided by those who do.

The late protein chemist Charles Tanford, for instance, poured scorn on Wrinch's best-known work, the 'cyclol theory' of protein structure, proposed in the 1930s. It was, he said, "not really worth more than a footnote... a theory built on nothing". Of Wrinch herself, he proclaimed "she was arrogant and felt persecuted when criticized, but in retrospect her miseries seem self-inflicted".

In a bid to rebalance such attacks, Senechal, co-editor of the journal *The Mathematical Intelligencer* — for whom Wrinch was a mentor at Smith College in Northampton,

Massachusetts — has written a sympathetic apologia. And whatever one feels about Wrinch and her research, she is a fascinating subject. Her circle of friends, colleagues and correspondents included many of the luminaries of early twentieth-century science and philosophy.

Wrinch, a Cambridge-trained mathematician, was the first woman to earn an Oxford DSc, in 1929. A student of Bertrand Russell, she was championed by D'Arcy Thompson and Irving Langmuir, worked alongside Robert Robinson, and knew Niels Bohr, G. H. Hardy, Kurt Gödel and John von Neumann. Several of them considered her brilliant. Calling for mathematicians to interest themselves in biology, Thompson wrote in 1931, "I do not know of anyone... so well qualified as Dr Wrinch." The polymathic mathematician and geophysicist Harold Jeffreys developed some of his ideas on statistical reasoning in collaboration with Wrinch at Cambridge, and wrote in *Nature* in 1976 of "the substantial contribution she

made to this work, which is the basis of all my later work on scientific inference".

Senechal's central question is: what went wrong? Why did an apparently so promising figure, a member of the pioneering Theoretical Biology Club that included Joseph Needham, J. Desmond Bernal and Conrad Waddington, end up relegated to obscurity?

The too-easy answer is: Linus Pauling. When, in a 1939 paper, Pauling comprehensively destroyed Wrinch's cyclol theory — which argued that globular proteins are polyhedral shells, in which amino acids link into a lattice of hexagonal rings — he also finished her career.

But a more complex reason for Wrinch's downfall emerges as the story unfolds. Part of her undoing was her magpie mind. Seemingly unable to decide how to use her substantial abilities, Wrinch never really made important contributions to one area before flitting to another — from Bayesian statistics to seismology, topology to mitosis. Warren Weaver, the astute director for natural sciences at the Rockefeller Foundation in New York, which funded Wrinch for some years, described her as "a queer fish, with a kaleidoscopic pattern of ideas, ever shifting and somewhat dizzying. She works, to a considerable extent, in the older English way, with heavy dependence on 'models' and intuitive ideas."

Senechal presents a selection of opinions that the foundation collected on Wrinch while assessing her funding application, many deeply unflattering: she is a fool; she is mad or 'preachy'; she dismisses facts that don't fit and poaches others' ideas. Frustratingly, we're left to decide for ourselves how much of this is justified, but the evidence for a problematic personality piles up.

She had a talent for making enemies. "Everyone in England in or near the protein field is more than antagonistic to her," said one of the Rockefeller interviewees. Bernal was incensed when Wrinch tried to argue that the diffraction data obtained by his student Hodgkin supported her cyclol theory — an assertion that was sloppy at best, and perhaps dishonest. In retaliation, Wrinch called Bernal "jealous, brutal and treacherous". (Hodgkin was charitably forgiving.)

Underlying all of this is the position of Wrinch as a female scientist. Like many educated women of the 1930s, Wrinch felt motherhood as a burden and barrier that only extreme measures could relieve. Her eugenic inclinations and call, in her pseudonymous *The Retreat from Parenthood* (1930),



I Died for Beauty: Dorothy Wrinch and the Cultures of Science

MARJORIE SENECHAL
Oxford Univ. Press:
2012. 312 pp. \$34.95

"Wrinch never really made important contributions to one area before flitting to another."

➔ **NATURE.COM**
Georgina Ferry
discusses Dorothy
Hodgkin:
go.nature.com/dwljite

for a state-run child-rearing service that farmed out children to professional carers, reinforce the fact that Aldous Huxley was only writing what he heard. Alarming though her approach to parenting now sounds, it is shameful that the professional structures of science have hardly made it any easier for mothers some 80 years on.

Wrinch's central problem, it seems, was that, working at a time when most male scientists assumed that women thought differently from them, she seemed to conform to their stereotype: headstrong, strident and reliant on intuition rather than facts. But those complaints could also be made of Wrinch's arch-enemy Pauling: Senechal rightly observes that "Dorothy and Linus were more alike than either of them ever admitted". She sees injustice in the way Pauling's blunders, such as the denial of quasicrystals, were forgiven, whereas Wrinch's were not.

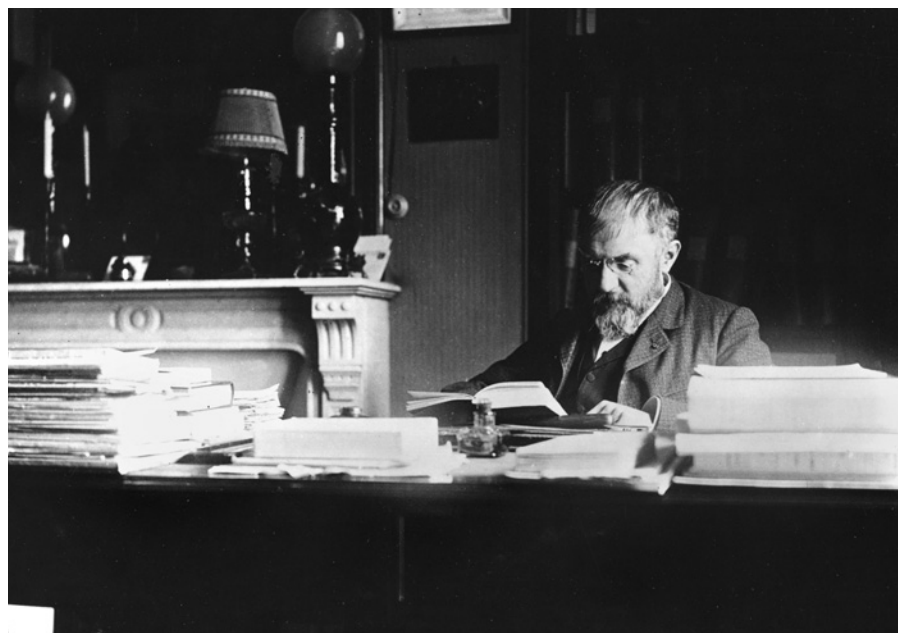
Did sexism play a part here? I think not. Unlike Wrinch, Pauling hit more than enough bullseyes to compensate for his errors. Nonetheless, Senechal's imagined scene of braying men and their snickering wives poring over Pauling's devastating paper has a depressing ring of truth.

Senechal's prose is mannered, but pleasantly so — a welcome alternative to chronological plod. Yet, primarily a mathematician herself, she doesn't always help the reader to understand what Wrinch was trying to do. Her interest in "the arrangement of genes on chromosomes" sounds tantalizingly modern, but it is impossible to figure out what Wrinch understood it to mean. Neither can one easily infer, from Senechal's criticisms of Pauling's attack, that the cyclol theory was way off beam even then. Tanford has pointed out that it predicted protein structures that were "sterically impossible" — the atoms just wouldn't fit (although cyclol rings have now been found in some natural products).

Fundamentally, Wrinch was in love with symmetry — to which the book's title, taken from the 1924 Emily Dickinson poem of the same name, alludes. It was this that drew her to crystallography, and her 1946 book *Fourier Transforms and Structure Factors* is still esteemed by some crystallographers today. But such Platonism can become a false refuge from the messiness of life, both in the biochemical and the personal sense.

It is tremendous that Senechal has excavated this story. She offers a gripping portrait of an era and of a scientist whose complications acquire a tragic glamour. It is a cautionary tale for which we must supply the moral ourselves. ■

Philip Ball is a writer based in London.
e-mail: p.ball@btinternet.com



Henri Poincaré posed a puzzle that remained unsolved for 99 years.

MATHEMATICS

Poet of the infinite

George Szpiro celebrates a biography of the multifaceted mathematician, physicist and philosopher Henri Poincaré.

Were it not for the Poincaré conjecture, it is doubtful whether many non-mathematicians today would know of Henri Poincaré. His vexed question in topology was solved only in 2003 — nearly a century after it was published and some years after its conqueror, Russian mathematician Grigori Perelman, began to unpick it. Perelman has vanished from public view. Poincaré remains a household name.

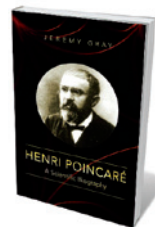
He was hardly unknown in his day. As John Gray recounts in his masterly *Henri Poincaré: A Scientific Biography*, Poincaré was one of France's great intellectuals in the late nineteenth and early twentieth centuries. When he died at just 58 in 1912, the French Minister of Education called him "a kind of poet of the infinite, a kind of bard of science", and his funeral cortège was a veritable who's who of the world's intellectual elite.

Poincaré was also a prodigiously versatile thinker. A brilliant mathematician, equalled in his time only by David Hilbert in Göttingen, Germany, Poincaré was also rightly considered a physicist and philosopher of science of the first order. Gray encapsulates Poincaré's multiple dimensions; his intellectual biography is both a tour de force and a triumph of readability. He leads us through Poincaré's life, and the vast array of subjects he touched on, covering practically the

entire corpus of what interested mathematicians and physicists at the turn of the twentieth century — from topology and algebraic geometry to Lie groups.

The field that Poincaré spawned is algebraic topology, which explores surfaces in higher-dimensional spaces using techniques from abstract algebra, the discipline concerned with mathematical structures. And, within topology, he formulated his conjecture.

Poincaré in fact posed a version of the conjecture four years before the one for which he is remembered: a theorem he decided to publish to "avoid making this work too prolonged", as he put it, with the promise of a proof to follow. Instead, he proved himself wrong by providing a counterexample. In 1904 he was much more cautious, and published the puzzle as a question. In essence, he asked whether a three-dimensional surface is equivalent to a three-dimensional sphere if rubber bands, wound around it, can be contracted, lasso-like, to a single point. He



**Henri Poincaré:
A Scientific
Biography**
JEREMY GRAY
Princeton Univ. Press:
2012. 616 pp. \$35

for a state-run child-rearing service that farmed out children to professional carers, reinforce the fact that Aldous Huxley was only writing what he heard. Alarming though her approach to parenting now sounds, it is shameful that the professional structures of science have hardly made it any easier for mothers some 80 years on.

Wrinch's central problem, it seems, was that, working at a time when most male scientists assumed that women thought differently from them, she seemed to conform to their stereotype: headstrong, strident and reliant on intuition rather than facts. But those complaints could also be made of Wrinch's arch-enemy Pauling: Senechal rightly observes that "Dorothy and Linus were more alike than either of them ever admitted". She sees injustice in the way Pauling's blunders, such as the denial of quasicrystals, were forgiven, whereas Wrinch's were not.

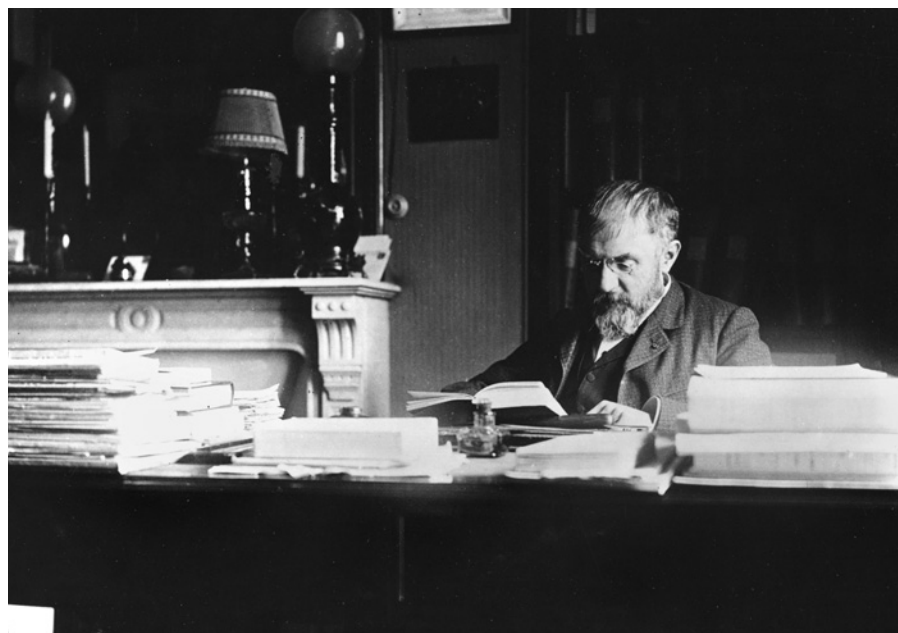
Did sexism play a part here? I think not. Unlike Wrinch, Pauling hit more than enough bullseyes to compensate for his errors. Nonetheless, Senechal's imagined scene of braying men and their snickering wives poring over Pauling's devastating paper has a depressing ring of truth.

Senechal's prose is mannered, but pleasantly so — a welcome alternative to chronological plod. Yet, primarily a mathematician herself, she doesn't always help the reader to understand what Wrinch was trying to do. Her interest in "the arrangement of genes on chromosomes" sounds tantalizingly modern, but it is impossible to figure out what Wrinch understood it to mean. Neither can one easily infer, from Senechal's criticisms of Pauling's attack, that the cyclol theory was way off beam even then. Tanford has pointed out that it predicted protein structures that were "sterically impossible" — the atoms just wouldn't fit (although cyclol rings have now been found in some natural products).

Fundamentally, Wrinch was in love with symmetry — to which the book's title, taken from the 1924 Emily Dickinson poem of the same name, alludes. It was this that drew her to crystallography, and her 1946 book *Fourier Transforms and Structure Factors* is still esteemed by some crystallographers today. But such Platonism can become a false refuge from the messiness of life, both in the biochemical and the personal sense.

It is tremendous that Senechal has excavated this story. She offers a gripping portrait of an era and of a scientist whose complications acquire a tragic glamour. It is a cautionary tale for which we must supply the moral ourselves. ■

Philip Ball is a writer based in London.
e-mail: p.ball@btinternet.com



Henri Poincaré posed a puzzle that remained unsolved for 99 years.

MATHEMATICS

Poet of the infinite

George Szpiro celebrates a biography of the multifaceted mathematician, physicist and philosopher Henri Poincaré.

Were it not for the Poincaré conjecture, it is doubtful whether many non-mathematicians today would know of Henri Poincaré. His vexed question in topology was solved only in 2003 — nearly a century after it was published and some years after its conqueror, Russian mathematician Grigori Perelman, began to unpick it. Perelman has vanished from public view. Poincaré remains a household name.

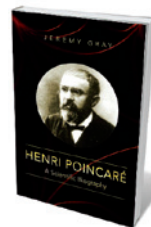
He was hardly unknown in his day. As John Gray recounts in his masterly *Henri Poincaré: A Scientific Biography*, Poincaré was one of France's great intellectuals in the late nineteenth and early twentieth centuries. When he died at just 58 in 1912, the French Minister of Education called him "a kind of poet of the infinite, a kind of bard of science", and his funeral cortège was a veritable who's who of the world's intellectual elite.

Poincaré was also a prodigiously versatile thinker. A brilliant mathematician, equalled in his time only by David Hilbert in Göttingen, Germany, Poincaré was also rightly considered a physicist and philosopher of science of the first order. Gray encapsulates Poincaré's multiple dimensions; his intellectual biography is both a tour de force and a triumph of readability. He leads us through Poincaré's life, and the vast array of subjects he touched on, covering practically the

entire corpus of what interested mathematicians and physicists at the turn of the twentieth century — from topology and algebraic geometry to Lie groups.

The field that Poincaré spawned is algebraic topology, which explores surfaces in higher-dimensional spaces using techniques from abstract algebra, the discipline concerned with mathematical structures. And, within topology, he formulated his conjecture.

Poincaré in fact posed a version of the conjecture four years before the one for which he is remembered: a theorem he decided to publish to "avoid making this work too prolonged", as he put it, with the promise of a proof to follow. Instead, he proved himself wrong by providing a counterexample. In 1904 he was much more cautious, and published the puzzle as a question. In essence, he asked whether a three-dimensional surface is equivalent to a three-dimensional sphere if rubber bands, wound around it, can be contracted, lasso-like, to a single point. He



**Henri Poincaré:
A Scientific
Biography**
JEREMY GRAY
Princeton Univ. Press:
2012. 616 pp. \$35

Children's edition

Books in brief

ends with the ominous words, "However, this question would carry us too far."

Mathematicians laboured over the problem for 99 years. Most tried to solve it in the affirmative; some attempted to find counterexamples. It was left to Perelman to prove that the answer to Poincaré's question was "Yes" — after which he refused both the US\$1-million Millennium Prize from the Clay Mathematics Institute and the Fields Medal.

Like many, Gray wonders why the Nobel Prize in Physics was never awarded to Poincaré for his work in, say, electromagnetism, optics or thermodynamics. As Gray tells us, Poincaré was ahead of Albert Einstein in speculating about a truly relativistic theory of gravity. Quoting Maurice de Broglie, who pioneered X-ray spectroscopy, Gray writes that the reason Poincaré did not take the decisive steps that Einstein did may have been his "too hypercritical turn of mind, due perhaps to his having first been a pure mathematician." Another reason that Poincaré did not win the prize, Gray suggests, was that he was a theorist in mathematical physics, and Nobel prizes at the time were awarded mainly for experimental discoveries. After all, even Einstein was awarded the Nobel prize only in 1921 — for the discovery of the law of the photoelectric effect.

It would be petty to find faults in a work of this calibre, but some reference to Louis Bachelier would have been welcome. He was the visionary of the Black-Scholes options pricing formula of modern financial theory — which gives the correct price of financial derivatives — and one of Poincaré's handful of doctoral students. And the bibliography seems to have omitted Perelman's postings to the Internet.

On the whole, however, this book is an achievement in its own right. Gray keeps the tone light and embeds each of the equations in explanatory text.

Fortunately, Gray also tells it like it was, warts and all. Poincaré's work could contain errors, and often lacked rigour. Aside from his initial, incorrect attempt at his conjecture, his first stab at a prize question — posed to honour the 60th birthday of Sweden's King Oscar II — contained a serious flaw. All copies of the journal that published it were pulped. But most of Poincaré's fumbles are there for all to see; and by studying such blunders, we may observe the meanderings of science as it advances by trial and error. Presenting only the finished product, as Isaac Newton did when he concealed his discovery of calculus, does injustice to the scientific process. ■

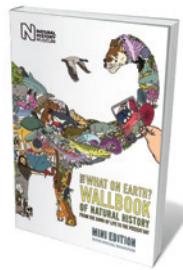
George Szpiro is a science and technology correspondent for the Swiss daily *Neue Zürcher Zeitung*. He is the author of *Poincaré's Prize*.
e-mail: georgeszpiro@gmail.com



Lift-the-Flap Questions and Answers

Katie Daynes and Marie-Eve Tremblay USBORNE 14 pp. £9.99 (2012). Age 3+

This interactive board book by Katie Daynes is food for enquiring minds, answering questions from 'How deep is the sea?' to 'What makes a car go?' and the age-old 'Why do I have to go to sleep?' Questions are divided into types — How? What? Why? — and each has a flap to lift to solve the mystery. Marie-Eve Tremblay's quirky cut-out illustrations give this the feel of a scrapbook, packed with drawings and detail. Simple and accessible, it could prove a boon to a parent asked for an early-morning explanation of how fish breathe.



The What on Earth? Wallbook of Natural History: From the Dawn of Life to the Present Day (MINI EDITION)

Christopher Lloyd and Andy Forshaw NATURAL HISTORY MUSEUM 16 pp. £6.99 (2012). Age 5+

Christopher Lloyd shows that Earth's entire history can be folded down to the size of a postcard. Once the timeline is unfurled, Andy Forshaw's 1,000-plus illustrations capture key events. On a backdrop divided into land, sea and sky, life forms from single-celled organisms to humans appear according to where they live and when they evolved, in a harmonious interplay of large evolutionary concepts and detailed examples.



How We Make Stuff: The Story Behind Our Everyday Things

Christiane Dorion and Beverley Young TEMPLAR 18 pp. £14.99 (2012). Age 7+

The latest in the *How It Works* series traces the journey that natural resources take as they are transformed into food, clothes, phones and 'things'. By revealing, say, that a cheeseburger can involve combined efforts from four continents, Christiane Dorion and Beverley Young could inspire thinking about the planetary impact of our need for stuff. The tabs, flaps and fold-out sections tell the stories of particular items; one of the most interesting is an interactive mix-and-match game to create an environmentally friendly outfit.



Deadly! The Truth About the Most Dangerous Creatures on Earth

Nicola Davies and Neal Layton WALKER 64 pp. £9.99 (2012). Age 8+ Zoologist Nicola Davies takes a spin on the hilarious side of death in a book that reveals the ingenious methods animals use to kill each other. The comedy comes from Neal Layton's cartoons, which deploy exaggerated expressions and amusing speech bubbles to puncture the killer beasts' fearsomeness. Davies' text goes into gruesome detail to describe killer whales' team hunts, the 'death roll' performed by crocodiles and much more. She also raises challenging and important concepts, such as the value of predators to biodiversity and the danger of humans viewing them simply as threats.



Eve & Adam: And Girl Creates Boy

Michael Grant and Katherine Applegate EGMONT 320 pp. £6.99 (2012). Age: 12+

Teen meets gene in this creation myth for the modern age. Evening Spiker's billionaire-geneticist mother gives her a computer program and a challenge: design the perfect boy. But it soon becomes clear that the project extends beyond the computer screen — Adam can become real. This portrayal of a world in which humans have "taken the reins of evolution" is unsettling, but at its heart lies a touching exploration of love and why perfect isn't always good enough.

Children's edition

Books in brief

ends with the ominous words, "However, this question would carry us too far."

Mathematicians laboured over the problem for 99 years. Most tried to solve it in the affirmative; some attempted to find counterexamples. It was left to Perelman to prove that the answer to Poincaré's question was "Yes" — after which he refused both the US\$1-million Millennium Prize from the Clay Mathematics Institute and the Fields Medal.

Like many, Gray wonders why the Nobel Prize in Physics was never awarded to Poincaré for his work in, say, electromagnetism, optics or thermodynamics. As Gray tells us, Poincaré was ahead of Albert Einstein in speculating about a truly relativistic theory of gravity. Quoting Maurice de Broglie, who pioneered X-ray spectroscopy, Gray writes that the reason Poincaré did not take the decisive steps that Einstein did may have been his "too hypercritical turn of mind, due perhaps to his having first been a pure mathematician." Another reason that Poincaré did not win the prize, Gray suggests, was that he was a theorist in mathematical physics, and Nobel prizes at the time were awarded mainly for experimental discoveries. After all, even Einstein was awarded the Nobel prize only in 1921 — for the discovery of the law of the photoelectric effect.

It would be petty to find faults in a work of this calibre, but some reference to Louis Bachelier would have been welcome. He was the visionary of the Black-Scholes options pricing formula of modern financial theory — which gives the correct price of financial derivatives — and one of Poincaré's handful of doctoral students. And the bibliography seems to have omitted Perelman's postings to the Internet.

On the whole, however, this book is an achievement in its own right. Gray keeps the tone light and embeds each of the equations in explanatory text.

Fortunately, Gray also tells it like it was, warts and all. Poincaré's work could contain errors, and often lacked rigour. Aside from his initial, incorrect attempt at his conjecture, his first stab at a prize question — posed to honour the 60th birthday of Sweden's King Oscar II — contained a serious flaw. All copies of the journal that published it were pulped. But most of Poincaré's fumbles are there for all to see; and by studying such blunders, we may observe the meanderings of science as it advances by trial and error. Presenting only the finished product, as Isaac Newton did when he concealed his discovery of calculus, does injustice to the scientific process. ■

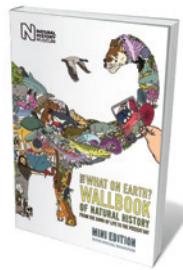
George Szpiro is a science and technology correspondent for the Swiss daily *Neue Zürcher Zeitung*. He is the author of *Poincaré's Prize*.
e-mail: georgeszpiro@gmail.com



Lift-the-Flap Questions and Answers

Katie Daynes and Marie-Eve Tremblay USBORNE 14 pp. £9.99 (2012). Age 3+

This interactive board book by Katie Daynes is food for enquiring minds, answering questions from 'How deep is the sea?' to 'What makes a car go?' and the age-old 'Why do I have to go to sleep?' Questions are divided into types — How? What? Why? — and each has a flap to lift to solve the mystery. Marie-Eve Tremblay's quirky cut-out illustrations give this the feel of a scrapbook, packed with drawings and detail. Simple and accessible, it could prove a boon to a parent asked for an early-morning explanation of how fish breathe.



The What on Earth? Wallbook of Natural History: From the Dawn of Life to the Present Day (MINI EDITION)

Christopher Lloyd and Andy Forshaw NATURAL HISTORY MUSEUM 16 pp. £6.99 (2012). Age 5+

Christopher Lloyd shows that Earth's entire history can be folded down to the size of a postcard. Once the timeline is unfurled, Andy Forshaw's 1,000-plus illustrations capture key events. On a backdrop divided into land, sea and sky, life forms from single-celled organisms to humans appear according to where they live and when they evolved, in a harmonious interplay of large evolutionary concepts and detailed examples.



How We Make Stuff: The Story Behind Our Everyday Things

Christiane Dorion and Beverley Young TEMPLAR 18 pp. £14.99 (2012). Age 7+

The latest in the *How It Works* series traces the journey that natural resources take as they are transformed into food, clothes, phones and 'things'. By revealing, say, that a cheeseburger can involve combined efforts from four continents, Christiane Dorion and Beverley Young could inspire thinking about the planetary impact of our need for stuff. The tabs, flaps and fold-out sections tell the stories of particular items; one of the most interesting is an interactive mix-and-match game to create an environmentally friendly outfit.



Deadly! The Truth About the Most Dangerous Creatures on Earth

Nicola Davies and Neal Layton WALKER 64 pp. £9.99 (2012). Age 8+ Zoologist Nicola Davies takes a spin on the hilarious side of death in a book that reveals the ingenious methods animals use to kill each other. The comedy comes from Neal Layton's cartoons, which deploy exaggerated expressions and amusing speech bubbles to puncture the killer beasts' fearsomeness. Davies' text goes into gruesome detail to describe killer whales' team hunts, the 'death roll' performed by crocodiles and much more. She also raises challenging and important concepts, such as the value of predators to biodiversity and the danger of humans viewing them simply as threats.



Eve & Adam: And Girl Creates Boy

Michael Grant and Katherine Applegate EGMONT 320 pp. £6.99 (2012). Age: 12+

Teen meets gene in this creation myth for the modern age. Evening Spiker's billionaire-geneticist mother gives her a computer program and a challenge: design the perfect boy. But it soon becomes clear that the project extends beyond the computer screen — Adam can become real. This portrayal of a world in which humans have "taken the reins of evolution" is unsettling, but at its heart lies a touching exploration of love and why perfect isn't always good enough.



Stranded Iceberg, by Camille Seaman, taken off the coast of Antarctica's Cape Bird in 2006.

Q&A Camille Seaman

Iceberg imager

Camille Seaman photographs icebergs and storm clouds. With an exhibition of her work opening in January in San Francisco, California, she talks about stalking supercell storms and watching hungry polar bears destroy a bird colony.



What do you aim for in your photos?

I try to allow myself to feel something. My main aim is to reveal beauty. We live in boxes, and most of us are not connected to the outside world.

Once people feel something, it is the start of a relationship. If we keep degrading our environment, it will hurt our lives. Every iceberg that I have photographed is gone. In a couple of hundred years, photographs such as mine will remind people what icebergs and penguins looked like.

How did you start to photograph icebergs?

In 1999, I got a free plane ticket. On a whim, I flew to the Bering Sea and naively decided to walk across the frozen ocean towards Russia. I returned with the sense that I had met my planet. In 2003, I boarded a Norwegian icebreaker in Svalbard; crashing through sea ice was exhilarating. In 2004, I travelled to Antarctica, near where Shackleton's ship was trapped and crushed a century ago. The scale of the icebergs was beyond belief. Since then, I have worked as an expedition photographer for companies in the Arctic and Antarctic.

Camille Seaman, *The Last Iceberg III*
Corden | Potts Gallery, San Francisco, California.
3 January–2 February 2013.

How do icebergs 'behave'?

Melting ice lowers the salinity of the seawater and releases minerals that allow krill to bloom, attracting fish, birds, seals and whales. After a glacier calves, the fallen ice creates a crackling sound like billions of pop rocks. My grandfather, a Shinnecock Indian, once asked me to sit still on a warm summer day and watch my own sweat evaporate. The vapour becomes part of a cloud, which falls as rain to feed plants and animals, which feed us. Each iceberg is different. Some are stalwart, refusing to break apart despite being pounded by waves. Others just collapse.

What have you learned from scientists?

Working on ships has allowed me to spend time with researchers in many disciplines. A marine biologist explained that whales became so scarce in the early twentieth century that some companies boiled penguins for bird oil. I didn't appreciate the courage of penguins until an ornithologist sat me down for hours to observe their behaviour. A geologist showed me a 3-billion-year-old stone. He was trained to see scales of time that are beyond an average human's comprehension.

Humanity may not survive, he said, but he wasn't worried about the planet.

How did you begin to chase storm clouds?

It was serendipitous. My daughter was watching *Storm Chasers* on television, and said, "Mom, you should do that." Three days later, I was in Kansas in a Chevy Suburban with storm expert Todd Thorn, chasing a supercell mesocyclone. When you stand under these supercell storm clouds, which have a persistent rotating updraft, it is like a nebula where stars are forming. The creation of these storms in our atmosphere involves the coalescence of gravity, wind and electrical current.

Have you ever feared for your life on the job?

I have no desire to end up dead. I want to photograph the beauty and structure of these storms, and to do that you have to get some distance. You can avoid tornadoes, but hail can be dangerous when it gets to baseball size. Lightning can strike anywhere at any time. Storms are unpredictable. One time in South Dakota, we had been chasing an epic supercell storm for several hours, when it started to collapse. All the energy that had built up was rushing out at 110 kilometres an hour, like a sandstorm in the desert. We had to drive at 150 kilometres an hour over dirt roads for quite some time to outrun the storm. The next morning, we found that a rear wheel on our vehicle had nearly come off.

How do you create your images?

Before I pick up my camera, I ask, what in my field of vision is making me feel a certain way? I use the camera like a Geiger counter to find the source of the emotion. Then I push the button. Nature is awesome without additives. I don't exaggerate colours or contrast, and I don't crop or straighten. My joy is in creating the image in the camera, not on the computer. I love analogue photographs but have begun to shoot digital since getting through airports with film has become difficult. Now that the files are large enough, you can get huge digital prints with the same tactile sense of detail as with film.

How has climate change affected your work?

I left the Arctic last summer heartbroken. The expedition got within 400 kilometres of the North Pole without the nuclear-powered icebreakers that are usually necessary. Our time on land was spent witnessing hungry polar bears destroying a full year of bird colonization. Last year, I realized that people are not willing to make the changes necessary to keep what we have now. I left knowing that the future is not about preservation or conservation, but about being able to handle the changes ahead. The changes are coming; the question is whether we will be prepared. ■

INTERVIEW BY JASCHA HOFFMAN

ILLUSTRATION: NICK HIGGINS; BASED ON PORTRAIT BY ROBERT LESUE

Correspondence

Research-reporting standards fall short

More than 150 journals and many research-funding charities have endorsed the ARRIVE guidelines for reporting research that uses animal models (C. Kilkenny *et al.* *PLoS Biol.* **8**, e1000412; 2010), but we find that they are being largely ignored. This could undermine data reproducibility and model credibility, and might obstruct translation into human therapy (S. Landis *et al.* *Nature* **490**, 187–191; 2012).

For example, of 180 papers on multiple sclerosis listed on PubMed in the past 6 months, we found that only 40% used appropriate statistics to compare the effects of gene-knockout or treatment. Appropriate statistics were applied in only 4% of neuroimmunological studies published in the past two years in Nature Publishing Group journals, *Science* and *Cell* (details available from D.B. on request). Many journals are therefore failing to ensure that the basics of experimental design and data analysis are respected.

Simply introducing guidelines is not enough. The issue requires greater editorial oversight (perhaps using a tick-box questionnaire at submission), stricter refereeing standards and engagement by learned societies. **David Baker**, **Katie Lidster**, **Ana Sottomayor** *Queen Mary, University of London, UK.* david.baker@qmul.ac.uk
Sandra Amor *Free University Amsterdam, the Netherlands.*

From pork lard to palm oil and back

The food industry is rapidly ramping up the production of palm oil, destroying tropical forest at an alarming rate to make way for more oil-palm plantations. Consumers might assume that palm oil is more heart-healthy than animal-based

lard. It is not: human metabolism recognizes the chemicals themselves, not their source.

The popularity of butter and lard declined in the 1940s and 1950s, giving way to margarine. This shift was fuelled by the belief that vascular health could be improved by switching from saturated animal fats to unsaturated plant oils. Margarine fell from grace around 1990, when it was discovered that plant-oil solidification produces metabolically harmful *trans*-fat.

The physical-chemical properties of lard make it ideal for baking, and palm oil is an effective substitute because its chemical composition is almost identical. In lard, the ratios of saturated, monounsaturated and polyunsaturated fatty acids are 43:47:10, whereas in palm oil they are 47:45:8. Neither type contains significant amounts of the more beneficial omega-3 fatty acids.

So we have come full circle. Why discard the pork fat from abattoirs only to replace it with essentially the same thing, but from an ecologically disastrous source?

José Bonner *Indiana University, Bloomington, Indiana, USA.* bonner@indiana.edu

Strength to strength for mouse models

Jessica Bolker's emphasis on choosing the right animal model (*Nature* **491**, 31; 2012) should not undermine the validity of the mouse as a model for human disease. Contrary to her implication, mouse researchers do take genetic background and environment into consideration.

Mouse models used to test therapies should reproduce closely the human disease being investigated — including the response to genetic and environmental factors. But this need not apply to models for understanding disease mechanisms: Nobel-prizewinning discoveries of embryonic stem cells, the mouse

major histocompatibility locus and monoclonal antibodies, for example, all relied on experimental mice and not disease models.

Researchers do not use only inbred strains of mice: they use genetically characterized mouse populations and deploy different genetic backgrounds to identify complex inherited traits. There are large collections of recombinant inbred mouse strains, as well as a public database of more than 3,000 traits (E. J. Chesler *Nature Neurosci.* **7**, 485–486; 2004). The Collaborative Cross reference panel, representing eight inbred strains of lab and wild-derived mice, contains twice the genetic diversity of the entire human population and allows high-resolution analysis of phenotypic variations (*Genetics* **190**, 389–401; 2012).

The full potential of the mouse as a model system has yet to be realized. The study of genetic reference populations, along with a library of mutants for every mouse gene, will continue to transform our understanding of human disease.

Klaus Schughart *SYSGENET, HZI Braunschweig, University of Veterinary Medicine Hanover, Germany; and University of Tennessee Health Science Center, Memphis, USA.* klaus.schughart@helmholtz-hzi.de
Claude Libert *SYSGENET, VIB-Ghent University, Ghent, Belgium.*
Martien J. Kas *SYSGENET, University Medical Center Utrecht, Utrecht, the Netherlands.*

Eritrea should choose its own science path

I find your perspective on the state of science in Eritrea too narrow and founded on questionable assumptions (*Nature* **491**, 8 and *Nature* **491**, 24–26; 2012).

You assume that links with Western institutions are inherently beneficial; that exiled individuals convey an

objective picture of the situation inside a closed country; and that disagreements between governments and academic institutions with Western links result from wrongdoing by the government.

Given the complex and difficult recent history of Eritrea, I suggest (without wishing to endorse the regime) that the interests of elite academics, often trained in the West, may not overlap with those of the country's poorer population. And, although international cooperation is part and parcel of academia, recipients of crucial aid are rarely in a position to stand up for their own interests against powerful donors.

Elements of the Eritrean regime want national institutions to survive and eventually flourish without foreign resources, even if that means serious difficulty in the short and medium term. A closed education system, for example, could take a generation to develop the technical expertise and facilities otherwise delivered immediately to a willing aid recipient.

States must decide for themselves on their path to independence. We may not like what they decide, but drawing a line between those who are with us or against us will not benefit the international scientific community, or the vast populations of countries such as Eritrea.

Andrew Isaac Meso *Institut de Neurosciences de la Timone, CNRS/Aix-Marseille University, Marseilles, France.* andrew.meso@univ-amu.fr

CORRECTION

A declaration of competing financial interests was omitted from the Correspondence 'NIH chimps: use existing facilities' (*Nature* **491**, 672; 2012). This has been added at <http://go.nature.com/aeqzhu>.

Farish A. Jenkins Jr

(1940–2012)

Palaeontologist, anatomist, explorer and artist.

With a rifle strapped to his back each summer, a scalpel in his hand each autumn and the eyes of an artist throughout the year, Farish Jenkins Jr seamlessly blended expeditionary palaeontology with experimental anatomy to establish how animals evolved to walk, run, jump and fly.

Jenkins, who died of complications from pneumonia on 11 November, was raised in Rye, New York. As a child, he showed no obvious draw towards a life of science and exploration. But two experiences transformed him. While studying philosophy at Princeton University in New Jersey in the early 1960s, Jenkins spent a summer as an undergraduate assistant to Glenn Lowell Jepsen. Jepsen ran a legendary field programme in Wyoming, digging up mammalian fossils, and Jenkins caught the bug for expeditionary palaeontology. After university he enlisted in the US Marine Corps, where he acquired the stamina, determination and confidence to execute the fieldwork that became a hallmark of his success.

In 1964, Jenkins began a PhD at Yale University in New Haven, Connecticut. Working with A. W. Crompton, the newly appointed director of the Yale Peabody Museum, Jenkins discovered an interest in early mammals and their closest relatives. His dissertation on the postcranial anatomy of these animals was a landmark study. It showed how careful anatomical observation and three-dimensional analysis of joint articulations could reveal major steps in the evolution of locomotion.

In 1971, Jenkins was recruited by Crompton to a post at Harvard University's Museum of Comparative Zoology (MCZ) in Cambridge, Massachusetts, where Crompton had assumed directorship. Here, the two launched a now famous laboratory. They employed electromyography, a technique for recording the electrical activity produced by muscles, along with a then-new cineradiographic device for creating movies from successive X-ray images. Crompton, Jenkins and their students revealed how the movement of bones in animals ranging from lizards and shrews to frogs is coupled to the activity of their muscles as they eat and move about. Armed with this new empirical evidence, Jenkins and his colleagues revised

nearly a century's worth of speculation about functional anatomy that had been based on fossils alone.

Jenkins's research output was as systematic as his military training had been. During the

a serendipitous expansion of his research programme to include other tetrapod groups. In the 1990s and 2000s, Jenkins used the same approach to open up the Triassic rocks of Greenland and the Devonian sediments of Arctic Canada to palaeontological discovery. He uncovered haramiyids (some of the earliest mammals) in the Triassic rocks and *Tiktaalik* (a genus of lobe-finned fish) in the Devonian ones.

Jenkins was president of the Society of Vertebrate Paleontology in 1981–82, and he received its Romer-Simpson Medal for life-time achievement in 2009. He will be remembered by generations of undergraduates, graduate and medical students and assistant professors at Harvard College and the Harvard-MIT Health Sciences and Technology Training Program for the humanity and compassion with which he supported their careers. Among his many awards, he was especially proud to receive a Harvard College Professorship for his role in undergraduate teaching.

The showmanship of Farish's Harvard lectures was legendary. To demonstrate gaits he would recite Herman Melville while limping like Captain Ahab; at other times, he would don a body stocking with a skeleton painted on it.

He cut a dashing figure — whether bearing a pocket watch, pressed white shirt and tie clip in the laboratory, or a miner's pick and fire-arm (to protect himself and others from polar bears) in the field. As well as an anatomist, palaeontologist and explorer, he was an artist. It was not unusual for him to arrive for class four hours early to draw three-dimensional anatomical diagrams on the blackboard. Indeed, his scientific papers typically contained renderings that took months to execute. If you wrote a paper with Farish, you finished images and art before penning a single word. ■

Neil Shubin is Robert R. Bensley Distinguished Service Professor at the University of Chicago, Chicago, Illinois 60637, USA. He collaborated with Jenkins on expeditions to Arizona, Greenland, Morocco, Namibia, Argentina, China and Ellesmere Island during the past 30 years. e-mail: nshubin@uchicago.edu



1970s, he published a succession of cogent analyses of the key joints of the mammalian body and their role in major functional transitions of evolution. Indeed, the 1970s were heady times to be at the MCZ. A menagerie of creatures walked, hopped and crawled under the cine X-ray beam. Students and colleagues came from around the world with fresh questions. All the while, Jenkins was developing the palaeontological expeditionary approach that led to his greatest breakthroughs.

Farish Jenkins's recipe for successful expeditions went thus: identify a crucial question, explore the rocks most likely to contain the fossils you need to answer it and add stubborn persistence to the mix.

To better understand the evolutionary origins of mammals, Jenkins began his search in the Cretaceous rocks of Montana, where he found early mammal fossils. From 1977 to 1983 he launched a series of expeditions to the Jurassic Kayenta Formation of Arizona. Others had famously found fossils in these rocks, but Jenkins brought a novel approach: if the goal was to understand mammalian origins, and the earliest representatives were small, then the search should be focused on those sediments most likely to hold the smallest fossils.

The result was stunning. His excavation of siltstones uncovered not just early mammals, but also salamanders, frogs and a group of amphibians called caecilians — prompting

Intimate neuronal whispers

It's a touching story of cohabitation and meaningful communication. Two neighbouring fruitfly neurons talk to each other not by means of synaptic junctions but by interactions through the surrounding electrical field. [SEE ARTICLE P.66](#)

KAZUMICHI SHIMIZU & MARK STOPFER

To process information, neurons almost always work as discrete, insulated building blocks of the nervous system — they interact only through specialized gateway structures known as synapses, but otherwise keep their cogitations to themselves. This view has been prevalent since Ramón y Cajal and other biologists formulated the 'neuron doctrine' more than a century ago. But on page 66 of this issue, Su *et al.*¹ describe a notable finding: multiple olfactory receptor neurons can directly influence one another non-synaptically, with their combined output forming a description of the olfactory environment*.

Su and colleagues observed this in the fruitfly *Drosophila*, an insect that offers experimenters a terrific toolkit for genetic manipulation. *Drosophila*'s olfactory receptor neurons (ORNs), like those of many animals, are packed into narrow, fluid-filled structures called sensilla. Most sensilla contain more than one ORN. The dendritic projections of these cells touch each other but the neurons themselves are not connected by synapses².

The authors focused on a sensillum called ab3, which contains two ORNs (ab3A and ab3B). They exposed the insects to two odorants — methyl hexanoate and 2-heptanone — each of which activates only one of these ORNs. While one odorant was presented continuously in the background, the second odorant was briefly pulsed. As expected, when methyl hexanoate was presented in the background, ab3A began to respond by firing a series of action potentials (spiking). When 2-heptanone was pulsed atop this background, ab3B responded by spiking. Intriguingly, however, as soon as ab3B began to fire, the ongoing response of ab3A suddenly and dramatically decreased (Fig. 1a–c).

To test whether spiking in ab3B was directly responsible for the diminished response of ab3A, Su *et al.* used a genetic trick — they destroyed ab3B to prevent it from firing, and then repeated the experiment. This time, pulsing 2-heptanone had no effect on the firing

*This article and the paper under discussion¹ were published online on 21 November 2012.

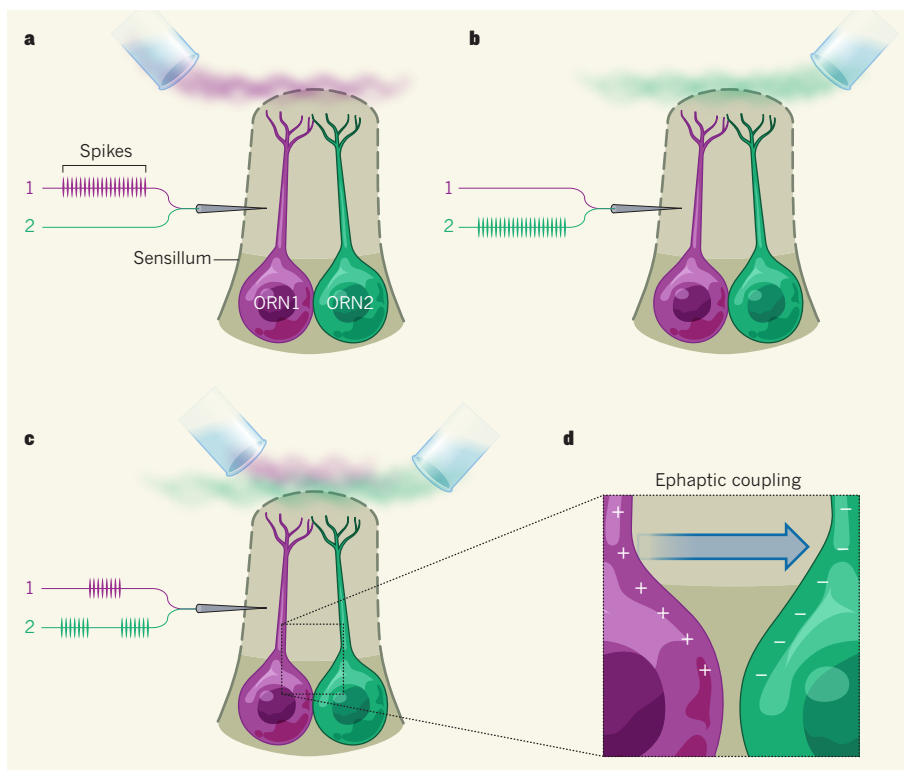


Figure 1 | Close neuronal couples. a,b, In this simplified example, olfactory receptor neurons 1 and 2 (ORN1 and ORN2) reside within the same sensillum, but do not make synaptic connections. From the spiking responses of these neurons, displayed separately on lines 1 and 2, ORN1 responds to the 'purple' odour (a), whereas ORN2 responds to the 'green' odour (b). c, When a pulse of the purple odour is briefly mixed into the ongoing background green odour, ORN1 transiently responds, and during this time ORN2 is inhibited. d, Su *et al.*¹ propose that this inhibition is mediated by a direct electrical field interaction between such closely apposed ORNs through the process of ephaptic coupling.

of ab3A. Through further complementary experiments in ab3, and experiments in other types of sensillum, the researchers showed that spiking in one ORN can inhibit the responses of other ORNs in the same sensillum.

Is this coupling effect powerful enough to influence the animal's behaviour? To test this, the authors studied another sensillum containing two ORNs, one of which mediates attraction to apple cider vinegar (ACV), and the other repulsion from carbon dioxide. Given a choice between a CO₂–ACV mixture and a CO₂–water–vapour mixture, flies typically prefer CO₂–ACV. Su and co-workers reasoned that this preference could be explained by a strong attraction to ACV;

by repulsion from CO₂ that is diminished by the presence of ACV; or by a combination of both. To determine which of these possibilities was true, they used genetic manipulations that allowed the ACV-responsive ORNs to fire action potentials, but blocked them from synaptically activating any 'follower' neurons.

Flies manipulated in this way showed reduced attraction to the CO₂–ACV mixture, but still preferred it to the CO₂–water–vapour blend. These insects could not have been directly attracted to ACV because the synaptic pathway mediating this attraction had been blocked. Moreover, a genetic manipulation that prevents ACV receptors from

responding but leaves CO₂ receptors intact reduced the fly's preference for CO₂-ACV over CO₂-water vapour. Together, these clever and elegant experiments suggest that the flies' behavioural preference for CO₂-ACV can be explained by two factors: attraction to ACV; and reduced repulsion from CO₂, mediated by ACV-receptor-driven inhibition of spiking in the CO₂-responsive neuron.

The authors' additional experiments showed that this receptor-driven inhibition is not mediated through synapses. Instead, they propose that the ORNs interact directly through the extracellular fluid surrounding the neurons by a mechanism called ephaptic coupling³ (Fig. 1d). When a neuron fires an action potential, electrical charges transiently flow into and out of its membrane. Usually, the impact of this current flow is diffuse and slight outside the neuron. But when the extracellular space is unusually tight and compartmentalized, the impact can, in theory, be strong enough to affect the electrical activity of neighbouring neurons, leading to ephaptic interactions⁴.

Ephaptic transmission is particularly

interesting in the context of the chemical senses because chemosensory receptors commonly cohabit. In insects, for instance, gustatory receptor neurons — like ORNs — are packed tightly together into sensilla⁵; and in vertebrates, gustatory receptors are intertwined within compact taste buds⁶. Thus, Su and colleagues' report calls for a systematic revision of long-standing views of the first stage of chemosensory processing. On the basis of their data, the receptors seem to function not as fully independent information channels, but rather as interactive components, with the sensillum serving as the autonomous building block of sensory transduction.

What benefits might this arrangement provide for coding sensory information? According to Su *et al.*, it enables the novelty of a stimulus to be detected and encoded right there in the periphery, when new, transient responses suppress ongoing activity of the neuron sensitive to the stimulus. Although little is known of the logic behind the distribution of different types of ORN into sensilla, the process of making behavioural choices might

often begin as interactive antagonisms between strategically paired, contiguous ORNs. Moreover, the timing of spiking in ORNs may be shaped in part by ORN-ORN interactions; this timing underlies the more elaborately patterned neural odour codes arising downstream⁷. More work is needed to determine the mechanistic details and behavioural consequences in this fascinating story. ■

Kazumichi Shimizu and Mark Stopfer are at the National Institute of Child Health and Human Development, National Institutes of Health, Bethesda, Maryland 20892, USA. e-mail: stopferm@mail.nih.gov

1. Su, C.-Y., Menz, K., Reiser, J. & Carlson, J. R. *Nature* **492**, 66–71 (2012).
2. Su, C.-Y., Menz, K. & Carlson, J. R. *Cell* **139**, 45–59 (2009).
3. Jefferys, J. G. *Physiol. Rev.* **75**, 689–723 (1995).
4. Vermeulen, A. & Rospars, J.-P. *Eur. Biophys. J.* **33**, 633–643 (2004).
5. Zacharuk, R. Y. *Annu. Rev. Entomol.* **25**, 27–47 (1980).
6. Chaudhari, N. & Roper, S. D. *J. Cell Biol.* **190**, 285–296 (2010).
7. Raman, B., Joseph, J., Tang, J. & Stopfer, M. *J. Neurosci.* **30**, 1994–2006 (2010).

ORGANIC CHEMISTRY

Toolkit of reagents to aid drug discovery

Reagents have been developed that allow carbon–hydrogen bonds on benzene-like compounds called heterocycles to be converted directly into carbon–carbon bonds. The finding will be a boon to medicinal chemists. SEE LETTER P.95

WILLIAM J. PITTS

When designing medicines, the difference between success and failure can hinge on small variations made to the molecular structures of candidate drugs during the optimization phase of drug discovery. In this issue, Fujiwara *et al.*¹ report the development of a toolkit of reagents that can be used to attach a variety of chemical groups to heterocycles — benzene-like rings containing atoms such as nitrogen, as well as carbon, that are frequently found in drug molecules. The toolkit should make it quicker to generate analogues of candidate drugs for biological testing, and improve the metabolic stability of compounds containing heterocycles. It also provides medicinal chemists with a powerful strategy for making 'substituted' heterocycles — heterocyclic compounds to which chemical groups are attached — and so offers a tactical advantage for the optimization phase of drug discovery*.

Fujiwara and colleagues' toolkit consists of ten zinc bis(alkanesulphonate) salts. These reagents, which have practical uses, are precursors to alkyl radicals — species known to react with a wide variety of heterocycles, including those contained in drugs and natural products. The authors found that their zinc salts typically react at carbon–hydrogen (C–H) bonds adjacent to nitrogen atoms in heterocycles, creating a carbon–carbon (C–C) bond to the alkyl group of the salt (Fig. 1). The resulting products are not commercially available and can be difficult to prepare using traditional synthetic approaches, requiring many steps to complete.

The reactions do not require 'pre-functionalized' sites in heterocycles — that is, there is no need to incorporate special groups at the reaction sites to allow C–C bond formation to occur. This makes it easier to synthesize substrates for the reactions, and means that substrates can be made from simple (and therefore often cheap) starting materials. What's more, Fujiwara *et al.* report that the reactions do not affect potentially reactive sites or groups that

might be present elsewhere in the starting material. This means that structurally complex compounds obtained as intermediates in the late stages of a synthetic pathway can be used as substrates for the reactions, making it easier to prepare several analogues of a compound from a common intermediate. It also means that there is no need for protection strategies, in which reactive sites are temporarily modified to stop them taking part in unwanted side reactions, reducing waste and expense.

Fujiwara *et al.* observed that when two different zinc bis(alkanesulphonate) salts were added sequentially to the same heterocycle, new C–C bonds formed specifically at two different sites in the substrate. This ability to perform sequential reactions further increases the complexity of the substituted heterocycles that can be produced using the toolkit. The researchers also report that the reactions can proceed under 'mild' conditions that are unlikely to cause substrates to decompose; that they tolerate several chemical groups known to be especially prone to side reactions; and that they can be performed in organic solvents, in water, and even in the isolated fluid contents of cells. Fujiwara and colleagues went on to demonstrate that the reactions proceed in buffer solution in the presence of an enzyme, β -lactamase, without adversely affecting the enzyme's activity. This result leads them to suggest that their chemical toolkit can facilitate the attachment of drugs to proteins such as antibodies, which can increase the therapeutic effect of the drug substance and target delivery to specific cells.

Several of the alkyl groups in the zinc bis(alkanesulphonate) salts contain fluorine atoms. This makes them particularly useful to medicinal chemists, who are increasingly

*This article and the paper under discussion¹ were published online on 28 November 2012.

responding but leaves CO₂ receptors intact reduced the fly's preference for CO₂-ACV over CO₂-water vapour. Together, these clever and elegant experiments suggest that the flies' behavioural preference for CO₂-ACV can be explained by two factors: attraction to ACV; and reduced repulsion from CO₂, mediated by ACV-receptor-driven inhibition of spiking in the CO₂-responsive neuron.

The authors' additional experiments showed that this receptor-driven inhibition is not mediated through synapses. Instead, they propose that the ORNs interact directly through the extracellular fluid surrounding the neurons by a mechanism called ephaptic coupling³ (Fig. 1d). When a neuron fires an action potential, electrical charges transiently flow into and out of its membrane. Usually, the impact of this current flow is diffuse and slight outside the neuron. But when the extracellular space is unusually tight and compartmentalized, the impact can, in theory, be strong enough to affect the electrical activity of neighbouring neurons, leading to ephaptic interactions⁴.

Ephaptic transmission is particularly

interesting in the context of the chemical senses because chemosensory receptors commonly cohabit. In insects, for instance, gustatory receptor neurons — like ORNs — are packed tightly together into sensilla⁵; and in vertebrates, gustatory receptors are intertwined within compact taste buds⁶. Thus, Su and colleagues' report calls for a systematic revision of long-standing views of the first stage of chemosensory processing. On the basis of their data, the receptors seem to function not as fully independent information channels, but rather as interactive components, with the sensillum serving as the autonomous building block of sensory transduction.

What benefits might this arrangement provide for coding sensory information? According to Su *et al.*, it enables the novelty of a stimulus to be detected and encoded right there in the periphery, when new, transient responses suppress ongoing activity of the neuron sensitive to the stimulus. Although little is known of the logic behind the distribution of different types of ORN into sensilla, the process of making behavioural choices might

often begin as interactive antagonisms between strategically paired, contiguous ORNs. Moreover, the timing of spiking in ORNs may be shaped in part by ORN-ORN interactions; this timing underlies the more elaborately patterned neural odour codes arising downstream⁷. More work is needed to determine the mechanistic details and behavioural consequences in this fascinating story. ■

Kazumichi Shimizu and Mark Stopfer are at the National Institute of Child Health and Human Development, National Institutes of Health, Bethesda, Maryland 20892, USA. e-mail: stopferm@mail.nih.gov

1. Su, C.-Y., Menz, K., Reiser, J. & Carlson, J. R. *Nature* **492**, 66–71 (2012).
2. Su, C.-Y., Menz, K. & Carlson, J. R. *Cell* **139**, 45–59 (2009).
3. Jefferys, J. G. *Physiol. Rev.* **75**, 689–723 (1995).
4. Vermeulen, A. & Rospars, J.-P. *Eur. Biophys. J.* **33**, 633–643 (2004).
5. Zacharuk, R. Y. *Annu. Rev. Entomol.* **25**, 27–47 (1980).
6. Chaudhari, N. & Roper, S. D. *J. Cell Biol.* **190**, 285–296 (2010).
7. Raman, B., Joseph, J., Tang, J. & Stopfer, M. *J. Neurosci.* **30**, 1994–2006 (2010).

ORGANIC CHEMISTRY

Toolkit of reagents to aid drug discovery

Reagents have been developed that allow carbon–hydrogen bonds on benzene-like compounds called heterocycles to be converted directly into carbon–carbon bonds. The finding will be a boon to medicinal chemists. SEE LETTER P.95

WILLIAM J. PITTS

When designing medicines, the difference between success and failure can hinge on small variations made to the molecular structures of candidate drugs during the optimization phase of drug discovery. In this issue, Fujiwara *et al.*¹ report the development of a toolkit of reagents that can be used to attach a variety of chemical groups to heterocycles — benzene-like rings containing atoms such as nitrogen, as well as carbon, that are frequently found in drug molecules. The toolkit should make it quicker to generate analogues of candidate drugs for biological testing, and improve the metabolic stability of compounds containing heterocycles. It also provides medicinal chemists with a powerful strategy for making 'substituted' heterocycles — heterocyclic compounds to which chemical groups are attached — and so offers a tactical advantage for the optimization phase of drug discovery*.

Fujiwara and colleagues' toolkit consists of ten zinc bis(alkanesulphonate) salts. These reagents, which have practical uses, are precursors to alkyl radicals — species known to react with a wide variety of heterocycles, including those contained in drugs and natural products. The authors found that their zinc salts typically react at carbon–hydrogen (C–H) bonds adjacent to nitrogen atoms in heterocycles, creating a carbon–carbon (C–C) bond to the alkyl group of the salt (Fig. 1). The resulting products are not commercially available and can be difficult to prepare using traditional synthetic approaches, requiring many steps to complete.

The reactions do not require 'pre-functionalized' sites in heterocycles — that is, there is no need to incorporate special groups at the reaction sites to allow C–C bond formation to occur. This makes it easier to synthesize substrates for the reactions, and means that substrates can be made from simple (and therefore often cheap) starting materials. What's more, Fujiwara *et al.* report that the reactions do not affect potentially reactive sites or groups that

might be present elsewhere in the starting material. This means that structurally complex compounds obtained as intermediates in the late stages of a synthetic pathway can be used as substrates for the reactions, making it easier to prepare several analogues of a compound from a common intermediate. It also means that there is no need for protection strategies, in which reactive sites are temporarily modified to stop them taking part in unwanted side reactions, reducing waste and expense.

Fujiwara *et al.* observed that when two different zinc bis(alkanesulphonate) salts were added sequentially to the same heterocycle, new C–C bonds formed specifically at two different sites in the substrate. This ability to perform sequential reactions further increases the complexity of the substituted heterocycles that can be produced using the toolkit. The researchers also report that the reactions can proceed under 'mild' conditions that are unlikely to cause substrates to decompose; that they tolerate several chemical groups known to be especially prone to side reactions; and that they can be performed in organic solvents, in water, and even in the isolated fluid contents of cells. Fujiwara and colleagues went on to demonstrate that the reactions proceed in buffer solution in the presence of an enzyme, β -lactamase, without adversely affecting the enzyme's activity. This result leads them to suggest that their chemical toolkit can facilitate the attachment of drugs to proteins such as antibodies, which can increase the therapeutic effect of the drug substance and target delivery to specific cells.

Several of the alkyl groups in the zinc bis(alkanesulphonate) salts contain fluorine atoms. This makes them particularly useful to medicinal chemists, who are increasingly

*This article and the paper under discussion¹ were published online on 28 November 2012.

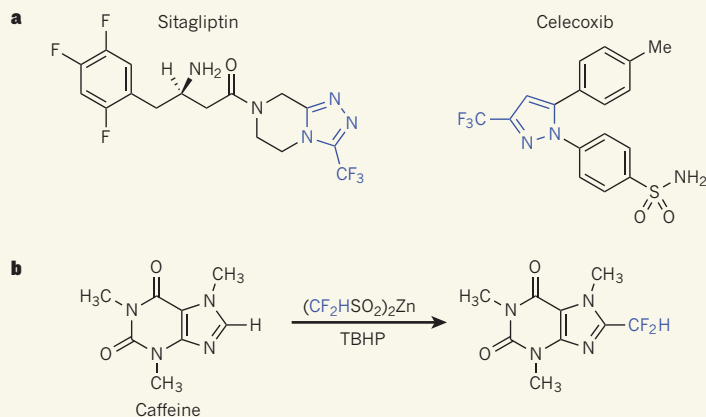


Figure 1 | Applications and synthesis of substituted heterocycles. **a**, Many drugs contain substituted heterocycles — benzene-like rings bearing one or more chemical groups. The antidiabetic drug sitagliptin and the anti-inflammatory agent celecoxib both contain heterocycles (blue) to which a fluorine-containing group (CF_3) is attached. **b**, Fujiwara *et al.*¹ report reagents known as zinc bis(alkylsulphonate) salts, $(\text{RSO}_2)_2\text{Zn}$ (where R is a carbon-containing alkyl group), which convert carbon–hydrogen bonds adjacent to nitrogen atoms in heterocycles to carbon–carbon bonds. In this example, a difluoromethyl (CF_2H) group is transferred from the zinc salt to the smaller heterocycle in caffeine; *t*-butyl hydroperoxide (TBHP) is also required to initiate the reaction.

incorporating fluorine into candidate drugs as part of their optimization plans². The antidiabetic drug Januvia (sitagliptin phosphate) and the anti-inflammatory medicine Celebrex (celecoxib), for example, contain heterocycles with fluoroalkyl groups attached (Fig. 1).

Incorporating fluoroalkyl groups into heterocycles is desirable for various reasons. Several of these groups are important bioisosteres — groups that can replace another group to produce a similar biological effect³. For example, difluoromethyl (CF_2H) groups are good replacements for hydroxyl (OH) groups because the electron-withdrawing effect of the fluorine atoms in CF_2H increases the acidity of the hydrogen atom to the point that it can take part in hydrogen bonding, just as the hydrogen in OH takes part in hydrogen bonding. When attached to heterocycles, the electron-withdrawing effect of fluoroalkyl groups can also decrease the extent to which those heterocycles are ionized at low pH. This is useful for a drug compound because it allows it to be absorbed into the bloodstream without being affected by the co-administration of drugs that raise the pH of the stomach (such as antacids). Finally, fluoroalkyl groups often increase the length of time a drug circulates in the body (its 'half-life'). This could mean that a drug need only be administered once a day, for example, rather than several times, increasing patient compliance with the treatment regime.

Fluoroalkyl groups can improve the half-life by several mechanisms. For example, they are more resistant than analogous hydrocarbon groups to oxidation by metabolic cytochrome P450 enzymes. But heterocycles can also be metabolized by the aldehyde oxidase

enzyme⁴. This oxidation process frequently occurs at C–H bonds adjacent to nitrogen atoms. Fujiwara and colleagues' toolkit incorporates fluoroalkyl groups at such positions, which is expected to decrease the contribution of aldehyde oxidase⁴ to the metabolism of candidate drugs. Taken together, these considerations make the toolkit a valuable addition to the armoury of methods used by medicinal chemists for drug optimization.

EVOLUTIONARY GENOMICS

Algae's complex origins

The nuclear genomes of two of nature's most complex cells have been sequenced. The data will help to determine the evolutionary path from symbioses between species to a multi-compartmental unicellular organism. [SEE ARTICLE P.59](#)

SVEN B. GOULD

The orchestration of cellular function from genetic information is a marvel, even in a typical cell that has a single genome. But a few unusual members of a group of microorganisms called protists pack four genomes, each of unique origin, into a single cell. In this issue, Curtis *et al.*¹ report the nuclear-genome sequences for two of these organisms: the unicellular algae *Guillardia theta* and *Bigelowiella natans*. These species are each the derivatives of symbiotic relationships between multiple cells, and their endowment of genetic and cellular relicts from these

Nevertheless, there are some minor limitations. The authors identify zinc bis(alkane-sulphonate) salts as optimal reagents, but the reactions generally provide only moderate product yields (typically 40–80%). Low-yielding reactions are acceptable in the early stages of drug optimization, especially if they allow a new analogue of a candidate drug to be made expediently. However, if large quantities of a candidate drug are needed at a later stage, for example for toxicology studies or to evaluate efficacy in animals, then the synthetic route may need to be redesigned to improve yields. Another potential drawback is that the reactions occur at more than one position in some heterocycles, resulting in a mixture of isomeric products. But as long as the isomers are separable, this can be useful for early optimization efforts, because each isomer can be tested for its biological activity and may even provide a serendipitous breakthrough.

Fujiwara and colleagues' toolkit will be extensively used and expanded to include salts that contain a wider range of alkyl groups. Medicinal chemists in particular will contribute to, and benefit from, this work and future developments. ■

William J. Pitts is in the Department of Molecular Sciences and Candidate Optimization, Bristol-Myers Squibb, Princeton, New Jersey 08543-4000, USA. e-mail: pittsw@bms.com

1. Fujiwara, Y. *et al.* *Nature* **492**, 95–99 (2012).
2. Hagmann, W. K. J. *Med. Chem.* **51**, 4359–4369 (2008).
3. Meanwell, N. A. J. *Med. Chem.* **54**, 2529–2591 (2011).
4. Pryde, D. C. *et al.* *J. Med. Chem.* **53**, 8441–8460 (2010).

symbioses makes them the most complex cells known. The genome sequences are the final pieces in a long-standing puzzle, and they will enrich our understanding of how this arrangement evolved and how the cells manage their intricate biochemistry*.

The unusual biology of these algae arose from endosymbiosis, which is when a cell lives in irreversible symbiosis within another cell. Endosymbiosis is an important concept — the photosynthetic organelles (plastids) of all photosynthetic eukaryotes ultimately trace back to a cyanobacterium that took up

*This article and the paper under discussion¹ were published online on 28 November 2012.

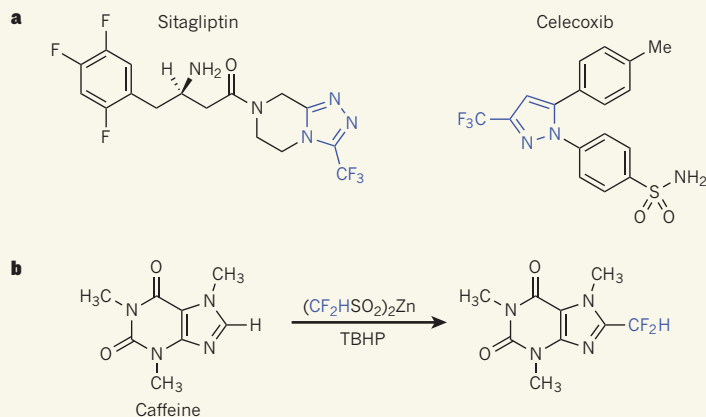


Figure 1 | Applications and synthesis of substituted heterocycles. **a**, Many drugs contain substituted heterocycles — benzene-like rings bearing one or more chemical groups. The antidiabetic drug sitagliptin and the anti-inflammatory agent celecoxib both contain heterocycles (blue) to which a fluorine-containing group (CF_3) is attached. **b**, Fujiwara *et al.*¹ report reagents known as zinc bis(alkylsulphonate) salts, $(\text{RSO}_2)_2\text{Zn}$ (where R is a carbon-containing alkyl group), which convert carbon–hydrogen bonds adjacent to nitrogen atoms in heterocycles to carbon–carbon bonds. In this example, a difluoromethyl (CF_2H) group is transferred from the zinc salt to the smaller heterocycle in caffeine; *t*-butyl hydroperoxide (TBHP) is also required to initiate the reaction.

incorporating fluorine into candidate drugs as part of their optimization plans². The antidiabetic drug Januvia (sitagliptin phosphate) and the anti-inflammatory medicine Celebrex (celecoxib), for example, contain heterocycles with fluoroalkyl groups attached (Fig. 1).

Incorporating fluoroalkyl groups into heterocycles is desirable for various reasons. Several of these groups are important bioisosteres — groups that can replace another group to produce a similar biological effect³. For example, difluoromethyl (CF_2H) groups are good replacements for hydroxyl (OH) groups because the electron-withdrawing effect of the fluorine atoms in CF_2H increases the acidity of the hydrogen atom to the point that it can take part in hydrogen bonding, just as the hydrogen in OH takes part in hydrogen bonding. When attached to heterocycles, the electron-withdrawing effect of fluoroalkyl groups can also decrease the extent to which those heterocycles are ionized at low pH. This is useful for a drug compound because it allows it to be absorbed into the bloodstream without being affected by the co-administration of drugs that raise the pH of the stomach (such as antacids). Finally, fluoroalkyl groups often increase the length of time a drug circulates in the body (its 'half-life'). This could mean that a drug need only be administered once a day, for example, rather than several times, increasing patient compliance with the treatment regime.

Fluoroalkyl groups can improve the half-life by several mechanisms. For example, they are more resistant than analogous hydrocarbon groups to oxidation by metabolic cytochrome P450 enzymes. But heterocycles can also be metabolized by the aldehyde oxidase

enzyme⁴. This oxidation process frequently occurs at C–H bonds adjacent to nitrogen atoms. Fujiwara and colleagues' toolkit incorporates fluoroalkyl groups at such positions, which is expected to decrease the contribution of aldehyde oxidase⁴ to the metabolism of candidate drugs. Taken together, these considerations make the toolkit a valuable addition to the armoury of methods used by medicinal chemists for drug optimization.

EVOLUTIONARY GENOMICS

Algae's complex origins

The nuclear genomes of two of nature's most complex cells have been sequenced. The data will help to determine the evolutionary path from symbioses between species to a multi-compartmental unicellular organism. SEE ARTICLE P.59

SVEN B. GOULD

The orchestration of cellular function from genetic information is a marvel, even in a typical cell that has a single genome. But a few unusual members of a group of microorganisms called protists pack four genomes, each of unique origin, into a single cell. In this issue, Curtis *et al.*¹ report the nuclear-genome sequences for two of these organisms: the unicellular algae *Guillardia theta* and *Bigelowiella natans*. These species are each the derivatives of symbiotic relationships between multiple cells, and their endowment of genetic and cellular relicts from these

Nevertheless, there are some minor limitations. The authors identify zinc bis(alkanesulphonate) salts as optimal reagents, but the reactions generally provide only moderate product yields (typically 40–80%). Low-yielding reactions are acceptable in the early stages of drug optimization, especially if they allow a new analogue of a candidate drug to be made expediently. However, if large quantities of a candidate drug are needed at a later stage, for example for toxicology studies or to evaluate efficacy in animals, then the synthetic route may need to be redesigned to improve yields. Another potential drawback is that the reactions occur at more than one position in some heterocycles, resulting in a mixture of isomeric products. But as long as the isomers are separable, this can be useful for early optimization efforts, because each isomer can be tested for its biological activity and may even provide a serendipitous breakthrough.

Fujiwara and colleagues' toolkit will be extensively used and expanded to include salts that contain a wider range of alkyl groups. Medicinal chemists in particular will contribute to, and benefit from, this work and future developments. ■

William J. Pitts is in the Department of Molecular Sciences and Candidate Optimization, Bristol-Myers Squibb, Princeton, New Jersey 08543-4000, USA. e-mail: pittsw@bms.com

1. Fujiwara, Y. *et al.* *Nature* **492**, 95–99 (2012).
2. Hagmann, W. K. J. *Med. Chem.* **51**, 4359–4369 (2008).
3. Meanwell, N. A. J. *Med. Chem.* **54**, 2529–2591 (2011).
4. Pryde, D. C. *et al.* *J. Med. Chem.* **53**, 8441–8460 (2010).

symbioses makes them the most complex cells known. The genome sequences are the final pieces in a long-standing puzzle, and they will enrich our understanding of how this arrangement evolved and how the cells manage their intricate biochemistry*.

The unusual biology of these algae arose from endosymbiosis, which is when a cell lives in irreversible symbiosis within another cell. Endosymbiosis is an important concept — the photosynthetic organelles (plastids) of all photosynthetic eukaryotes ultimately trace back to a cyanobacterium that took up

*This article and the paper under discussion¹ were published online on 28 November 2012.

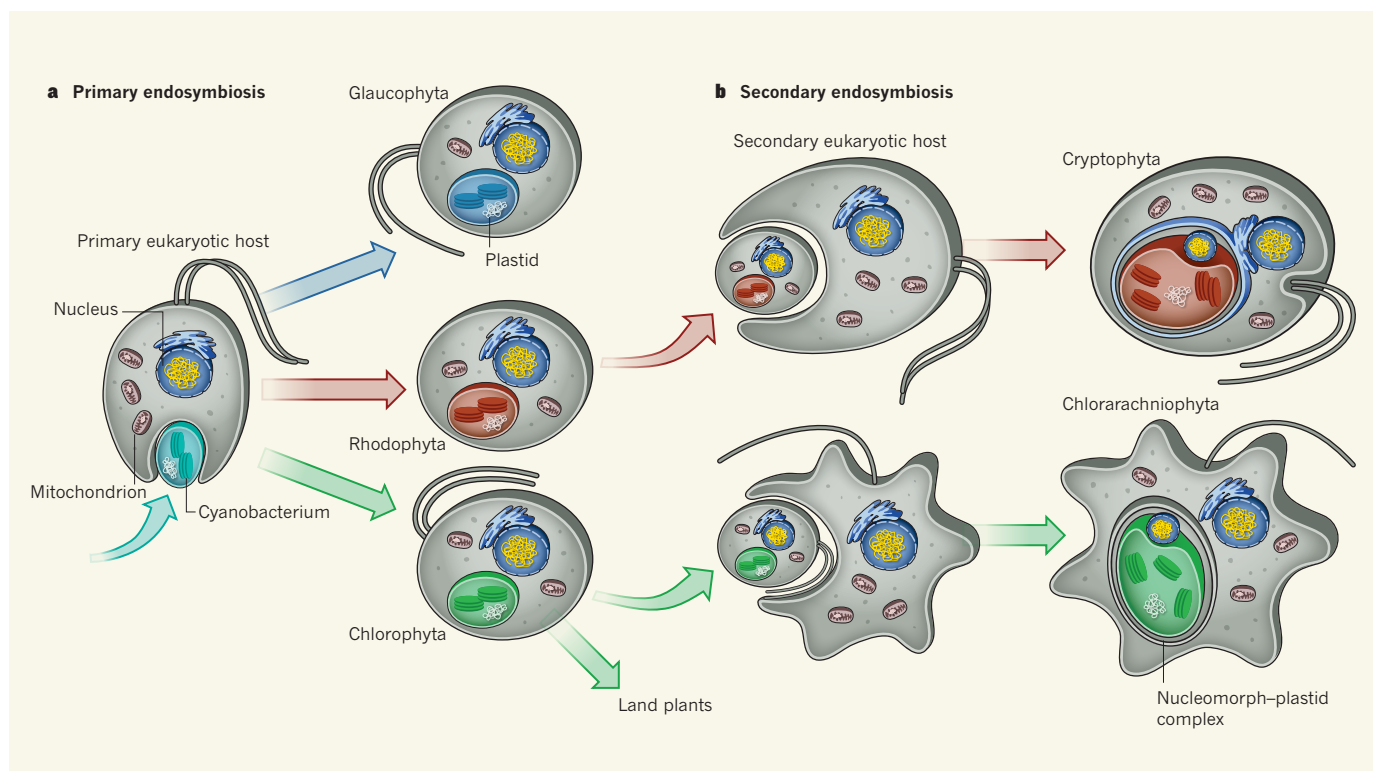


Figure 1 | The rise of photosynthetic eukaryotes. **a**, During an evolutionary event referred to as primary endosymbiosis, a eukaryotic cell irreversibly assimilated a prokaryotic cell called a cyanobacterium. This generated three lineages of alga (glaucophyta, rhodophyta and chlorophyta) that contain a photosynthetic organelle (plastid), which is the remnant of the cyanobacterium, and mitochondria, which are organelles derived from the integration of other prokaryotes early in eukaryotic evolution. Members of one of these lineages, the chlorophytes, gave rise

to all extant complex land plants. **b**, In two independent evolutionary events, other non-photosynthetic eukaryotic hosts then engulfed cells from both the rhodophyta (red algae) and chlorophyta (green algae) lineages. This secondary wave of endosymbiosis led to two further algal groups, the cryptophytes and the chlorarachniophytes. These unicellular organisms contain not only plastids and mitochondria, but also an organelle called the nucleomorph, which is the relict of the nucleus of the engulfed algae.

residence within a eukaryotic host more than 1.2 billion years ago². (Eukaryotes are organisms with nucleated cells, such as animals, plants and fungi, whereas cyanobacteria are prokaryotes, whose cells do not have a nucleus or other membrane-bound organelles.) This fateful encounter is called the primary endosymbiosis (Fig. 1a), because it led to all plastids known today.

Plastids are usually surrounded by two membranes, which are derived from the inner and outer cell membranes of that ancestral cyanobacterium³. But the plastids of some algae have additional membranes — a further two in the case of the algal groups studied by Curtis *et al.* — and the origin of these extra membranes is the story of secondary endosymbiosis⁴. Secondary endosymbiosis occurs when a eukaryotic host acquires a eukaryotic alga as its endosymbiont; the extra membranes around the plastid are the telltale relicts of what was once a whole eukaryotic cell that became an organelle of another (Fig. 1b).

The idea of secondary endosymbiosis was proved correct by the discovery of nucleomorphs — the remnant nuclei of these eukaryotic endosymbionts. Nucleomorph-carrying organisms retain not only the membranes of this relict nucleus, but also many of its genes:

nucleomorph genomes consist of three linear ‘bonsai’ chromosomes, each less than 200 kilobases in size (for *Guillardia* species) and are the smallest eukaryotic genomes known⁵. Many extant protist groups display organellar evidence of secondary endosymbiotic events, such as the dinoflagellates (the cause of red tides) and the apicomplexa (parasitic organisms that include the *Plasmodium* species that cause malaria).

The algae that Curtis *et al.* studied are from two groups that independently evolved to bear nucleomorphs — the cryptophytes (*G. theta*) and the chlorarachniophytes (*B. natans*). These cells express, and make use of, four distinct sets of protein-synthesis machinery known as ribosomes. Two types of ribosome are prokaryotic, belonging to the plastids and the mitochondria (which are eukaryotic organelles also originally derived from endosymbiotic prokaryotes). The other two types are eukaryotic: the cytoplasmic ribosome and that of the periplastidial compartment, which is the remnant cytoplasm of the engulfed alga. At some evolutionary stage, these organisms had five genomes: two nuclear and two mitochondrial (from the two eukaryotic symbionts) and one plastidal. Over time, however, the mitochondrial genome of the endosymbiont

was lost, leaving four genomes in the extant cells. Sounds complex? It is! Which is why Curtis and colleagues’ genome sequences provide rich insight into cell and genome evolution, and the opportunity to study sophisticated intracellular communication and molecular logistics.

The different types of membrane-bound compartment in nucleomorph-bearing cells all have to be serviced by proteins coded for by nuclear genes, and some of these proteins have to cross five membranes before they reach their destination⁶. The number of these compartment-destined proteins predicted from Curtis and colleagues’ nuclear genome is much greater than expected. This may be the final curtain for an old idea that some genes fail to be transferred from organelles to the nucleus because the hydrophobic nature of their protein products would make it difficult for them to be transported across multiple membranes⁷. Further experiments will be needed to clarify the biochemical compartmentalization in these cells and how the complex trafficking of proteins and metabolites is organized.

Curtis *et al.* also found that RNA transcripts produced by *Bigelowiella* algae undergo more alternative splicing than any other unicellular

eukaryote that has been studied. (Alternative splicing is when segments of a transcript can be joined in different conformations to produce different forms of a given protein or lead to different subcellular localization.) Why this organism splices so wildly and how this influences its biology are questions for the years to come.

Both algal genomes also harbour what evolutionary biologists call conflicting phylogenetic signals: there are a surprisingly large number of genes of apparent green-algal origin in *Guillardia*, which actually harbours the remnants of a red alga, and too many red-algal genes in the green-alga-harbours *Bigelowiella* (Fig. 1b). This Pandora's box was first opened when such 'green signals' were identified in related heterokontophyte algae, and additional layers of endosymbiotic events were proposed to explain this apparent conflict⁸. However, more recent analyses favour phylogenetic errors and sampling bias as the explanation^{9,10}. As more red algal genomes are sequenced and a more balanced set of reference genomes becomes available, the conundrum of what early evolutionary track these complex cells took will probably be solved.

Perhaps the most exciting insight revealed by the two genomes is why these cells have not lost the nucleomorph — a question that has puzzled researchers since the discovery of these organelles. Eukaryotic nuclear genomes are typically replete with copies of mitochondrial or plastid DNA¹¹. Humans, for example, have about 500 kilobases of mitochondrial DNA strewn across their chromosomes¹². These insertions arise when one of these organelles lyses and releases its DNA, fragments of which then enter the nucleus, with some being successfully integrated into the nuclear DNA.

But what if there were only one mitochondrion per cell? Its lysis would mean no mitochondrion-bearing progeny and the death of that cell lineage (because mitochondria are essential for cellular energy provision). Notably, only one nucleomorph-plastid complex exists per cell in *Guillardia* and *Bigelowiella*. So, although Curtis *et al.* find mitochondrial DNA in both nuclear genomes, indicating that recent gene transfer from the mitochondrial organelles has occurred, they find no recently transferred copies of nucleomorph or plastid DNA. This implies that the presence of a single nucleomorph-plastid complex prevents any further gene transfer in that cell, such that the nucleomorph is evolutionarily frozen. This constellation tells us that it takes two to tango on the route to becoming an enduring secondary organelle. ■

Sven B. Gould is at the Institute for Molecular Evolution, Heinrich Heine University, 40225 Düsseldorf, Germany.
e-mail: gould@hhu.de

1. Curtis, B. A. *et al.* *Nature* **492**, 59–65 (2012).
2. Parfrey, L. W., Lahr, D. J. G., Knoll, A. H. & Katz, L. A. *Proc. Natl Acad. Sci. USA* **108**, 13624–13629 (2011).
3. Cavalier-Smith, T. *Trends Plant Sci.* **5**, 174–182 (2000).
4. Gibbs, S. *Can. J. Bot.* **56**, 2883–2889 (1978).
5. Douglas, S. E., Murphy, C. A., Spencer, D. F. & Gray, M. W. *Nature* **350**, 148–151 (1991).
6. Gould, S. B., Fan, E., Hempel, F., Maier, U.-G. & Klösgen, R. B. *J. Biol. Chem.* **282**, 30295–30302 (2007).
7. Barbrook, A. C., Howe, C. J. & Purton, S. *Trends Plant Sci.* **11**, 101–108 (2006).
8. Moustafa, A. *et al.* *Science* **324**, 1724–1726 (2009).
9. Stiller, J. W., Huang, J., Ding, Q., Tian, J. & Goodwillie, C. *BMC Genomics* **10**, 484 (2009).
10. Woehle, C., Dagan, T., Martin, W. F. & Gould, S. B. *Genome Biol. Evol.* **3**, 1220–1230 (2011).
11. Hazkani-Covo, E., Zeller, R. M. & Martin, W. *PLoS Genet.* **6**, e1000834 (2010).
12. Ricchetti, M., Tekaia, F. & Dujon, B. *PLoS Biol.* **2**, e273 (2004).

EXTRASOLAR PLANETS

Astrophysical false positives

The probability that giant-planet-like signals detected by the Kepler spacecraft are not from planets is higher than expected. The result underscores the importance of making follow-up observations to confirm the nature of the signals.

ANDREW COLLIER CAMERON

For the past three years, the mosaic of detectors on board NASA's Kepler mission have been staring at 150,000 stars in a region roughly halfway between the bright stars Vega and Deneb. They have been hunting for the recurring dips in light that betray the presence of planets whose orbital planes are nearly edge-on to the line of sight. In that short time, the Kepler team has announced some 2,300 candidate planetary systems. Writing in *Astronomy & Astrophysics*, Santerne *et al.*¹ report that 35% of giant, close-in candidate planets found by Kepler are astrophysical false positives — that is, stars in binary systems that eclipse their companions with a change in brightness (depth) and duration similar to that expected for planets. This value is several times larger than expected.

Santerne and colleagues' team studied 46 giant, close-in Kepler candidates over several weeks using the SOPHIE spectrograph mounted on the 1.93-metre telescope at the Haute-Provence Observatory in wooded hill country north of Marseille, France. The goal of the study was to determine the masses of the putative planets, by measuring the parent star's reflex orbital motion — the back-and-forth 'wobble' caused by the gravitational pull of the planet — around its common centre of mass with the planet. A planetary-mass determination is an unambiguous means of ruling out astrophysical false positives, as well as determining the bulk density, and hence the likely composition, of a planet.

The target stars were selected carefully. They had to be bright enough to yield useful results in a reasonable allocation of telescope time. The candidate planets to be investigated

were also selected carefully. Their passages in front of the host stars (transits) had to decrease the brightness of the star sufficiently (a deep enough transit) to indicate that they had high mass and would thus yield a detectable reflex motion. Finally, the suspected planets had to have orbital periods shorter than 25 days, to ensure that their orbital motion could be detected unambiguously.

The 35% rate of false positives in the sample of 46 candidate planets came as a surprise. A model developed by Morton and Johnson² — based on transit depths, orbital periods and a detailed model of the Milky Way's population of binary stars in the direction of Kepler's field of view — had predicted false-positive probabilities no greater than about 5% for most of the objects in the set of giant, close-in candidate planets observed by Santerne and colleagues. The authors' high rate of false positives calls into question^{1,3} the validity of models of the Galactic binary population in Kepler's direction, and the assumptions on which they are based.

This is important, because the main scientific legacy of data collected by Kepler is a two-dimensional scatter plot of derived planet radius as a function of orbital separation (the distance from host star to planet). This plot contains a wealth of clues concerning planet formation and migration processes, and has the potential to reveal the incidence of Earth-sized planets orbiting at distances at which they could harbour liquid water on their surfaces. A detailed understanding of the stellar binary population as a function of eclipse depth and orbital period is essential to our understanding of the rate of false positives in different parts of the radius-separation plot.

Eclipsing binary stars can mimic transiting giant planets in three common ways (Fig. 1).

eukaryote that has been studied. (Alternative splicing is when segments of a transcript can be joined in different conformations to produce different forms of a given protein or lead to different subcellular localization.) Why this organism splices so wildly and how this influences its biology are questions for the years to come.

Both algal genomes also harbour what evolutionary biologists call conflicting phylogenetic signals: there are a surprisingly large number of genes of apparent green-algal origin in *Guillardia*, which actually harbours the remnants of a red alga, and too many red-algal genes in the green-alga-harbours *Bigelowiella* (Fig. 1b). This Pandora's box was first opened when such 'green signals' were identified in related heterokontophyte algae, and additional layers of endosymbiotic events were proposed to explain this apparent conflict⁸. However, more recent analyses favour phylogenetic errors and sampling bias as the explanation^{9,10}. As more red algal genomes are sequenced and a more balanced set of reference genomes becomes available, the conundrum of what early evolutionary track these complex cells took will probably be solved.

Perhaps the most exciting insight revealed by the two genomes is why these cells have not lost the nucleomorph — a question that has puzzled researchers since the discovery of these organelles. Eukaryotic nuclear genomes are typically replete with copies of mitochondrial or plastid DNA¹¹. Humans, for example, have about 500 kilobases of mitochondrial DNA strewn across their chromosomes¹². These insertions arise when one of these organelles lyses and releases its DNA, fragments of which then enter the nucleus, with some being successfully integrated into the nuclear DNA.

But what if there were only one mitochondrion per cell? Its lysis would mean no mitochondrion-bearing progeny and the death of that cell lineage (because mitochondria are essential for cellular energy provision). Notably, only one nucleomorph-plastid complex exists per cell in *Guillardia* and *Bigelowiella*. So, although Curtis *et al.* find mitochondrial DNA in both nuclear genomes, indicating that recent gene transfer from the mitochondrial organelles has occurred, they find no recently transferred copies of nucleomorph or plastid DNA. This implies that the presence of a single nucleomorph-plastid complex prevents any further gene transfer in that cell, such that the nucleomorph is evolutionarily frozen. This constellation tells us that it takes two to tango on the route to becoming an enduring secondary organelle. ■

Sven B. Gould is at the Institute for Molecular Evolution, Heinrich Heine University, 40225 Düsseldorf, Germany.
e-mail: gould@hhu.de

1. Curtis, B. A. *et al.* *Nature* **492**, 59–65 (2012).
2. Parfrey, L. W., Lahr, D. J. G., Knoll, A. H. & Katz, L. A. *Proc. Natl Acad. Sci. USA* **108**, 13624–13629 (2011).
3. Cavalier-Smith, T. *Trends Plant Sci.* **5**, 174–182 (2000).
4. Gibbs, S. *Can. J. Bot.* **56**, 2883–2889 (1978).
5. Douglas, S. E., Murphy, C. A., Spencer, D. F. & Gray, M. W. *Nature* **350**, 148–151 (1991).
6. Gould, S. B., Fan, E., Hempel, F., Maier, U.-G. & Klösgen, R. B. *J. Biol. Chem.* **282**, 30295–30302 (2007).
7. Barbrook, A. C., Howe, C. J. & Purton, S. *Trends Plant Sci.* **11**, 101–108 (2006).
8. Moustafa, A. *et al.* *Science* **324**, 1724–1726 (2009).
9. Stiller, J. W., Huang, J., Ding, Q., Tian, J. & Goodwillie, C. *BMC Genomics* **10**, 484 (2009).
10. Woehle, C., Dagan, T., Martin, W. F. & Gould, S. B. *Genome Biol. Evol.* **3**, 1220–1230 (2011).
11. Hazkani-Covo, E., Zeller, R. M. & Martin, W. *PLoS Genet.* **6**, e1000834 (2010).
12. Ricchetti, M., Tekaia, F. & Dujon, B. *PLoS Biol.* **2**, e273 (2004).

EXTRASOLAR PLANETS

Astrophysical false positives

The probability that giant-planet-like signals detected by the Kepler spacecraft are not from planets is higher than expected. The result underscores the importance of making follow-up observations to confirm the nature of the signals.

ANDREW COLLIER CAMERON

For the past three years, the mosaic of detectors on board NASA's Kepler mission have been staring at 150,000 stars in a region roughly halfway between the bright stars Vega and Deneb. They have been hunting for the recurring dips in light that betray the presence of planets whose orbital planes are nearly edge-on to the line of sight. In that short time, the Kepler team has announced some 2,300 candidate planetary systems. Writing in *Astronomy & Astrophysics*, Santerne *et al.*¹ report that 35% of giant, close-in candidate planets found by Kepler are astrophysical false positives — that is, stars in binary systems that eclipse their companions with a change in brightness (depth) and duration similar to that expected for planets. This value is several times larger than expected.

Santerne and colleagues' team studied 46 giant, close-in Kepler candidates over several weeks using the SOPHIE spectrograph mounted on the 1.93-metre telescope at the Haute-Provence Observatory in wooded hill country north of Marseille, France. The goal of the study was to determine the masses of the putative planets, by measuring the parent star's reflex orbital motion — the back-and-forth 'wobble' caused by the gravitational pull of the planet — around its common centre of mass with the planet. A planetary-mass determination is an unambiguous means of ruling out astrophysical false positives, as well as determining the bulk density, and hence the likely composition, of a planet.

The target stars were selected carefully. They had to be bright enough to yield useful results in a reasonable allocation of telescope time. The candidate planets to be investigated

were also selected carefully. Their passages in front of the host stars (transits) had to decrease the brightness of the star sufficiently (a deep enough transit) to indicate that they had high mass and would thus yield a detectable reflex motion. Finally, the suspected planets had to have orbital periods shorter than 25 days, to ensure that their orbital motion could be detected unambiguously.

The 35% rate of false positives in the sample of 46 candidate planets came as a surprise. A model developed by Morton and Johnson² — based on transit depths, orbital periods and a detailed model of the Milky Way's population of binary stars in the direction of Kepler's field of view — had predicted false-positive probabilities no greater than about 5% for most of the objects in the set of giant, close-in candidate planets observed by Santerne and colleagues. The authors' high rate of false positives calls into question^{1,3} the validity of models of the Galactic binary population in Kepler's direction, and the assumptions on which they are based.

This is important, because the main scientific legacy of data collected by Kepler is a two-dimensional scatter plot of derived planet radius as a function of orbital separation (the distance from host star to planet). This plot contains a wealth of clues concerning planet formation and migration processes, and has the potential to reveal the incidence of Earth-sized planets orbiting at distances at which they could harbour liquid water on their surfaces. A detailed understanding of the stellar binary population as a function of eclipse depth and orbital period is essential to our understanding of the rate of false positives in different parts of the radius-separation plot.

Eclipsing binary stars can mimic transiting giant planets in three common ways (Fig. 1).

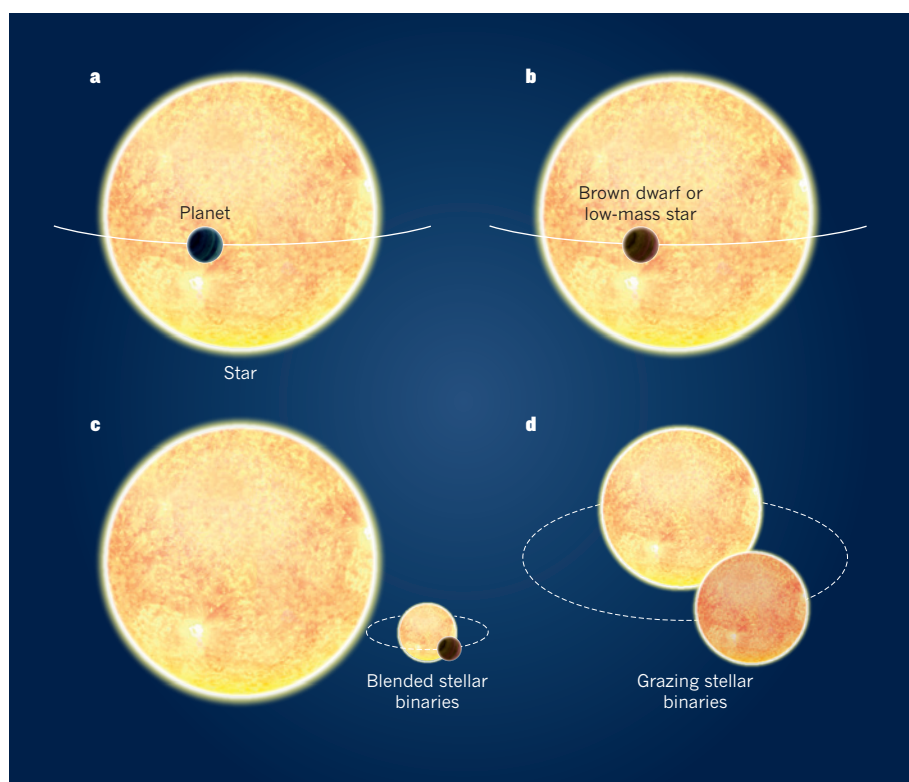


Figure 1 | Mimicking a planetary transit. **a**, A gas-giant planet blocks a small amount of starlight as it passes in front of its host star. The resulting drop in light is similar to that produced by other systems, as follows: **b**, an orbiting brown-dwarf or low-mass star, both of which have radii similar to gas-giant planets; **c**, blended stellar binaries in a triple-star system that have deep eclipses strongly diluted by a bright neighbouring star, mimicking the much shallower transits of a planet; **d**, grazing binary stars, in which the stars' disks overlap by only a tiny amount at each eclipse. The latter systems are the most common type of 'impostor' in Santerne and colleagues' sample of candidate planets¹.

First and simplest, brown-dwarf stars and stars with masses less than 10% that of the Sun have very similar radii to those of gas-giant planets such as Jupiter. As a result, planets can be distinguished from such eclipsing binaries only by determining their mass. A second type of impostor is a triple-star system, in which a bright single star dilutes the light of a nearby, dimmer, eclipsing binary pair to the point at which the eclipses seem to be as shallow as those caused by planets. A third possibility is grazing binary systems, in which the stars' disks overlap by only a tiny amount at each eclipse, so that the reduction in brightness is similarly small.

Some of these options can be easily eliminated. Kepler's high-precision imaging delineates the shape of a planetary transit clearly. The light from the host star changes rapidly when the planet (which is generally much smaller than the star) is moving on or off the edge of the star's disk, giving a characteristic 'U-shaped' light variation. Grazing stellar binaries have 'V-shaped' profiles. The duration of the transit is also a clue. It gives a direct dynamical measure of the host star's bulk density, which is closely related to its temperature. Therefore, a measurement of the density that is inconsistent with that inferred from the star's temperature is a good indicator that

the system could be an impostor.

This and other validation tests are vital for confirming the planetary nature of Kepler candidates, and do not require expensive follow-up observations — they are simply based on stellar properties determined from existing ground-based surveys, and on the Kepler data.

For single-planet systems, confirmation requires follow-up measurements of the orbital reflex motion caused by the orbiting planet. But this approach is expensive because it requires a large amount of ground-based telescope time. The vast majority of Kepler small-planet candidates are simply too faint to be confirmed in this way. Santerne and colleagues' result, which is based on such follow-up measurements of giant-planet candidates, comes as a salutary lesson on the importance of checking, wherever possible, that individual Kepler candidates are not impostors. It also serves as a good example of the painstaking way in which science is advanced. The problem with Morton and Johnson's model was traced³ quickly to an inadequate treatment of the population of grazing binaries. This has already led Morton to develop an improved validation method³, which reproduces the rate of false positives in Santerne and colleagues' sample more reliably, by taking better account of the shape of the Kepler



50 Years Ago

Natural History of Infectious

Diseases. By Sir MacFarlane Burnet

— It is a pleasure to review this, the third edition, of such a well-known work, which now presents an up-to-date account of the ramifications of an important subject ... Throughout it adopts a Darwinian attitude, often overstepping the realms of human pathology into all kinds of unexpected avenues ... In its ambit it presents a picture of the ravages by bacteria, protozoa and viruses ... He discredits the practical value of antityphoid inoculation and would rather attribute the favourable results obtained to military sanitation ...

The readers will find here important information about such diverse subjects as myxomatosis in rabbits, the common cold, plague, German measles, poliomyelitis, the sweating sickness of the Middle Ages and Q. fever (from personal experience). An epilogue on new diseases and the rather bleak outlook for the future finds the author in a gloomy mood in an appraisal of bacteriological warfare.

From *Nature* 8 December 1962

100 Years Ago

Mr. E. G. Bryant ... asks a question regarding the effect of moonlight in "turning" fish. I have lived many years in South Africa, and have encountered the same belief, that moonlight will hasten the turning bad of fish ... It seems curious, at first sight, that moonlight, which has so little effect on meteorological instruments, should have this effect on fish. I have thought it probably due to insects or some low form of life which would be abroad, or be stimulated to action, on moonlit nights and not on dark nights. The action of moonlight in stimulating the rise of sap in trees is widely believed in by practical wood cutters in almost every quarter of the world.

From *Nature* 5 December 1912

planetary-transit profile as well as the transit depth and orbital period.

We should not, however, expect the story to end here. Estimates of the true fraction of planetary systems among Kepler candidates over the full range of transit depths and orbital periods are only as good as our understanding

of the binary-star population. Wherever we have the opportunity to test the predictions of the currently favoured Galactic models, we should do so. ■

Andrew Collier Cameron is at the SUPA School of Physics and Astronomy, University of

St Andrews, St Andrews KY16 9SS, UK.
e-mail: acc4@st-andrews.ac.uk

1. Santerne, A. *et al.* *Astron. Astrophys.* **545**, A76 (2012).
2. Morton, T. D. & Johnson, J. A. *Astrophys. J.* **738**, 170 (2011).
3. Morton, T. D. Preprint at <http://arxiv.org/abs/1206.1568> (2012).

BIOCHEMISTRY

Another aspect of nature's ingenuity

Eyewitnesses are sometimes asked to identify a culprit from a line-up of people associated with a crime scene. An enzyme — iridoid synthase — that catalyses an unusual reaction has been identified by a similar approach. SEE LETTER P.138

JOE CHAPPELL

Compounds known as iridoids are common in plants¹, having vital roles in the interactions between a plant and its environment — for example, offering protection against herbivore attack or microbial pathogens. Perhaps the most widely encountered iridoid is nepetalactone, which mimics feline sex hormones and was first isolated from the catnip plant. Iridoids also form the basis of a diverse array of drugs obtained from natural sources, but, surprisingly, the mechanism responsible for their biosynthesis has remained elusive. On page 138 of this issue, Geu-Flores *et al.*² identify iridoid synthase, the enzyme responsible for the formation of iridoids. The discovery opens the door to the synthesis of a wide range of iridoid derivatives and related compounds through manipulation of the naturally occurring biosynthetic machinery*.

Iridoids belong to the monoterpene family of chemicals, which themselves constitute a family within the much larger constellation of terpenes. Terpenes arise from isoprene, a common biosynthetic building block that contains five carbon atoms. Multiple isoprene units link together to yield chemical classes such as the monoterpenes (which contain 10 carbons), sesquiterpenes (15 carbons), diterpenes (20 carbons) and so on.

As with many other classes of natural product, the impressive structural diversity of the terpene family depends on how the carbon atoms in biosynthetic precursors can be rearranged to form new three-dimensional configurations. The mechanisms involved in the formation of molecular scaffolds and in carbon-atom positioning for terpenes have been dominated by the 'biogenic isoprene

rule'³ — the idea, which won its discoverer Leopold Ruzicka a Nobel prize, that all terpenes are assembled from chains of isoprene units in reactions that include cationic intermediates called carbocations. This concept led to the discovery and characterization of many terpene cyclase enzymes^{4,5} (now more appropriately termed terpene synthases). These enzymes initiate cyclization reactions, in which

linear precursor molecules are converted into ring-containing products through the generation of reactive carbocations (Fig. 1a). The carbocation intermediates also drive myriad complex reactions that lead to hundreds of structurally diverse scaffolds within each of the terpene classes.

But something different happens with iridoids — indeed, these compounds are sometimes called irregular monoterpenes because their biosynthesis could not be deduced from conventional carbocation chemistry. Iridoids are derived from geranyl diphosphate, which is first converted to geraniol, then successively oxidized to form 10-oxogeranial, a direct precursor to iridoids (Fig. 1b). The iridoid-forming cyclization reaction had previously been studied only in plant extracts⁶, and was found to depend on NADPH, a naturally occurring reducing agent.

To identify the iridoid synthase enzyme responsible for the cyclization reaction, Geu-Flores *et al.* examined data on the full

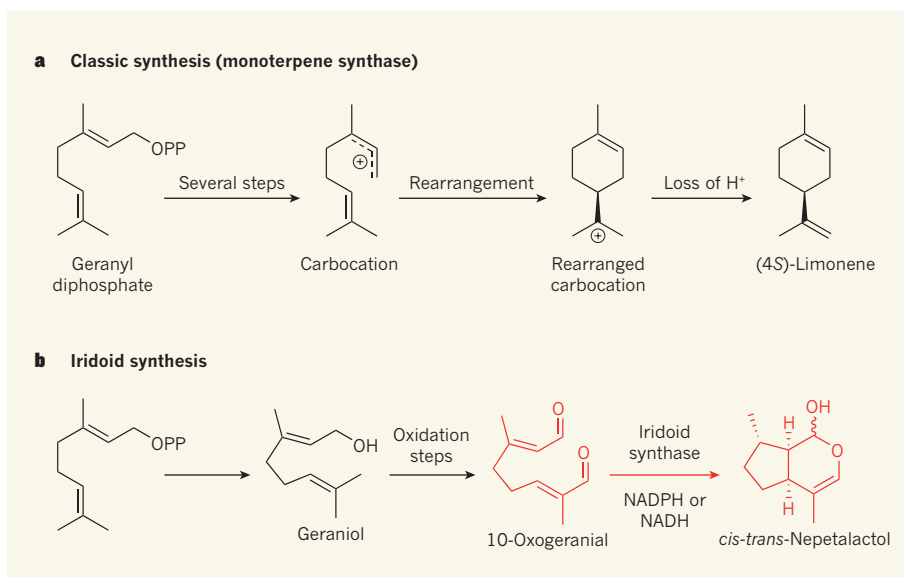


Figure 1 | Mechanisms of monoterpene biosynthesis. Monoterpenes are naturally occurring compounds derived from geranyl diphosphate (GPP); OPP is a diphosphate group. **a**, Monoterpene biosynthesis usually involves positively charged intermediates known as carbocations. Here, a carbocation forms from GPP in several steps (broken bonds in the carbocation indicate charge delocalization), then rearranges to form a new carbocation, which loses a H⁺ ion to form (4S)-limonene as the final product. All the steps are catalysed by a single monoterpene synthase enzyme. The wedge-shaped bonds project above the plane of the page. **b**, The biosynthesis of iridoid monoterpenes, such as *cis-trans*-nepetalactol, does not involve carbocations. Instead, GPP is first converted to geraniol and then to 10-oxogeranial, the direct precursor of iridoids. Geu-Flores *et al.*² have identified the enzyme that converts 10-oxogeranial to *cis-trans*-nepetalactol (reaction shown in red), a process that requires the naturally occurring reducing agent NADPH, or its analogue NADH. The wavy line in *cis-trans*-nepetalactol indicates that the compound forms as a mixture of isomers in which the bond points either above or below the plane of the page; dashed bonds project below the plane of the page.

*This article and the paper under discussion² were published online on 21 November 2012.

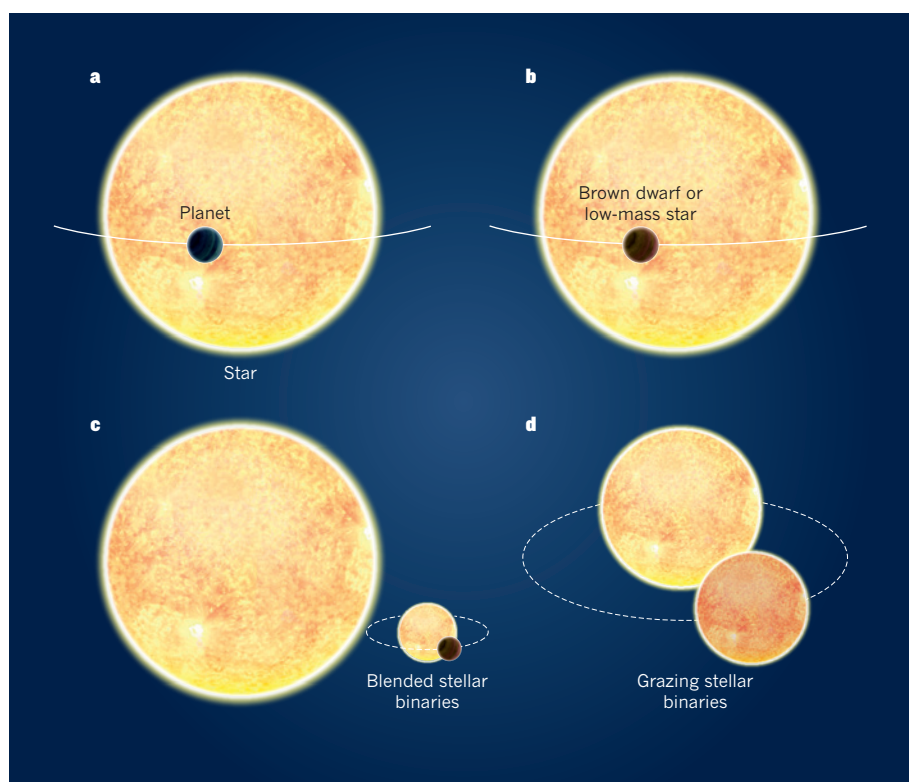


Figure 1 | Mimicking a planetary transit. **a**, A gas-giant planet blocks a small amount of starlight as it passes in front of its host star. The resulting drop in light is similar to that produced by other systems, as follows: **b**, an orbiting brown-dwarf or low-mass star, both of which have radii similar to gas-giant planets; **c**, blended stellar binaries in a triple-star system that have deep eclipses strongly diluted by a bright neighbouring star, mimicking the much shallower transits of a planet; **d**, grazing binary stars, in which the stars' disks overlap by only a tiny amount at each eclipse. The latter systems are the most common type of 'impostor' in Santerne and colleagues' sample of candidate planets¹.

First and simplest, brown-dwarf stars and stars with masses less than 10% that of the Sun have very similar radii to those of gas-giant planets such as Jupiter. As a result, planets can be distinguished from such eclipsing binaries only by determining their mass. A second type of impostor is a triple-star system, in which a bright single star dilutes the light of a nearby, dimmer, eclipsing binary pair to the point at which the eclipses seem to be as shallow as those caused by planets. A third possibility is grazing binary systems, in which the stars' disks overlap by only a tiny amount at each eclipse, so that the reduction in brightness is similarly small.

Some of these options can be easily eliminated. Kepler's high-precision imaging delineates the shape of a planetary transit clearly. The light from the host star changes rapidly when the planet (which is generally much smaller than the star) is moving on or off the edge of the star's disk, giving a characteristic 'U-shaped' light variation. Grazing stellar binaries have 'V-shaped' profiles. The duration of the transit is also a clue. It gives a direct dynamical measure of the host star's bulk density, which is closely related to its temperature. Therefore, a measurement of the density that is inconsistent with that inferred from the star's temperature is a good indicator that

the system could be an impostor.

This and other validation tests are vital for confirming the planetary nature of Kepler candidates, and do not require expensive follow-up observations — they are simply based on stellar properties determined from existing ground-based surveys, and on the Kepler data.

For single-planet systems, confirmation requires follow-up measurements of the orbital reflex motion caused by the orbiting planet. But this approach is expensive because it requires a large amount of ground-based telescope time. The vast majority of Kepler small-planet candidates are simply too faint to be confirmed in this way. Santerne and colleagues' result, which is based on such follow-up measurements of giant-planet candidates, comes as a salutary lesson on the importance of checking, wherever possible, that individual Kepler candidates are not impostors. It also serves as a good example of the painstaking way in which science is advanced. The problem with Morton and Johnson's model was traced³ quickly to an inadequate treatment of the population of grazing binaries. This has already led Morton to develop an improved validation method³, which reproduces the rate of false positives in Santerne and colleagues' sample more reliably, by taking better account of the shape of the Kepler



50 Years Ago

Natural History of Infectious

Diseases. By Sir MacFarlane Burnet

— It is a pleasure to review this, the third edition, of such a well-known work, which now presents an up-to-date account of the ramifications of an important subject ... Throughout it adopts a Darwinian attitude, often overstepping the realms of human pathology into all kinds of unexpected avenues ... In its ambit it presents a picture of the ravages by bacteria, protozoa and viruses ... He discredits the practical value of antityphoid inoculation and would rather attribute the favourable results obtained to military sanitation ...

The readers will find here important information about such diverse subjects as myxomatosis in rabbits, the common cold, plague, German measles, poliomyelitis, the sweating sickness of the Middle Ages and Q. fever (from personal experience). An epilogue on new diseases and the rather bleak outlook for the future finds the author in a gloomy mood in an appraisal of bacteriological warfare.

From *Nature* 8 December 1962

100 Years Ago

Mr. E. G. Bryant ... asks a question regarding the effect of moonlight in "turning" fish. I have lived many years in South Africa, and have encountered the same belief, that moonlight will hasten the turning bad of fish ... It seems curious, at first sight, that moonlight, which has so little effect on meteorological instruments, should have this effect on fish. I have thought it probably due to insects or some low form of life which would be abroad, or be stimulated to action, on moonlit nights and not on dark nights. The action of moonlight in stimulating the rise of sap in trees is widely believed in by practical wood cutters in almost every quarter of the world.

From *Nature* 5 December 1912

planetary-transit profile as well as the transit depth and orbital period.

We should not, however, expect the story to end here. Estimates of the true fraction of planetary systems among Kepler candidates over the full range of transit depths and orbital periods are only as good as our understanding

of the binary-star population. Wherever we have the opportunity to test the predictions of the currently favoured Galactic models, we should do so. ■

Andrew Collier Cameron is at the SUPA School of Physics and Astronomy, University of

St Andrews, St Andrews KY16 9SS, UK.
e-mail: acc4@st-andrews.ac.uk

1. Santerne, A. *et al. Astron. Astrophys.* **545**, A76 (2012).
2. Morton, T. D. & Johnson, J. A. *Astrophys. J.* **738**, 170 (2011).
3. Morton, T. D. Preprint at <http://arxiv.org/abs/1206.1568> (2012).

BIOCHEMISTRY

Another aspect of nature's ingenuity

Eyewitnesses are sometimes asked to identify a culprit from a line-up of people associated with a crime scene. An enzyme — iridoid synthase — that catalyses an unusual reaction has been identified by a similar approach. SEE LETTER P.138

JOE CHAPPELL

Compounds known as iridoids are common in plants¹, having vital roles in the interactions between a plant and its environment — for example, offering protection against herbivore attack or microbial pathogens. Perhaps the most widely encountered iridoid is nepetalactone, which mimics feline sex hormones and was first isolated from the catnip plant. Iridoids also form the basis of a diverse array of drugs obtained from natural sources, but, surprisingly, the mechanism responsible for their biosynthesis has remained elusive. On page 138 of this issue, Geu-Flores *et al.*² identify iridoid synthase, the enzyme responsible for the formation of iridoids. The discovery opens the door to the synthesis of a wide range of iridoid derivatives and related compounds through manipulation of the naturally occurring biosynthetic machinery*.

Iridoids belong to the monoterpene family of chemicals, which themselves constitute a family within the much larger constellation of terpenes. Terpenes arise from isoprene, a common biosynthetic building block that contains five carbon atoms. Multiple isoprene units link together to yield chemical classes such as the monoterpenes (which contain 10 carbons), sesquiterpenes (15 carbons), diterpenes (20 carbons) and so on.

As with many other classes of natural product, the impressive structural diversity of the terpene family depends on how the carbon atoms in biosynthetic precursors can be rearranged to form new three-dimensional configurations. The mechanisms involved in the formation of molecular scaffolds and in carbon-atom positioning for terpenes have been dominated by the 'biogenic isoprene

rule'³ — the idea, which won its discoverer Leopold Ruzicka a Nobel prize, that all terpenes are assembled from chains of isoprene units in reactions that include cationic intermediates called carbocations. This concept led to the discovery and characterization of many terpene cyclase enzymes^{4,5} (now more appropriately termed terpene synthases). These enzymes initiate cyclization reactions, in which

linear precursor molecules are converted into ring-containing products through the generation of reactive carbocations (Fig. 1a). The carbocation intermediates also drive myriad complex reactions that lead to hundreds of structurally diverse scaffolds within each of the terpene classes.

But something different happens with iridoids — indeed, these compounds are sometimes called irregular monoterpenes because their biosynthesis could not be deduced from conventional carbocation chemistry. Iridoids are derived from geranyl diphosphate, which is first converted to geraniol, then successively oxidized to form 10-oxogeranial, a direct precursor to iridoids (Fig. 1b). The iridoid-forming cyclization reaction had previously been studied only in plant extracts⁶, and was found to depend on NADPH, a naturally occurring reducing agent.

To identify the iridoid synthase enzyme responsible for the cyclization reaction, Geu-Flores *et al.* examined data on the full

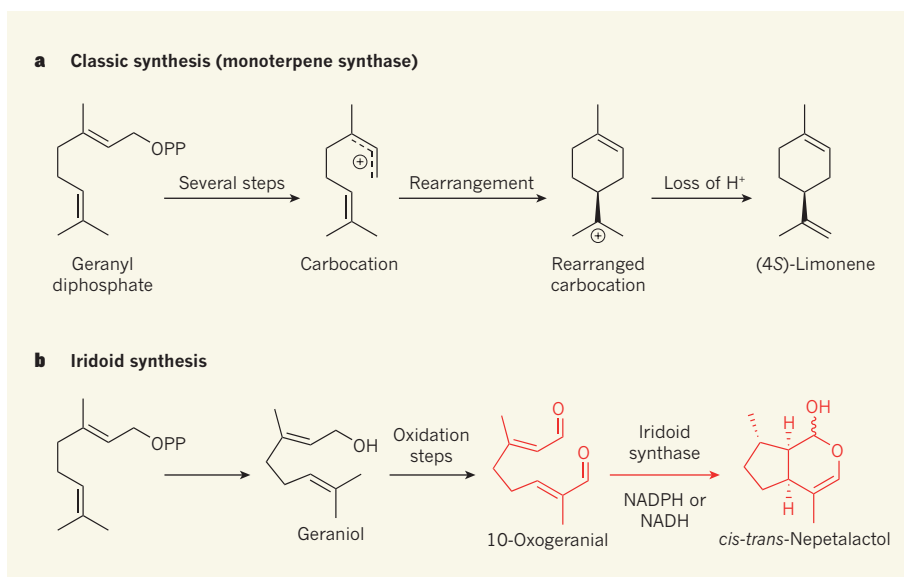


Figure 1 | Mechanisms of monoterpene biosynthesis. Monoterpenes are naturally occurring compounds derived from geranyl diphosphate (GPP); OPP is a diphosphate group. **a**, Monoterpene biosynthesis usually involves positively charged intermediates known as carbocations. Here, a carbocation forms from GPP in several steps (broken bonds in the carbocation indicate charge delocalization), then rearranges to form a new carbocation, which loses a H⁺ ion to form (4S)-limonene as the final product. All the steps are catalysed by a single monoterpene synthase enzyme. The wedge-shaped bonds project above the plane of the page. **b**, The biosynthesis of iridoid monoterpenes, such as *cis-trans*-nepetalactol, does not involve carbocations. Instead, GPP is first converted to geraniol and then to 10-oxogeranial, the direct precursor of iridoids. Geu-Flores *et al.*² have identified the enzyme that converts 10-oxogeranial to *cis-trans*-nepetalactol (reaction shown in red), a process that requires the naturally occurring reducing agent NADPH, or its analogue NADH. The wavy line in *cis-trans*-nepetalactol indicates that the compound forms as a mixture of isomers in which the bond points either above or below the plane of the page; dashed bonds project below the plane of the page.

*This article and the paper under discussion² were published online on 21 November 2012.

complement of RNA molecules transcribed from DNA in many different tissues of the Madagascar periwinkle, *Catharanthus roseus* — the plant from which we get potent and widely used anticancer agents known as monoterpene indole alkaloids (MIAs). These compounds arise from the reaction of a derivative of the amino acid tryptophan with an iridoid derivative, which generates a molecule that is further modified to yield the final MIA products. The authors surmised that the genes encoding enzymes known to be involved in the complex biosynthesis of MIAs would be expressed coordinately and in parallel with previously unidentified genes coding for other steps in the biosynthesis. That is, all of the genes involved in MIA biosynthesis would be expressed together in tissues in which the biosynthesis was occurring.

Geu-Flores *et al.* therefore assembled a list of candidate genes that have expression profiles similar to those of genes known to be involved in MIA biosynthesis. To home in on the gene that encodes iridoid synthase, they narrowed down the list by selecting candidate genes encoding enzymes that were likely to use NADPH or similar cofactors. In this way, they identified a gene similar to the one that encodes an enzyme called progesterone 5β -reductase. Lo and behold, when the authors incubated 10-oxogeranial with extracts prepared from *Escherichia coli* bacteria that had been engineered to express this periwinkle gene, they observed that nepetalactol was biosynthesized in an NADPH- or NADH-dependent manner (NADH is the non-phosphorylated version of NADPH). Geu-Flores *et al.* confirmed that this seemingly unlikely gene encodes iridoid synthase in plants by analysing the enzyme's kinetics, and by observing that MIA formation was lost when levels of the messenger RNA transcripts of the gene were lowered in *C. roseus* leaves.

The authors went on to examine the substrate specificity of the iridoid synthase, and concluded that the cyclization reaction probably requires the formation of an enol intermediate (a compound that contains a C=C-OH group). This implies that variants of reductase enzymes — either naturally occurring ones or those developed using artificial molecular evolution — might be able to generate previously unknown reaction products from 10-oxogeranial. To test this theory, Geu-Flores *et al.* incubated 10-oxogeranial with a fungal reductase enzyme that is unrelated to iridoid synthase, and did indeed recover two novel products. It might be possible to expand the range of reaction products that can be formed by incubating similar reductases with several analogues of 10-oxogeranial. If organisms could be engineered to biosynthesize such analogues as substrates for these reductases, this, too, would open up opportunities for the production of new iridoid derivatives.

Irregular terpenes are found in almost

every class of the terpene family. Geu-Flores and colleagues' results therefore lead one to wonder whether as-yet-undiscovered biosynthetic reactions responsible for other irregular cyclic structures will also involve novel mechanisms catalysed by enzymes in unexpected ways. This will be a difficult possibility to confirm. It will be equally difficult to overcome the various technical hurdles that must be faced before the reductase cyclization mechanism for producing diverse chemicals can be harnessed in biotechnological applications. The challenges for the field are therefore great, but such goals would not even have been possible before Geu-Flores and colleagues developed their approach to addressing an outstanding biochemical

question — and, of course, without the chemical ingenuity that nature has provided. ■

Joe Chappell is in the Department of Plant and Soil Sciences, University of Kentucky, Lexington, Kentucky 40546-0312, USA.
e-mail: chappell@uky.edu

1. Dinda, B., Debnath, S. & Banik, R. *Chem. Pharm. Bull.* **59**, 803–833 (2011).
2. Geu-Flores, F. *et al. Nature* **492**, 138–142 (2012).
3. Ruzicka, L., Eschenmoser, A. & Heusser, H. *Experientia* **9**, 357–367 (1953).
4. Croteau, R. *Chem. Rev.* **87**, 929–954 (1987).
5. Cane, D. E. *Chem. Rev.* **90**, 1089–1103 (1990).
6. Uesato, S., Ikeda, H., Fujita, T., Inouye, H. & Zenk, M. H. *Tetrahedron Lett.* **28**, 4431–4434 (1987).

APPLIED PHYSICS

An optical trampoline

A neat study shows that a sheet of laser light can be used to reflect light-absorbing liquid droplets and manipulate their trajectories. This observation may open up new ways of controlling and studying aerosols.

DAVID MCGLOIN

We think of light as an ephemeral thing with no substance. We appreciate its warming effect when we step outside on a sunny day, but the idea that light can have a mechanical effect, producing forces, seems counter-intuitive. It seems plausible that a small droplet can bounce off a pool of water, unable to break the surface tension. But can we say the same of a droplet hitting a sheet of light? Writing in *Applied Physics Letters*, Esseling and colleagues¹ describe such a phenomenon: an optical 'trampoline'.

In the 1970s, Arthur Ashkin and his co-workers at Bell Laboratories pioneered a new field of research — the manipulation of microscopic particles using light². Ashkin showed that by using a laser he was able to push objects such as glass beads immersed in water and droplets of liquid dispersed in air along the direction of propagation of the laser beam. This radiation pressure could also be used to trap particles by holding them against gravity or, by using two counter-propagating beams, to confine them where the radiation pressure from each beam balanced.

The idea that light could exert these forces was nothing new: James Clerk Maxwell had

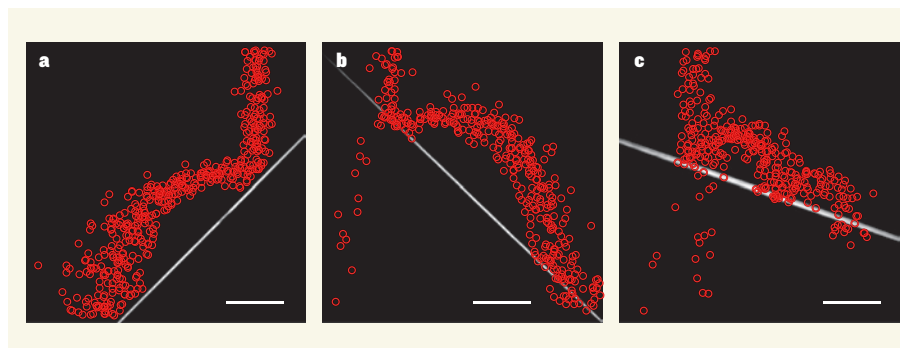


Figure 1 | Bouncing droplets. Esseling *et al.*¹ have used a sheet of laser light (white) to manipulate the trajectory of liquid droplets for several light-sheet inclinations; red circles represent the tracked centres of the droplets. **a**, For an inclination of 45°, droplets starting from the top make a single bounce off the light sheet. **b**, For an inclination of -45°, one bounce is also observed, and some droplets are seen to leak through the light sheet at the initial contact point. **c**, For an inclination of -20°, the droplets bounce twice, passing through the light sheet at the start of the third 'bounce'. Scale bars, 300 micrometres. (Images taken from ref. 1.)

complement of RNA molecules transcribed from DNA in many different tissues of the Madagascar periwinkle, *Catharanthus roseus* — the plant from which we get potent and widely used anticancer agents known as monoterpene indole alkaloids (MIAs). These compounds arise from the reaction of a derivative of the amino acid tryptophan with an iridoid derivative, which generates a molecule that is further modified to yield the final MIA products. The authors surmised that the genes encoding enzymes known to be involved in the complex biosynthesis of MIAs would be expressed coordinately and in parallel with previously unidentified genes coding for other steps in the biosynthesis. That is, all of the genes involved in MIA biosynthesis would be expressed together in tissues in which the biosynthesis was occurring.

Geu-Flores *et al.* therefore assembled a list of candidate genes that have expression profiles similar to those of genes known to be involved in MIA biosynthesis. To home in on the gene that encodes iridoid synthase, they narrowed down the list by selecting candidate genes encoding enzymes that were likely to use NADPH or similar cofactors. In this way, they identified a gene similar to the one that encodes an enzyme called progesterone 5β -reductase. Lo and behold, when the authors incubated 10-oxogeranial with extracts prepared from *Escherichia coli* bacteria that had been engineered to express this periwinkle gene, they observed that nepetalactol was biosynthesized in an NADPH- or NADH-dependent manner (NADH is the non-phosphorylated version of NADPH). Geu-Flores *et al.* confirmed that this seemingly unlikely gene encodes iridoid synthase in plants by analysing the enzyme's kinetics, and by observing that MIA formation was lost when levels of the messenger RNA transcripts of the gene were lowered in *C. roseus* leaves.

The authors went on to examine the substrate specificity of the iridoid synthase, and concluded that the cyclization reaction probably requires the formation of an enol intermediate (a compound that contains a C=C-OH group). This implies that variants of reductase enzymes — either naturally occurring ones or those developed using artificial molecular evolution — might be able to generate previously unknown reaction products from 10-oxogeranial. To test this theory, Geu-Flores *et al.* incubated 10-oxogeranial with a fungal reductase enzyme that is unrelated to iridoid synthase, and did indeed recover two novel products. It might be possible to expand the range of reaction products that can be formed by incubating similar reductases with several analogues of 10-oxogeranial. If organisms could be engineered to biosynthesize such analogues as substrates for these reductases, this, too, would open up opportunities for the production of new iridoid derivatives.

Irregular terpenes are found in almost

every class of the terpene family. Geu-Flores and colleagues' results therefore lead one to wonder whether as-yet-undiscovered biosynthetic reactions responsible for other irregular cyclic structures will also involve novel mechanisms catalysed by enzymes in unexpected ways. This will be a difficult possibility to confirm. It will be equally difficult to overcome the various technical hurdles that must be faced before the reductase cyclization mechanism for producing diverse chemicals can be harnessed in biotechnological applications. The challenges for the field are therefore great, but such goals would not even have been possible before Geu-Flores and colleagues developed their approach to addressing an outstanding biochemical

question — and, of course, without the chemical ingenuity that nature has provided. ■

Joe Chappell is in the Department of Plant and Soil Sciences, University of Kentucky, Lexington, Kentucky 40546-0312, USA.
e-mail: chappell@uky.edu

1. Dinda, B., Debnath, S. & Banik, R. *Chem. Pharm. Bull.* **59**, 803–833 (2011).
2. Geu-Flores, F. *et al. Nature* **492**, 138–142 (2012).
3. Ruzicka, L., Eschenmoser, A. & Heusser, H. *Experientia* **9**, 357–367 (1953).
4. Croteau, R. *Chem. Rev.* **87**, 929–954 (1987).
5. Cane, D. E. *Chem. Rev.* **90**, 1089–1103 (1990).
6. Uesato, S., Ikeda, H., Fujita, T., Inouye, H. & Zenk, M. H. *Tetrahedron Lett.* **28**, 4431–4434 (1987).

APPLIED PHYSICS

An optical trampoline

A neat study shows that a sheet of laser light can be used to reflect light-absorbing liquid droplets and manipulate their trajectories. This observation may open up new ways of controlling and studying aerosols.

DAVID MCGLOIN

We think of light as an ephemeral thing with no substance. We appreciate its warming effect when we step outside on a sunny day, but the idea that light can have a mechanical effect, producing forces, seems counter-intuitive. It seems plausible that a small droplet can bounce off a pool of water, unable to break the surface tension. But can we say the same of a droplet hitting a sheet of light? Writing in *Applied Physics Letters*, Esseling and colleagues¹ describe such a phenomenon: an optical 'trampoline'.

In the 1970s, Arthur Ashkin and his co-workers at Bell Laboratories pioneered a new field of research — the manipulation of microscopic particles using light². Ashkin showed that by using a laser he was able to push objects such as glass beads immersed in water and droplets of liquid dispersed in air along the direction of propagation of the laser beam. This radiation pressure could also be used to trap particles by holding them against gravity or, by using two counter-propagating beams, to confine them where the radiation pressure from each beam balanced.

The idea that light could exert these forces was nothing new: James Clerk Maxwell had

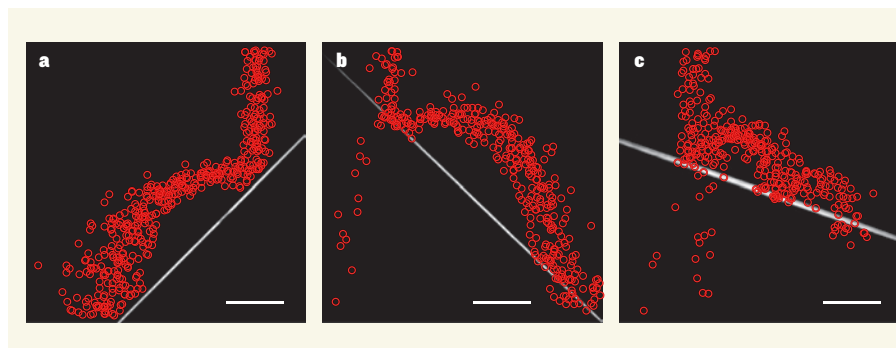


Figure 1 | Bouncing droplets. Esseling *et al.*¹ have used a sheet of laser light (white) to manipulate the trajectory of liquid droplets for several light-sheet inclinations; red circles represent the tracked centres of the droplets. **a**, For an inclination of 45°, droplets starting from the top make a single bounce off the light sheet. **b**, For an inclination of -45°, one bounce is also observed, and some droplets are seen to leak through the light sheet at the initial contact point. **c**, For an inclination of -20°, the droplets bounce twice, passing through the light sheet at the start of the third 'bounce'. Scale bars, 300 micrometres. (Images taken from ref. 1.)

predicted³ it as a consequence of his electromagnetic theory nearly 100 years previously. However, observing the effect had proved difficult owing to the problem of distinguishing optical forces from thermal effects. Indeed, William Crookes (of Crookes radiometer fame) was able to demonstrate thermal forces on matter in 1901, long before optical forces were definitively observed.

Ashkin's great insight was to understand that, by using optically transparent microscopic objects, he could rely on the forces generated by scattering, reflection and refraction alone and remove the strong, masking thermal forces. His work has led to many applications, with optical-trapping techniques being widely used for studying minuscule forces and microscopic motion in systems ranging from molecular motors to the evaporation dynamics of aerosols.

Ashkin's techniques are limited in part by the types of object that they can trap. It is challenging to work with particles that strongly absorb the laser light being used, because they tend to heat up, and a process called thermophoresis starts to come into play. By heating one side of an object, a thermal gradient is established that results in it moving away from the hotter region and towards the colder one, driving it along the direction of the laser beam. Although this sounds very much like Ashkin's original experiments, thermal forces are up to 1,000 times stronger than radiation pressure.

Previous optical-manipulation techniques have used thermophoresis to trap and control solid particles such as carbon⁴. Esseling *et al.* have now extended this to optically absorbing liquid particles and, by using sheets of laser light instead of simple laser beams, have produced a surface made of light off which liquid droplets can bounce. This behaviour has previously been observed with droplets in emulsions⁵, but here the manipulation is carried out in air. By using an inkjet printer head, the authors were able to produce droplets of a uniform diameter of 50 micrometres; ink that absorbed at the laser wavelength of 532 nanometres was used. They then fired the droplets at the light sheet. Depending on the power of the laser and the angle of the light sheet, the droplets could be made to pass through the light or to bounce with well-defined, controllable trajectories (Fig. 1). Multiple bounces could be seen at certain light-sheet inclinations, mimicking a rubber ball bouncing down a smooth slope. A horizontal sheet made with a laser power of 1.8 watts and with a peak intensity of $115 \mu\text{W} \mu\text{m}^{-2}$ prevented droplets from passing through.

This idea opens up avenues for the control of droplet streams. In particular, the ability to shape optical beams means that parabolic light 'bowls' could be created and used to focus droplets in air and carry out controlled chemical reactions; particles in aerosols could be

sorted by rapidly altering the light path down which they travel. Furthermore, the behaviour observed suggests that light-absorbing liquid droplets can be trapped in a similar manner to solid particles. An interest in aerosol particles of all types underpins many areas of atmospheric science as well as combustion studies, for example, and new ways to handle aerosols should allow better and more flexible experiments to be carried out.

Another interesting application is in the development of novel forms of optofluidics — a technique in which light and liquid interact, usually on prefabricated, miniaturized devices called microfluidic chips. A recent advance in aerosol manipulation has been to use such devices to probe the properties of aerosols⁶, and the opportunities afforded by Esseling and colleagues' technique would mean that light could be used to route nearly any type of microscopic particle around such a chip, as well as being used to avoid interactions with the chip's walls (not desirable when using liquid droplets). Their technique may also provide opportunities to analyse particles in confined geometries, such as hollow optical fibres⁷.

The major open question about this type of technique is how the heating of a droplet caused by its interaction with the light sheet

influences the droplet's dynamics and composition. If the goal of manipulating droplets is to investigate the real-world properties of aerosols, then their interaction with the light sheet must have a negligible effect, otherwise the properties of interest will be masked or destroyed. Additionally, many aerosol processes take place in much smaller droplets than those used here. Future experiments will be required to test the limits of the technique. But if all goes to plan, next year's must-have fashion accessory could well be an umbrella made of light. ■

David McGloin is at the Division of Physics, University of Dundee, Dundee DD1 4HN, UK.

e-mail: d.mcglain@dundee.ac.uk

1. Esseling, M., Rose, P., Alpmann, C. & Denz, C. *Appl. Phys. Lett.* **101**, 131115 (2012).
2. Ashkin, A. *Phys. Rev. Lett.* **24**, 156–159 (1970).
3. Maxwell, J. C. *A Treatise on Electricity and Magnetism* Vol. 2 (Oxford Clarendon Press, 1873).
4. Shvedov, V. G. *et al. Phys. Rev. Lett.* **105**, 118103 (2010).
5. Cordero, M. L., Burnham, D. R., Baroud, C. N. & McGloin, D. *Appl. Phys. Lett.* **93**, 034107 (2008).
6. Horstmann, M., Probst, K. & Fallnich, C. *Appl. Phys. B* **103**, 35–39 (2011).
7. Schmidt, O. A., Garbos, M. K., Euser, T. G. & Russell, P. St. J. *Phys. Rev. Lett.* **109**, 024502 (2012).

ASTRONOMY

A truly embryonic star

The discovery of what may be the best example yet of a forming star caught in the moments just before birth provides a missing link in our understanding of how giant gas clouds collapse to form fully fledged stars. [SEE LETTER P.83](#)

DAVID A. CLARKE

In the known Universe there are some 10^{22} stars, give or take a factor of ten. Within our own Milky Way, around 20% of the mass can be accounted for by about 2×10^{11} luminous stars, and another 20% or more may be locked up in 'failed' stars — brown dwarfs, which are too small to ignite thermonuclear fusion — and in stellar remnants such as black holes, neutron stars and white dwarfs¹. That nature has found a way to routinely bring together far-flung wisps of matter, condense it by 24 orders of magnitude, and form the nuclear engines responsible for illuminating the Universe is at the same time astonishing and undeniable. Precisely what that mechanism is, however, is only now being understood by astronomers, and the paper by Tobin *et al.*² on page 83 of this issue brings to bear a central and previously missing piece: the first detection and measurement of a truly embryonic star.

The overall picture of how a star forms is as follows³. About 5% of the interstellar medium, the rarefied gas filling the regions among the stars, consists of vast (6–150 parsecs in diameter) and cold (tens of kelvin) clouds of molecular gas (mainly hydrogen, with traces of carbon monoxide, water and other molecules). These clouds have densities of about 300 particles per cubic centimetre. Random perturbations, such as nearby supernovae, trigger slightly over-dense regions called clumps to collapse under their own gravity, forming molecular 'cloud cores', which are considerably denser — about 10^5 particles per cubic centimetre.

Cloud cores represent a pseudo-stable midpoint in which built-up internal turbulence provides almost enough support to stop further gravitational collapse. However, through dynamic friction, magnetic braking and the relentless pull of gravity, material gradually rains down towards the centre of the cloud core, where the higher pressure and

predicted³ it as a consequence of his electromagnetic theory nearly 100 years previously. However, observing the effect had proved difficult owing to the problem of distinguishing optical forces from thermal effects. Indeed, William Crookes (of Crookes radiometer fame) was able to demonstrate thermal forces on matter in 1901, long before optical forces were definitively observed.

Ashkin's great insight was to understand that, by using optically transparent microscopic objects, he could rely on the forces generated by scattering, reflection and refraction alone and remove the strong, masking thermal forces. His work has led to many applications, with optical-trapping techniques being widely used for studying minuscule forces and microscopic motion in systems ranging from molecular motors to the evaporation dynamics of aerosols.

Ashkin's techniques are limited in part by the types of object that they can trap. It is challenging to work with particles that strongly absorb the laser light being used, because they tend to heat up, and a process called thermophoresis starts to come into play. By heating one side of an object, a thermal gradient is established that results in it moving away from the hotter region and towards the colder one, driving it along the direction of the laser beam. Although this sounds very much like Ashkin's original experiments, thermal forces are up to 1,000 times stronger than radiation pressure.

Previous optical-manipulation techniques have used thermophoresis to trap and control solid particles such as carbon⁴. Esseling *et al.* have now extended this to optically absorbing liquid particles and, by using sheets of laser light instead of simple laser beams, have produced a surface made of light off which liquid droplets can bounce. This behaviour has previously been observed with droplets in emulsions⁵, but here the manipulation is carried out in air. By using an inkjet printer head, the authors were able to produce droplets of a uniform diameter of 50 micrometres; ink that absorbed at the laser wavelength of 532 nanometres was used. They then fired the droplets at the light sheet. Depending on the power of the laser and the angle of the light sheet, the droplets could be made to pass through the light or to bounce with well-defined, controllable trajectories (Fig. 1). Multiple bounces could be seen at certain light-sheet inclinations, mimicking a rubber ball bouncing down a smooth slope. A horizontal sheet made with a laser power of 1.8 watts and with a peak intensity of $115 \mu\text{W} \mu\text{m}^{-2}$ prevented droplets from passing through.

This idea opens up avenues for the control of droplet streams. In particular, the ability to shape optical beams means that parabolic light 'bowls' could be created and used to focus droplets in air and carry out controlled chemical reactions; particles in aerosols could be

sorted by rapidly altering the light path down which they travel. Furthermore, the behaviour observed suggests that light-absorbing liquid droplets can be trapped in a similar manner to solid particles. An interest in aerosol particles of all types underpins many areas of atmospheric science as well as combustion studies, for example, and new ways to handle aerosols should allow better and more flexible experiments to be carried out.

Another interesting application is in the development of novel forms of optofluidics — a technique in which light and liquid interact, usually on prefabricated, miniaturized devices called microfluidic chips. A recent advance in aerosol manipulation has been to use such devices to probe the properties of aerosols⁶, and the opportunities afforded by Esseling and colleagues' technique would mean that light could be used to route nearly any type of microscopic particle around such a chip, as well as being used to avoid interactions with the chip's walls (not desirable when using liquid droplets). Their technique may also provide opportunities to analyse particles in confined geometries, such as hollow optical fibres⁷.

The major open question about this type of technique is how the heating of a droplet caused by its interaction with the light sheet

influences the droplet's dynamics and composition. If the goal of manipulating droplets is to investigate the real-world properties of aerosols, then their interaction with the light sheet must have a negligible effect, otherwise the properties of interest will be masked or destroyed. Additionally, many aerosol processes take place in much smaller droplets than those used here. Future experiments will be required to test the limits of the technique. But if all goes to plan, next year's must-have fashion accessory could well be an umbrella made of light. ■

David McGloin is at the Division of Physics, University of Dundee, Dundee DD1 4HN, UK.

e-mail: d.mcglain@dundee.ac.uk

1. Esseling, M., Rose, P., Alpmann, C. & Denz, C. *Appl. Phys. Lett.* **101**, 131115 (2012).
2. Ashkin, A. *Phys. Rev. Lett.* **24**, 156–159 (1970).
3. Maxwell, J. C. *A Treatise on Electricity and Magnetism* Vol. 2 (Oxford Clarendon Press, 1873).
4. Shvedov, V. G. *et al. Phys. Rev. Lett.* **105**, 118103 (2010).
5. Cordero, M. L., Burnham, D. R., Baroud, C. N. & McGloin, D. *Appl. Phys. Lett.* **93**, 034107 (2008).
6. Horstmann, M., Probst, K. & Fallnich, C. *Appl. Phys. B* **103**, 35–39 (2011).
7. Schmidt, O. A., Garbos, M. K., Euser, T. G. & Russell, P. St. J. *Phys. Rev. Lett.* **109**, 024502 (2012).

ASTRONOMY

A truly embryonic star

The discovery of what may be the best example yet of a forming star caught in the moments just before birth provides a missing link in our understanding of how giant gas clouds collapse to form fully fledged stars. [SEE LETTER P.83](#)

DAVID A. CLARKE

In the known Universe there are some 10^{22} stars, give or take a factor of ten. Within our own Milky Way, around 20% of the mass can be accounted for by about 2×10^{11} luminous stars, and another 20% or more may be locked up in 'failed' stars — brown dwarfs, which are too small to ignite thermonuclear fusion — and in stellar remnants such as black holes, neutron stars and white dwarfs¹. That nature has found a way to routinely bring together far-flung wisps of matter, condense it by 24 orders of magnitude, and form the nuclear engines responsible for illuminating the Universe is at the same time astonishing and undeniable. Precisely what that mechanism is, however, is only now being understood by astronomers, and the paper by Tobin *et al.*² on page 83 of this issue brings to bear a central and previously missing piece: the first detection and measurement of a truly embryonic star.

The overall picture of how a star forms is as follows³. About 5% of the interstellar medium, the rarefied gas filling the regions among the stars, consists of vast (6–150 parsecs in diameter) and cold (tens of kelvin) clouds of molecular gas (mainly hydrogen, with traces of carbon monoxide, water and other molecules). These clouds have densities of about 300 particles per cubic centimetre. Random perturbations, such as nearby supernovae, trigger slightly over-dense regions called clumps to collapse under their own gravity, forming molecular 'cloud cores', which are considerably denser — about 10^5 particles per cubic centimetre.

Cloud cores represent a pseudo-stable midpoint in which built-up internal turbulence provides almost enough support to stop further gravitational collapse. However, through dynamic friction, magnetic braking and the relentless pull of gravity, material gradually rains down towards the centre of the cloud core, where the higher pressure and

temperature break the molecular bonds, strip the atoms of their electrons and couple this ionized gas to the entrained magnetic field. This hot, ionized region of the cloud core forms an 'envelope' about a central condensate that eventually distinguishes itself enough from its surroundings to be designated a protostar, whose luminosity — mostly in the far infrared — is derived from the release of gravitational energy, rather than from the thermonuclear fusion that fuels a fully developed star.

In the same way that figure skaters increase their spin by bringing their arms in to their bodies, the spin of a protostar increases as more material accretes onto it. Indeed, its spin becomes so rapid that centrifugal force completely stymies further collapse, and were it not for an ingenious mechanism for ridding the protostar of most of its angular momentum, stars as we know them would not exist. By the combined action of magnetic, centrifugal and gravitational forces, about 10% of the infalling material is redirected and focused into narrow beams of outflowing gas called protostellar jets¹. These jets transport about 70% of the angular momentum back into the molecular cloud⁵, reducing the spin of the protostar and allowing its collapse to continue.

Young stellar objects (YSOs), which include protostars as their youngest members, are divided into four classes according to their light spectra⁶: 0, I, II and III. This classification is thought to represent an evolutionary track, with higher classification numbers corresponding to older YSOs. Class 0 objects — embryonic stars that many refer to as 'true' protostars — have masses lower than those of their envelopes, whereas class I objects are protostars whose masses are in excess of those of their envelopes. Somewhere during the class II or III phase, thermonuclear fusion is ignited, and this sudden release of energy blows away much of what remains of the envelope and cloud core. Left behind is what is known as a pre-main-sequence star, around which dust and gas trapped in a disk within the star's equatorial plane coalesce into planets, comets and other assorted rubble that remain in orbit about the new star. The entire evolutionary process, from initial collapse of the giant molecular cloud to the emergence of a pre-main-sequence star, happens within 10^8 years, with the true protostellar phase lasting less than 10^5 years. For a star such as our Sun, whose lifetime is about 10^{10} years, this



Figure 1 | The Orion nebula. The giant molecular cloud M42, seen here in the lower half of this image of the Orion nebula, is the closest significant 'stellar nursery' to Earth, in which stars at all stages of early evolution may be found.

phase corresponds to roughly 7 hours in a human lifespan.

This brief but critical period in a star's evolution has evaded astronomers' best efforts to observe it. Although molecular clouds have been observed since antiquity (the most famous example being M42, visible to the naked eye in the sword of Orion; Fig. 1), they have been appreciated for their role in star formation only since the 1960s^{7,8}. And whereas cloud cores⁹ and class I–III YSOs¹⁰ have been observed for some time, there is an enormous conceptual gulf between a cloud core and a class I YSO. A great deal of physics must happen on a very short timescale during the class 0 phase to bridge this gap, and the lack of any observations of it has presented astronomers with their own 'missing link' in stellar evolution. It is for this reason that the detection of true protostars has been referred to as "the holy grail of infrared astronomy"¹¹.

Class 0 protostars are difficult to detect directly because of their very short duration, their weak luminosity and the fact that they are — by definition — enshrouded in gas and dust many times their own mass. It is only once enough of the surrounding material has been accreted onto and/or blown away from the protostar that we have a direct line of sight for observation. Fortunately, wavelengths in the far infrared can pass through much gas and

dust. However, it is only recently that telescopes such as the Submillimeter Array and the Combined Array for Millimeter-wave Astronomy, both used by Tobin *et al.*, have had the resolution necessary to distinguish something as tiny as a protostellar disk from the surrounding envelope. Incidentally, it isn't the class 0 protostar that is imaged directly. Rather, Tobin *et al.* infer its existence by detecting the accretion disk around it (see Fig. 2 of the paper²) and, using Kepler's laws of motion, determining what the mass of the nascent protostar must be to account for the observed rotational velocity of the disk.

Tobin and colleagues may not be the first to measure the mass of a protostar, but the protostar they have observed (known as L1527 IRS) is by far the best example of a class 0 protostar to date. With a mass 0.19 ± 0.04 that of the Sun, its mass as a fraction of its surrounding envelope (0.2) is ten times smaller than the previous best example. In many ways, L1527 IRS is a protostar 'caught in the act' of transition between the gradual collapse of the cloud core and the emergence of a class I YSO.

Is L1527 IRS the holy grail of infrared astronomy and stellar evolution? That will be for historians of science to determine. In the meantime, it is undoubtedly a major discovery, and future studies of it will help to broaden our understanding of how stars form. ■

David A. Clarke is at the Institute for Computational Astrophysics, Department of Astronomy and Physics, Saint Mary's University, Halifax, Nova Scotia B3H 3C3, Canada.
e-mail: dclarke@ap.smu.ca

1. Binney, J. & Tremaine, S. *Galactic Dynamics* 2nd edn (Princeton Univ. Press, 2008).
2. Tobin, J. J. *et al. Nature* **492**, 83–85 (2012).
3. McKee, C. F. & Ostriker, E. C. *Annu. Rev. Astron. Astrophys.* **45**, 565–687 (2007).
4. Clarke, D. A., MacDonald, N. R., Ramsey, J. P. & Richardson, M. *Phys. Can.* **64**, 47–53 (2008).
5. Woitas, J. *et al. Astron. Astrophys.* **432**, 149–160 (2005).
6. Barsony, M. in *Clouds, Cores, and Low Mass Stars* ASP Conf. Ser. Vol. 65 (eds Clemens, D. P. & Barvainis, R.) 197–206 (Astron. Soc. Pacif., 1994).
7. Elmegreen, B. G. & Lada, C. J. *Astrophys. J.* **14**, 725–741 (1977).
8. Blaauw, A. *Annu. Rev. Astron. Astrophys.* **2**, 213–246 (1964).
9. Myers, P. C. & Benson, P. J. *Astrophys. J.* **266**, 309–320 (1983).
10. Lada, C. J. & Wilking, B. A. *Astrophys. J.* **287**, 610–621 (1984).
11. Wynn-Williams, C. G. *Annu. Rev. Astron. Astrophys.* **20**, 587–618 (1982).

NOBEL 2012

As the recipients of the 2012 science Nobel prizes gather in Stockholm to celebrate and be celebrated, News & Views shares some expert opinions on the achievements honoured.

ECONOMICS

Stable allocations and market design

What is the best way to match up entities that have different preferences for one another, if price cannot be used to determine the allocation? The 2012 Sveriges Riksbank Prize in Economic Sciences in Memory of Alfred Nobel went to Lloyd S. Shapley and Alvin E. Roth for the theory and practical demonstration that such processes are optimized by achieving stable matches (see figure).

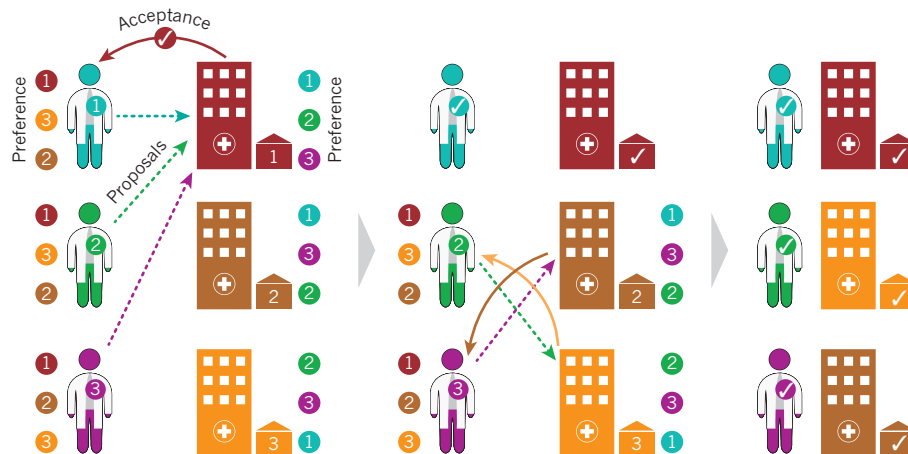
EXPERIMENTAL ECONOMICS

by Yan Chen

In a seminal paper, Gale and Shapley¹ outline an algorithm that always produces stable matching in situations in which legal or ethical obligations preclude the use of price to determine the allocations. Extensions of this algorithm have been applied to several important fields, including the labour market for doctors², school admissions³ and kidney exchange⁴, to improve the stability and reduce gaming of the matching systems in use.

In such system redesigns, controlled laboratory experiments are frequently used to compare the performance of the systems at a level of detail that cannot be obtained from field data. For example, Kagel and Roth's experiments⁵ on regional medical markets in Britain allowed a comparison of the performance of two algorithms for assigning doctors to hospitals, and this demonstrated that the stability of the algorithm contributes to the functioning of such markets. Laboratory experiments can also generate the first data on the performance of a theoretically superior mechanism for which there are no field data. For example, the first school-choice experiment⁶ helped to persuade the public-school authorities in Boston, Massachusetts,

THE PROBLEM: Three doctors each have a preference list of where they would like to work, but the three hospitals have different ideas of whom they most want to employ.



THE PROCESS:

A matching system based on the Gale–Shapley algorithm uses a series of proposals and acceptances to pair up the doctors and hospitals.

THE OUTCOME:

Not everyone ends up with their first choice, but the matches are stable, because no pair can be found in which both parties would prefer each other over their current match.

to switch in 2005 from the Boston mechanism then in use to the Gale–Shapley mechanism.

These examples demonstrate how laboratory experiments can serve as a wind tunnel for evaluating new institutions. Matching and auction theories thus provide new areas for experimental research and are canonical examples of scenarios in which theory, laboratory experiments and real-world implementations form a healthy feedback loop. For these reasons, more economists are now conducting laboratory experiments to evaluate policies and institutions.

AN ENGINEERING APPROACH

by Jacob Goeree

Roth's early work illuminated how the Gale–Shapley algorithm¹ led to the successful matching of newly qualified doctors to hospitals, where decentralized systems had failed. New challenges arose, however, when a growing number of couples graduated from medical school and started to contact hospitals directly, causing instabilities. So Roth and Peranson designed an algorithm that could

accommodate joint applications by doctors. Many entry-level labour markets now use this algorithm, which produces stable outcomes even when the applicants are couples.

In the process, Roth came to realize that many practical problems could not be solved by theory alone, and that computer simulations and laboratory experiments were invaluable tools for comparing alternative matching mechanisms. This 'engineering' approach inspired an entirely new field, referred to as market design, which draws on insights from game theory, experimental economics and computer science to improve the functioning of economic and social institutions.

The tools of market design are now being applied to a host of settings, including auctions to privatize public assets⁷ and cap-and-trade programmes to reduce greenhouse-gas emissions⁸. In an interview about the Nobel award, a reporter asked Roth's opinion on the European debt crisis, and he modestly replied that he is not "that kind of economist". And yet his engineering approach to market design could help to create stable financial markets that avoid excessive risk-taking and taxpayer bailouts of banks

or countries, such as those that are currently plaguing economies around the world. ■

Yan Chen is in the School of Information, University of Michigan, Ann Arbor, Michigan 48109-1285, USA.

e-mail: yanchen@umich.edu

Jacob Goeree is in the ESEI Group for Market

Design, University of Zurich, CH-8006 Zurich, Switzerland.
e-mail: jacob.goeree@econ.uzh.ch

1. Gale, D. & Shapley, L. S. *Am. Math. Mon.* **69**, 9–15 (1962).
2. Roth, A. E. *J. Polit. Econ.* **92**, 991–1016 (1984).
3. Abdulkadiroğlu, A. & Sönmez, T. *Am. Econ. Rev.* **93**, 729–747 (2003).

4. Roth, A. E., Sönmez, T. & Ünver, M. U. *Q. J. Econ.* **119**, 457–488 (2004).
5. Kagel, J. H. & Roth, A. E. *Q. J. Econ.* **115**, 201–235 (2000).
6. Chen, Y. & Sönmez, T. *J. Econ. Theory* **127**, 202–231 (2006).
7. Goeree, J. K. & Holt, C. A. *Games Econ. Behav.* **70**, 146–169 (2010).
8. Ishikida, T., Ledyard, J., Olson, M. & Porter, D. *Res. Exp. Econ.* **8**, 185–220 (2001).

PHYSICS

Manipulating individual quantum systems

Serge Haroche and David J. Wineland have been awarded the Nobel Prize in Physics for developing techniques to measure and manipulate single particles without destroying their quantum properties. Haroche traps photons and measures and controls their quantum states with atoms. Conversely, Wineland traps ions and controls them with light (see figure).

SINGLE-PHOTON CONTROL

by Ed Hinds

Serge Haroche and his colleagues have developed an experiment to study the quantum mechanics of microwave light trapped between two mirrors (a cavity)¹. They show that the quantum of light — the photon — can be controlled at an astonishing level of precision, and have used this to bring the abstract ideas of quantum entanglement to life in the laboratory.

Light is usually detected by destroying it: for example, a light sensor called a photodiode generates an electrical pulse when it absorbs, and so destroys, a photon. But Haroche's group measures the intensity of trapped light using a non-destructive method that probes the light using atoms flying through the trap. Each atom acts as a clock whose ticking rate depends on its energy level. As an atom flies through the cavity, its energies are shifted by the trapped light, and the total number of ticks of the clock changes accordingly, without any light being absorbed.

When a kind of excited atom called a Rydberg atom is used, the technique is sensitive enough to detect a single photon, and repeated measurements allow the same photon to be observed as it lives and eventually dies in the cavity². Similarly, starting with several photons, the researchers can watch the photons disappearing one by one as they are absorbed by the cavity mirrors. The group has even prepared photons in a 'Schrödinger's cat' state — a fragile quantum

state in which many photons are collectively doing two things at once (being dead and alive in the case of the cat) — to study how the state is destroyed by photon loss in the cavity³. These studies allow deep insight into the way quantum systems work, and provide a practical basis for developing powerful devices based on the strange laws of quantum mechanics.

MASTERING SINGLE IONS

by Rainer Blatt

A consummate experimentalist, David Wineland pioneered the use of electromagnetic devices known as Paul traps to hold single trapped ions for quantum metrology. Along the way, he has developed a plethora of groundbreaking experimental methods that have since become standard means of manipulating single atoms.

Armed with efficient single-atom detection through a technique called electron shelving, together with laser cooling to bring an ion to its lowest-energy vibrational state, Wineland masterfully conducted ultra-high-precision spectroscopy of single ions. Using precisely timed and tuned laser pulses, he tailored the coupling between the ions' internal states and their quantized vibration⁴.

Notably, it is with this technology that he laid the groundwork for unprecedented control of a single trapped particle's electronic and motional degrees of freedom, which he in turn applied to generate many kinds of non-classical states that could otherwise be observed only

through light-matter interactions in a cavity⁵.

These methods culminated in Wineland's quantum-logic clock, in which the ions' motion is used to transfer otherwise inaccessible spectroscopic information to a read-out ion⁶. This technology has produced the most precise measurement of an atomic frequency ever obtained, with a fractional uncertainty of less than 10^{-17} . Moreover, Wineland's spectacular quantum mastery will continue to have a major impact. His techniques are already a crucial element of the exciting field of quantum information processing, and will prove invaluable for both fundamental tests of quantum physics and future quantum technologies. ■

Ed Hinds is at the Centre for Cold Matter, Department of Physics, Imperial College London, London SW7 2AZ, UK.

e-mail: ed.hinds@imperial.ac.uk

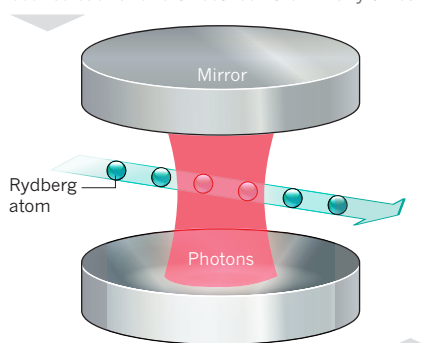
Rainer Blatt is at the Institute for Experimental Physics, University of Innsbruck, and the Institute for Quantum Optics and Quantum Information, Austrian Academy of Sciences, A-6020 Innsbruck, Austria.

e-mail: rainer.blatt@uibk.ac.at

1. Haroche, S. & Raimond, J.-M. *Exploring the Quantum, Atoms, Cavities and Photons* (Oxford Univ. Press, 2006).
2. Gleyzes, S. et al. *Nature* **446**, 297–300 (2007).
3. Deléglise, S. et al. *Nature* **455**, 510–514 (2008).
4. Monroe, C., Meekhof, D. M., King, B. E., Itano, W. M. & Wineland, D. J. *Phys. Rev. Lett.* **75**, 4714–4717 (1995).
5. Meekhof, D. M., Monroe, C., King, B. E., Itano, W. M. & Wineland, D. J. *Phys. Rev. Lett.* **76**, 1796–1799 (1996).
6. Schmidt, P. O. et al. *Science* **309**, 749–752 (2005).

HAROCHÉ METHOD

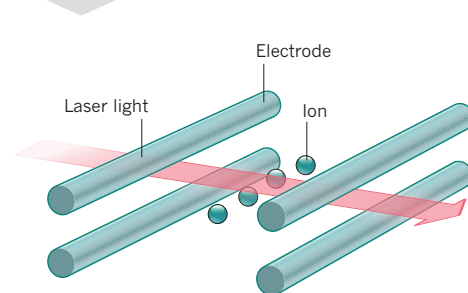
Microwave photons are placed between two highly reflective mirrors that enable an individual photon to bounce back and forth between them many times.



Rydberg atoms, which have one electron in a high-energy level, are sent through the system to measure and manipulate the photon's quantum state.

WINELAND METHOD

An electric field produced by an arrangement of electrodes holds one or several ions inside a trap.



Laser light is shone on the ion, suppressing its thermal vibration and allowing its quantum state to be measured and controlled.

or countries, such as those that are currently plaguing economies around the world. ■

Yan Chen is in the School of Information, University of Michigan, Ann Arbor, Michigan 48109-1285, USA.

e-mail: yanchen@umich.edu

Jacob Goeree is in the ESEI Group for Market

Design, University of Zurich, CH-8006 Zurich, Switzerland.
e-mail: jacob.goeree@econ.uzh.ch

1. Gale, D. & Shapley, L. S. *Am. Math. Mon.* **69**, 9–15 (1962).
2. Roth, A. E. *J. Polit. Econ.* **92**, 991–1016 (1984).
3. Abdulkadiroğlu, A. & Sönmez, T. *Am. Econ. Rev.* **93**, 729–747 (2003).

4. Roth, A. E., Sönmez, T. & Ünver, M. U. *Q. J. Econ.* **119**, 457–488 (2004).
5. Kagel, J. H. & Roth, A. E. *Q. J. Econ.* **115**, 201–235 (2000).
6. Chen, Y. & Sönmez, T. *J. Econ. Theory* **127**, 202–231 (2006).
7. Goeree, J. K. & Holt, C. A. *Games Econ. Behav.* **70**, 146–169 (2010).
8. Ishikida, T., Ledyard, J., Olson, M. & Porter, D. *Res. Exp. Econ.* **8**, 185–220 (2001).

PHYSICS

Manipulating individual quantum systems

Serge Haroche and David J. Wineland have been awarded the Nobel Prize in Physics for developing techniques to measure and manipulate single particles without destroying their quantum properties. Haroche traps photons and measures and controls their quantum states with atoms. Conversely, Wineland traps ions and controls them with light (see figure).

SINGLE-PHOTON CONTROL

by Ed Hinds

Serge Haroche and his colleagues have developed an experiment to study the quantum mechanics of microwave light trapped between two mirrors (a cavity)¹. They show that the quantum of light — the photon — can be controlled at an astonishing level of precision, and have used this to bring the abstract ideas of quantum entanglement to life in the laboratory.

Light is usually detected by destroying it: for example, a light sensor called a photodiode generates an electrical pulse when it absorbs, and so destroys, a photon. But Haroche's group measures the intensity of trapped light using a non-destructive method that probes the light using atoms flying through the trap. Each atom acts as a clock whose ticking rate depends on its energy level. As an atom flies through the cavity, its energies are shifted by the trapped light, and the total number of ticks of the clock changes accordingly, without any light being absorbed.

When a kind of excited atom called a Rydberg atom is used, the technique is sensitive enough to detect a single photon, and repeated measurements allow the same photon to be observed as it lives and eventually dies in the cavity². Similarly, starting with several photons, the researchers can watch the photons disappearing one by one as they are absorbed by the cavity mirrors. The group has even prepared photons in a 'Schrödinger's cat' state — a fragile quantum

state in which many photons are collectively doing two things at once (being dead and alive in the case of the cat) — to study how the state is destroyed by photon loss in the cavity³. These studies allow deep insight into the way quantum systems work, and provide a practical basis for developing powerful devices based on the strange laws of quantum mechanics.

MASTERING SINGLE IONS

by Rainer Blatt

A consummate experimentalist, David Wineland pioneered the use of electromagnetic devices known as Paul traps to hold single trapped ions for quantum metrology. Along the way, he has developed a plethora of groundbreaking experimental methods that have since become standard means of manipulating single atoms.

Armed with efficient single-atom detection through a technique called electron shelving, together with laser cooling to bring an ion to its lowest-energy vibrational state, Wineland masterfully conducted ultra-high-precision spectroscopy of single ions. Using precisely timed and tuned laser pulses, he tailored the coupling between the ions' internal states and their quantized vibration⁴.

Notably, it is with this technology that he laid the groundwork for unprecedented control of a single trapped particle's electronic and motional degrees of freedom, which he in turn applied to generate many kinds of non-classical states that could otherwise be observed only

through light-matter interactions in a cavity⁵.

These methods culminated in Wineland's quantum-logic clock, in which the ions' motion is used to transfer otherwise inaccessible spectroscopic information to a read-out ion⁶. This technology has produced the most precise measurement of an atomic frequency ever obtained, with a fractional uncertainty of less than 10^{-17} . Moreover, Wineland's spectacular quantum mastery will continue to have a major impact. His techniques are already a crucial element of the exciting field of quantum information processing, and will prove invaluable for both fundamental tests of quantum physics and future quantum technologies. ■

Ed Hinds is at the Centre for Cold Matter, Department of Physics, Imperial College London, London SW7 2AZ, UK.

e-mail: ed.hinds@imperial.ac.uk

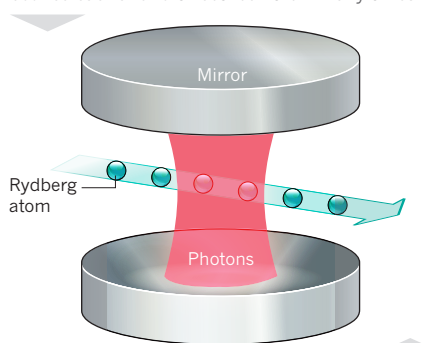
Rainer Blatt is at the Institute for Experimental Physics, University of Innsbruck, and the Institute for Quantum Optics and Quantum Information, Austrian Academy of Sciences, A-6020 Innsbruck, Austria.

e-mail: rainer.blatt@uibk.ac.at

1. Haroche, S. & Raimond, J.-M. *Exploring the Quantum, Atoms, Cavities and Photons* (Oxford Univ. Press, 2006).
2. Gleyzes, S. et al. *Nature* **446**, 297–300 (2007).
3. Deléglise, S. et al. *Nature* **455**, 510–514 (2008).
4. Monroe, C., Meekhof, D. M., King, B. E., Itano, W. M. & Wineland, D. J. *Phys. Rev. Lett.* **75**, 4714–4717 (1995).
5. Meekhof, D. M., Monroe, C., King, B. E., Itano, W. M. & Wineland, D. J. *Phys. Rev. Lett.* **76**, 1796–1799 (1996).
6. Schmidt, P. O. et al. *Science* **309**, 749–752 (2005).

HAROCHÉ METHOD

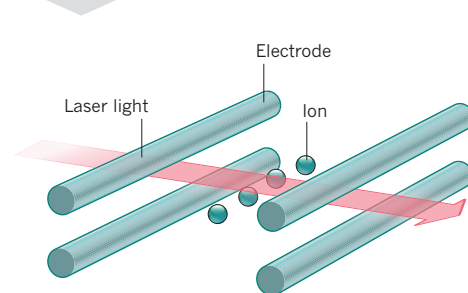
Microwave photons are placed between two highly reflective mirrors that enable an individual photon to bounce back and forth between them many times.



Rydberg atoms, which have one electron in a high-energy level, are sent through the system to measure and manipulate the photon's quantum state.

WINELAND METHOD

An electric field produced by an arrangement of electrodes holds one or several ions inside a trap.



Laser light is shone on the ion, suppressing its thermal vibration and allowing its quantum state to be measured and controlled.

PHYSIOLOGY
OR MEDICINEMature cells can be
rejuvenated

The recipients of the Nobel Prize in Physiology or Medicine are John B. Gurdon and Shinya Yamanaka, whose research — spanning more than four decades — showed that differentiated adult cells can be reprogrammed to become immature cells capable of developing into all the cell types of an organism (see figure).

FROM SCIENCE FICTION TO SCIENCE FACT
by Janet Rossant

Even though the cloned animals John Gurdon produced were only tadpoles, the publication of his experiments¹ caused a media stir: the production of armies of identical cloned humans seemed to be moving from science fiction towards science fact.

But it took decades before cloning was achieved in mammals. Ian Wilmut and colleagues' 1997 creation of Dolly² — a sheep generated by transfer of an adult cell nucleus into an oocyte — opened up practical applications for cloning. This technology has been key to the generation of genetically modified pigs, sheep and cows, and cloned animals have been used to make pharmaceutical products in milk, to generate rejection-resistant pigs

for organ transplantation into humans, and as preclinical models of human disease. But it has also caused controversy: the spectre of human cloning still looms large in the public eye, despite the absence of any evidence that nuclear transfer from adult human cells could ever be effective or safe.

Nonetheless, a specialized form of nuclear transfer, in which the nucleus from an egg containing faulty mitochondria in its cytoplasm is transferred to the healthy cytoplasm of another egg³, has the potential to treat mitochondrial disease and is being developed for use in humans. From frogs to sheep to humans, the impact of Gurdon's experiments continues to challenge nature and to break boundaries.

A CELLULAR VERSION OF A PATIENT
by Christine Mummery

Yamanaka and his co-author⁴ showed that induced pluripotent stem (iPS) cells, which can form any kind of differentiated cell, can be derived from anyone. These cells are genetically identical to the person from whom they are obtained. So, once the technical hurdles are overcome, differentiated cells derived from iPS cells could be transplanted back into a patient without being rejected, to replace cells that have been damaged or lost through disease or trauma.

These cells are also fantastic disease models. In other words, the iPS cells can essentially become 'the patient'. They may carry the same disease-causing mutations present in a patient, or have genetic variants associated with predisposition (or resistance) to a disease. Once the iPS cells differentiate to form the cell types associated with the illness, the effects of these genetic variants may reveal the underlying causes of its symptoms. Moreover, researchers

might discover how a disease develops and look for ways to slow this down or even reverse it. Looking ahead, such insights might reveal windows of opportunity for treating the condition before symptoms appear.

Generating patient-specific cells from iPS cells is an exciting development for the pharmaceutical industry too. Reagents that restore gene or protein expression to normal levels in its derived cells may form the basis of therapies for disorders for which there is no treatment. Similarly, these cell models should help to identify drug targets or reveal side effects of medications. Moreover, they could recapitulate human diseases for which there are no good animal models, such as heart failure and some forms of muscular dystrophy.

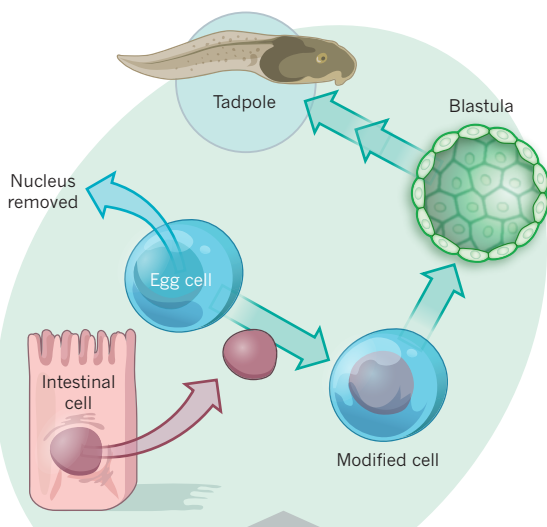
Because iPS cells can be derived from individuals of any ethnic background, they may eventually reveal why some conditions affect certain races more than others, why some drugs are preferentially toxic to some people and why patients may not respond to certain treatments. The potential of iPS cells is almost limitless, and there are exhilarating times ahead. ■

Janet Rossant is at the Hospital for Sick Children, Departments of Molecular Genetics and of Obstetrics and Gynecology, University of Toronto, Toronto, Ontario M5G 1X8, Canada. e-mail: janet.rossant@sickkids.ca

Christine Mummery is in the Department of Anatomy and Embryology, Leiden University Medical Center, 2300 RC Leiden, the Netherlands.

e-mail: c.l.mummery@lumc.nl

1. Gurdon, J. B. *J. Embryol. Exp. Morphol.* **10**, 622–640 (1962).
2. Wilmut, I., Schnieke, A. E., McWhir, J., Kind, A. J. & Campbell, K. H. S. *Nature* **385**, 810–813 (1997).
3. Craven, L. et al. *Nature* **465**, 82–85 (2010).
4. Takahashi, K. & Yamanaka, S. *Cell* **126**, 663–676 (2006).

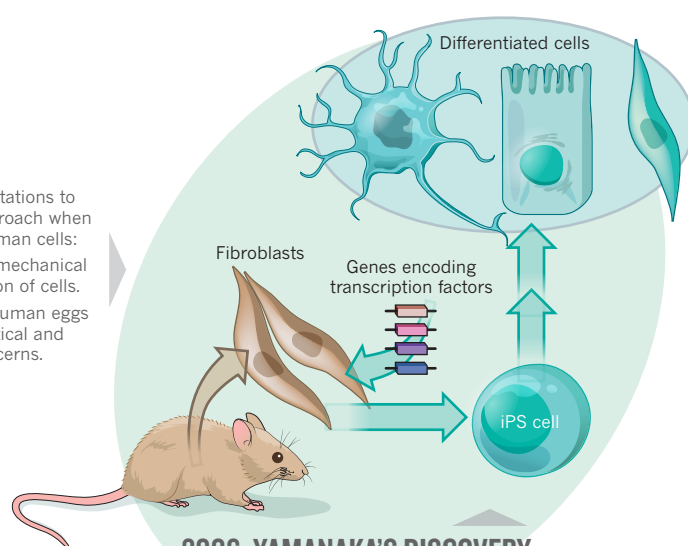


1962: GURDON'S DISCOVERY

When the nucleus of a differentiated intestinal cell is transferred into a nucleus-free egg, the resulting modified cell can go through normal embryonic development to form a blastula, which can generate a tadpole.

There are limitations to Gurdon's approach when applied to human cells:

1. It requires mechanical manipulation of cells.
2. Access to human eggs raises practical and ethical concerns.



2006: YAMANAKA'S DISCOVERY

Introduction of genes encoding just four transcription factors into an intact, differentiated fibroblast can reprogram it into an induced pluripotent stem (iPS) cell that can differentiate into various cell types of the body.

CHEMISTRY

Studies of a ubiquitous receptor family

The Nobel Prize in Chemistry was awarded to Robert J. Lefkowitz and Brian K. Kobilka for their work in characterizing G-protein-coupled receptors (GPCRs) — the proteins that enable cells to sense and respond to their environment (see figure).

BIOLOGICAL INSIGHTS

by Bryan L. Roth

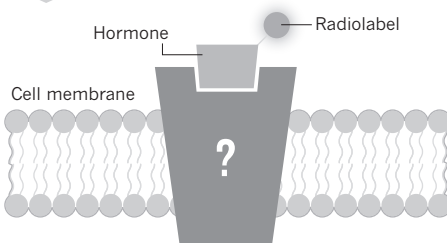
The idea that drugs exert their effects through specific interactions with receptors has captivated scientists' imagination¹ since 1905. But it was not until 1986 that Lefkowitz, Kobilka and colleagues' cloning of β -adrenergic receptors, which mediate the effects of adrenaline and noradrenaline, provided the first definitive proof that receptors are physical entities encoded by the human genome. This finding ushered in one of the most exciting eras of pharmacology and biochemistry, because it allowed other GPCRs to be identified on the basis of their similar transmembrane-domain architecture. Perhaps as many as 900 human GPCRs have been discovered in this way².

The identification of these GPCRs has revealed that more than 50% are 'orphan' receptors^{3,4} — those for which ligands have not been identified. Working out the function of even one orphan GPCR, as Kobilka, Lefkowitz and co-workers did for the 5-HT_{1A} receptor⁵ (the most abundant of the receptors that bind the signalling molecule serotonin), is a great achievement and can open up entire fields of research. 'De-orphanizing' such GPCRs represents a major challenge for scientists.

Lefkowitz and colleagues also discovered that GPCRs have two signalling modes: one that acts through G proteins and another facilitated by cell-scaffolding proteins such as β -arrestins⁶. It seems that β -arrestin-facilitated signalling is responsible for many of the physiological effects of GPCR activation, although the full panoply of events mediated by β -arrestins is unknown. Elucidation of the molecular basis of these effects should reveal the full repertoire of β -arrestin-mediated signalling and provide ample opportunities for drug-discovery programmes for years to come.

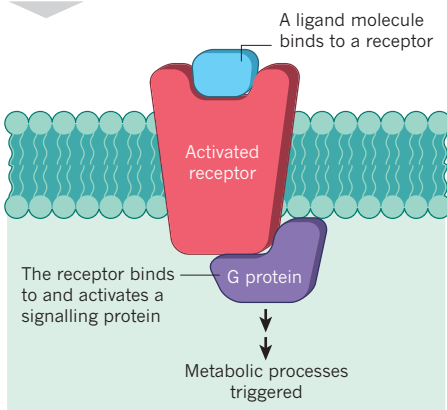
1968

Lefkowitz began using radiolabelled hormones to identify several of the receptors that enable cells to sense their environment.



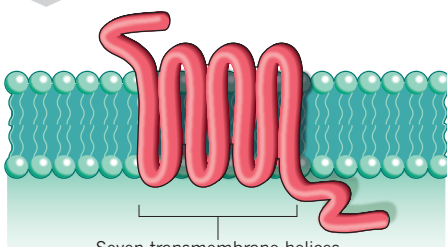
1980

Lefkowitz and colleagues proposed the widely accepted 'ternary complex model' for receptor activation.



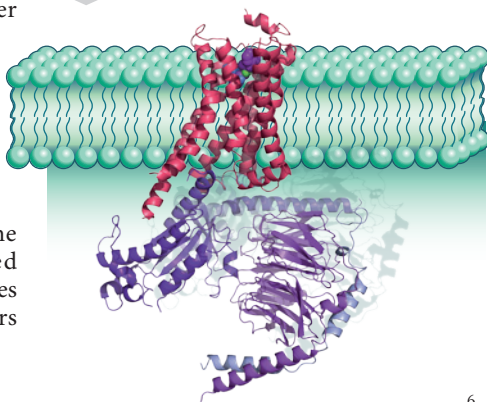
1986

Lefkowitz, Kobilka and co-workers cloned the gene that encodes the β_2 -adrenergic receptor, revealing its transmembrane structure. They concluded that it was part of a family of functionally similar receptors.



2011

Kobilka and colleagues solved the crystal structure of the β_2 -adrenergic receptor in complex with an activating ligand and a G protein.



ENABLING DRUG DISCOVERY

by Fiona H. Marshall

For many years, pharmaceutical companies screened for drugs that act at GPCRs by using live animal tissues suspended in baths to test chemicals related to natural hormones. The introduction of assays based on radio-labelled ligands, such as those developed by Lefkowitz, was a breakthrough, because it allowed larger numbers of compounds to be tested, together with accurate measurement of their affinities for their receptors. This allowed medicinal chemists to identify the relationships between the molecular structure of a ligand and its biological activity.

Lefkowitz, Kobilka and colleagues' cloning of GPCR genes had two notable effects on drug discovery. It enabled the high-throughput screening of libraries of millions of compounds against human receptors, and led to the identification of many GPCRs. A range of genomic technologies has since been applied to discover the function of these orphan receptors, and drugs that target them — for example, suvorexant, a treatment for insomnia⁷ — are now approaching the market.

Despite some successes, high-throughput screening is a hit-and-miss process. The availability of X-ray structures of GPCRs instigated a new era of rational design⁸ for drug discovery that targets these receptors — compounds that fit perfectly into 'pockets' of the receptors can now be selected using computational techniques. Kobilka and colleagues' recently reported structure of the active form of a GPCR in complex with its signalling protein suggests that drugs that activate the receptor, rather than just block it, can also be designed. GPCR-targeting drugs discovered using such structure-based techniques are already in development. ■

Bryan L. Roth is in the Department of Pharmacology, University of North Carolina Medical School, Chapel Hill, North Carolina 27514, USA.

e-mail: bryan_roth@med.unc.edu

Fiona H. Marshall is at Heptares Therapeutics Ltd, Welwyn Garden City AL7 3AX, UK.

e-mail: fiona.marshall@heptares.com

1. Langley, J. N. *J. Physiol. (Lond.)* **33**, 374–413 (1905).
2. Zhang, Y., DeVries, M. E. & Skolnick, J. *PLoS Comput. Biol.* **2**, e13 (2006).
3. Kroeze, W. K., Sheffler, D. J. & Roth, B. L. *J. Cell Sci.* **116**, 4867–4869 (2003).
4. Allen, J. A. & Roth, B. L. *Annu. Rev. Pharmacol. Toxicol.* **51**, 117–144 (2011).
5. Fargn, A. et al. *Nature* **335**, 358–360 (1988).
6. Luttrell, L. M. et al. *Science* **283**, 655–661 (1999).
7. Cox, C. D. et al. *J. Med. Chem.* **53**, 5320–5332 (2010).
8. Congreve, M. et al. *J. Med. Chem.* **55**, 1898–1903 (2012).

F.H.M. declares competing financial interests. See go.nature.com/mo5rfy for details.

Algal genomes reveal evolutionary mosaicism and the fate of nucleomorphs

Bruce A. Curtis^{1,2,3}, Goro Tanifuji^{1,2,3}, Fabien Burki^{3,4}, Ansgar Gruber^{5†}, Manuel Irimia⁶, Shinichiro Maruyama^{1,2,3}, Maria C. Arias⁷, Steven G. Ball⁷, Gillian H. Gile^{1,2,3}, Yoshihisa Hirakawa^{3,4}, Julia F. Hopkins^{1,2,3}, Alan Kuo⁸, Stefan A. Rensing^{9†}, Jeremy Schmutz^{8,10}, Aikaterini Symeonidi⁹, Marek Elias¹¹, Robert J. M. Eveleigh^{1,2,12}, Emily K. Herman¹³, Mary J. Klute¹³, Takuro Nakayama^{1,2,3}, Miroslav Oborník^{14,15,16}, Adrian Reyes-Prieto^{3,17}, E. Virginia Armbrust¹⁸, Stephen J. Aves¹⁹, Robert G. Beiko²⁰, Pedro Coutinho²¹, Joel B. Dacks¹³, Dion G. Durnford¹⁷, Naomi M. Fast⁴, Beverley R. Green⁴, Cameron J. Gridale⁴, Franziska Hempel²², Bernard Henrissat²¹, Marc P. Höppner²³, Ken-Ichiro Ishida²⁴, Eunsoo Kim²⁵, Luděk Kořený^{14,15}, Peter G. Kroth⁵, Yuan Liu^{19,26}, Shehre-Banoo Malik^{1,2,3}, Uwe G. Maier²², Darcy McRose²⁷, Thomas Mock²⁸, Jonathan A. D. Neilson¹⁷, Naoko T. Onodera^{1,2,3}, Anthony M. Poole²⁹, Ellen J. Pritham³⁰, Thomas A. Richards²⁶, Gabrielle Roca¹⁸, Scott W. Roy³¹, Chihiro Sarai²⁴, Sarah Schaack³², Shu Shirato²⁴, Claudio H. Slamovits^{1,2,3}, David F. Spencer^{1,2,3}, Shigekatsu Suzuki²⁴, Alexandra Z. Worden²⁷, Stefan Zauner²², Kerrie Barry⁸, Callum Bell³³, Arvind K. Bharti³³, John A. Crow³³, Jane Grimwood^{8,10}, Robin Kramer³³, Erika Lindquist⁸, Susan Lucas⁸, Asaf Salamov⁸, Geoffrey I. McFadden³⁴, Christopher E. Lane^{1,2,3,35}, Patrick J. Keeling^{3,4}, Michael W. Gray^{1,2,3}, Igor V. Grigoriev⁸ & John M. Archibald^{1,2,3}

Cryptophyte and chlorarachniophyte algae are transitional forms in the widespread secondary endosymbiotic acquisition of photosynthesis by engulfment of eukaryotic algae. Unlike most secondary plastid-bearing algae, miniaturized versions of the endosymbiont nuclei (nucleomorphs) persist in cryptophytes and chlorarachniophytes. To determine why, and to address other fundamental questions about eukaryote–eukaryote endosymbiosis, we sequenced the nuclear genomes of the cryptophyte *Guillardia theta* and the chlorarachniophyte *Bigelowiella natans*. Both genomes have >21,000 protein genes and are intron rich, and *B. natans* exhibits unprecedented alternative splicing for a single-celled organism. Phylogenomic analyses and subcellular targeting predictions reveal extensive genetic and biochemical mosaicism, with both host- and endosymbiont-derived genes servicing the mitochondrion, the host cell cytosol, the plastid and the remnant endosymbiont cytosol of both algae. Mitochondrion-to-nucleus gene transfer still occurs in both organisms but plastid-to-nucleus and nucleomorph-to-nucleus transfers do not, which explains why a small residue of essential genes remains locked in each nucleomorph.

The photosynthetic organelles (plastids) of algae evolved from cyanobacteria by endosymbiosis^{1,2}. The ‘primary’ plastids of red algae, glaucophyte algae and green algae, and their land-plant descendants, probably arose just once, more than a billion years ago^{3,4}. Subsequent to this key event, the primary plastids of red and green algae were laterally transferred to other eukaryotes by secondary and tertiary endosymbioses, spawning some of the most abundant and ecologically important aquatic photosynthesizers on Earth such as diatoms, giant kelp, bloom-forming haptophytes and toxic dinoflagellates, as well as parasites such as the malaria pathogen *Plasmodium*³.

We have sequenced the nuclear genomes of two unicellular algae that are remarkable in their genetic and cellular complexity: the cryptophyte *Guillardia theta* and the chlorarachniophyte *Bigelowiella natans*. The secondary plastids of these independently evolved algae are unique in retaining a relict endosymbiont nucleus (the nucleomorph). Cryptophyte and chlorarachniophyte cells thus have four genomes and require complex subcellular protein-targeting machinery and inter-compartment coordination (Fig. 1). The *B. natans* nuclear genome is the first to be sequenced from a rhizarian protist, and the *G. theta* nuclear genome sequence is the first from a cryptophyte. They

¹Department of Biochemistry and Molecular Biology, Dalhousie University, Halifax, Nova Scotia B3H 4R2, Canada. ²Centre for Comparative Genomics and Evolutionary Bioinformatics, Dalhousie University, Halifax, Nova Scotia B3H 4R2, Canada. ³Integrated Microbial Biodiversity Program, Canadian Institute for Advanced Research, University of British Columbia, Vancouver, British Columbia V6T 1Z4, Canada. ⁴Department of Botany, University of British Columbia, Vancouver, British Columbia V6T 1Z4, Canada. ⁵Fachbereich Biologie, Universität Konstanz, 78457 Konstanz, Germany. ⁶Banting and Best Department of Medical Research and Donnelly Centre, University of Toronto, Toronto, Ontario M5S 3E1, Canada. ⁷Unité de Glycobiologie Structurale et Fonctionnelle, UMR 8576 CNRS-USTL, Université des Sciences et Technologies de Lille, 59655 Villeneuve d'Ascq Cedex, France. ⁸US Department of Energy Joint Genome Institute, Walnut Creek, California 94598, USA. ⁹Faculty of Biology and BIOS Centre for Biological Signalling Studies, University of Freiburg, 79085 Freiburg, Germany. ¹⁰HudsonAlpha Genome Sequencing Center, 601 Genome Way, Huntsville, Alabama 35806, USA. ¹¹University of Ostrava, Faculty of Science, Department of Biology and Ecology, Life Science Research Centre, 710 00 Ostrava, Czech Republic. ¹²Genome Quebec, 740 Docteur-Penfield Avenue, Montreal, Quebec H3A 1A4, Canada. ¹³Department of Cell Biology, University of Alberta, Edmonton, Alberta T6G 2H7, Canada. ¹⁴University of South Bohemia, Faculty of Science, Branišovská 31, 37005 České Budějovice, Czech Republic. ¹⁵Biology Centre, Academy of Sciences of the Czech Republic, Institute of Parasitology, Branišovská 31, 37005 České Budějovice, Czech Republic. ¹⁶Institute of Microbiology, Academy of Sciences of the Czech Republic, 37981 Třeboň, Czech Republic. ¹⁷Department of Biology, University of New Brunswick, Fredericton, New Brunswick E3B 5A3, Canada. ¹⁸School of Oceanography, University of Washington, Seattle, Washington 98195-7940, USA. ¹⁹Biosciences, College of Life and Environmental Sciences, University of Exeter, Stocker Road, Exeter EX4 4QD, UK. ²⁰Faculty of Computer Science, Dalhousie University, Halifax, Nova Scotia B3H 4R2, Canada. ²¹Architecture et Fonction des Macromolécules Biologiques, Aix-Marseille Université, CNRS UMR 7257, 163 avenue de Luminy, 13228 Marseille, France. ²²LOEWE-Zentrum für Synthetische Mikrobiologie (Synmikro), Hans-Meerwein-Straße, D-35032 Marburg, Germany. ²³Science for Life Laboratory, Department of Medical Biochemistry and Microbiology Uppsala University, SE-751 23 Uppsala, Sweden. ²⁴Graduate School of Life and Environmental Sciences, University of Tsukuba, Tsukuba, Ibaraki 305-8572, Japan. ²⁵American Museum of Natural History, Division of Invertebrate Zoology, New York, New York 10024, USA. ²⁶The Natural History Museum, Cromwell Road, London SW7 5BD, UK. ²⁷Monterey Bay Aquarium Research Institute (MBARI), 7700 Sandholdt Road, Moss Landing, California 95039, USA. ²⁸School of Environmental Sciences, University of East Anglia, Norwich Research Park, Norwich NR47TJ, UK. ²⁹Biomolecular Interaction Centre & School of Biological Sciences, University of Canterbury, Christchurch 8140, New Zealand. ³⁰Eccles Institute of Human Genetics, Salt Lake City, Utah 84112, USA. ³¹San Francisco State University, San Francisco, California 94132, USA. ³²Reed College, Portland, Oregon 97202, USA. ³³National Center for Genome Resources, Rodeo Park Drive East, Santa Fe, New Mexico 87505, USA. ³⁴School of Botany, University of Melbourne, Victoria 3010, Australia. ³⁵University of Rhode Island, Kingston, Rhode Island 02881, USA. †Present addresses: Department of Biochemistry and Molecular Biology, Dalhousie University, Halifax, Nova Scotia B3H 4R2, Canada (A.G.); Fachbereich Biologie, Philipps-Universität Marburg, Karl-von-Frisch Straße 8, 35043 Marburg, Germany (S.A.R.).

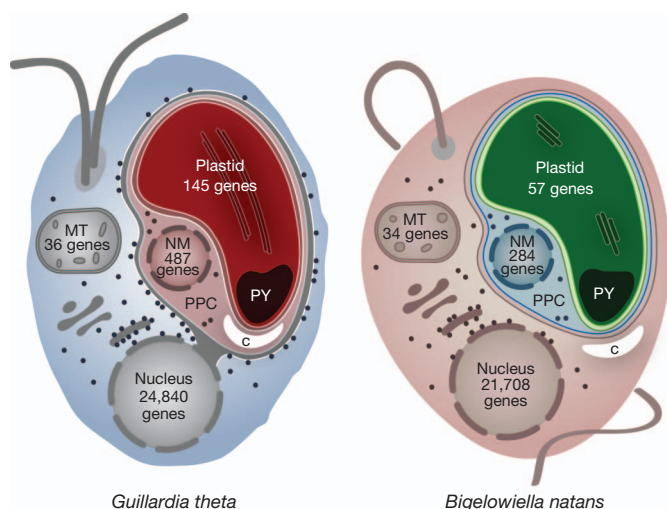


Figure 1 | Cryptophyte and chlorarachniophyte cell biology. The cryptophyte alga *G. theta* and the chlorarachniophyte alga *B. natans* have plastids bound by four membranes. In cryptophytes, the outermost plastid membrane is continuous with the nuclear envelope and its surface is studded with ribosomes, which co-translationally insert nucleus-encoded, organelle-targeted proteins. Between the inner and outer membrane pairs is the periplastidial compartment (PPC), which contains the nucleomorph (NM), the relict nucleus of the eukaryotic endosymbiont. The predicted numbers of protein-coding genes in the plastid, mitochondrial (MT), nucleomorph and nuclear genomes of *G. theta* and *B. natans* are shown. Additional abbreviations: C, carbohydrate; PY, pyrenoid.

fill critical gaps on the tree of eukaryotic life, shed light on the pattern and process of host–endosymbiont integration, and reveal why nucleomorphs persist in cryptophytes and chlorarachniophytes but have been lost in other algae and parasites with secondary plastids.

Genomic and transcriptomic complexity

The nuclear genomes of *B. natans* and *G. theta* are approximately 95 and 87 megabase pairs (Mb) in size, respectively (Table 1 and Supplementary Tables 1.4.1 and 1.4.2; see Supplementary Information for sequencing and assembly details). Compared to the genomes of other secondary plastid-bearing algae, such as the diatoms *Phaeodactylum tricornutum*⁵ and *Thalassiosira pseudonana*⁶, and the filamentous brown alga *Ectocarpus siliculosus*⁷, the *B. natans* and *G. theta* genomes are gene rich (>21,000 predicted protein genes each, >85% of which are supported by RNA-seq data). Of the inferred proteins, 51% in *G. theta* and 47% in *B. natans* are unique, that is, have no detectable homologues in any other organism. Both genomes contain a large number of paralogues, constituting 2,636 multi-gene families in *B. natans* and 3,284 in *G. theta* (Supplementary Table 1.6.2).

As inferred from functional classifications based on the eukaryotic Orthologous Groups (KOG) database⁸, and protein family analyses (Supplementary Information 2.6), the *G. theta* and *B. natans* genomes are essentially ‘complete’ with respect to the major hallmarks of eukaryotic cellular complexity (>97% of a set of ‘core eukaryotic genes’⁹ are present in both organisms). These include components of the endomembrane system (Supplementary Information 2.6.3), transcription, RNA processing and modification, post-translational modification and

protein turnover, and cytoskeleton. Examples of particularly large gene families include RNA processing and modification proteins, ankyrin repeat-containing proteins in *B. natans* (Supplementary Figs 1.6.3 and 1.6.5) and putative tyrosine kinases in *G. theta* (Supplementary Figs 1.6.4 and 1.6.6).

B. natans and *G. theta* protein genes are rich in spliceosomal introns. Examination of *B. natans* RNA-seq data revealed an unexpected finding: unlike all characterized unicellular species—indeed, unlike all characterized non-metazoans—*B. natans* shows complex and ubiquitous alternative splicing (Supplementary Information 2.2). Heavy use of various major alternative-splicing mechanisms was observed, including intron retention or inclusion (22% of *B. natans* introns were retained in >20% of the gene transcripts; Supplementary Fig. 2.2.1a) and exon skipping, which was found at levels higher than those observed in all characterized unicellular and multicellular species, and human tissues, being comparable only to the level observed in the human cerebral cortex (Supplementary Fig. 2.2.1b; exon skipping was confirmed by RNA-seq and expressed-sequence-tag (EST) data as well as polymerase chain reaction with reverse transcription (RT–PCR)). Hundreds of cases of alternative 5′ and 3′ splice-site usage were also identified, many involving alternative splicing at 3′ AG dinucleotides spaced three nucleotides apart (NAGNAG boundaries, Supplementary Fig. 2.2.5c), and whose role in expanding mammalian proteomes has been reported recently¹⁰.

We next examined the possible biological significance of the observed transcriptional complexity in *B. natans*. Two features of the *B. natans* alternative exons suggest that much of the exon skipping reflects spliceosomal ‘noise’ (that is, splicing errors). First, most skipped exons are nearly constitutively spliced (that is, skipped only occasionally), perhaps suggesting that exon skipping is not regulated (Supplementary Fig. 2.2.4b). Second, the proportion of exons that maintain reading frame (that is, are a multiple of three nucleotides) is close to random expectation (and similar to constitutive exons) (Supplementary Fig. 2.2.4c). This proportion is lower than that observed for cassette exons in human and fly, in which maintenance of the reading frame is associated with functional (and evolutionarily conserved) alternative splicing (for example, refs 11, 12). Nevertheless, even if most of the splicing complexity seen in *B. natans* simply reflects mis-splicing, many of these alternative transcripts might have important functions. A systematic survey of RNA-seq data identified 246 cases of genes whose alternative isoforms differentially include or exclude amino-terminal signal-peptide-encoding regions (three of which were verified by RT–PCR), suggesting that alternative splicing has a role in the generation of proteins targeted to different subcellular compartments (below). Alternative splicing has recently been shown to mediate dual targeting of glycolytic enzymes to the cytosol and peroxisome in fungi¹³.

Subcellular proteomes

Cryptophyte and chlorarachniophyte nucleomorphs are residual, endosymbiotic nuclei with tiny genomes <1 Mb in size^{14–17}. The *G. theta* and *B. natans* nucleomorph genomes have only 487 (ref. 17) and 331 (ref. 15) protein genes, respectively, comprised of a limited set of ‘housekeeping’ genes, 31 or fewer genes for plastid-targeted proteins, and an abundance of ‘ORFan’ genes that typically show no detectable sequence similarity to known proteins¹⁴.

Table 1 | Features of the *Guillardia theta* and *Bigelowiella natans* genomes relative to those of select algae and plants

Features	<i>Guillardia theta</i>	<i>Bigelowiella natans</i>	<i>Phaeodactylum tricornutum</i>	<i>Chlamydomonas reinhardtii</i>	<i>Arabidopsis thaliana</i>
Genome size (Mb)	87.2	94.7	27.4	121	140
G + C (%)	53	45	49	64	36
Protein-coding genes	24,840	21,708	10,402	15,143	26,341
Genes with introns (%)	80	86	47	92	79
Mean intron length (bp)	110	184	123	373	164
Mean exons per gene	6.4	8.8	1.8	8.3	5.2

Like plastids and mitochondria, nucleomorphs and their genomes are reduced beyond self-sufficiency; they depend on nucleus-encoded proteins that are targeted to the periplastidial compartment (PPC), the residual endosymbiont cytoplasm in which the nucleomorph resides (Fig. 1). However, only a handful of PPC-targeted proteins are known (for example, see refs 18–21) and the true extent of this dependence is unclear. Indeed, why nucleomorph genomes have been retained at all is a long-standing mystery of plastid evolution. Bearing in mind our knowledge of the *G. theta* and *B. natans* plastid^{22,23}, nucleomorph^{15,17} and mitochondrial (this study) genome sequences, we carried out a comprehensive examination of nucleus-encoded proteins predicted to be targeted to each subcellular compartment (Supplementary Information 1.9), with emphasis on the PPC.

Our *in silico*-predicted mitochondrial, plastid, and PPC and nucleomorph proteomes for *G. theta* and *B. natans* are summarized in Supplementary Table 1.9.1 and Supplementary Fig. 1.9.4.1.2, together with a predicted set of >600 evolutionarily conserved endoplasmic reticulum and Golgi proteins (Supplementary Information 1.9). The limited overlap in proteins predicted to be targeted to different compartments suggests that the search strategies successfully differentiated among plastid-, PPC- and nucleomorph-, and host endoplasmic-reticulum- and Golgi-targeted proteins, which is important because in both cryptophytes and chlorarachniophytes the signal peptide secretion system is the first step in trafficking proteins to each of these compartments¹. We analysed these proteomes in order to compare and contrast the biology of the independently evolved plastid and periplastidial compartments in *G. theta* and *B. natans*.

G. theta is predicted to have twice as many PPC- and nucleomorph-targeted proteins as *B. natans* (2,401 versus 1,002, after removal of ambiguously assigned proteins). A KOG-based breakdown of the unique (that is, non-overlapping) proteins in the PPC or nucleomorph proteomes revealed three KOG categories that are particularly 'enriched' in *G. theta* relative to *B. natans*: post-translational modification, protein turnover and chaperones; signal transduction; and carbohydrate transport and metabolism (Fig. 2a and Supplementary Table 1.9.4.1.1). The biological significance of these observations was further revealed through the mapping of nucleomorph- and nucleus-encoded, PPC-targeted proteins to KEGG (Kyoto Encyclopedia of Genes and Genomes) metabolic pathways (Supplementary Information 2.4). The *G. theta* PPC possesses canonical components of the protein-degrading proteasome, which *B. natans* seems to have lost entirely (KEGG pathway map 03050, Supplementary Fig. 2.4.1). *G. theta* also seems to have more PPC-localized proteins dedicated to protein folding (molecular chaperones) and RNA degradation, and a much greater diversity of metabolic enzymes, including those involved in amino acid biosynthesis (Supplementary Information 2.6.1 and Supplementary Fig. 2.4.1). In contrast, *B. natans* has a larger number of predicted nucleomorph-localized, spliceosome-associated proteins than does *G. theta* (Supplementary Fig. 2.4.1), which correlates with the marked difference in intron abundance: 852 in the *B. natans* nucleomorph genome¹⁵ versus just 17 in *G. theta*¹⁷.

Host nuclear control over organelle biology is apparent in both *G. theta* and *B. natans* in the form of nucleus-encoded transcription-associated proteins (presumably regulating nucleomorph gene expression; Supplementary Information 2.6.1), putative DNA replication machinery, and 'cell cycle-related' proteins (for example, protein kinases) (Supplementary Fig. 2.4.1). Other processes in the PPC and nucleomorph are driven mainly by nucleomorph-encoded proteins, translation being a prominent example (Fig. 2a; KOG category J (translation, ribosomal structure and biogenesis)). Near-complete repertoires of small and large PPC ribosomal subunits could be inferred for *G. theta*, somewhat less so for *B. natans*, and in both cases the bulk of the constituent proteins are nucleomorph-encoded (Supplementary Fig. 2.4.2). This mirrors the pattern seen in plastid genomes²⁴, in which core processes such as transcription and translation primarily involve proteins synthesized 'on-site'.

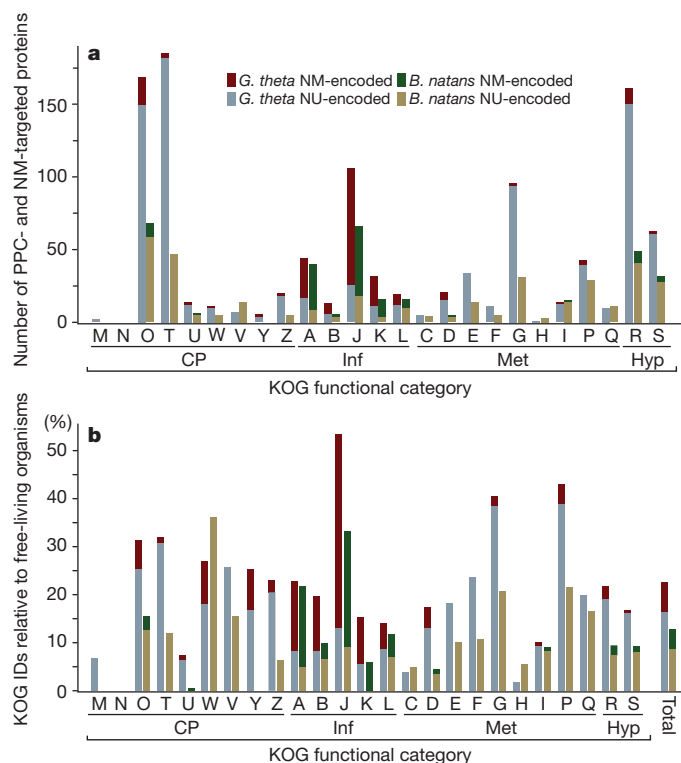


Figure 2 | Complexity of the periplastidial compartment in cryptophytes and chlorarachniophytes. **a**, Histogram showing the number of proteins predicted to be targeted to the PPC of *G. theta* and *B. natans* broken down by KOG functional category. For each KOG category, nucleomorph (NM)- and nucleus (NU)-encoded proteins are shown (PPC proteins predicted to be targeted to more than one subcellular compartment were removed; see Supplementary Fig. 1.9.4.1.2). **b**, Histogram showing the diversity of protein functions in the *G. theta* and *B. natans* PPC relative to free-living organisms (colour-coding as in **a**). Numbers of distinct KOG identifiers (IDs) in the PPC proteomes are plotted as a percentage of the average number of KOG IDs across 25 KOG categories for 6 organisms: *Chlamydomonas reinhardtii*, *Ostreococcus tauri*, *Arabidopsis lyrata*, *Emiliania huxleyi*, *Dictyostelium purpureum* and *Phaeodactylum tricornutum* (see Supplementary Information 1.9.4.3). Plastid and mitochondrial proteins were removed before calculating the averages (see Supplementary Information). KOG categories are as follows: A, RNA processing and modification; B, chromatin structure and dynamics; C, energy production and conversion; D, cell cycle control, cell division and chromosome partitioning; E, amino acid transport and metabolism; F, nucleotide transport and metabolism; G, carbohydrate transport and metabolism; H, coenzyme transport and metabolism; I, lipid transport and metabolism; J, translation, ribosomal structure and biogenesis; K, transcription; L, replication, recombination and repair; M, cell wall, membrane or envelope biogenesis; N, cell motility; O, post-translational modification, protein turnover, chaperones; P, inorganic ion transport and metabolism; Q, secondary metabolites biosynthesis, transport and catabolism; R, general function prediction only; S, function unknown; T, signal transduction; U, intracellular trafficking, secretion and vesicular transport; V, defence mechanisms; W, extracellular structures; Y, nuclear structure; Z, cytoskeleton. Higher KOG categories are as follows: CP, cellular processing and signalling; Hyp, poorly characterized; Inf, information storage and processing; Met, metabolism.

Carbon metabolism differs substantially in *G. theta* and *B. natans* as inferred from the identification of putative carbohydrate-active enzymes (Supplementary Information 1.11 and Tables 2.3.1 and 2.3.2). Subcellular mapping of putative glycolysis-associated proteins in *G. theta* (Supplementary Fig. 2.4.5) reveals many PPC-localized reactions catalysed by key enzymes such as glucan, water dikinase, alpha-amylase, hexokinase, 6-phosphofructokinase and phosphoglucosyltransferase. These enzymes form a link to the synthesis and degradation of starch, which occurs in the PPC in *G. theta*²⁵. Thirty-six candidate proteins for PPC, plastid or cytosol metabolite shuttling

in *G. theta* were identified from a set of 757 putative membrane-transport-associated proteins (Supplementary Information 1.10 and Supplementary Table 1.10.2). The distribution of glycolytic enzymes in *B. natans* is very different from that of *G. theta*, with a more heterogeneous mix of PPC-, plastid-, mitochondrion- and host cytosol-localized proteins (Supplementary Figs 2.4.3 and 2.4.4). In chlorarachniophytes the main carbohydrate storage product is a β -1,3-glucan located in the host cytoplasm²⁶ (Fig. 1), and we identified numerous enzymes that are likely to have roles in β -glucan metabolism (Supplementary Information 2.3.2.1 and Supplementary Table 2.3.4).

We next examined the reduction in the PPC and nucleomorph proteomes of cryptophytes and chlorarachniophytes relative to the free-living organisms from which they evolved. We used the number of different KOG identifiers present in each of the 25 KOG functional categories as a measure of the diversity of biochemical processes taking place in the *B. natans* and *G. theta* PPC (taking into account nucleomorph-encoded proteins) (Supplementary Information 1.9.4.3). A total of 237 and 452 unique KOG identifiers were assigned to the *B. natans* and *G. theta* PPC proteome data sets, respectively (Supplementary Table 1.9.4.3.1). For most KOG categories the number of KOG identifiers in *G. theta* and *B. natans* is <25% of the average calculated from a set of 6 free-living organisms (algae with primary and secondary plastids plus a heterotrophic amoeba; Fig. 2b and Supplementary Information 1.9.4.3). Some functional categories are, predictably, completely absent in both organisms (for example, *n* = cell motility), whereas in *G. theta* the number of KOG identifiers in three different KOG categories exceeds 40% of the 'free-living' average (category J (translation, ribosomal structure and biogenesis), G (carbohydrate transport and metabolism) and P (inorganic ion transport and metabolism); Fig. 2b). On balance, the PPC of cryptophytes and chlorarachniophytes is highly reduced, but has retained an unexpectedly broad range of biochemical processes. These data provide the basis for addressing many fundamental questions about algal cell biology, including how many homologues of *G. theta* and *B. natans* PPC proteins are retained in the nucleomorph-lacking PPC of algae such as diatoms and haptophytes²¹, and what exactly are the biochemical determinants of the protein trafficking pathways in cryptophytes, chlorarachniophytes and other secondary plastid-bearing algae^{1,27}. Making sense of the hundreds of predicted PPC and nucleomorph proteins in *G. theta* and *B. natans* with unknown functions (Supplementary Table 1.9.4.1.1) will be a substantial challenge.

Endosymbiotic gene transfer and replacement

Endosymbiotic gene transfer (EGT)—the movement of DNA from endosymbiont to host before, during and after the evolution of an organelle—has had a notable role in the evolution of algae and their nuclear genomes^{28,29}. The genomes of eukaryotes that are known or proposed to have undergone secondary endosymbioses involving red or green algal endosymbionts are now regularly queried for the presence or absence of so-called 'red' genes or 'green' genes (for example, see refs 30, 31). Organisms with (or thought to have once had) red algal secondary plastids are predicted to have 'red' genes in their nuclear genomes and 'green' genes should be found in the nuclei of organisms with green algal secondary plastids. Quantification of these algal signatures has the potential to answer fundamental questions about the spread and secondary loss of plastids across the eukaryotic tree but has led to conflicting results. For example, a large and unexpected number of 'green' genes were found in the genomes of diatoms³² and were interpreted to be evidence of a cryptic secondary endosymbiosis involving a green alga before the establishment of the red alga-derived plastid that diatoms currently harbour. However, these results were re-evaluated and found to be unconvincing³³. The ability to detect genes of algal origin in nuclear genomes and to accurately distinguish between 'red' and 'green' has been shown to

be complicated by a number of factors including taxonomic sampling bias, phylogenetic artefacts and large data sets consisting of thousands of complex trees that are invariably processed in an automated fashion^{31,33,34}. We carried out a comprehensive phylogenomic investigation of EGT in the nuclear genomes of *B. natans* and *G. theta*, whose plastids and nucleomorphs are of green and red algal ancestry, respectively, using protocols and programs designed to address, to the extent possible, those issues mentioned above and other potential problems (Supplementary Information 1.12 and Supplementary Fig. 1.12.3).

From a set of 6,181 *B. natans* genes for which protein-based phylogenetic trees could be generated, automated tree sorting and manual curation resulted in the identification of 353 genes (5.7%) for which an algal origin could be confidently inferred (Fig. 3 and Supplementary Fig. 1.12.3). As expected, a large proportion (207; 59%) of these were green algal in nature, although 45 (22%) were classified as being derived from red algae. This pattern resembles that seen in an early EST-based analysis of *B. natans* proteins and was attributed to the mixotrophic lifestyle of chlorarachniophyte algae³⁵. For *G. theta*, 508 of 7,451 genes (6.8%) were deemed to be algal in origin (Fig. 3 and Supplementary Fig. 1.12.3). Interestingly, more than twice as many *G. theta* genes in the manually curated set were classified as green (252) than red (100), and 9 examples of apparently glaucophyte-derived genes were identified. These results should be interpreted with caution, however, because although our analyses included all available red algal protein data sets (Supplementary Table 1.12.1), taxon sampling is still biased towards 'green' lineages. In fact, the majority (143 out of 252) of the protein trees for 'green' genes in *G. theta* contained no red algal homologues (Fig. 3) and 147 out of 508 were considered 'algal' but ambiguous with respect to which type. Thus, increased taxon sampling from red algae will presumably affect several predictions and perhaps enable more meaningful interpretation of others, as underscored by recent authors investigating 'red' and 'green' signals in other organisms with red secondary plastids^{31,33,34}. The same can be said for interpretation of the red algal genes in *B. natans*, which has a green alga-derived secondary plastid. These uncertainties are exacerbated further by the still-unresolved phylogenetic position of the host component of cryptophytes relative to primary and secondary plastid-bearing algae³⁶. Consequently, testing hypotheses about possible biological explanations for the diversity of algal nuclear genes seen in *G. theta* and *B. natans*, such as the relative contributions of endosymbiotic versus horizontal gene transfer, cannot currently be carried out without careful consideration of taxon sampling and methodological artefacts.

Nevertheless, phylogenomic data taken together with subcellular targeting predictions show that the *B. natans* and *G. theta* nuclear genomes possess a complex mosaic of genes whose evolutionary histories do not reliably predict where their protein products function within the cell. A large portion of the alga-derived proteins identified in both organisms seem to function in their host cytosolic compartments, and clear examples of algal proteins targeted to the mitochondrion, endoplasmic reticulum or Golgi apparatus, plastid, and PPC or nucleomorph were also found (Fig. 3b). These results show that during the course of host–endosymbiont integration proteins often acquire new functions and/or new locations in which to function.

Gene duplication has also played a part in the 're-purposing' of *G. theta* and *B. natans* nuclear genes of both host and endosymbiont ancestry (Supplementary Information 2.5.2 and Supplementary Fig. 2.5.2.2). Of the 508 'algal' genes in the *G. theta* nuclear genome, 71 were found to belong to paralogous gene clusters (that is, genes that have duplicated subsequent to EGT); in ~25% of these cases, paralogues encode proteins predicted to be targeted to multiple compartments, most often the PPC and host cytosol (Supplementary Fig. 2.5.2.1). A similar picture is seen in *B. natans*. In other cases the opposite pattern is observed, that is, duplication of apparent host-derived genes followed by organelle targeting of one or more

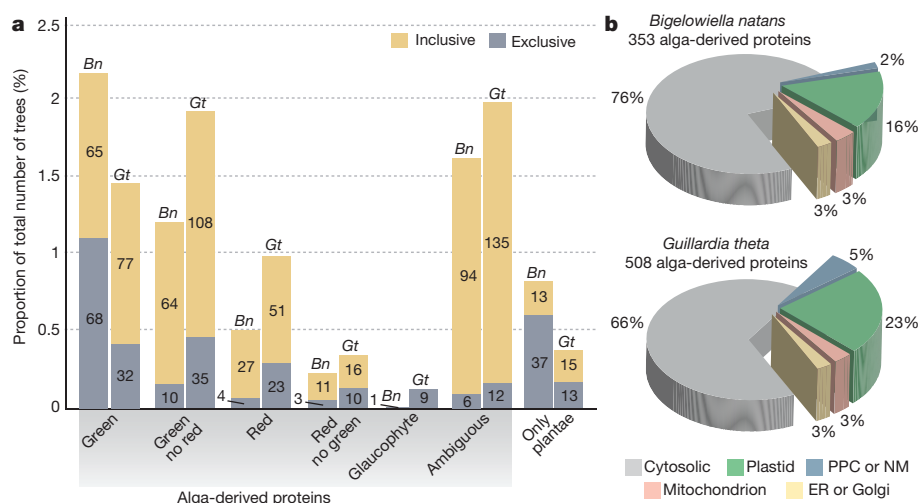


Figure 3 | Algal genes in the *Bigeloviella natans* and *Guillardia theta* nuclear genomes and the predicted subcellular locations of their protein products. **a**, Histogram showing the proportion of ‘algal’ genes or proteins and their inferred origin by automated tree sorting and manual curation; bar height is relative to the total number of trees built for each organism and the raw counts are indicated on the bars (Supplementary Fig. 1.12.3). Exclusive affiliations are those in which the *B. natans* or *G. theta* homologue forms a clade solely with the group in question (for example, red algae), whereas inclusive affiliations enable sequences from other secondary and/or tertiary plastid-bearing algae within the clade to be present. ‘Green’ is defined as chlorophyte

and/or streptophyte algae (including land plants). ‘Only plantae’ means trees containing only sequences from green algae and/or red algae and/or glaucophytes; algal origin therefore cannot be inferred with confidence. Only trees in the ‘red’, ‘green’ and ‘glaucophyte’ categories provide unambiguous information on the specific evolutionary origin of the *B. natans* or *G. theta* proteins. **b**, Pie charts showing the predicted locations of the algal proteins presented in **a**. Endoplasmic reticulum and Golgi proteins are those identified at the level of 75% confidence (see Supplementary Information 1.9.3). The ‘cytosolic’ category includes all proteins with no positive prediction for any of the four proteomes investigated.

of the protein products, sometimes as compensation for the loss of a nucleomorph gene (below). The present-day composition of the *G. theta* and *B. natans* subcellular proteomes is the product of extensive mixing and matching of proteins derived from their hosts and from endosymbionts that have become organelles. No clear pattern in the fates of individual endosymbiont-derived genes (loss, retention, duplication or re-purposing) is apparent.

Why do nucleomorphs persist?

Nuclear mitochondrial DNAs (NUMTs) and/or nuclear plastid DNAs (NUPTs) have been found in most eukaryotes studied so far; rates of EGT seem to vary substantially from lineage to lineage^{37,38}. Although most such transfers involve small, apparently random fragments of organellar DNA that have no notable impact on the nuclear genome, entire genes can be transferred and expressed in their new environment (for example, see refs 39, 40). Instances in which NUMTs have altered existing genes by introducing new introns or truncating the gene through frameshifts have also been observed (for example, see refs 41–43).

Nuclear genome sequences from a rhizarian and a cryptophyte provide the first opportunity to test if NUMTs, NUPTs and, most importantly, nucleomorph-derived DNAs (NUNMs) reside in these genomes. Given that these types of ‘recent’ EGT recapitulate an important process by which endosymbiont and organellar genomes are initially reduced and can ultimately be lost, the presence or absence of NUPTs and NUNMs has the potential to provide insight into the fate of plastid and nucleomorph genomes of secondary endosymbiotic origin. A bioinformatic screen (Supplementary Information 2.5) revealed seven NUMTs in the *B. natans* nuclear genome (Supplementary Table 2.5.3.1) and 13 in *G. theta* (Supplementary Table 2.5.3.2). All of the fragments were small (<320 nucleotides) and none contained entire genes. Their point of origin in their respective mitochondrial genomes seems random both in terms of content and position, and most were integrated into non-coding regions.

In marked contrast, no recent transfers of NUPTs or NUNMs were observed in *B. natans* or *G. theta*. The presence of NUMTs in both nuclear genomes demonstrates that EGT happens, so there is no

obvious impediment to the incorporation of organelle-donated DNA. One explanation for the apparent absence of NUNMs and NUPTs in the *B. natans* and *G. theta* genomes is the ‘limited transfer window’ hypothesis, which posits that cells with multiple copies of an organelle are more likely to have EGTs than those with single organelles because lysis of a single organelle to release DNA into the host nucleocytoplasm would be catastrophic^{44,45}. Consistent with our observations, *G. theta* and *B. natans* cells have a single plastid–nucleomorph complex per cell, the lysis of which would presumably be fatal. In contrast, cryptophytes can have large, reticulate mitochondria that undergo fission and fusion⁴⁶, and in chlorarachniophytes each cell generally has multiple mitochondria that reside in both the cytoplasm and (when present) filopodia⁴⁷. The ability of the limited transfer window hypothesis to explain the absence of NUPTs and NUNMs in *G. theta* and *B. natans* could be tested further by searching the nuclear genomes of cryptophytes and chlorarachniophytes that contain multiple plastid–nucleomorph complexes per cell^{48,49}.

The consequences of the lack of NUNMs and NUPTs in the *B. natans* and *G. theta* nuclear genomes are considerable. In the absence of EGT, inactivation and loss of essential plastid and nucleomorph genes cannot be compensated for by the classical gene transfer–protein re-targeting scenario, as occurs in other systems^{39,50}. Our results show that indirect ‘solutions’ have evolved, most notably the duplication and functional reassignment of host-derived nuclear genes. For example, a nucleus-encoded cyclin-dependent kinase regulatory subunit protein (also known as kin(cdc)) predicted to function in the *G. theta* PPC or nucleomorph is not specifically related to kin(cdc) homologues encoded in the nucleomorph genomes of two other cryptophytes^{14,16}, but instead is a recent duplicate of an apparently host-derived homologue (Supplementary Fig. 2.5.2.2a). A similar pattern is seen in a variety of other nucleus-encoded, PPC-targeted proteins in *G. theta* (Supplementary Information 2.5.5 and Supplementary Table 2.5.5.1). In *B. natans*, alternative splicing may serve as an additional mechanism for increasing proteome complexity and compensating for the loss of organellar genes. Over recent evolutionary time scales, nucleomorph genome reduction seems to have slowed markedly for lack of an easy solution to the problem of nucleomorph gene loss.

Extensive EGT has nevertheless occurred in the ancestors of *B. natans* and *G. theta*. Some of the protein products of these transferred genes are targeted to the plastid and PPC but most are not (Fig. 3b). Genetic and biochemical mosaicism is thus rampant in both organisms, with host-, endosymbiont- and foreign alga-derived proteins contributing to processes taking place in their various subcellular compartments. The extent to which such mosaicism exists in other cryptophytes and chlorarachniophytes remains unknown. Nevertheless, it seems likely that close inspection of the genomes of all algae that evolved by eukaryote–eukaryote endosymbiosis will reveal a level of mosaicism beyond that which is typically assumed. This conclusion has important implications for the use of genomic data to infer a robust tree of eukaryotes that includes secondary and tertiary plastid-bearing phototrophs, and more generally, for our understanding of the evolution of the eukaryotic cell.

METHODS SUMMARY

DNA was extracted from axenic cultures established from single-cell isolates of *Guillardia theta* and *Bigelowiella natans* (Bigelow Laboratory for Ocean Sciences). Three different-sized libraries, 3-kb, 8-kb and 34-kb fosmids, were generated and sequenced at the Joint Genome Institute (JGI) using Sanger sequencing. Additional 454 sequencing was used to fill gaps, and sequence reads were assembled using a modified version of Arachne. Gene models were generated and annotated for the resulting genomic scaffolds using JGI's gene modelling pipeline with additional manual curation. Gene modelling, annotation and alternative splicing analyses were assisted by three messenger RNA data sets: ESTs generated before the genome projects, JGI-generated ESTs and RNA-seq data. Proteome predictions for the plastid, mitochondrion, endoplasmic reticulum or Golgi, and periplastidial compartment were generated using independent bioinformatic pipelines. Maximum likelihood phylogenetic trees were generated from protein sequences retrieved from a local database and the positions of the *B. natans* and *G. theta* proteins were assessed using a combination of automated filtering and manual curation. Complete materials and methods are described in the Supplementary Information.

Received 20 August; accepted 18 October 2012.

Published online 28 November 2012.

- Gould, S. B., Waller, R. F. & McFadden, G. I. Plastid evolution. *Annu. Rev. Plant Biol.* **59**, 491–517 (2008).
- Gray, M. W. The endosymbiont hypothesis revisited. *Int. Rev. Cytol.* **141**, 233–357 (1992).
- Palmer, J. D. The symbiotic birth and spread of plastids: how many times and whodunnit? *J. Phycol.* **39**, 4–11 (2003).
- Yoon, H. S., Hackett, J. D., Ciniglia, C., Pinto, G. & Bhattacharya, D. A molecular timeline for the origin of photosynthetic eukaryotes. *Mol. Biol. Evol.* **21**, 809–818 (2004).
- Bowler, C. *et al.* The *Phaeodactylum* genome reveals the evolutionary history of diatom genomes. *Nature* **456**, 239–244 (2008).
- Armbrust, E. V. *et al.* The genome of the diatom *Thalassiosira pseudonana*: ecology, evolution, and metabolism. *Science* **306**, 79–86 (2004).
- Cock, J. M. *et al.* The *Ectocarpus* genome and the independent evolution of multicellularity in brown algae. *Nature* **465**, 617–621 (2010).
- Koonin, E. V. *et al.* A comprehensive evolutionary classification of proteins encoded in complete eukaryotic genomes. *Genome Biol.* **5**, R7 (2004).
- Parra, G., Bradnam, K. & Korf, I. CEGMA: a pipeline to accurately annotate core genes in eukaryotic genomes. *Bioinformatics* **23**, 1061–1067 (2007).
- Bradley, R. K., Merkin, J., Lambert, N. J. & Burge, C. B. Alternative splicing of RNA triplets is often regulated and accelerates proteome evolution. *PLoS Biol.* **10**, e1001229 (2012).
- Irimia, M. *et al.* Widespread evolutionary conservation of alternatively spliced exons in *Caenorhabditis*. *Mol. Biol. Evol.* **25**, 375–382 (2008).
- Sorek, R., Shamir, R. & Ast, G. How prevalent is functional alternative splicing in the human genome? *Trends Genet.* **20**, 68–71 (2004).
- Freitag, J., Ast, J. & Bolker, M. Cryptic peroxisomal targeting via alternative splicing and stop codon read-through in fungi. *Nature* **485**, 522–525 (2012).
- Tanifuji, G. *et al.* Complete nucleomorph genome sequence of the nonphotosynthetic alga *Cryptomonas paramecium* reveals a core nucleomorph gene set. *Genome Biol. Evol.* **3**, 44–54 (2011).
- Gilson, P. R. *et al.* Complete nucleotide sequence of the chlorarachniophyte nucleomorph: nature's smallest nucleus. *Proc. Natl Acad. Sci. USA* **103**, 9566–9571 (2006).
- Lane, C. E. *et al.* Nucleomorph genome of *Hemiselmis anderseni* reveals complete intron loss and compaction as a driver of protein structure and function. *Proc. Natl Acad. Sci. USA* **104**, 19908–19913 (2007).
- Douglas, S. E. *et al.* The highly reduced genome of an enslaved algal nucleus. *Nature* **410**, 1091–1096 (2001).
- Gould, S. B. *et al.* Nucleus-to-nucleus gene transfer and protein retargeting into a remnant cytoplasm of cryptophytes and diatoms. *Mol. Biol. Evol.* **23**, 2413–2422 (2006).
- Gile, G. H. & Keeling, P. J. Nucleus-encoded periplastid-targeted EFL in chlorarachniophytes. *Mol. Biol. Evol.* **25**, 1967–1977 (2008).
- Hirakawa, Y., Burki, F. & Keeling, P. J. Nucleus- and nucleomorph-targeted histone proteins in a chlorarachniophyte alga. *Mol. Microbiol.* **80**, 1439–1449 (2011).
- Moog, D., Stork, S., Zauner, S. & Maier, U. G. *In silico* and *in vivo* investigations of the proteins of a minimized eukaryotic cytoplasm. *Genome Biol. Evol.* **3**, 375–382 (2011).
- Douglas, S. E. & Penny, S. L. The plastid genome of the cryptophyte alga, *Guillardia theta*: complete sequence and conserved synteny groups confirm its common ancestry with red algae. *J. Mol. Evol.* **48**, 236–244 (1999).
- Rogers, M. B., Gilson, P. R., Su, V., McFadden, G. I. & Keeling, P. J. The complete chloroplast genome of the chlorarachniophyte *Bigelowiella natans*: evidence for independent origins of chlorarachniophyte and euglenid secondary endosymbionts. *Mol. Biol. Evol.* **24**, 54–62 (2007).
- Martin, W. & Herrmann, R. G. Gene transfer from organelles to the nucleus: how much, what happens, and why? *Plant Physiol.* **118**, 9–17 (1998).
- Deschamps, P. *et al.* Nature of the periplastidial pathway of starch synthesis in the cryptophyte *Guillardia theta*. *Eukaryot. Cell* **5**, 954–963 (2006).
- McFadden, G. I., Gilson, P. R. & Sims, I. M. Preliminary characterization of carbohydrate stores from chlorarachniophytes (Division: Chlorarachniophyta). *Phycol. Res.* **45**, 145–151 (1997).
- Hirakawa, Y., Gile, G. H., Ota, S., Keeling, P. J. & Ishida, K. Characterization of periplastidial compartment-targeting signals in chlorarachniophytes. *Mol. Biol. Evol.* **27**, 1538–1545 (2010).
- Martin, W., Brinkmann, H., Savonna, C. & Cerff, R. Evidence for a chimeric nature of nuclear genomes: eubacterial origin of eukaryotic glyceraldehyde-3-phosphate dehydrogenase genes. *Proc. Natl Acad. Sci. USA* **90**, 8692–8696 (1993).
- Timmis, J. N., Ayiliffe, M. A., Huang, C. Y. & Martin, W. Endosymbiotic gene transfer: organelle genomes forge eukaryotic chromosomes. *Nature Rev. Genet.* **5**, 123–135 (2004).
- Stiller, J. W., Huang, J., Ding, Q., Tian, J. & Goodwillie, C. Are algal genes in nonphotosynthetic protists evidence of historical plastid endosymbioses? *BMC Genomics* **10**, 484 (2009).
- Woehle, C., Dagan, T., Martin, W. F. & Gould, S. B. Red and problematic green phylogenetic signals among thousands of nuclear genes from the photosynthetic and apicomplexa-related *Chromera velia*. *Genome Biol. Evol.* **3**, 1220–1230 (2011).
- Moustafa, A. *et al.* Genomic footprints of a cryptic plastid endosymbiosis in diatoms. *Science* **324**, 1724–1726 (2009).
- Deschamps, P. & Moreira, D. Reevaluating the green contribution to diatom genomes. *Genome Biol. Evol.* **4**, 683–688 (2012).
- Burki, F. *et al.* Re-evaluating the green versus red signal in eukaryotes with secondary plastid of red algal origin. *Genome Biol. Evol.* **4**, 738–747 (2012).
- Archibald, J. M., Rogers, M. B., Toop, M., Ishida, K. & Keeling, P. J. Lateral gene transfer and the evolution of plastid-targeted proteins in the secondary plastid-containing alga *Bigelowiella natans*. *Proc. Natl Acad. Sci. USA* **100**, 7678–7683 (2003).
- Burki, F., Okamoto, N., Pombert, J. F. & Keeling, P. J. The evolutionary history of haptophytes and cryptophytes: phylogenomic evidence for separate origins. *Proc. R. Soc. B* **279**, 2246–2254 (2012).
- Richly, E. & Leister, D. NUMTs in sequenced eukaryotic genomes. *Mol. Biol. Evol.* **21**, 1081–1084 (2004).
- Richly, E. & Leister, D. NUPTs in sequenced eukaryotes and their genomic organization in relation to NUMTs. *Mol. Biol. Evol.* **21**, 1972–1980 (2004).
- Adams, K. L. & Palmer, J. D. Evolution of mitochondrial gene content: gene loss and transfer to the nucleus. *Mol. Phylogenet. Evol.* **29**, 380–395 (2003).
- Stegemann, S. & Bock, R. Experimental reconstruction of functional gene transfer from the tobacco plastid genome to the nucleus. *Plant Cell* **18**, 2869–2878 (2006).
- Ricchetti, M., Tekai, F. & Dujon, B. Continued colonization of the human genome by mitochondrial DNA. *PLoS Biol.* **2**, e273 (2004).
- Noutsos, C., Kleine, T., Armbruster, U., DalCorso, G. & Leister, D. Nuclear insertions of organellar DNA can create novel patches of functional exon sequences. *Trends Genet.* **23**, 597–601 (2007).
- Curtis, B. A. & Archibald, J. M. A spliceosomal intron of mitochondrial DNA origin. *Curr. Biol.* **20**, R919–R920 (2010).
- Barbrook, A. C., Howe, C. J. & Purton, S. Why are plastid genomes retained in non-photosynthetic organisms? *Trends Plant Sci.* **11**, 101–108 (2006).
- Smith, D. R., Crosby, K. & Lee, R. W. Correlation between nuclear plastid DNA abundance and plastid number supports the limited transfer window hypothesis. *Genome Biol. Evol.* **3**, 365–371 (2011).
- Hill, D. R. A. & Wetherbee, R. *Proteomonas sulcata* gen. et sp. nov. (Cryptophyceae), a cryptomonad with two morphologically distinct and alternating forms. *Phycologia* **25**, 521–543 (1986).
- Hibberd, D. J. & Norris, R. E. Cytology and ultrastructure of *Chlorarachnion reptans* (Chlorarachniophyta divisio nova, Chlorarachniophyceae classis nova). *J. Phycol.* **20**, 310–330 (1984).
- Kugrens, P. & Clay, B. L. In *Freshwater Algae of North America* 715–755 (Elsevier Science, 2003).
- Ota, S., Kudo, A. & Ishida, K.-I. *Gymnochloa dimorpha* sp. nov., a new chlorarachniophyte with unique daughter cell behavior. *Phycologia* **50**, 317–326 (2011).

50. Martin, W. *et al.* Gene transfer to the nucleus and the evolution of chloroplasts. *Nature* **393**, 162–165 (1998).

Supplementary Information is available in the online version of the paper.

Acknowledgements The work conducted by the US Department of Energy Joint Genome Institute is supported by the Office of Science of the US Department of Energy under Contract no. DE-AC02-05CH11231. RNA-seq data used in the paper were generated by the National Center for Genome Resources as part of the Gordon and Betty Moore Foundation's Marine Microbial Eukaryote Transcriptome Project. B.A.C. and J.F.H. were supported by a Special Research Opportunities Grant from the Natural Sciences and Engineering Research Council of Canada awarded to J.M.A. and M.W.G. J.M.A., P.J.K., M.W.G. and C.H.S. are members of the Canadian Institute for Advanced Research, Program in Integrated Microbial Biodiversity. G.I.M. is an Australian Research Council Federation Fellow and a Howard Hughes International Scholar. We thank R. A. Andersen (Bigelow Laboratories) for assistance with single-cell isolations, C. X. Chan for a tree-sorting PERL script, H. Gutierrez for help with SM protein family annotation, and B. Read for permission to analyse the *Emiliania huxleyi* genome sequenced by the JGI.

Author Contributions Nucleic acid sample preparation: C.E.L., D.F.S. and J.F.H. Genome and transcriptome sequencing and assembly: J.S., J.G., C.B., A.K.B., J.A.C., R.K., E.L. and S.L. Genome annotation and/or analysis: B.A.C., G.T., F.B., A.G., M.I., S.M., M.C.A., S.G.B., G.H.G., Y.H., J.F.H., A.K., S.A.R., J.S., A. Symeonidi, M.E., R.J.M.E., E.K.H., M.J.K., T.N.,

M.O., A.R.-P., E.V.A., S.J.A., R.G.B., P.C., J.B.D., D.G.D., N.M.F., B.R.G., C.J.G., F.H., B.H., M.P.H., K.-I.I., E.K., L.K., P.G.K., Y.L., S.-B.M., U.G.M., D.M., T.M., J.A.D.N., N.T.O., A.M.P., E.J.P., T.A.R., G.R., S.W.R., C.S., S. Schaack, S. Shirato, C.H.S., S. Suzuki, A.Z.W., S.Z., J.G., A. Salamov, C.E.L., M.W.G. and J.M.A. Project management: K.B., I.V.G. and J.S. Project coordination: J.M.A., M.W.G., P.J.K., C.E.L. and G.I.M. Writing: J.M.A., B.A.C., M.W.G., G.I.M., P.J.K., C.E.L., G.T., F.B., A.G., M.I., S.M., M.C.A., S.G.B., G.H.G., J.F.H., A.K., S.A.R., J.S., A. Symeonidi, R.J.M.E., E.K.H., M.J.K., T.N., A.R.-P., J.B.D., E.K., P.G.K., E.J.P., S.W.R., S.S., A.K.B. and I.V.G.

Author Information The *G. theta* and *B. natans* genome sequences and annotations are available through the JGI Genome Portal at <http://jgi.doe.gov/Gtheta> and <http://jgi.doe.gov/Bnatans> and have been deposited in GenBank under the accession numbers AEIE00000000 and ADNK00000000, respectively. Reprints and permissions information is available at www.nature.com/reprints. The authors declare no competing financial interests. Readers are welcome to comment on the online version of the paper. Correspondence and requests for materials should be addressed to J.M.A. (john.archibald@dal.ca).



This work is licensed under a Creative Commons Attribution-NonCommercial-Share Alike 3.0 Unported licence. To view a copy of this licence, visit <http://creativecommons.org/licenses/by-nc-sa/3.0>

Non-synaptic inhibition between grouped neurons in an olfactory circuit

Chih-Ying Su¹, Karen Menuz¹, Johannes Reisert² & John R. Carlson¹

Diverse sensory organs, including mammalian taste buds and insect chemosensory sensilla, show a marked compartmentalization of receptor cells; however, the functional impact of this organization remains unclear. Here we show that compartmentalized *Drosophila* olfactory receptor neurons (ORNs) communicate with each other directly. The sustained response of one ORN is inhibited by the transient activation of a neighbouring ORN. Mechanistically, such lateral inhibition does not depend on synapses and is probably mediated by ephaptic coupling. Moreover, lateral inhibition in the periphery can modulate olfactory behaviour. Together, the results show that integration of olfactory information can occur via lateral interactions between ORNs. Inhibition of a sustained response by a transient response may provide a means of encoding salience. Finally, a CO₂-sensitive ORN in the malaria mosquito *Anopheles* can also be inhibited by excitation of an adjacent ORN, suggesting a broad occurrence of lateral inhibition in insects and possible applications in insect control.

An intriguing feature of a number of sensory systems is the compartmentalization of their primary sensory cells. These cells are housed together in specialized structures such as the taste buds of vertebrates and the chemosensory sensilla of invertebrates. The compartmentalized primary sensory cells often respond to diverse stimuli. The functional consequence of such organization is unknown.

Olfactory receptor neurons (ORNs) are the primary units of odour perception¹. ORNs are widely believed to function as autonomous units, each responding to odorants independent of other ORNs. In some organisms, such as insects, ORNs are compartmentalized into sensilla (Fig. 1a). An individual sensillum encapsulates the dendrites of neurons^{2–4}. The neighbouring ORNs exhibit differing spike amplitudes and odorant sensitivities⁵. In *Drosophila melanogaster*, each ORN is assigned a designation indicating the type of sensillum in which it is housed and its relative spike amplitude among the ORNs of the sensillum. Thus, the ab3A neuron is located in antennal basiconic sensilla of type 3, and the 'A' indicates that its spike amplitude is greater than that of the neighbouring 'B' neuron. In fruitflies, moths and mosquitoes, ORNs are grouped in stereotyped combinations^{5–9}.

The functional significance of this widespread pattern of ORN organization is unknown. In *Drosophila*, neighbouring ORNs do not have obvious functional relationships¹⁰, and they do not project to adjacent regions in the brain¹¹. In certain sensilla of flies, moths and beetles, the activation of neighbouring ORNs elicits opposing behaviours^{6,8,9,12–16}. There are theoretical predictions based on electrical circuit modelling that the transient activation of one ORN may interfere with the signalling of a neighbouring ORN¹⁷, and there is precedent for olfactory stimuli that activate one neuron and inhibit its neighbour^{15,16}, but in the absence of molecular genetic analysis it is difficult to determine whether such stimuli act uniquely on one ORN or directly on both. Similar examples can also be found in insect taste sensilla^{18–22}, but in *Drosophila* some bitter compounds have been shown to act directly both on a sugar neuron and on a bitter neuron, inhibiting one and exciting the other²³.

Here we use the molecular genetics of *Drosophila* to examine the coding of pairs of odours by the ORNs of olfactory sensilla. We find that the prolonged activation of one ORN is inhibited by the transient

excitation of its neighbour. This lateral inhibition is observed within diverse types of *Drosophila* sensilla, and the activation of a mosquito ORN laterally inhibits the response of a neighbouring ORN to CO₂, a key cue used by mosquitoes to find their human hosts. The communication between neurons does not require a synapse, and probably proceeds via ephaptic coupling. Finally, we find that this lateral inhibition at the periphery of the olfactory circuit can modulate olfactory behaviour. Together, our results indicate that ORNs do not signal cell-autonomously in all circumstances, but rather their responses can be regulated by the activity of their ORN neighbours in a sensillum.

Activation of an ORN inhibits its neighbour

To analyse the relationship between two ORNs in a sensillum, we used a paradigm that allows us to deliver two odours, one for each neuron (Fig. 1b, c). One odorant, the 'background odorant', is provided continuously via an airstream and elicits the sustained firing of one ORN, the A neuron in most experiments. Superimposed on this background stimulus, a short pulse of a second odorant is delivered to activate the other ORN, usually the B neuron. This paradigm of odour presentation is distinct from the single-odorant paradigm used commonly in many studies^{5,10,24}, but it simulates a coding problem that the system encounters in its natural environment, for example when a fly receiving sustained olfactory input from a local source receives a superimposed, transient stimulus from a distant source delivered by a gust of wind.

When the ab3 sensillum is stimulated with a prolonged dose of methyl hexanoate, the ab3A neuron responds with a sustained train of action potentials (large action potentials in Fig. 1d). When a pulse of 2-heptanone is superimposed on this background, not only does ab3B fire (small action potentials) but there is a marked reduction in the firing of ab3A (Fig. 1d).

This inhibitory effect could, in principle, be due to direct inhibition of OR22A, the receptor of ab3A, by 2-heptanone. However, ablation of ab3B by expression of the cell death gene *reaper* (*rpr*) completely abolished the inhibition of ab3A (Fig. 1d, bottom). This result indicates that the inhibition of the A neuron depends on the excitation of the B neuron.

¹Department of Molecular, Cellular and Developmental Biology, Yale University, New Haven, Connecticut 06520, USA. ²Monell Chemical Senses Center, Philadelphia, Pennsylvania 19104, USA.

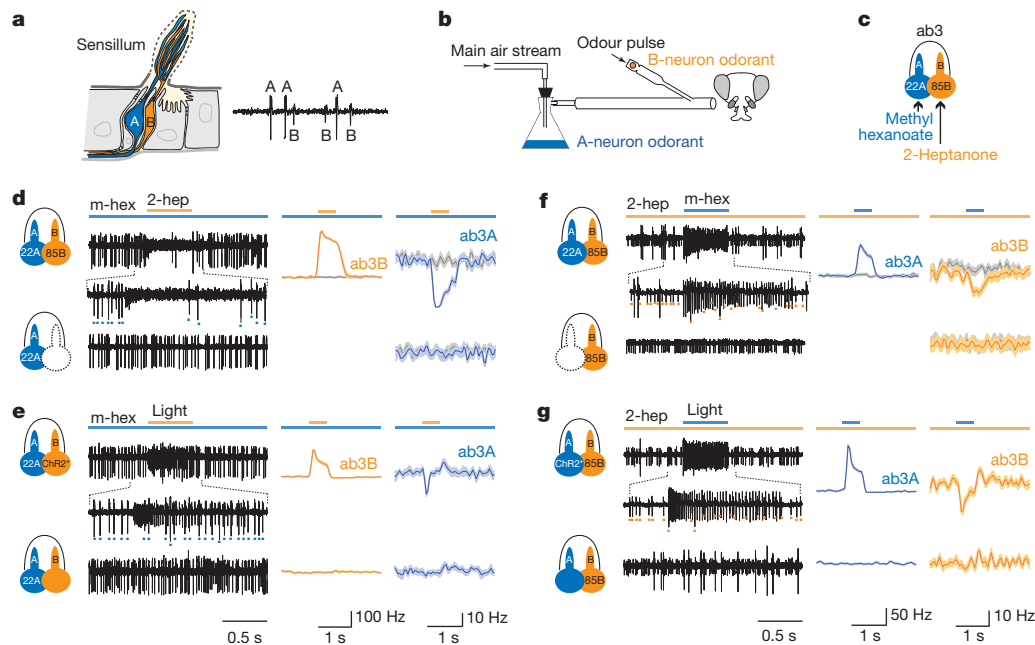


Figure 1 | Lateral inhibition of ORNs. **a**, An olfactory sensillum that houses two ORNs, A and B. Inset: a single-unit recording. 'A' has a larger spike amplitude than 'B'. **b**, The two-odour paradigm. **c**, The ab3 sensillum, the ORNs of which express the OR22A and OR85B receptors, which are sensitive to the indicated odorants. **d**, Top: a sustained stimulus of methyl hexanoate (m-hex, 10^{-7} dilution, long blue bar) elicits a response from ab3A (large spikes, ~ 37 spikes s^{-1}). A 500-ms pulse of 2-heptanone (2-hep, 10^{-4} dilution, orange bar) activates ab3B (small spikes). The response of ab3A is inhibited by the 2-heptanone stimulus. Right, averaged responses. Grey traces indicate responses when a pulse of diluent is delivered instead of 2-heptanone. Shaded areas represent s.e.m. Inset: blue dots indicate ab3A spikes. Bottom: genetic

To test further the possibility that activation of the ab3B neuron can inhibit the ab3A neuron, we expressed Channelrhodopsin2 (H134R-ChR2)²⁵ in ab3B. As expected, blue light elicited an excitatory response in ab3B of these engineered flies (Fig. 1e). Activation of ab3B by light also inhibited the tonic firing of ab3A elicited by methyl hexanoate. Blue light had no effect on ab3A firing in control flies lacking H134R-ChR2 (Fig. 1e, bottom), indicating that it does not inhibit ab3A directly. The simplest interpretation of these results is that activation of ab3B inhibits the firing of ab3A.

We next asked whether activation of ab3A can inhibit ab3B. We first elevated ab3B activity by delivering 2-heptanone as the background odorant and then presented a pulse of methyl hexanoate to activate ab3A. Indeed, the pulse of methyl hexanoate inhibited the activity of ab3B (Fig. 1f, top). Genetic ablation of ab3A demonstrated that this inhibition depended on ab3A (Fig. 1f, bottom). Similarly, when H134R-ChR2 was expressed in ab3A, a blue-light stimulus activated ab3A and inhibited the tonic firing of ab3B (Fig. 1g).

Lateral inhibition in other sensilla

There are four morphological types of antennal sensilla: large basiconic sensilla, small basiconic sensilla, coeloconic sensilla and trichoid sensilla^{1,26,27}. ab3 is a large basiconic sensillum containing two ORNs. We analysed four other sensilla, chosen for their morphological diversity and their functional specificities. Their ORNs express receptors that have been functionally characterized, and odorants have been identified that at certain concentrations selectively activate the receptor of only one ORN in each sensillum^{10,24}.

Lateral inhibition between ORNs was observed in all sensillar types examined: a large basiconic sensillum containing four ORNs (ab1); a large basiconic sensillum with two ORNs (ab2); a small basiconic sensillum (ab5); and a coeloconic sensillum (ac3). In each case, a short

ablation of ab3B prevented inhibition. **e**, In flies expressing ChR2* in ab3B (top), a 500-ms pulse of blue light (473 nm, ~ 10 mW mm^{-2}) excited ab3B, which inhibited the response of ab3A to methyl hexanoate (~ 32 spikes s^{-1} , 10^{-6}). The more phasic inhibition is probably due to the kinetics of ChR2-dependent activation. Bottom: flies without ChR2*. **f**, Top: activation of ab3B by a pulse of methyl hexanoate (10^{-6}) inhibited the response of ab3B to 2-heptanone (~ 38 spikes s^{-1} , 5×10^{-7}). Bottom: genetic ablation of ab3A prevented inhibition. Inset: orange dots indicate ab3B spikes. Very large spikes represent the coincidence of A and B spikes. **g**, ChR2* expressed in ab3A. A pulse of blue light (~ 25 mW mm^{-2}) excited ab3A, inhibiting the response of ab3B to 2-heptanone (~ 35 spikes s^{-1} , 5×10^{-7}). $n = 12$ in **d–g**.

odorant pulse that activated one target ORN inhibited the tonic firing of a neighbouring ORN (Fig. 2a–d). When the targeted ORN was ablated or non-functional, the short odorant pulse showed no inhibition of the neighbouring ORN (Supplementary Fig. 1). We note also that the pulsed odorant alone did not directly inhibit the spontaneous firing of the A neuron (Supplementary Fig. 2). These results indicate that lateral inhibition is observed broadly in the *Drosophila* antenna.

Lateral inhibition in a mosquito sensillum

ORNs are compartmentalized in sensilla in a wide variety of insects. We examined a sensillum of the malaria vector *Anopheles gambiae* that responds to CO₂ (ref. 7), a human volatile that attracts many mosquito species²⁸. This sensillum contains an ORN, cpA, that responds to CO₂, and a neighbouring ORN, cpB, that is excited by 1-octen-3-ol (ref. 7).

We used a prolonged CO₂ stimulus to elicit a sustained response from cpA. When a short pulse of 1-octen-3-ol was superimposed, the cpB neuron was excited and cpA was robustly inhibited (Fig. 2e). We note that when 1-octen-3-ol was delivered in the absence of CO₂, it did not inhibit the spontaneous firing of the CO₂-responsive cpA neuron directly (Supplementary Fig. 2d), consistent with previous results⁷.

Taken together, our results show that lateral inhibition occurs in olfactory sensilla of multiple insect species, in sensilla of radically different morphology, and in sensilla containing two, three or four ORNs.

Inhibition is dose-dependent

When ab3A was tonically excited with a constant concentration of methyl hexanoate, increasing doses of 2-heptanone produced increasing excitation of ab3B and increasing inhibition of ab3A (Fig. 3a, b). When the scales of the firing ranges are adjusted (Fig. 3b), the dose-response functions seem to be symmetrical.

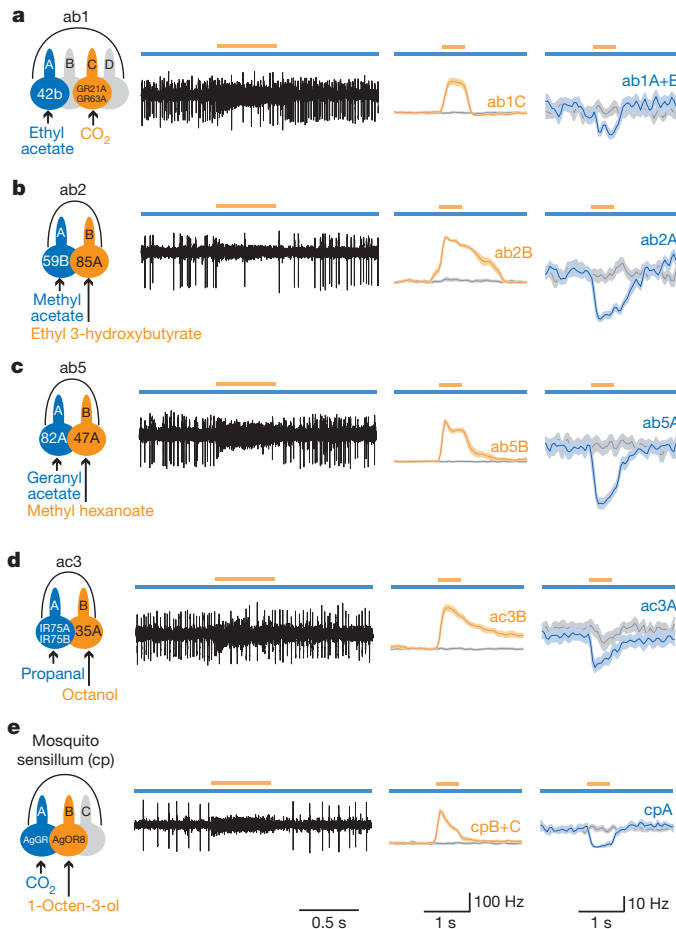


Figure 2 | Lateral inhibition in diverse sensilla. Odorants at the tested concentrations activate only one ORN in each sensillum. **a–d**, *Drosophila* sensilla. Activation of the target ORN (orange) inhibited the response of the neighbouring ORN (blue) to the background odorant. In **a**, ab1A and ab1B spikes could not be sorted reliably and were grouped. **e**, In the capitae-peg sensillum of *Anopheles*, activation of the cpB neuron by 1-octen-3-ol (10^{-4}) inhibited the response of cpA to CO_2 . cpB and cpC spikes were combined. $n = 11$ –13. Odour dilutions and A neuron basal activities are in Supplementary Table 2.

When the background odorant, methyl hexanoate, was delivered at increasing concentrations, the rate of ab3A tonic firing increased across a range of $\sim 15 \text{ spikes s}^{-1}$ to $\sim 50 \text{ spikes s}^{-1}$ (Fig. 3c, d, and Supplementary Table 2). Inhibition by a strong ab3B stimulus was potent across all these concentrations; in all of these cases the rate of firing was reduced to approximately the same level. A genetic ablation experiment confirmed that these reductions depended on ab3B (Supplementary Fig. 3). We note that 2-heptanone alone did not directly inhibit ab3A spontaneous activity (Fig. 3c, d, 'no bkg').

Transmission without a synapse

Next we asked whether the intrasensillar communication is mediated by synapses. First we used tetanus toxin (TNT)²⁹ to block synaptic transmission. We expressed TNT in ORNs using the *Orco* promoter and the *GAL4/UAS* system, which is expected to drive expression in all basiconic ORNs³⁰ except the CO_2 -sensitive ab1C neuron^{31,32}. Activation of ab3B inhibited the tonic excitation of ab3A in these TNT-expressing flies (Fig. 4a, top). Moreover, the degree of inhibition was comparable to that in control flies (Fig. 4a, bottom). T-maze behavioural tests confirmed that synaptic transmission was blocked in the targeted ORNs (Fig. 4b).

Second, we performed single-unit recordings from isolated antennae, severed from the heads of flies. Activation of ab3B again inhibited

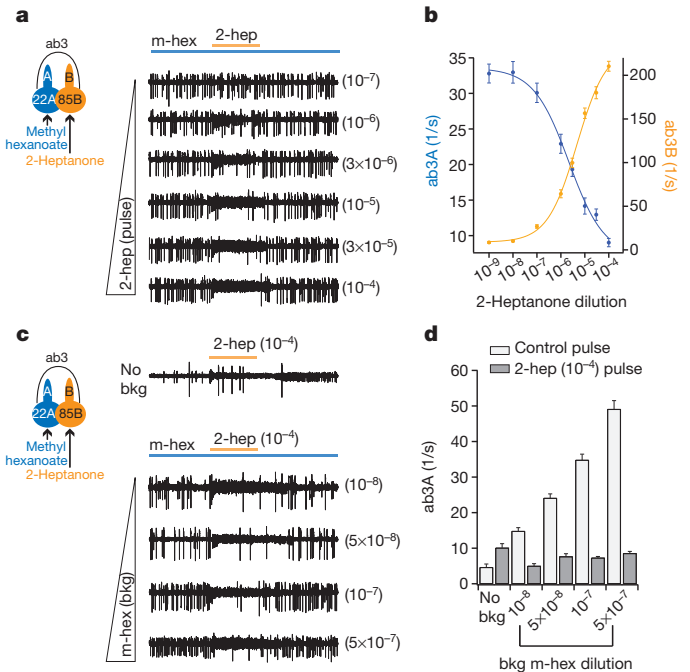


Figure 3 | Lateral inhibition is dose-dependent. **a**, Responses of ab3A and ab3B to a 500-ms pulse of 2-heptanone (orange) superimposed on a background odorant, methyl hexanoate (10^{-7} dilution; $\sim 37 \text{ spikes s}^{-1}$). At these low concentrations, methyl hexanoate and 2-heptanone selectively activate ab3A and ab3B, respectively. 2-Heptanone dilutions are at the right of the panel. **b**, Activities of ab3A and ab3B during 2-heptanone pulses. Fit is with the Hill equation; $n = 12$. **c**, Responses to a pulse of 2-heptanone (10^{-4}) in the presence of varying levels of methyl hexanoate, indicated at the right of the panel. **d**, Responses of ab3A during 500-ms exposures to paraffin oil (control) or 2-heptanone with varying concentrations of background methyl hexanoate; $n = 12$. In the absence of sustained stimulation of the A neuron ('no bkg'), strong activation of the B neuron elicited a small increase in the firing of A, which may represent passive depolarization of A resulting from close apposition of the neuronal membranes^{43,44}. This effect seems to be overwhelmed by the passive hyperpolarization produced by ephaptic interactions (discussed below) when B is activated during sustained stimulation of A. Differences are significant in all conditions ($P < 0.002$, paired t -test); $n = 12$.

the tonic excitation of ab3A (Fig. 4c), supporting the conclusion that lateral inhibition between neighbouring ORNs occurs in the periphery without involvement of central synapses.

Third, we tested the possibility of axo-axonic synapses between ORNs with a cross-correlation analysis³³. Analysis of ab3A and ab3B spontaneous spikes did not reveal coordinated spiking patterns and thus provided no evidence for axo-axonic synaptic interactions (Fig. 4d), similar to what has been found between homotypic ORNs in *Drosophila*³⁴.

Finally, we used Cd^{2+} to block synaptic neurotransmission³⁵. We included a high concentration of Cd^{2+} in the recording pipette so as to allow Cd^{2+} to diffuse into the sensillum lymph and block any peripheral dendro-dendritic synapses in sensilla of *Orco-GAL4; UAS-TNT* flies. We observed little if any effect on the inhibition of ab3A firing after ab3B excitation (Fig. 4e; compare with Fig. 4a). To verify the efficacy of our drug delivery method, we applied the Orco agonist VUAA1 (ref. 36) via the recording pipette and observed elevated ORN spike activities, as expected (Fig. 4f). Together, these results indicate that lateral inhibition does not depend on chemical synapses.

Intrasensillar communication could, in principle, be mediated via gap junctions; however, the activation of one ORN would then probably lead to the activation, rather than the inhibition, of its neighbour. Moreover, we found that nitric oxide signalling inhibitors had

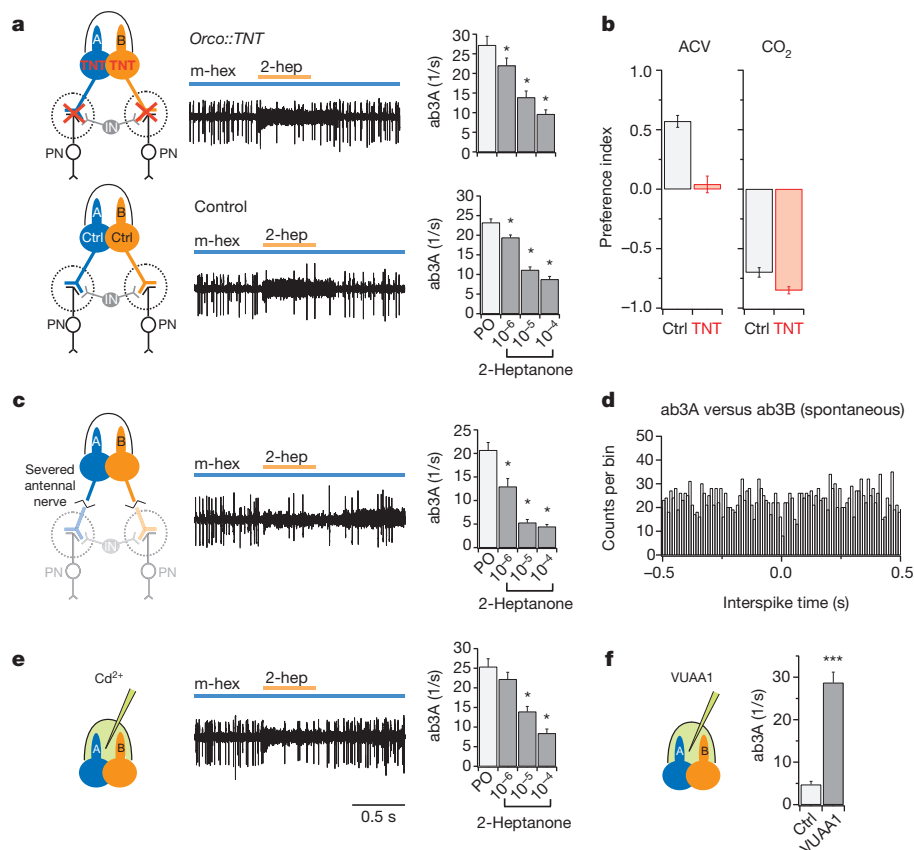


Figure 4 | Lateral inhibition does not require synapses. **a**, ab3 sensilla in flies expressing TNT in ORNs via the *Orco* promoter. Neurons were exposed to a 500-ms pulse of the ab3B odorant, 2-heptanone (orange, 10^{-4}), superimposed on the background ab3A odorant, methyl hexanoate (blue, 10^{-7}). IN, representative interneuron. Right: ab3A activity during a 500-ms exposure to paraffin oil (PO) or 2-heptanone in the presence of methyl hexanoate. Error bars indicate s.e.m.; * $P < 0.05$, one-way repeated measures ANOVA, multiple comparison versus control group (PO) with Dunnett's method ($n = 12$). **b**, T-maze choice between water and 25% ACV or between air and 0.67% CO_2 .

CO_2 neurons do not express *Or* genes. ($n = 9$). **c**, Recordings were performed as in **a** except that the antenna was severed from the head ($n = 7$). **d**, Cross-correlation analysis of spontaneous spikes from an ab3 sensillum, showing intervals between ab3A spikes and ab3B spikes, binned in 10-ms increments. Each ab3B spike is used as a reference. Another ab3 sensillum gave similar results. **e**, Recordings made 15 min after introduction of Cd^{2+} ($n = 12$). **f**, VUAA1 (1 mM) or vehicle (1% dimethylsulphoxide (DMSO)) was delivered via the recording electrode³⁶. ab3A responses were recorded for 10 s. *** $P < 0.001$, t -test ($n = 12$).

no effect on lateral inhibition (not shown). In summary, conventional forms of neuronal communication are unlikely to mediate lateral inhibition in a sensillum.

Lateral inhibition modulates behaviour

To determine whether intra-sensillar neuronal inhibition can modulate olfactory behaviour, we examined a pair of neighbouring ORNs, the activation of which leads to opposing behavioural outputs (Fig. 5). ab1A mediates attraction to apple cider vinegar (ACV)¹³, whereas its neighbour ab1C mediates aversion to low concentrations of CO_2 (refs 12, 32, 37, 38). We confirmed that in a T-maze assay, when given a choice between CO_2 and air alone, flies avoid CO_2 , whereas when faced with a choice between ACV and water, they are attracted to ACV (Fig. 5a, black bars).

We then tested whether the two behavioural pathways interact. When both arms of the T-maze contained CO_2 , the flies showed no preference (Fig. 5a). When ACV was added to one of the CO_2 -containing arms, the flies preferred that arm. The preference for the arm containing both CO_2 and ACV could have two sources: the attraction to its ACV that is mediated by ab1A, and a reduction in the avoidance of its CO_2 that is mediated by ab1C.

To evaluate the contributions of these sources, we used *Orco*-*GAL4*; *UAS*-*TNT*, which blocks synaptic transmission from ab1A but not ab1C. Consistent with the expected specificity of this block, these flies did not respond to ACV but avoided CO_2 (Fig. 5b, black

bars). We note that in these flies, physiological recordings confirmed that ab1A neurons respond to ACV (not shown). When given a choice between two arms, one with CO_2 and one with CO_2 and ACV, these flies preferred the arm with ACV (Fig. 5b). Because synaptic transmission from ab1A neurons is blocked and the flies have no attraction to ACV, the simplest interpretation of these results is that activation of ab1A attenuated the response of ab1C to CO_2 via lateral inhibition: the reduced CO_2 response decreased the avoidance of the arm containing CO_2 and ACV relative to the arm containing CO_2 alone, and this decreased avoidance is seen as an attraction to the arm containing CO_2 and ACV.

If this interpretation is correct, and the preference for the arm containing CO_2 and ACV depends on the activation of ab1A, then the preference should be abolished in *Orco* mutants, which lack a co-receptor required for the response of ab1A but not ab1C. Consistent with this prediction, *Orco* mutants showed no preference between the arm containing CO_2 and the arm containing CO_2 and ACV (Fig. 5c). We note that ACV does not inhibit ab1C directly (Supplementary Fig. 4). Taken together, these results provide evidence that lateral inhibition within a sensillum can modulate behaviour.

Discussion

Integration of olfactory information has long been known to occur in the CNS, and has more recently been shown to occur in individual ORNs³⁹. We have demonstrated that integration also occurs at a third

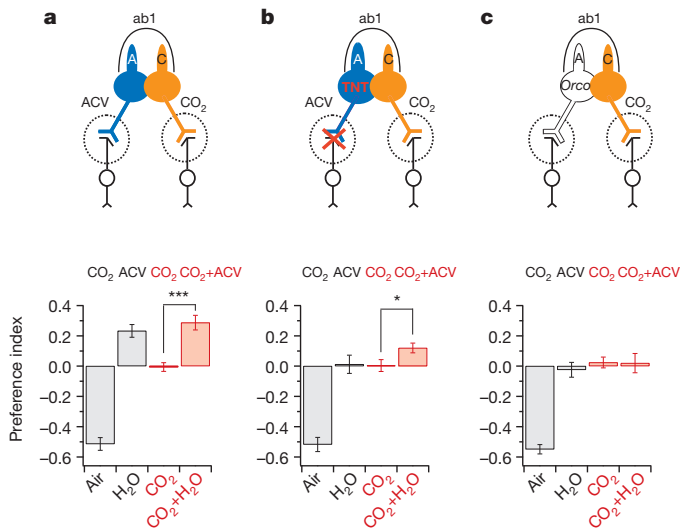


Figure 5 | Lateral inhibition modulates behaviour. a–c, Activation of ab1A mediates attraction to ACV; activation of ab1C mediates aversion to CO₂. Two of the four ORNs in ab1 are depicted. Preference indices of control (a), *Orco-GAL4; UAS-TNT* (b) and *Orco* (c) are shown (mean \pm s.e.m.). The ab1A neurons of the TNT-expressing flies respond to ACV but are expected not to transmit information to postsynaptic neurons, whereas ab1A neurons in *Orco* are expected not to respond to ACV. In each T-maze assay, ~50 flies were allowed 2 min to choose. In single-odour experiments (black bars) the test arm contained either CO₂ or ACV. * $P < 0.05$; *** $P < 0.001$, t -test ($n = 16$). CO₂ was 0.13%; ACV was 100%, pH 7.5. In physiological recordings from *Orco* flies, ACV did not inhibit the spontaneous firing of the CO₂ neuron.

level, the sensillum, via lateral inhibition between ORNs responding to different components of a mixture. The sensillum thus acts as a processing unit in olfactory computation.

Lateral inhibition of a prolonged signal by a transient signal may provide a neural representation of the salience of an odour that has recently reached the fly⁴⁰. Sustained responses were inhibited more strongly by stronger transient pulses. This graded pattern of lateral inhibition may give rise to a potent form of contrast enhancement in which the output of a sensillum is dominated by a pulse of a strong odour. Graded lateral inhibition may provide a peripheral mechanism for evaluating countervailing signals and allowing one to prevail. We note that in *Drosophila*, an ORN that responds to a pheromone^{41,42} is the only ORN that does not have a neighbour, as if to ensure that its sustained response is not inhibited by a pulse of any other odorant.

Our finding that lateral inhibition does not require synapses is consistent with anatomical data. Electron microscopy in *Drosophila* has not revealed synaptic structures or gap junctions between ORNs housed in the same sensillum^{2,3}. Rather, as detailed below, the physiological features of olfactory sensilla suggest another mechanism of lateral information flow: ephaptic transmission, which refers to non-synaptic communication between adjacent neurons through an extracellular electrical field^{43,44}. The ability of either neuron in a two-neuron sensillum to inhibit the other, as well as the grossly similar temporal dynamics of activation and lateral inhibition (Supplementary Fig. 5), are consistent with ephaptic transmission.

In insect olfactory sensilla, a substantial electrical potential exists between two isolated compartments: the sensillum lymph, which bathes the dendrites, and the haemolymph, which surrounds the somata (Fig. 1a and Supplementary Fig. 6). This ‘transepithelial’ potential serves as the primary driving force for odorant-induced transduction currents of the ORNs^{17,45}. Elaboration of an established electrical circuit model^{17,45} based on these physiological features predicts that strong activation of one ORN will hyperpolarize the soma of a co-compartmentalized ORN (Supplementary Fig. 6), resulting in a reduced firing rate. This prediction is consistent with the results of

our molecular genetic analysis and with our interpretation that lateral inhibition is due to ephaptic interactions.

The model further predicts that the magnitude of the hyperpolarization of the neighbouring neuron, and hence its reduction in firing rate, is reflected by the change in the transepithelial potential (V_A) (Supplementary Fig. 6), measured experimentally as a local field potential (LFP) (Supplementary Fig. 7a). Although strong activation of an ORN can influence the LFP in a neighbouring sensillum⁴⁶, we found that the magnitude of the LFP change in nearby unstimulated sensilla is small (Supplementary Fig. 7). Consistent with this observation, lateral inhibition does not spread among homotypic sensilla that are in close proximity to one another (Supplementary Fig. 8). These results further support the conclusion that the lateral inhibition is due to local electrical interactions between neighbouring ORNs within a sensillum.

The two-odour paradigm used in this analysis, in which a transient odour is superimposed upon a sustained odour, differs from the classic one-odour paradigm in which a transient pulse of a single odour is delivered. A priori one might expect to observe ephaptic effects in the one-odour paradigm if one ORN were excited sufficiently strongly, but the effects may be expected to be less pronounced than in the two-odour paradigm. ORN spike frequency is determined not only by the somatic transmembrane potential V_m , but also by its rate of change, dV_m/dt (ref. 46). According to the model, transient activation of ORN₂ reduces the depolarizing current of ORN₁ (Supplementary Fig. 6). In the two-odour paradigm, activation of ORN₂ has a marked effect on the value of dV_{m1}/dt , which changes from 0 to a negative value ($dV_{m1}/dt \leq 0$; Supplementary Fig. 6). By contrast, in the one-odour paradigm, the activation of ORN₂ has a more subtle effect on dV_{m1}/dt when the sensillum is stimulated with an odour that activates both neurons: dV_{m1}/dt is positive either in the presence or absence of ORN₂ activation, only somewhat less positive when ORN₂ is activated. The more subtle influence of ORN₂ activation on dV_{m1}/dt in the one-odour paradigm may explain why in the one-odour paradigm, the excitatory responses of an ORN containing an ectopically expressed receptor were markedly similar to those of the ORN that endogenously expresses the same receptor²⁴, despite major differences in the response profiles of their neighbours.

We note finally that our results indicate the possibility of a new approach to insect control: the inhibition of key insect ORNs by activation of their neighbours with odorants.

METHODS SUMMARY

Fly antennal preparations and single-unit recordings were performed essentially as described²⁴, except for the isolated antennal preparation in which the stabilized antenna was severed from the head using the broken tip of a tapered glass microcapillary tube. Recordings were performed on adult female flies 5–7 days after eclosion, except that flies 24–36 h after eclosion were used in *UAS-TNT* experiments because TNT-expressing ORNs began to lose spike activities in older flies. Supplementary Table 1 lists fly genotypes for all experiments. Female *Anopheles gambiae* mosquitoes were used ~4 days after eclosion. Extracellular recordings from the capitae-peg sensilla on the maxillary palp were performed as described^{7,47}. AC signals (300–2,000 Hz) were recorded, except for local field potential recordings where DC signals (low-pass filtered at 2 kHz) were recorded. ORN spikes were detected and sorted based on spike amplitude using routines in Igor Pro 6.01 and binned at 50-ms intervals.

For optogenetic experiments, flies were reared in constant darkness on fly food supplemented with ~100 μ M all trans-retinal³⁷. Recordings were performed on adult females 7 days after eclosion using an established optics set-up⁴⁸. For pharmacological experiments, chemicals were delivered inside the sensillum via the recording glass electrode.

T-maze behavioural tests were performed essentially as described¹². For experiments shown in Fig. 4b, flies were given 1 min to choose between the two arms: air versus CO₂ (0.67%) or H₂O versus ACV (25%). For experiments shown in Fig. 5, four experimental conditions were used: (1) air versus CO₂ (0.13%); (2) H₂O versus ACV (100%, pH 7.5); (3) CO₂ (0.13%) versus CO₂ (0.13%); (4) CO₂ (0.13%) plus H₂O versus CO₂ (0.13%) plus ACV (100%, pH 7.5). Preference

index was calculated as the fraction of flies entering the test arm minus the fraction of flies entering the control arm.

Full Methods and any associated references are available in the online version of the paper.

Received 9 March; accepted 25 October 2012.

Published online 21 November 2012.

- Su, C. Y., Menz, K. & Carlson, J. R. Olfactory perception: receptors, cells, and circuits. *Cell* **139**, 45–59 (2009).
- Shanbhag, S. R., Muller, B. & Steinbrecht, R. A. Atlas of olfactory organs of *Drosophila melanogaster* 1. Types, external organization, innervation and distribution of olfactory sensilla. *Int. J. Insect Morphol. Embryol.* **28**, 377–397 (1999).
- Shanbhag, S. R., Muller, B. & Steinbrecht, R. A. Atlas of olfactory organs of *Drosophila melanogaster* 2. Internal organization and cellular architecture of olfactory sensilla. *Arthropod Struct. Dev.* **29**, 211–229 (2000).
- Keil, T. A. Reconstruction and morphometry of silkworm olfactory hairs: A comparative study of sensilla trichodea on the antennae of male *Antheraea polyphemus* and *Antheraea pernyi* (Insecta, Lepidoptera). *Zoomorphology* **104**, 147–156 (1984).
- de Bruyne, M., Foster, K. & Carlson, J. R. Odor coding in the *Drosophila* antenna. *Neuron* **30**, 537–552 (2001).
- Kaissling, K. E. Peripheral mechanisms of pheromone reception in moths. *Chem. Senses* **21**, 257–268 (1996).
- Lu, T. et al. Odor coding in the maxillary palp of the malaria vector mosquito *Anopheles gambiae*. *Curr. Biol.* **17**, 1533–1544 (2007).
- Akers, R. P. & O'Connell, R. J. The contribution of olfactory receptor neurons to the perception of pheromone component ratios in male redbanded leafroller moths. *J. Comp. Physiol. A* **163**, 641–650 (1988).
- Takanashi, T. et al. Unusual response characteristics of pheromone-specific olfactory receptor neurons in the Asian corn borer moth, *Ostrinia furnacalis*. *J. Exp. Biol.* **209**, 4946–4956 (2006).
- Hallem, E. A. & Carlson, J. R. Coding of odors by a receptor repertoire. *Cell* **125**, 143–160 (2006).
- Couto, A., Alenius, M. & Dickson, B. J. Molecular, anatomical, and functional organization of the *Drosophila* olfactory system. *Curr. Biol.* **15**, 1535–1547 (2005).
- Suh, G. S. et al. A single population of olfactory sensory neurons mediates an innate avoidance behaviour in *Drosophila*. *Nature* **431**, 854–859 (2004).
- Semmelhack, J. L. & Wang, J. W. Select *Drosophila* glomeruli mediate innate olfactory attraction and aversion. *Nature* **459**, 218–223 (2009).
- Berg, B. G. & Mustaparta, H. The significance of major pheromone components and interspecific signals as expressed by receptor neurons in the oriental tobacco budworm moth, *Helioverpa assulta*. *J. Comp. Physiol. A* **177**, 683–694 (1995).
- Nikonov, A. A. & Leal, W. S. Peripheral coding of sex pheromone and a behavioral antagonist in the Japanese beetle, *Popillia japonica*. *J. Chem. Ecol.* **28**, 1075–1089 (2002).
- O'Connell, R. J. Responses to pheromone blends in insect olfactory receptor neurons. *J. Comp. Physiol. A* **156**, 747–761 (1985).
- Vermeulen, A. & Rospars, J. P. Why are insect olfactory receptor neurons grouped into sensilla? The teachings of a model investigating the effects of the electrical interaction between neurons on the transepithelial potential and the neuronal transmembrane potential. *Eur. Biophys. J.* **33**, 633–643 (2004).
- Mitchell, B. K. Interactions of alkaloids with galeal chemosensory cells of Colorado potato beetle. *J. Chem. Ecol.* **13**, 2009–2022 (1987).
- Schoonhoven, L. M. & Van Loon, J. J. A. An inventory of taste in caterpillars: each species its own key. *Acta Zool. Hung.* **48** (suppl. 1), 215–263 (2002).
- Jorgensen, K., Almaas, T. J., Marion-Poll, F. & Mustaparta, H. Electrophysiological characterization of responses from gustatory receptor neurons of sensilla chaetica in the moth *Heliothis virescens*. *Chem. Senses* **32**, 863–879 (2007).
- de Brito Sanchez, M. G., Giurfa, M., de Paula Mota, T. R. & Gauthier, M. Electrophysiological and behavioural characterization of gustatory responses to antennal 'bitter' taste in honeybees. *Eur. J. Neurosci.* **22**, 3161–3170 (2005).
- Dethier, V. G. & Bowdan, E. The effect of alkaloids on sugar receptors and the feeding behaviour of the blowfly. *Physiol. Entomol.* **14**, 127–136 (1989).
- Meunier, N., Marion-Poll, F., Rospars, J. P. & Tanimura, T. Peripheral coding of bitter taste in *Drosophila*. *J. Neurobiol.* **56**, 139–152 (2003).
- Hallem, E. A., Ho, M. G. & Carlson, J. R. The molecular basis of odor coding in the *Drosophila* antenna. *Cell* **117**, 965–979 (2004).
- Pulver, S. R., Pashkovski, S. L., Hornstein, N. J., Garrity, P. A. & Griffith, L. C. Temporal dynamics of neuronal activation by Channelrhodopsin-2 and TRPA1 determine behavioral output in *Drosophila* larvae. *J. Neurophysiol.* **101**, 3075–3088 (2009).
- Kwon, Y. et al. *Drosophila* TRPA1 channel is required to avoid the naturally occurring insect repellent citronellal. *Curr. Biol.* **20**, 1672–1678 (2010).
- Benton, R., Vannice, K. S., Gomez-Diaz, C. & Vosshall, L. B. Variant ionotropic glutamate receptors as chemosensory receptors in *Drosophila*. *Cell* **136**, 149–162 (2009).
- Takken, W. & Knols, B. G. Odor-mediated behavior of Afrotropical malaria mosquitoes. *Annu. Rev. Entomol.* **44**, 131–157 (1999).
- Keller, A., Sweeney, S. T., Zars, T., O'Kane, C. J. & Heisenberg, M. Targeted expression of tetanus neurotoxin interferes with behavioral responses to sensory input in *Drosophila*. *J. Neurobiol.* **50**, 221–233 (2002).
- Larsson, M. C. et al. Or83b encodes a broadly expressed odorant receptor essential for *Drosophila* olfaction. *Neuron* **43**, 703–714 (2004).
- Kwon, J. Y., Dahanukar, A., Weiss, L. A. & Carlson, J. R. The molecular basis of CO₂ reception in *Drosophila*. *Proc. Natl Acad. Sci. USA* **104**, 3574–3578 (2007).
- Jones, W. D., Cayirlioglu, P., Kadow, I. G. & Vosshall, L. B. Two chemosensory receptors together mediate carbon dioxide detection in *Drosophila*. *Nature* **445**, 86–90 (2007).
- Gaffin, D. D. Electrophysiological analysis of synaptic interactions within peg sensilla of scorpion pectines. *Microsc. Res. Tech.* **58**, 325–334 (2002).
- Kazama, H. & Wilson, R. I. Origins of correlated activity in an olfactory circuit. *Nature Neurosci.* **12**, 1136–1144 (2009).
- Yaksi, E. & Wilson, R. I. Electrical coupling between olfactory glomeruli. *Neuron* **67**, 1034–1047 (2010).
- Jones, P. L., Pask, G. M., Rinker, D. C. & Zwiebel, L. J. Functional agonism of insect odorant receptor ion channels. *Proc. Natl Acad. Sci. USA* **108**, 8821–8825 (2011).
- Suh, G. S. et al. Light activation of an innate olfactory avoidance response in *Drosophila*. *Curr. Biol.* **17**, 905–908 (2007).
- Ai, M. et al. Acid sensing by the *Drosophila* olfactory system. *Nature* **468**, 691–695 (2010).
- Su, C. Y., Martelli, C., Emonet, T. & Carlson, J. R. Temporal coding of odor mixtures in an olfactory receptor neuron. *Proc. Natl Acad. Sci. USA* **108**, 5075–5080 (2011).
- Martin, J. P. et al. The neurobiology of insect olfaction: sensory processing in a comparative context. *Prog. Neurobiol.* **95**, 427–447 (2011).
- van der Goes van Naters, W. & Carlson, J. R. Receptors and neurons for fly odors in *Drosophila*. *Curr. Biol.* **17**, 606–612 (2007).
- Kurtovic, A., Widmer, A. & Dickson, B. J. A single class of olfactory neurons mediates behavioural responses to a *Drosophila* sex pheromone. *Nature* **446**, 542–546 (2007).
- Jefferys, J. G. Nonsynaptic modulation of neuronal activity in the brain: electric currents and extracellular ions. *Physiol. Rev.* **75**, 689–723 (1995).
- Faber, D. S. & Korn, H. Electrical field effects: their relevance in central neural networks. *Physiol. Rev.* **69**, 821–863 (1989).
- Kaissling, K. E. Chemo-electrical transduction in insect olfactory receptors. *Annu. Rev. Neurosci.* **9**, 121–145 (1986).
- Nagel, K. I. & Wilson, R. I. Biophysical mechanisms underlying olfactory receptor neuron dynamics. *Nature Neurosci.* **14**, 208–216 (2011).
- Pellegrino, M., Nakagawa, T. & Vosshall, L. B. Single sensillum recordings in the insects *Drosophila melanogaster* and *Anopheles gambiae*. *J. Vis. Exp.* **36**, 1–5 (2010).
- Cardin, J. A. et al. Targeted optogenetic stimulation and recording of neurons *in vivo* using cell-type-specific expression of Channelrhodopsin-2. *Nature Protocols* **5**, 247–254 (2010).

Supplementary Information is available in the online version of the paper.

Acknowledgements We thank J. Cardin for help with establishing the optogenetics system; Y. Zhao and E. Fikrig for providing mosquitoes; A. Tzingounis and G. Lowe for suggestions; Z. Berman and P. Graham for technical assistance; T. Koh for suggestions and for sharing reagents; and G. Thomas, F. Marion-Poll, R. Wyman and D. McCormick for comments on the manuscript. This work was funded by National Institutes of Health (NIH) grants to J.R.C. and by a grant from the Foundation for the NIH through the Grand Challenges in Global Health Initiative (GCGH no. 121); an NRSA postdoctoral fellowship to K.M. (NIH F32DC011242); and an NIH grant to J.R. (NIH DC009613).

Author Contributions C.-Y.S. designed, performed the experiments and analysed the data, except for coeloconic sensillum recordings and cross-correlation analysis, which were performed by K.M. and J.R., respectively. The model was elaborated primarily by K.M. C.-Y.S., K.M. and J.R.C. wrote the manuscript. All authors contributed to the interpretation of the study.

Author Information Reprints and permissions information is available at www.nature.com/reprints. The authors declare no competing financial interests. Readers are welcome to comment on the online version of the paper. Correspondence and requests for materials should be addressed to J.R.C. (john.carlson@yale.edu).

METHODS

Drosophila stocks. Recordings were performed on adult female flies 5 days after eclosion, except that 7-day flies were used in *UAS-rpr* experiments, and flies 24–36 h after eclosion were used in *UAS-TNT* experiments because TNT-expressing ORNs began to lose spike activities in older flies. Flies were reared at 25 °C in an incubator with a 12-h light/dark cycle. The following fly stocks were used: (1) *UAS-rpr* (ref. 49), (2) *w¹¹¹⁸* and *PBac[WH]Or35a^{f02057}*, (3) *UAS-TNT* (ref. 29), (4) *UAS-H134R-ChR2* (ref. 25), (5) *Or-GAL4* lines (Bloomington stock centre), (6) *Gr21a-GAL4* (ref. 31). Supplementary Table 1 lists genotypes for all experiments.

Mosquitoes. Female *Anopheles gambiae* mosquitoes were used ~4 days after eclosion. Extracellular recordings from the capitae-peg sensilla on the maxillary palp were performed as described^{7,47}.

Electrophysiology and data analysis. For the standard antennal preparation, a fly was wedged into the narrow end of a truncated plastic pipette tip to expose the antenna, which was subsequently stabilized between a tapered glass microcapillary tube and a coverslip covered with double-sided tape. For the isolated antennal preparation, a standard antennal preparation was made first and the stabilized antenna was gently severed from the head using the broken tip of a tapered glass microcapillary tube. Extracellular single-unit recordings were performed essentially as described²⁴. Briefly, electrical activity of the ORNs was recorded extracellularly by placing a sharp electrode filled with Ringer solution²⁴ into a sensillum and the reference electrode filled with the same Ringer solution was placed in the eye (standard antennal preparation) or in the first antennal segment (severed antennal preparation). No more than four sensilla from the same antenna were recorded in the standard preparation, and no more than two sensilla from the same antenna were recorded in the severed preparation. For each sensillum, one trial of each odour concentration was presented. AC signals (300–2,000 Hz) were recorded on an Iso-DAM amplifier (World Precision Instruments), except for local field potential recordings where DC signals (low-pass-filtered at 2 kHz) were recorded and digitized at 5 kHz with Axoscope 10.2 (Molecular Devices). ORN spikes were detected and sorted based on spike amplitude using routines in Igor Pro 6.01 (Wavemetrics). Peri-stimulus time histograms (PSTHs) were obtained by averaging spike activities in 50-ms bins and smoothed using a binomial algorithm (Igor Pro 6.01, Wavemetrics).

Odour stimuli. Odorants were diluted in paraffin oil (v/v). For short odour pulses, odour stimuli (50 µl applied to a filter disc) were delivered from a Pasteur pipette via a pulse of air (200 ml min⁻¹) into the main air stream (2,000 ml min⁻¹) as described previously²⁴. In Fig. 2a, stimulation with CO₂ was by filling the Pasteur pipette with pure CO₂, which was subsequently puffed into the main air stream. On the basis of the published dose–response relationships of ab1A to CO₂ (refs 31, 50), the concentration of CO₂ was estimated to be ~1% (mean ab1C response shown in Fig. 2a: 163 Hz). Background odour stimuli were delivered from a 125-ml flask containing 3 ml of odour dilutions (or 25 ml of carbonated water for background CO₂) directly downstream of the main air stream (2,000 ml min⁻¹).

Optogenetic stimulation. Flies expressing H134R-ChR2 in targeted ORNs and control flies (*UAS-H134R-ChR2*; +) were reared in constant darkness on fly food supplemented with ~100 µM all trans-retinal (Sigma) as described³⁷. Recordings were performed on adult females 7 days after eclosion using an established optics setup⁴⁸. Briefly, a light stimulus was generated via a blue laser (MBL-III-473/30 mW, Opto Engine LLC) and delivered by an optical fibre (200-µm core diameter, BFH22-200, Thorlabs). The tip of the optical fibre was positioned above the antenna. Light pulses (500-ms duration) were controlled by an isolated pulse stimulator (Model 2100, A-M Systems). Light output at the tip of the optical fibre was measured with an optical power meter (Model 1916-C, Newport).

Cross-correlation analysis. The basal spike activity was investigated using 30 sweeps of 10-s duration. Action potentials of the ab3A and ab3B neuron were identified based on size and their triphasic (ab3A neuron) or more biphasic (ab3B neuron) shape using Origin software (OriginLab Corporation). Spike times of

ab3A and ab3B neurons of individual sweeps were cross-correlated using Matlab software (MathWorks). Interspike times were accumulated across all recorded sweeps and binned in 10-ms intervals. Such an analysis can reveal coordinated spiking patterns and was used to identify axo-axonic synapses between neighbouring scorpion ORNs³³.

Pharmacology. Drugs were prepared as concentrated stock solutions and diluted in Ringer solution before experiments. Chemicals were delivered inside the sensillum via the recording glass electrode. Recordings were performed in flies expressing TNT in the ORNs ~15 min after drug introduction, except for the experiments with VUAA1, where recordings were performed within minutes after electrode insertion. The electrode stayed inside the sensillum throughout the 15-min period. VUAA1 (Chemical Diversity Research Institute, Joint Stock Company) was used at 1 mM (stock: 100 mM in DMSO). CdCl₂ (Aldrich) was used at 1 mM (stock: 100 mM in Ringer solution).

T-maze assay. Flies were collected within ~8 h after eclosion without using CO₂ anaesthesia. Flies were tested 24–32 h after eclosion after ~24 h starvation. For starvation, flies were gently tapped into empty vials with moistened foam plugs and kept at 25 °C in an incubator.

Behavioural tests were performed as described previously¹² at room temperature in a dark room. About 40–60 flies were transferred by an aspirator into a 15-ml centrifuge tube (Corning 430791), which was subsequently connected to the sliding chamber (elevator) of the T-maze apparatus. Flies were gently tapped into the elevator, which was then lowered to the opening where the test arm and the control arm were connected. A 16-inch 15-W fluorescent bulb was placed horizontally behind the test and control arms, and the light was on only for the duration of the assay. Phototaxis drew flies out of the elevator. Flies were given 1 min to choose between the two arms, after which the elevator was partially lifted to block any further choices. Preference index was calculated as the fraction of the flies entering the test arm minus the fraction of the flies entering the control arm. The total number of flies used in calculation of the preference index included flies in both arms and in the elevator.

For the experiment shown in Fig. 4b, 10 µl of apple cider vinegar solution or 10 µl of water was added to a Whatman filter disc (1/2 inch diameter) that was positioned around the 1.5-ml mark of the 15-ml centrifuge tube. Twenty-five per cent apple cider vinegar was used because it attracted flies in a T-maze assay without triggering the acid-mediated avoidance pathway³⁸. Ten minutes of equilibrium time was allowed before the tubes were connected to the T-maze apparatus immediately before the assay. For the experiment in Fig. 4b using CO₂, 0.1 ml of pure CO₂ (UN1013, Airgas) was injected into the tube immediately before the assay. The positions of the test and control tubes were alternated for each trial. New groups of flies and new tubes were used for each test. The air inside the 15-ml tube was equilibrated with the air in the room for at least 4 h before use.

For experiments shown in Fig. 5 to address the behavioural relevance of lateral inhibition, we used four experimental conditions: (1) air versus CO₂; (2) H₂O versus ACV; (3) CO₂ versus CO₂; and (4) CO₂ plus H₂O versus CO₂ plus ACV. Thirty microlitres of neutralized apple cider vinegar (100%, pH 7.5) or water was added to a Whatman filter disc that was positioned horizontally via permanent double-sided tape (Scotch, 3M) around the 10-ml mark of the centrifuge tube. When CO₂ was used, 0.1 ml of 20% CO₂ was injected into the tube(s) (near the 5-ml mark) immediately before the assay. When CO₂ was used in both arms, the CO₂ was injected, the two tubes were connected to the T-maze apparatus, and then the apparatus was inverted gently ~10 times and allowed to equilibrate for an additional minute to ensure that CO₂ was distributed evenly between the two arms. The elevator was then lowered to release the flies. The positions of the test and control tubes were alternated for each trial.

49. Yoo, S. J. *et al.* Hid, Rpr and Grim negatively regulate DIAP1 levels through distinct mechanisms. *Nature Cell Biol.* **4**, 416–424 (2002).

50. Yao, C. A. & Carlson, J. R. Role of G-proteins in odor-sensing and CO₂-sensing neurons in *Drosophila*. *J. Neurosci.* **30**, 4562–4572 (2010).

The entorhinal grid map is discretized

Hanne Stensola^{1*}, Tor Stensola^{1*}, Trygve Solstad¹, Kristian Frøland¹, May-Britt Moser¹ & Edvard I. Moser¹

The medial entorhinal cortex (MEC) is part of the brain's circuit for dynamic representation of self-location. The metric of this representation is provided by grid cells, cells with spatial firing fields that tile environments in a periodic hexagonal pattern. Limited anatomical sampling has obscured whether the grid system operates as a unified system or a conglomerate of independent modules. Here we show with recordings from up to 186 grid cells in individual rats that grid cells cluster into a small number of layer-spanning anatomically overlapping modules with distinct scale, orientation, asymmetry and theta-frequency modulation. These modules can respond independently to changes in the geometry of the environment. The discrete topography of the grid-map, and the apparent autonomy of the modules, differ from the graded topography of maps for continuous variables in several sensory systems, raising the possibility that the modularity of the grid map is a product of local self-organizing network dynamics.

A cardinal feature of mammalian neural organization is the topographic mapping of the external environment onto sensory areas of the neocortex. These sensory areas are further organized into layer-spanning spatial modules, or columns, consisting of cells that represent similar features of the sensory input^{1–4}. In the somatosensory cortex, cells form columns that respond to specific somatic stimulus modalities¹. In the visual cortex, cells may be organized into stripes or patches with similar eye dominance^{2,3}, orientation preference^{4–7} or direction preference^{8–11}. The topography of these and other sensory maps is thought to result from the formation of precise connections between sensory receptors and central target cells during early development^{12–14}.

Much less is known about functional circuit organization in higher-order non-sensory cortices. One of the few non-sensory systems with sufficiently distinct behavioural correlates to investigate structure–function relationships is the hippocampal–entorhinal space circuit. Many neurons in this circuit have known spatial firing correlates. ‘Place cells’ in the hippocampus fire only when animals visit certain locations^{15–17}. These cells are probably generated, in part, from grid cells in the MEC, one synapse upstream^{17–22}. Grid cells have multiple periodic firing fields, arranged for each cell in a hexagonal lattice that provides the network with a metric that place cells do not have on their own^{17,19,21}. In both the hippocampus and the MEC, different cells fire at different locations^{16,19}, such that, collectively, the cells form neural maps of all locations in local space^{16–18}. These maps are different from sensory maps in that spatial firing fields are not derived by extraction of features from a particular sensory input, but probably originate from pattern-formation processes in the circuit itself^{17,21–28}. The mechanisms for topographical organization may thus be very dissimilar from those of the columnar sensory cortices.

The functional organization of the network that generates the grid pattern is not yet understood. We know that the grid map is distributed and topographical at the same time. The phase of the grid has a distributed representation in that firing fields of neighbouring grid cells do not overlap more than those of distant grid cells¹⁹. In contrast, grid scale is mapped topographically, in the sense that co-localized grid cells have similar grid spacing and grid spacing increases progressively from dorsal to ventral MEC^{18–20}. However, because of limited sampling across MEC of individual animals, it has not been

possible, despite theoretical suggestions^{21,23} and experimental indications^{29,30}, to determine whether the gradient in grid spacing is continuous or modular and whether it is accompanied by changes in other properties of the grid. To establish whether the grid map is organized into discrete autonomous units, similar to those of some sensory cortices, and to reveal the organization and functional properties of any such modules, we recorded sequentially or simultaneously from 968 widespread grid cells in 15 animals, with up to 186 grid cells per animal.

We used two strategies (Fig. 1a). Five rats were implanted with a single bundle of 4 adjacent tetrodes angled tangentially to the MEC surface to allow grid cells to be recorded sequentially along a continuous dorsoventral strip of the superficial cell layers. Ten rats were implanted with a 1.0 mm × 1.25 mm oval array of 12 independently movable tetrodes, enabling parallel recording from grid cells across large parts of the MEC. Neural activity was sampled while the rats foraged in 100–220-cm-wide square boxes.

Grid scale has a discrete organization

We first investigated whether the progression in grid scale along the entorhinal dorsoventral axis is discrete or continuous. In rats with tangential tetrode implants, the recording tracks covered up to 1,800 μm of layers II and III, or more than one-third of the dorsoventral length of the MEC in the sagittal plane (1333 ± 349 μm, mean ± s.d., Supplementary Fig. 1). Within this range, we recorded up to 62 grid cells per animal (45.6 ± 19.0 , mean ± s.d.). Grid spacing spanned from 35.2 cm to 171.7 cm (74.4 ± 35.6 cm, mean range ± s.d.). There was a strong positive correlation between grid spacing and tetrode depth across animals (Spearman rank correlation: $\rho = 0.34$, $P < 0.001$, $n = 228$ grid cells)^{18–20} and within animals (mean $\rho \pm$ s.e.m.: 0.48 ± 0.09) (Fig. 1b).

The large number of grid cells obtained with the tangential tetrode tracks made it possible to determine, in individual animals, whether grid scale increases gradually or in discrete steps along the dorsoventral axis. The data pointed to a discrete organization in every single animal (Figs 1 and 2 and Supplementary Figs 1 and 2). Within animals, grid spacing clustered at distinct values, often with considerable gaps between successive clusters (Fig. 1d). To quantify the discreteness of the scale distribution, we counted the number of grid cells within successive bins of grid spacing, using a range of bin widths. Then,

¹Kavli Institute for Systems Neuroscience and Centre for the Biology of Memory, Norwegian University of Science and Technology, Olav Kyrres gate 9, MTF5, 7491 Trondheim, Norway.

*These authors contributed equally to this work.

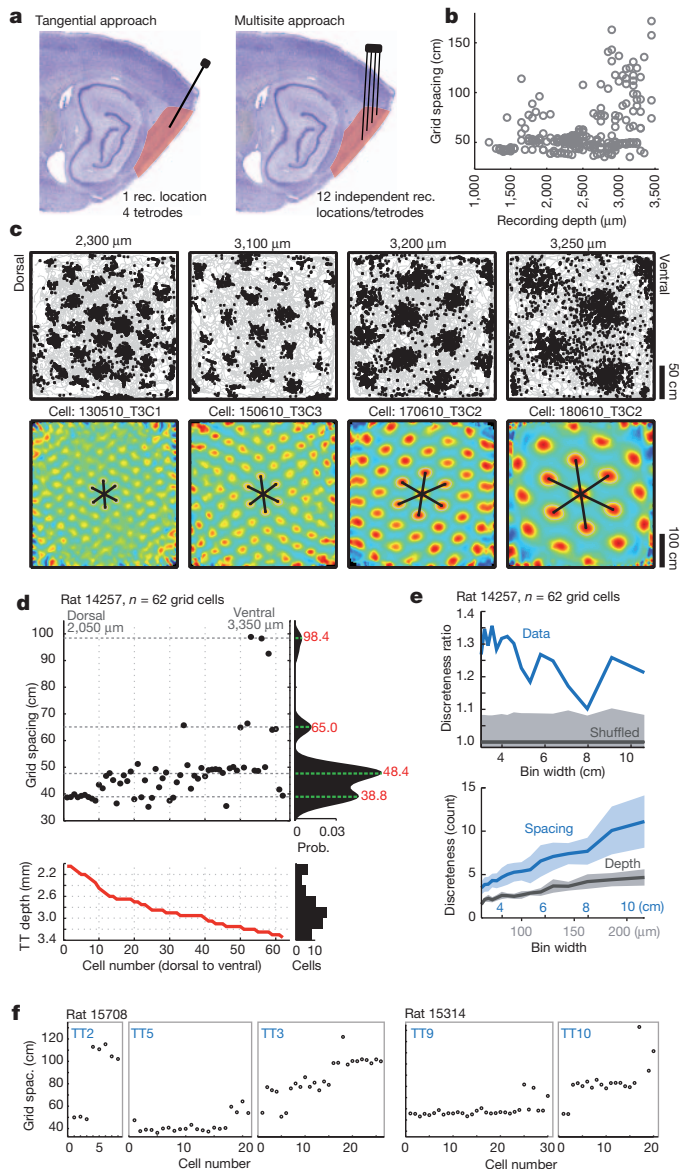


Figure 1 | Step-like increases in grid scale along the entorhinal dorsoventral axis. **a**, Schematic representation of tangential and multisite recording approaches (Nissl-stained sagittal sections, MEC highlighted in red). **b**, Scatterplot showing grid spacing as a function of dorsoventral recording position (all grid cells of all 'tangential' animals; increased recording depth corresponds to a more ventral location). **c**, Example grids at successive dorsoventral positions in a representative 'tangential' animal (rat 14257). Dorsoventral location from brain surface is indicated. Top, neuronal spikes (extracellular action potentials) overlaid on trajectory of rat (grey). Bottom, corresponding colour-coded autocorrelograms with colour scale (−1, 1; blue is correlation of −1, red is correlation of 1). Grid spacing was determined from the innermost polygon (black axes). The spatial autocorrelogram reveals repeating activity patterns in the spatial rate map and is generated by correlating the rate map with itself at all spatial offsets. **d**, Grid spacing at successive dorsoventral levels in a single rat (TT, tetrode). Dots correspond to individual cells. Cells are plotted sequentially to avoid overlap between cells at similar depths. Right, kernel smoothed density (KSD) estimate of the distribution. Red text, spacing in cm for the estimated peaks. **e**, Top, the discreteness of the frequency distribution was calculated across multiple bin widths (Supplementary Fig. 3). Blue line, ratio of discreteness in recorded data and shuffled data in rat 14257. Light grey area, s.d. of shuffled data (mean 1.0, dark grey line). Bottom, discreteness of grid spacing compared to discreteness of recording depth for the same cells. Shadowed areas show s.d. of bin-count difference from mean. **f**, Grid scale of successively recorded cells at increasing dorsoventral depth on different tetrodes with the multisite approach. Tetrode numbering is arbitrary.

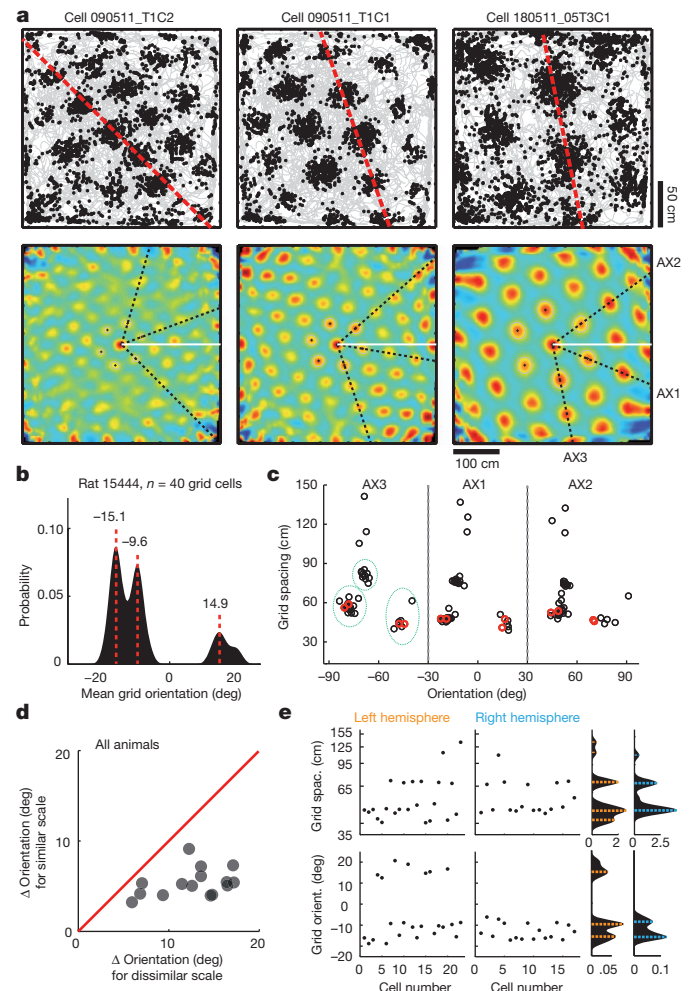


Figure 2 | Comodular organization of grid orientation and grid scale. **a**, Distinct grid orientations within one animal (rat 15444). Spike and autocorrelation maps as in Fig. 1c. Dashed lines indicate grid axes (AX). The white line is the horizontal reference (0 deg). Cells T1C1 and T1C2 were recorded simultaneously. **b**, KSD estimate of grid orientation in all cells from rat 15444. Each circle within each axis is one cell. Cells in red are from the same recording session. Note comodularity of orientation and spacing (green dashed outlines). **c**, Grid spacing against grid orientation for all three grid axes in rat 15444. Each circle within each axis is one cell. Cells in red are from the same recording session. Note comodularity of orientation and spacing (green dashed outlines). **d**, Comparison of average orientation differences for pairs of grid cells with similar grid spacing (<5th percentile of scale differences) and pairs with different grid spacing (>5th percentile) in all 15 animals (one circle per data set). **e**, Left, scatter plots showing successively recorded values for grid spacing (top) and grid orientation (bottom) in separate hemispheres. Corresponding KSD estimates shown on right.

for each bin width, we calculated the standard deviation of differences in cell counts between bins and referred to this standard deviation as the discreteness of the distribution (Supplementary Fig. 3 and Supplementary Methods). Across all animals with more than 15 cells and a grid-spacing range of more than 20 cm, the discreteness was consistently larger for the observed data than for shuffled distributions of the same data (3.06 ± 0.58 ; mean $Z \pm$ s.e.m.; Fig. 1e, top). The mean discreteness for the distribution of recording depth was significantly lower than the mean discreteness for grid spacing in the same cell sample (Fig. 1e, bottom; discreteness ratio (spacing/depth) across bin widths, $P < 0.001$ in all animals). Collectively, these findings indicate that the distribution of grid spacing is discontinuous and that discontinuity is not caused by uneven cell sampling.

The discreteness of the scale gradient in animals with tangential tetrode tracks was reinforced by data from animals with semi-vertical

tetrode tracks at several locations. With the multisite approach, we recorded grid cells at distances up to approximately 1,000 μm apart along the mediolateral axis and 2,000 μm along the dorsoventral axis (Supplementary Fig. 4). These recordings produced high yields of grid cells (up to 186 cells in individual animals; 61.7 ± 67.0 cells, mean \pm s.d.). The dorsoventral span of these recordings was sufficient to reveal steps in grid scale that mirrored those observed with the tangential approach (Fig. 1f and Supplementary Figs 2d–f and 4).

Grid orientation is discretized

We next asked whether other properties of the grid map follow a similar modular organization and whether the boundaries for any such modules are the same as for grid scale. We began by addressing the organization of grid orientation. Early studies of grid cells showed that co-localized cells express largely the same grid orientation¹⁹, but the anatomically restricted sampling area of those studies precluded conclusions about whether all grid cells express the same orientation, or whether cells with different orientations exist in the same network. The widespread distribution of recording locations in the present study allowed us to address this question.

Two key observations were made. First, multiple discrete grid orientations were observed within animals and within recording sessions (Fig. 2a–c and Supplementary Figs 1 and 5). Second, the boundaries between these orientation modules coincided with boundaries between scale modules. Cells that belonged to the same scale module had similar grid orientations, whereas members of different scale modules often differed also in orientation (Fig. 2b, c and Supplementary Figs 5b and 6). In all 15 animals, grid orientation was more similar for cell pairs with similar grid scale (<5th percentile of all pairwise differences in grid scale) than for pairs with different scale (>5th percentile) (Fig. 2d and Supplementary Figs 6 and 7; mean ratio of orientation differences for pairs with different compared with similar scale: 2.73 ± 0.36 , mean \pm s.e.m., $t(15) = 8.37$ $P < 0.001$, 16 data sets, Student's t -test). In an animal with bihemispheric implants, mean values for grid scale and grid orientation were almost identical for left and right cluster pairs (Fig. 2e and Supplementary Fig. 1; mean peak differences \pm s.e.m. of 1.4 ± 1.0 cm for scale and 0.6 ± 0.5 degrees for orientation).

Modular distortions of the grid pattern

Grid patterns can be distorted by changes in the shape of the environment. When a square test box is changed to a rectangle, the grid pattern may rescale selectively along the axis of transformation^{30,31}. Similar asymmetries were observed in the present data, without preceding changes in the geometry of the environment (Fig. 3a and Supplementary Fig. 8). In many recordings, grid fields of co-localized neurons were consistently elongated in one direction (Fig. 3a, b). We asked whether these distortions were coherent across cells, and if they were not, whether differences followed the boundaries of modules for grid spacing and grid orientation. To quantify the distortions, we fitted ellipses to the six field centres of the inner polygon of the spatial autocorrelogram (Fig. 3a, b). From these ellipses, we determined ellipse tilt direction, ellipticity and eccentricity (see Supplementary Methods).

Grid cells with different distortion patterns could be observed within individual animals. Boundaries between cell clusters with different tilt directions coincided with boundaries between scale and orientation modules (Fig. 3a–d and Supplementary Fig. 9). In all 15 animals (16 data sets), the degree of grid distortion (Supplementary Fig. 8d and Supplementary Methods) was more similar for cell pairs with similar grid scale (<5th percentile of all pairwise differences in grid scale) than for pairs with different scale (>5th percentile) (Fig. 3d, ratio of grid distortion in cell pairs with different compared with similar scale: 3.17 ± 0.30 , mean \pm s.e.m., $t(15) = 10.33$, $P < 0.001$, Student's t -test).

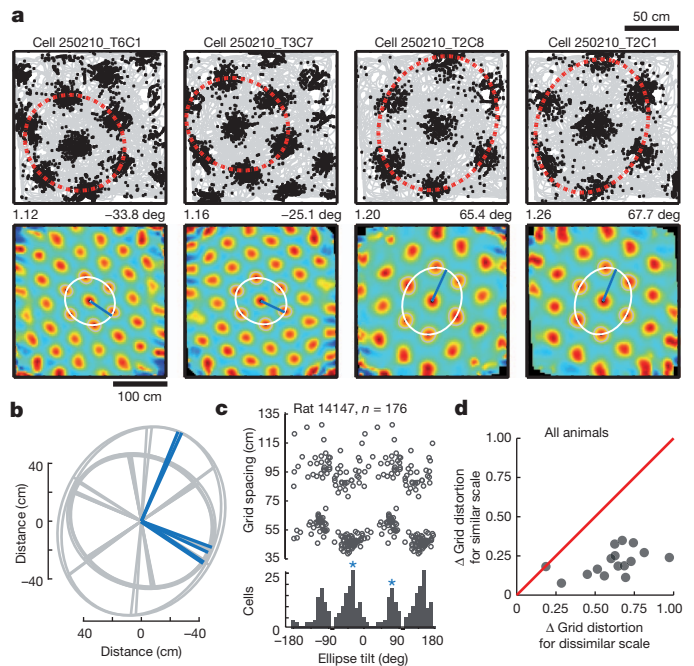


Figure 3 | Distortions in grid shape are comodular with grid spacing.

a, Bimodal grid asymmetry within a single recording session (3 tetrodes, rat 14147). Maps as in Fig. 1c. Ellipses (white) were fitted to the inner polygon of the autocorrelogram. Corresponding ellipses on spike maps are shown in red. Blue lines and text on the upper right: ellipse-tilt (direction of semi-major axis). Text on the upper right: ellipticity. **b**, Ellipses calculated for all grids recorded in **a** ($n = 6$, 4 recording locations). **c**, Ellipse tilt as a function of grid scale (scatter plot and frequency distribution). Note the orthogonal bimodality (blue asterisks). Ellipse tilt ranged from -90 to 90 degrees, shown here from -180 to 180 for clarity. **d**, Comparison of average differences in grid eccentricity for pairs of grid cells with similar grid spacing (<5th percentile of scale differences) and pairs with different spacing (>5th percentile) in all 15 animals (methods as in Fig. 2d).

In animals with a bimodal distribution of ellipse tilt, the orientations were always close to orthogonal (Fig. 3b, c and Supplementary Fig. 8), indicating that the distortions were determined by the square shape of the recording environment. When an animal with a bimodal distribution was exposed to a circular environment, the distribution became unimodal, without any loss of ellipticity (Supplementary Fig. 10). The results indicate that asymmetries are coherent for grid cells within the same module, but may differ between modules depending on the environment.

Anatomical organization of grid modules

We next asked how modules with distinct grid scale, grid orientation and grid distortions are organized in anatomical space. We used a k -means algorithm based on grid scale, grid orientation and grid eccentricity to establish for the entire cell sample, with minimal experimenter bias, which cells belonged to which grid module (Supplementary Fig. 11 and Supplementary Methods). The k -value for each animal was determined from the number of local maxima detected in a two-dimensional kernel-smoothed-density estimate of distributions of grid scale and grid orientation (Supplementary Figs 11a and 12). The maximum k value was 5 (rat 14147).

First, in the tangential experiments, we noticed that the dorsoventral locations of the k -means-identified grid modules exhibited considerable overlap (Fig. 4a, b). The proportion of recording locations containing cells from more than one grid module was $37.0 \pm 7.3\%$. A total of $10.3 \pm 3.8\%$ locations had more than two modules. The number of simultaneously recorded modules increased from dorsal to ventral MEC (mean correlation between dorsoventral location and s.d. of grid scale \pm s.e.m., 0.68 ± 0.11 , $P < 0.005$). The same sets of grid modules were identified in layers II and III (Supplementary

Fig. 13). Taken together these data indicate that grid modules are extensive and interspersed and cut across cortical layers.

One limitation of the tangential approach is that cells were sampled along a single track. To estimate the anatomical extent of the grid-cell modules, we turned to the multisite implants, which yielded from 2 to 10 grid-cell recording tracks in each animal (4.8 ± 2.8 , mean \pm s.d., predominantly MEC layers II and III, Supplementary Fig. 4). Surprisingly, the addition of recording tracks did not increase the number of *k*-means-identified grid modules (Fig. 4c, d). The dispersion of recording locations was determined by plotting them onto entorhinal flat maps in which the MEC is unfolded onto a two-dimensional

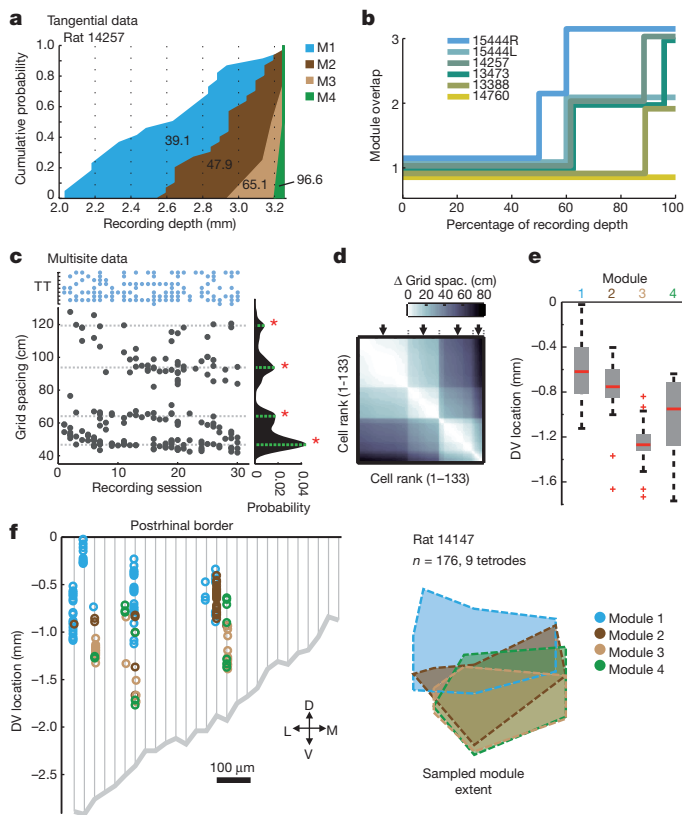


Figure 4 | Grid modules are organized as overlapping horizontal bands.

a, Cumulative distribution of grid modules as a function of dorsoventral position in rat 14257 (62 grid cells, *k*-means-determined modules are colour-coded). Mean grid spacings in cm are indicated. **b**, Proportion of recording sites that had grid cells assigned to 1, more than 1, or more than 2 grid modules (all 'tangential' animals; L, left hemisphere; R, right hemisphere). **c**, Grid spacing for all grid cells in rat 14147. The same four grid modules were detected at other recording sites (KSD estimate and green lines/red asterisks on right). See Supplementary Fig. 17 for a possible fifth module. Top, tetrodes with grid cells on successive recording sessions. Each row corresponds to one tetrode; dots indicate sessions with grid cells. **d**, Similarity matrix showing differences in grid spacing for all grid-cell pairs from 20 sessions after experience-dependent stabilization³⁰. Cells are ranked with respect to spacing (top and left, lowest value). Differences are coded by brightness (scale bar). Four blocks of grid spacing appear as abrupt transitions along the diagonal (black arrows). **e**, Boxplot showing dorsoventral (DV) distribution of recording locations for each module. Red lines, individual medians; grey boxes, 25th–75th percentile range; whiskers extend to extreme data points that are not considered outliers; red crosses, individual outlier data points ($n = 176$ in this plot). **f**, Left, flat map of the medial half of the MEC showing grid cell-containing recording positions in the same animal as in **c**. The *x* axis shows mediolateral position, *y* axis shows dorsoventral distance from the dorsal MEC border. Circles indicate recording locations for individual grid cells. Colour indicates module identity. Grid cells were recorded over approximately 50% of the dorsoventral axis and 20% of the mediolateral extent of the MEC (~1,900 μ m and ~500 μ m, respectively). Right, outline of each module (extrapolated from flat map, same scale).

surface (Fig. 4f). In animals with grid-cell recording locations spread apart as much as 900 μ m along the mediolateral axis at a single dorsoventral level, only one cluster was identified (Supplementary Fig. 14). In animals with more extensive dorsoventral sampling and more than one grid module, values for grid scale and grid orientation were similar at widely separated mediolateral locations (Fig. 4e, f and Supplementary Figs 15 and 16), irrespective of cell layer (Supplementary Figs 4 and 13–15), indicating that, within the recording area in medial MEC, the modules may be organized as horizontal bands parallel to the dorsal border of the MEC. The maximum number of modules detected in any animal was four or five, with some uncertainty about the fifth module because the putative grids were too large for periodicity to be detected in this study (Supplementary Fig. 17). The largest area covered by tetrodes in any animal spanned nearly 50% of the dorsoventral axis and 32% of the mediolateral axis of MEC (Fig. 4e and Supplementary Fig. 14b), implying that the number of grid modules within MEC is small and, by extrapolation, in the upper single-digit range.

Scale relations across modules

We asked whether module averages for grid spacing vary across animals and if there is a fixed scale relationship within animals. Mean grid-spacing values were widely distributed between rats, with no apparent peaks in the distribution (Fig. 5a, b and Supplementary Fig. 18). A significant scale relationship was revealed, however, when increases in grid spacing were plotted across animals as a function of module number, with modules ranked according to their mean grid spacing. Increments in grid spacing increased linearly between successive pairs of modules (from M2–M1 through M3–M2 to M4–M3) (Fig. 5c, $R^2 = 0.20$, $P = 0.027$). The ratio between successive module averages (M2/M1, M3/M2, M4/M3) fluctuated around a constant value of 1.42 (s.d. = 0.02; Fig. 5d), indicating that grid scale follows

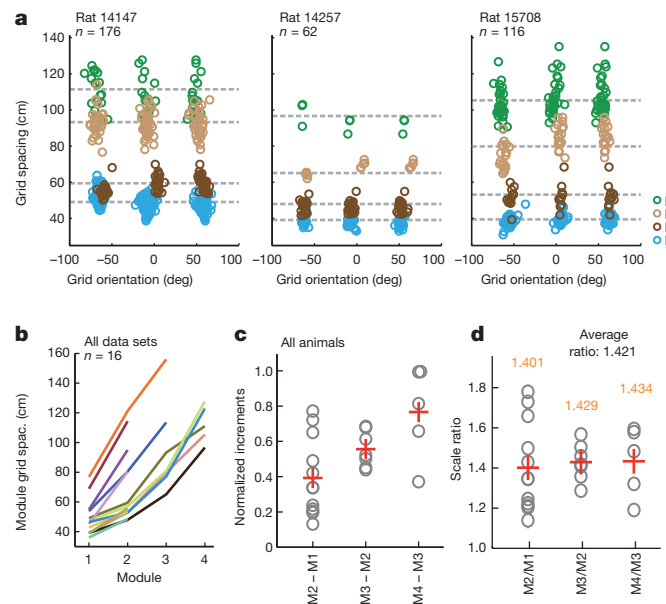


Figure 5 | Scale relationship between grid modules. **a**, Scatterplots showing difference in module grid-scale relationship for 3 animals, each with 4 detected modules (circles correspond to individual cells, modules are colour-coded). Spacing and orientation for all three axes are shown. Dashed lines, mean spacing of each module. **b**, Mean grid spacing for all modules (M1–M4) in all animals (animals colour-coded). Note variable module means and scale relationships across animals. **c**, Normalized increments in grid spacing (mean per module) as a function of module pair (M2 – M1: difference in mean grid spacing between module with lowest and second-lowest value, etc.). Individual module pairs are in grey, means across animals are in red. **d**, Ratios between successive module means for grid spacing. Individual module pairs in grey, means indicated by red crosses (values in orange).

a geometric progression rule. Note that a progression of approximately $1.42 (\sqrt{2})$ translates to a near-perfect doubling of the area of the grid hexagon between modules of successive grid scale.

Grid modules have a discrete temporal organization

When MEC neurons fire in grid patterns, the local network activity is dominated by the theta rhythm^{32,33}. To establish whether the organization of this rhythm is modular, we estimated the intrinsic theta frequency (ITF) of each cell in all eight animals with more than 35 grid cells in 2 or more modules. ITF was defined as the peak frequency in the theta band of the cell's spike-time autocorrelogram (Fig. 6). ITF was not uniformly distributed in MEC. When data were pooled across animals, there was a weak but significant negative correlation between ITF and grid spacing ($r = -0.12$, $P < 0.001$), as reported previously^{32,34}. Within animals, this correlation was not reliable (-0.12 ± 0.05 , mean \pm s.e.m., $P > 0.05$ in 6 out of 8 animals), despite widespread sampling (Supplementary Fig. 19). However, the ITF was more similar for grid cells from the same module than grid cells from different modules (Fig. 6b, c). In 7 out of 8 animals, the ITF was more similar for cell pairs with similar grid scale (<5th percentile of all pairwise differences in grid scale) than for pairs with different scale (>5th percentile) (Fig. 6c; ratio of 1.33 ± 0.08 , mean \pm s.e.m., $t(7) = 4.37$, $P < 0.005$, Student's t -test). This comodularity was not caused by any relationship between grid theta frequency and grid spacing, as

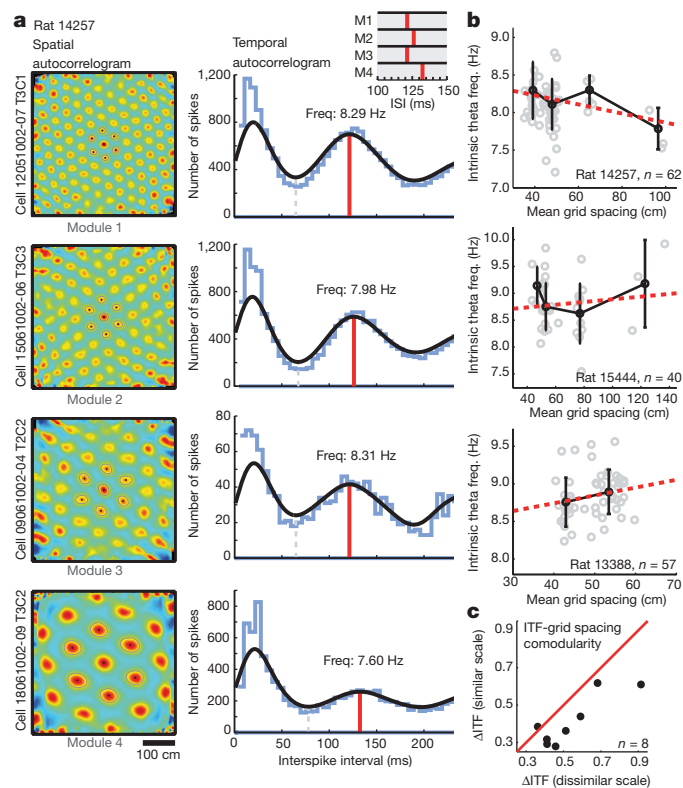


Figure 6 | Comodularity between grid spacing and theta frequency. **a**, Theta modulation in four cells from four grid modules in rat 14527. Left, spatial autocorrelograms. Right, spike-time autocorrelograms for the same cells. Peaks (red line) in the theta range were used to calculate each grid cell's intrinsic theta frequency (ITF, indicated above each peak). Top inset, close-up of peak interspike interval (ISI) for each module. **b**, ITF as a function of grid spacing in three animals. Circles indicate cells. Mean and s.d. of ITF are shown for each module. Red dashed lines indicate best linear fits. Note modular appearance of the theta modulation as well as lack of linear or monotonic relationship between grid spacing and theta modulation. **c**, Comparison of average differences in ITF for pairs of grid cells with similar grid spacing (<5th percentile of scale differences) and pairs with different spacing (>5th percentile) (all animals, methods as in Fig. 2d).

the residuals of the linear regression between ITF and grid spacing remained more similar for cell pairs with similar grid scale (7 of 8 animals, ratio of 1.26 ± 0.10 , $t(7) = 2.59$, $P < 0.05$). Taken together, these observations show that modules of grid cells with similar geometric properties are discrete also with regard to temporal organization, and that this temporal organization does not exhibit any strong linear or monotonic relationship to grid spacing.

Functional independence of grid modules

We have found that grid scale, grid orientation and grid distortion, as well as temporal organization in the theta frequency range, are determined independently for different modules of the same grid network. To address directly the question of whether the modules are also decoupled in their responses to changes in the environment, we tested four animals in an environmental compression task known to induce temporary rescaling in grid cells³⁰.

Grid cells from different modules were first recorded in a familiar 150 cm \times 150 cm environment, then in a novel 150 cm \times 100 cm version of the same environment, and then again in the original environment (Fig. 7a–c). To quantify any rescaling in the compressed environment, we stretched each rectangular rate map iteratively in small increments and correlated, for each step, the stretched map with the overlapping region of the cell's square map. This yielded

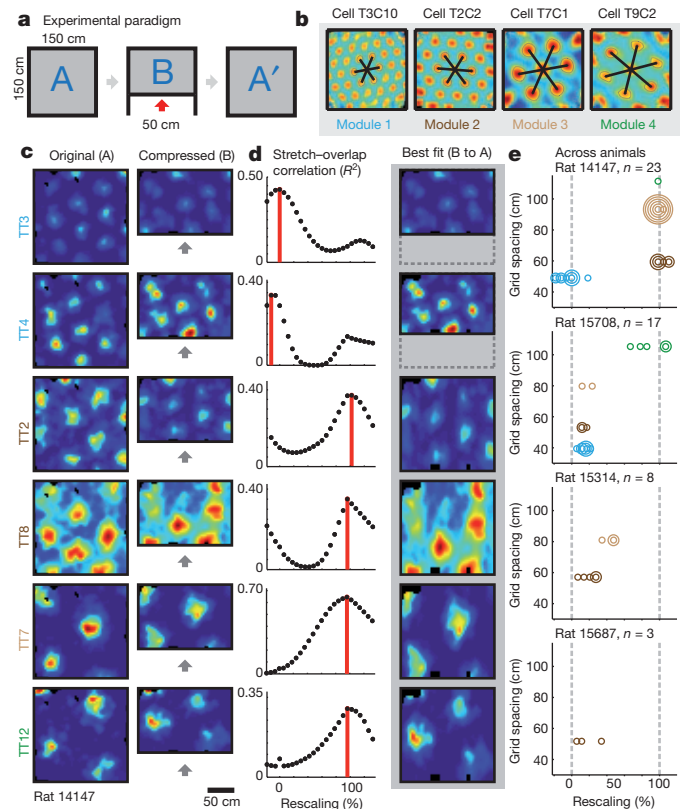


Figure 7 | Grid modules are functionally independent. **a**, Schematic of the box-compression experiment. **b**, Spatial autocorrelograms from individual cells representing 4 modules in rat 14147. **c**, Rate maps from 6 grids on 6 different tetrodes in the box-compression task (rat 14147). Tetrode numbering is arbitrary. Only configurations A and B are shown. Wall relocation indicated by grey arrows. **d**, Left, stretch-correlation curves showing spatial correlation between the rate map in B and the overlapping part of A for successive expansions of the map in B. Peak values are indicated by red lines. Best fits are shown to the right. Note distinct responses of grids in module M1 (TT3, TT4) as compared to grids in M2–M4 (remaining tetrodes, all with larger grid spacing). **e**, Rescaling as a function of module scale. Circles correspond to individual cells. Concentric rings represent overlapping data points. For clarity, individual grids are represented by the mean grid spacing of the respective module. Colour code as in **b**.

stretch-correlation curves from which we could define each cell's rescaling level as the amount of stretch that gave rise to the largest correlation (Fig. 7d). The degree of rescaling varied substantially (from -18 to 110% ; mean \pm s.e.m. = $35.1 \pm 17.0\%$; 4 animals, 51 grid cells). Within individual rats, the distribution of rescaling values was generally bimodal, with clusters forming near 0% and 100% (Fig. 7e and Supplementary Fig. 20); cells either rescaled fully with the environment or did not rescale at all.

The key finding is that simultaneously recorded grid modules responded independently to the relocation of the wall (Fig. 7c–e and Supplementary Fig. 20). Grid cells in Module M1, with the smallest grid-scale values, showed only minimal rescaling, with peak correlations appearing between -18.4% and 21.4% of the stretch distance. At the same time, grid cells in the larger modules rescaled completely, such that all fields of the original environment were maintained, but with reduced grid-field distances in the compressed direction. Cells that belonged to the same module always responded coherently (Fig. 7c–e). Taken together, these data provide proof-of-principle evidence that grid modules can operate independently on geometric inputs from the same environment.

Discussion

Our understanding of population dynamics in the entorhinal grid network has lagged behind that of individual grid cells for the very reason that, until now, experimenters have not been able to collect data from more than a dozen grid cells in the same animal^{18–20,30–38}. By increasing this number by an order of magnitude, and by recording from multiple locations within the same MEC circuit at the same time, we were able to obtain sufficiently dense cell sampling to show that the grid-cell population is discretized into functionally independent sub-populations. Whereas the scale of the grid map was found to increase topographically from dorsal to ventral MEC when the data were pooled across animals, as in previous work^{19,20,30,36}, there was no corresponding smoothness in individual animals. In every single animal, the progression of grid scale was step-like. Because step sizes and step ratios were unique for each animal, the discrete nature of the distribution is masked in the pooled data. Our study further showed that more than one grid orientation can be expressed simultaneously in the same animal³⁷, and that discontinuities in grid orientation coincide with discontinuities in grid scale. The presence of only a single grid orientation in previous work³⁸ probably reflects limited sampling. Finally, cell populations with different grid properties were found to respond independently to changes in the geometry of the environment, indicating that modules of grid cells can be anchored separately to external cues or boundaries. The discrete but interspersed topography of the grid map, and the apparent autonomy of the modules, differs from the graded topography of maps for continuous variables in well-studied sensory systems, such as the orientation and direction maps of the feline, weasel and primate visual cortex^{4–11}.

The cellular substrate of the grid modules remains to be determined. The MEC has several architectonic features that might favour modular operations²⁹, such as the organization of entorhinal neurons into a mosaic of alternating cytochrome-oxidase-rich and cytochrome-oxidase-poor clusters^{39,40} or the segregation of cell groups by bundles of axons and dendrites from cells in the intermediate and deep layers⁴¹. However, none of these, or other known structural variations²⁹, match the anatomical distribution of grid modules. First, the number of MEC clusters formed by bundling or variations in cytochrome oxidase expression is probably in the order of hundreds, whereas the number of grid-cell modules, identified within a range that covered up to 50% of the dorsoventral axis of the MEC, on the medial side, never exceeded 4 or 5. Second, the horizontal band-like appearance of the grid modules, with detectable clustering in the dorsoventral but not the mediolateral dimension, is inconsistent with the patchy patterns observed in the anatomical stains. Finally, grid modules exhibit considerable anatomical overlap, cutting across cell layers as well as widespread regions

along both axes of the MEC sheet. The data indicate that grid modules are partly entangled and raise the possibility that, within the same anatomical space, there are multiple cell groups with strong internal connectivity and weak cross-connectivity. How overlapping networks are segregated remains to be determined, but the invariance of the average scale ratio, across animals and successive modules, implies a genetic mechanism, possibly one in which the formation of modules is determined by self-organizing cortical mechanisms during cortical development²¹, at the same time as the variability in actual values for grid spacing across animals retains a role for experience in calibrating the grid modules to the external environment. The emergence of grid patterns from local inhibitory coupling^{26,42}, and the absence of precise spatial periodicity before the maturation of such coupling^{43,44}, point to inhibitory networks as a possible component of the mechanism for developmental segregation of grid modules.

The modular nature of the grid-cell network has implications for the mechanisms of grid formation. Computational models of grid cells fall into two main classes—oscillatory interference models and attractor-network models^{17,22}. Both types of models make predictions relevant to the functional organization of the grid-cell network. The interference models suggest that grid patterns emerge from velocity-dependent beat frequencies in the membrane potential formed by interference between multiple theta oscillators at slightly different frequencies^{24,45,46}. Following this idea, increases in grid scale must be paralleled by proportional decreases in the cells' theta modulation frequency. The lack of such a linear relationship across modules does not support a theta frequency-based mechanism for grid cells and reinforces the recent observation that grid cells persist in the absence of theta rhythmicity³⁶. In the second class of models—the attractor models—the changing location of a moving animal is represented instead by translation of activity across an array of grid cells arranged in network space according to their grid phase, with direction and distance of displacement in this array being proportional to the actual movement of the animal in the environment^{21,23,26,42}. This proposed correspondence between velocity of movement and displacement in the neural sheet can only be maintained if the local network has a common grid scale and grid orientation, that is if the network is organized into discrete space and orientation modules. The present work confirms this prediction. By showing that grid modules with different spacing and orientation can interact independently with the environment, the present study further raises the possibility that the MEC comprises multiple path-integrating grid networks, each operating at a unique grid scale, possibly as the result of a unique amplification of incoming speed signals²¹.

The modular organization of grid cells may further influence how information is processed and stored downstream in the hippocampus. If hippocampal place cells are excited by convergent input from multiple grid modules, two types of effects can be envisaged. First, convergence of signals from multiple grid modules would prevent propagation of noise that is uncorrelated across modules, allowing the hippocampus to estimate location with a precision that exceeds that of the individual grid modules^{26,47}. Second, such convergence might facilitate the formation of new and unique representations for new environments. If converging modules respond independently to displacement or reconfiguration of the environment, the altered co-activity may activate a new subset of hippocampal neurons at each location in the changed environment³⁵. A similarly effective redistribution would not necessarily be seen if the entire grid map responded coherently. Computational simulations have shown that convergence of signals from only 2 to 4 independently aligned grid modules may be sufficient to obtain near-complete remapping in downstream place cells⁴⁸. Each change in relative phase and orientation among a set of grid modules might lead to a unique hippocampal activation pattern, suggesting that the number of distinct representations that can be formed is large^{49,50}. By combining input from a small number of independently operating grid modules, hippocampal cell

populations may thus acquire the ability to generate discrete representations individualized to specific places and experiences, an ability that may lie at the heart of the contribution of the hippocampus to episodic and semantic memory formation.

METHODS SUMMARY

Male Long-Evans rats were implanted with a microdrive carrying a single bundle of 4 tetrodes angled tangentially to the MEC surface (5 rats) or with a 'hyperdrive' carrying 12 independently movable tetrodes targeted semi-vertically to widespread regions of the MEC (10 rats). The tetrodes were advanced in small increments over weeks until large numbers of stable grid cells appeared. Neural activity was recorded while the rats foraged in 100–220-cm-wide open-field boxes. Cells were assigned to modules using a *k*-means clustering algorithm. A complete description of the materials and methods is provided in Supplementary Information.

Received 16 May; accepted 28 September 2012.

- Mountcastle, V. B. Modality and topographic properties of single neurons of cat's somatic sensory cortex. *J. Neurophysiol.* **20**, 408–434 (1957).
- Hubel, D. H. & Wiesel, T. Receptive fields, binocular interaction, and functional architecture of cat striate cortex. *J. Physiol. (Lond.)* **160**, 106–154 (1962).
- Hubel, D. H. & Wiesel, T. Functional architecture of macaque monkey visual cortex. *Proc. R. Soc. Lond. B Biol. Sci.* **198**, 1–59 (1977).
- Hubel, D. H. & Wiesel, T. Sequence regularity and geometry of orientation columns in the monkey striate cortex. *J. Comp. Neurol.* **158**, 267–293 (1974).
- Blasdel, G. G. & Salama, G. Voltage sensitive dyes reveal a modular organization in monkey striate cortex. *Nature* **321**, 579–585 (1986).
- Bonhoeffer, T. & Grünwald, A. Orientation columns in cat are organized in pin-wheel like patterns. *Nature* **353**, 429–431 (1991).
- Ohki, K. *et al.* Highly ordered arrangement of single neurons in orientation pinwheels. *Nature* **442**, 925–928 (2006).
- Payne, B. R., Berman, N. & Murphy, E. H. Organization of direction preferences in cat visual cortex. *Brain Res.* **211**, 445–450 (1981).
- Tolhurst, D. J., Dean, A. F. & Thompson, I. D. Preferred direction of movement as an element in the organization of cat visual cortex. *Exp. Brain Res.* **44**, 340–342 (1981).
- Weliky, M., Bosking, W. H. & Fitzpatrick, D. A systematic map of direction preference in primary visual cortex. *Nature* **379**, 725–728 (1996).
- Ohki, K., Chung, S., Ch'ng, Y. H., Kara, P. & Reid, R. C. Functional imaging with cellular resolution reveals precise micro-architecture in visual cortex. *Nature* **433**, 597–603 (2005).
- Sperry, R. W. Visuomotor coordination in the newt (*Triturus viridescens*) after regeneration of the optic nerve. *J. Comp. Neurol.* **79**, 33–55 (1943).
- Drescher, U. *et al.* In vitro guidance of retinal ganglion cell axons by RAGS, a 25 kDa tectal protein related to ligands for Eph receptor tyrosine kinases. *Cell* **82**, 359–370 (1995).
- Cheng, H. J., Nakamoto, M., Bergemann, A. D. & Flanagan, J. G. Complementary gradients in expression and binding of ELF-1 and Mek4 in development of the topographic retinotectal projection map. *Cell* **82**, 371–381 (1995).
- O'Keefe, J. & Dostrovsky, J. The hippocampus as a spatial map. Preliminary evidence from unit activity in the freely-moving rat. *Brain Res.* **34**, 171–175 (1971).
- O'Keefe, J. & Nadel, L. *The Hippocampus as a Cognitive Map* (Oxford Univ. Press, 1978).
- Moser, E. I., Kropff, E. & Moser, M.-B. Place cells, grid cells, and the brain's spatial representation system. *Annu. Rev. Neurosci.* **31**, 69–89 (2008).
- Fyhn, M., Molden, S., Witter, M. P., Moser, E. I. & Moser, M. B. Spatial representation in the entorhinal cortex. *Science* **305**, 1258–1264 (2004).
- Hafting, T., Fyhn, M., Molden, S., Moser, M.-B. & Moser, E. I. Microstructure of a spatial map in the entorhinal cortex. *Nature* **436**, 801–806 (2005).
- Sargolini, F. *et al.* Conjunctive representation of position, direction, and velocity in entorhinal cortex. *Science* **312**, 758–762 (2006).
- McNaughton, B. L., Battaglia, F. P., Jensen, O., Moser, E. I. & Moser, M.-B. Path integration and the neural basis of the 'cognitive map'. *Nature Rev. Neurosci.* **7**, 663–678 (2006).
- Giocomo, L. M., Moser, M.-B. & Moser, E. W. I. Computational models of grid cells. *Neuron* **71**, 589–603 (2011).
- Fuhs, M. C. & Touretzky, D. S. A spin glass model of path integration in rat medial entorhinal cortex. *J. Neurosci.* **26**, 4266–4276 (2006).
- Burgess, N., Barry, C. & O'Keefe, J. An oscillatory interference model of grid cell firing. *Hippocampus* **17**, 801–812 (2007).
- Kropff, E. & Treves, A. The emergence of grid cells: intelligent design or just adaptation? *Hippocampus* **18**, 1256–1269 (2008).
- Burak, Y. & Fiete, I. R. Accurate path integration in continuous attractor network models of grid cells. *PLOS Comput. Biol.* **5**, e1000291 (2009).
- Zilli, E. A. & Hasselmo, M. E. Coupled noisy spiking neurons as velocity-controlled oscillators in a model of grid cell spatial firing. *J. Neurosci.* **30**, 13850–13860 (2010).
- Mhatre, H., Gorchetchnikov, A. & Grossberg, S. Grid cell hexagonal patterns formed by fast self-organized learning within entorhinal cortex. *Hippocampus* **22**, 320–334 (2012).
- Witter, M. P. & Moser, E. I. Spatial representation and the architecture of the entorhinal cortex. *Trends Neurosci.* **29**, 671–678 (2006).
- Barry, C., Hayman, R., Burgess, N. & Jeffery, K. J. Experience-dependent rescaling of entorhinal grids. *Nature Neurosci.* **10**, 682–684 (2007).
- Solstad, T., Boccara, C. N., Kropff, E., Moser, M.-B. & Moser, E. I. Representation of geometric borders in the entorhinal cortex. *Science* **322**, 1865–1868 (2008).
- Brun, V. H. *et al.* Progressive increase in grid scale from dorsal to ventral medial entorhinal cortex. *Hippocampus* **18**, 1200–1212 (2008).
- Hafting, T., Fyhn, M., Bonnevie, T., Moser, M.-B. & Moser, E. I. Hippocampus-independent phase precession in entorhinal grid cells. *Nature* **453**, 1248–1252 (2008).
- Jeewajee, A., Barry, C., O'Keefe, J. & Burgess, N. Grid cells and theta as oscillatory interference: electrophysiological data from freely moving rats. *Hippocampus* **18**, 1175–1185 (2008).
- Fyhn, M., Hafting, T., Treves, A., Moser, M. B. & Moser, E. I. Hippocampal remapping and grid realignment in entorhinal cortex. *Nature* **446**, 190–194 (2007).
- Yartsev, M. M., Witter, M. P. & Ulanovsky, N. Grid cells without theta oscillations in the entorhinal cortex of bats. *Nature* **479**, 103–107 (2011).
- Krupic, J., Burgess, N. & O'Keefe, J. Neural representations of location composed of spatially periodic bands. *Science* **337**, 853–857 (2012).
- Doeller, C. F., Barry, C. & Burgess, N. Evidence for grid cells in a human memory network. *Nature* **463**, 657–661 (2010).
- Hevner, R. F. & Wong-Riley, M. T. Entorhinal cortex of the human, monkey, and rat: metabolic map as revealed by cytochrome oxidase. *J. Comp. Neurol.* **326**, 451–469 (1992).
- Burgalossi, A. *et al.* Microcircuits of functionally identified neurons in the rat medial entorhinal cortex. *Neuron* **70**, 773–786 (2011).
- Ikeda, J., Mori, K., Oka, S. & Watanabe, Y. A columnar arrangement of dendritic processes of entorhinal cortex neurons revealed by a monoclonal antibody. *Brain Res.* **505**, 176–179 (1989).
- Couey, J. J. *et al.* Medial entorhinal cortex layer II stellate cells are embedded within a recurrent inhibitory network. *Soc. Neurosci. abstr.* 702.06 (2012).
- Langston, R. F. *et al.* Development of the spatial representation system in the rat. *Science* **328**, 1576–1580 (2010).
- Wills, T. J., Cacucci, F., Burgess, N. & O'Keefe, J. Development of the hippocampal cognitive map in preweanling rats. *Science* **328**, 1573–1576 (2010).
- Hasselmo, M. E., Giocomo, L. M. & Zilli, E. A. Grid cell firing may arise from interference of theta frequency membrane potential oscillations in single neurons. *Hippocampus* **17**, 1252–1271 (2007).
- Blair, H. T., Welday, A. C. & Zhang, K. Scale-invariant memory representations emerge from moiré interference between grid fields that produce theta oscillations: a computational model. *J. Neurosci.* **27**, 3211–3229 (2007).
- Sreenivasan, S. & Fiete, I. Grid cells generate an analog error-correcting code for singularly precise neural computation. *Nature Neurosci.* **14**, 1330–1337 (2011).
- Monaco, J. D. & Abbott, L. F. Modular realignment of entorhinal grid cell activity as a basis for hippocampal remapping. *J. Neurosci.* **31**, 9414–9425 (2011).
- Muller, R. U. & Kubie, J. L. The effects of changes in the environment on the spatial firing of hippocampal complex-spike cells. *J. Neurosci.* **7**, 1951–1968 (1987).
- Colgin, L. L., Moser, E. I. & Moser, M.-B. Understanding memory through hippocampal remapping. *Trends Neurosci.* **31**, 469–477 (2008).

Supplementary Information is available in the online version of the paper.

Acknowledgements We thank A. M. Amundgård, K. Haugen, K. Jenssen, E. Kråkvik, R. Skjerpeng, and H. Waade for technical assistance, J. Whitlock for implanting an animal in the tangential group, and T. Bonhoeffer, B. Dunn, B. McNaughton, Y. Roudi, A. Treves and A. Witoelar for helpful discussion. The work was supported by an Advanced Investigator Grant from the European Research Council ('CIRCUIT', Grant Agreement no. 232608), the Kavli Foundation and the Centre of Excellence scheme of the Research Council of Norway.

Author Contributions T.St., H.S., T.So., M.-B.M. and E.I.M. designed experiments and analyses; H.S., T.St. and T.So. implanted tetrodes; H.S. recorded multisite data; T.So. and K.F. tested animals with tangential implants; T.St. performed the majority of the analyses; and T.St. and E.I.M. wrote the paper with input from all authors.

Author Information Reprints and permissions information is available at www.nature.com/reprints. The authors declare no competing financial interests. Readers are welcome to comment on the online version of the paper. Correspondence and requests for materials should be addressed to E.I.M. (edvard.moser@ntnu.no) or H.S. (hanne.stensola@ntnu.no) or T.St. (tor.stensola@ntnu.no).

Extremely metal-poor gas at a redshift of 7

Robert A. Simcoe¹, Peter W. Sullivan¹, Kathy L. Cooksey¹, Melodie M. Kao^{1,2}, Michael S. Matejek¹ & Adam J. Burgasser³

In typical astrophysical environments, the abundance of heavy elements ranges from 0.001 to 2 times the solar value. Lower abundances have been seen in selected stars in the Milky Way's halo^{1–3} and in two quasar absorption systems at redshift $z = 3$ (ref. 4). These are widely interpreted as relics from the early Universe, when all gas possessed a primordial chemistry. Before now there have been no direct abundance measurements from the first billion years after the Big Bang, when the earliest stars began synthesizing elements. Here we report observations of hydrogen and heavy-element absorption in a spectrum of a quasar at $z = 7.04$, when the Universe was just 772 million years old (5.6 per cent of its present age). We detect a large column of neutral hydrogen but no corresponding metals (defined as elements heavier than helium), limiting the chemical abundance to less than 1/10,000 times the solar level if the gas is in a gravitationally bound protogalaxy, or to less than 1/1,000 times the solar value if it is diffuse and unbound. If the absorption is truly intergalactic^{5,6}, it would imply that the Universe was neither ionized by starlight nor chemically enriched in this neighbourhood at $z \approx 7$. If it is gravitationally bound, the inferred abundance is too low to promote efficient cooling^{7,8}, and the system would be a viable site to form the predicted but as yet unobserved massive population III stars.

We observed the recently discovered $z = 7.085$ quasar ULAS J1120+0641 (ref. 6) in January 2012 with the FIRE infrared spectrometer⁹ on the Magellan/Baade telescope. Our data provide a 12-fold increase in spectral resolution over the discovery spectrum at similar signal-to-noise ratio, enabling study of weak heavy-element absorption lines that are diluted by the instrumental profile at lower resolution.

Our spectrum (Fig. 1) confirms the presence of unusually strong Lyman α ($\text{Ly}\alpha$) resonance absorption from neutral hydrogen (H I) in the immediate foreground of the quasar. This absorption is clearly visible in Fig. 1a, b as a contrast between the observed flux (black) and an intrinsic source spectrum model (red) at wavelengths $\lambda < 0.98 \mu\text{m}$. However, the data also fall well below the source template at wavelengths redder than the $\text{Ly}\alpha$ transition at the quasar's systemic redshift ($\lambda > 0.9829 \mu\text{m}$). This has been interpreted^{5,6} as a Lorentzian damping wing of the H I $\text{Ly}\alpha$ line at a redshift very close to that of the quasar, indicating a high neutral-hydrogen column density¹⁰. Such absorption could be caused by a long column of low-density, intergalactic hydrogen with a high neutral fraction in the vicinity of the quasar. Or, it could arise in compact, high-density gas gravitationally bound to an early galaxy. Such proximate damped $\text{Ly}\alpha$ (DLA) absorption systems have numerous analogues at lower redshift.

At $z = 5$ and below, every known absorption system with sufficient neutral hydrogen to elicit damping wings also exhibits absorption from heavy-element lines^{11–13}. However, we find no evidence of heavy-element absorption despite the sensitivity of the FIRE data, which is sufficient to detect metals (defined as elements heavier than helium) at abundance levels characteristic of lower-redshift DLAs. We do detect narrow metal absorption lines from highly ionized gas at the redshift of the quasar, manifested in C IV and N V. However these are offset from the damped H I absorption by $\Delta v = +711 \text{ km s}^{-1}$ (equivalent to

800 kpc in proper distance units if Δv is purely cosmological), and there is substantial flux transmission at the associated H I wavelength for these lines. The heavy-element lines are therefore most probably internal to the quasar host itself and not physically coincident with the neutral gas.

Quantitative chemical abundance estimates are usually impossible for $z > 5.5$ quasar absorbers because the benchmark neutral-hydrogen line is severely blended and saturated in the forest of neighbouring $\text{Ly}\alpha$ systems. However the damping wing near the emission redshift of ULAS J1120 offers a unique opportunity to measure its H I column density. In conjunction with upper limits on the heavy-element column density, this yields a straightforward upper limit on the chemical abundance of metals.

The H I column density estimate is sensitive to the detailed shape of the damping profile, which is fitted to the ratio of emitted to observed flux (the ratio of the red to black lines in Fig. 1). This ratio depends

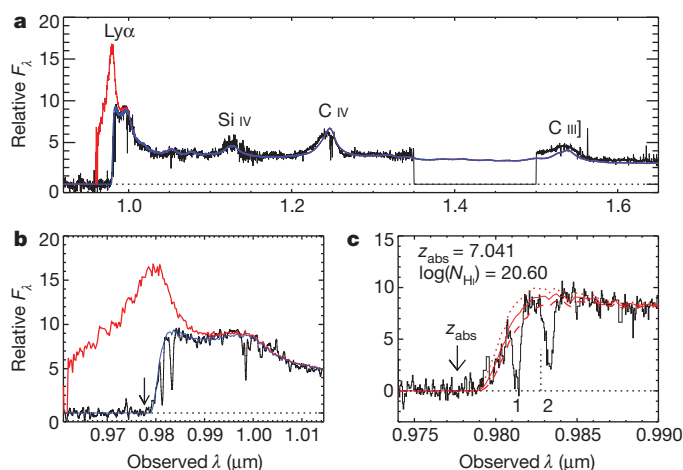


Figure 1 | Infrared spectrum of ULAS J1120+0641, compared to our estimate of the intrinsic quasar spectrum without foreground absorption.

a, The unabsorbed continuum is shown in red, and the blue curve includes the absorption. The continuum template is constructed from a composite of quasars in the Sloan Digital Sky Survey^{14,16} shifted to a redshift of $z_{\text{templ}} = 7.07$. C IV absorption intrinsic to the quasar host galaxy is seen to the red of the labelled C IV emission peak. However, the C IV emission line is anomalously blueshifted⁶ in ULAS J1120, so we compute the redshift distance between the absorber and quasar host using its Mg II (ref. 6) or [C II] (ref. 25) redshift. **b**, Magnified view of the $\text{Ly}\alpha$ region of the spectrum with unabsorbed continuum model (red) and absorbed continuum (blue). The vertical arrow marks the location of $\text{Ly}\alpha$ absorption at $z_{\text{abs}} = 7.04$. **c**, Detail of the damping wing with best-fit H I absorption model (solid line) centred on z_{abs} with $\log(N_{\text{HI}}) = 20.6 \text{ cm}^{-2}$. Dotted and dashed lines indicate the $\pm 1\sigma$ fit uncertainty. The quasar's emission redshift²⁶ (7.0842) is indicated with the vertical dashed line. Two additional optically thin $\text{Ly}\alpha$ absorbers (labelled 1 and 2) are apparent in the quasar's near zone at $z = 7.0721 \pm 0.0001$ and $z = 7.0855 \pm 0.0001$ ($\Delta v = -424, +161 \text{ km s}^{-1}$ from the host, respectively, see Supplementary Information). These data have not been continuum normalized, so a slight downward slope is visible towards redder wavelengths.

¹MIT-Kavli Institute for Astrophysics and Space Research, 77 Massachusetts Avenue, Building 37, Room 664L, Cambridge, Massachusetts 02139, USA. ²Department Of Astronomy, California Institute of Technology, 1200 East California Boulevard, MC 249-17, Pasadena, California 01125, USA. ³Center for Astrophysics and Space Science, University of California San Diego, MC 0424, 9500 Gilman Drive, La Jolla, California 92093, USA.

critically on how the intrinsic (that is, unabsorbed) shape of the quasar's Ly α emission line is modelled, including both its absolute flux density and its redshift, which fixes the location of the emission peak. The details of this procedure are described in Supplementary Information, but to summarize, we experimented with several different prescriptions, including four different quasar composite spectra generated from low-redshift surveys^{14–17}, and additionally a principal-component analysis fit¹⁸ extrapolated over the Ly α region. For each of these continua, we calculated the H I column density required to produce the damping wing redward of the systemic Ly α line via Voigt profile model fitting, finding a best-fit value of $\log(N_{\text{HI}}) = 20.60 \text{ cm}^{-2}$. For any one continuum model, the formal fit error for $\log(N_{\text{HI}})$ was of the order of 0.02–0.03 dex, but the true error is much more likely to be dominated by systematic uncertainty in the continuum. By experimenting with different choices of continuum and absorber redshift, we estimated the range of allowable $\log(N_{\text{HI}})$ as 20.45–21.0, at a best-fit absorption redshift of $z = 7.041^{+0.003}_{-0.008}$ (95% confidence).

We estimated upper limits to the metal line column densities (Fig. 2) both by curve-of-growth analysis and by direct Voigt profile fitting (Table 1, see also Supplementary Information). For systems with $\log(N_{\text{HI}}) > 20.3$, the transitions in Table 1 represent the predominant ionization states for their respective elements^{19,20}. The one exception to this is C IV, which is secondary to C II but which we include as an ionization constraint (discussed below). We therefore follow the usual practice for DLA systems and do not apply ionization corrections when estimating abundances^{19,20}.

Considering first the DLA scenario, our strongest abundance limit is derived from Si II, which yields a 1σ (2σ) upper bound of 1/20,000 (1/10,000) times the solar metallicity. With such unusual abundances, one must consider the possible effects of ionization, particularly given the proximity of the brightest known object in the $z = 7$ Universe. However, prior studies of other proximate DLA systems indicate that ionization plays only a minor role and may be counterbalanced by a tendency for such systems to have higher than average metallicities^{13,21}. Additionally, our spectrum places strong constraints on the lack of ionized gas seen in C IV, which would yield a tenfold lower abundance limit than C II if it dominated the ionization balance (on account of its higher signal-to-noise ratio and larger atomic cross-section). This rules out an ionized phase as a major source of missing metals in this absorber.

The limits presented above assume that the absorbing gas resides in a compact structure that is well-represented by a discrete line or cloud, which is appropriate for DLAs at lower redshift. However at $z = 7$ the absorption could also result from the integrated contribution of diffuse intergalactic gas if the neighbourhood of ULAS J1120 has not yet been ionized by starlight. Using Monte Carlo simulations of intergalactic H I and heavy-element absorption (described in Supplementary Information), we find that for physical conditions leading to an intergalactic damping wing our spectrum still restricts heavy element absorption to the $<10^{-3}$ times the solar level, even with no DLA.

These chemical abundance limits have significant implications for either of the two physical scenarios considered. If the diffuse absorption model is correct, then at $z = 7$ the intergalactic medium must be both metal-poor and substantially neutral, even in the neighbourhood of a bright quasar. Such intergalactic material would not yet have mixed with the chemically polluted interstellar by-products of galaxies, so it should not be surprising for its heavy-element content to be small. At later epochs ($z = 2$ – 4), heavy elements are actually observed in intergalactic space, with abundances distributed log-normally between 1/300 and 1/3,000 times solar^{22,23}. Our $z = 7$ limit excludes the upper half of this distribution, but enrichment at the low end could elude detection in the FIRE data. Nevertheless, if this one object proves to be representative of the Universe at these epochs, it is plausible that $z = 7$ pre-dates both the radiative feedback and the chemical feedback thought to be hallmarks of reionization.

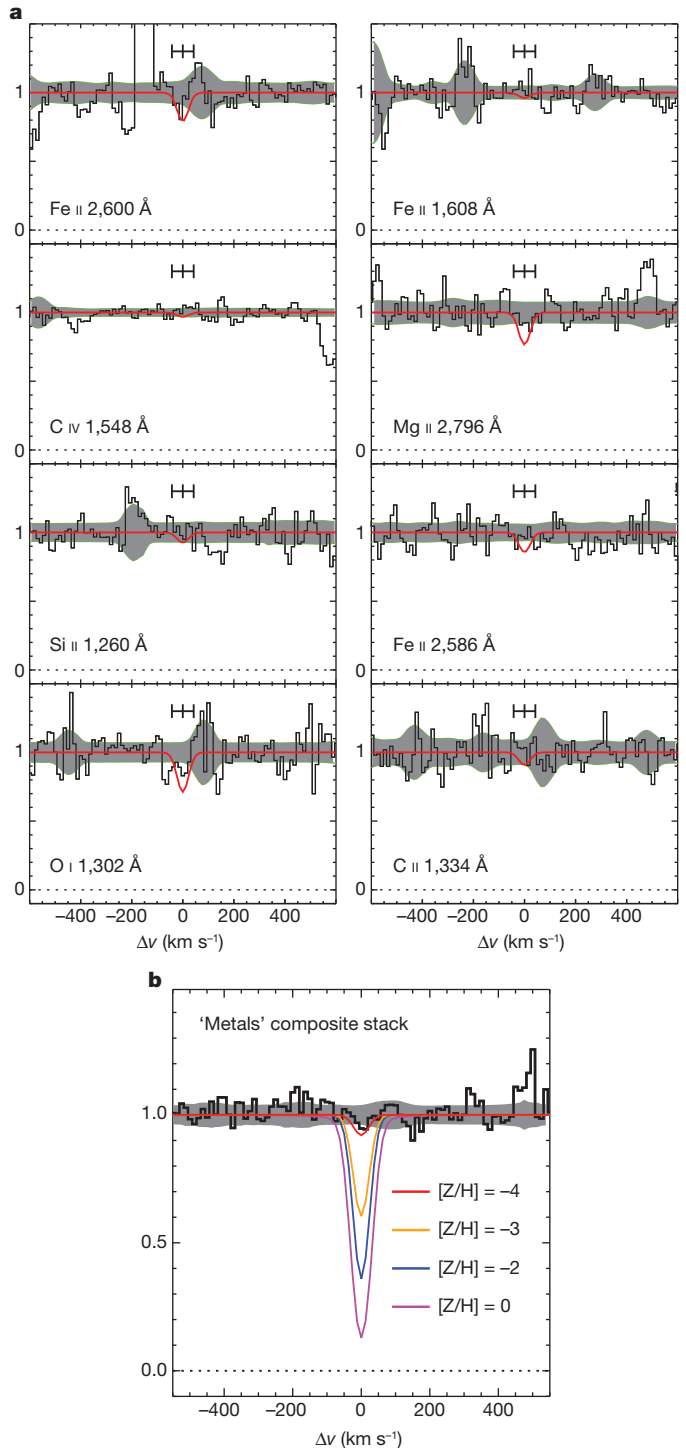


Figure 2 | Continuum-normalized transmitted flux in spectral regions where expected heavy-element transitions would appear for a DLA at redshift $z = 7.041$. **a**, Spectral regions with transition given; 1σ error contours are shaded grey, and the extraction aperture is indicated with horizontal bars. A Voigt profile with $b = 10 \text{ km s}^{-1}$ and N set by our column-density upper limit is shown in red for each panel. Velocity offsets are relative to the rest frame of the H I absorber. **b**, Composite stack of all heavy-element transitions, generated using an inverse-variance weighted mean and solar relative abundances. Each transition is scaled to the cross-section and relative abundance of O I. Overlaid curves show predicted metal absorption profiles for a DLA of $\log(N_{\text{HI}}) = 20.6$ and varying metallicity levels. The stack shows no statistically significant absorption, though there is a fluctuation at the 1σ level, corresponding to an effective $[\text{O}/\text{H}] < -4$.

Table 1 | Upper limits on chemical abundance

Measured ion and line wavelength	Chemical abundance
O I 1,302 Å	[O/H] ≤ −3.39 (−3.25)
C II 1,334 Å	[C/H] ≤ −4.16 (−3.86)
Si II 1,260 Å	[Si/H] ≤ −4.35 (−4.03)
Fe II 2,586 Å	[Fe/H] ≤ −3.09 (−2.92)
Fe II 2,600 Å	[Fe/H] ≤ −3.43 (−3.41)
Mg II 2,796 Å	[Mg/H] ≤ −3.89 (−3.74)
Stacked composite	[Z/H] ≤ −4.07 (−3.90)

These limits are for the $z = 7.041$ absorber when modelled as a single-component DLA. Values reflect the logarithm of the elemental abundance (by number) relative to solar abundance, calculated using $[X/H] = \log_{10}(N_X) - \log_{10}(N_H) - \log_{10}(X/H)_\odot$ and standard solar abundance values²⁴. Quoted levels are 1σ upper limits, with 2σ limits shown in parentheses. If the absorption arises in unbound intergalactic gas rather than a collapsed DLA, we derive upper limits of $[X/H] < -3.0$ using simulated sensitivity calculations described in Supplementary Information.

Alternatively, the observed hydrogen may sample the interstellar medium of a very early proto-galaxy. In this case, our limit of $<10^{-4}$ times the solar abundance is an order of magnitude lower than any previously measured in a predominantly neutral gas reservoir (Fig. 3). Comparably low heavy-element abundances have recently been reported in two Lyman limit systems at $z \approx 3$ (ref. 4), but the gas in those environments is at most 0.8% neutral⁴, and their total neutral hydrogen column is 2–3 orders of magnitude smaller. In contrast, the system producing the ULAS J1120 damping wing is at least 10% neutral and possibly much more so⁵. Figure 3 shows that metal-poor gas clouds represent a small percentage of all known systems at lower redshift^{11,12,22}. At $z = 7$, the first chemical abundance measured in any non-AGN (active galactic nucleus) environment would already be as pristine as the most metal-poor absorption systems at $z = 3$ and below.

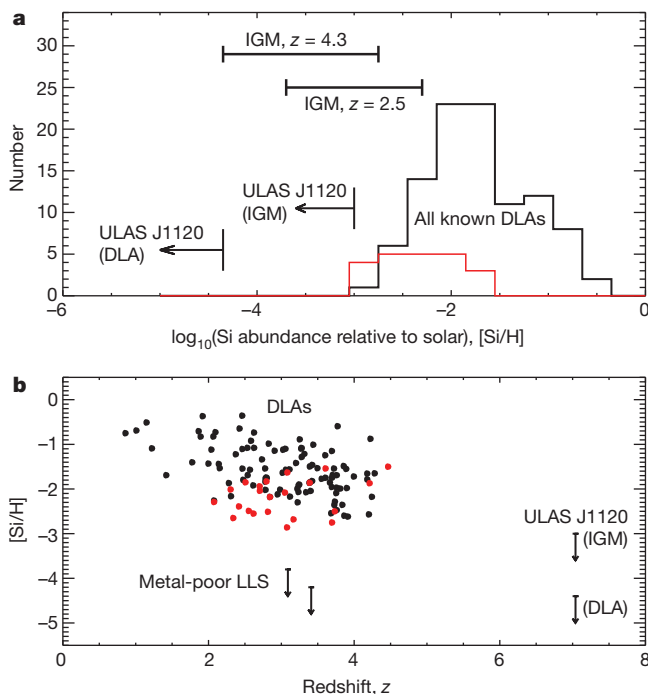


Figure 3 | Comparison of our $z = 7.04$ abundance measurement in ULAS J1120 with existing values from the literature. **a**, Histogram of the silicon abundance for known DLAs^{11,12,21}; **b**, silicon abundance for the same systems as **a**, at their respective redshifts. Panel **a** includes the $\pm 1\sigma$ abundance ranges for absorption systems in the intergalactic medium (IGM)^{22,23} at redshift 2.5 and 4.3; **b** also shows the locations of two recently reported metal-poor Lyman limit system (LLS) QSO absorbers⁴ at $z \approx 3$. DLAs at lower redshift exhibit $-2.5 < [Si/H] < -0.5$ (ref. 11), with the lowest previously known system having $[Si/H] = -2.75$ (ref. 13). Surveys designed expressly to uncover metal-poor DLAs (shown with red histogram and points) find $-2.86 < [Si/H] < -1.5$ (ref. 12).

DLA gas is commonly said to be a fuel supply for star formation, but our limits on the abundance in this geometry are sufficiently low that normal gas cooling channels for population I and II star formation would be suppressed. Theoretical calculations suggest that below an abundance of $[C/H] \approx -3.5$ (see Table 1 footnote for a definition of this nomenclature), the normal fine-structure atomic cooling mechanisms lose their effectiveness, and the predominant mode of star formation occurs through molecular H_2 cooling, resulting in high-mass population III stars^{7,8}. Taken together with its high redshift, this fact renders the $z = 7.04$ absorber in ULAS J1120 a viable site for population III star formation if the neutral gas is organized into a bound halo.

We warn that many more observations of $z > 7$ absorption systems will be required to establish whether the trends of large neutral-hydrogen column and low metal content are representative of the overall Universe at this early epoch. Indeed, the existence of heavy elements in both emission and absorption in the background quasar host indicates that local enrichment is underway in some environments. However, the confluence of neutral gas and extremely low chemical abundance, taken together with the young age of the Universe (772 Myr) at this redshift, suggests that current observations may already be reaching the era corresponding to the onset of star formation and cosmic chemical enrichment.

Received 20 March; accepted 19 September 2012.

- Christlieb, N. *et al.* A stellar relic from the early Milky Way. *Nature* **419**, 904–906 (2002).
- Frebel, A. *et al.* Nucleosynthetic signatures of the first stars. *Nature* **434**, 871–873 (2005).
- Caffau, E. *et al.* An extremely primitive star in the Galactic halo. *Nature* **477**, 67–69 (2011).
- Fumagalli, M., O'Meara, J. M. & Prochaska, J. X. Detection of pristine gas two billion years after the Big Bang. *Science* **334**, 1245–1249 (2011).
- Bolton, J. S. *et al.* How neutral is the intergalactic medium surrounding the redshift $z = 7.085$ quasar ULAS J1120+0641? *Mon. Not. R. Astron. Soc.* **416**, L70–L74 (2011).
- Mortlock, D. J. *et al.* A luminous quasar at a redshift of $z = 7.085$. *Nature* **474**, 616–619 (2011).
- Bromm, V., Ferrara, A., Coppi, P. S. & Larson, R. B. The fragmentation of pre-enriched primordial objects. *Mon. Not. R. Astron. Soc.* **328**, 969–976 (2001).
- Frebel, A., Johnson, J. L. & Bromm, V. Probing the formation of the first low-mass stars with stellar archaeology. *Mon. Not. R. Astron. Soc.* **380**, L40–L44 (2007).
- Simcoe, R. A. *et al.* FIRE: a near-infrared cross-dispersed echellette spectrometer for the Magellan telescopes. *Proc. SPIE* **7014**, 27–37 (2008).
- Miralda-Escude, J. Reionization of the intergalactic medium and the damping wing of the Gunn-Peterson trough. *Astrophys. J.* **501**, 15–22 (1998).
- Prochaska, J. X. *et al.* The UCSD/Keck damped Ly α abundance database: a decade of high-resolution spectroscopy. *Astrophys. J. Suppl. Ser.* **171**, 29–60 (2007).
- Cooke, R., Pettini, M., Steidel, C. C., Rudie, G. C. & Nissen, P. E. The most metal-poor damped Ly α systems: insights into chemical evolution in the very metal-poor regime. *Mon. Not. R. Astron. Soc.* **417**, 1534–1558 (2011).
- Ellison, S. L. *et al.* The nature of proximate damped Lyman α systems. *Mon. Not. R. Astron. Soc.* **406**, 1435–1459 (2010).
- Richards, G. T. *et al.* Unification of luminous type 1 quasars through C IV emission. *Astron. J.* **141**, 167–183 (2011).
- Vanden Berk, D. E. *et al.* Composite quasar spectra from the Sloan Digital Sky Survey. *Astron. J.* **122**, 549–564 (2001).
- Hewett, P. C. & Wild, V. Improved redshifts for SDSS quasar spectra. *Mon. Not. R. Astron. Soc.* **405**, 2302–2316 (2010).
- Zheng, W., Kriss, G. A., Telfer, R. C., Grimes, J. P. & Davidsen, A. F. A. Composite HST spectrum of quasars. *Astrophys. J.* **475**, 469–478 (1997).
- Yip, C. W. *et al.* Spectral classification of quasars in the Sloan Digital Sky Survey: eigenspectra, redshift, and luminosity effects. *Astron. J.* **128**, 2603–2630 (2004).
- Prochaska, J. X. & Wolfe, A. M. A. Keck HIRES investigation of the metal abundances and kinematics of the $z = 2.46$ damped Ly α system toward Q0201+365. *Astrophys. J.* **470**, 403–443 (1996).
- Vladilo, G., Centurión, M., Bonifacio, P. & Howk, J. C. Ionization properties and elemental abundances in damped Ly α systems. *Astrophys. J.* **557**, 1007–1020 (2001).
- Ellison, S. L., Prochaska, J. X. & Mendel, J. T. Metallicities and dust content of proximate damped Lyman α systems in the Sloan Digital Sky Survey. *Mon. Not. R. Astron. Soc.* **412**, 448–468 (2011).
- Simcoe, R. A. The carbon content of intergalactic gas at $z = 4.25$ and its evolution toward $z = 2.4$. *Astrophys. J.* **738**, 159–180 (2011).
- Schaye, J. *et al.* Metallicity of the intergalactic medium using pixel statistics. II. The distribution of metals as traced by C IV. *Astrophys. J.* **596**, 768–796 (2003).
- Asplund, M., Grevesse, N., Sauval, A. J. & Scott, P. The chemical composition of the Sun. *Annu. Rev. Astron. Astrophys.* **47**, 481–522 (2009).

25. Venemans, B. P. *et al.* Detection of atomic carbon [CII] 158 μm and dust emission from a $z=7.1$ quasar host galaxy. *Astrophys. J.* **751**, L25 (2012).

Supplementary Information is available in the online version of the paper.

Acknowledgements We thank J. O'Meara and A. Frebel for comments during the preparation of this Letter. M. Haehnelt also provided advice on methods for modelling the quasar near-zone, and G. Richards shared his composite QSO spectra in electronic form. This work includes data gathered with the 6.5-m Magellan Telescopes located at Las Campanas Observatory, Chile. R.A.S. acknowledges support from the NSF under awards AST-0908920 and AST-1109115. K.L.C. is supported by the NSF Astronomy and Astrophysics Postdoctoral Fellowship programme.

Author Contributions R.A.S. constructed the FIRE instrument, and together with P.W.S. designed and executed the observations, performed the analysis and prepared the manuscript. K.L.C. prepared observations and edited the manuscript. M.S.M. assisted with the pipeline software used to reduce the spectroscopic data, and M.M.K. wrote the software to perform eigenspectrum continuum fits. A.J.B. contributed to the spectrograph construction, and executed observations for the program. All authors helped with the scientific interpretations and commented on the manuscript.

Author Information Reprints and permissions information is available at www.nature.com/reprints. The authors declare no competing financial interests. Readers are welcome to comment on the online version of the paper. Correspondence and requests for materials should be addressed to R.A.S. (simcoe@space.mit.edu).

A ~ 0.2 -solar-mass protostar with a Keplerian disk in the very young L1527 IRS system

John J. Tobin¹, Lee Hartmann², Hsin-Fang Chiang^{3,4}, David J. Wilner⁵, Leslie W. Looney³, Laurent Loinard^{6,7}, Nuria Calvet² & Paola D'Alessio⁶

In their earliest stages, protostars accrete mass from their surrounding envelopes through circumstellar disks. Until now, the smallest observed protostar-to-envelope mass ratio was about 2.1 (ref. 1). The protostar L1527 IRS is thought to be in the earliest stages of star formation². Its envelope contains about one solar mass of material within a radius of about 0.05 parsecs (refs 3, 4), and earlier observations suggested the presence of an edge-on disk⁵. Here we report observations of dust continuum emission and ^{13}CO (rotational quantum number $J = 2 \rightarrow 1$) line emission from the disk around L1527 IRS, from which we determine a protostellar mass of 0.19 ± 0.04 solar masses and a protostar-to-envelope mass ratio of about 0.2. We conclude that most of the luminosity is generated through the accretion process, with an accretion rate of about 6.6×10^{-7} solar masses per year. If it has been accreting at that rate through much of its life, its age is approximately 300,000 years, although theory suggests larger accretion rates earlier⁶, so it may be younger. The presence of a rotationally supported disk is confirmed, and significantly more mass may be added to its planet-forming region as well as to the protostar itself in the future.

The protostar L1527 IRS (hereafter L1527), at a distance of about 140 pc, is one of the nearest class 0 protostars; this is the earliest phase of the star formation process², and we show a schematic diagram of a protostellar system in Fig. 1. Observations of dust continuum emission towards L1527 were obtained with the Submillimeter Array (SMA) and Combined Array for Millimeter-wave Astronomy (CARMA) at wavelengths of 870 μm , 1.3 mm and 3.4 mm, following up indications from previous Gemini results⁵ that L1527 harboured an edge-on disk. The 870- μm and 3.4-mm data are shown in Fig. 2 with sufficient resolution to resolve the emission from the disk midplane, finding it to be extended north-south, like the 3.8- μm dark lane. The observed disk is $\sim 180 \pm 12$ astronomical units (AU) in diameter (radius $R \approx 90$ AU), measured from inside the outer contour plotted in Fig. 2; the dust emission appears smaller than the mid-infrared dark lane because the lower-density outer disk is fainter than the sensitivity limit. (1 AU is the distance from the Earth to the Sun, 1.496×10^{13} cm.) Other studies did not conclusively detect disks around L1527 and other class 0 protostars because the spatial resolution was too low to distinguish the disk emission from the envelope and/or the disks were too small^{7,8}. We estimate a disk mass of $0.007 \pm 0.0007 M_{\odot}$ from the 870- μm flux density ($F_{870\mu\text{m}} = 213.6 \pm 8.1$ mJy); details are given in Supplementary Information section 3. We consider this mass a lower limit because the adopted dust opacity is large ($3.5 \text{ cm}^2 \text{ g}^{-1}$ at 850 μm)⁹, and we have not accounted for spatial filtering by the interferometer.

We observed the ^{13}CO ($J = 2 \rightarrow 1$) molecular line transition with CARMA at a wavelength of 1.3 mm. This line traces the outflow in most class 0 protostars¹⁰; however, Fig. 3 shows that the ^{13}CO emission primarily traces the inner envelope and disk in L1527. The outflow is detected at velocities less than $\pm 1 \text{ km s}^{-1}$, but does not affect our

analysis (Supplementary Information section 2). The ^{13}CO data have lower resolution than the 870- μm and 3.4-mm observations ($1''$, 140 AU); however, the positional accuracy of line emission is comparable to the resolution divided by the signal-to-noise ratio (typically 5 or higher), enabling us to determine the location of emission accurately in each velocity channel. Figure 3 shows the ^{13}CO emission from the blueshifted and redshifted components to be on opposite sides of protostar, consistent with Keplerian rotation. The emission from the disk is most probably confined to $\pm 1''$; at larger radii and lower velocities we expect the flattened envelope to contribute to the kinematics, as shown by lower-resolution ^{13}CO ($J = 1 \rightarrow 0$) observations¹¹. The observations shown in Figs 2 and 3 as a whole provide definitive evidence for a large, rotationally supported disk in this class 0 protostellar system. Such a disk at this early phase may be inconsistent with some disk formation models that consider strong magnetic braking^{12,13}; however, large disks can form at this stage in models with weak magnetic fields^{14,15} or if the magnetic field is not aligned with the rotation axis¹⁶.

Assuming that the disk is rotationally supported and that the mass of the protostar is dominant, we can use the position-velocity information from the molecular line data to determine the protostellar mass.

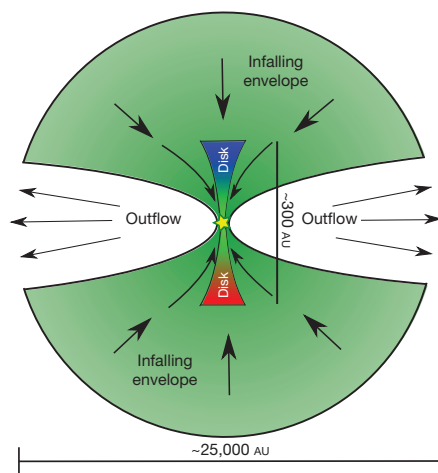


Figure 1 | Cartoon of a protostellar system rotated to match the orientation of L1527. Green shading highlights the large ($R \approx 12,500$ AU) infalling envelope surrounding the protostar and disk; the envelope geometry on 10,000-AU scales is generally more complex than shown here²⁷. Because the infalling material has some net rotation, it falls onto a disk due to conservation of angular momentum rather than directly onto the protostar. The disk is coloured with a red-to-blue velocity gradient to illustrate Keplerian rotation around the protostar. Mass is transported from the envelope to the disk and then it is accreted through the disk and onto the protostar. The protostar and disk both work together and drive a bipolar outflow¹⁰ that evacuates the polar regions of the envelope.

¹National Radio Astronomy Observatory, Charlottesville, Virginia 22903, USA. ²Department of Astronomy, University of Michigan, Ann Arbor, Michigan 48109, USA. ³Department of Astronomy, University of Illinois, Urbana, Illinois 61801, USA. ⁴Institute for Astronomy and NASA Astrobiology Institute, University of Hawaii at Manoa, Hilo, Hawaii 96720, USA. ⁵Harvard-Smithsonian Center for Astrophysics, Cambridge, Massachusetts 02138, USA. ⁶Centro de Radioastronomía y Astrofísica, UNAM, Apartado Postal 3-72 (Xangari), 58089 Morelia, Michoacán, Mexico. ⁷Max-Planck-Institut für Radioastronomie, Auf dem Hügel 69, 53121 Bonn, Germany.

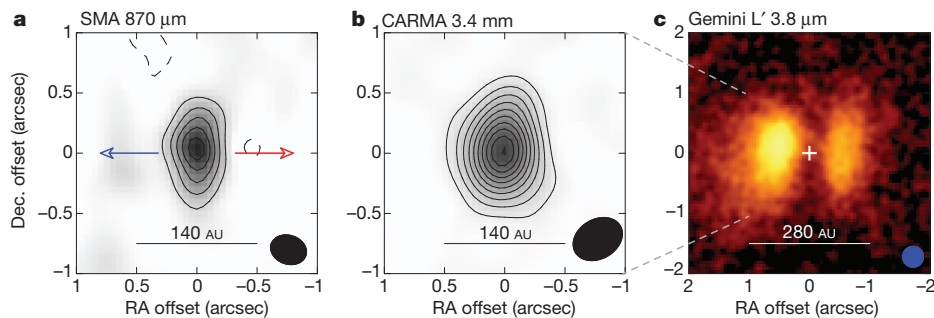


Figure 2 | Images of the edge-on disk around the protostar L1527.

a–c, High-resolution images of L1527 are shown at wavelengths of 870 μm from the SMA (**a**), 3.4 mm from CARMA (**b**) and 3.8 μm from Gemini (**c**), showing the disk in dust continuum emission and scattered light. The Gemini image is shown on a larger scale to fully capture the scattered light features, the dashed grey lines mark the outer edge of the region shown in the submillimetre images. The submillimetre images are elongated in the direction of the dark lane shown in **c**, consistent with an edge-on disk in this class 0

protostellar system. The outflow direction is indicated by the red and blue arrows in **a**, denoting the respective directions of the outflow. The white cross in **c** marks the central position of the disk from the SMA images. The contours in the 870- μm and 3.4-mm images start at three times the noise level and increase at this interval; the noise level is 5.0 mJy per beam and 0.24 mJy per beam for the SMA and CARMA data, respectively. The ellipses in the lower right corner of each image give the resolution of the observations, approximately $0.25''$ (**a**), $0.35''$ (**b**) and $0.35''$ (**c**). RA, right ascension; dec., declination.

This has been done for more evolved sources, but not for a class 0 protostar^{17,18}. To determine the mass, we measured the positional offset of the line emission relative to the protostar (1.3-mm continuum source) in each velocity channel (binned to 0.3 km s^{-1}) and the position–velocity data were fitted with a Keplerian rotation curve (velocity $v = (GM/r)^{1/2}$, where G is the gravitational constant, M is the protostellar mass and r is the radius at which the velocity is being measured). These data are plotted in Fig. 4 and least-squares fitting yields a protostellar mass of $0.19 \pm 0.04 M_{\odot}$; the flattening of radius at velocities less than $\sim 1.5 \text{ km s}^{-1}$ can be attributed to the superposition of rotation velocities projected along the line of sight at large radii. We do not expect contributions from the envelope to affect the fit because its emission is at lower velocities and larger scales¹¹. The almost edge-on nature of L1527 facilitates this analysis because the $\sim 85^\circ$ inclination^{5,19} does not significantly affect any calculations. Although the model fit in Fig. 4 is simplistic, it highlights the important physics of the problem, and the method is consistent with simulated observations of more complicated line radiative transfer models that require many assumptions (Supplementary Information section 4).

Masses have previously been estimated for binary Class 0 protostellar systems using proper motion measurements at very high resolution²⁰, but with substantial uncertainty due to unconstrained orbital parameters. The primary uncertainty in our measurement is whether the protostellar mass is dominant over the disk/envelope mass at the scales we are probing. The disk mass of $0.007 M_{\odot}$ could be up to a few

times higher owing to opacity uncertainties, and the envelope mass within $R = 150 \text{ AU}$ is only expected to be $\sim 0.01 M_{\odot}$, because most mass is on large scales. If we allow for a factor of four times higher disk and envelope masses, they would combine to contribute at most $\sim 35\%$ to the total mass. The kinematic effect of this additional mass should become apparent at larger disk radii, but the current data are insufficient to distinguish this effect. Moreover, the possibility of additional mass would only cause the protostellar mass to be overestimated.

The ratio of protostellar mass to envelope mass in L1527 is only $\sim 20\%$; all other protostellar systems with dynamical mass measurements from disk rotation have protostellar masses greater than twice the surrounding envelope mass¹. Therefore, in contrast to these more evolved systems, L1527 will probably accumulate significantly more mass. Accreting protostars are expected to follow a ‘birthline’, with rising effective temperature and luminosity with increasing mass; the birthline is also the starting point of pre-main-sequence evolution once the protostar has stopped accreting significantly²¹. If L1527 is on the birthline, we can estimate its stellar parameters from the mass. We use the birthline model²¹ with an accretion rate of $2 \times 10^{-6} M_{\odot} \text{ yr}^{-1}$; for a $0.19 M_{\odot}$ protostar, this model gives a radius of $1.7 R_{\odot}$, an effective temperature of 3,300 K, and a luminosity of $0.3 L_{\odot}$. This indicates that $\sim 90\%$ of the protostar’s total luminosity ($2.75 L_{\odot}$; ref. 19) is supplied by accretion of mass onto the protostar. Thus, the accretion rate of the disk onto the protostar is $\sim 6.6 \times 10^{-7} M_{\odot} \text{ yr}^{-1}$, assuming $L_{\text{acc}} = GM\dot{M}/R_*$ (here L_{acc} is the luminosity generated by accretion,

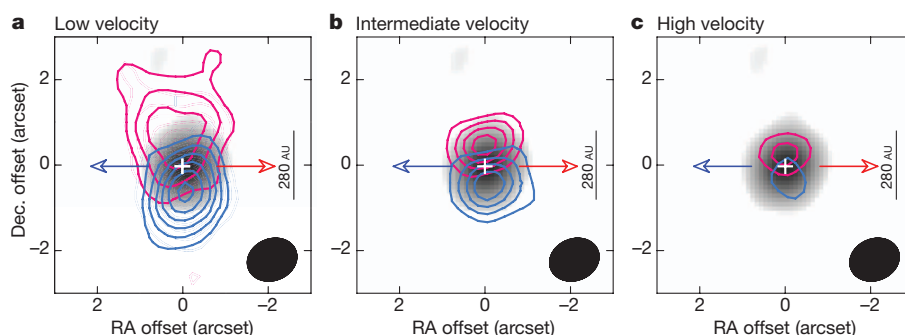


Figure 3 | ^{13}CO emission from the disk around L1527 exhibiting a Keplerian rotation signature. **a–c**, The CARMA 1.3-mm continuum image is shown (greyscale) with the red and blue contours showing ^{13}CO emission integrated at low velocities (**a**), intermediate velocities (**b**) and high velocities (**c**). The white cross in all panels marks the location of the protostar. The blueshifted and redshifted emission centroids show a clear signature of rotation on the size scale of the protostellar disk and no extension of emission along the outflow. The low-velocity emission probably includes contributions from the

envelope, while the intermediate- to high-velocity emission is dominated by the disk. The low-velocity range (**a**; in km s^{-1}) is 6.35–7.25 (shown red) and 4.55–5.3 (shown blue); the intermediate-velocity range (**b**; in km s^{-1}) is 7.25–8.0 (red) and 3.8–4.55 (blue); the high-velocity range (**c**; in km s^{-1}) is 8.0–8.6 (red) and 3.2–3.8 (blue). The contours start and increase in intervals three times the noise level (σ) where $\sigma = 0.85 \text{ K km s}^{-1}$ (red) and 0.75 K km s^{-1} (blue). The angular resolution of these data are given by the ellipse in the lower right corners, $1.1'' \times 0.95''$.

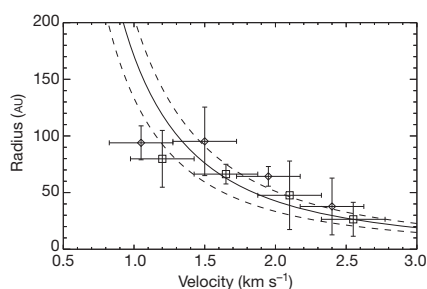


Figure 4 | Plots of radius versus velocity, showing the rotation curve derived from the ^{13}CO emission. We fitted the function $v = (GM/r)^{1/2}$ to the data, assuming a rotationally supported disk around a central point mass, and we find a best-fitting mass of $M_* = 0.19 \pm 0.04 M_\odot$. We used simulated data from molecular line radiative transfer models to confirm that using this method will yield accurate protostellar masses (Supplementary Information section 4). The velocity profile for the best-fitting mass is shown as the solid line; the dashed lines show the 1 s.d. uncertainty level. The diamonds show data on the south, blue-shifted side of the disk; the squares show data on the north, red-shifted side of the disk. The uncertainty in the observed data points is derived as follows: on the x axis, from the fixed velocity channel width; on the y axis, from the 1 s.d. error derived by adding in quadrature the positional uncertainty of the Gaussian fit to the ^{13}CO emission and the error in the position of the protostellar source. The flattening of the data points at velocities less than 1.5 km s^{-1} is due to the superposition of rotation velocities projected to our line of sight at large disk radii; such flattening was also seen in the data from the line radiative transfer models (Supplementary Information section 4).

and R_* is the radius of the protostar). If the protostar has been accreting at this rate throughout its life, its age is only $\sim 300,000$ yr, within the expected lifetime of the class 0 phase²². However, theoretical studies indicate that mass infall/accretion rates may be larger initially and decrease with time⁶; in addition, protostars are expected to have variable accretion rates²³, so L1527 could be younger. The dynamical time of the 0.3 pc outflow (red and blue sides) as measured by a recent survey of the Taurus star-forming region is $\sim 30,000$ yr (ref. 24). This time, calculated from the outflow's velocity and size, gives an estimate of the age of the outflow, a rough proxy for the protostellar age.

The detection of a proto-planetary disk and a measurement of protostellar mass have made L1527 one of the best characterized class 0 protostellar systems. Its high accretion rate is nearly a factor of 100 greater than those of the more evolved pre-main-sequence stars with disks; this rate is high enough to heat the inner disk to temperatures consistent with early Solar System conditions²⁵. Although we cannot say definitively what L1527 will look like at the end of its formation phase, it does have the potential to gain as much mass as the Sun from its envelope and it already has a proto-planetary disk of at least seven Jupiter masses, similar to presumed planet-forming disks²⁶. Therefore, L1527 already has all the elements of a solar system in the making.

Received 6 June; accepted 19 September 2012.

1. Takakuwa, S. *et al.* A Keplerian circumbinary disk around the protostellar system L1551 NE. *Astrophys. J.* **754**, 52 (2012).
2. Andre, P., Ward-Thompson, D. & Barsony, M. Submillimeter continuum observations of Rho Ophiuchi A — the candidate protostar VLA 1623 and prestellar clumps. *Astrophys. J.* **406**, 122–141 (1993).
3. Chandler, C. J. & Richer, J. S. The structure of protostellar envelopes derived from submillimeter continuum images. *Astrophys. J.* **530**, 851–866 (2000).
4. Tobin, J. J. *et al.* Complex structure in class 0 protostellar envelopes. II. Kinematic structure from single-dish and interferometric molecular line mapping. *Astrophys. J.* **740**, 45 (2011).
5. Tobin, J. J., Hartmann, L. & Loinard, L. The inner envelope and disk of L1527 revealed: Gemini L'-band-scattered light imaging. *Astrophys. J.* **722**, L12–L17 (2010).
6. Foster, P. N. & Chevalier, R. A. Gravitational collapse of an isothermal sphere. *Astrophys. J.* **416**, 303–311 (1993).
7. Jørgensen, J. K. *et al.* PROSAC: a submillimeter array survey of low-mass protostars. I. Overview of program: envelopes, disks, outflows, and hot cores. *Astrophys. J.* **659**, 479–498 (2007).

8. Maury, A. J. *et al.* Toward understanding the formation of multiple systems. A pilot IRAM-PdBI survey of Class 0 objects. *Astron. Astrophys.* **512**, A40 (2010).
9. Andrews, S. M. & Williams, J. P. Circumstellar dust disks in Taurus-Auriga: the submillimeter perspective. *Astrophys. J.* **631**, 1134–1160 (2005).
10. Arce, H. G. & Sargent, A. I. The evolution of outflow-envelope interactions in low-mass protostars. *Astrophys. J.* **646**, 1070–1085 (2006).
11. Ohashi, N., Hayashi, M., Ho, P. T. P. & Momose, M. Interferometric imaging of IRAS 04368+2557 in the L1527 molecular cloud core: a dynamically infalling envelope with rotation. *Astrophys. J.* **475**, 211–223 (1997).
12. Dapp, W. B. & Basu, S. Averting the magnetic braking catastrophe on small scales: disk formation due to Ohmic dissipation. *Astron. Astrophys.* **521**, L56 (2010).
13. Hennebelle, P. & Fromang, S. Magnetic processes in a collapsing dense core. I. Accretion and ejection. *Astron. Astrophys.* **477**, 9–24 (2008).
14. Yorke, H. W. & Bodenheimer, P. The formation of protostellar disks. III. The influence of gravitationally induced angular momentum transport on disk structure and appearance. *Astrophys. J.* **525**, 330–342 (1999).
15. Vorobyov, E. I. Embedded protostellar disks around (sub-)solar protostars. I. Disk structure and evolution. *Astrophys. J.* **723**, 1294–1307 (2010).
16. Joos, M., Hennebelle, P. & Ciardi, A. Protostellar disk formation and transport of angular momentum during magnetized core collapse. *Astron. Astrophys.* **543**, A128 (2012).
17. Simon, M., Dutrey, A. & Guilloteau, S. Dynamical masses of T Tauri stars and calibration of pre-main-sequence evolution. *Astrophys. J.* **545**, 1034–1043 (2000).
18. Jørgensen, J. K. *et al.* PROSAC: a submillimeter array survey of low-mass protostars. II. The mass evolution of envelopes, disks, and stars from the Class 0 through I stages. *Astron. Astrophys.* **507**, 861–879 (2009).
19. Tobin, J. J., Hartmann, L., Calvet, N. & D'Alessio, P. Constraining the envelope structure of L1527 IRS: infrared scattered light modeling. *Astrophys. J.* **679**, 1364–1384 (2008).
20. Rodríguez, L. F. *et al.* Very Large Array observations of proper motions in L1551 IRS 5. *Astrophys. J.* **583**, 330–333 (2003).
21. Hartmann, L., Cassen, P. & Kenyon, S. J. Disk accretion and the stellar birthline. *Astrophys. J.* **475**, 770–785 (1997).
22. Evans, N. J. *et al.* The Spitzer c2d legacy results: star-formation rates and efficiencies; evolution and lifetimes. *Astrophys. J.* **181** (Supp.), 321–350 (2009).
23. Dunham, M. M., Evans, N. J., Terebey, S., Dullemond, C. P. & Young, C. H. Evolutionary signatures in the formation of low-mass protostars. II. Toward reconciling models and observations. *Astrophys. J.* **710**, 470–502 (2010).
24. Narayanan, G., Snell, R. & Bemis, A. Molecular outflows identified in the FCRAO CO survey of the Taurus molecular cloud. *Mon. Not. R. Astron. Soc.* **425**, 2641 (2012).
25. Bell, K. R., Cassen, P. M., Wasson, J. T. & Woolum, D. S. in *Protostars and Planets IV* (eds Mannings, V., Boss, A. P. & Russell, S. S.) 897–926 (Univ. Arizona Press, 2000).
26. Andrews, S. M., Wilner, D. J., Hughes, A. M., Qi, C. & Dullemond, C. P. Protoplanetary disk structures in Ophiuchus. II. Extension to fainter sources. *Astrophys. J.* **723**, 1241–1254 (2010).
27. Tobin, J. J., Hartmann, L., Looney, L. W. & Chiang, H. Complex structure in class 0 protostellar envelopes. *Astrophys. J.* **712**, 1010–1028 (2010).

Supplementary Information is available in the online version of the paper.

Acknowledgements We thank E. Bergin for comments on the manuscript and W. Kwon for discussing improvements to the data reduction. J.J.T. was supported by NASA through Hubble Fellowship grant HSTHF-51300.01-A awarded by the Space Telescope Science Institute, which is operated by the Association of Universities for Research in Astronomy, Inc., for NASA, under contract NAS 5-26555. L.H. and J.J.T. acknowledge partial support from the University of Michigan. H.-F.C. was supported by NASA through the NASA Astrobiology Institute under cooperative agreement NNA09DA77A issued through the Office of Space Science. L.W.L. and H.-F.C. acknowledge support from the Laboratory for Astronomical Imaging at the University of Illinois and the NSF under grant AST-07-09206. P.D. acknowledges a grant from PAPIIT-UNAM. L.L. was supported by DGAPA, UNAM, CONACyT (México) and the Alexander von Humboldt Stiftung. Support for CARMA construction was derived from the states of Illinois, California and Maryland, the James S. McDonnell Foundation, the Gordon and Betty Moore Foundation, the Kenneth T. and Eileen L. Norris Foundation, the University of Chicago, the Associates of the California Institute of Technology, and the NSF. Continuing CARMA development and operations are supported by the NSF under a cooperative agreement, and by the CARMA partner universities. The Submillimeter Array is a joint project between the Smithsonian Astrophysical Observatory and the Academia Sinica Institute of Astronomy and Astrophysics and is funded by the Smithsonian Institution and the Academia Sinica. The National Radio Astronomy Observatory is a facility of the NSF operated under cooperative agreement by Associated Universities, Inc.

Author Contributions J.J.T., H.-F.C., D.J.W. and L.W.L. participated in data acquisition and reduction. All authors contributed to the data analysis, discussed the results and commented on the manuscript.

Author Information Reprints and permissions information is available at www.nature.com/reprints. The authors declare no competing financial interests. Readers are welcome to comment on the online version of the paper. Correspondence and requests for materials should be addressed to J.J.T. (jtobin@nrao.edu).

Controlled-reflectance surfaces with film-coupled colloidal nanoantennas

Antoine Moreau^{1,2,3}, Cristian Ciraci¹, Jack J. Mock¹, Ryan T. Hill⁴, Qiang Wang^{5,6}, Benjamin J. Wiley⁵, Ashutosh Chilkoti^{4,7} & David R. Smith¹

Efficient and tunable absorption is essential for a variety of applications, such as designing controlled-emissivity surfaces for thermophotovoltaic devices¹, tailoring an infrared spectrum for controlled thermal dissipation² and producing detector elements for imaging³. Metamaterials based on metallic elements are particularly efficient as absorbing media, because both the electrical and the magnetic properties of a metamaterial can be tuned by structured design⁴. So far, metamaterial absorbers in the infrared or visible range have been fabricated using lithographically patterned metallic structures^{2,5–9}, making them inherently difficult to produce over large areas and hence reducing their applicability. Here we demonstrate a simple method to create a metamaterial absorber by randomly adsorbing chemically synthesized silver nanocubes onto a nanoscale-thick polymer spacer layer on a gold film, making no effort to control the spatial arrangement of the cubes on the film. We show that the film-coupled nanocubes provide a reflectance spectrum that can be tailored by varying the geometry (the size of the cubes and/or the thickness of the spacer). Each nanocube is the optical analogue of a grounded patch antenna, with a nearly identical local field structure that is modified by the plasmonic response of the metal's dielectric function, and with an anomalously large absorption efficiency that can be partly attributed to an interferometric effect¹⁰. The absorptivity of large surface areas can be controlled using this method, at scales out of reach of lithographic approaches (such as electron-beam lithography) that are otherwise required to manipulate matter on the nanoscale.

To enhance the light absorbed within a medium, both the reflectance and the transmittance of the medium must be minimized. Although any opaque material, such as a metal, can essentially eliminate transmittance, eliminating the reflectance is more difficult. For a material defined by its electric permittivity, ϵ , and magnetic permeability, μ , the Fresnel reflection coefficient for the s polarization has the form

$$r_s = \frac{z_2 \cos(\theta_i) - z_1 \cos(\theta_t)}{z_2 \cos(\theta_i) + z_1 \cos(\theta_t)} \quad (1)$$

where $z_j = \sqrt{\mu_j/\epsilon_j}$ is the wave impedance for material j , and θ_i and θ_t are the incident and transmitted angle of the wave with respect to the surface normal. For normal incidence, for which $\theta_i = \theta_t = 0$, equation (1) shows that if $z_1 = z_2$ then reflection is eliminated. In particular, for normal incidence any medium whose wave impedance has the vacuum value, $z_0 = \sqrt{\mu_0/\epsilon_0}$, will be reflectionless in the vacuum. An opaque, impedance-matched structure can be considered an ideal absorber, because all incident light (at least that incident normally) must be absorbed.

Because magnetic response is far more limited in naturally occurring materials than in metamaterials, especially beyond frequencies of a few terahertz, impedance-matching a medium by introducing higher permeability materials is not generally feasible. In contrast, artificially

structured metamaterials can have controlled magnetic as well as controlled electric properties at nearly any wavelength in the electromagnetic spectrum¹¹ (including the visible); metamaterials have thus been suggested as ideal absorbers⁴. It has been shown that a metamaterial composite comprising lithographically patterned resonant conducting elements on top of a conducting back plane can be made reflectionless for light incident over a broad range of angles^{2,12}. To achieve the requisite magnetic response at infrared and visible wavelengths, a variety of metallic metamaterial structures have been used, such as cut-wire pairs^{13,14}. By combining different types of metamaterial elements together into a single composite, more complicated reflectance spectra can be engineered, achieving the level of control needed in certain spectroscopy and energy-harvesting applications^{7,12}.

Because an absorbing structure does not require any substantial volume, the appropriateness of defining bulk constitutive parameters, such as ϵ and μ , which are rigorously defined only over a volume, can be called into question; thus, alternative descriptions have been proposed⁸. Here we similarly find it instructive to adopt a related model of reflection (Fig. 1). We view the metamaterial surface, or metasurface^{15–17}, as supporting both electric as well as fictitious magnetic surface current densities that are excited by the incident wave. Because both currents produce reflected waves that are exactly out of phase with each other, their sum can cancel out entirely if the total induced effective magnetic current exactly balances the total induced electric current¹⁷.

Although magnetic conductors do not physically exist, many devices are commonly said to scatter waves via the excitation of effective magnetic currents. One example is that of the grounded patch antenna, which consists of a conducting metallic patch positioned above a conducting (ground) plane (Fig. 1e). The patch antenna supports a series of cavity-like resonances in which the electromagnetic field is localized within the gap between the ground plane and the patch element. For modes in which the electric field is maximum at the patch edges, the patch can be equivalently described as having a magnetic surface current density, K_M , that flows along the periphery of the patch, with magnitude given by $2E \times n$, where the field is determined at the patch edge and n is a unit vector normal to the surface. Thus, adding a population of patch antennas at some critical density to an otherwise conducting sheet can generate enough fictitious magnetic surface current density to offset the electric surface current density of an incident wave.

The underlying mode description of the patch is extensible to any wavelength as long as the patch and surface behave as conductors. Although metals are often described as lossy dielectric materials at optical wavelengths, they nevertheless support currents and can be used to form the optical equivalent of patch antennas¹⁸. We note that the particular arrangement of antennas on the surface should not matter for an isotropic absorber, because it is necessary to introduce only enough magnetic current to offset the electric current. Thus, an

¹Center for Metamaterials and Integrated Plasmonics, Duke University, Durham, North Carolina 27708, USA. ²Clermont Université, Université Blaise Pascal, Institut Pascal, BP 10448, 63000 Clermont-Ferrand, France. ³CNRS, UMR 6602, IP, 63171 Aubière, France. ⁴Center for Biologically Inspired Materials and Material Systems, Duke University, Durham, North Carolina, 27708, USA. ⁵Department of Chemistry, Duke University, Durham, North Carolina 27708, USA. ⁶Laboratory for Micro-sized Functional Materials & College of Elementary Education, Capital Normal University, Beijing 100048, China. ⁷Department of Biomedical Engineering, Duke University, Durham, North Carolina 27708, USA.

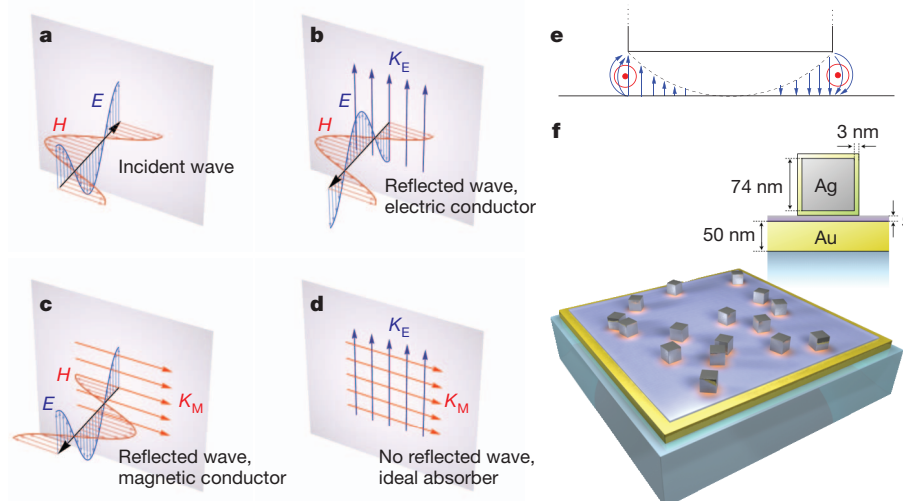


Figure 1 | Forming an ideal absorber. **a–d**, Light incident on a conductor **(a)** reflects due to either the excitation of electric surface current densities, K_E **(b)**, or fictitious magnetic surface current densities, K_M **(c)**. If both are excited then the back reflected wave represents the sum of the waves in **b** and **c**, for

artificially structured ideal absorber should not be reliant on any sort of patterning methods, and we can make use of colloidal self-assembly processes to very simply produce a randomized patch antenna geometry.

In plasmonic systems, field localization is generally correlated with local field enhancement, $f = E_l/E_0$, where E_l is the local electric field and E_0 is the electric field of the incident wave. In the present context, the enhancement serves to increase the effective magnetic surface current that flows in response to the applied field. Equivalently, the resonance can be viewed as enhancing the coupling between the gap modes and the incident field, enabling the incident fields to penetrate the gap region. In the latter interpretation, the enhanced absorption in the nanocube system can be considered to be closely related to the enhanced transmission in very thin slit arrays¹⁹ and the large absorption that can be obtained with extremely shallow metallic gratings²⁰.

As a means of demonstrating the proposed colloidal approach to an ideal optical absorber, we consider nanocubes, with edge length ℓ , separated by a nanoscale distance from a gold film by a dielectric spacer layer with a refractive index of 1.54. To estimate the absorption efficiency of the nanoantennas, we perform numerical simulations over a domain containing a single absorber, and apply either periodic (Fourier modal method²¹) or absorbing (COMSOL) boundary conditions. As has been noted previously, square patches have scattering behaviour very similar to that of strips⁸ because they share the same underlying mechanisms^{7,18}; we are thus able to run two-dimensional simulations in many cases to perform quick optimizations, followed by fewer confirmative three-dimensional simulations.

A gap-plasmon guided mode, whose profile is shown Fig. 2, is supported under the cube. The constructive interferences of this mode, reflected back and forth at the edges of the cube, create a cavity resonance as in a Fabry–Pérot interferometer. This mechanism makes the resonance insensitive to the angle of incidence as well as to the polarization of the incident wave (see Supplementary Information for a detailed analysis).

When the thickness of the spacer layer is decreased, the effective index, n_e , of the mode increases, and can reach arbitrarily large values. Because the relation between the resonance wavelength and the cavity size, ℓ , is roughly $\ell \approx \lambda/2n_e$, resonances can thus be excited under cubes for which ℓ is only one-tenth of the wavelength, especially for very thin spacer layers. Figure 2 shows that the effective absorption efficiency, which is defined as the power absorbed by the nanocube divided by the incident intensity and normalized with respect to the actual surface occupied by a cube, is maximum for a spacer layer that is between 5

and 10 nm thick. For thicker spacer layers, the resonance is not as well formed, the reflection coefficient of the mode being relatively low. For extremely thin layers, the resonance is poorly excited by the incident field. The effective absorption efficiency can be as large as 30, meaning that in theory around 3% of the surface needs to be covered with cubes to reach almost complete absorption (Fig. 2).

Because the cavity is excited uniformly on both sides of the cube at normal incidence, it constitutes a perfect example of interferometrically controlled absorption¹⁰: the field amplitude is twice as large as if the cavity was excited from one side only, and the absorption is thus four times larger (especially compared with a structure like the shallow grating described in ref. 20, where the absorption mechanism is very similar). This phenomenon contributes to the very large absorption efficiency and explains why second-order resonances are not likely to be excited (Supplementary Information).

Having evaluated the underlying mechanisms of the nanoparticle-based ideal absorber, we next seek to implement the concept experimentally using chemically synthesized metal nanocubes that are randomly

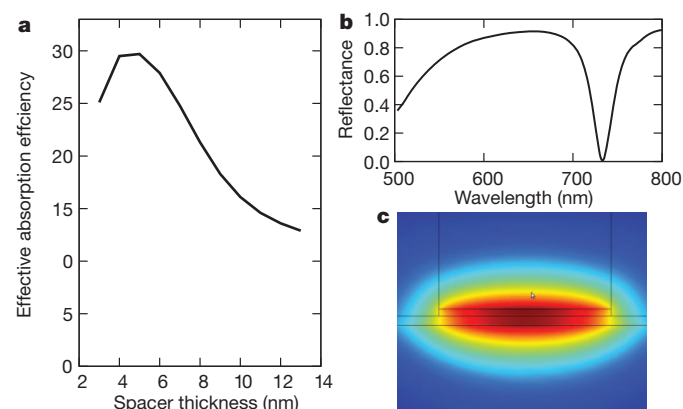


Figure 2 | Theoretical absorption efficiency of the nanocubes. **a**, Effective absorption efficiency as a function of the spacer thickness, defined as the ratio of the absorption cross-section to the physical cross-section for a single nanocube. The absorption cross-section is computed as the ratio of the energy absorbed to the illumination intensity. **b**, Reflectance spectrum for cubes that are 70 nm in size, periodically (350 nm) distributed and separated from the metallic film by a 8-nm-thick dielectric layer. **c**, Modulus of the magnetic field (red, high values; blue, low values) for the mode that is guided under the cube (out-of-plane wavevector). Black lines show the edges of the different materials in the COMSOL simulation.

adsorbed on an organic insulating spacer layer (of precisely controlled thickness) above a gold film. Because the synthetic chemistry for nanocubes favours silver rather than gold, we synthesized silver nanocubes with an edge length of 74 nm according to previously published protocols^{22,23}. Electron microscopy images of the cubes are shown in Fig. 3. We note that a periodic arrangement of nanocubes would entirely suppress scattering, which is not the case for the random distributions considered here. Substantial scattering can thus be expected to occur from the nanoantennas, as confirmed by the dark-field optical images shown in Fig. 3c. The scattering places an upper limit on the reflectivity away from the absorption dip, as well as a lower limit on the reflectivity at the peak absorption.

Reflectance spectra were obtained from samples where 4.2% of the surface of the gold film was occupied by nanocubes and the nanocube–film separation distance was modulated by polyelectrolyte molecular spacer layers of increasing thicknesses^{24–28}. Figure 4a shows the position of the measured resonance as a function of the overall thickness under the cubes, assuming that the nanocube–film separation distance is the sum of the polyelectrolyte spacer layer thickness and the 3-nm thickness of the stabilizer coating that surrounds the cubes. The position of the resonances can be accurately determined by three-dimensional simulations²¹ if the coating and the rounded corners of the cubes are taken into account (by using a somewhat smaller cube dimension of 62 nm). Again, as is typical with nanoplasmonic systems, the resonance properties are crucially sensitive to the thickness and dielectric properties of the spacer layer, making the reflectance properties of the surface easily tunable by slightly changing the gap dimension.

On the basis of our three-dimensional simulations, which used a perfectly uniform population of cubes, we would expect a small reflectance even for such low surface coverage. However, the silver cubes as prepared varied in size. This variation contributes to a broader and shallower absorption dip in the reflectance. To achieve very low reflectance (without preparing a more uniform population of silver nanocubes), the concentration of cubes on the surface had to be increased. Figure 4b shows the relative reflectance observed from two nanocube–film samples. For one of them the surface coverage with imperfect cubes was 7.3%, and for the other it was 17.1%. For both, the nanocubes were separated from the gold film by a 6-nm polyelectrolyte layer. Figure 4b

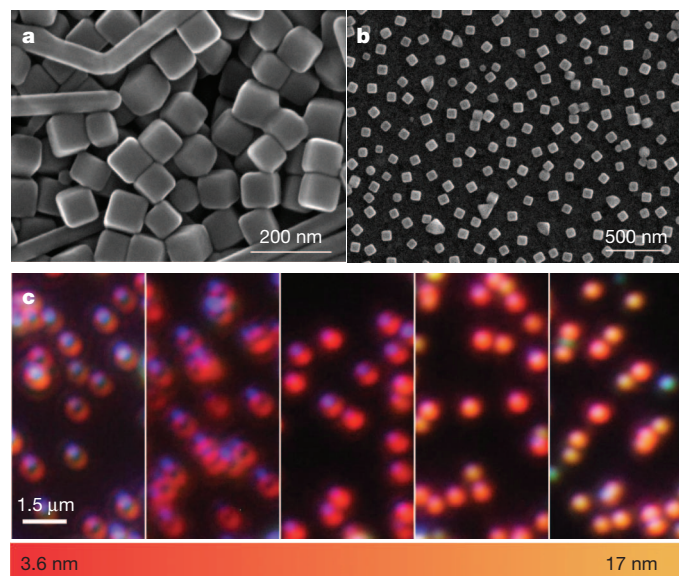


Figure 3 | Silver nanocubes. **a, b**, Scanning electronic microscopy images of the silver nanocubes as fabricated (**a**) and after deposition on the gold film with 17.1% surface coverage and remarkably uniform spacing (**b**). **c**, Dark-field images of the nanocubes randomly adsorbed on a nanoscale polymer spacer on a gold film, showing the light scattered by the individual nanocubes for less than 1% surface coverage. The spacer ranges in thickness from 3.6 to 17 nm.

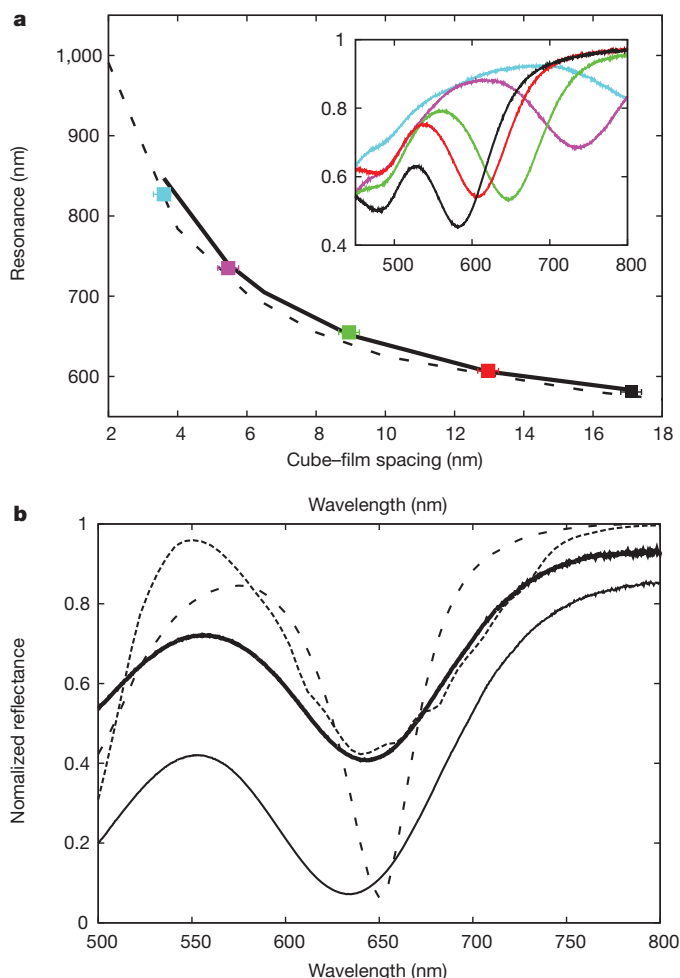


Figure 4 | Tunability of the reflectance. **a**, Position of the resonance as a function of the spacer thickness. Measured positions (black squares) for a cube surface density of 4.18% agree with three-dimensional simulations (solid line) and two dimensional simulations (dotted line) for 74-nm-wide gold nanorods surrounded by air. Inset, corresponding experimental reflectances for an angle of incidence of 25° and for the different spacer thicknesses. **b**, Experimental reflectance for normal incidence, normalized to the gold film, for surface coverages of 7.3% (thin solid line) and 17.1% (thick solid line), compared with simulations of uniform cubes (4.2% surface coverage, dotted line) and a model including size dispersion (dashed line; see Supplementary Information).

also shows the simulated reflectance for both perfectly uniform cubes and cubes with a size distribution similar to the experimental one. A reflectance of less than 7% is observed for normal incidence at 637 nm from samples with 17.1% surface coverage, further demonstrating the ease and extent to which the reflectance can be controlled.

For many applications, a narrow absorption band may be desirable. Size dispersion seems to be the primary limitation on achieving much narrower spectroscopic features. This limitation can probably be overcome by using either fabrication processes that allow greater control or nanoparticle separation techniques^{29,30}. The very small size and highly efficient optical response of the cubes suggests that mixed cube populations with controlled sized dispersion could be used further to tailor the absorption at will. Although those structures can be designed to operate in the infrared, we predict the introduction of alternative materials that would have better thermal properties. It is, however, worth underscoring that the extreme sensitivity of the resonant modes supported by the nanocubes can be exploited for immediate biosensor applications³⁰. The gap-dependent cavity resonances have a completely different character from the classical resonances of spherical nanoparticles coupled to a film²⁸, so that in addition to their higher sensitivity, they can be excited very conveniently for normal incidence.

The spectral control available from absorbing metasurfaces forms the basis for a growing number of promising applications, including thermal detectors, light sources, energy-harvesting systems and even biosensors. Until now, structured absorbers have been successfully demonstrated across the entire electromagnetic spectrum, relying on top-down lithographic patterning as the fabrication approach. Although such patterning can produce highly uniform arrays of structures with high tolerances, it does not scale well to the large areas that will probably be needed in most applications of interest. By contrast, the bottom-up, colloidal approach described here is simple, rapid, inexpensive and easily scalable, and could lead to the eventual cost-effective manufacture of large-area metasurfaces with controlled reflectance.

METHODS SUMMARY

A 5-nm chromium adhesion layer and a 50-nm gold film were deposited by electron-beam evaporation onto a Nexterion Glass B slide. The surface of the gold film was then treated with a layer-by-layer deposition²⁴ of polyallylamine hydrochloride and polystyrene sulphonate to create a polyelectrolyte spacer layer with a controllable thickness²⁵. The thickness of the polyelectrolyte layer was measured before deposition of the nanocubes using a J. A. Woolam Co. M-88 spectroscopic ellipsometer. The silver nanocubes were immobilized on the polyelectrolyte surface by a brief exposure to the colloidal solution followed by rinsing with water and drying under a stream of nitrogen. In an effort to limit the number of aggregates accumulating on the surface of the film, the exposure to the colloidal solution was carried out with the gold film facing down so that in theory aggregates would sink away from the surface. The nanocube coverage density on the gold film was controlled by varying the concentration of colloids in solution and the time that the surface was exposed to the solution. Scanning electron microscope images were used to determine the surface density of the cubes and their size distribution, which was found to have a standard deviation of the order of 10 nm (Supplementary Information). To measure the normal-incidence reflectance properties of the samples, white light from a 75-W xenon source was directed at the sample through a microscope objective with a numerical aperture of 0.13 and $\times 5$ magnification, and the reflected signal was collected by the same objective and directed through a 50/50 beam splitter to a spectrometer. For off-normal specular reflectance, 1-mm-diameter multimode fibres terminated with collimating lens adapters formed both the excitation path (from the light source to the sample) and the collection path (of the reflected signal from the sample to the spectrometer).

Full Methods and any associated references are available in the online version of the paper.

Received 18 April; accepted 24 September 2012.

- Bermel, P. *et al.* Design and global optimization of high-efficiency thermophotovoltaic systems. *Opt. Express* **18**, A314–A334 (2010).
- Hao, J. *et al.* High performance optical absorber based on a plasmonic metamaterial. *Appl. Phys. Lett.* **96**, 251104 (2010).
- Niesler, F., Gansel, J., Fischbach, S. & Wegener, M. Metamaterial metal-based bolometers. *Appl. Phys. Lett.* **100**, 203508 (2012).
- Landy, N. I., Sajuyigbe, S., Mock, J. J., Smith, D. R. & Padilla, W. J. Perfect metamaterial absorber. *Phys. Rev. Lett.* **100**, 207402 (2008).
- Avitzour, Y., Urzhumov, Y. A. & Shvets, G. Wide-angle infrared absorber based on a negative-index plasmonic metamaterial. *Phys. Rev. B* **79**, 045131 (2009).
- Liu, N., Mesch, M., Weiss, T., Hentschel, M. & Giessen, H. Infrared perfect absorber and its application as plasmonic sensor. *Nano Lett.* **10**, 2342–2348 (2010).
- Koechlin, C. *et al.* Total routing and absorption of photons in dual color plasmonic antennas. *Appl. Phys. Lett.* **99**, 241104 (2011).
- Wu, C. *et al.* Large-area wide-angle spectrally selective plasmonic absorber. *Phys. Rev. B* **84**, 075102 (2011).

- Tittl, A., Mai, P., Taubert, R., Dregely, D. & Giessen, N. L. H. Palladium-based plasmonic perfect absorber in the visible wavelength range and its application to hydrogen sensing. *Nano Lett.* **11**, 4366–4369 (2011).
- Wan, W. *et al.* Time-reversed lasing and interferometric control of absorption. *Science* **331**, 889–892 (2011).
- Shalaev, V. Optical negative-index metamaterials. *Nature Photon.* **1**, 41–48 (2007).
- Liu, X. *et al.* Taming the blackbody with infrared metamaterials as selective thermal emitters. *Phys. Rev. Lett.* **107**, 045901 (2011).
- Dolling, G. *et al.* Cut-wire pairs and plate pairs as magnetic atoms for optical metamaterials. *Opt. Lett.* **30**, 3198–3200 (2005).
- Shalaev, V. M. *et al.* Negative index of refraction in optical metamaterials. *Opt. Lett.* **30**, 3356–3358 (2005).
- Yu, N. *et al.* Light propagation with phase discontinuities: generalized laws of reflection and refraction. *Science* **334**, 333–337 (2011).
- Shadrivov, I. V., Kapitanova, P., Maslovski, S. & Kivshar, Y. Metamaterials controlled with light. *Phys. Rev. Lett.* **109**, 083902 (2012).
- Albooyeh, M. & Simovski, C. Maximal absorption and local field enhancement in planar plasmonic arrays. Preprint at <http://arxiv.org/abs/1203.2100v1> (2012).
- Bozhevolnyi, S. I. & Søndergaard, T. General properties of slow-plasmon resonant nanostructures: nano-antennas and resonators. *Opt. Express* **15**, 10869–10877 (2007).
- Moreau, A., Lafarge, C., Laurent, N., Edee, K. & Granet, G. Enhanced transmission of slits arrays in an extremely thin metallic film. *J. Opt. A* **9**, 165–169 (2007).
- Le Perche, J., Quemerais, P., Barbara, A. & Lopez-Ros, T. Why metallic surfaces with grooves a few nanometers deep and wide may strongly absorb visible light. *Phys. Rev. Lett.* **100**, 066408 (2008).
- Granet, G. & Plumey, J. Parametric formulation of the Fourier modal method for crossed surface-relief gratings. *J. Opt. A* **4**, S145 (2002).
- Sun, Y. & Xia, Y. Shape-controlled synthesis of gold and silver nanoparticles. *Science* **298**, 2176–2179 (2002).
- Im, S. H., Lee, Y. T., Wiley, B. & Xia, Y. Large-scale synthesis of silver nanocubes: the role of HCl in promoting cube perfection and monodispersity. *Angew. Chem. Int. Ed.* **44**, 2154–2195 (2005).
- Decher, G. Fuzzy nanoassemblies: toward layered polymeric multicomposites. *Science* **277**, 1232–1237 (1997).
- Marinakos, S. M., Chen, S. & Chilkoti, A. Plasmonic detection of a model analyte in serum by a gold nanorod sensor. *Anal. Chem.* **79**, 5278–5283 (2007).
- Michota, A., Kudelski, A. & Bukowska, J. Molecular structure of cysteamine monolayers on silver and gold substrates: comparative studies by surface-enhanced Raman scattering. *Surf. Sci.* **502–503**, 214–218 (2002).
- Wallwork, M. L., Smith, D. A., Zhang, J., Kirkham, J. & Robinson, C. Complex chemical force titration behavior of amine-terminated self-assembled monolayers. *Langmuir* **17**, 1126–1131 (2001).
- Mock, J. J. *et al.* Distance-dependent plasmon resonant coupling between a gold nanoparticle and gold film. *Nano Lett.* **8**, 2245–2252 (2008).
- Hanauer, M., Pierrat, S., Zins, I., Lotz, A. & Sönnichsen, C. Separation of nanoparticles by gel electrophoresis according to size and shape. *Nano Lett.* **7**, 2881–2885 (2007).
- Anker, J. N. *et al.* Biosensing with plasmonic nanosensors. *Nature Mater.* **7**, 442–453 (2008).

Supplementary Information is available in the online version of the paper.

Acknowledgements This work was supported by the US Air Force Office of Scientific Research (grant no. FA9550-09-1-0562) and by the US Army Research Office through a Multidisciplinary University Research Initiative (grant no. W911NF-09-1-0539). Additional support includes US NIH grant R21EB009862, to A.C., and US NIH F32 award (F32EB009299), to R.T.H.

Author Contributions A.M. and C.C. ran the simulations. A.M., C.C., J.J.M. and D.R.S. conducted the physical analysis. Q.W. fabricated and characterized the nanocubes. R.T.H. made the substrates (gold and polyelectrolyte layers), measured their characteristics and deposited the cubes. J.J.M. built the experimental set-up and made the measurements. All the authors provided technical and scientific insight and contributed to the writing of the manuscript.

Author Information Reprints and permissions information is available at www.nature.com/reprints. The authors declare no competing financial interests. Readers are welcome to comment on the online version of the paper. Correspondence and requests for materials should be addressed to D.R.S. (drsmith@ee.duke.edu).

METHODS

A 50-nm-thick gold film was deposited by electron-beam evaporation (CHA Industries), at 2 \AA s^{-1} onto a Nexterion Glass B slide (Schott North America, Inc.), including a 5-nm chromium adhesion layer (deposited at 1 \AA s^{-1}).

The surface of the gold film was then treated by layer-by-layer deposition²⁴ of polyallylamine hydrochloride (Aldrich) and polystyrene sulphonate (Aldrich) to create a polyelectrolyte spacer layer with a controllable thickness²⁸. For each deposition step, the gold-coated glass slides were immersed for 30 min in polyelectrolyte at a concentration of 0.003 moles of monomer per litre and 1 M NaCl, rinsed thoroughly with a gentle stream of ultrapure water (18 M Ω , used throughout) and immersed in fresh ultrapure water for 1 min, after which the substrates were either immersed in 1 M NaCl for 30 s before repeating the same steps for deposition of the oppositely charged polyelectrolyte or dried with a stream of high-purity nitrogen for analysis. All layer-by-layer depositions were initiated and terminated with the cationic polyallylamine hydrochloride layer to facilitate both the attachment of the first polyelectrolyte layer to the gold film through amine–gold interactions^{25–27} and the electrostatic immobilization of the silver nanocubes.

The nanocubes, which were made following a previously published protocol²², were immobilized on the polyelectrolyte surface by brief exposure to the colloidal solution followed by rinsing with water and drying under a stream of nitrogen. In an effort to limit the number of aggregates accumulating on the surface of the film during this attachment process, the nanocube solution was sonicated briefly and the slide was lowered gold side down onto a coverslip containing a 30- μl droplet of

the colloidal solution, whereupon the coverslip was picked up by the slide using the capillary force of the droplet spreading onto the film surface. Under these conditions, aggregates would theoretically sink away from the surface of the gold film during the incubation. The density of coverage of nanocubes on the surface of the gold film was controlled by varying the concentration of colloids in solution and the time that the surface was exposed to the colloidal solution.

Scanning electronic microscope images were used to determine both the surface density of the cubes after deposition on the layers and the size distribution of the cubes. This distribution was found to have a standard deviation of the order of 10 nm (Supplementary Information). The thickness of the polyelectrolyte layer was measured before deposition of the nanocubes using a J. A. Woolam Co. M-88 spectroscopic ellipsometer.

To measure the normal-incidence specular reflectance properties of the samples, white light from a 75-W xenon source (ORIEL) was directed at the sample through a microscope objective with a numerical aperture of 0.13 and $\times 5$ magnification (Nikon), and the reflected signal was collected by the same objective and directed through a 50/50 beam splitter to a spectrometer (ACTON 2300i). For off-normal (25°) specular reflectance, 1-mm-diameter multimode fibres terminated with collimating lens adapters formed both the excitation path (from the light source to the sample) and the collection path (of the reflected signal from the sample to the spectrometer). With this technique, the beam diameter at the surface of the sample is approximately 3 mm. In all of the presented data, the reflectivity of the cube-covered film is normalized by the reflectance spectrum of the bare gold film.

Continuous gas-phase synthesis of nanowires with tunable properties

Magnus Heurlin¹, Martin H. Magnusson², David Lindgren¹, Martin Ek³, L. Reine Wallenberg³, Knut Deppert¹ & Lars Samuelson¹

Semiconductor nanowires are key building blocks for the next generation of light-emitting diodes¹, solar cells² and batteries³. To fabricate functional nanowire-based devices on an industrial scale requires an efficient methodology that enables the mass production of nanowires with perfect crystallinity, reproducible and controlled dimensions and material composition, and low cost. So far there have been no reports of reliable methods that can satisfy all of these requirements. Here we show how aerotaxy, an aerosol-based growth method⁴, can be used to grow nanowires continuously with controlled nanoscale dimensions, a high degree of crystallinity and at a remarkable growth rate. In our aerotaxy approach, catalytic size-selected Au aerosol particles induce nucleation and growth of GaAs nanowires with a growth rate of about 1 micrometre per second, which is 20 to 1,000 times higher than previously reported for traditional, substrate-based growth of nanowires made of group III–V materials^{5–7}. We demonstrate that the method allows sensitive and reproducible control of the nanowire dimensions and shape—and, thus, controlled optical and electronic properties—through the variation of growth temperature, time and Au particle size. Photoluminescence measurements reveal that even as-grown nanowires have good optical properties and excellent spectral uniformity. Detailed transmission electron microscopy investigations show that our aerotaxy-grown nanowires form along one of the four equivalent $\langle 111 \rangle_B$ crystallographic directions in the zincblende unit cell, which is also the preferred growth direction for III–V nanowires seeded by Au particles on a single-crystal substrate. The reported continuous and potentially high-throughput method can be expected substantially to reduce the cost of producing high-quality nanowires and may enable the low-cost fabrication of nanowire-based devices on an industrial scale.

Semiconductor nanowires are typically grown using a bottom-up approach whereby metal particles positioned on top of a single-crystalline substrate enhance growth in one dimension, forming high-aspect-ratio nanostructures⁸. The nanowire growth mechanism allows sensitive control of the nanowire dimensions, crystal structure

and material composition (in terms of, for example, doping⁹ or heterostructure design¹⁰) if the growth method used is flexible enough to accommodate a wide set of growth parameters. Common methods for producing these structures include metalorganic vapour-phase epitaxy (MOVPE), molecular-beam epitaxy and chemical-beam epitaxy. However, these methods are slow compared with other methods, as well as costly because of the need for expensive single-crystal substrates. Alternative approaches based on, for example, solution^{11,12} and gas-phase¹³ growth, although potentially cheaper, are typically associated with restrictions or allow only poor control of basic nanowire properties such as crystallinity, diameter, length and shape.

In this Letter, we show that an aerotaxy-based growth method can overcome all of these issues when growing nanowires. The principle of aerotaxy—which so far has been used only for the controlled conversion of droplets of a group-III material, such as Ga, into crystalline III–V nanocrystals, such as GaAs⁴—is based on the formation and manipulation of nanoparticles and nanowires in a continuous stream of gas. Our aerotaxy method therefore eliminates the need for single-crystal substrates to induce nucleation and circumvents the limitations of batch-wise growth by providing a continuous process. Comparing our growth equipment with a 2-inch MOVPE reactor, where Au particles have been deposited on a wafer at a density of $1 \mu\text{m}^{-2}$ it is possible to increase the nanowire production rate by a factor of 50 using our aerotaxy system (Supplementary Information). Because the high cost of single-crystal semiconductor devices has so far been a limiting factor in large-scale implementations of, for example, energy-relevant semiconductor applications, such as solar cells and light-emitting diodes, we anticipate that the aerotaxy-based nanowire growth method reported here could provide a scalable methodology for fabricating large-area nanowire-based applications.

In our experiments, we use Au nanoparticles to catalyse the one-dimensional growth of GaAs nanowires that all form in the aerosol phase (Fig. 1). The nanoparticles are size-selected with a high degree of control¹⁴, to allow sensitive tuning of the nanowire lateral dimension and, thereby, material properties such as quantum confinement and

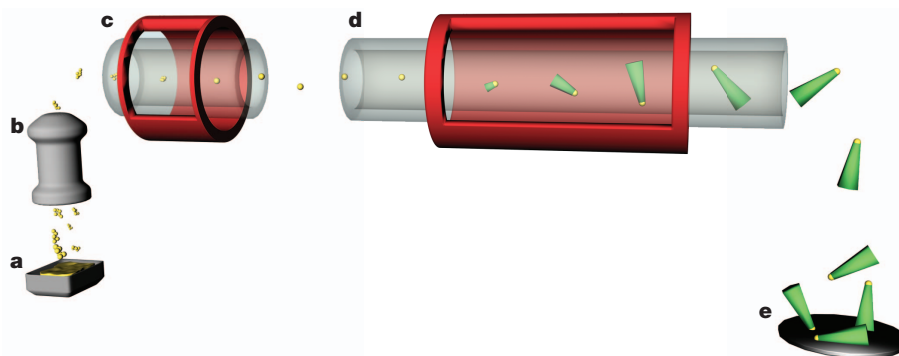


Figure 1 | Aerotaxy growth of nanowires. a, Au agglomerate formation; b, Au agglomerate size sorting using a DMA; c, Au agglomerate compaction into spherical particles in a furnace; d, nanowire growth; e, nanowire deposition.

¹Division of Solid State Physics, Lund University, 22100 Lund, Sweden. ²Sol Volts AB, Ideon Science Park, 22370 Lund, Sweden. ³Division of Polymer and Materials Chemistry, Lund University, 22100 Lund, Sweden.

electron scattering, which allow the optical¹⁵ and electrical¹⁶ properties of the nanowires to be fine-tuned. Particle size selection is achieved by generating and size-selecting Au aerosol particles in a set-up that consists of an evaporation–condensation step for the formation of Au agglomerates, a particle charger, a differential mobility analyser (DMA) for the size selection of the Au agglomerates and a sintering furnace for particle compaction¹⁷. A similar method has previously been used successfully to provide seed particles for gas-phase growth of a related class of one-dimensional materials, carbon nanotubes, where it was possible to control and tune the nanotube diameter¹⁸.

To initiate the reaction forming the nanowires, the size-selected Au particles are first mixed with reactants (precursors) carrying the constituents of the nanowire material and are then heated in a tube furnace for a well-controlled period, the growth time. We used trimethylgallium (TMGa) and arsine (AsH₃), which are commonly used for the growth of thin-film GaAs crystals and nanowires by MOVPE. According to our present understanding of nanowire growth, an alloyed nanoparticle of Au–Ga should form, and new atomic planes should subsequently nucleate at the crystal–nanoparticle–vapour triple phase boundary¹⁹ during the time spent in the tube furnace. In our case, the crystal–nanoparticle interface is not present at the start of the process but is generated on the nanoparticle surface through the formation of a GaAs crystallite from which the nanowire can grow, such that the Au particle acts as the ‘substrate’ from which the nanowire nucleates. We have found that the nanowires preferentially form under relatively low group-V/group-III ratios compared with nanowires nucleated using Au particles and grown using MOVPE with the same precursors. Because there is no substrate that can provide Ga to supersaturate the Au particle, this must instead be provided directly from the gas phase. A high V/III ratio would decrease this supersaturation, inhibiting nanowire nucleation and instead favouring GaAs particle formation. After the nanowires have formed they are transported, still in the aerosol phase, to a deposition chamber, where they are deposited, with the use of an electric field, on a surface of choice.

The nanowire diameter, length and shape can be controlled by changing the Au particle size (Fig. 2a–d), the growth temperature

(Fig. 2e–h) and the growth time (Fig. 2j, k), respectively. Controlling these parameters results in nanowires with reproducible properties, which is of importance in large-scale semiconductor applications, where millions of nanowires need to be incorporated in parallel to build up a functional device. The growth time is controlled by the gas velocity through the reactor tube (for a given furnace length) and can be varied by, for example, changing the diameter of the reactor tube. The Au particle size is determined by the DMA, and our current set-up can produce Au particles with diameters ranging from 5 to 80 nm. The effect of temperature is more complex than a change in particle size or growth time because it affects both the length (Fig. 2i) and the shape of the nanowire. This is due to an increase in the reaction rate at higher temperatures, both at the interface between the Au particle and the nanowire and on the side facets of the nanowire. This phenomenon is well known from conventional nanowire growth. The increased reaction rate at higher temperatures also leads to parasitic reactions between TMGa and AsH₃ in the gas phase, which can form small GaAs particles (Fig. 2g).

Investigations show that the axial growth rate, which can exceed $1\ \mu\text{m s}^{-1}$, has an Arrhenius dependence on temperature between 450 and 550 °C (Supplementary Fig. 1). From this, we extract an activation energy of $97\ \text{kJ mol}^{-1}$ for the axial growth. This is within the range of previously reported values for the activation energy of substrate-nucleated GaAs nanowires ($67\text{--}102\ \text{kJ mol}^{-1}$ (refs 20, 21)). It is not possible to conclude whether the rate-limiting step for aerotaxy-grown nanowires differs in any considerable way. An apparent difference is, however, the absence of a reduced growth rate at higher temperatures for aerotaxy-grown nanowires. When nanowires are seeded on a native single-crystalline substrate, growth on the substrate surface becomes more dominant at higher temperatures, reducing the nanowire growth rate. The absence of a substrate in aerotaxy eliminates this effect, enabling a high growth rate to be maintained over a broader temperature interval.

In addition to affecting the growth rate, the growth temperature also affects the crystal structure of the nanowires (Fig. 3). III–V nanowires commonly have a polytypic crystal structure where the cubic

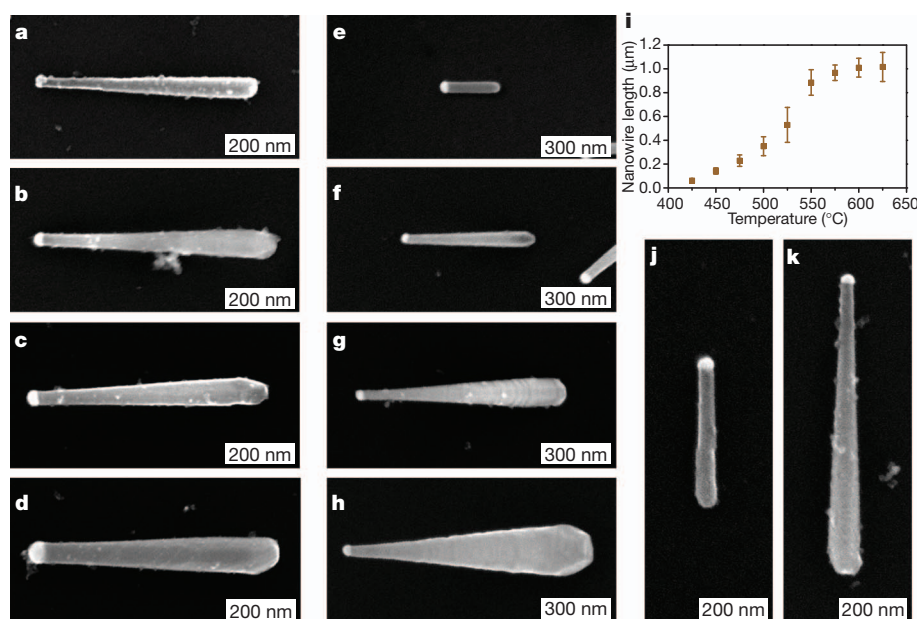


Figure 2 | Scanning electron microscope images of GaAs nanowires grown by aerotaxy under different growth conditions. a–d, Nanowires grown with 35- (a), 50- (b), 70- (c) and 120-nm (d) diameter Au agglomerates at a furnace temperature of 525 °C. After particle compaction and nanowire growth, this results in average nanowire-top diameters (where the nanowire meets the Au particle) of 30, 41, 51 and 66 nm, respectively. e–h, Nanowires grown at furnace temperatures of 450 (e), 500 (f), 550 (g) and 600 °C (h), using 50-nm Au

agglomerates and a growth time of 1 s. i, Temperature dependence of the nanowire length (errors, s.d. of measured nanowire length). Each measurement point contains between four and ten nanowire measurements (Supplementary Information) j, k, Nanowires grown with reactor tube diameters of 18 (j) and 32 mm (k), resulting in growth times of approximately 0.3 and 1 s, respectively. In each series of images, only the growth parameter specified was varied.

zincblende and hexagonal wurtzite phases are intermixed²². Between 425 °C (the lowest temperature at which we achieved nanowire growth) and 525 °C, the nanowires have a pure zincblende crystal structure, where polytypism-related modulations in the potential landscape for an electron travelling in the axial direction of a nanowire are avoided (Fig. 3a, b). At higher temperatures, intermixing of the crystal phases is observed with the formation of twin planes and small wurtzite inclusions in the zincblende-dominated nanowires (Fig. 3c, d). The relatively large temperature interval in which single-crystal phase nanowires can be grown using our technique further demonstrates the applicability of this technique and its ability to control nanowire properties.

The nanowire crystal growth direction was determined to be along a $\langle 111 \rangle$ direction in more than 99% of the investigated nanowires, using high-resolution transmission electron microscope images. Ten nanowires were further investigated using convergent-beam electron diffraction (CBED) to differentiate the two types of $\langle 111 \rangle$ growth direction, $\langle 111 \rangle_A$ or $\langle 111 \rangle_B$, which are respectively defined by having either a group-III- or a group-V-terminated $\{111\}$ surface. In all cases, the growth was found to have occurred in a $\langle 111 \rangle_B$ direction (Supplementary Fig. 4), as is most commonly reported for substrate-grown III–V nanowires. This shows that the growth direction and polarity of nanowires remain the same as when using a crystalline substrate during growth, indicating that this fundamental property is dictated at the seed-particle/nanowire interface and not by the substrate.

Photoluminescence measurements reveal spectra of excellent uniformity (Fig. 4 and Supplementary Fig. 5) despite the fact that no surface treatment or high-bandgap passivation was used to reduce

surface recombination. This indicates that as-grown nanowires have good optical properties. A peak maximum can be observed at 1.514 eV, which falls in the known range for bound and free excitons in bulk GaAs (1.513–1.516 eV (ref. 23)) and corresponds well with previous reports of MOVPE-grown nanowires²⁴. The average peak full-width at half-maximum of eight measured spectra is 23 meV. The measurements were performed on nanowires grown using an Au agglomerate size of 50 nm, a growth temperature of 625 °C and a growth time of 0.3 s. We found that nanowires grown in this shorter time typically show a lower density of stacking defects than do nanowires grown over a longer time (~ 1 s) at the same temperature. Transmission electron microscope images of nanowires grown with the parameters stated above show a twinned zincblende crystal structure in which the distance between two adjacent twin planes varies from a few nanometres to 60 nm (Supplementary Fig. 6). In view of this, we attribute the luminescence observed below the main peak to type-II transitions at the twin plane boundaries²⁵. Our photoluminescence results are better, in terms of homogeneity and full-width at half-maximum, than those in previous reports of GaAs nanowires grown in a solution or gas phase, where only very broad luminescence, if any, was observed^{26,27}. The reported data are better or comparable to those for GaAs nanowires grown on single-crystalline Si (ref. 28). Increased control of nanowire polytypism at high nanowire growth temperatures and the addition of a surface passivating shell could improve the optical characteristics to match those of state-of-the-art GaAs nanowires grown on a native substrate, which can have photoluminescence spectra with full-widths at half-maximum as low as 3 meV (ref. 24).

We expect that the presented aerotaxy-based growth method will have a substantial impact on how the field of nanoscale devices, primarily those based on nanowires, will develop in the future. The method is general and is expected to be applicable to other common precursor materials and techniques of seed nanoparticle formation. For large-area applications, the throughput, that is, the number of nanowires produced per unit time, is of high importance. Although we have so far used production rates that exceed those available for substrate-nucleated nanowires, further improvements are possible. Because our system is currently limited by the number of seed particles that can be produced, an increase in particle production will result in a similar increase in nanowire production and, thus, a reduction in the cost of nanowire fabrication. Increasing particle production is possible by, for example, adding additional high-temperature furnaces for agglomerate formation or by implementing different nanoparticle

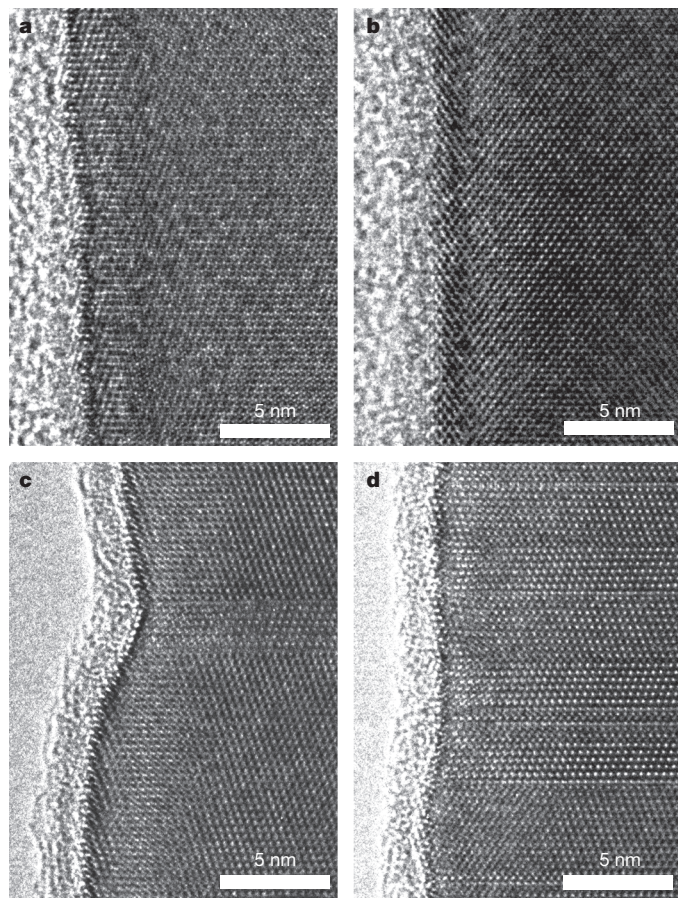


Figure 3 | Temperature dependence of the nanowire crystal structure. Transmission electron microscope images of nanowires grown at temperatures of 450 (a), 500 (b), 550 (c) and 600 °C (d). The nanowires were grown with 50-nm Au agglomerates and a growth time of 1 s. The nanowires are viewed along a $\langle 110 \rangle$ direction perpendicular to the growth direction.

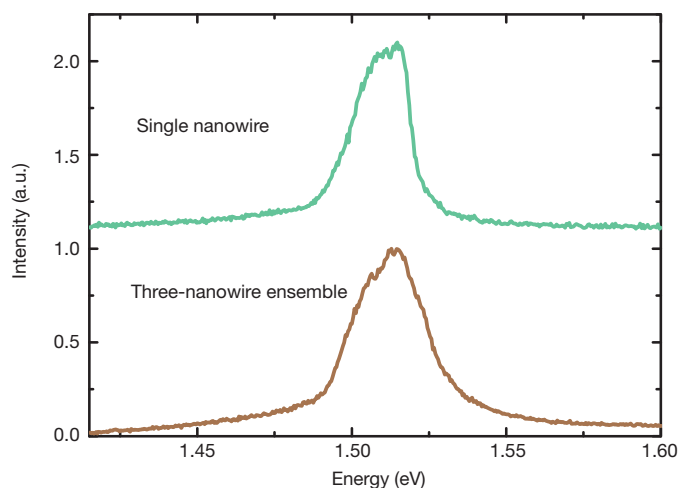


Figure 4 | Photoluminescence spectra. Nanowire microphotoluminescence measurements performed on a single nanowire and on a three-nanowire ensemble at 4 K. Nanowires were grown from 50-nm Au agglomerates at a growth temperature of 625 °C and a growth time of approximately 0.3 s. a.u. arbitrary units.

generation processes with higher throughput, for example spark or arc discharge.

Doping of the nanowires and, in particular, the realization of p–n junctions are important considerations for future applications. We are currently working on these issues. Preliminary results from secondary-ion mass spectrometry measurements on single-segment nanowires show that Zn is incorporated during growth in the presence of the precursor diethylzinc. Forming a p–n junction containing segments with different dopants and doping concentrations should be possible by implementing sequential growth furnaces, with different precursors introduced in each furnace. Challenges related to the altered reaction chemistry and contacting, which has proven troublesome for small-diameter GaAs nanowires, need to be studied and addressed in more detail. Another key issue that needs to be resolved relates to the doping profile, which could be non-uniform if the dopant precursor is depleted during growth. This non-uniformity would in turn affect the contact formation. However, it should be possible to resolve these issues by optimizing the process design and doing chemical and kinetic modelling.

Another consideration for some device and system applications is the ability to align the non-substrate-bound nanowires. This can be done with, for example, electric fields, a method that has previously been demonstrated to result in nanowire alignment with remarkably high yields²⁹. Our use of charged aerosol particles also raises the possibility of deposition and simultaneous alignment (Supplementary Fig. 7) of nanowires directly from the gas phase. To control the vertical orientation of the p- and n-doped segments in the alignment process of nanowires containing p–n junctions, which is important for applications involving solar cells and, to some extent, those involving light-emitting diodes, the built-in potential of the p–n junction can be exploited, with nanowires forming small dipoles under illumination. As an alternative to the above methods, the aerotaxy-produced nanowires can also be extracted directly from the gas phase into a liquid using various scrubber techniques. The nanowire solution can thereafter be stored and used in further processing steps in which the nanowires are deposited using, for example, fluidic alignment³⁰, which might be ideal for thermoelectric applications^{31,32}. However, many applications, such as Li-ion batteries, do not require nanowire alignment. Li-ion batteries with Si nanowires as the anode material have received considerable attention over the past few years because Si has the highest known theoretical charge potential and in nanowire form undergoes less performance deterioration due to charge cycling³. With further developments in the areas of growth and device processing, aerotaxy could thus provide a scalable means of production of perfect semiconductor nanowire device structures for applications such as large-area solar cells, solid-state lighting and Li-ion batteries.

METHODS SUMMARY

Nanowire synthesis. The size-selected Au aerosol particles were generated using a set-up similar to one described previously¹⁷. The main differences were that only one DMA was used and the particles were charged using a ⁶³Ni β -radiation charger. The Au particles were mixed with the precursor gases AsH₃ and TMGa and passed through a reaction furnace consisting of a sintered Al₂O₃ reactor tube surrounded by a resistive heater. The reactor tube was exchangeable and two tubes with different inner diameters (18 and 32 mm) were used in the experiments. The AsH₃ molar fraction was 3×10^{-6} (6×10^{-6} in the growth time comparison (Fig. 2j, k)) with a total gas flow of 1.68 l min^{-1} , and the V/III ratio was 0.9 in all experiments. The electric field strength in the deposition chamber was 10^5 V m^{-1} . During our experiments a Si substrate was used to collect the nanowires.

Characterization. All samples were investigated with a scanning electron microscope, operated at 10 kV, and selected samples were singled out for further analysis to determine atomic structure and optical properties. The crystal structure was investigated using a JEOL 3000F TEM (300 kV) with a point resolution of 1.7 Å. The crystal polarity was determined using CBED by observing the asymmetrical contrast between the 002 and $\bar{0}02$ diffraction discs, which arises from dynamical diffraction when odd-index, high-order reflections are excited simultaneously³³. Optical properties were investigated using a microphotoluminescence set-up at 4 K with a spectral resolution of 1.3 meV. The 532-nm line from a frequency-doubled Nd:YAG laser was used as the excitation source, with an intensity of

approximately 10 W cm^{-2} . To make measurements on single nanowires and small nanowire ensembles, some nanowires were transferred to an Au-coated Si substrate.

Full Methods and any associated references are available in the online version of the paper.

Received 13 February; accepted 27 September 2012.

Published online 28 November 2012.

- Qian, F., Gradečak, S., Li, Y., Wen, C.-Y. & Lieber, C. M. Core/multishell nanowire heterostructures as multicolor, high-efficiency light-emitting diodes. *Nano Lett.* **5**, 2287–2291 (2005).
- Borgström, M. T. et al. Nanowires with promise for photovoltaics. *IEEE J. Sel. Top. Quantum Electron.* **17**, 1050–1061 (2011).
- Chan, C. K. et al. High-performance lithium battery anodes using silicon nanowires. *Nature Nanotechnol.* **3**, 31–35 (2008).
- Deppert, K. & Samuelson, L. Self-limiting transformation of monodisperse Ga droplets into GaAs nanocrystals. *Appl. Phys. Lett.* **68**, 1409–1411 (1996).
- Joyce, H. J. et al. Unexpected benefits of rapid growth rate for III–V nanowires. *Nano Lett.* **9**, 695–701 (2009).
- Borgström, M. T., Immink, G., Ketelaars, B., Algra, R. & Bakkers, E. P. A. M. Synergetic nanowire growth. *Nature Nanotechnol.* **2**, 541–544 (2007).
- Ramdani, M. R. et al. Fast growth synthesis of GaAs nanowires with exceptional length. *Nano Lett.* **10**, 1836–1841 (2010).
- Yazawa, M., Koguchi, M., Muto, A., Ozawa, M. & Hiruma, K. Effect of one monolayer of surface gold atoms on the epitaxial growth of InAs nanowhiskers. *Appl. Phys. Lett.* **61**, 2051–2053 (1992).
- Haraguchi, K., Katsuyama, T. & Hiruma, K. Polarization dependence of light emitted from GaAs p–n junctions in quantum wire crystals. *J. Appl. Phys.* **75**, 4220–4225 (1994).
- Björk, M. T. et al. One-dimensional steeplechase for electrons realized. *Nano Lett.* **2**, 87–89 (2002).
- Holmes, J. D., Johnston, K. P., Doty, R. C. & Korgel, B. A. Control of thickness and orientation of solution-grown silicon nanowires. *Science* **287**, 1471–1473 (2000).
- Wang, F. et al. Solution–liquid–solid growth of semiconductor nanowires. *Inorg. Chem.* **45**, 7511–7521 (2006).
- Duan, X. & Lieber, C. M. General synthesis of compound semiconductor nanowires. *Adv. Mater.* **12**, 298–302 (2000).
- Karlsson, L., Deppert, K. & Malm, J.-O. Size determination of Au aerosol nanoparticles by off-line TEM/STEM observations. *J. Nanopart. Res.* **8**, 971–980 (2006).
- Gudiksen, M. S., Wang, J. & Lieber, C. M. Size-dependent photoluminescence from single indium phosphide nanowires. *J. Phys. Chem. B* **106**, 4036–4039 (2002).
- Ford, A. C. et al. Diameter-dependent electron mobility of InAs nanowires. *Nano Lett.* **9**, 360–365 (2009).
- Magnusson, M. H., Deppert, K., Malm, J.-O., Bovin, J.-O. & Samuelson, L. Size-selected gold nanoparticles by aerosol technology. *Nanostruct. Mater.* **12**, 45–48 (1999).
- Kim, S. H. & Zachariah, M. R. Gas-phase growth of diameter-controlled carbon nanotubes. *Mater. Lett.* **61**, 2079–2083 (2007).
- Wacaser, B. A. et al. Preferential interface nucleation: an expansion of the VLS growth mechanism for nanowires. *Adv. Mater.* **21**, 153–165 (2009).
- Soci, C., Bao, X.-Y., Aplin, D. P. R. & Wang, D. A systematic study on the growth of GaAs nanowires by metal–organic chemical vapor deposition. *Nano Lett.* **8**, 4275–4282 (2008).
- Borgström, M., Deppert, K., Samuelson, L. & Seifert, W. Size- and shape-controlled GaAs nano-whiskers grown by MOVPE: a growth study. *J. Cryst. Growth* **260**, 18–22 (2004).
- Caroff, P., Bolinsson, J. & Johansson, J. Crystal phases in III–V nanowires: from random toward engineered polytypism. *IEEE J. Sel. Top. Quantum Electron.* **17**, 829–846 (2011).
- Bogardus, E. H. & Bebb, H. B. Bound-exciton, free-exciton, band-acceptor, donor-acceptor, and Auger recombination in GaAs. *Phys. Rev.* **176**, 993–1002 (1968).
- Morral, A. F. Gold-free GaAs nanowire synthesis and optical properties. *IEEE J. Sel. Top. Quantum Electron.* **17**, 819–828 (2011).
- Heiss, M. et al. Direct correlation of crystal structure and optical properties in wurtzite/zinc-blende GaAs nanowire heterostructures. *Phys. Rev. B* **83**, 045303 (2011).
- Dong, A., Yu, H., Wang, F. & Buhro, W. E. Colloidal GaAs quantum wires: solution–liquid–solid synthesis and quantum-confinement studies. *J. Am. Chem. Soc.* **130**, 5954–5961 (2008).
- Duan, X., Wang, J. & Lieber, C. M. Synthesis and optical properties of gallium arsenide nanowires. *Appl. Phys. Lett.* **76**, 1116–1118 (2000).
- Moewe, M., Chuang, L. C., Crankshaw, S., Chase, C. & Chang-Hasnain, C. Atomically sharp catalyst-free wurtzite GaAs/AlGaAs nanoneedles grown on silicon. *Appl. Phys. Lett.* **93**, 023116 (2008).
- Freer, E. M., Grachev, O., Duan, X., Martin, S. & Stumbo, D. P. High-yield self-limiting single-nanowire assembly with dielectrophoresis. *Nature Nanotechnol.* **5**, 525–530 (2010).
- Huang, Y., Duan, X., Wei, Q. & Lieber, C. M. Directed assembly of one-dimensional nanostructures into functional networks. *Science* **291**, 630–633 (2001).
- Dresselhaus, M. S. et al. New directions for low-dimensional thermoelectric materials. *Adv. Mater.* **19**, 1043–1053 (2007).
- Boukai, A. I. et al. Silicon nanowires as efficient thermoelectric materials. *Nature* **451**, 168–171 (2008).

33. Taftø, J. & Spence, J. C. H. A simple method for the determination of structure-factor phase relationships and crystal polarity using electron diffraction. *J. Appl. Crystallogr.* **15**, 60–64 (1982).

Supplementary Information is available in the online version of the paper.

Acknowledgements We thank M. Borgström for discussions on the nanowire growth, B. Meuller for technical assistance with the growth setup, D. Csontos for reviewing our manuscript before submission and B. Pedersen for supporting this project by making the infrastructure of Sol Voltaics AB available. We acknowledge G. Alcott and E. Nilsson for sharing their preliminary results on doping. This project is performed within the Nanometer Structure Consortium at Lund University (nmC@LU) and with financial support from the Swedish Research Council, the

Swedish Foundation for Strategic Research, the Knut and Alice Wallenberg Foundation and VINNOVA.

Author Contributions M.H., M.H.M., K.D. and L.S. designed the growth experiments. M.H. and M.H.M. performed the growth experiments. M.H., M.H.M., D.L. and M.E. performed the characterization and data analysis. K.D., L.R.W. and L.S. supervised the project. M.H. and L.S. wrote the main part of the paper. All authors reviewed and commented on the manuscript.

Author Information Reprints and permissions information is available at www.nature.com/reprints. The authors declare no competing financial interests. Readers are welcome to comment on the online version of the paper. Correspondence and requests for materials should be addressed to L.S. (lars.samuelson@ftf.lth.se).

METHODS

Nanowire synthesis. The size-selected Au aerosol particles were generated in a set-up similar to one described previously¹⁷. In the set-up, Au agglomerates are formed by an evaporation–condensation process in a high-temperature furnace working at between 1,750 and 1,850 °C. Size selection of the Au agglomerates was performed using a DMA with a sheath flow of 10 l min^{−1} and a variable voltage determining the Au agglomerate size. For the agglomerates to be size-selected they required a single electron charge supplied by a ⁶³Ni β-radiation charger positioned before the DMA. After size selection, the agglomerates were compacted into spherical particles using a sinter furnace working at 450 °C. The Au particles were mixed with the precursor gases AsH₃ and TMGa, the AsH₃ being supplied from a gas bottle through a mass-flow controller. The TMGa was supplied from a standard temperature- and pressure-controlled metalorganic bubbler, with H₂ carrier gas supplied through a second mass-flow controller. The AsH₃ molar fraction was 3×10^{-6} (6×10^{-6} in the growth time comparison (Fig. 2j, k)), with a total gas flow of 1.68 l min^{−1}. The V/III ratio was 0.9 in all experiments. The main carrier gas was N₂. The mixture of Au particles and gas was passed through a reaction furnace consisting of a sintered Al₂O₃ reactor tube surrounded by a resistive heater. The reactor tube was exchangeable and two tubes with different inner diameters (18 and 32 mm) were used in the experiments. After the reaction furnace, the nanowires were passed either to an electrometer measuring the amount

of charge in the aerosol or to a deposition chamber, where the nanoparticles or nanowires were deposited using an electric field. The electric field strength in the deposition chamber was 10⁵ V m^{−1}. During our experiments, a Si substrate was used to collect the nanowires.

Characterization. All samples were investigated with a scanning electron microscope operated at 10 kV, and selected samples were singled out for further analysis to determine atomic structure and optical properties. The crystal structure was investigated using a JEOL 3000F TEM (300 kV) with a point resolution of 1.7 Å. The CBED measurements were made by tilting approximately 7° in the (002) plane until the Bragg condition was fulfilled for either the 002 or the 00 $\bar{2}$ reflection and two weak, odd-indexed reflections ($\bar{1}\bar{1}\bar{1}$ and $\bar{1}\bar{1}$ 9 in the case of 002). After setting the convergence angle to approximately 3.7 mrad, we saw a bright interference pattern in the centre of the 00 $\bar{2}$ disc (dark in the 002 disc). This difference allowed the diffraction pattern to be indexed unambiguously³³. A comparison with GaAs nanowires grown by MOVPE on (111)B substrates was used to resolve the 180° ambiguity due to possible image inversions. Optical properties were investigated using a microphotoluminescence set-up at 4 K with a spectral resolution of 1.3 meV. The 532-nm line from a frequency-doubled Nd:YAG laser was used as the excitation source, with an intensity of approximately 10 W cm^{−2}. To make measurements on single nanowires and small nanowire ensembles, some nanowires were transferred to an Au-coated Si substrate.

Practical and innate carbon–hydrogen functionalization of heterocycles

Yuta Fujiwara^{1*}, Janice A. Dixon^{1*}, Fionn O'Hara^{1*}, Erik Daa Funder¹, Darryl D. Dixon¹, Rodrigo A. Rodriguez¹, Ryan D. Baxter¹, Bart Herlé¹, Neal Sach^{1,2}, Michael R. Collins^{1,2}, Yoshihiro Ishihara¹ & Phil S. Baran¹

Nitrogen-rich heterocyclic compounds have had a profound effect on human health because these chemical motifs are found in a large number of drugs used to combat a broad range of diseases and pathophysiological conditions. Advances in transition-metal-mediated cross-coupling have simplified the synthesis of such molecules; however, C–H functionalization of medicinally important heterocycles that does not rely on pre-functionalized starting materials is an underdeveloped area^{1–9}. Unfortunately, the innate properties of heterocycles that make them so desirable for biological applications—such as aqueous solubility and their ability to act as ligands—render them challenging substrates for direct chemical functionalization. Here we report that zinc sulphinate salts can be used to transfer alkyl radicals to heterocycles, allowing for the mild (moderate temperature, 50 °C or less), direct and operationally simple formation of medicinally relevant C–C bonds while reacting in a complementary fashion to other innate C–H functionalization methods^{2–6} (Minisci, borono-Minisci, electrophilic aromatic substitution, transition-metal-mediated C–H insertion and C–H deprotonation). We prepared a toolkit of these reagents and studied their reactivity across a wide range of heterocycles (natural products, drugs and building blocks) without recourse to protecting-group chemistry. The reagents can even be used in tandem fashion in a single pot in the presence of water and air.

The strategy that we describe here was conceived with a strong desire to make use of the native chemical reactivity¹ of nitrogen-rich heterocycles rather than attempting to override it with pre-functionalization (Fig. 1a). Minisci's pioneering work demonstrated the ability of heterocycles to react with certain alkyl and acyl radicals² (derived from carboxylic acids and halides (Fig. 1b)). This form of innate C–H functionalization, however, is limited to a subset of alkyl and acyl donors, and often requires higher temperatures (for example, greater than 70 °C), transition-metal additives and strongly oxidizing conditions³. In 2010, it was reported that aryl boronic acids can be used as aryl radical precursors for heterocycle functionalization⁴. Later, it was shown that alkyl boronic acids and trifluoroborate salts can serve as radical precursors^{5,6}. In 2011, it was demonstrated that sodium trifluoromethanesulphonate, a reagent extensively studied by Langlois⁸, was capable of trifluoromethylating heterocycles via a radical mechanism⁷. Shortly thereafter, a procedure was described for difluoromethylation that relied upon the use of a zinc-derived sulphinate salt⁹.

Zinc sulphinate salts are easily prepared, bench-stable, free-flowing solids (with the exception of zinc triethyleneglycolsulphonate (TEGS; F) (Fig. 1c)) that show remarkably enhanced reactivity compared with sodium-derived analogues in radical additions to heterocycles (see below). Here we describe a modular, innate C–H functionalization of heterocycles using zinc sulphinate salts following a mild and practical reaction protocol. We use a zinc bis(alkanesulphonate) salt toolkit, much like available toolkits for cross-coupling chemistry, for the direct functionalization of a variety of heterocycles, all of which result in

products that cannot be efficiently generated by standard Minisci protocols and would otherwise require programmed, multistep processes. These salts represent examples of what we anticipate to be a general

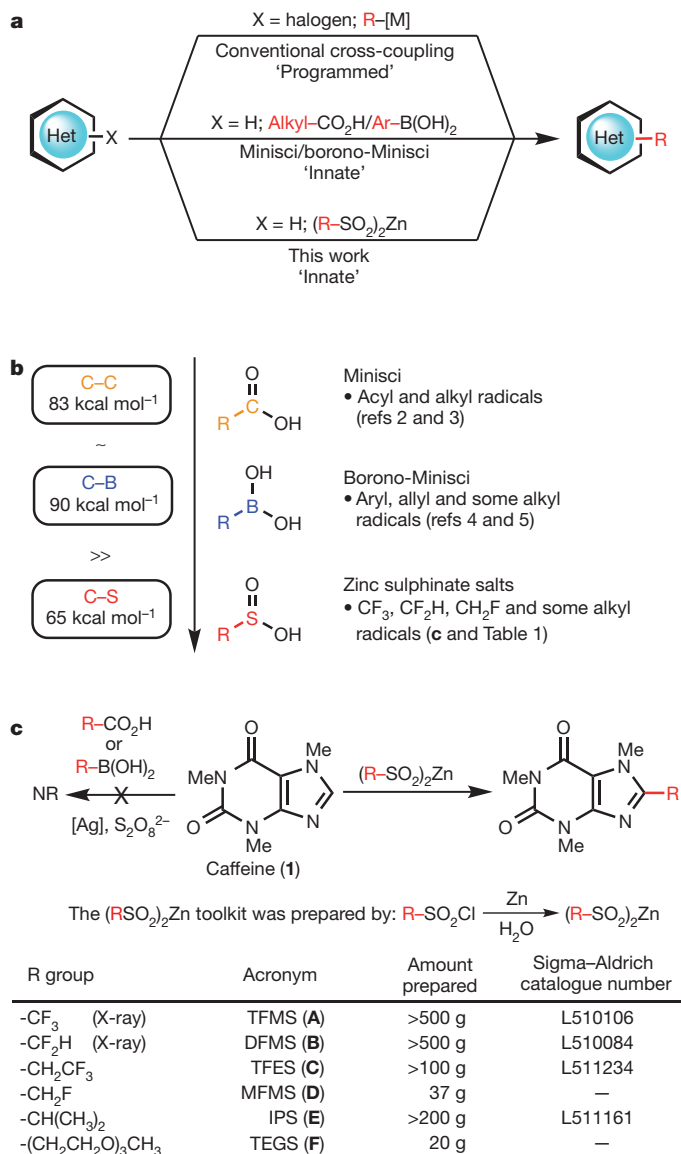


Figure 1 | Development of a reagent toolkit for an innate C–H functionalization of heterocycles. **a**, Comparison of different methods of heterocycle functionalization. **b**, Evolution of the radical precursor. **c**, Invention of new reagents for heterocycle functionalization.

¹Department of Chemistry, The Scripps Research Institute, 10550 North Torrey Pines Road, La Jolla, California 92037, USA. ²Department of Chemistry, La Jolla Laboratories, Pfizer Inc., 10770 Science Center Drive, San Diego, California 92121, USA.

*These authors contributed equally to this work.

reagent class that will permit the rapid diversification of heterocycles using an operationally simple protocol¹⁰. Functionalization using zinc bis(alkanesulphinate) salts affords a marked improvement over functionalization with sodium-based sulphinate salts⁷ and is a generalization of the zinc difluoromethanesulphinate chemistry developed previously⁹.

We identified a modular set of zinc sulphinate salts as being highly desirable for the installation of medicinally relevant moieties (Fig. 1c): zinc trifluoromethanesulphinate (TFMS; **A**), zinc difluoromethanesulphinate (DFMS; **B**), zinc trifluoroethanesulphinate (TFES; **C**), zinc monofluoromethanesulphinate (MFMS; **D**), zinc isopropylsulphinate (IPS; **E**), and zinc triethyleneglycolsulphinate (TEGS; **F**). The fluoroalkyl and alkyl groups that we wish to introduce hold privileged positions in drug discovery and are described in detail below.

The CF₃ group is an excellent bioisostere of a methyl group because the former is similar in size to the latter but does not suffer metabolic oxidation¹¹. It can also be used to tune the steric and electronic properties of a known scaffold, and to grant favourable physicochemical attributes to a lead target^{12,13}. For these reasons, trifluoromethylation methodology has received much attention, with nucleophilic CF₃ reagents¹⁴ (for example carbonyl functionalization), electrophilic CF₃ reagents¹⁴ (for example enolate functionalization) and cross-coupling procedures dominating arene functionalization^{15,16}. (Metal-catalysed C–H activation for trifluoromethylation is also known¹⁷.) However, the trifluoromethylation of heterocycles is less common owing to substrate-mediated reagent or catalyst deactivation in these strongly basic, acidic or transition-metal-catalysed reactions.

To fill this gap in methodology, we have begun to study a radical-based approach to trifluoromethylation⁷. Although the introduction of the CF₃ group by a radical pathway is known, reagents that achieve this radical transformation are difficult to handle and are toxic (CF₃I (ref. 18), a gas), ozone-depleting (CF₃Br (ref. 19), a gas) or corrosive (CF₃SO₂Cl (refs 20, 21), a low-boiling liquid). Furthermore, CF₃CO₂H does not generate radicals under Minisci conditions, and CF₃B(OH)₂, as an analogy to borono-Minisci chemistry, is an unknown chemical species (other CF₃–boron sources such as CF₃–B(OMe)₃K and CF₃–BF₃K are not viable radical precursors⁷). Although sodium trifluoromethanesulphinate (CF₃SO₂Na, a stable solid) addressed many of the above difficulties for heterocycle trifluoromethylation, TFMS (**A**) was found to be superior in terms of both stability and reactivity (47% yield was obtained for a reaction of pentoxifylline (**2**) with CF₃SO₂Na in 2.5:1 CH₂Cl₂:H₂O at room temperature for 48 h (ref. 7), 79% yield was obtained for a reaction of pentoxifylline (**2**) with TFMS in 2.5:1 CH₂Cl₂:H₂O at room temperature for 3 h (Table 1) and 99% yield was obtained for a reaction of **2** with TFMS in 2.5:1 CH₂Cl₂:H₂O at 50 °C for 3 h; also see comparisons of reaction conversions for various substrates in Supplementary Information).

The CF₂H group can act as a lipophilic hydrogen-bond donor and has been used in bioisostere design variously to mimic a thiol, a hydroxamic acid, a hydroxyl and an amide¹¹. Although the CF₂H group can be formed using (diethylamino)sulphur trifluoride on an aldehyde and can be introduced using (trimethylsilyl)difluoromethane²² or other difluoromethyl precursors²³, direct difluoromethylation strategies on heterocycles had not been explored before the invention of DFMS⁹ (**B**).

The CH₂CF₃ group is an excellent bioisostere of an ethyl group and acts as a mild electron-withdrawing group (trifluoroethanol is about 3.5 orders of magnitude more acidic than ethanol). Appendage of the CH₂CF₃ group is typically achieved by multistep strategies (such as nucleophilic addition of CF₃ into an aldehyde followed by deoxygenation), and a catalytic cross-coupling method for this purpose was reported only recently²⁴. A direct, free-radical-based approach for the introduction of the CH₂CF₃ group was unknown, and therefore TFES (**C**) was developed to fill this gap in methodology.

Much like the CF₃ group, the CH₂F group can act as a useful bioisostere of a methyl group because the fluorine atom can also prevent metabolic oxidation owing to its electron-withdrawing effect. Furthermore, the CH₂F group has also been considered bioisosteric

with hydroxymethyl (CH₂OH) and methoxymethyl (CH₂OCH₃) groups²⁵. However, monofluoromethylation methods are limited and less well studied compared with trifluoromethylation and are typically introduced using ‘auxiliary’ approaches²³, for example appending a fluoro(phenylsulphonyl)methyl group and then removing the phenylsulphonyl group²⁶. The generation of a monofluoromethyl radical is almost unknown, with only one report made on its characterization by a matrix reaction of bromofluoromethane with alkali metals, without demonstration of synthetic applicability²⁷. As fluoroacetic acid (CH₂F–CO₂H) cannot generate radicals under standard Minisci conditions, a practical CH₂F radical precursor and its application to synthetic chemistry is required; MFMS (**D**) is a new reagent devised for this purpose.

The ability to add steric bulk and lipophilicity where needed may prove valuable when probing for structure–activity relationships or when blocking metabolically labile positions. Methods for the direct introduction of this hindered group include the use of toxic isopropylmercurial reagent ((CH₃)₂CH–HgCl (ref. 28)) or the use of air- and water-sensitive isopropyllithium or isopropylmagnesium chloride. Furthermore, the use of (CH₃)₂CH–CO₂H or (CH₃)₂CH–I with the Minisci protocol on caffeine (**1**) did not afford the desired product at room temperature or higher temperatures. A ‘programmed’ approach to installing an isopropyl group is often low-yielding and problematic using Suzuki- or Negishi-type couplings (with a few notable exceptions²⁹) and we therefore designed an ‘innate’ approach using IPS (**E**).

Ethylene glycol units are excellent solubilizing units, and the utility of poly(ethylene glycol) chains in drug delivery has been extensively investigated³⁰. As a proof of concept for the appendage of poly(ethylene glycol) units onto heterocycles, we planned to introduce a shorter, tri(ethylene glycol), chain that might retain the ability to increase the hydrophilicity of a lead target. Methods to directly append an oligo(ethylene glycol) unit onto heterocyclic frameworks are unknown, and TEGS (**F**) was therefore devised.

The ability to incorporate fluoroalkyl, alkyl and alkoxyalkyl groups into heterocyclic frameworks is highly desirable; however, until now the chemistry to access substituted heterocycles rapidly has been underdeveloped and of limited scope. The power of the zinc sulphinate toolkit is demonstrated here with a synthesis of an exemplary set of medicinally relevant heterocycles (>50 examples), most of which represent new chemical entities.

As shown in Table 1, we used an operationally simple procedure to functionalize xanthines (**1** and **2**), pyridines (**3** and **4**), quinoxalines (**5**), pyrimidines (**6**), pyridazines (**7**) and pyrroles (**8**): the heterocycle substrate and the zinc sulphinate salt were combined with a mixture of organic solvent and water and cooled in an ice-water bath, *tert*-butyl hydroperoxide (TBHP) was added and this mixture was warmed to room temperature or 50 °C. Exclusion of air or purification of solvents is unnecessary, and the reaction flask is sealed only with a plastic cap to prevent solvent evaporation. Fluoroalkylated zinc sulphinate reagents (**A–D**) performed best in halogenated solvents such as CH₂Cl₂, ClCH₂CH₂Cl, perfluorotoluene and perfluorohexane, whereas alkylated zinc salts (**E** and **F**) reacted more favourably in DMSO or in an electron-rich aromatic solvent such as anisole. For substrates that showed low conversion, addition of one or more of the following was performed: zinc sulphinate salt, TBHP or trifluoroacetic acid.

Perhaps the most notable aspect of C–C bond formation using zinc sulphinate chemistry is the mildness of the reaction conditions. As shown in Table 1, reactive groups such as nitriles, ketones and esters are tolerated. The level of functional group compatibility can be extended even to reactive heteroaryl halides, free carboxylic acids and boronate esters, three groups of particular utility in pharmaceutical chemistry owing to the ease of further functionalization via cross-coupling methods or amide bond formation (Fig. 2a). These groups are typically incompatible with most organic reactions, much less C–H functionalization strategies; however, under our reaction conditions, simple pyridine building blocks bearing a reactive chloro (**9**), pinacolboron (**10**) or carboxylic acid (**11**) moiety can be functionalized with

Table 1 | Substrate scope of the zinc sulphinate salt toolkit

Zinc sulphinate salt
Open flask, operational simplicity, >50 examples

Heterocycle	Zn salt, R					
	CF ₃ (A)	CF ₂ H (B)	CH ₂ CF ₃ (C)	CH ₂ F (D)	CH(CH ₃) ₂ (E)	(CH ₂ CH ₂ O) ₃ CH ₃ (F)
1 	89 (100) [†] 1A	73 (57) [†] ^{§§} 1B	51 [#] 1C	80 [#] 1D	41 ^{**} 1E	40 ^{††} 1F
2 	79 (100) [†] 2A	72 (41) [†] ^{§§} 2B	44 [#] 2C	75 [#] 2D	37 ^{**} 2E	49 ^{††} 2F
3 	35 (77) [†] [4:1 C2:C3] 3A	66 (100) [†] [only C2] 3B	18 (85) [#] [4:1 C2:C3] 3C	73 ^{†††} [17:1 C2:C2&C6] 3D	47 [§] [C2:C2&C6 1.4:1] 3E	41 ^{††} [only C2] 3F
4 	66 (65) [†] ^{§§} [2.3:1 C6:C2] 4A	60 (96) [†] [C2:C6:C4 3:2:1] 4B	33 [#] [1.4:1 C6:C4] 4C	NR 4D	41 ^{††} [only C6] 4E	NR 4F
5 	75 (100) [†] [5 products] 5A	50 (67) [†] 5B	31 (77) [‡] 5C	56 [#] 5D	43 ^{**} 5E	32 ^{**} 5F
6 	42 (44) [2.7:1 C4:C5] 6A	21 (44) [1.6:1 C4:C5] 6B	21 ^{**} [only C5] 6C	NR 6D	46 ^{**} [2.1:1 C4:C5] 6E	16 ^{††} [3.4:1 C4:C5] 6F
7 	45 (90) [only C4] 7A	57 (71) [6:1 C4:C5] 7B	NR 7C	NR 7D	49 ^{**} [10:1 C4:C5] 7E	32 (38) ^{††} [only C4] 7F
8 	76 (91) [†] [7.4:1 C2:C5] 8A	65 (100) [†] [only C2] 8B	58 ^{**} [1.4:1 C2:C5] 8C	40 [§] [only C2] 8D	17 ^{**} [only C2] 8E	10 (43) ^{††} [only C2] 8F

Isolated yields are shown. Percentage conversions by gas chromatography (GC) mass spectrometry are indicated in parentheses, and regioisomeric ratios are shown in square brackets. Compounds **1A**, **2A**, **3A**, **4A** and **5A** have been previously synthesized with Langlois reagent (ref. 7), and compounds **1B**, **2B**, **3B**, **4B**, **5B** and **8B** have been previously prepared using DFMS (ref. 9) and are included for completeness; all other compounds in this table are new.

* Standard conditions involve heterocycle (1.0 equiv.), zinc salt (2.0–3.0 equiv.), TBHP (3.0–5.0 equiv.) and solvent:water (2.5:1) at a specified temperature for a period of 3–12 h.

Solvent and temperature: [†]CH₂Cl₂, RT; [‡]ClCH₂CH₂Cl, RT; [§]ClCH₂CH₂Cl, 50 °C; ^{||}perfluorohexane, RT; ^{††}perfluorotoluene, RT; [#]perfluorotoluene, 50 °C; ^{**}DMSO, 50 °C; ^{†††}anisole, 50 °C (the reaction time for anisole is 0.5–96 h; see Supplementary Information).

^{‡‡} TFA was used as an additive.

^{§§} When the GC percentage conversion is lower than the isolated yield, it signifies that only one addition of Zn salt was made for the 'GC yield reaction', but that a second addition of Zn salt and TBHP was performed after 12 h for the 'isolated yield reaction'.

Et, ethyl; Me, methyl; NR, no reaction; RT, room temperature (25 °C); TBHP, *tert*-butyl hydroperoxide; TFA, trifluoroacetic acid.

CF₃ or CF₂H groups. In particular, carboxylic acid **11** is a quintessential example of the unique chemoselectivity and mildness of the reaction conditions, because Minisci or borono-Minisci conditions would not leave the carboxylic acid unit intact. It is of note that the modest yields observed in these reactions are due to difficulties in product isolation, for example the high volatility of difluoromethylated product **12**. It is of further note that **12** is commercially available but is prohibitively expensive (US\$3,500 per gram from Accel Pharmtech)

and was previously prepared from 4-chloro-2-pyridinecarbaldehyde (US\$432 per gram from Matrix Scientific) using (diethylamino)sulphur trifluoride or from 2-picolinic acid using a laborious six-step protocol; the zinc sulphinate procedure allowed the synthesis of **12** from a cheap precursor (US\$1.1 per gram from Oakwood Products), 4-chloropyridinium hydrochloride (**9**).

To further test the specificity of this transformation to react at the position defined by the innate reactivity of the given heterocycle, we

performed a one-pot sequential C–H functionalization of the anti-malarial drug dihydroquinine (**15**; Fig. 2b). Because our previous studies suggested that electrophilic radicals add to the C7 position of **15** (ref. 7) and that nucleophilic radicals add to the C2 position of **15** (ref. 9), we expected **15** to react sequentially when an electrophilic and a nucleophilic radical were added in one pot. To test this, we added TFMS (**A**) and then IPS (**E**) to a reaction vessel containing **15**, after which difunctionalized dihydroquinine derivative **16** was isolated in 30% yield. The scope of this sequential functionalization was further extended to examples including pyridines (**17** and **18**) and purines (**19**). This strategy is particularly useful for the construction of

lipophilic derivatives of hydrophilic molecules such as dihydroquinine and 6-chloropurine, because the isolation of water-soluble intermediates can be avoided and only the lipophilic bis-substituted product is isolated.

Finally, the versatile nature of this transformation is demonstrated by the ability to carry out difluoromethylation and trifluoromethylation in unconventional media (conversion to product confirmed by high-performance liquid chromatography), including cell lysate (Fig. 2c, i), tea (Fig. 2c, ii) and a Tris buffer solution in the presence of a serine-based β -lactamase (Fig. 2c, iii), which retained its functional activity after reisolation. These findings may have important implications in the area of bioconjugation¹⁰.

Although zinc sulphinate chemistry can provide a great number of new chemical entities that are difficult or impossible to access in other ways, and yet have high levels of chemoselectivity, this procedure, much like other methods, is not without limitations. For instance, some nucleophilic radicals gave markedly lower yields when reacting with certain electron-rich substrates, for example a 17% yield in the reaction of IPS (**E**) with pyrrole **8** (Table 1). We found that many solvents sometimes had to be screened to achieve the desired reaction (for example for MFMS (**D**)). Nevertheless, we believe that the practicality, versatility and functional group tolerance of this innate functionalization of heterocycles makes it a valuable addition to the range of C–H functionalization methods that can be used to construct pharmaceutically important targets. In addition, comparison of traditional programmed approaches (of which none exist for three of the six salts described in Table 1) with the synthesis of compounds in Table 1 and, especially, those in Fig. 2 shows that it would be extremely difficult to devise a faster, simpler or cheaper way to make such molecules.

In most contexts of discovery chemistry, reactions that can be conducted open to the air on unprotected, late-stage molecules in 10–50% yield are preferable to time-intensive, multistep routes, especially when the overall yield of such routes (for instance a typical sequence of protection, lithiation, iodination, cross-coupling and deprotection) is comparable to this direct approach. It is of note that 50 of the 52 compounds reported here have not been prepared before (or have only previously been described by our laboratory^{7,9}; several other methods are listed in compound databases but no preparations are reported). Zinc sulphinate chemistry is not limited to the six salts presented above. Salts have also been prepared for the transfer of CH_2Cl , $\text{CH}_2\text{CO}_2\text{Me}$, cyclohexyl (for example, see **18** in Fig. 2b) and perfluoroalkyl (for example C_6F_{13}) groups, and the extent of their scope is currently being examined (Supplementary Information).

We have described the invention of a zinc sulphinate toolkit containing ten different groups (CF_3 , CF_2H , CH_2CF_3 , CH_2F , $\text{CH}(\text{CH}_3)_2$, $(\text{CH}_2\text{CH}_2\text{O})_3\text{CH}_3$, CH_2Cl , $\text{CH}_2\text{CO}_2\text{CH}_3$, cyclohexyl and C_6F_{13}) for the simple and rapid diversification of heterocycles. Four of these reagents are currently commercially available from Sigma-Aldrich (TFMS, catalogue no. L510106; DFMS, catalogue no. L510084; TFES, catalogue no. L511234; IPS, catalogue no. L511161). Particular advantages of this chemistry include (1) the superiority of zinc over sodium alkylsulphinates, which led to the identification of a highly active counter-cation and allowed for an efficient radical generation from alkylsulphinates; (2) the mildness of the reaction conditions, which tolerated highly sensitive functional groups such as chloro and boron groups; (3) a different, transition-metal-free mode of radical generation compared with Minisci chemistry, as benzylic carboxylic acids were tolerated; (4) the feasibility of a sequential, one-pot operation that allowed for a site-selective bis-alkylation of heterocycles using two different alkylating agents; and (5) the ability to conduct these reactions under open air, without organic co-solvent and in the presence of extensive impurities in the reaction medium, which may have potential applications in bioconjugation.

This chemistry has already been ‘field-tested’ and is now widely used for medicinal chemistry at Pfizer; several of the building blocks reported in this work are currently in use there (**3–5**, **7**, **13** and **14**).

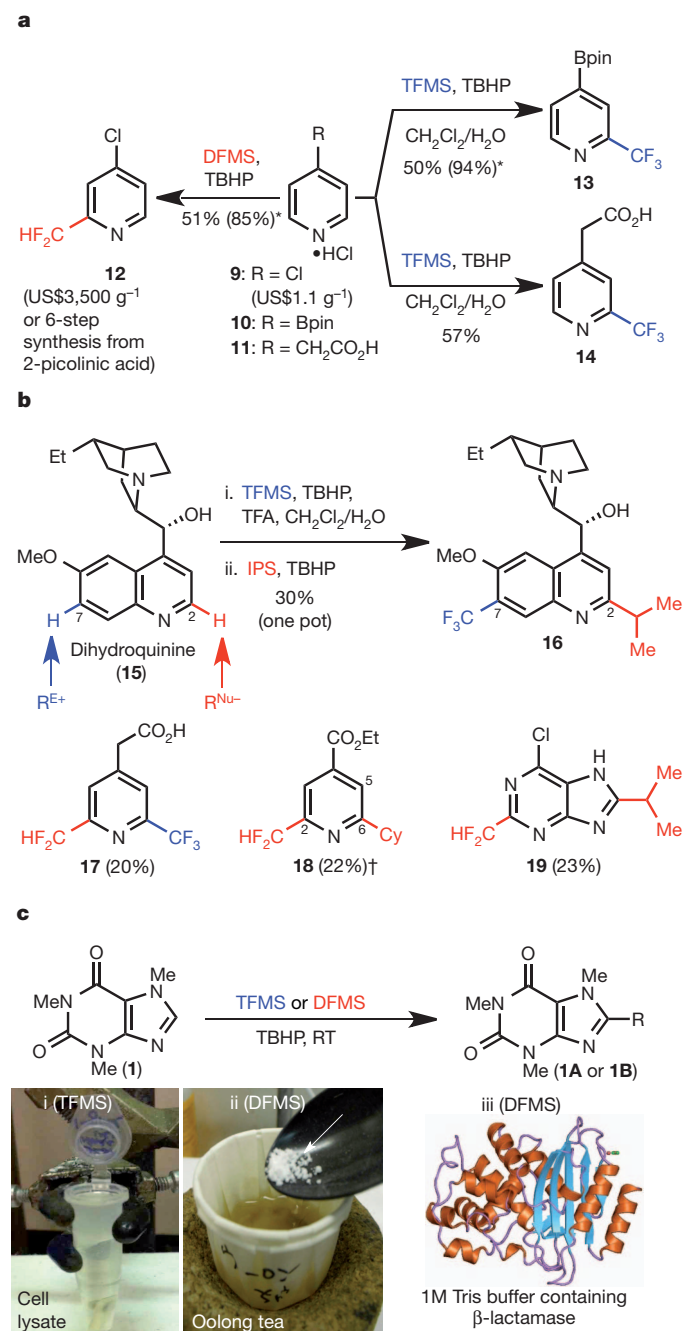


Figure 2 | Chemoselectivity, rapid diversity and complexity generation, and practical utility. **a**, Functional group tolerance and cost-effective synthesis of **12**. Bpin, pinacolboron. *Percentage conversion as observed by gas chromatography mass spectrometry analysis. **b**, One-pot sequential addition in water and under air. Cy, cyclohexyl. †Six per cent yield of the C5-cyclohexyl isomer was also obtained. **c**, Operational simplicity in unconventional media.

In many cases, building blocks that would be regarded as ‘low priority’ at Pfizer owing to prohibitively high cost or lengthy synthetic routes are now easily accessible. The extreme operational ease, functional group tolerance and ability to run reactions in unconventional media open to air bode well for the widespread application of zinc sulphinate salts in chemical synthesis. As a further outlook for the utility of innate heterocycle functionalization, zinc sulphinate reagents could potentially be used to cap metabolically susceptible positions in bioactive molecules and to identify the most reactive sites of a given heteroarene. The development of such a ‘profiling system’, providing a set of empirically determined reactivity rules to organic chemists, is a topic of ongoing research in our laboratory.

METHODS SUMMARY

All reactions were carried out under an atmosphere of air. Reagents were of the highest commercial quality and were used without further purification, unless otherwise stated. Yields refer to chromatographically and spectroscopically (^1H NMR) homogeneous material, unless otherwise stated. Reactions were monitored by thin-layer chromatography carried out on 0.25-mm E. Merck silica plates (60F-254), using ultraviolet light as the visualizing agent and KMnO_4 as a developing agent. For full experimental details and procedures for all reactions performed and full characterization (^1H , ^{13}C and ^{19}F NMR, high-resolution mass spectrometry, infrared spectroscopy, melting point and R_f value) of all new compounds, see Supplementary Information.

Full Methods and any associated references are available in the online version of the paper.

Received 1 June; accepted 16 October 2012.

Published online 28 November 2012.

- Brückl, T., Baxter, R. D., Ishihara, Y. & Baran, P. S. Innate and guided C–H functionalization logic. *Acc. Chem. Res.* **45**, 826–839 (2012).
- Minisci, F., Vismara, E. & Fontana, F. Recent developments of free-radical substitutions of heteroaromatic bases. *Heterocycles* **28**, 489–519 (1989).
- Dunston, M. A. J. Minisci reactions: versatile CH-functionalizations for medicinal chemists. *Med. Chem. Comm.* **2**, 1135–1161 (2011).
- Seiple, I. B. et al. Direct C–H arylation of electron-deficient heterocycles with arylboronic acids. *J. Am. Chem. Soc.* **132**, 13194–13196 (2010).
- Fujiwara, Y. et al. Practical C–H functionalization of quinones with boronic acids. *J. Am. Chem. Soc.* **133**, 3292–3295 (2011).
- Molander, G. A., Colombel, V. & Braz, V. A. Direct alkylation of heteroaryls using potassium alkyl- and alkoxyethyltrifluoroborates. *Org. Lett.* **13**, 1852–1855 (2011).
- Ji, Y. et al. Innate C–H trifluoromethylation of heterocycles. *Proc. Natl Acad. Sci. USA* **108**, 14411–14415 (2011).
- Langlois, B. R., Laurent, E. & Roidot, N. Trifluoromethylation of aromatic compounds with sodium trifluoromethanesulfinate under oxidative conditions. *Tetrahedr. Lett.* **32**, 7525–7528 (1991).
- Fujiwara, Y. et al. A new reagent for direct difluoromethylation. *J. Am. Chem. Soc.* **134**, 1494–1497 (2012).
- Kolb, H. C., Finn, M. G. & Sharpless, K. B. Click chemistry: diverse chemical function from a few good reactions. *Angew. Chem. Int. Ed.* **40**, 2004–2021 (2001).
- Meanwell, N. A. Synopsis of some recent tactical application of bioisosteres in drug design. *J. Med. Chem.* **54**, 2529–2591 (2011).
- Purser, S., Moore, P. R., Swallow, S. & Gouverneur, V. Fluorine in medicinal chemistry. *Chem. Soc. Rev.* **37**, 320–330 (2008).
- Kirk, K. L. Fluorination in medicinal chemistry: methods, strategies, and recent developments. *Org. Process Res. Dev.* **12**, 305–321 (2008).
- Ma, J.-A. & Cahard, D. Strategies for nucleophilic, electrophilic, and radical trifluoromethylations. *J. Fluor. Chem.* **128**, 975–996 (2007).
- Cho, E. J. et al. The palladium-catalyzed trifluoromethylation of aryl chlorides. *Science* **328**, 1679–1681 (2010).
- Morimoto, H., Tsubogo, T., Litvinas, N. D. & Hartwig, J. F. A broadly applicable copper reagent for trifluoromethylations and perfluoroalkylations of aryl iodides and bromides. *Angew. Chem. Int. Ed.* **50**, 3793–3798 (2011).
- Wang, X., Truesdale, L. & Yu, J.-Q. Pd(II)-catalyzed *ortho*-trifluoromethylation of arenes using TFA as a promoter. *J. Am. Chem. Soc.* **132**, 3648–3649 (2010).
- Kino, T. et al. Trifluoromethylation of various aromatic compounds by CF_3I in the presence of Fe(II) compound, H_2O_2 and dimethylsulfoxide. *J. Fluor. Chem.* **131**, 98–105 (2010).
- Qi, Q., Shen, Q. & Lu, L. Polyfluoroalkylation of 2-aminothiazoles. *J. Fluor. Chem.* **133**, 115–119 (2012).
- Kamigata, N., Ohtsuka, T., Fukushima, T., Yoshida, M. & Shimizu, T. Direct perfluoroalkylation of aromatic and heteroaromatic compounds with perfluoroalkanesulfonyl chlorides catalysed by a ruthenium(II) phosphine complex. *J. Chem. Soc. Perkin Trans. I* 1339–1346 (1994).
- Nagib, D. A. & MacMillan, D. W. C. Trifluoromethylation of arenes and heteroarenes by means of photoredox catalysis. *Nature* **480**, 224–228 (2011).
- Fier, P. S. & Hartwig, J. F. Copper-mediated difluoromethylation of aryl and vinyl iodides. *J. Am. Chem. Soc.* **134**, 5524–5527 (2012).
- Hu, J., Zhang, W. & Wang, F. Selective difluoromethylation and monofluoromethylation reactions. *Chem. Commun.* 7465–7478 (2009).
- Zhao, Y. & Hu, J. Palladium-catalyzed 2,2,2-trifluoroethylation of organoboronic acids and esters. *Angew. Chem. Int. Ed.* **51**, 1033–1036 (2012).
- Müller, K., Faeh, C. & Diederich, F. Fluorine in pharmaceuticals: looking beyond intuition. *Science* **317**, 1881–1886 (2007).
- Li, Y. et al. Stereoselective nucleophilic monofluoromethylation of *N*-(*tert*-butanesulfinyl)imines with fluoromethyl phenyl sulfone. *Org. Lett.* **8**, 1693–1696 (2006).
- Raymond, J. I. & Andrews, L. Matrix reactions of fluorohalomethanes with alkali metals. Infrared spectrum and bonding in the monofluoromethyl radical. *J. Phys. Chem.* **75**, 3235–3242 (1971).
- Russell, G. A., Guo, D. & Khanna, R. K. Alkylation of pyridine in free radical chain reactions utilizing alkylmercurials. *J. Org. Chem.* **50**, 3423–3425 (1985).
- Han, C. & Buchwald, S. L. Negishi coupling of secondary alkylzinc halides with aryl bromides and chlorides. *J. Am. Chem. Soc.* **131**, 7532–7533 (2009).
- Knop, K., Hooogenboom, R., Fischer, D. & Schubert, U. S. Poly(ethylene glycol) in drug delivery: pros and cons as well as potential alternatives. *Angew. Chem. Int. Ed.* **49**, 6288–6308 (2010).

Supplementary Information is available in the online version of the paper.

Acknowledgements We thank D.-H. Huang and L. Pasternack for NMR spectroscopic assistance, A. Schuyler and W. Uritboonthai for mass spectrometry assistance and D. Cayer for the analysis of the β -lactamase activity. Financial support for this work was provided by the US NIH/NIGMS (GM-073949), the Uehara Memorial Foundation (postdoctoral fellowship for Y.F.), the US–UK Fulbright Commission (postdoctoral fellowship for F.O.), Aarhus University, OChem Graduate School, CDNA, CFIN and NABIT (fellowship for E.D.F.), the US NIH (graduate fellowship for R.A.R.) and Pfizer Inc. (postdoctoral fellowship for R.D.B.).

Author Contributions Y.F., J.A.D., D.D.D., R.A.R. and P.S.B. conceived the work; Y.F., J.A.D., F.O., E.D.F., D.D.D., R.A.R., R.D.B., B.H., N.S. and M.R.C. performed the experiments; Y.F., J.A.D., F.O., E.D.F., D.D.D., R.A.R., R.D.B., B.H., N.S., M.R.C. and P.S.B. designed the experiments and analysed the data; and F.O., R.A.R., Y.I. and P.S.B. wrote the manuscript.

Author Information Reprints and permissions information is available at www.nature.com/reprints. The authors declare no competing financial interests. Readers are welcome to comment on the online version of the paper. Correspondence and requests for materials should be addressed to P.S.B. (pbaran@scripps.edu).

METHODS

Our standard procedure for the functionalization of heterocycles was as follows. A solution of heterocycle (0.125–0.250 mmol, 1.0 equiv.) and Zn salt (2.0–3.0 equiv.) in an organic solvent was cooled in an ice-water bath, and this was followed by the slow addition of TBHP (70% solution in water, 54–179 μ l, 3.0–5.0 equiv.) using an Eppendorf pipette (metal needles should not be used as they decompose the reagent) with vigorous stirring. The reaction mixture was warmed to room temperature or 50 °C and monitored by thin-layer chromatography until reaction completion. For substrates that do not achieve reaction completion in 12–24 h,

a second addition of Zn salt (2.0–3.0 equiv.) and TBHP (3.0–5.0 equiv.) may be added to drive the reaction further. On consumption of the starting material, the reaction was partitioned between EtOAc (5.0 ml) and saturated NaHCO₃ (5.0 ml) or CH₂Cl₂ (5.0 ml) and saturated NaHCO₃ (5.0 ml). The organic layer was separated, and the aqueous layer was extracted with EtOAc or CH₂Cl₂ (3 \times 5.0 ml). The organic layers were dried with Na₂SO₄, concentrated and purified by column chromatography on silica gel. We note that if the TBHP is added too rapidly, the resulting exotherm can result in reduced yield and selectivity. This is especially important on larger scales, where a syringe pump may be used to add the TBHP.

The root of branching river networks

J. Taylor Perron¹, Paul W. Richardson¹, Ken L. Ferrier¹ & Mathieu Lapôtre²

Branching river networks are one of the most widespread and recognizable features of Earth's landscapes and have also been discovered elsewhere in the Solar System^{1,2}. But the mechanisms that create these patterns and control their spatial scales are poorly understood. Theories based on probability^{3–5} or optimality^{3,6–8} have proven useful⁹, but do not explain how river networks develop over time through erosion and sediment transport. Here we show that branching at the uppermost reaches of river networks is rooted in two coupled instabilities: first, valleys widen at the expense of their smaller neighbours, and second, side slopes of the widening valleys become susceptible to channel incision. Each instability occurs at a critical ratio of the characteristic timescales for soil transport and channel incision. Measurements from two field sites demonstrate that our theory correctly predicts the size of the smallest valleys with tributaries. We also show that the dominant control on the scale of landscape dissection in these sites is the strength of channel incision, which correlates with aridity and rock weakness, rather than the strength of soil transport. These results imply that the fine-scale structure of branching river networks is an organized signature of erosional mechanics, not a consequence of random topology.

Observers have long recognized that branching river networks, in which tributaries merge in the downstream direction, are a fundamental outcome of erosion by flowing water. Early field observations led to conceptual models in which hierarchical drainage networks result from progressive integration of initially separate drainages through divide migration and stream capture^{10,11}. More than a century of study of erosional mechanics has culminated in numerical models that produce landscapes dissected by branching river networks^{12–14} and lend some support to the early conceptual models,

but a physically based theory that explains the form of tributary networks has proven elusive¹⁵.

One of the main reasons for this shortcoming is that there is no clear consensus about what such a theory should be able to predict. Early efforts to identify unique geometric characteristics of natural river networks^{11,16,17} failed when the proposed scaling laws were subsequently shown to apply to all hierarchical networks, riverine or otherwise^{3,4,18}. This fuelled a broader class of studies based on principles other than erosional mechanics, including probabilistic models of topologically random networks^{3–5} and optimality arguments based on energy dissipation or entropy^{3,6–8}. Such studies have provided new insights into the structure of natural river networks⁹, but cannot directly relate river network form to the erosional mechanisms that shape the topography: we know what the skeleton of a landscape looks like, but not how it grows.

Thus, despite progress in characterizing the geometry of drainage networks and modelling landscape evolution, it remains unclear how the form of drainage networks records the dominant factors that shape landscapes, such as bedrock properties, tectonic deformation, climate and life. Here we use a simplified model to show that branching tributary networks form through two coupled instabilities, and propose that the scale of the smallest valleys with tributaries is a signature of this process. We then present field measurements from two sites with drainage networks that differ considerably in scale, and show that both are consistent with our theory. This comparison reveals how the spatial structure of river networks records fundamental geological and environmental factors such as rock type and rainfall.

To identify characteristic scales in tributary networks, we mapped the valley networks in two landscapes with similar erosion processes but different scales of fluvial dissection (Fig. 1). The Allegheny Plateau

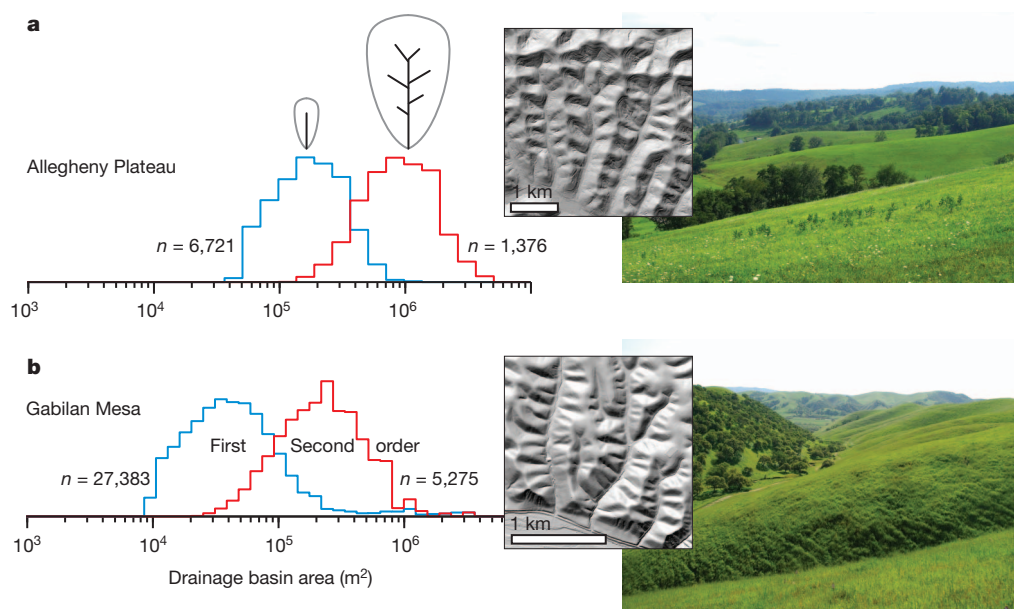


Figure 1 | Properties of the study sites. **a**, The Allegheny Plateau, Pennsylvania; **b**, Gabilan Mesa, California. Left, area distributions of first- and second-order drainage basins, with inset sketches showing examples of first- and second-order basins. Coloured lines are histograms with counts weighted by drainage basin area to compensate for the greater abundance of smaller basins. Insets at centre, shaded relief maps of small portions of the study sites generated from laser altimetry, with vegetation filtered out. Right, photographs showing views from the tops of ridgelines, with first-order valleys in the near distance. See Methods for data sources.

¹Department of Earth, Atmospheric and Planetary Sciences, Massachusetts Institute of Technology, Cambridge, Massachusetts 02139, USA. ²École et Observatoire des Sciences de la Terre, Université de Strasbourg, F-67084 Strasbourg, France.

in southwest Pennsylvania and northern West Virginia consists of horizontally bedded Permian sandstone with minor lenses of limestone, siltstone, shale and coal¹⁹. Land cover is dominantly pasture and deciduous forest, and mean annual precipitation is 105 cm. Gabilan Mesa is an elevated area on the eastern margin of California's Salinas Valley where rivers have incised into nearly horizontally bedded Pliocene and Pleistocene conglomerate, sandstone and siltstone²⁰. The Mesa is an oak savanna that receives 32 cm of rain per year. Both landscapes are shaped dominantly by soil creep due to bioturbation, particularly animal burrowing, and by river channel incision that, in the small drainage basins studied here, is episodic²¹, occurring at estimated intervals of years to many decades.

We mapped the valley network over a large area of each landscape (Methods). We then applied the Horton-Strahler stream ordering scheme^{11,16} to identify first-order drainage basins (those with no tributaries) and second-order drainage basins (those with at least one first-order tributary) (Fig. 1). The upstream areas drained by basins of a given order are log-normally distributed around a well-defined modal value (Fig. 1). Moreover, we find that the modal drainage areas of first- and second-order basins in the Allegheny Plateau and Gabilan Mesa differ considerably. The smallest basins with tributaries are typically four times larger in the Allegheny Plateau, despite the similar appearance of the landscape (Fig. 1). We seek an explanation for this fundamental scale difference.

Valleys bounded by smooth ridgelines emerge in soil-mantled landscapes from a competition between river channel incision, which amplifies topographic perturbations, and soil creep, which damps perturbations. The extent of valley incision can also be limited by a threshold for runoff production or surface erosion²², but we make the simplification that soil creep is the dominant effect, an assumption supported by previous analyses^{21,23}. The smoothing effect of soil creep can be characterized with a diffusion time, $t_{\text{diff}} = L^2/D$, where L is a horizontal length scale and D is the soil transport coefficient (in $\text{m}^2 \text{yr}^{-1}$). Channel incision can be characterized by an advection time that describes the rate at which changes in elevation propagate through the drainage network, $t_{\text{adv}} = L^{1-2m}/K$, where m is a constant and K is a channel incision rate coefficient (in $\text{m}^{1-2m} \text{yr}^{-1}$). The ratio $t_{\text{diff}}/t_{\text{adv}}$, which describes the strength of channel incision relative to soil creep at a chosen scale L , is analogous to a Péclet number, $\text{Pe} = KL^{1+2m}/D$ (refs 21, 23).

We suggest that branching valley networks will develop at a finer scale in landscapes where channel incision is stronger relative to soil creep. To test this idea, we used a landscape evolution model (Methods) to simulate the development of a ridgeline bounded by two incising channels for many different values of Pe . Each simulation formed drainage basins extending from the bounding channels up towards the drainage divide (Supplementary Fig. 5). The length scale L was chosen to be the half-width of the ridgeline, which roughly equals the length of the largest basins (Fig. 2a, inset). (Throughout this study, L is taken to be the length of a drainage basin, or the length of a slope on which a drainage basin may develop.) From the final, equilibrium topography in each experiment, we measured the drainage areas of the basins. A plot of normalized drainage area versus Pe for all the simulations (Fig. 2a) reveals a transition at $250 < \text{Pe} < 300$. For $\text{Pe} < 250$, drainage basins have a uniform size. For $\text{Pe} > 300$, the distribution of basin size is bimodal, with each basin either extending all the way from a lowering boundary to the central drainage divide, or extending only part way to the divide and occupying a small space between larger basins. Nearly all of the larger basins for $\text{Pe} > 300$ developed tributaries (Supplementary Fig. 5).

We interpret this transition in landscape form in terms of a stability diagram (Fig. 2a). At $\text{Pe} < 250$, an array of parallel, uniformly sized basins is a stable configuration: additional numerical experiments confirmed that if any one basin in such a configuration is perturbed by increasing its drainage area, the topographic divides separating the enlarged basin from its neighbours will migrate back towards the

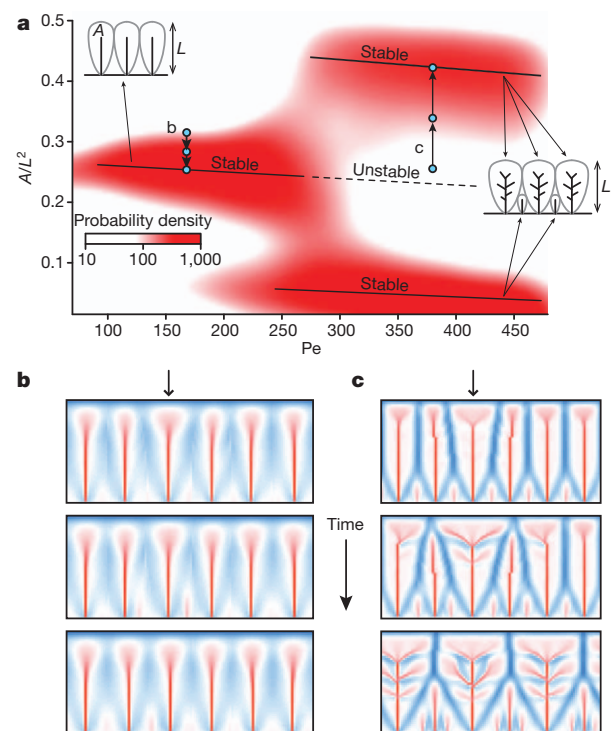


Figure 2 | Branching instability in valley networks. **a**, Stability diagram for first- and second-order drainage basins as a function of Péclet number, Pe . Insets illustrate the definitions of ridgeline half-width, L , and basin area, A . Background colour (see key) indicates probability density distribution of drainage basins generated in numerical experiments, which partly reflects variable initial conditions (Methods). Paths with blue points and arrows trace the evolution of the numerical experiments in **b** and **c**, which illustrate the response of an array of parallel valleys to a perturbation in which one valley (marked with an arrow) is enlarged slightly. Colours in **b** and **c** denote drainage area, with blues corresponding to ridgelines and reds to valleys.

centre of the enlarged basin, such that it shrinks back to the size of its neighbours (Fig. 2b). At $\text{Pe} > 300$, an array of parallel, uniformly sized basins is unstable: enlarging the drainage area of any one basin causes the topographic divides to continue to migrate away from the centre of the enlarged basin, such that it widens at the expense of its neighbours (Fig. 2c). This instability propagates through the landscape until all drainage basins have either grown or shrunk to reach one of the two stable sizes. Supplementary Fig. 3 shows several drainage basins in Gabilan Mesa that may have experienced this instability. This transformation of the drainage network is comparable to an effect observed in laboratory analogue experiments²⁴, and may explain the uniform aspect ratios of basins that drain to linear boundaries²⁵.

The qualitative explanation for the critical value of Pe concerns the feedbacks that operate when a basin is enlarged. The increase in drainage area increases channel discharge, and therefore channel incision rate. Faster incision further deepens the basin, driving the surrounding ridgelines towards neighbouring basins and enlarging the drainage area—a positive feedback. Competing against this is a negative feedback in which deeper valleys with a sharper “V” shape are filled in faster by diffusive soil creep. For $\text{Pe} > \sim 300$, the positive feedback is stronger.

This instability explains the enlargement of some of the basins, but it does not explain why the enlarged basins develop tributaries on their side slopes (Fig. 2c). To determine why the tributaries grow, we performed a second experiment in which we subjected an inclined, planar surface with a prescribed Péclet number (intended to mimic the side slopes of a drainage basin) to a series of small-amplitude perturbations with a range of wavelengths, and measured the growth or decay rate of the perturbations (Fig. 3). The length scale L used to calculate Pe was

chosen to be the horizontal length of this sloping surface, which is the length of the incipient valleys. For $Pe < \sim 60$, perturbations of all wavelengths decay, and no tributary valleys form. At $Pe \approx 60$, wavelengths of roughly one-third of the slope length become unstable, and grow into incipient tributary valleys. The range of unstable wavelengths widens as Pe increases above this critical value. A similar wavelength selection has been inferred in analytical studies of incipient channelization under sheet flow^{26,27}.

To relate this instability to tributary valleys like those in Fig. 2c, we calculate Péclet numbers for the side slopes of drainage basins with and without tributaries in the numerical model solutions, using the horizontal lengths of the basin side slopes as L (Fig. 3 inset). This comparison confirms that the difference between valleys with and without tributaries is whether Pe for their side slopes is greater than or less than the critical value of ~ 60 . For example, the side slopes of the first-order basins in Fig. 2b have $Pe = 12$, whereas those of the second-order basins in Fig. 2c have $Pe = 75$. Thus, the basin-widening instability shown in Fig. 2 is accompanied by the formation of tributary valleys because the lengthening side slopes exceed the critical Pe for growth of incipient valleys.

Together, these two instabilities provide an explanation for the characteristic branching pattern of fine-scale tributary networks. In addition, our theory makes a testable prediction: second-order drainage basins should have Péclet numbers that exceed the critical value of ~ 300 (Fig. 2a), regardless of the absolute spatial scale of the landscape. To test this prediction, we calculated Pe for drainage basins in the Allegheny Plateau and Gabilan Mesa. This requires measurements of K/D , m and drainage basin length, L , each of which can be estimated from topographic data. K/D and m have been estimated²¹ for representative sites in each landscape from an independent analysis of the topography (Supplementary Table 2). Combining these values with our measurements of L (Methods), we compiled frequency distributions of Pe (Fig. 4). Unlike the drainage area distributions in Fig. 1, which differ between sites by a factor of four, the Pe distributions are quite similar. The critical range of $250 < Pe < 300$ (Fig. 2) falls between the modal values for first- and second-order basins in both landscapes, consistent with the prediction that most second-order basins should exceed this range, whereas most first-order basins should not. The match is slightly better for the Allegheny Plateau, whereas the gap between the modes occurs at approximately $300 < Pe < 350$ for Gabilan Mesa, but this difference is small compared with the scale discrepancy in Fig. 1. In addition, most first-order basins in both landscapes exceed the critical value of $Pe \approx 60$ for the development of incipient valleys (Figs 3 and 4). Thus, drainage

networks in both the Allegheny Plateau and Gabilan Mesa are consistent with our proposed mechanism for tributary network development, despite their difference in spatial scale.

This result implies that the ratio of coefficients describing the long-term rates of channel incision and soil creep, K/D , can be estimated from a drainage basin's stream order and size. Because m is typically ~ 0.5 (ref. 28, Supplementary Table 2), $Pe \approx KL^2/D$ as a rule of thumb. Thus, $K/D \approx Pe_n/L^2$, where Pe_n is the modal Péclet number for a basin of order n (from Fig. 4, for example, $Pe_2 \approx 600$). With this approach, it may be possible to use remote imagery to help calibrate long-term erosion laws, a result with promise for both terrestrial and planetary landscapes. The specific expressions presented here only apply to low-order, steady-state drainage basins shaped by regolith creep and ephemeral channel incision. Nonetheless, the principle that stream order and basin size provide a proxy for long-term process rates may also apply to higher-order drainage basins and landscapes shaped by different hillslope and channel erosion mechanisms. We show in the Supplementary Information that the branching mechanism documented in Figs 2 and 3 occurs even with different erosion and transport laws, provided that channel incision depends on drainage area and regolith transport depends on slope.

To understand how the geological, climatic and biological characteristics of a landscape control the scale of the drainage network, we performed an additional calculation. Gabilan Mesa is made of weaker rocks than the Allegheny Plateau, receives less rainfall in a more seasonal distribution, and has vegetation dominated by grasses rather than forest; it also has larger K/D (Supplementary Table 2) and therefore a finer-scale drainage network (Fig. 1). We determined K and D independently to discover whether this larger ratio reflects stronger channel incision, less mobile soil, or both. Combining long-term erosion rates inferred from cosmogenic ¹⁰Be in river sediment (Methods, Supplementary Table 1) with surveys of hillslope topography, we calculated D for the Allegheny Plateau and Gabilan Mesa, and divided D by K to obtain K (Methods, Supplementary Table 2). This calculation clearly shows that the main difference between the sites is the strength of channel incision: whereas D differs by only 25% (and is actually larger at Gabilan Mesa, the opposite of what would be expected if D were responsible for the scale difference), the channel incision rate factor for a reference drainage area, KA_{ref}^m , is roughly seven times larger at Gabilan Mesa (Supplementary Table 2). The magnitudes and uniformity of the soil diffusivities measured here are consistent with measurements from other landscapes in Mediterranean to humid climates²⁹, and probably reflect similar soil mechanical properties and bioturbation intensities. There are two likely and

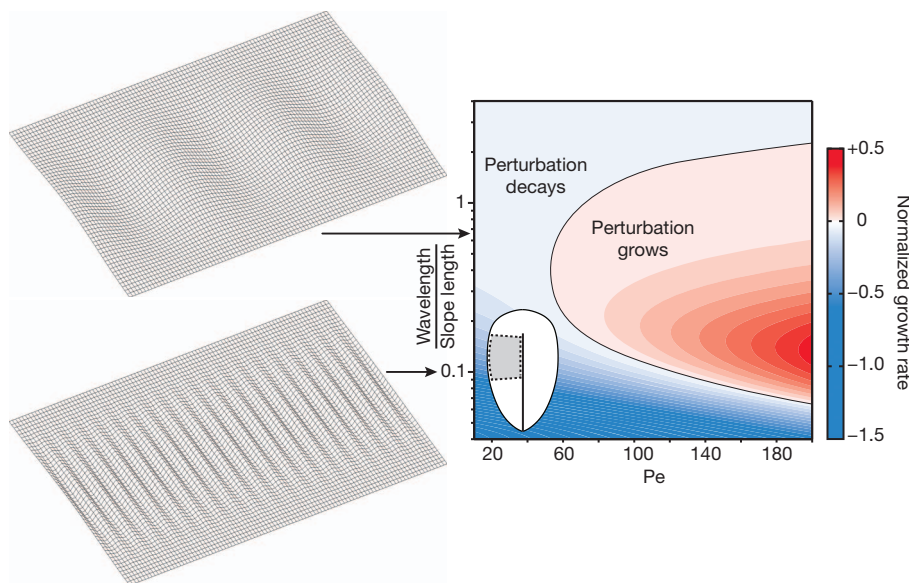


Figure 3 | Growth rates of incipient valleys on inclined slopes. Left, wire mesh plots showing vertically exaggerated examples of sinusoidal perturbations on inclined, planar slopes. Right, normalized growth rate (colour coded) of sinusoidal perturbations as a function of Péclet number, Pe , and aspect ratio (wavelength divided by slope length). Normalized growth rate is proportional to the fractional rate of change of the standard deviation of surface elevation after the background slope has been removed. Contour interval is 0.05, and the black line is the zero contour. Inset, illustration of the hypothetical position of such a slope within a larger drainage basin.

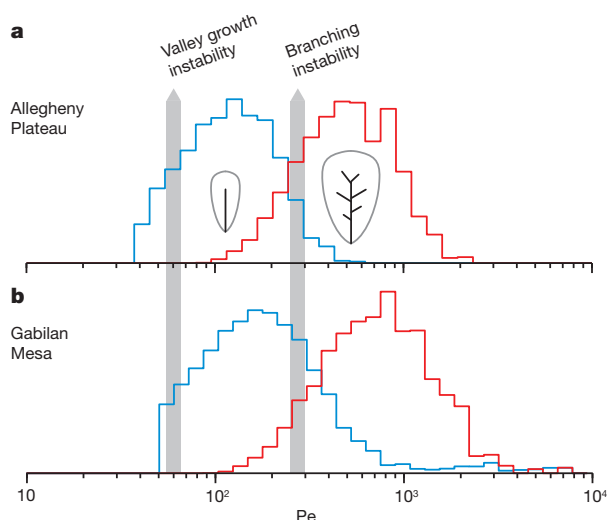


Figure 4 | Péclet number distributions of first- and second-order drainage basins in the study sites. a, Allegheny Plateau; b, Gabilan Mesa. Coloured lines are histograms with counts weighted by drainage basin area to compensate for the greater abundance of smaller basins. Inset sketches are examples of first- and second-order basins. Grey bars indicate critical values of Pe for valley growth (Fig. 3) and branching (Fig. 2). Basins analysed are the same as in Fig. 1.

non-exclusive explanations for the difference in channel incision: first, the weaker rocks at Gabilan Mesa are easier to erode; and second, highly seasonal rainfall and sparser vegetation at Gabilan Mesa promote runoff and inhibit infiltration, such that larger surface flows occur at a given drainage area and mean rainfall rate. The broader implication of this result is that the finely branched tips of river networks, which form both the skeleton and the circulatory system of Earth's landscapes, carry a fundamental signature of rock strength, climate and life. A remaining challenge is to further quantify this signature by relating specific materials, mechanisms and conditions to the rate constants used to describe landscape evolution over geologic time.

METHODS SUMMARY

Topographic analysis. We identified valleys in laser altimetry data as areas of anomalously positive contour curvature (Supplementary Fig. 1). We then traced valley networks over a larger region using a steepest-descent flow routing procedure and a drainage area threshold based on the curvature criterion, and assigned Strahler stream orders to these networks (Supplementary Fig. 2). Drainage basin areas, A , are determined just upstream of the junction with a higher-order link. We approximated²² drainage basin length as $L \approx \sqrt{3A}$, and calculated the Péclet number as $Pe = (K/D)(3A)^{m+1/2}$.

Landscape evolution model. The model^{21,23} solves an equation for the time evolution of an elevation surface due to rock uplift or boundary lowering, channel incision and downslope soil transport. We solved this equation forward in time with a finite difference method²³ on a rectangular grid with periodic x boundaries, lowering y boundaries, and a low-relief, randomly rough initial surface. We varied the Péclet number by varying K/D and performed 1,600 runs with different initial conditions to determine the probability densities in Fig. 2a.

Cosmogenic nuclides. We estimated long-term erosion rates by measuring the concentration of cosmogenic ^{10}Be in quartz grains in stream sediment (Supplementary Table 1) and converting these concentrations to surface erosion rates based on rates of ^{10}Be production and decay.

Calculation of K and D . We assumed steady state hillslope topography and calculated the soil transport coefficient as $D = -E/\nabla^2 z_h$, where E is the surface erosion rate determined from cosmogenic ^{10}Be and $\nabla^2 z_h$ is the Laplacian of elevation on hilltops, which has been measured from laser altimetry²¹ (Supplementary Table 2). The channel incision coefficient K was calculated by dividing D by previous estimates²¹ of D/K , and the channel incision coefficient for a reference drainage area, KA_{ref}^m , was calculated with previous estimates²¹ of m and $A_{\text{ref}} = 10^4 \text{ m}^2$ (Supplementary Table 2).

Full Methods and any associated references are available in the online version of the paper.

Received 16 April; accepted 27 September 2012.

- Mars Channel Working Group. Channels and valleys on Mars. *Geol. Soc. Am. Bull.* **94**, 1035–1054 (1983).
- Tomasko, M. G. *et al.* Rain, winds and haze during the Huygens probe's descent to Titan's surface. *Nature* **438**, 765–778 (2005).
- Leopold, L. B. & Langbein, W. B. The concept of entropy in landscape evolution. *Prof. Pap. US Geol. Surv.* **500-A**, 1–20 (1962).
- Shreve, R. L. Infinite topologically random channel networks. *J. Geol.* **75**, 178–186 (1967).
- Howard, A. Simulation of stream networks by headward growth and branching. *Geogr. Anal.* **3**, 29–50 (1971).
- Howard, A. Theoretical model of optimal drainage networks. *Wat. Resour. Res.* **26**, 2107–2117 (1990).
- Sun, T., Meakin, P. & Jøssang, T. Minimum energy dissipation model for river basin geometry. *Phys. Rev. E* **49**, 4865–4872 (1994).
- Rigon, R., Rinaldo, A., Rodriguez-Iturbe, I., Bras, R. L. & Ijjasz-Vasquez, E. Optimal channel networks: a framework for the study of river basin morphology. *Wat. Resour. Res.* **29**, 1635–1646 (1993).
- Rodriguez-Iturbe, I. & Rinaldo, A. *Fractal River Basins: Chance and Self-Organization* (Cambridge Univ. Press, 2001).
- Gilbert, G. K. *Report on the Geology of the Henry Mountains* (US Govt Printing Office, 1877).
- Horton, R. E. Erosional development of streams and their drainage basins: hydrophysical approach to quantitative morphology. *Bull. Geol. Soc. Am.* **56**, 275–370 (1945).
- Willgoose, G., Bras, R. L. & Rodriguez-Iturbe, I. Results from a new model of river basin evolution. *Earth Surf. Process. Landf.* **16**, 237–254 (1991).
- Howard, A. D. A detachment-limited model of drainage basin evolution. *Wat. Resour. Res.* **30**, 2261–2286 (1994).
- Tucker, G. E. & Slingerland, R. Drainage basin responses to climate change. *Wat. Resour. Res.* **33**, 2031–2047 (1997).
- Dunne, T. Formation and controls of channel networks. *Prog. Phys. Geogr.* **4**, 211–239 (1980).
- Strahler, A. N. Quantitative analysis of watershed geomorphology. *Trans. Am. Geophys. Union* **38**, 913–920 (1957).
- Schumm, S. A. Evolution of drainage systems and slopes in badlands at Perth Amboy, New Jersey. *Geol. Soc. Am. Bull.* **67**, 597–646 (1956).
- Kirchner, J. W. Statistical inevitability of Horton's laws and the apparent randomness of stream channel networks. *Geology* **21**, 591–594 (1993).
- Berg, T. M. *et al.* *Geologic Map of Pennsylvania* (Pennsylvania Geological Survey, 1980).
- Durham, D. L. Geology of the southern Salinas Valley area, California. *Prof. Pap. US Geol. Surv.* **819**, 1–111 (1974).
- Perron, J. T., Kirchner, J. W. & Dietrich, W. E. Formation of evenly spaced ridges and valleys. *Nature* **460**, 502–505 (2009).
- Montgomery, D. R. & Dietrich, W. E. Channel initiation and the problem of landscape scale. *Science* **255**, 826–830 (1992).
- Perron, J. T., Dietrich, W. E. & Kirchner, J. W. Controls on the spacing of first-order valleys. *J. Geophys. Res.* **113**, F04016, <http://dx.doi.org/10.1029/2007JF000977> (2008).
- Bonnet, S. Shrinking and splitting of drainage basins in orogenic landscapes from the migration of the main drainage divide. *Nature Geosci.* **2**, 766–771 (2009).
- Hovius, N. Regular spacing of drainage outlets from linear mountain belts. *Basin Res.* **8**, 29–44 (1996).
- Smith, T. R. & Bretherton, F. P. Stability and the conservation of mass in drainage basin evolution. *Wat. Resour. Res.* **8**, 1506–1529 (1972).
- Izumi, N. & Parker, G. Inception of channelization and drainage basin formation: upstream-driven theory. *J. Fluid Mech.* **283**, 341–363 (1995).
- Snyder, N. P., Whipple, K. X., Tucker, G. E. & Merritts, D. J. Landscape response to tectonic forcing: digital elevation model analysis of stream profiles in the Mendocino triple junction region, northern California. *Geol. Soc. Am. Bull.* **112**, 1250–1263 (2000).
- Fernandes, N. F. & Dietrich, W. E. Hillslope evolution by diffusive processes: the timescale for equilibrium adjustments. *Wat. Resour. Res.* **33**, 1307–1318 (1997).

Supplementary Information is available in the online version of the paper.

Acknowledgements This study was supported by the US National Science Foundation Geomorphology and Land Use Dynamics programme through award EAR-0951672 to J.T.P. and by the US Department of Defense through a National Defense Science and Engineering Graduate Fellowship to P.W.R. J.T.P. is a Scholar in the Canadian Institute for Advanced Research (CIFAR). The authors thank T. Clifton and G. Chmiel for assistance with sample preparation, and the Orradre family of San Ardo, California, and numerous landowners in Greene County, Pennsylvania, for granting access to their land.

Author Contributions J.T.P. conceived of the study, performed the numerical modelling, and wrote the paper. J.T.P., P.W.R. and K.L.F. conducted the fieldwork. P.W.R. processed the ^{10}Be samples, and P.W.R. and K.L.F. analysed the ^{10}Be data. J.T.P. and M.L. performed the topographic analyses.

Author Information Reprints and permissions information is available at www.nature.com/reprints. The authors declare no competing financial interests. Readers are welcome to comment on the online version of the paper. Correspondence and requests for materials should be addressed to J.T.P. (perron@mit.edu).

METHODS

Topographic analysis. We mapped valley networks in the central Gabilan Mesa (GM) in California, between the towns of King City and San Miguel, and the Waynesburg Hills area of the Allegheny Plateau (AP) in Pennsylvania and West Virginia, in the Dunkard Creek, Fish Creek and South Fork Ten Mile Creek watersheds, using a combination of airborne laser altimetry and the US National Elevation Dataset (NED). Laser altimetry for GM was acquired and processed by the National Center for Airborne Laser Mapping (NCALM), and laser altimetry for AP was produced by the PAMAP program of the Pennsylvania Department of Conservation and Natural Resources. Both laser altimetry data sets were filtered to remove vegetation and gridded to a horizontal point spacing of 1 m.

We first used the laser altimetry to map valley networks over subregions of roughly 25 km². We mapped valleys rather than channels to focus on the long-term topographic signature of channel incision rather than the most recent episodes (particularly since the latter may have been influenced by human land use). To objectively map the valley network, we used a procedure that identifies valleys as areas with anomalously convergent topography, as defined below, and then uses flow routing to bridge any gaps in the resulting map. The steps in this procedure are illustrated in Supplementary Fig. 1. First, elevations were smoothed with a Gaussian filter with a standard deviation of 10 m (GM) or 20 m (AP) to reduce fine-scale roughness (Supplementary Fig. 1a). Contour curvature (Supplementary Fig. 1b) was then calculated as^{30,31}:

$$\kappa_c = \frac{\left(\frac{\partial z}{\partial y}\right)^2 \frac{\partial^2 z}{\partial x^2} - 2 \frac{\partial z}{\partial x} \frac{\partial z}{\partial y} \frac{\partial^2 z}{\partial x \partial y} + \left(\frac{\partial z}{\partial x}\right)^2 \frac{\partial^2 z}{\partial y^2}}{\left(\left(\frac{\partial z}{\partial x}\right)^2 + \left(\frac{\partial z}{\partial y}\right)^2\right)^{\frac{3}{2}}} \quad (1)$$

Following a recently proposed procedure^{32,33}, we identified valleys as areas in which contour curvature is sufficiently positive that it deviates from the approximately Gaussian frequency distribution of curvature over most of the terrain. Specifically, we defined valleys as clusters of points with κ_c greater than two standard normal quantiles above the mean, which is the value at which the frequency distribution of κ_c begins to deviate substantially from a Gaussian distribution (Supplementary Fig. 1c). To exclude small, scattered local minima on hillslopes that satisfy the curvature criterion, we additionally required that the clusters be at least 10 m² in size. To exclude depressions in nearly planar topography (such as on alluviated valley floors) that are not part of the valley network, we required that clusters include at least one point with a drainage area (calculated with the D-infinity algorithm³⁴) greater than two standard normal quantiles above the mean.

Applying the curvature criterion produced a binary map of pixel clusters that lie within areas of strongly convergent topography (Supplementary Fig. 1d). We then routed flow over the entire landscape using a steepest-descent algorithm³⁵, identified the pixel in each cluster with the largest drainage area, and traced flow paths downslope from these pixels to the boundaries of the elevation grid. The resulting network of clusters joined by flow paths (Supplementary Fig. 1e) contained some parallel flow paths in areas with subtly varying slope directions, because the steepest-descent algorithm is insensitive to changes in flow direction of less than 45°. Parallel flow paths were merged (Supplementary Fig. 1f) by applying a morphological closing operation³⁶ with a disk-shaped structuring element with a radius of 10 m. The resulting skeleton was thinned to a network one pixel wide and pruned to remove spurs less than 10 m long (Supplementary Fig. 1g).

We then used this laser altimetry-based drainage network to calibrate a procedure for mapping the drainage network over a much larger area using coarser elevation data. In this procedure, the steepest-descent flow-routing algorithm was applied to the 10 m resolution (GM) or 30 m resolution (AP) NED over the same area covered by the laser altimetry, the drainage network was identified as the set of points with drainage area greater than a minimum value, A_{\min} , and the network was pruned to remove spurs less than 20 m (GM) or 30 m (AP) in length. The laser altimetry-based network was then compared with the NED-based network. For each study site, we identified the value of A_{\min} that maximized the number of valleys appearing as first-order links in both networks, and found $A_{\min} = 10,000$ m² for GM and 50,400 m² for AP. Using these values, we mapped the drainage networks over larger geographic areas with the NED, increasing our sample size from tens of drainage basins to several thousand, and assigned Strahler stream orders^{11,16} to the networks. For each first-order or second-order link in a network, we identified the associated drainage basin as the area that drains to the point on the link just upstream of the junction with a higher-order link. Comparison of the laser altimetry-based valley network with NED-based drainage basin boundaries (Supplementary Fig. 2) indicates that the calibrated analysis of NED elevation data correctly identifies the boundaries of most first-order and

second-order drainage basins, despite the coarser resolution. The mapped valley network corresponds to areas that have experienced significant channel incision over geologic time, but does not necessarily coincide with the extent of the currently active channel network³⁷. Recent episodes of channel incision may extend further upslope than the long-term average in some locations (such as the small gullies visible in Supplementary Fig. 2), while in others, valleys that have experienced significant long-term incision may lack currently active channels.

To transform drainage basin areas into the lengths, L , used to calculate the Péclet number, Pe , we used the well-known observation that drainage basin area scales with the square of basin length to a good approximation over many orders of magnitude in basin size³⁸. It has been found²² that $L \approx \sqrt{3A}$, with the factor of $\sqrt{3}$ describing the non-square shape of drainage basins. Thus, for a drainage basin with an area A , we calculate $Pe = (K/D)(3A)^{m+\frac{1}{2}}$. We used drainage area to calculate equivalent basin lengths rather than measuring basin length directly because drainage area is an integrated measure of basin size that is less sensitive to differences in basin shape.

In addition to this quantitative test of the proposed mechanisms for the development of tributary networks, visual inspection of the topography provides a qualitative means of identifying evidence that these mechanisms have operated in a landscape. For example, Supplementary Fig. 3 shows several adjacent drainage basins that appear to have undergone the instabilities illustrated in Figs 2c and 3.

Landscape evolution model. The landscape evolution model is a modified version of the Tadpole model^{21,23}, which solves an equation for the time evolution of an elevation surface, $z(x, y)$, derived^{13,23,39} from conservation of mass and rate laws for soil creep and channel incision,

$$\frac{\partial z}{\partial t} = DV^2 z - KA^m |\nabla z| + E \quad (2)$$

where z is elevation, t is time, D is the soil transport coefficient, A is drainage area, K and m are constants, and E is the rate of boundary lowering. Elevation is measured relative to the lowering boundary, such that E appears in equation (2) as a surface uplift rate. The linear diffusion term is based on the theoretical expectation^{40,41}, supported by field measurements^{42–47}, that soil creep flux on hillslopes with gentle to moderate gradients is driven by isotropic disturbance (due to animal burrowing, for example) and gravitational settling, such that soil flux is proportional to the topographic gradient. The nonlinear kinematic wave term is based on studies of erosional channels^{28,48–50} suggesting that channel incision rate is proportional to the rate of energy expenditure by the flow of water⁵¹, or ‘stream power’, per unit area of the bed under normal flow. A term with the same form—that is, a power law dependence of channel incision rate on drainage area and slope—is obtained if incision rate is instead assumed to be proportional to shear stress⁵².

The linear diffusion term describes the smoothing effect of slope-dependent soil creep, and the nonlinear kinematic wave term describes how changes in elevation at the boundaries propagate upslope through the landscape, including a strong positive feedback in valley incision through the dependence on drainage area. The boundary lowering (or, equivalently, uplift relative to the boundaries), E , drives the development of the landscape by steepening the topography. The competition between these effects gives rise to a landscape with smooth, concave down ridgelines and sharper, concave-up valleys. As noted in the main text, the Péclet number describes the relative magnitudes of the soil creep and channel incision terms²³.

The use of a continuum model with constant coefficients implicitly averages in space and time over many erosion and transport events, which would be difficult to describe individually. For example, this model assumes that channel incision and soil creep can occur in the same location, in a time-averaged sense, and is therefore appropriate for low-order drainage basins in which episodes of channelization are interspersed with periods of diffusive infilling (Supplementary Fig. 4). The modelling approach employed here makes it possible to explore the main controls on landscape form in terms of a few parameters.

Equation (2) was solved numerically on a 300×100 ($N_x \times N_y$) regular grid with $\Delta x, \Delta y = 5$ m using a finite difference method²³. The grid was subject to a constant lowering of the y boundaries intended to mimic a set of parallel, incising channels. The x boundaries were periodic, such that the topography repeats with a period equal to the length of the domain in the x direction. Experiments began with an initial surface of uncorrelated Gaussian noise with a variance of 1 m², and continued until the topography reached a dynamic equilibrium in which all points were lowering at the same rate. In each experiment, incipient drainage basins formed at the lowering y boundaries and advanced towards the interior of the grid in a direction perpendicular to the y boundaries. A central drainage divide formed where the basins advancing in opposite directions met roughly halfway between the y boundaries. Supplementary Fig. 5 shows steady-state solutions for three experiments.

We varied the Péclet number in the model by setting $m = 0.5$ and changing the ratio K/D . The length scale L was defined as half of the length of the domain in the y direction, which is the approximate length of drainage basins that extend from the central drainage divide to one of the lowering boundaries. In each model solution, we identified drainage basin outlets as points adjacent to one of the lowering boundaries with $\nabla^2 z \geq 0.005 \text{ m}^{-1}$, measured the drainage area at each outlet, and normalized the areas by L^2 . While the mean characteristics of drainage basins at steady state for a given Péclet number are independent of initial conditions, the characteristics of individual basins are sensitive to initial conditions, and vary about the mean⁵³. To better characterize the size distribution of drainage basins for a given Pe, we performed an ensemble of 1,600 simulations with identical parameters and boundary conditions, but different initial surfaces. A probability density map of the resulting population of more than 60,000 drainage basins as a function of drainage basin size and Péclet number reveals a transition from a unimodal to a bimodal size distribution over the interval $250 < \text{Pe} < 300$ (Fig. 2).

Cosmogenic nuclides. We estimated long-term erosion rates in AP and GM by measuring the concentration of cosmogenic ^{10}Be in quartz grains in stream sediment, following an established procedure⁵⁴. This yields erosion rates that are spatially averaged over the sampled drainage basins and temporally averaged over the characteristic time of ^{10}Be accumulation in the sampled quartz, which is typically 10^3 – 10^5 yr in most eroding landscapes. We collected sediment samples from three drainage basins in AP and two in GM in 2009 and 2010. All sampled basins have quartz-rich lithologies (sandstone in AP, sandstone and quartzite conglomerate in GM). We separated and dissolved quartz from each sample following a standard procedure⁵⁵ and isolated ^{10}Be using cation exchange⁵⁶. $^{10}\text{Be}/^{9}\text{Be}$ ratios were measured with Accelerator Mass Spectrometry at PRIME Lab, Purdue University, in February 2011. The mean location and elevation of each drainage basin were used to determine ^{10}Be production rates⁵⁷. For small drainage basins like those analysed here, the uncertainty introduced by using a single location and elevation to approximate the production rate is typically much smaller than uncertainties associated with other assumptions required to calculate basin-averaged erosion rates⁵⁷. A correction factor accounting for topographic shielding from cosmic rays⁵⁷ was calculated at each pixel in a 4 m per pixel version of the laser altimetry map of GM, and the mean value for each drainage basin was used. The shielding correction at all of the AP sites was found to be negligible.

Because the sediments that make up GM are young, and might therefore have been exposed at the surface recently, we corrected the ^{10}Be concentrations in the GM samples by subtracting the inherited concentration measured in three shielded samples with the same lithology. The shielded samples were collected in 2002 from recently excavated drill platforms near the 2009–10 surface sample locations. When the samples were originally buried to depths much deeper than 1 m, they were shielded from subsequent production and the ^{10}Be concentration was altered only by radioactive decay. The shielded samples were processed at the University of California, Berkeley, and $^{10}\text{Be}/^{9}\text{Be}$ ratios were measured with Accelerator Mass Spectrometry at Lawrence Livermore National Laboratory in 2005. The mean ^{10}Be concentration of the shielded samples was subtracted from the ^{10}Be concentrations of the surface samples to determine the ^{10}Be concentration accumulated during recent exposure (Supplementary Table 1). Given the close vertical proximity of the shielded samples and the 1.36 Myr half-life of ^{10}Be , we interpret the difference in ^{10}Be concentration in the shielded samples to reflect slightly different source and transport histories rather than different durations of burial.

^{10}Be concentrations of the surface samples at both sites were converted into erosion rates using the CRONUS calculator⁵⁷, version 2.2. Measured quantities used in this calculation, and the resulting erosion rates, are summarized in Supplementary Table 1. The uniform relief of both landscapes and the consistency of the erosion rates among sampling locations suggest that these rates are representative of the surrounding landscape. We therefore average the erosion rates to arrive at a single rate for each landscape: $92 \pm 5 \text{ t km}^{-2} \text{ yr}^{-1}$ for AP, and $206 \pm 27 \text{ t km}^{-2} \text{ yr}^{-1}$ for GM. The uncertainties were taken to be the larger of the standard error of the mean of the site-specific rates and the pooled site-specific uncertainties.

For comparison with the model predictions, these mass removal rates must be converted to surface erosion rates with units of $[\text{L T}^{-1}]$. Dividing by measured soil densities of $1,660 \pm 110 \text{ kg m}^{-3}$ in AP and $1,400 \pm 100 \text{ kg m}^{-3}$ in GM yields surface erosion rates of $55 \pm 5 \text{ m Myr}^{-1}$ in AP and $147 \pm 22 \text{ m Myr}^{-1}$ in GM. This calculation assumes that chemical mass removal by dissolution is negligible.

Calculation of K and D . At steady state ($\partial z/\partial t = 0$), the surface erosion rate at any location equals the boundary lowering rate, and equation (2) reduces to:

$$-E = D\nabla^2 z - KA^m|\nabla z| \quad (3)$$

On hilltops, where drainage area and slope are small, $A^m|\nabla z| \approx 0$, and

$$D = -\frac{E}{\nabla^2 z_h} \quad (4)$$

where $\nabla^2 z_h$ is the Laplacian of elevation on hilltops. We used equation (4) to estimate D for AP and GM, using the surface erosion rates measured with cosmogenic nuclides as an estimate of E , and the hilltop Laplacian measured in ref. 21 (Supplementary Table 2). The uniform value of the Laplacian over each hillslope supports the steady-state assumption in equation (3). Given D and an estimate of D/K (ref. 21), it is straightforward to calculate K . The units of K depend on the value of m . To facilitate comparisons among different landscapes where m can vary, we compare the quantity KA_{ref}^m , where A_{ref} is a reference drainage area, here taken to be 10^4 m^2 . The estimated m values for AP and GM are very similar (Supplementary Table 2), so the difference in KA_{ref}^m is due almost entirely to the difference in K . Note that KA_{ref}^m is faster than the actual channel incision rate, which also depends on slope.

30. Mitášová, H. & Hofierka, J. Interpolation by regularized spline with tension: II. Application to terrain modeling and surface geometry analysis. *Math. Geol.* **25**, 657–669 (1993).
31. Peckham, S. D. in *Geomorphometry 2011* (eds Hengl, T. Evans, I. S., Wilson, J. P. & Gould, M.) 27–30 (2011); available at <http://geomorphometry.org/Peckham2011a> (2011).
32. Lashermes, B., Foufoula-Georgiou, E. & Dietrich, W. E. Channel network extraction from high resolution topography using wavelets. *Geophys. Res. Lett.* **34**, L23S04, <http://dx.doi.org/10.1029/2007GL031140> (2007).
33. Passalacqua, P., Do Trung, T., Foufoula-Georgiou, E., Sapiro, G. & Dietrich, W. E. A geometric framework for channel network extraction from lidar: nonlinear diffusion and geodesic paths. *J. Geophys. Res.* **115**, F01002, <http://dx.doi.org/10.1029/2009JF001254> (2010).
34. Tarboton, D. G. A new method for the determination of flow directions and upslope areas in grid digital elevation models. *Wat. Resour. Res.* **33**, 309–319 (1997).
35. Jensen, S. K. & Domingue, J. O. Extracting topographic structure from digital elevation data for geographic information system analysis. *Photogramm. Eng. Remote Sensing* **54**, 1593–1600 (1988).
36. Gonzalez, R. C., Woods, R. E. & Eddins, S. L. *Digital Image Processing Using MATLAB* (Pearson Prentice Hall, 2004).
37. Dietrich, W. E. & Dunne, T. in *Channel Network Hydrology* (eds Beven, K. & Kirkby, M. J.) 175–219 (Wiley & Sons, 1993).
38. Hack, J. T. Studies of longitudinal stream profiles in Virginia and Maryland. *Prof. Pap. US Geol. Surv.* **294-B**, 1–97 (1957).
39. Tucker, G. E. & Slingerland, R. Predicting sediment flux from fold and thrust belts. *Basin Res.* **8**, 329–349 (1996).
40. Culling, W. E. H. Analytical theory of erosion. *J. Geol.* **68**, 336–344 (1960).
41. Culling, W. E. H. Soil creep and the development of hillside slopes. *J. Geol.* **71**, 127–161 (1963).
42. Nash, D. Morphologic dating of degraded normal fault scarps. *J. Geol.* **88**, 353–360 (1980).
43. Hanks, T. C., Bucknam, R. C., Lajoie, K. R. & Wallace, R. E. Modification of wave-cut and faulting-controlled landforms. *J. Geophys. Res.* **89**, 5771–5790 (1984).
44. Rosenbloom, N. A. & Anderson, R. S. Hillslope and channel evolution in a marine terraced landscape, Santa Cruz, California. *J. Geophys. Res.* **99**, 14013–14029 (1994).
45. Monaghan, M. C., McKean, J., Dietrich, W. & Klein, J. ^{10}Be chronometry of bedrock-to-soil conversion rates. *Earth Planet. Sci. Lett.* **111**, 483–492 (1992).
46. McKean, J. A., Dietrich, W. E., Finkel, R. C., Southon, J. R. & Caffee, M. W. Quantification of soil production and downslope creep rates from cosmogenic ^{10}Be accumulations on a hillslope profile. *Geology* **21**, 343–346 (1993).
47. Small, E. E., Anderson, R. S. & Hancock, G. S. Estimates of the rate of regolith production using ^{10}Be and ^{26}Al from an alpine hillslope. *Geomorphology* **27**, 131–150 (1999).
48. Seidl, M. A., Dietrich, W. E. & Kirchner, J. W. Longitudinal profile development into bedrock: an analysis of Hawaiian channels. *J. Geol.* **102**, 457–474 (1994).
49. Stock, J. D. & Montgomery, D. R. Geologic constraints on bedrock river incision using the stream power law. *J. Geophys. Res.* **104**, 4983–4994 (1999).
50. Snyder, N. P., Whipple, K. X., Tucker, G. E. & Merritts, D. J. Channel response to tectonic forcing: field analysis of stream morphology and hydrology in the Mendocino triple junction region, northern California. *Geomorphology* **53**, 97–127 (2003).
51. Seidl, M. A. & Dietrich, W. E. The problem of channel erosion into bedrock. *Catena* **23**, 101–124 (1992).
52. Howard, A. D. & Kerby, G. Channel changes in badlands. *Bull. Geol. Soc. Am.* **94**, 739–752 (1983).
53. Perron, J. T. & Fagherazzi, S. The legacy of initial conditions in landscape evolution. *Earth Surf. Process. Landf.* **37**, 52–63 (2012).
54. Granger, D., Kirchner, J. & Finkel, R. Spatially averaged long-term erosion rates measured from in situ-produced cosmogenic nuclides in alluvial sediment. *J. Geol.* **104**, 249–257 (1996).
55. Kohl, C. P. & Nishiizumi, K. Chemical isolation of quartz for measurement of in-situ-produced cosmogenic nuclides. *Geochim. Cosmochim. Acta* **56**, 3583–3587 (1992).
56. Ditchburn, R. G. & Whitehead, N. E. The separation of ^{10}Be from silicates. In *Proc. Third Workshop of the South Pacific Environmental Radioactivity Association* 4–7 (1994).
57. Balco, G., Stone, J. O., Lifton, N. A. & Dunai, T. J. A complete and easily accessible means of calculating surface exposure ages or erosion rates from ^{10}Be and ^{26}Al measurements. *Quat. Geochronol.* **3**, 174–195 (2008).

Identification of a rudimentary neural crest in a non-vertebrate chordate

Philip Barron Abitua¹, Eileen Wagner¹, Ignacio A. Navarrete¹ & Michael Levine¹

Neural crest arises at the neural plate border, expresses a core set of regulatory genes and produces a diverse array of cell types, including ectomesenchyme derivatives that elaborate the vertebrate head^{1,2}. The evolution of neural crest has been proposed to be a key event leading to the appearance of new cell types that fostered the transition from filter feeding to active predation in ancestral vertebrates³. However, the origin of neural crest remains controversial, as homologous cell types have not been unambiguously identified in non-vertebrate chordates^{1,4}. Here we show that the tunicate *Ciona intestinalis* possesses a cephalic melanocyte lineage (a9.49) similar to neural crest that can be reprogrammed into migrating 'ectomesenchyme' by the targeted misexpression of *Twist* (also known as twist-like 2). Our results suggest that the neural crest melanocyte regulatory network pre-dated the divergence of tunicates and vertebrates. We propose that the co-option of mesenchyme determinants, such as *Twist*, into the neural plate ectoderm was crucial to the emergence of the vertebrate 'new head'³.

Whole-genome phylogenetic analyses place the tunicates as the true sister clade to vertebrates⁵, and consequently they are well suited for investigating the evolutionary origins of the neural crest. In a previous report on the mangrove tunicate, a migratory cell population originating from the vicinity of the neural tube was likened to the neural crest⁶. However, subsequent studies of eleven additional tunicates provided unequivocal evidence that these cells arise from the mesoderm flanking the neural tube⁷. It was then suggested that a mesoderm-derived mesenchyme lineage (A7.6) in *Ciona* possessed some of the properties of the neural crest⁸, although these cells do not arise from the neural plate border and lack expression of key neural crest regulatory genes.

We present evidence that the bilateral a9.49 pigment cell lineage of *Ciona* embryos represents a rudimentary neural crest. It arises at the neural plate border and expresses several neural plate border genes, as well as a number of neural crest specification genes, including *Id*, *Snail*, *Ets* and *FoxD*^{8–13} (Fig. 1a and Supplementary Fig. 1). In vertebrates, MITF (microphthalmia-associated transcription factor) directly activates several target genes required for melanogenesis of neural-crest-derived melanocytes, including *TYR* and *TYRP1* (ref. 14). In tunicates, *Mitf* is expressed in the a9.49 lineage¹⁵, which can be labelled by electroporation of a reporter, *Mitf*>*lacZ* (*Mitf* regulatory sequence driving the expression of *lacZ*) (Fig. 1b). The posterior daughters of the lineage (a10.97) intercalate at the dorsal midline and form the gravity-sensing otolith and melanocyte of the light-detecting ocellus (Fig. 1c)¹⁶. We sought to understand the basis for the differential specification of these pigmented cells.

Wnt signalling has a conserved role in neural crest induction, and promotes melanocyte formation from cephalic neural crest in zebrafish¹⁷. Both a10.97 cells express *Tcf/Lef*, the transcriptional effector of Wnt signalling¹³, thus Wnt may also have a role in *Ciona* melanogenesis. We found that *Wnt7* is expressed along the dorsal midline just posterior to the presumptive ocellus (Fig. 1b), suggesting that it might serve

as a positional cue to trigger differentiation of the posterior a10.97 melanocyte.

Wnt signalling was selectively perturbed in the a9.49 lineage by the targeted misexpression of *Wnt7*, stable β -catenin and dominant-negative *Tcf* (ΔTcf , which lacks the β -catenin amino-terminal binding domain) using the *Mitf* enhancer (Fig. 1c–f). A $\beta\gamma$ -crystallin reporter was used to distinguish the melanocytes, as it is expressed in the otolith but not the ocellus (Fig. 1c). Both pigmented precursors were converted

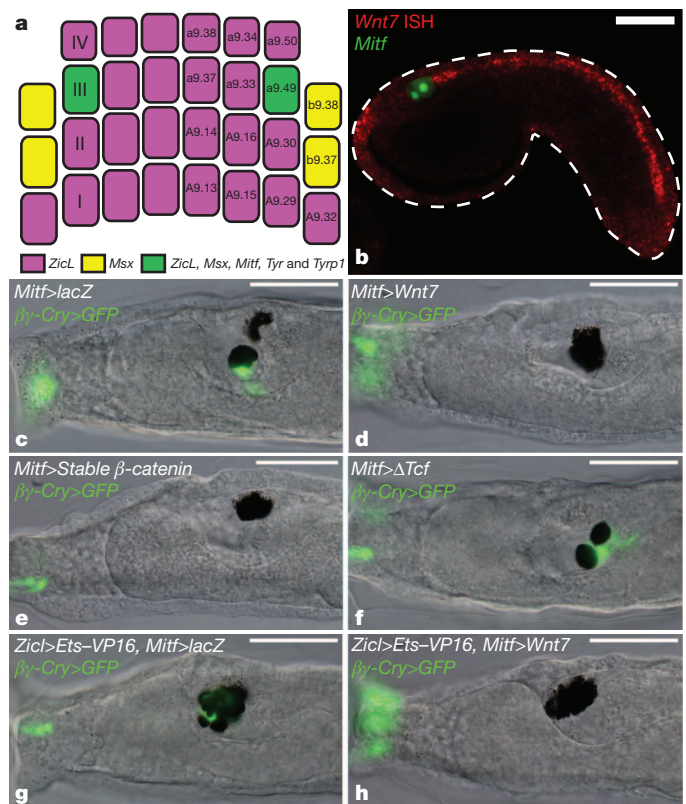


Figure 1 | Wnt signalling promotes ocellus formation. **a**, Schematic of neural plate at gastrulation, indicating the lineage-specific expression of enhancers in this study. **b**, Tailbud embryo electroporated with *Mitf*>*lacZ*, detected with an antibody (green) and hybridized with a *Wnt7* probe (red). ISH, *in situ* hybridization. **c–f**, Larvae electroporated with $\beta\gamma$ -crystallin>*GFP* ($\beta\gamma$ -cry>*GFP*) marks the otolith and anterior palps. **c**, Larva co-electroporated with *Mitf*>*lacZ* (166 of 196 had an otolith and ocellus). **d**, Larva co-electroporated with *Mitf*>*Wnt7* (172 of 205 had two ocelli). **e**, Larva co-electroporated with *Mitf*>stable β -catenin (189 of 205 had two ocelli). **f**, Larva co-electroporated with *Mitf*> ΔTcf (dominant-negative *Tcf*) (100 of 205 had two otoliths). **g, h**, Larvae electroporated with *ZicL*>*Ets*-VP16 and $\beta\gamma$ -crystallin>*GFP*. **g**, Larva co-electroporated with *Mitf*>*lacZ* (75 of 100 had extra otoliths). **h**, Larva co-electroporated with *Mitf*>*Wnt7* (only 11 of 100 had extra otoliths). Scale bars, 50 μ m.

¹Center for Integrative Genomics, Division of Genetics, Genomics and Development, Department of Molecular and Cell Biology, University of California, Berkeley, California 94720, USA.

to ocelli after misexpression of *Wnt7* in the a9.49 lineage (*Wnt7* is not normally expressed in this lineage) (Fig. 1d). A similar transformation was observed after targeted expression of a stabilized form of β -catenin, the coactivator of *Tcf* (Fig. 1e). In contrast, misexpression of a dominant-negative form of *Tcf* (*Mitf*> Δ *Tcf*) produced the reciprocal transformation: both a10.97 melanocytes differentiated into otoliths and expressed the β -crystallin reporter (Fig. 1f).

Supernumerary otoliths were induced by the expression of a constitutively active form of the transcription factor for MAPK signalling, *Ets1/2* (also known as *Ets/pointed2*) (Fig. 1g and Supplementary Fig. 2). Co-electroporation of *Mitf*>*Wnt7* transformed these extra otoliths into ocelli (Fig. 1h). These results suggest that *Wnt7* signalling is crucial in transforming otoliths to ocelli; it specifies the ocellus and suppresses the development of the otolith. To determine the underlying mechanism we sought to identify neural crest specification genes that are selectively activated in the presumptive ocellus in response to *Wnt7* signalling.

In vertebrates, *FoxD3* has been shown to repress melanogenesis of neural crest cells through downregulation of *Mitf*^{4,18}. In *Ciona*, *FoxD* is activated directly by the accumulation of nuclear β -catenin in the early embryo, indicating a potential link between *Wnt* signalling and *FoxD* expression¹⁹. We found that *FoxD* is selectively expressed in the presumptive ocellus, (Fig. 2a, b) adjacent to the site of *Wnt7* expression in the dorsal midline (Fig. 1b). A *FoxD* enhancer recapitulates this

expression in the presumptive ocellus (Fig. 2c), and is dependent on *Wnt* signalling, as expression is lost in the presence of Δ *Tcf* (Fig. 2d).

To investigate the role of *FoxD* in melanogenesis, we expressed variants of *FoxD* in the midline of the CNS, including the a9.49 lineage, using 5' regulatory sequences from the *Msx* gene (Fig. 1a and Supplementary Fig. 3). Targeted expression of either full-length *FoxD* or the N-terminal third of *FoxD* (non-DNA binding) abolished expression of the *Mitf*>*GFP* reporter gene (Fig. 2e, f and Supplementary Fig. 3). However, misexpression of a constitutive repressor form of *FoxD* (DNA-binding domain fused to a WRPW repressor motif) had little effect on *Mitf* expression (Supplementary Fig. 3). These results suggest that *FoxD* represses *Mitf* independent of its DNA-binding domain, which is consistent with its mode of regulation in avian embryos, in which *Foxd3*-mediated repression of *Mitf* is thought to occur through the sequestration of the transcriptional activator Pax3 (ref. 18).

Our results suggest a simple gene regulatory network (*Wnt7* signalling activates *FoxD*, which inhibits *Mitf* expression) for the differential specification of the otolith and ocellus in the *Ciona* tadpole (Supplementary Fig. 4). Both a10.97 cells express *Mitf* before neurulation and during the convergence of the two cells along the dorsal midline of the anterior neural tube. Subsequently, the posterior a10.97 cell receives a localized *Wnt7* signal and activates *FoxD*, which attenuates *Mitf* leading to diminished pigmentation in the ocellus. *Mitf* expression is sustained in the anterior a10.97 cell, which forms the densely pigmented otolith.

Notably, zebrafish uses a very similar mechanism to specify neural crest-derived pigmented melanophores and iridophores, which derive

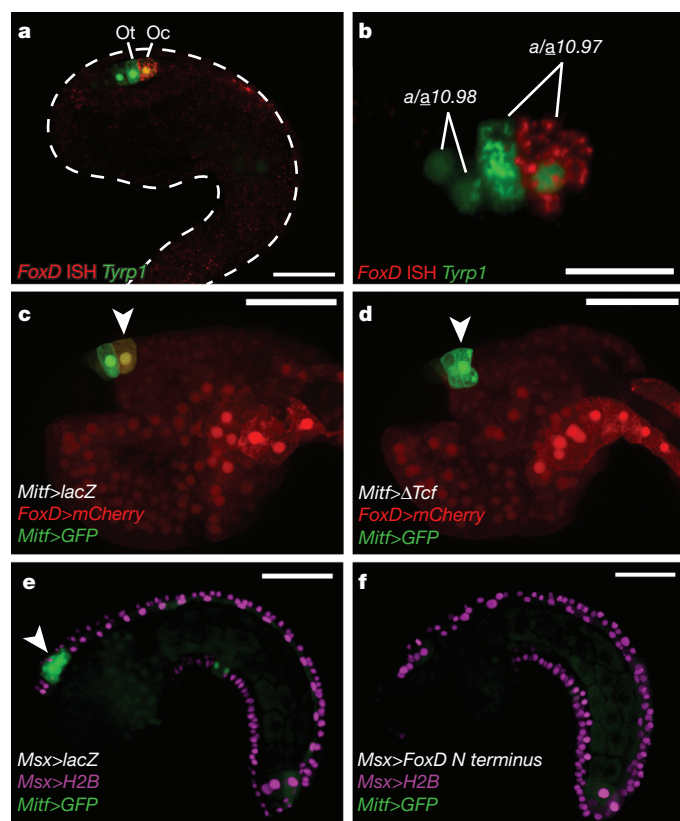


Figure 2 | *FoxD* represses *Mitf* in the ocellus. **a**, Tailbud embryo electroporated with *Tyrp1*>*lacZ* detected with an antibody (green) marking the precursors of the otolith and ocellus, and hybridized with a *FoxD* probe (red). **b**, *FoxD* is expressed in the posterior a10.97 cell. **c**, **d**, Tailbud embryos electroporated with *FoxD*>*mCherry* and *Mitf*>*GFP*. Arrowheads mark the presumptive ocellus. **c**, Co-electroporated with *Mitf*>*lacZ* (126 of 180 expressed *mCherry*). **d**, Co-electroporated with *Mitf*> Δ *Tcf* (only 30 of 180 expressed *mCherry*). **e**, **f**, Tailbuds electroporated with *Msx*>histone *H2B* *mCherry* and *Mitf*>*GFP*. Arrowhead shows GFP expression in a9.49 derivatives. **e**, Co-electroporated with *Msx*>*lacZ*. **f**, Co-electroporated with *Msx*>*FoxD* N terminus. Scale bars, 50 μ m (**a**, **c**–**f**); 25 μ m (**b**). Oc, ocellus; Ot, otolith.

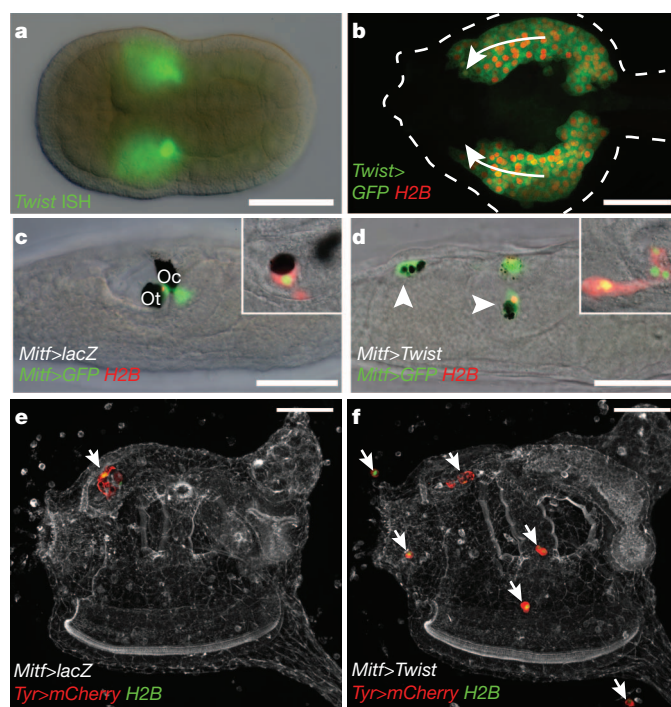


Figure 3 | *Twist* reprograms the a9.49 lineage. **a**, Neurula hybridized with a *Twist* probe. **b**, Tailbud embryo during mesenchyme migration (arrows) co-electroporated with *Twist*>*GFP* and *Twist*>*H2B* *mCherry*. **c**, **d**, Larvae electroporated with *Mitf*>*GFP* and *Mitf*>*H2B* *mCherry*. Insets show lineage marked with *Tyr*>*mCherry* and *Tyr*>*H2B* YFP (yellow fluorescent protein); both the *Tyr* and *Mitf* reporters label the same a9.49 cells. **c**, Co-electroporated with *Mitf*>*lacZ*. Oc, ocellus; Ot, otolith. **d**, Co-electroporated with *Mitf*>*Twist*. Arrowheads indicate ectopic position of a9.49 derivatives. **e**, **f**, Juveniles electroporated with *Tyr*>*mCherry* and *Tyr*>*H2B* YFP. Arrows identify the position of a9.49 derivatives. **e**, Juvenile co-electroporated with *Mitf*>*lacZ*. **f**, Co-electroporated with *Mitf*>*Twist*. Scale bars, 50 μ m.

from a common bipotent *Mitf*⁺ progenitor¹⁴. The conservation of this network strengthens the argument that the a9.49 lineage of *Ciona* represents a rudimentary neural crest. However, the a9.49 lineage lacks some of the defining properties of cephalic neural crest, such as long-range migration and the potential to form ectomesenchyme derivatives.

We therefore sought to identify vertebrate neural crest determinants that are not expressed in the *Ciona* a9.49 lineage. In vertebrates, the craniofacial mesenchyme is derived from primary mesoderm and the ectomesenchyme arising from cephalic neural crest^{2,20}. Both sources of cranial mesenchyme express the conserved mesodermal determinant *Twist*²¹ and produce diverse cranial tissues including muscle, cartilage and bone. In tetrapods, it seems that only the cephalic neural crest expresses *Twist* and produces ectomesenchyme^{21–23}, whereas trunk neural crest lacks *Twist* expression and generates non-ectomesenchymal derivatives (for example, neurons, glia and melanocytes)². Disruption of *Twist* activity causes severe cephalic neural crest phenotypes, including defects in cell migration and survival, as well as morphological defects of the skull vault and heart^{21,22,24}.

There are three *Twist*-related genes in *Ciona*. In this study we focused on the gene most similar to *Twist1* in vertebrates (Supplementary Fig. 5). In *Ciona*, *Twist* is expressed solely in mesoderm-derived

mesenchyme (Fig. 3a). It is not expressed in any region of the neural plate, including the a9.49 lineage. *Twist*-expressing mesoderm undergoes long-range migration (Fig. 3b) and produces a number of diverse tissues in juveniles and adults, including body-wall muscles, tunic cells (which populate the protective covering of the adult) and blood cells²⁵. The migration and differentiation of these mesoderm tissues are inhibited when *Twist* expression is reduced²⁵.

To determine whether ectomesenchyme could be formed in *Ciona*, we misexpressed *Twist* in the a9.49 lineage using the *Mitf* enhancer (Fig. 3c, d). The manipulated cells exhibit a mesenchymal phenotype, including protrusive activity, proliferation and long-range migration, which was not observed by the misexpression of other related genes (Supplementary Video 1 and Supplementary Fig. 6). Moreover, misexpression of *Twist* in the notochord and motor ganglion causes some disruptions in terminal differentiation, but does not transform these tissues into mesenchyme (Supplementary Fig. 7). The reprogrammed a9.49 cells exhibit expression of mesenchyme genes, including *Erg* (Supplementary Fig. 8), which is expressed in the ectomesenchyme of mouse embryos²⁶. The affected lineage was visualized in juveniles using reporters for *Tyr*, a gene that is activated by *Mitf* in melanocytes¹⁴ (Fig. 3e, f). Normally the a9.49 derivatives are located solely in an anterior region of the CNS (Fig. 3e). In contrast, embryos expressing

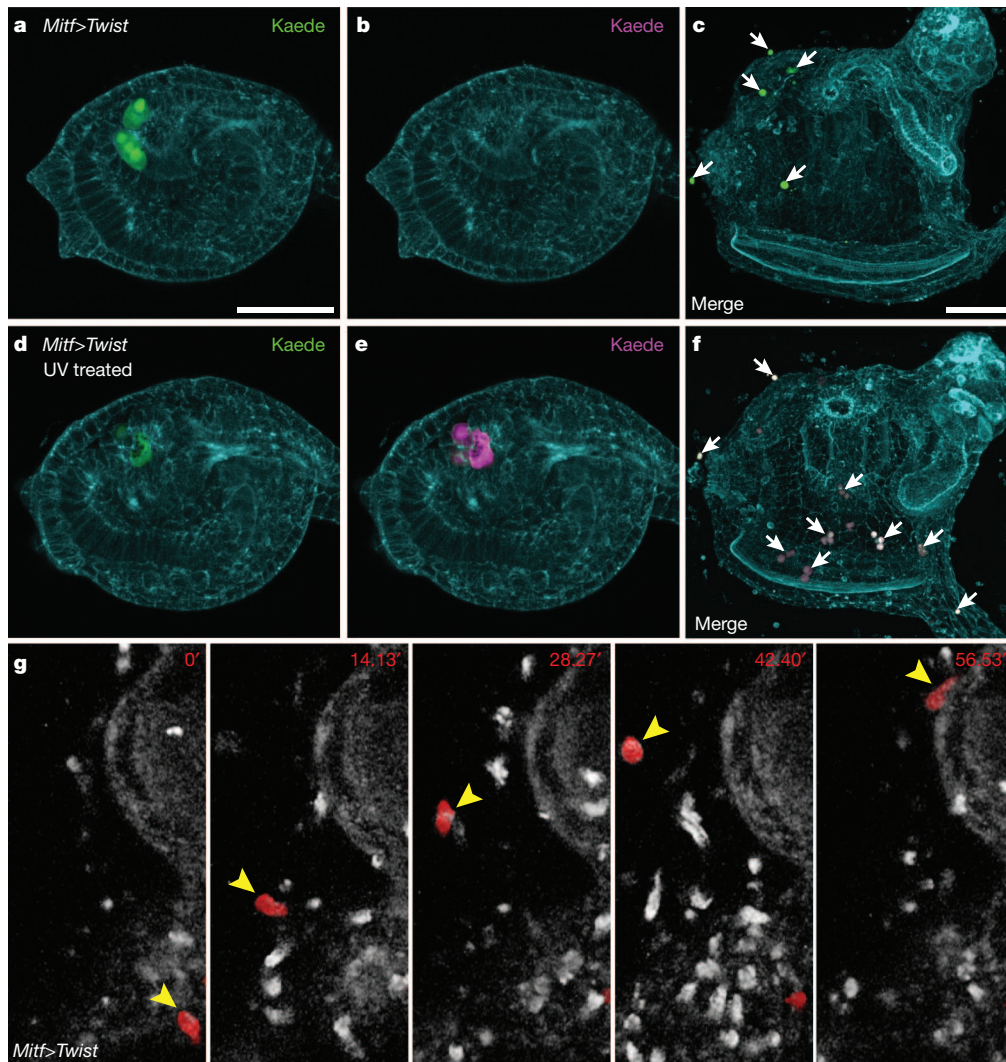


Figure 4 | Lineage tracing of reprogrammed a9.49 cells. a–f, *Ciona* electroporated with *Mitf*>*Twist* and *Tyr*>*Kaede*. a, b, Non-ultraviolet (UV)-treated tailbud embryo shows only green fluorescence. c, Embryo never exposed to UV results in a juvenile with only green ectopic cells (arrows). d, e, UV-treated tailbud embryos show green and red fluorescence, respectively.

f, UV-treated embryo results in a juvenile with green and red ectopic cells (arrows). g, Time-lapse frames of Supplementary Video 2 (frames were taken from the times indicated) shows the migration of reprogrammed a9.49 cell labelled with *Tyr*>*mCherry* (arrowhead). The white cells correspond to endogenous tunic cells. Scale bars, 50 μ m.

Mitf>*Twist* result in juveniles with ectopic a9.49 cells (Fig. 3f). The reprogrammed cells seem to produce mesodermal derivatives, such as tunic cells, based on their location and distinct, rounded morphology (Supplementary Fig. 9).

Additional evidence for the reprogramming of the a9.49 lineage was obtained with Kaede, a photoconvertible fluorescent protein that was previously used in *Ciona* to trace the formation of the CNS²⁷. Embryos were co-electroporated with *Mitf*>*Twist* and *Tyr*>*Kaede*, which mediate expression in the a9.49 lineage (Fig. 4a). Tailbud embryos that were not exposed to ultraviolet light show no red fluorescence (Fig. 4b) and result in juveniles that have only green a9.49 descendants (Fig. 4c). In contrast, tailbud embryos treated with ultraviolet light (Fig. 4d, e) develop into juveniles that display red cells throughout the body (Fig. 4f). Control juveniles lacking *Mitf*>*Twist* exhibit the expected expression solely in the CNS (Supplementary Fig. 10). Finally, time-lapse microscopy was used to examine the *Mitf*>*Twist* expressing cells in juveniles. Some of these cells migrate like the normal tunic cells derived from the mesenchyme (Fig. 4g and Supplementary Video 2). Thus, the misexpression of *Twist* is sufficient to reprogram the a9.49 lineage into migrating mesenchymal cells, reminiscent of vertebrate ectomesenchyme.

The mesenchymal properties of neural crest were proposed to be the last features to appear during its evolution^{3,28}. Our studies of the non-vertebrate chordate *Ciona intestinalis* support this hypothesis. We propose that cephalic neural crest arose from the co-option of one or more mesenchyme determinants (for example, *Twist*) in a rudimentary neural crest cell type. Thus, this enigmatic cell population should not be considered a vertebrate innovation but an elaboration of an ancestral chordate gene network.

Note added in proof: After this paper was accepted for publication, our time-lapse imaging revealed that the a10.97 cells undergo an additional division just before their intercalation at the dorsal midline. This finding does not alter any of the preceding conclusions.

METHODS SUMMARY

Ciona intestinalis transgenesis, and protein–RNA double-labelling assays, were performed as described previously²⁹. All enhancer and misexpression sequences were cloned into a pCESA vector using the primer pairs shown in Supplementary Table 1. The *ZicL*, *Msx*, *FoxD*, *Tyr*, *Tyrr1*, *Brachyury* and *Dmbx* enhancers have been described previously^{10,13,19,29,30}. Photoconversion of Kaede was achieved by treating tailbud embryos with ultraviolet light using a fluorescence stereomicroscope. All images were generated on a Zeiss Axio Imager A2 or a Zeiss LSM 700 microscope.

Full Methods and any associated references are available in the online version of the paper.

Received 19 March; accepted 13 September 2012.

Published online 7 November 2012.

1. Bronner, M. E. & Le Douarin, N. M. Evolution and development of the neural crest: An overview. *Dev. Biol.* **366**, 2–9 (2012).
2. Le Douarin, N. M. et al. Neural crest cell plasticity and its limits. *Development* **131**, 4637–4650 (2004).
3. Gans, C. & Northcutt, R. G. Neural crest and the origin of vertebrates: a new head. *Science* **220**, 268–273 (1983).
4. Yu, J. K., Meulemans, D., McKeown, S. J. & Bronner-Fraser, M. Insights from the amphioxus genome on the origin of vertebrate neural crest. *Genome Res.* **18**, 1127–1132 (2008).
5. Delsuc, F., Brinkmann, H., Chourrout, D. & Philippe, H. Tunicates and not cephalochordates are the closest living relatives of vertebrates. *Nature* **439**, 965–968 (2006).
6. Jeffery, W. R., Strickler, A. G. & Yamamoto, Y. Migratory neural crest-like cells form body pigmentation in a urochordate embryo. *Nature* **431**, 696–699 (2004).

7. Jeffery, W. R. Ascidian neural crest-like cells: phylogenetic distribution, relationship to larval complexity, and pigment cell fate. *J. Exp. Zool. B* **306B**, 470–480 (2006).
8. Jeffery, W. R. et al. Trunk lateral cells are neural crest-like cells in the ascidian *Ciona intestinalis*: Insights into the ancestry and evolution of the neural crest. *Dev. Biol.* **324**, 152–160 (2008).
9. Tassy, O. et al. The ANISEED database: digital representation, formalization, and elucidation of a chordate developmental program. *Genome Res.* **20**, 1459–1468 (2010).
10. Russo, M. T. et al. Regulatory elements controlling *Ci-msxb* tissue-specific expression during *Ciona intestinalis* embryonic development. *Dev. Biol.* **267**, 517–528 (2004).
11. Imai, K. S., Levine, M., Satoh, N. & Satou, Y. Regulatory blueprint for a chordate embryo. *Science* **312**, 1183–1187 (2006).
12. Wada, H. & Makabe, K. Genome duplications of early vertebrates as a possible chronicle of the evolutionary history of the neural crest. *Int. J. Biol. Sci.* **2**, 133–141 (2006).
13. Squarzon, P., Parveen, F., Zanetti, L., Ristatore, F. & Spagnuolo, A. FGF/MAPK/Ets signaling renders pigment cell precursors competent to respond to Wnt signal by directly controlling *Ci-Tcf* transcription. *Development* **138**, 1421–1432 (2011).
14. Curran, K. et al. Interplay between *Foxd3* and *Mitf* regulates cell fate plasticity in the zebrafish neural crest. *Dev. Biol.* **344**, 107–118 (2010).
15. Yajima, I. et al. Cloning and functional analysis of ascidian *Mitf* in vivo: insights into the origin of vertebrate pigment cells. *Mech. Dev.* **120**, 1489–1504 (2003).
16. Nishida, H. & Satoh, N. Determination and regulation in the pigment cell lineage of the ascidian embryo. *Dev. Biol.* **132**, 355–367 (1989).
17. Dorsky, R. I., Moon, R. T. & Raible, D. W. Control of neural crest cell fate by the Wnt signalling pathway. *Nature* **396**, 370–373 (1998).
18. Thomas, A. J. & Erickson, C. A. *FOXD3* regulates the lineage switch between neural crest-derived glial cells and pigment cells by repressing *Mitf* through a non-canonical mechanism. *Development* **136**, 1849–1858 (2009).
19. Imai, K. S., Satoh, N. & Satou, Y. An essential role of a *Foxd* gene in notochord induction in *Ciona* embryos. *Development* **129**, 3441–3453 (2002).
20. Yoshida, T., Vivatbutsiri, P., Morris-Kay, G., Saga, Y. & Iseki, S. Cell lineage in mammalian craniofacial mesenchyme. *Mech. Dev.* **125**, 797–808 (2008).
21. Bildsoe, H. et al. Requirement for *Twist1* in frontonasal and skull vault development in the mouse embryo. *Dev. Biol.* **331**, 176–188 (2009).
22. Soo, K. et al. *Twist* function is required for the morphogenesis of the cephalic neural tube and the differentiation of the cranial neural crest cells in the mouse embryo. *Dev. Biol.* **247**, 251–270 (2002).
23. Hopwood, N. D., Pluck, A. & Gurdon, J. B. A *Xenopus* mRNA related to *Drosophila* *twist* is expressed in response to induction in the mesoderm and the neural crest. *Cell* **59**, 893–903 (1989).
24. Vincentz, J. W. et al. An absence of *Twist1* results in aberrant cardiac neural crest morphogenesis. *Dev. Biol.* **320**, 131–139 (2008).
25. Tokuoka, M., Satoh, N. & Satou, Y. A bHLH transcription factor gene, *Twist-like 1*, is essential for the formation of mesodermal tissues of *Ciona* juveniles. *Dev. Biol.* **288**, 387–396 (2005).
26. Vlaeminck-Guillem, V. et al. The *Ets* family member *Erg* gene is expressed in mesodermal tissues and neural crests at fundamental steps during mouse embryogenesis. *Mech. Dev.* **91**, 331–335 (2000).
27. Horie, T. et al. Ependymal cells of chordate larvae are stem-like cells that form the adult nervous system. *Nature* **469**, 525–528 (2011).
28. Shimeld, S. M. & Holland, P. W. H. Vertebrate innovations. *Proc. Natl Acad. Sci. USA* **97**, 4449–4452 (2000).
29. Shi, W. & Levine, M. Ephrin signaling establishes asymmetric cell fates in an endomesoderm lineage of the *Ciona* embryo. *Development* **135**, 931–940 (2008).
30. Stolfi, A. & Levine, M. Neuronal subtype specification in the spinal cord of a protovertebrate. *Development* **138**, 995–1004 (2011).

Supplementary Information is available in the online version of the paper.

Acknowledgements We thank A. Stolfi for his continued support and guidance, Y. Satou for isolating the *Twist* enhancer, N. Ellis for cloning *Dmbx*>*Twist* and B. Gainous for critical reading of the manuscript. P.B.A. is supported by a graduate fellowship from the US National Science Foundation. This work was supported by a grant from the US National Institutes of Health (NS 076542).

Author Contributions P.B.A. designed and performed most experiments in consultation with M.L. E.W. isolated the *cis*-regulatory element for the β_1 -crystallin reporter and made the stable β -catenin transgene. I.A.N. examined *Mech2* and *Erg* expression in wild-type and reprogrammed tailbud embryos. P.B.A., M.L. and E.W. wrote the manuscript.

Author Information Reprints and permissions information is available at www.nature.com/reprints. The authors declare no competing financial interests. Readers are welcome to comment on the online version of the paper. Correspondence and requests for materials should be addressed to M.L. (mlevine@berkeley.edu).

METHODS

Embryo preparation and imaging. *Ciona intestinalis* adults were obtained, *in vitro* fertilized and electroporated for transient transgenesis as described²⁹. For each electroporation, typically 70 µg of DNA was resuspended in 100 µl buffer. Embryos were fixed at the appropriate developmental stage for 15 min in 4% formaldehyde. The tissue was then cleared in a series of washes of 0.01% Triton-X in PBS. Actin was stained overnight with Alexa-647-conjugated phalloidin at a dilution of 1:500. Samples were mounted in 50% glycerol in PBS with 2% DABCO compound for microscopy. Differential interference-contrast microscopy was used to obtain transmitted light micrographs with a Zeiss Axio Imager A2 using the ×40 EC Plan Neofluar objective. Confocal images were acquired on a Zeiss LSM 700 microscope using a plan-apochromat ×20 or ×40 objective. Confocal stacks contained approximately 50 optical slices at a thickness of 1 to 2 µm each. Images were rendered in three dimensions using Volocity 6 with the three-dimension opacity visualization tool. For time-lapse microscopy, larvae and juveniles were anaesthetized in artificial sea water supplemented with 0.04% tricaine mesylate in a glass-bottom dish. Time-lapse images were taken on a Zeiss LSM 700 microscope at intervals of 3 to 4 min.

Molecular cloning. The University of California Santa Cruz Genome Browser Gateway facilitated the identification of conserved non-coding sequences between *Ciona intestinalis* and *Ciona savignyi*. Primers (Supplementary Table 1) were used to PCR (polymerase chain reaction) amplify these putative enhancer sequences which were cloned into a pCESA vector using either *AscI* or *NotI* restriction sites for *Prop1*, *Twist* and *βγ-crystallin*, or *AscI* and *XhoI* for *Mitf*. The *Mitf* enhancer

sequence was cloned 5' of a basal friend of GATA (Zfp1) promoter. The *lacZ* coding sequence of the pCESA vector was replaced with UNC-76-GFP, UNC-76-mCherry, H2B-mCherry, enhanced GFP or Kaede. The *ZicL*, *Msx*, *FoxD*, *Tyr*, *Tyrp1* *Brachyury* and *Dmbx* enhancers have been previously described^{10,13,19,29,30}. A similar cloning strategy was used to create misexpression vectors using *NotI* or *EcoRI* sites for control group A basic helix-loop-helix genes, *Wnt7*, *FoxD* and *FoxD* N-terminal, or *NotI* or *BlpI* sites for stabilized *β-catenin* and *Twist* (Supplementary Table 1). The *FoxD-DBD-WRPW* coding sequence was made by amplifying the DBD (DNA-binding domain) of *FoxD* (Supplementary Table 1), which was subcloned into a pCESA vector containing an HA-NLS peptide and a WRPW repressor motif using *NheI* or *SpeI* sites. Additional coding sequences for *Ets-VP16*, *Ets-WRPW* and *ΔTcf* were subcloned from existing expression vectors¹³.

In situ hybridization and immunohistochemistry. The double-fluorescent *in situ* hybridizations and immunohistochemistry were performed as described³⁰ using linearized complementary DNA clones for *Wnt7* (cilv33g04), *FoxD* (citb8o13), *Erg* (cilv04i11), *Mech2* (cicl04m09), and *Twist* (cicl20p07) from the cDNA library of N. Satoh.

Kaede lineage tracing. Embryos electroporated with *Tyr>Kaede* and co-electroporated with *Mitf>lacZ* or *Mitf>Twist* were developed in the dark until the late tailbud stage. Tailbuds expressing Kaede were then photoconverted with UV light using the DAPI filter on a Zeiss Stereo Lumar.V12 for 3 min. Embryos were continuously reared in the dark from tailbud stages and prepared for imaging.

EZH2 inhibition as a therapeutic strategy for lymphoma with EZH2-activating mutations

Michael T. McCabe¹, Heidi M. Ott¹, Gopinath Ganji¹, Susan Korenchuk¹, Christine Thompson¹, Glenn S. Van Aller¹, Yan Liu¹, Alan P. Graves², Anthony Della Pietra III¹, Elsie Diaz², Louis V. LaFrance¹, Mark Mellinger¹, Celine Duquenne¹, Xinrong Tian¹, Ryan G. Kruger¹, Charles F. McHugh¹, Martin Brandt², William H. Miller¹, Dashyant Dhanak¹, Sharad K. Verma¹, Peter J. Tummino¹ & Caretha L. Creasy¹

In eukaryotes, post-translational modification of histones is critical for regulation of chromatin structure and gene expression. EZH2 is the catalytic subunit of the polycomb repressive complex 2 (PRC2) and is involved in repressing gene expression through methylation of histone H3 on lysine 27 (H3K27). EZH2 overexpression is implicated in tumorigenesis and correlates with poor prognosis in several tumour types^{1–5}. Additionally, somatic heterozygous mutations of Y641 and A677 residues within the catalytic SET domain of EZH2 occur in diffuse large B-cell lymphoma (DLBCL) and follicular lymphoma^{6–10}. The Y641 residue is the most frequently mutated residue, with up to 22% of germinal centre B-cell DLBCL and follicular lymphoma harbouring mutations at this site. These lymphomas have increased H3K27 tri-methylation (H3K27me3) owing to altered substrate preferences of the mutant enzymes^{9,11–13}. However, it is unknown whether specific, direct inhibition of EZH2 methyltransferase activity will be effective in treating EZH2 mutant lymphomas. Here we demonstrate that GSK126, a potent, highly selective, S-adenosyl-methionine-competitive, small-molecule inhibitor of EZH2 methyltransferase activity, decreases global H3K27me3 levels and reactivates silenced PRC2 target genes. GSK126 effectively inhibits the proliferation of EZH2 mutant DLBCL cell lines and markedly inhibits the growth of EZH2 mutant DLBCL xenografts in mice. Together, these data demonstrate that pharmacological inhibition of EZH2 activity may provide a promising treatment for EZH2 mutant lymphoma.

To identify inhibitors of EZH2 methyltransferase activity, a high-throughput biochemical screen with a five-member PRC2 protein complex was performed¹⁴. This work identified a small-molecule EZH2 inhibitor with a $K_i^{app} = 700$ nM. Extensive optimization of this compound through medicinal chemistry generated GSK126 (Fig. 1a). GSK126 potently inhibits both wild-type and mutant EZH2 methyltransferase activity with similar potencies ($K_i^{app} = 0.5–3$ nM) independent of substrate used, and is competitive with S-adenosyl-methionine (SAM) and non-competitive with peptide substrates (Fig. 1b and Supplementary Fig. 1a, b). GSK126 is highly selective against other methyltransferases and multiple other protein classes (Supplementary Tables 1–4). In particular, GSK126 is more than 1,000-fold selective for EZH2 versus 20 other human methyltransferases, including both SET-domain-containing and non-SET-domain-containing methyltransferases¹⁵. Even EZH1, which is 96% identical to EZH2 within the SET domain, and 76% identical overall, is inhibited more than 150-fold less potently ($K_i^{app} = 89$ nM). Using an EZH2 homology model⁹, combined with enzyme mechanism-of-action and inhibitor structure–activity relationship data, *in silico* docking revealed the SAM binding pocket as the most plausible docking site for GSK126. Here it is predicted to make extensive contacts with the post-SET domain which forms one side of the SAM binding pocket (Supplementary Fig. 2a–d). Interestingly, within 10 Å of the predicted

GSK126-binding site, four of the six residue differences between EZH2 and EZH1 lie within the post-SET domain, and these may contribute to the decreased potency for EZH1.

The altered substrate preferences of EZH2 mutants lead to an imbalance in cellular H3K27 methylation states (Supplementary Fig. 3a)^{9,11}. Nonetheless, GSK126 induced a 50% loss of H3K27me3 in both EZH2 wild-type and mutant DLBCL cell lines at concentrations ranging from 7–252 nM independent of EZH2 mutation status (*t*-test, $P = 0.27$) (Fig. 1c). Further analyses demonstrated that inhibition of H3K27me3 began before 24 h and potency was maximal after 2 days (Supplementary Fig. 3b). GSK126 most potently inhibited H3K27me3, followed by H3K27me2, and H3K27me1 was only weakly reduced at the highest inhibitor concentration (Fig. 1d and Supplementary Fig. 3c). Total histone H3 and PRC2 components were not affected by GSK126 (Supplementary Figs 3c and 4), thus reduction of H3K27 methylation is due to direct inhibition of EZH2 methyltransferase activity and not degradation of histone H3 or PRC2.

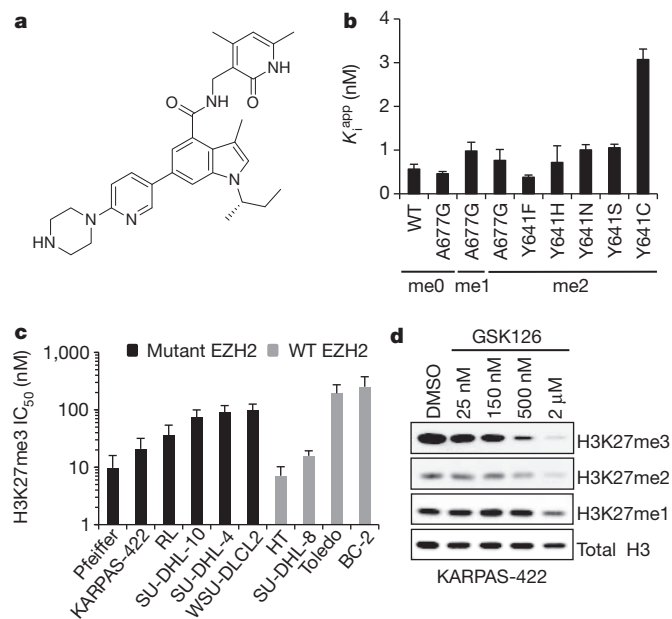


Figure 1 | Biochemical and cellular mechanistic activity of GSK126.

a, Structure of GSK126. **b**, Potency of GSK126 against wild-type and mutant EZH2. Histone H3 peptides (21–44) with K27me0, K27me1 or K27me2 were used as substrates ($n = 2$; mean values \pm s.d. are shown). **c**, Effect of GSK126 on H3K27me3 in lymphoma cell lines treated with GSK126 for 48 h. IC_{50} values were determined using an H3K27me3 ELISA ($n \geq 2$; mean values \pm s.d. are shown). **d**, Evaluation of H3K27me3/2/1 in KARPAS-422 cells following treatment for 72 h. Total histone H3 is shown as a loading control.

¹Cancer Epigenetics Discovery Performance Unit, Cancer Research, Oncology R&D, GlaxoSmithKline, 1250 S. Collegeville Road, Collegeville, Pennsylvania 19426, USA. ²Platform Technology and Sciences, GlaxoSmithKline, 1250 S. Collegeville Road, Collegeville, Pennsylvania 19426, USA.

This is in contrast to 3-deazaneplanocin A (DZNep), an inhibitor of S-adenosyl-L-homocysteine (SAH) hydrolase that promotes degradation of the PRC2 complex and indirectly inhibits EZH2 through effects on intracellular SAH concentrations¹⁶.

We evaluated the effect of GSK126 on cell proliferation in a panel of B-cell lymphoma cell lines. DLBCL cell lines were the most sensitive to EZH2 inhibition (Fig. 2a). Six of the seven most sensitive DLBCL cell lines harboured Y641N, Y641F or A677G EZH2 mutations (growth IC_{50} = 28–861 nM) (Fig. 2a, Supplementary Table 5 and Supplementary Fig. 5). The exception was the cell line HT, which is wild type for EZH2 (growth IC_{50} = 516 nM). Interestingly, HT harbours a mutation in UTX (R1111C), a H3K27 demethylase frequently inactivated in multiple tumour types¹⁷. Only two of the 11 remaining DLBCL cell lines harboured EZH2 mutations indicating that, in most cases, DLBCL cell lines with mutant EZH2 are dependent on EZH2 activity for cell growth. However, in some situations co-occurring

alterations may override the dependence of the cell on EZH2 activity, making it less sensitive to EZH2 inhibition. Among EZH2 mutant cell lines, sensitivity to GSK126 is independent of BCL2 translocation or p53 mutation, common alterations found within DLBCL (Supplementary Table 5). There was a modest correlation between inhibition of H3K27me3 and cell growth (Pearson, $r = 0.62$), but there was no correlation between sensitivity to GSK126 and EZH2 protein levels (Supplementary Fig. 6a–c). Interestingly, two of the most sensitive DLBCL cell lines, WSU-DLCL2 and KARPAS-422, are derived from patients with refractory disease^{18,19} indicating that DLBCL cells that are resistant to standard-of-care may be sensitive to EZH2 inhibition. Burkitt lymphoma and Hodgkin's lymphoma cell lines were generally less sensitive to EZH2 inhibition (growth IC_{50} > 1.3 μ M) with the exception of Jiyoye (growth IC_{50} = 232 nM), a Burkitt lymphoma cell line with wild-type EZH2. Evaluation of GSK126 in additional lymphoma cell lines and extensive genomic and epigenomic

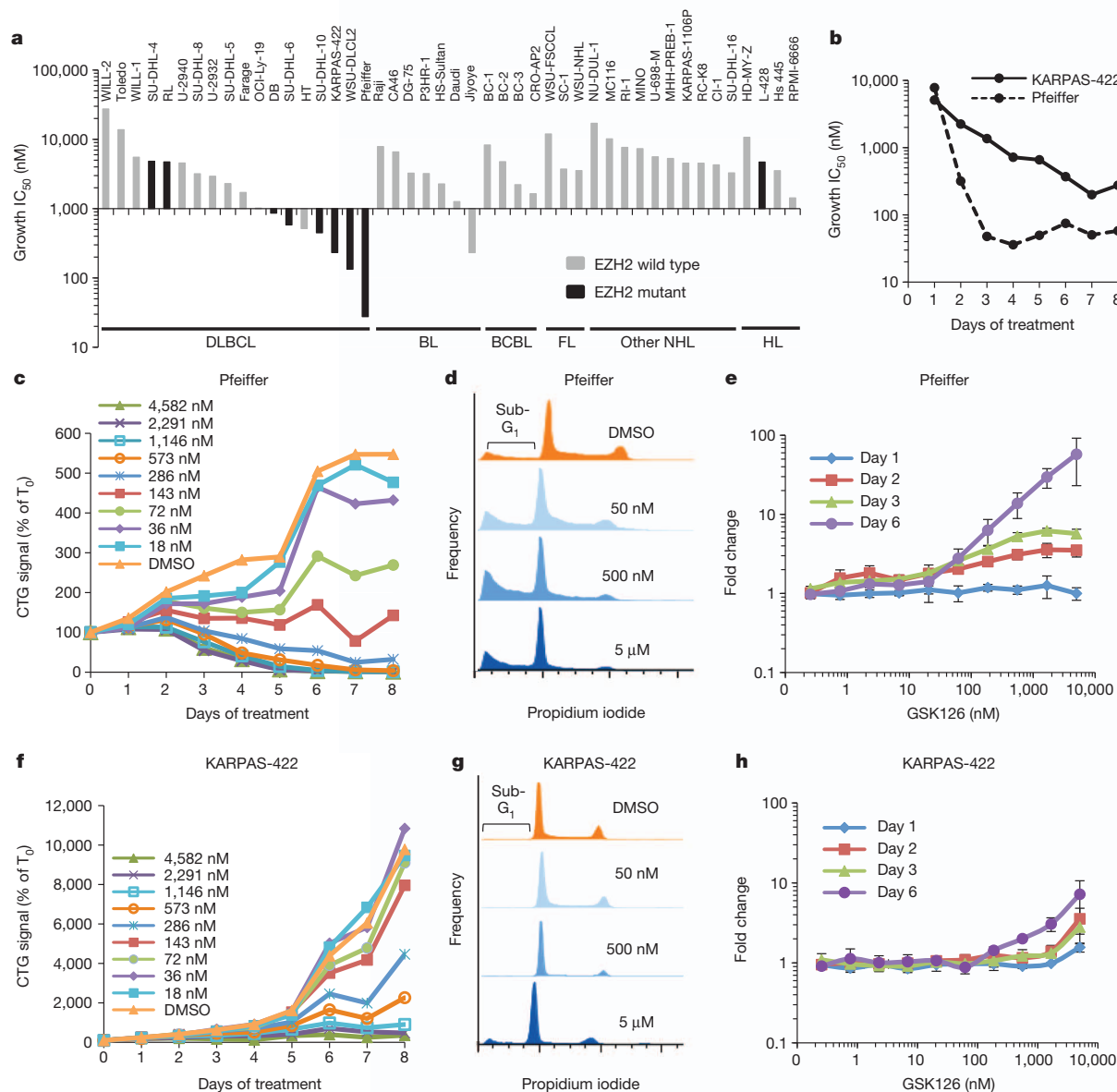


Figure 2 | GSK126 inhibits the proliferation of several EZH2 mutant lymphoma cell lines. **a**, The effect of GSK126 on the growth of 46 lymphoma cell lines after 6 days represented as the concentration of GSK126 required to inhibit 50% of growth (growth IC_{50}). BCBL, AIDS body cavity-based lymphoma; BL, Burkitt lymphoma; DLBCL, diffuse large B-cell lymphoma; FL, follicular lymphoma; HL, Hodgkin's lymphoma; NHL, non-Hodgkin's

lymphoma. **b**, Potency of GSK126 on growth of Pfeiffer and KARPAS-422 cells over time represented as growth IC_{50} . **c**, **f**, Dose-dependent effects of GSK126 on cell proliferation over time in Pfeiffer or KARPAS-422 cells. Growth is expressed as a percentage of CTG at time zero (T_0). **d**, **g**, DNA content histograms showing the effect of GSK126 on the cell cycle after 72 h. **e**, **h**, Mean fold-change in caspase 3/7 activity over vehicle control \pm s.d. is shown ($n = 4$).

characterization will be required to fully elucidate the determinants of sensitivity among lymphoma subtypes.

Both cytostatic and cytotoxic responses were observed among the most sensitive cell lines (Supplementary Table 5); therefore, the timing of GSK126-induced effects on proliferation and cell death was examined in detail in two of the most sensitive cell lines. In the Pfeiffer cell line, potent inhibition of cell proliferation was observed after 2 days (Fig. 2b) and net decreases in cell number were evident after 3 days (Fig. 2c). This cell death seems to be driven by caspase-mediated apoptosis as indicated by the increase in the sub-G₁ population (Fig. 2d) and dose-dependent induction of caspase activity (Fig. 2e). The response in the KARPAS-422 cell line was slower with 6–7 days required for maximal potency (Fig. 2b). Furthermore, a primarily cytostatic effect was observed in KARPAS-422 cells as demonstrated by CellTiter-Glo (CTG) values remaining above day 0 levels, a G₁ arrest (43% and 77% of cells in G₁ with dimethylsulphoxide (DMSO) and 500 nM GSK126, respectively) with little sub-G₁ content, and minimal caspase activity with <1 μ M GSK126 (Fig. 2f–h). Consistent with these observations, short-hairpin-RNA-mediated knockdown of EZH2 led to profound cytotoxic and apoptotic responses in Pfeiffer cells, and decreased cell proliferation and no caspase

activation in KARPAS-422 cells, demonstrating that the phenotypic effects observed with GSK126 are due to inhibition of EZH2 (Supplementary Fig. 7).

Because EZH2 is associated with transcriptional repression, we evaluated the effect of GSK126 on gene expression in DLBCL cell lines with a range of sensitivity to GSK126. Robust transcriptional activation was noted in the most sensitive cell lines (Fig. 3a, Supplementary Fig. 8a and Supplementary Table 6). Not surprisingly, considering the repressive nature of H3K27me_{2/3}, the majority of transcriptional changes involved upregulation. The high degree of similarity between gene expression changes observed with GSK126 treatment and EZH2 knockdown in KARPAS-422 and Pfeiffer cells indicates that these transcriptional changes are due to loss of EZH2 activity and not off-target effects (Supplementary Figs 9 and 10). Additionally, analysis of data from chromatin immunoprecipitation followed by sequencing (ChIP-seq) for the three most responsive cell lines showed that before treatment upregulated genes exhibited broad enrichment of H3K27me₃, indicating that these genes are EZH2 targets marked by H3K27me₃ (Fig. 3b and Supplementary Fig. 11).

In contrast to the response observed in the sensitive cell lines, minimal transcriptional changes occurred with GSK126 treatment in

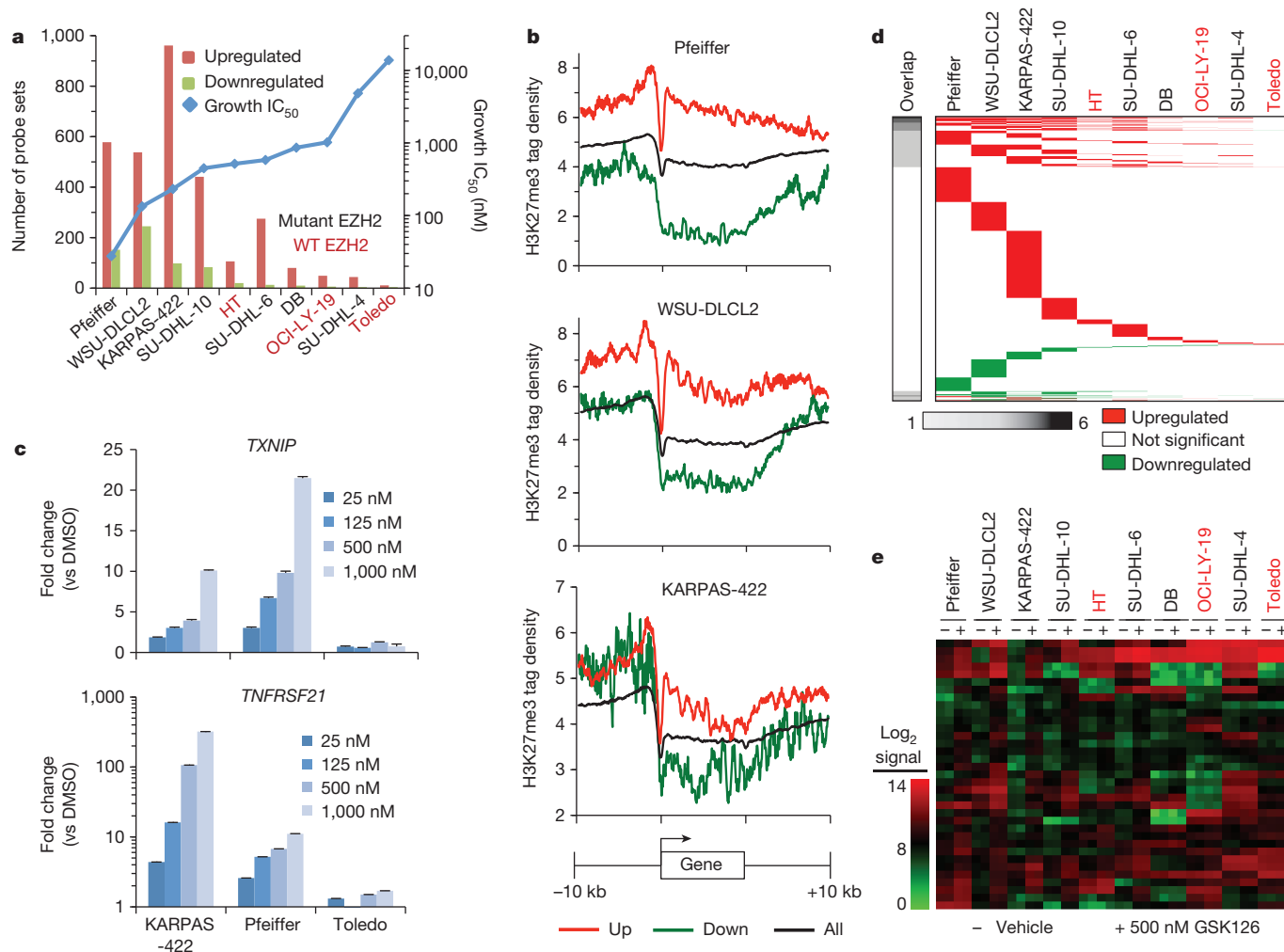


Figure 3 | GSK126 induces transcriptional activation in sensitive cell lines.

a, The number of probe sets showing significantly altered gene expression (false discovery rate (FDR) < 0.1 and fold-change > 2 or < -2) following 72 h treatment with 500 nM GSK126 ($n = 2$). **b**, Basal H3K27me₃ ChIP-seq enrichment profiles of genes upregulated (red), downregulated (green), or all human transcripts (black) following GSK126 treatment. **c**, qRT-PCR analysis of *TXNIP* and *TNFRSF21* following 72 h treatment with GSK126 ($n = 3$; mean

values \pm s.d. are shown). **d**, The overlap of up- and downregulated probe sets between 10 DLBCL cell lines using a twofold expression change cut-off. **e**, Heat map showing the average gene expression intensities of the 35 probe sets exhibiting significantly increased expression in at least four of the five most sensitive mutant DLBCL cell lines (Pfeiffer, KARPAS-422, WSU-DLCL2, SU-DHL-10 and SU-DHL-6).

Toledo cells, a cell line with wild-type EZH2 whose growth is not affected by EZH2 inhibition (Fig. 3a). Even at 2 μ M GSK126, very few transcriptional changes were observed in Toledo cells (23 upregulated and 10 downregulated probe sets), despite a near complete loss of H3K27me3 at this dose and time (Supplementary Table 6 and Supplementary Fig. 3c). Likewise, quantitative PCR with reverse transcription (qRT-PCR) performed for quantitative mRNA expression analysis of two H3K27me3-enriched genes revealed dose-responsive increases in gene expression with as little as 25 nM GSK126 in Pfeiffer and KARPAS-422 cells, but no transcriptional changes in Toledo cells with up to 1 μ M GSK126 (Fig. 3c and Supplementary Table 7). Interestingly, even in the most sensitive wild-type EZH2 cell line, HT, the transcriptional response was less pronounced when compared to EZH2 mutant DLBCL cell lines with similar sensitivity (Fig. 3a). Relaxing the transcriptional fold-change criteria from 2.0 to 1.5 revealed additional modest transcriptional changes in HT cells (Supplementary Fig. 8b). This muted transcriptional response in wild-type EZH2 and less sensitive mutant cell lines indicates that other compensatory mechanisms (such as H3K9, H4K20 or DNA methylation) may exist in these cell lines to dampen the transcriptional response.

Among the EZH2 mutant cell lines, global H3K27me3 levels were statistically higher in transcriptionally responsive lines (*t*-test, $P = 0.019$), indicating that EZH2 mutation status together with global H3K27me3 levels may be a better predictive biomarker than mutation status alone (Supplementary Fig. 8c). Whereas the five most sensitive EZH2 mutant cell lines showed a preponderance of upregulated gene expression changes (69–95%), little overlap was observed among the differentially regulated probe sets using either twofold or 1.5-fold significance criteria (Fig. 3d and Supplementary Fig. 8d). Only 35 upregulated probe sets were common to at least four of these five mutant cell lines (Supplementary Table 8). Examination of these commonly upregulated probe sets revealed that many are enriched for H3K27me3 (32/35) (Supplementary Tables 7 and 8). Additionally, many of these probe sets are induced, albeit weakly, in the other cell lines, indicating that additional time or chromatin factors may be required for complete gene activation in these settings (Fig. 3e and Supplementary Table 8). Lastly, whereas no single pathway or process was significantly enriched among the limited set of genes commonly upregulated, gene ontology enrichment analysis of regulated gene sets in each cell line individually revealed several common processes including cell cycle regulation, cell death and regulation of biological/cellular processes (Supplementary Fig. 12 and Supplementary Table 9). These data demonstrate that the global loss of H3K27me3 following inhibition of EZH2 with GSK126 is associated with transcriptional activation of EZH2 target genes that correlates well with sensitivity, and that mutant EZH2 de-regulates H3K27me3 in a global, rather than targeted, manner. The significant variation between the upregulated gene sets of sensitive cell lines is a surprising observation that likely highlights the complexity and uniqueness of the epigenome in each cell line, and the diversity of selective pressures during the development of individual lymphomas.

On the basis of its potent effects in cell culture, we evaluated GSK126 in mice using subcutaneous xenografts of KARPAS-422 and Pfeiffer cells. Following 10 days of once-daily dosing of GSK126, global H3K27me3 decreased and gene expression increased in a dose-dependent fashion consistent with observations from cell culture (Fig. 4a, b). Although GSK126 was initially cleared rapidly from the blood, there was an extended terminal phase where drug elimination from blood and tumour was slower (Supplementary Fig. 13a, b). With daily 50 mg per kg dosing, complete tumour growth inhibition was observed in both KARPAS-422 and Pfeiffer cell models (Fig. 4c and Supplementary Fig. 14a). When higher dosing regimens were examined with KARPAS-422 xenografts, marked tumour regression was observed (Fig. 4c). Upon cessation of dosing, tumours in the 50 mg per kg once daily group showed tumour stasis whereas complete tumour eradication was observed in the 150 mg per kg once daily and 300 mg per kg twice per week groups. Tumour growth inhibition

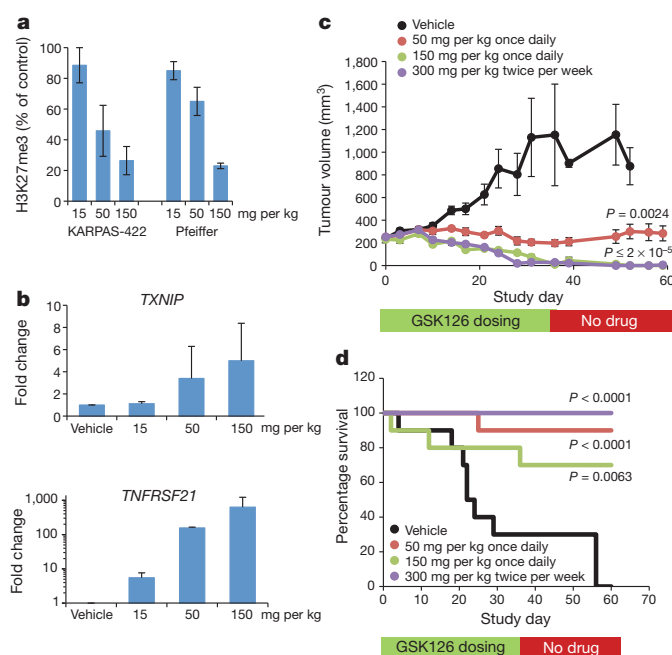


Figure 4 | In vivo inhibition of H3K27me3 and tumour growth response with GSK126. **a**, Response of H3K27me3 in tumour xenografts following 10 days of once daily dosing with GSK126. **b**, qRT-PCR analysis of EZH2 target genes in KARPAS-422 tumour xenografts. Mean values \pm s.d. ($n = 3$) are shown (**a**, **b**). **c**, Activity of GSK126 on the growth of subcutaneous KARPAS-422 xenografts. Mean tumour volume \pm s.e.m. is shown ($n = 10$). **d**, Kaplan-Meier survival curve of mice treated in **c**. Significant P values, calculated using a nonparametric log-rank test, between vehicle and treatment groups are indicated. No significant differences were observed between treatment groups (P values = 0.07–0.32).

also correlated with statistically significant increased survival of mice bearing the more aggressive KARPAS-422 tumours, where spontaneous deaths occurred in vehicle-treated animals (Fig. 4d). On the basis of these striking observations, intermittent dosing regimens with lower doses of GSK126 given weekly or with a 1 week drug holiday were examined in KARPAS-422 tumour xenografts with large tumours (Supplementary Fig. 14b). All schedules demonstrated tumour growth inhibition (91–100%, *t*-test, P values = 0.0008–0.0024). These results indicate that the response to GSK126 is durable and that intermittent dosing schedules may be effective in a clinical setting even in advanced tumours.

GSK126 was well tolerated at the doses and schedules examined as measured by little to no decrease in body weight, normal grooming and behaviour, and vastly improved survival in mice carrying KARPAS-422 xenografts (Supplementary Fig. 15a–c and Fig. 4d). Given the role of EZH2 in normal haematopoiesis and the identification of EZH2 loss-of-function mutations in myeloid malignancies^{20–23}, we investigated the effects of GSK126 treatment on peripheral blood of immunocompetent mice. Complete blood count analysis revealed no significant changes in any blood cell types at doses and times where efficacy was observed in tumour xenografts (Supplementary Fig. 15d).

Over the past decade, the development of targeted agents that specifically inhibit oncoproteins with activating somatic alterations has provided profound clinical benefit for cancer patients^{24,25}. The data shown here provide compelling evidence that inhibition of EZH2 methyltransferase activity may be a viable strategy for the treatment of DLBCL and non-indolent follicular lymphoma harbouring activating mutations in EZH2. GSK126 also provides a means to evaluate whether EZH2 activity is required for the survival of tumours where EZH2 overexpression has been linked to poor prognosis^{2–5}, and tumours harbouring loss-of-function mutations in UTX^{17,21,26}.

Although we do not expect GSK126 to be effective in treating myeloid malignancies bearing loss-of-function mutations in EZH2 (refs 21–23), GSK126 should be an important tool to assess the role of EZH2 in normal myeloid development and to understand the oncogenic role of EZH2 in myeloproliferative neoplasms. Lastly, the identification of a selective EZH2 inhibitor which does not lead to degradation of the PRC2 complex provides a useful tool to understand the role of EZH2 methyltransferase activity versus its scaffolding role in development, tumorigenesis and tumour progression that could not be elucidated through conventional genetic manipulation studies.

METHODS SUMMARY

Biochemical assays used the five-member PRC2 complex (human Flag-EZH2, EED, SUZ12, AEBP2, RbAp48) containing either wild-type or mutant EZH2, [³H]-SAM and the indicated peptide substrate; reactions were incubated for 30 min. Global histone modification levels were determined by enzyme-linked immunosorbent assay (ELISA) or western blot methods using antibodies specific for total histone H3, H3K27me1, H3K27me2 or H3K27me3. Cell proliferation and caspase-3/7 activity were assessed using CellTiter-Glo and Caspase-Glo 3/7 (Promega), respectively. Gene expression profiling was conducted using Affymetrix Human Genome U133 Plus 2.0 microarrays. Differentially expressed probe sets were determined by fitting the data to a linear model using the limma statistical package (<http://www.bioconductor.org>) and carrying out pair-wise contrasts of treated versus control. Significant probe sets were filtered for detection (\log_2 signal threshold of 8), an average fold-change >2 or <-2 , or >1.5 or <-1.5 , where indicated, with *P* values adjusted for multiple testing correction by false discovery rate (FDR; Benjamini–Hochberg) < 0.1 . H3K27me3 ChIP reads were aligned using Bowtie²⁷. H3K27me3 enrichment peaks were identified using SICER²⁸ with optimized parameters. A custom PERL script was used to quantify the average basal H3K27me3 ChIP-seq tag density across gene sets. All *in vivo* studies were conducted after review by the Institutional Animal Care and Use Committee at GSK and in accordance with the GSK Policy on the Care, Welfare and Treatment of Laboratory Animals. GSK126 and vehicle were administered to mice intraperitoneally. Two-tailed *t*-tests were conducted assuming two samples of equal variance. A complete description of the materials and methods is provided in Supplementary Information.

Full Methods and any associated references are available in the online version of the paper.

Received 25 June; accepted 24 September 2012.

Published online 10 October 2012.

1. Varambally, S. *et al.* Genomic loss of microRNA-101 leads to overexpression of histone methyltransferase EZH2 in cancer. *Science* **322**, 1695–1699 (2008).
2. Varambally, S. *et al.* The polycomb group protein EZH2 is involved in progression of prostate cancer. *Nature* **419**, 624–629 (2002).
3. Kleer, C. G. *et al.* EZH2 is a marker of aggressive breast cancer and promotes neoplastic transformation of breast epithelial cells. *Proc. Natl Acad. Sci. USA* **100**, 11606–11611 (2003).
4. Wagener, N. *et al.* Enhancer of zeste homolog 2 (EZH2) expression is an independent prognostic factor in renal cell carcinoma. *BMC Cancer* **10**, 524 (2010).
5. Takawa, M. *et al.* Validation of the histone methyltransferase EZH2 as a therapeutic target for various types of human cancer and as a prognostic marker. *Cancer Sci.* **102**, 1298–1305 (2011).
6. Morin, R. D. *et al.* Frequent mutation of histone-modifying genes in non-Hodgkin lymphoma. *Nature* **476**, 298–303 (2011).
7. Morin, R. D. *et al.* Somatic mutations altering EZH2 (Tyr641) in follicular and diffuse large B-cell lymphomas of germinal-center origin. *Nature Genet.* **42**, 181–185 (2010).

8. Pasqualucci, L. *et al.* Analysis of the coding genome of diffuse large B-cell lymphoma. *Nature Genet.* **43**, 830–837 (2011).
9. McCabe, M. T. *et al.* Mutation of A677 in histone methyltransferase EZH2 in human B-cell lymphoma promotes hypertrimethylation of histone H3 on lysine 27 (H3K27). *Proc. Natl Acad. Sci. USA* **109**, 2989–2994 (2012).
10. Ryan, R. J. *et al.* EZH2 codon 641 mutations are common in BCL2-rearranged germinal center B cell lymphomas. *PLoS ONE* **6**, e28585 (2011).
11. Sneeringer, C. J. *et al.* Coordinated activities of wild-type plus mutant EZH2 drive tumor-associated hypertrimethylation of lysine 27 on histone H3 (H3K27) in human B-cell lymphomas. *Proc. Natl Acad. Sci. USA* **107**, 20980–20985 (2010).
12. Wigle, T. J. *et al.* The Y641C mutation of EZH2 alters substrate specificity for histone H3 lysine 27 methylation states. *FEBS Lett.* **585**, 3011–3014 (2011).
13. Yap, D. B. *et al.* Somatic mutations at EZH2 Y641 act dominantly through a mechanism of selectively altered PRC2 catalytic activity, to increase H3K27 trimethylation. *Blood* **117**, 2451–2459 (2011).
14. Diaz, E. *et al.* Development and validation of reagents and assays for EZH2 peptide and nucleosome high-throughput screens. <http://dx.doi.org/10.1177/1087057112453765> *J. Biomol. Screen.* (2012).
15. Schubert, H. L., Blumenthal, R. M. & Cheng, X. Many paths to methyltransferase: a chronicle of convergence. *Trends Biochem. Sci.* **28**, 329–335 (2003).
16. Miranda, T. B. *et al.* DZNep is a global histone methylation inhibitor that reactivates developmental genes not silenced by DNA methylation. *Mol. Cancer Ther.* **8**, 1579–1588 (2009).
17. van Haaften, G. *et al.* Somatic mutations of the histone H3K27 demethylase gene *UTX* in human cancer. *Nature Genet.* **41**, 521–523 (2009).
18. Dyer, M. J., Fischer, P., Nacheva, E., Labastide, W. & Karpas, A. A new human B-cell non-Hodgkin's lymphoma cell line (Karpas 422) exhibiting both t(14;18) and t(4;11) chromosomal translocations. *Blood* **75**, 709–714 (1990).
19. Al-Katib, A. M. *et al.* Bryostatins 1 down-regulates *mdr1* and potentiates vincristine cytotoxicity in diffuse large cell lymphoma xenografts. *Clin. Cancer Res.* **4**, 1305–1314 (1998).
20. Chou, R. H., Yu, Y. L. & Hung, M. C. The roles of EZH2 in cell lineage commitment. *Am. J. Transl. Res.* **3**, 243–250 (2011).
21. Jankowska, A. M. *et al.* Mutational spectrum analysis of chronic myelomonocytic leukemia includes genes associated with epigenetic regulation: *UTX*, *EZH2*, and *DNMT3A*. *Blood* **118**, 3932–3941 (2011).
22. Ernst, T. *et al.* Inactivating mutations of the histone methyltransferase gene *EZH2* in myeloid disorders. *Nature Genet.* **42**, 722–726 (2010).
23. Makishima, H. *et al.* Novel homo- and hemizygous mutations in *EZH2* in myeloid malignancies. *Leukemia* **24**, 1799–1804 (2010).
24. Chapman, P. B. *et al.* Improved survival with vemurafenib in melanoma with BRAF V600E mutation. *N. Engl. J. Med.* **364**, 2507–2516 (2011).
25. Kwak, E. L. *et al.* Anaplastic lymphoma kinase inhibition in non-small-cell lung cancer. *N. Engl. J. Med.* **363**, 1693–1703 (2010).
26. Gui, Y. *et al.* Frequent mutations of chromatin remodeling genes in transitional cell carcinoma of the bladder. *Nature Genet.* **43**, 875–878 (2011).
27. Langmead, B., Trapnell, C., Pop, M. & Salzberg, S. L. Ultrafast and memory-efficient alignment of short DNA sequences to the human genome. *Genome Biol.* **10**, R25 (2009).
28. Zang, C. *et al.* A clustering approach for identification of enriched domains from histone modification ChIP-Seq data. *Bioinformatics* **25**, 1952–1958 (2009).

Supplementary Information is available in the online version of the paper.

Acknowledgements We acknowledge members of GlaxoSmithKline's Platform Technology and Sciences group for reagent generation and sequencing, Ocimum Biosolutions for bioinformatic support, A. Anderson for statistical analysis, P. Hoffman for assistance with the manuscript, and all members of the Cancer Epigenetics Discovery Performance Unit for their guidance and support.

Author Contributions M.T.M., G.G., R.G.K., C.F.M., M.B., S.K.V. and C.L.C. designed studies; M.T.M., H.M.O., S.K., C.T., G.S.V.A., E.D., Y.L., A.P.G., A.D.P., L.V.L., M.M., C.D., X.T. and C.F.M. performed research; M.T.M., G.G., R.G.K., A.P.G., C.F.M., S.K.V., W.H.M., D.D., P.J.T. and C.L.C. analysed data and M.T.M., G.G., R.G.K., A.P.G. and C.L.C. wrote the paper.

Author Information The gene expression data are accessible on GEO through accession number GSE40972 and the ChIP-seq data through accession number GSE40970. Reprints and permissions information is available at www.nature.com/reprints. The authors declare no competing financial interests. Readers are welcome to comment on the online version of the paper. Correspondence and requests for materials should be addressed to C.L.C. (caretha.l.creasy@gsk.com).

METHODS

Determination of K_i^{app} values for GSK126 inhibition of wild-type and mutant EZH2. The five-member PRC2 complex (Flag-EZH2, EED, SUZ12, AEBP2, RbAp48) containing either wild-type or mutant (A677G, Y641N, Y641C, Y641H, Y641S or Y641F) EZH2 was prepared as previously described⁹. GSK126 was dissolved in DMSO and tested at concentrations of 0.6 nM to 300 nM with a final DMSO concentration of 2.5%. In contrast to wild-type EZH2 which prefers H3K27me0 as a substrate *in vitro*, EZH2 Y641 mutants prefer H3K27me2 and have little activity with H3K27me0 or H3K27me1. The A677G mutant is distinct from both the wild-type and Y641 mutant forms of EZH2 in that it efficiently methylates H3K27me0, H3K27me1, and H3K27me2; therefore, histone H3 peptides (residues 21–44; 10 μ M final) with either K27me0 (wild type, A677G EZH2), K27me1 (A677G EZH2), or K27me2 (A677G, Y641N, Y641C, Y641H, Y641S and Y641F EZH2) were used as methyltransferase substrates. GSK126 was added to plates followed by addition of 6 nM EZH2 complex and peptide. As the potency of GSK126 is at or near the tight binding limit of an assay run at $[SAM] = K_m$, we used a method where IC_{50} values were measured at a high concentration of the competitive substrate SAM relative to its K_m (7.5 μ M SAM where the SAM K_m is 0.3 μ M). Under these conditions, the contribution from the enzyme concentration becomes relatively small (see equation (1)) and accurate estimates of K_i can be calculated²⁹. Reactions were initiated with [3 H]-SAM, incubated for 30 min, quenched with the addition of 500-fold excess unlabelled SAM, and the methylated product peptide was captured on phosphocellulose filters according to the vendor supplied protocol for MSPH Multiscreen plates (EMD Millipore). Plates were read on a TopCount after adding 20 μ l of Microscint-20 cocktail (both from PerkinElmer). Apparent K_i values \pm s.d. were calculated using the Cheng–Prusoff relationship³⁰ for a competitive inhibitor ($n = 2$).

$$IC_{50} = K_i(1 + [S]/K_m) + [E]/2 \quad (1)$$

where E is the enzyme and S is the substrate.

Mechanism of GSK126 inhibition of EZH2. IC_{50} values were determined for GSK126 inhibition of EZH2 at several SAM concentrations ranging from 0.9 μ M to 15 μ M and then separately at several peptide concentrations ranging from 16 μ M to 60 μ M using the assay conditions described above. The resulting IC_{50} values were plotted against the $[SAM]/K_m$ ratio or the $[peptide]/K_m$ ratio, respectively.

Cell culture and immunoblotting. Cell lines were obtained from the American Type Culture Collection or the Deutsche Sammlung von Mikroorganismen und Zellkulturen and maintained in the recommended cell culture media at 37 °C in 5% CO₂. Cells were lysed with radioimmunoprecipitation (RIPA) buffer (Thermo Scientific) and western blot analysis was conducted as previously described⁹. Antibodies were obtained as previously described⁹ or from Cell Signaling Technology (SUZ12, 3737), or Santa Cruz Biotechnology (EED, sc-28701).

H3K27 methylation status and PRC2 components following GSK126 treatment. Cells (2×10^5 per well) were seeded into six-well tissue culture plates in the appropriate cell culture media 24 h before treatment. Cells were then exposed to 0.1% DMSO or varying concentrations of GSK126 (range = 25 nM–2 μ M) for 24, 72 or 144 h.

Enzyme-linked immunosorbent assay (ELISA)-based quantification of total histone H3 and H3K27me3 levels. Following tissue homogenization, tumour tissue lysates were prepared using the Epigentek Histone Extraction kit (OP-0006). Alternatively, cells were seeded at 2,000 cells per well in a 96-well plate and were treated with a 10-point threefold dilution series of GSK126 (dose range = 2 nM–38 μ M) for 48 h. Cells were lysed with 0.2 N HCl for 30 min to extract histones, the acid-insoluble portion was pelleted by centrifugation, and the supernatant was neutralized with neutralization buffer (1 M Na₂HPO₄, pH 12.5; ActiveMotif) containing protease inhibitors (Roche). Lysates were added to Maxisorp ELISA plates (Nunc) in duplicate on each of two plates plus blocking buffer (1% BSA). Plates were incubated for 1 h, washed four times with imidazole buffered saline containing Tween-20 (Kirkegaard & Perry Laboratories), incubated with primary antibodies for H3K27me3 or total H3, washed, incubated with horseradish peroxidase (HRP)-linked secondary anti-rabbit IgG antibody, and washed again. Luminata Forte substrate (Millipore) was added 5 min before chemiluminescence was quantified with an EnVision multi-label plate reader (PerkinElmer). H3K27me3 levels were normalized to total H3 values and IC_{50} values were determined using a four-parameter curve fit.

Cell proliferation assay. The optimal cell seeding was determined empirically for all cell lines by examining the growth of a wide range of seeding densities in a 384-well format to identify conditions that permitted proliferation for 6 days. Cells were then plated at the optimal seeding density 24 h before treatment (in duplicate) with a 20-point twofold dilution series of GSK126 or 0.15% DMSO. Plates were incubated for 6 days at 37 °C in 5% CO₂. Cells were then lysed with

CellTiter-Glo (CTG) (Promega) and chemiluminescent signal was detected with a TECAN Safire2 microplate reader. In addition, an untreated plate of cells was harvested at the time of compound addition (T_0) to quantify the starting number of cells. CTG values obtained after the 6 day treatment were expressed as a percent of the T_0 value and plotted against compound concentration. Data were fit with a four-parameter equation to generate a concentration response curve and the concentration of GSK126 required to inhibit 50% of growth (growth IC_{50}) was determined.

Caspase 3/7 assay. For detection of caspase-3/7 activity, cells were cultured in 96-well plates, treated with a 10-point threefold dilution series of GSK126 (range 0.03 nM to 5 μ M) and evaluated using Caspase-Glo 3/7 (Promega) as per the manufacturer's instructions. Values were normalized to CTG (Promega) levels at each time point and expressed as a percentage of vehicle treated control. Data represent an average of $n = 4$.

Cell cycle analysis. Cell cycle phase distribution was examined by flow cytometry. Twenty-four hours after seeding cells in a six-well culture plate, cells were treated with GSK126 or 0.1% DMSO (vehicle) for 3 days. Cells were washed with PBS, pelleted in CycleTest solution B (BD Biosciences, catalogue no. 340242b), flash frozen, and stored at –80 °C. CycleTest PLUS DNA reagent kit (BD Biosciences, catalogue no. 340242) was used according to the manufacturer's instructions to prepare and stain nuclei with propidium iodide. Samples were evaluated using a FACSCalibur flow cytometer (BD Biosciences) and data were analysed using FlowJo software (Tree Star).

Gene expression profiling. Cells (2×10^5 per well) were seeded into six-well tissue culture plates in the appropriate cell culture media 24 h before treatment. Duplicate wells were then exposed to 0.1% DMSO, 500 nM or 2 μ M GSK126 for 72 h. Cells were collected into TRIzol reagent (Invitrogen) and total RNA was isolated via phenol:chloroform extraction and the RNeasy kit (Qiagen) according to the manufacturer's instructions. Total RNA was labelled and hybridized to Affymetrix Human Genome U133 Plus 2.0 oligonucleotide microarrays arrays according to the manufacturer's instructions (Affymetrix) at Expression Analysis, Inc. These data are accessible through GEO via accession number GSE40972. Principal component and correlation analysis were used to confirm data reproducibility (Supplementary Fig. 16).

Affymetrix gene chip data analysis. CEL files, corresponding to individual samples, were processed by the Micro Array Suite 5.0 (MAS5) algorithm (<http://www.affymetrix.com/support/index.affx>) where signal values were scaled to a target intensity of 500 and log₂ transformed. Differentially expressed probe sets were determined by fitting the data to a linear model and carrying out pair-wise contrasts of treated versus control. Significant probe sets were filtered for detection (log₂ signal threshold of 8), an average fold-change >2 or <–2, or >1.5 or <–1.5, where indicated, with P-values adjusted for multiple testing correction by false discovery rate (FDR) (Benjamini–Hochberg) <0.1. Statistical analyses were performed using the limma package from Bioconductor (<http://www.bioconductor.org/>). Functional analyses of differentially expressed probe sets were performed using DAVID (<http://david.abcc.ncifcrf.gov/>). Significantly over-represented GO Biological Process and Molecular Function terms (levels 3–5) were filtered for EASE P-value <0.01.

qRT–PCR. Cells were treated for 72 h with 0.1% DMSO or a range of concentrations of GSK126 (range = 25 nM–1 μ M) and total RNA was isolated as described above. RNA (2.8 μ g) was reverse transcribed with MultiScribe Reverse Transcriptase (Applied Biosystems) according to the manufacturer's recommendations. The resulting cDNA was diluted and used along with TaqMan gene expression assays (Applied Biosystems; GAPDH, Hs03929097_g1; TNFRSF21, Hs00205419_m1; TXNIP, Hs00197750_m1). TaqMan Gene Expression Master Mix (Applied Biosystems) and a Viia 7 Real-Time PCR System (Applied Biosystems) were used according to the manufacturer's recommendations to quantify gene expression.

ChIP-seq. Cells (5×10^7) were maintained in the appropriate cell culture media for 24 h before fixation. Cells were fixed for 15 min at room temperature with freshly prepared formaldehyde solution (final concentrations 1% formaldehyde, 10 mM NaCl, 0.1 mM EDTA pH 8.0, 5 mM HEPES pH 7.9) followed by the addition of glycine to 125 mM. Fixed cells were rinsed twice in PBS containing 0.5% Igepal CA-630 (Sigma) and cell pellets were flash frozen. ChIP assays were performed using a custom assay protocol at Active Motif Inc. H3K27me3 ChIP and input libraries were prepared for 35 nucleotide single-end sequencing on an Illumina GAIIx sequencer according to manufacturer's instructions. These data are accessible through GEO via accession number GSE40970. Reads were assessed for quality (base quality <20 were excluded) and aligned to human reference sequence (hg19 build) using the Bowtie²⁷ algorithm allowing for up to two mismatches. Only uniquely mapped reads were used for subsequent analyses.

ChIP-seq analysis. The average basal H3K27me3 ChIP-seq tag count was quantified across genes that were upregulated, downregulated or unchanged following

treatment with GSK126 using a custom PERL script. In addition to the gene body, a region encompassing 10 kilobases (kb) upstream of the transcription initiation site and 10 kb downstream of the transcription termination site were evaluated. All genes were oriented by strand, and the variable length of gene bodies were standardized to 10,000 bins. After averaging the numbers of sequence tags at each base pair the values were normalized to the total number of mapped sequence tags per ChIP. A 500 base pair (bp) centred moving average was then applied to highlight larger trends and smooth out short-range fluctuations. MultiExperiment Viewer (<http://www.tm4.org/mev/>) was used to evaluate enrichment across individual genes. Peaks of H3K27me3 enrichment were identified using the peak calling software SICER²⁸ with the following parameters: fragment size, 250 bp; effective genome size fraction, 0.86; window size, 750 bp; gap size, 3; redundancy threshold, 1; FDR, 0.001. Statistically significant peaks (FDR < 0.001) enriched in the ChIP sample relative to its corresponding input sample were annotated for genomic location and were assigned to genes within ± 10 kb from transcription start site (TSS) to identify target genes: upstream (-10 to 2.5 kb relative to TSS), promoter (-2.5 kb to $+2.5$ kb), 5'UTR, coding region, 3'UTR. All genes were considered in the 5'→3' orientation. Bedtools was used for manipulation and analysis of data and IGV (<http://www.broadinstitute.org/igv/>) was used for visualization. Annotation files were downloaded from UCSC.

RNA isolation from tumour xenografts. QIAzol (300 μ l per mg tumour) (Qiagen) was added to tumour xenograft tissue. The tumour was lysed and homogenized using the Qiagen TissueLyzer and stainless steel beads. Chloroform was added to the QIAzol lysate. The QIAzol/chloroform homogenate was then added to a Qiagen MaXtract High Density tube (Qiagen). The aqueous phase was transferred to a fresh tube and mixed with an equal volume of 70% ethanol and applied to a Qiagen RNeasy column (Qiagen). The remaining RNA isolation was carried out according to the manufacturer's protocol.

In vivo studies. All studies were conducted after review by the Institutional Animal Care and Use Committee at GSK and in accordance with the GSK

Policy on the Care, Welfare and Treatment of Laboratory Animals. For all *in vivo* studies, GSK126 or vehicle was administered intraperitoneally at a dose volume of 0.2 ml per 20 g body weight in 20% captisol adjusted to pH 4–4.5 with 1 N acetic acid. Pfeiffer or KARPAS-422 cells (1×10^7) in 100% Matrigel (BD Biosciences) were implanted subcutaneously in female beige SCID mice. Tumours were measured with calipers, and block randomized according to tumour size into treatment groups. For efficacy studies, 10 mice were randomized in each treatment group before the initiation of dosing and GSK126 treatment was initiated once the tumour volumes were approximately 200 mm³ in the Pfeiffer and KARPAS-422 studies (Fig. 4c and Supplementary Fig. 14a) and 500 mm³ in the KARPAS-422 intermittent dosing study (Supplementary Fig. 14b). Mice were weighed and tumours measured with calipers twice weekly. Two-tailed *t*-tests were conducted assuming two samples of equal variance. For mouse pharmacokinetic studies, tumour and blood samples were harvested from euthanized mice at the indicated time. Blood and tumour homogenates were flash frozen and subsequently analysed by HPLC/MS/MS to evaluate the concentration of GSK126. For pharmacodynamic studies, a portion of each tumour was frozen for H3K27me3/H3 ELISAs or placed in RNeasy (Qiagen) for RNA isolation. For peripheral blood analyses, blood was harvested via cardiac puncture from euthanized, immunocompetent female CD-1 mice (three mice per group) on day 18. Blood was immediately placed into a Microtainer EDTA tube (BD) and gently mixed by inverting. A complete blood count analysis was conducted using the Advia 2120 haematology analyser (Siemens Medical Solutions) using multi-species software as per manufacturer's instructions.

29. Tornheim, K. Kinetic applications using high substrate and competitive inhibitor concentrations to determine K_i or K_m . *Anal. Biochem.* **221**, 53–56 (1994).
30. Yung-Chi, C. & Prusoff, W. H. Relationship between the inhibition constant (K_i) and the concentration of inhibitor which causes 50 per cent inhibition (I_{50}) of an enzymatic reaction. *Biochem. Pharmacol.* **22**, 3099–3108 (1973).

Fucose sensing regulates bacterial intestinal colonization

Alline R. Pacheco^{1,2}, Meredith M. Curtis^{1,2}, Jennifer M. Ritchie³, Diana Munera³, Matthew K. Waldor³, Cristiano G. Moreira^{1,2} & Vanessa Sperandio^{1,2}

The mammalian gastrointestinal tract provides a complex and competitive environment for the microbiota¹. Successful colonization by pathogens requires scavenging nutrients, sensing chemical signals, competing with the resident bacteria and precisely regulating the expression of virulence genes². The gastrointestinal pathogen enterohaemorrhagic *Escherichia coli* (EHEC) relies on inter-kingdom chemical sensing systems to regulate virulence gene expression^{3,4}. Here we show that these systems control the expression of a novel two-component signal transduction system, named FusKR, where FusK is the histidine sensor kinase and FusR the response regulator. FusK senses fucose and controls expression of virulence and metabolic genes. This fucose-sensing system is required for robust EHEC colonization of the mammalian intestine. Fucose is highly abundant in the intestine⁵. *Bacteroides thetaiotaomicron* produces multiple fucosidases that cleave fucose from host glycans, resulting in high fucose availability in the gut lumen⁶. During growth in mucin, *B. thetaiotaomicron* contributes to EHEC virulence by cleaving fucose from mucin, thereby activating the FusKR signalling cascade, modulating the virulence gene expression of EHEC. Our findings suggest that EHEC uses fucose, a host-derived signal made available by the microbiota, to modulate EHEC pathogenicity and metabolism.

The gastrointestinal tract is inhabited by trillions of commensal bacteria that play crucial roles in human physiology¹. This fundamental relationship between the host and microbiota relies on chemical signalling and nutrient availability², and invading pathogens compete for these resources through the precise coordination of virulence traits. EHEC colonizes the colon, leading to haemorrhagic colitis⁷. EHEC colonization depends on the locus of enterocyte effacement (LEE) pathogenicity island⁷. This pathogenicity island encodes a regulator for its own expression, *ler*, and a type III secretion system, a molecular syringe which injects effectors into the host cell, leading to the formation of attaching and effacing lesions on enterocytes. Attaching and effacing lesions are characterized by remodelling of the host cell cytoskeleton, leading to the formation of a pedestal-like structure beneath the bacteria⁷. LEE expression is regulated by an inter-kingdom chemical signalling system involving the host hormones adrenaline and/or noradrenaline and the microbial flora produced signal autoinducer-3 (AI-3)⁸. These signals are sensed by two histidine sensor kinases, QseC (ref. 3) and QseE (ref. 4), which initiate a signalling cascade that promotes virulence.

Histidine sensor kinases, together with response regulators, comprise a two-component system, which plays a major role in bacterial signal transduction. Upon sensing a signal, the histidine sensor kinases autophosphorylates and then transfers its phosphate to the response regulator. Subsequently, most response regulators bind DNA, promoting changes in gene expression⁹. The cognate response regulator for QseC is QseB and for QseE it is QseF (Fig. 1a). QseBC and QseEF repress expression of the *z0462* and *z0463* genes (Fig. 1b)^{10,11}. QseB repression of *z0462/z0463* expression is direct, whereas QseF-mediated

repression is indirect (Fig. 1c, d), in agreement with QseF being a σ^{54} -dependent transcriptional activator¹². QseF activates the expression of a repressor of *z0462/z0463*.

The *z0462/z0463* genes are within a pathogenicity island (O-island 20 (OI-20))¹³, which is found in EHEC O157:H7 strains and enteropathogenic *E. coli* strains exclusively from the O55:H7 serotype (which gave rise to the O157:H7 serotype), but absent in all other *E. coli* strains whose genomes are currently publicly available. This pathogenicity island is organized in three transcriptional units (Supplementary Fig. 1). The genes *z0462/z0463* encode for a putative two-component system: *z0462* encodes a histidine sensor kinase with eight transmembrane domains that shares similarity (around 30% similarity at the amino acid level) with a glucose-6-phosphate sensor, UhpB; *z0463* encodes a response regulator with a receiver and a DNA-binding

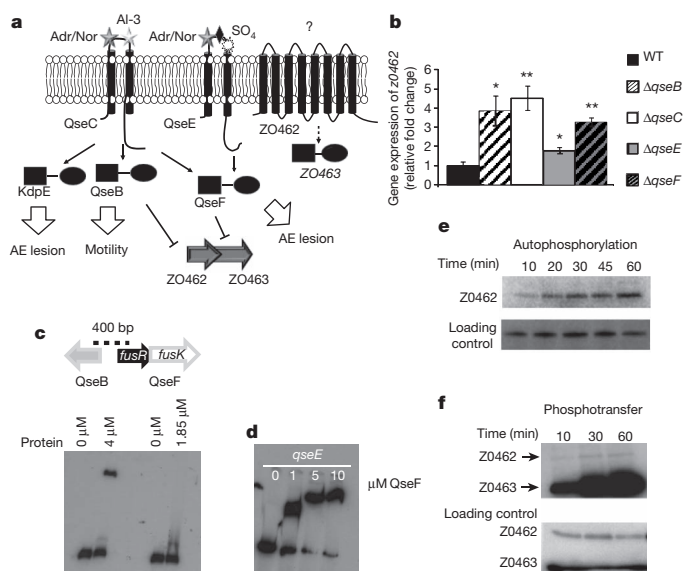


Figure 1 | The two-component system FusKR of EHEC. **a**, The QseC/QseE signalling cascade. QseC senses AI-3 and adrenaline and noradrenaline. QseE senses adrenaline and noradrenaline and SO_4 and PO_4 . QseC phosphorylates QseB (which activates flagella), KdpE (activates the LEE) and QseF. QseE only phosphorylates QseF. QseBC and QseEF repress the expression of *z0462* and *z0463*. AE, attaching and effacing. **b**, qRT-PCR of *z0462* in wild type (WT), $\Delta qseB$, $\Delta qseC$, $\Delta qseE$ and $\Delta qseF$ in DMEM media. Gene expression is represented as fold differences normalized to wild type. Error bars indicate standard deviations of ΔddCt values ($n = 18$ biological samples per strain; $*P < 0.01$, $**P < 0.001$, Student's *t*-test). **c**, Electrophoretic mobility shift assay (EMSA) of *z0463* with QseB and QseF. **d**, EMSA of *qseE* (positive control) with QseF. **e**, Autophosphorylation of Z0462 in liposomes (top panel), and a Coomassie gel of Z0462 (lower panel) (loading control). **f**, Phosphotransfer from Z0462 (in liposomes) to Z0463 (ratio 1 HK: 4 RR) (top panel), loading control Coomassie gel of Z0462 and Z0463 (lower panel).

¹Department of Microbiology, University of Texas Southwestern Medical Center, Dallas, Texas 75390-9048, USA. ²Department of Biochemistry, University of Texas Southwestern Medical Center, Dallas, Texas 75390-9048, USA. ³Division of Infectious Diseases, Brigham and Women's Hospital, Harvard Medical School, Boston, Massachusetts 02115, USA.

domain (Supplementary Fig. 2). Z0462 in liposomes is a functional histidine sensor kinase (Fig. 1e) and it transfers its phosphate to Z0463 (Fig. 1f). Hence, Z0462 and Z0463 constitute a cognate two-component system.

Transcriptomic studies (Supplementary Tables 4 and 5) indicated that Z0462/Z0463 act mainly as repressors of transcription. Z0462 and Z0463 represses LEE gene expression (Supplementary Fig. 3). Transcription of all LEE operons is increased in $\Delta z0462$ (deletion mutant of *z0462*) and $\Delta z0463$ (deletion mutant of *z0463*) and plasmid complementation restored the expression of *ler* to wild-type levels (Fig. 2a–d). Transcription of the LEE genes is activated by *Ler*¹⁴. The response regulator Z0463 directly represses *ler* transcription, and subsequently the other LEE operons, and phosphorylation of Z0463 increases its affinity to *ler* (Fig. 2e, f and Supplementary Figs 6–8).

As expected with the increased LEE transcription, both $\Delta z0462$ and $\Delta z0463$ secreted more EspB, a LEE-encoded protein (Fig. 2g), and formed more pedestals than wild type (Fig. 2h, i). Therefore, Z0462/Z0463 repress attaching and effacing lesion formation. However, expression of other genes encoding non-LEE-encoded type III secretion system effectors, not involved in attaching and effacing lesion formation, are activated by Z0462/Z0463 (Supplementary Fig. 4).

Expression of *z0463* is increased by the mucus produced by intestinal HT29 cells. EHEC-infected undifferentiated HT29 cells were used as negative controls, because they do not produce mucus (Fig. 3a and Supplementary Fig. 9). Z0462 is a predicted hexose-phosphate sensor, hence, Z0462 may sense sugars in the mucus. Fucose is a major component of mucin glycoproteins, it is abundant in the intestine⁵, and fucose utilization is important for EHEC intestinal colonization^{15,16}. In

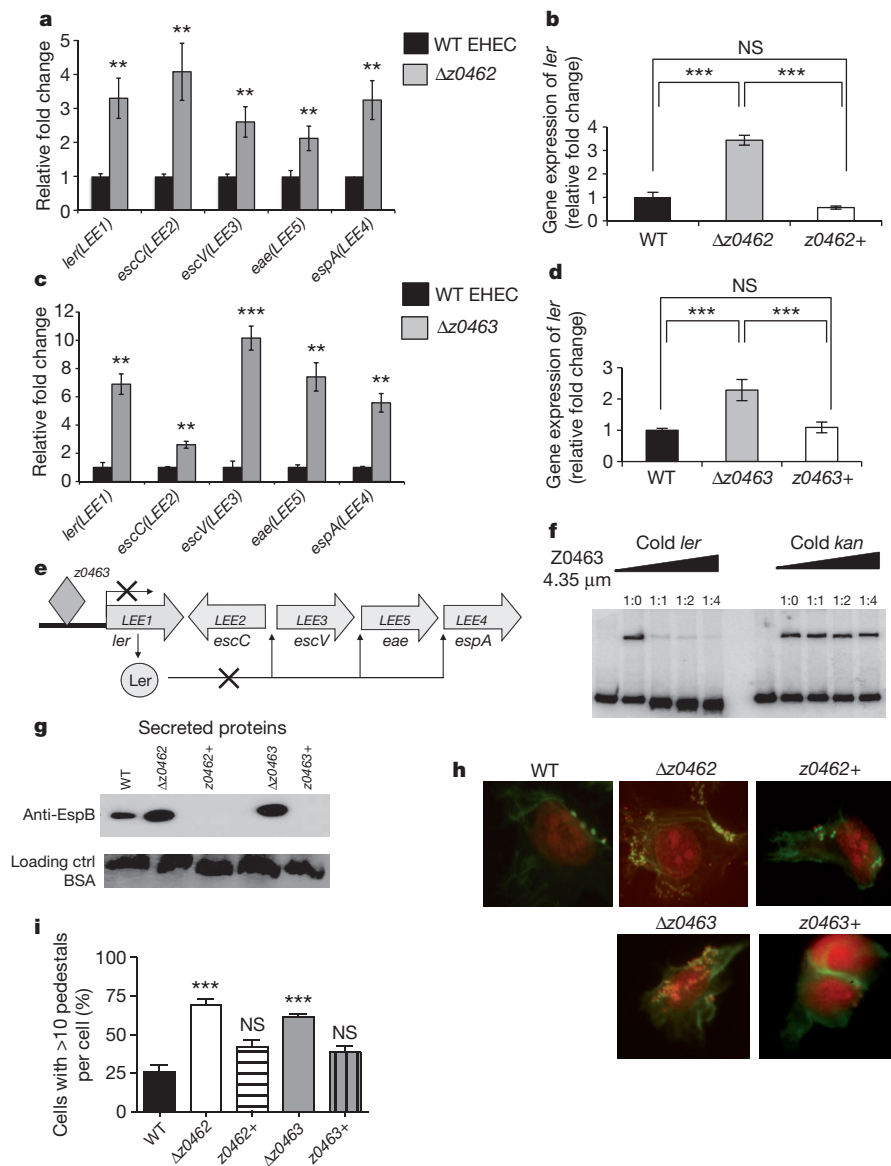


Figure 2 | *z0462/z0463* regulates LEE expression. **a**, qRT-PCR of LEE genes in wild type and $\Delta z0462$ in DMEM media ($n = 18$; error bars, s.d.; ** $P < 0.001$). **b**, qRT-PCR of *ler* in wild type, $\Delta z0462$ and *z0462+* ($\Delta z0462$ rescued with plasmid complementation of *z0462*) in DMEM media ($n = 18$; error bars, s.d.; NS, not significant; *** $P < 0.0001$). **c**, qRT-PCR of LEE genes in WT and $\Delta z0463$ in DMEM media ($n = 18$; error bars, s.d.; ** $P < 0.001$, *** $P < 0.0001$). **d**, qRT-PCR of *ler* in WT, $\Delta z0463$ and *z0463+* ($\Delta z0463$ rescued with plasmid complementation of *z0463*) in DMEM ($n = 18$; ** $P \leq 0.001$, *** $P < 0.0001$; NS, not significant $P > 0.05$; Student's *t*-test). **e**, Representation of the Ler and

Z0463 regulation of the LEE operons. **f**, EMSA of *ler* with Z0463 with *ler* and *kan* (kanamycin) cold probes. Ratios represent hot:cold probe. **g**, Western blot of EspB in supernatants of wild type, $\Delta z0462$, *z0462+*, $\Delta z0463$ and *z0463+* strains. BSA was added as a loading control. **h**, Fluorescent actin staining assay of HeLa cells infected with wild-type EHEC, $\Delta z0462$, *z0462+*, $\Delta z0463$ and *z0463+*, stained with fluorescein isothiocyanate-phalloidin (actin, green) and propidium iodide (bacterial and HeLa DNA, red). Original magnification, $\times 63$. **i**, Quantification of fluorescent actin staining assay ($n = 600$ cells; *** $P < 0.0001$; $P > 0.05 = NS$; Student's *t*-test; error bars, s.d.).

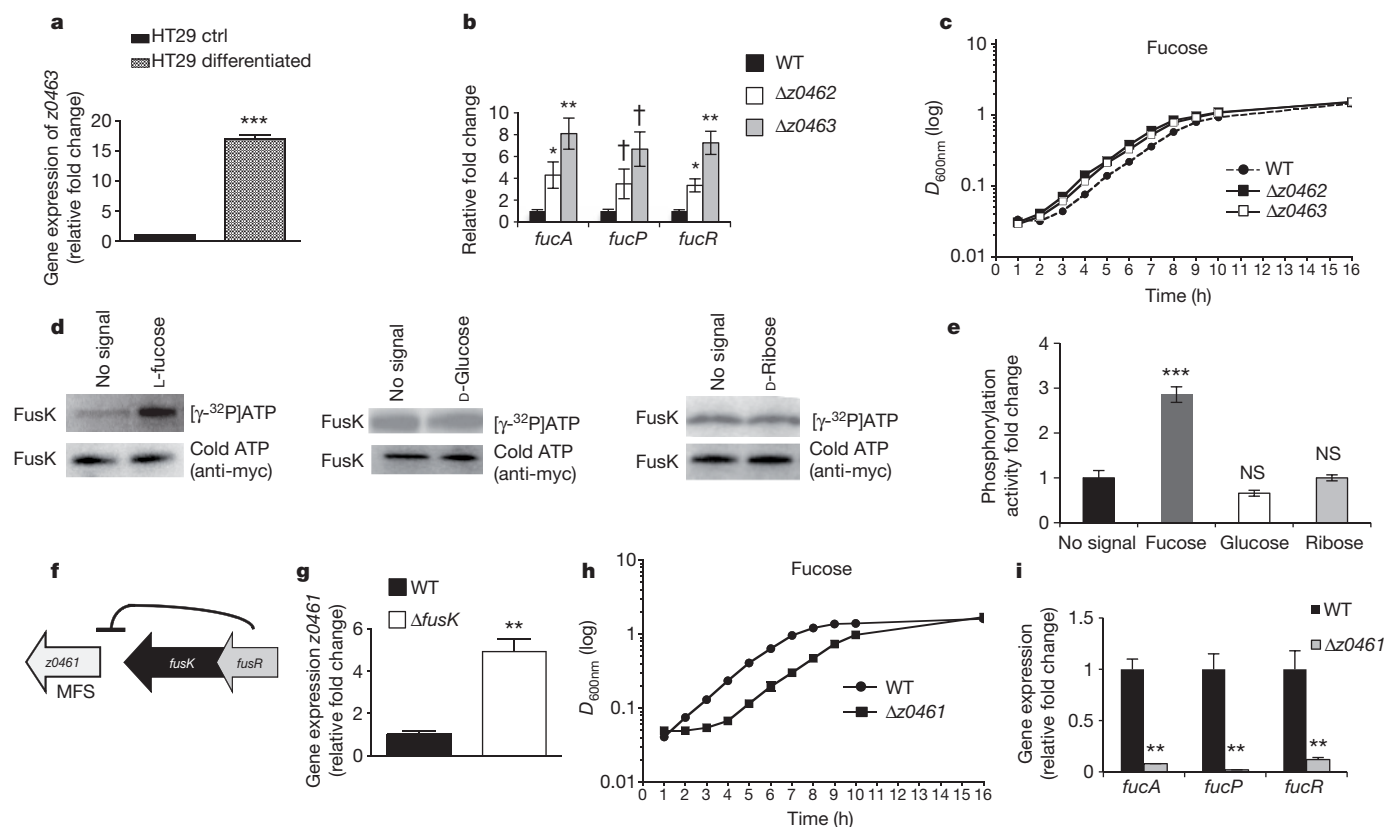


Figure 3 | Z0462 and Z0463 is a fucose-sensing two-component system.

a, qRT-PCR of *z0463* in wild type in the presence of undifferentiated non-mucus-producing HT29 or differentiated mucus-producing HT29 cells. Error bar indicates standard deviations of $\Delta\Delta Ct$ values ($n = 18$; *** $P < 0.0001$; Student's *t*-test). **b**, qRT-PCR of fucose-utilization genes in wild-type EHEC, $\Delta z0462$ and $\Delta z0463$ in DMEM ($D_{600nm} = 1.0$) ($n = 18$; † $P \leq 0.05$; * $P \leq 0.01$; ** $P \leq 0.001$; Student's *t*-test). **c**, Growth curves of wild type, $\Delta z0462$ and $\Delta z0463$ strains in M9 minimal-media with L-fucose as a sole carbon source. ($n = 6$; significance between generation times calculated through analysis of variance (ANOVA) $P \leq 0.01$, error bars too small to be visible on the graph). **d**, FusK autophosphorylation (in liposomes) in the presence of L-fucose, D-glucose or D-ribose (top panel), and Coomassie gel of FusK in liposomes

(lower panel) (loading control). No signal indicates no activating sugar signal added. **e**, Quantification of FusK autophosphorylation. Phosphorylation represented as fold-change compared to absence of signal. Error bar, standard deviation of fold-change values. ($n = 3$; *** $P < 0.0001$; $P > 0.05 = NS$; Student's *t*-test). **f**, Schematic representation of the *fusRK* operon to *z0461*. MFS, major facilitator superfamily. **g**, qRT-PCR of *z0461* in wild type and $\Delta fusK$ (also called $\Delta z0462$) ($n = 18$; ** $P < 0.001$; Student's *t*-test). **h**, Growth curves of wild type and $\Delta z0461$ in M9 medium with fucose as a sole carbon source ($n = 6$; significance between generation times calculated through ANOVA $P \leq 0.01$, error bars too small to be visible on the graph). **i**, qRT-PCR of *fucA*, *fucP* and *fucR* in wild type and $\Delta z0461$ ($n = 18$; ** $P < 0.001$; Student's *t*-test).

E. coli, L-fucose utilization requires the *fuc* genes and their activator FucR (ref. 17). Z0462/Z0463 repress the expression of the *fuc* genes (Fig. 3b), and $\Delta z0462$ and $\Delta z0463$ grow faster with L-fucose as a sole carbon source compared to wild type (generation times of 92.4 min for wild type, 64 min for $\Delta z0462$ and 74 min for $\Delta z0463$) (Fig. 3c). Therefore, Z0462/Z0463 regulates fucose utilization, and this response is specific to fucose, with the mutants and wild type growing at similar rates with other carbon sources (Supplementary Fig. 10). Z0462 senses fucose, but not glucose or D-ribose (Fig. 3d, e). The concentration of fucose used (100 μM) is physiologically relevant to the mammalian intestine¹⁸. Hence we renamed the Z0462 protein as FusK for fucose-sensing histidine kinase and its cognate response regulator, and Z0463 as FusR for fucose-sensing response regulator.

FusKR shares homology to the UhpAB two-component system. UhpAB senses glucose-6-phosphate and activates expression of the *uhpT* gene which encodes a hexose-phosphate major facilitator superfamily transporter^{19–21}. FusKR represses transcription of the *z0461* gene downstream of *fusKR*, which encodes a predicted major superfamily transporter (Fig. 3f, g and Supplementary Figs 3, 11). $\Delta z0461$ has decreased growth (lower concentration of cells) with fucose as a sole carbon source (generation times of 88.2 min for wild type and 96.6 min for $\Delta z0461$) (Fig. 3h), but grows with glucose similarly to wild type (Supplementary Fig. 12), indicating that *z0461* is involved in optimal fucose import. Transcription of the *fuc* operons is linked to

fucose uptake, fucose yields fucose-1-phosphate which is the inducer of the FucR activator of the *fuc* operons^{17,21–23}. Transcription of the *fuc* genes is decreased in $\Delta z0461$ (Fig. 3i). Fucose induces FusKR, which represses *z0461*, decreasing fucose import and the intracellular levels of the fucose-1-phosphate inducer of FucR. In further support of this indirect regulation of the *fuc* genes, FusR does not bind to the *fucPIKUR* promoter region (Supplementary Fig. 13), in contrast to the direct regulation of the LEE (Fig. 2).

The $\Delta fusK$ is not responsive to fucose, given that expression of *ler* is repressed by fucose in wild type, but not in $\Delta fusK$ (Fig. 4a). *B. thetaiotaomicron* produces multiple fucosidases that cleave fucose from host glycans, resulting in high fucose availability in the lumen². *B. thetaiotaomicron* supplies mucin-derived fucose to EHEC, reducing *ler* expression, whereas in free fucose there is no change in *ler* expression whether *B. thetaiotaomicron* is present or not (Fig. 4b). Expression of *ler* is decreased when EHEC is grown in mucin compared to fucose (Fig. 4b), consistent with the increased expression of *fusR* in mucin (Fig. 3a).

In vitro competitions between $\Delta fusK$ and wild type, and $\Delta fusK$ and Δler (which does not express the LEE) in the presence or absence of *B. thetaiotaomicron*, with either fucose or mucin as a sole carbon source were performed. The competition index between $\Delta fusK$ and wild type was 1 (Supplementary Fig. 14a) both in the absence or presence of *B. thetaiotaomicron* during growth in fucose, indicating

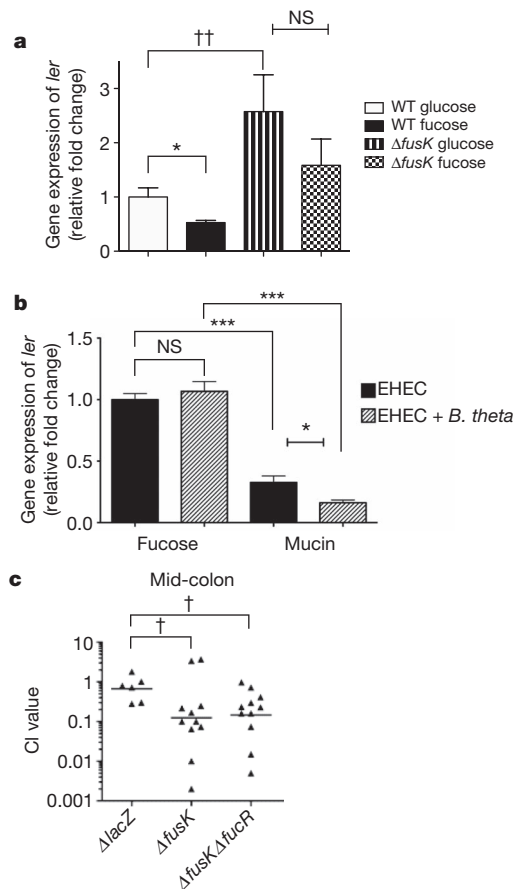


Figure 4 | FusK in pathogen-microbiota-host associations. **a**, qRT-PCR of *ler* in WT or $\Delta fusK$ RNAs extracted from cultures grown in M9 with either D-glucose or L-fucose as sole carbon sources. Error bar indicates standard deviations of ΔAddCt values ($n = 18$; †† $P < 0.02$; * $P < 0.01$; $P > 0.05 = \text{NS}$; Student's *t*-test). **b**, qRT-PCR of *ler* in WT in the presence or absence of *B. thetaiaomicon*. RNA samples from cultures grown in DMEM containing L-fucose or mucin. Error bar, standard deviations of ΔAddCt values. ($n = 18$; ** $P < 0.01$; *** $P < 0.0001$; $P > 0.05 = \text{NS}$; Student's *t*-test). **c**, Competition assays between WT and $\Delta fusK$ or $\Delta fusK \Delta fusR$. Infant rabbits were orogastrically inoculated with 1:1 mixtures of $\Delta fusK$ and wild-type EHEC or $\Delta lacZ$ and wild-type EHEC (which is *lacZ*+) or $\Delta fusK \Delta fusR$ and wild-type EHEC. Colony-forming units in the mid-colon were determined 2 days post-inoculation. Each point represents a competition index (CI). Horizontal lines represent the geometric mean value for each group ($n = 2$ litters (6–11 animals) $\Delta lacZ$ and $\Delta fusK \Delta fusR$, $n = 3$ litters (11 animals) $\Delta fusK$; asterisk, † $P < 0.05$; Mann-Whitney test).

that, in the presence of free fucose, *B. thetaiaomicon* does not affect the competition between $\Delta fusK$ and wild type, and that the growth advantage of $\Delta fusK$ in fucose is counteracted by decreased LEE expression in wild type. When these experiments were performed with mucin as a sole carbon source the competition index between $\Delta fusK$ and WT was 0.1 in the absence, and 1 in the presence of *B. thetaiaomicon* (Supplementary Fig. 14b). In the absence of *B. thetaiaomicon* there is no free fucose, therefore $\Delta fusK$ will not have a growth advantage. Furthermore, the $\Delta fusK$ overexpresses genes from the LEE, which constitutes an energy burden. Meanwhile, expression of *fusR* is activated in mucus (Fig. 3a), further repressing the LEE genes in the wild type. This scenario, however, reverts to a competition index of 1 in the presence of *B. thetaiaomicon*, which releases fucose from mucin, conferring a growth advantage to $\Delta fusK$, counteracting the wild type previous growth advantage (Supplementary Fig. 14b). Similar results were obtained in competitions between $\Delta fusK$ and Δler , consistent with the role of LEE gene expression being an energy burden in $\Delta fusK$ (Supplementary Fig. 14c).

The important role FusK has in the metabolism and virulence of EHEC means it is also important for intestinal colonization. Competition assays in infant rabbits demonstrated that the wild type outcompeted $\Delta fusK$ tenfold (competition index of 0.12), which is statistically different ($P = 0.039$) from a control competition assay, in which the wild type (*lacZ*+) was competed against a $\Delta lacZ$ (competition index of 0.7) (Fig. 4c). Hence, a functional FusK is necessary for robust EHEC intestinal colonization. To determine whether the decreased ability of $\Delta fusK$ to colonize the mammalian intestine was due to uncontrolled expression of the LEE and/or fucose utilization, we performed competition experiments between wild type and $\Delta fusK \Delta fusR$, which does not express the *fuc* genes. The double mutant was outcompeted by the wild type with a similar competition index to the $\Delta fusK$ and wild type competition (Fig. 4c), indicating that fucose utilization does not play a major role in FusK-mediated intestinal colonization, and the burden of LEE overexpression by $\Delta fusK$ is a stronger determinant of its decreased fitness within the intestine.

FusKR repression of LEE expression in the mucus layer prevents superfluous energy expenditure. Once in close contact to the epithelial surface, the QseCE adrenergic-sensing systems are triggered to activate virulence both directly through the QseCE cascade, and indirectly by repression of *fusKR* (Supplementary Fig. 15). EHEC competes with commensal *E. coli* (γ -Proteobacteria), but not with *B. thetaiaomicon*, for the same carbon sources (for example, fucose) within the mammalian intestine^{15,24–28}. Commensal *E. coli*, however, are not found in close contact with the epithelia, being in the mucus layer, where it is counterproductive for EHEC to invest resources to utilize fucose, when EHEC can efficiently use other carbon sources such as galactose, hexorunates or mannose, which are not used by commensal *E. coli* within the intestine¹⁵. Additionally, in contrast to commensal *E. coli*, EHEC is found closely associated with the intestinal epithelium²⁵. Therefore, EHEC can utilize nutrients exclusively available at the surface of the epithelial cells. Consequently, the decreased expression of the *fuc* operon through fucose-sensing by FusKR (Fig. 3) may prevent EHEC from expending energy in fucose utilization in the mucus layer, where it competes with commensal *E. coli* for this resource, and focus on using other carbon sources, not used by that competitor. Thus, the colonization defect of $\Delta fusK$ results from its inability to correctly time virulence and metabolic gene expression.

METHODS SUMMARY

Strains and plasmids are listed in Supplementary Tables 1 and 2. Molecular biology techniques were performed as previously described²⁹. Primers used in quantitative reverse transcription PCR (qRT-PCR) and cloning are listed in Supplementary Table 3. Construction of isogenic mutants was performed using a lambda-red method as previously described³⁰. FusK liposome studies were performed as previously described³.

Full Methods and any associated references are available in the online version of the paper.

Received 23 May; accepted 27 September 2012.

Published online 18 November 2012.

- Kau, A. L., Ahern, P. P., Griffin, N. W., Goodman, A. L. & Gordon, J. I. Human nutrition, the gut microbiome and the immune system. *Nature* **474**, 327–336 (2011).
- Fischbach, M. A. & Sonnenburg, J. L. Eating for two: how metabolism establishes interspecies interactions in the gut. *Cell Host Microbe* **10**, 336–347 (2011).
- Clarke, M. B., Hughes, D. T., Zhu, C., Boedeker, E. C. & Sperandio, V. The QseC sensor kinase: a bacterial adrenergic receptor. *Proc. Natl Acad. Sci. USA* **103**, 10420–10425 (2006).
- Reading, N. C., Rasko, D. A., Torres, A. G. & Sperandio, V. The two-component system QseEF and the membrane protein QseG link adrenergic and stress sensing to bacterial pathogenesis. *Proc. Natl Acad. Sci. USA* **106**, 5889–5894 (2009).
- Robbe, C., Capon, C., Coddeville, B. & Michalski, J. C. Structural diversity and specific distribution of O-glycans in normal human mucins along the intestinal tract. *Biochem. J.* **384**, 307–316 (2004).
- Xu, J. *et al.* A genomic view of the human-Bacteroides *thetaiaomicon* symbiosis. *Science* **299**, 2074–2076 (2003).
- Kaper, J. B., Nataro, J. P. & Mobley, H. L. Pathogenic *Escherichia coli*. *Nature Rev. Microbiol.* **2**, 123–140 (2004).

8. Sperandio, V., Torres, A. G., Jarvis, B., Nataro, J. P. & Kaper, J. B. Bacteria–host communication: the language of hormones. *Proc. Natl Acad. Sci. USA* **100**, 8951–8956 (2003).
9. Stock, A. M., Robinson, V. L. & Goudreau, P. N. Two-component signal transduction. *Annu. Rev. Biochem.* **69**, 183–215 (2000).
10. Hughes, D. T., Clarke, M. B., Yamamoto, K., Rasko, D. A. & Sperandio, V. The QseC adrenergic signaling cascade in enterohemorrhagic *E. coli* (EHEC). *PLoS Pathog.* **5**, e1000553 (2009).
11. Reading, N. C., Rasko, D., Torres, A. G. & Sperandio, V. A transcriptome study of the QseEF two-component system and the QseG membrane protein in enterohaemorrhagic *Escherichia coli* O157:H7. *Microbiology* **156**, 1167–1175 (2010).
12. Barrios, H., Valderrama, B. & Moret, E. Compilation and analysis of σ^{54} -dependent promoter sequences. *Nucleic Acids Res.* **27**, 4305–4313 (1999).
13. Perna, N. T. *et al.* Genome sequence of enterohaemorrhagic *Escherichia coli* O157:H7. *Nature* **409**, 529–533 (2001).
14. Mellies, J. L., Barron, A. M. & Carmona, A. M. Enteropathogenic and enterohemorrhagic *Escherichia coli* virulence gene regulation. *Infect. Immun.* **75**, 4199–4210 (2007).
15. Fabich, A. J. *et al.* Comparison of carbon nutrition for pathogenic and commensal *Escherichia coli* strains in the mouse intestine. *Infect. Immun.* **76**, 1143–1152 (2008).
16. Snider, T. A., Fabich, A. J., Conway, T. & Clinkenbeard, K. D. *E. coli* O157:H7 catabolism of intestinal mucin-derived carbohydrates and colonization. *Vet. Microbiol.* **136**, 150–154 (2009).
17. Chen, Y. M., Zhu, Y. & Lin, E. C. The organization of the *fuc* regulon specifying L-fucose dissimilation in *Escherichia coli* K12 as determined by gene cloning. *Mol. Gen. Genet.* **210**, 331–337 (1987).
18. Jaswal, V. M., Babbar, H. S. & Mahmood, A. Changes in sialic acid and fucose contents of enterocytes across the crypt-villus axis in developing rat intestine. *Biochem. Med. Metab. Biol.* **39**, 105–110 (1988).
19. Island, M. D., Wei, B. Y. & Kadner, R. J. Structure and function of the *uhp* genes for the sugar phosphate transport system in *Escherichia coli* and *Salmonella typhimurium*. *J. Bacteriol.* **174**, 2754–2762 (1992).
20. Weston, L. A. & Kadner, R. J. Identification of Uhp polypeptides and evidence for their role in exogenous induction of the sugar phosphate transport system of *Escherichia coli* K-12. *J. Bacteriol.* **169**, 3546–3555 (1987).
21. Weston, L. A. & Kadner, R. J. Role of *uhp* genes in expression of the *Escherichia coli* sugar-phosphate transport system. *J. Bacteriol.* **170**, 3375–3383 (1988).
22. Zhu, Y. & Lin, E. C. An evolvant of *Escherichia coli* that employs the L-fucose pathway also for growth on L-galactose and D-arabinose. *J. Mol. Evol.* **23**, 259–266 (1986).
23. Chen, Y. M., Tobin, J. F., Zhu, Y., Schleif, R. F. & Lin, E. C. Cross-induction of the L-fucose system by L-rhamnose in *Escherichia coli*. *J. Bacteriol.* **169**, 3712–3719 (1987).
24. Kamada, N. *et al.* Regulated virulence controls the ability of a pathogen to compete with the gut microbiota. *Science* **336**, 1325–1329 (2012).
25. Miranda, R. L. *et al.* Glycolytic and gluconeogenic growth of *Escherichia coli* O157:H7 (EDL933) and *E. coli* K-12 (MG1655) in the mouse intestine. *Infect. Immun.* **72**, 1666–1676 (2004).
26. Chang, D. E. *et al.* Carbon nutrition of *Escherichia coli* in the mouse intestine. *Proc. Natl Acad. Sci. USA* **101**, 7427–7432 (2004).
27. Autieri, S. M. *et al.* L-fucose stimulates utilization of D-ribose by *Escherichia coli* MG1655 $\Delta fucAO$ and *E. coli* Nissle 1917 $\Delta fucAO$ mutants in the mouse intestine and in M9 minimal medium. *Infect. Immun.* **75**, 5465–5475 (2007).
28. Fox, J. T., Drouillard, J. S., Shi, X. & Nagaraja, T. G. Effects of mucin and its carbohydrate constituents on *Escherichia coli* O157 growth in batch culture fermentations with ruminal or fecal microbial inoculum. *J. Anim. Sci.* **87**, 1304–1313 (2009).
29. Sambrook, J., Fritsch, E. F. & Maniatis, T. *Molecular Cloning: a Laboratory Manual* 2nd edn (Cold Spring Harbor Laboratory Press, 1989).
30. Datsenko, K. A. & Wanner, B. L. One-step inactivation of chromosomal genes in *Escherichia coli* K-12 using PCR products. *Proc. Natl Acad. Sci. USA* **97**, 6640–6645 (2000).

Supplementary Information is available in the online version of the paper.

Acknowledgements We thank M. Kendall for comments. We thank the microarray core facility. This work was supported by the National Institutes of Health (NIH) Grants AI053067, AI77853 and AI077613, and the Burroughs Wellcome Fund (to V.S.) and NIH Grant AI42347 and HHMI (to M.K.W.). M.M.C. was supported through NIH Training Grant 5 T32 AI7520-14. The contents are solely the responsibility of the authors and do not represent the official views of the NIH NIAID.

Author Contributions A.R.P. led the project and performed experiments, designed experiments and wrote the paper. M.M.C. J.M.R., D.M., M.K.W. and C.G.M. helped with some experiments. V.S. designed experiments and wrote the paper.

Author Information Microarray data are deposited in the Gene Expression Omnibus under accession number GSE34991. Reprints and permissions information is available at www.nature.com/reprints. The authors declare no competing financial interests. Readers are welcome to comment on the online version of the paper. Correspondence and requests for materials should be addressed to V.S. (vanessa.sperandio@utsouthwestern.edu).

METHODS

Bacterial strains, plasmids and growth conditions. Strains and plasmids are listed in Supplementary Tables 1 and 2. *E. coli* strains were grown aerobically at 37 °C in DMEM (Gibco) or LB media unless otherwise stated. For studies involving fucose utilization, bacterial cultures were grown in M9 minimal media containing 0.4% L-fucose, D-glucose, L-rhamnose, D-galactose or D-xylose (Sigma) as the sole carbon source. For the co-culture experiments between EHEC and *B. thetaiotaomicron*, these strains were grown anaerobically at 37 °C in DMEM buffer (lacking glucose and pyruvate) with or without mucin or free fucose, at a 1:1 ratio of EHEC to *B. thetaiotaomicron*. Enumeration of EHEC was performed through serial dilution of these cultures in McConkey agar containing streptomycin (EHEC strain 86-24 is streptomycin resistant, whereas *B. thetaiotaomicron* is streptomycin sensitive). Enumeration of *B. thetaiotaomicron* was performed through serial plating in TYG medium supplemented with 10% horse blood in the presence of gentamycin (*B. thetaiotaomicron* is gentamycin resistant, whereas EHEC is gentamycin sensitive).

Recombinant DNA techniques. Molecular biology techniques were performed as previously described²⁹. Primers used in qRT-PCR and cloning are listed in Supplementary Table 2.

Isogenic mutant construction. Construction of isogenic $\Delta fusK$, $\Delta fusR$, $\Delta z0461$, Δler and $\Delta fusK\Delta fusR$ mutants was performed using a lambda-red mediated recombination method as previously described³⁰. Primers used to construct these knockouts are depicted in Supplementary Table 3. Briefly, a PCR product used to create a mutation was generated using primers containing homologous regions to sequences flanking *z0462* (for $\Delta fusK$ mutant), *z0463* (for $\Delta fusR$ mutant), *z0461*, *ler*, and *fucR* to amplify a chloramphenicol resistance gene from pKD3. EHEC 86-24 cells harbouring pKD46 were electroporated using the PCR product and selected for chloramphenicol resistance. Nonpolar mutants were generated by resolving the chloramphenicol-resistant clones with resolvase encoded by pCP20. For complementation of the mutants, *z0462* and *z0463* previously cloned into ZeroBlunt TOPO (Invitrogen), were digested with BamHI and SalI then cloned into pACYC184, generating the plasmids pARP12 and pARP13, respectively. pARP12 was electroporated into $\Delta fusK$ to generate the ARP09-complemented strain; pARP13 was electroporated into $\Delta fusR$ cells to generate the ARP10-complemented strain.

FusR purification. FusR was cloned into ZeroBlunt TOPO, digested using XhoI and HindIII restriction enzymes and then cloned into pBADMyHisA, generating pARP11. pARP11 was subsequently transformed into TOP10 cells, generating the ARP04 strain. ARP04 strain was grown in LB to $D_{600nm} = 0.6$ at 37 °C, then protein expression was induced by addition of arabinose (final concentration of 0.2%) and overnight growth at 25 °C. FusR was subsequently purified using nickel columns (Qiagen).

Nested deletion analyses. Transcriptional fusions of the *ler* promoter with promoterless *lacZ* have been described previously³¹. To integrate the transcriptional fusions into the chromosome, *E. coli* MC4100 was lysogenized with phage λ 45, generating strains FS14 and FS16.

FusK purification and reconstitution into liposomes. FusK was cloned into ZeroBlunt TOPO, digested using XhoI and HindIII restriction enzymes and then cloned into pBADMyHisA. This plasmid was subsequently transformed into TOP10 cells, generating the ARP03 strain. The ARP03 strain was grown in LB media at 37 °C until $D_{600nm} = 0.5$ then protein expression was induced by addition of arabinose (final concentration of 0.2%) and growth for 5 h at 30 °C. Cells were collected, resuspended in 50 ml of lysis buffer (50 mM phosphate buffer pH 8.0, 1% deoxycholic acid, 10 mM imidazol, 300 mM NaCl, 15% glycerol, 5 mM dithiothreitol (DTT) and 100 μ l protease inhibitor cocktail), then lysed using emulsiflex. Lysates were incubated for 1 h for solubilization and then isolated by centrifugation at 18,000 r.p.m. for 30 min. Soluble fraction was collected by ultracentrifugation at 45,000 r.p.m. for 1 h to obtain membrane fraction, then membranes were resuspended in lysis buffer and incubated with nickel beads for 1 h at 4 °C with gentle agitation. The membrane suspension and clear lysates were loaded into nickel-nitrilotriacetic acid (Ni-NTA) columns, washed with wash buffer (50 mM phosphate buffer pH 8.0, 20 mM imidazol, 300 mM NaCl, 5 mM DTT and 0.1% deoxycholic acid) and eluted in three steps with elution buffer (250 mM imidazol, 300 mM NaCl, 1 mM DTT and 0.1% deoxycholic acid). Protein was concentrated using centricons with a molecular cutoff of 30,000 kDa, then protein concentration was determined by the Bradford protein assay method. Liposomes were loaded with FusK at a ratio of 20:1. Liposomes were reconstituted as described previously³². FusK presence in liposomes was confirmed by western blot using anti-Myc antibody (Invitrogen).

Autophosphorylation and phosphotransfer assays. Autophosphorylation assays were performed as described previously³. A concentration of 100 μ M L-fucose or D-glucose was used. The bands were quantified using ImageQuant software version 3.2. Quantification of triplets was performed. The Student's *t*-test was used

to determine statistical significance. A *P*-value of less than 0.05 was considered significant.

RNA extraction and qRT-PCR. RNA from six biological replicates (experiments performed three independent times, for a total of 18 independent biological replicates) was extracted using RiboPure kit according to the manufacturer's instructions (Invitrogen). Primer validation and real-time PCR was performed as described previously³³. Gene expression is represented as fold differences compared to the wild type EHEC strain 86-24. Error bars indicate the standard deviations of the $\Delta\Delta C_t$ values. The Student *t*-test was used to determine statistical significance. A *P* value of less than 0.05 was considered significant.

Microarrays. Microarray experiments and analysis were performed as previously described³⁴. The GeneChip *E. coli* Genome 2.0 array system (Affymetrix) was used to compare the gene expression in EHEC strain 86-24 to that of $\Delta fusK$ and $\Delta fusR$ strains. The output from scanning the Affymetrix GeneChip *E. coli* 2.0 was obtained using GCOS software v 1.4 according to the manufacturer's instructions. Comparisons were performed using the analysis tools within GCOS v 1.4, by selecting the appropriate array, CHP file for comparison and baseline values. Custom analysis scripts were written in Perl to complete multiple array analyses. Expression data can be accessed using accession number (GSE34991) at the NCBI GEO database.

Fluorescent actin staining (FAS) assay. Fluorescein actin staining (FAS) assays were performed as previously described³⁵. Pedestal enumeration was performed in 600 infected cells. The Student *t*-test was used to determine statistical significance. A *P*-value of less than 0.05 was considered significant.

In vitro competition assays. Bacterial strains were grown for 18 h in LB at 37 °C, resuspended in DMEM without glucose and inoculated 1:100 in DMEM (without glucose, without pyruvate) containing fucose or mucin as the sole carbon source. *B. thetaiotaomicron* was grown in TYG medium, resuspended in DMEM (without glucose) and inoculated at a 1:9 ratio. *In vitro* competitions were carried out anaerobically and samples were collected hourly for serial dilution and plating for the colony-forming units count. A competition index was determined by the ratio of $\Delta fusK$ to wild-type EHEC or the ratio of $\Delta fusK$ to Δler .

Infant rabbit infection studies. Litters of 3-day-old infant rabbits were infected as described previously³⁶. Individual rabbits were orogastrically inoculated (approximately 5×10^8 colony-forming units per 90 g of animal's weight) with 1:1 mixtures of wild-type ($\Delta lacZ$) EHEC and the $\Delta fusK$ of $\Delta fusK\Delta fusR$. The animals were killed 2 days postinoculation and colonic tissue samples removed and homogenized before microbiological analysis. The number of wild-type and *fusK* mutant cells present in the tissue homogenate was determined by serial dilution and plating on media containing streptomycin and 5-bromo-4-chloro-3-indolyl- β -D-galactoside (X-gal) as previously described³⁶. Competition indexes were calculated as the ratio of $\Delta fusK$ to wild type or $\Delta fusK\Delta fusR$ to wild type in tissue homogenates divided by the ratio of $\Delta fusK$ to wild type or $\Delta fusK\Delta fusR$ to wild type in the input. The competition index was compared to the competition index value obtained when otherwise isogenic *lacZ* (wild type) and $\Delta lacZ$ strains were given to rabbits. Differences in *cis* were compared using the Mann-Whitney test, where a *P*-value of less than 0.05 was considered significant. All animal experiments performed were approved by the IACUC offices of University of Texas Southwestern Medical Center and Brigham and Women's Hospital. ($\Delta lacZ$ *n* = 2 litters (6–11 animals) and $\Delta fusK\Delta fusR$, *n* = 3 litters (11 animals)).

β -galactosidase activity assays. The bacterial strains FS14, FS15 and FS16 were transformed with pFusR or empty vector (pBADMyHisA) and grown in aerobically in DMEM containing 0.2% arabinose at 37 °C to $D_{600nm} = 0.8$. The cultures were diluted 1:100 in Z buffer (60 mM Na₂HPO₄·7H₂O and 50 mM β -mercaptoethanol) and assayed for β -galactosidase activity by using *o*-nitrophenyl- β -D-galactopyranoside as substrate as previously described³⁷.

Electrophoretic mobility shift assay (EMSA). EMSAs were performed using purified FusR-Myc-His and radiolabelled probes. Primers were end-labelled using [³²P]ATP and T4 polynucleotide kinase (NEB), and subsequently used on a PCR to generate radiolabelled probes. End-labelled amplicons were run on a 6% polyacrylamide gel, excised and purified using a Qiagen gel extraction kit. To test the ability of FusR to bind directly to its target promoters, increasing amounts of FusR (0 to 4.35 μ M) were incubated with end-labelled probe (10 ng) for 20 min at 4 °C in binding buffer (500 μ g ml⁻¹ BSA, 50 ng poly(deoxyinosinic-deoxycytidylic) (dIdC) acid, 6 mM HEPES, pH 7.5, 5 mM EDTA, 3 mM DTT, 300 mM KCl and 25 mM MgCl₂). A sucrose solution was used to stop the reaction³⁹. The reactions were run on a 6% polyacrylamide gel for 6.5 h at 180 V. The gels were dried under vacuum and EMSAs were visualized by autoradiography.

DNase I footprinting. DNase I footprint was performed as previously described³⁸. Briefly: primer Ler-18FP-R (Supplementary Table 2) was end-labelled using [³²P]ATP and T4 polynucleotide kinase (NEB) and used in a PCR with cold primer Ler-299FP-F (Supplementary Table 2) to generate probe LerFP. The resulting end-labelled probe was used in a binding reaction (described in the EMSA subsection) for 20 min at room temperature. At this time, a 1:100 dilution of

DNase I (NEB) and the manufacturer-supplied buffer were added to the reaction and digestion proceeded for 7 min at room temperature. The digestion reaction was stopped by addition of 100 µl of stop buffer (200 mM NaCl, 2 mM EDTA and 1% SDS). Protein extraction was performed using phenol-chloroform and DNA was precipitated using 5 M NaCl, 100% ethanol and 1 µl glycogen. The DNase reactions were run in a 6% polyacrylamide-urea gel next to a sequencing reaction (Epicentre). Amplicon generated using primers Ler-299FP-F and Ler-18FP-R (radiolabelled) was used as a template for the sequencing reaction. The footprint was visualized by autoradiography.

31. Sharp, F. C. & Sperandio, V. QseA directly activates transcription of *LEE1* in enterohemorrhagic *Escherichia coli*. *Infect. Immun.* **75**, 2432–2440 (2007).
32. Janausch, I. G., Garcia-Moreno, I., Lehnen, D., Zeuner, Y. & Uden, G. Phosphorylation and DNA binding of the regulator DcuR of the fumarate-responsive two-component system DcuSR of *Escherichia coli*. *Microbiology* **150**, 877–883 (2004).
33. Walters, M. & Sperandio, V. Quorum sensing in *Escherichia coli* and *Salmonella*. *Int. J. Med. Microbiol.* **296**, 125–131 (2006).
34. Kendall, M. M., Rasko, D. A. & Sperandio, V. Global effects of the cell-to-cell signaling molecules autoinducer-2, autoinducer-3, and epinephrine in a *luxS* mutant of enterohemorrhagic *Escherichia coli*. *Infect. Immun.* **75**, 4875–4884 (2007).
35. Knutton, S., Baldwin, T., Williams, P. H. & McNeish, A. S. Actin accumulation at sites of bacterial adhesion to tissue culture cells: basis of a new diagnostic test for enteropathogenic and enterohemorrhagic *Escherichia coli*. *Infect. Immun.* **57**, 1290–1298 (1989).
36. Ritchie, K. M., Thorpe, C. M., Rogers, A. B. & Waldor, M. K. Critical roles for *stx₂*, *eae*, and *tir* in *Escherichia coli*-induced diarrhea and intestinal inflammation in infant rabbits. *Infect. Immun.* **71**, 7129–7139 (1989).
37. Miller, J. H. *Experiments in Molecular Genetics*. (Cold Spring Harbor Laboratory Press, 1972).
38. Sperandio, V. How the bacterial flora and the epithelial cell get along. *Trends Microbiol.* **8**, 544 (2000).

HIV therapy by a combination of broadly neutralizing antibodies in humanized mice

Florian Klein¹, Ariel Halper-Stromberg^{1*}, Joshua A. Horwitz^{1*}, Henning Gruell^{1,2}, Johannes F. Scheid^{1,3}, Stylianos Bournazos⁴, Hugo Mouquet¹, Linda A. Spatz^{1,5}, Ron Diskin⁶, Alexander Abadir¹, Trinity Zang⁷, Marcus Dorner⁸, Eva Billerbeck⁸, Rachael N. Labitt⁸, Christian Gaebler^{1,9}, Paola M. Marcovecchio⁶, Reha-Baris Incesu¹, Thomas R. Eisenreich¹, Paul D. Bieniasz^{7,10}, Michael S. Seaman¹¹, Pamela J. Bjorkman^{6,12}, Jeffrey V. Ravetch⁴, Alexander Ploss⁸ & Michel C. Nussenzweig^{1,10}

Human antibodies to human immunodeficiency virus-1 (HIV-1) can neutralize a broad range of viral isolates *in vitro* and protect non-human primates against infection^{1,2}. Previous work showed that antibodies exert selective pressure on the virus but escape variants emerge within a short period of time^{3,4}. However, these experiments were performed before the recent discovery of more potent anti-HIV-1 antibodies and their improvement by structure-based design^{5–9}. Here we re-examine passive antibody transfer as a therapeutic modality in HIV-1-infected humanized mice. Although HIV-1 can escape from antibody monotherapy, combinations of broadly neutralizing antibodies can effectively control HIV-1 infection and suppress viral load to levels below detection. Moreover, in contrast to antiretroviral therapy^{10–12}, the longer half-life of antibodies led to control of viraemia for an average of 60 days after cessation of therapy. Thus, combinations of potent monoclonal antibodies can effectively control HIV-1 replication in humanized mice, and should be re-examined as a therapeutic modality in HIV-1-infected individuals.

Treatment of HIV-1 infection was ineffective until antiretroviral drugs were applied in combination, permitting sustained suppression of viraemia^{13,14}. Despite this resounding success, the burden of daily medication, side effects and resistance to antiretroviral drugs necessitate a continuing search for additional complementary therapeutic modalities¹⁵.

To examine the potential of recently discovered antibodies to control HIV-1 infection effectively, we used non-obese diabetic (NOD) mice that carry targeted disruptions of the recombinase activating gene 1 (*Rag1*^{−/−}) and interleukin receptor common gamma chain (*Il2rg*^{null}) reconstituted with human fetal liver-derived CD34⁺ haematopoietic stem cells^{16,17}. Humanized mice were preferred to non-human primates for these experiments because the latter produce anti-human antibodies that can alter the bioavailability of the injected human antibodies after only one to two weeks.

Humanized mice were analysed for engraftment (Supplementary Fig. 1) and infected intraperitoneally (i.p.) with a CCR5-tropic HIV-1 isolate (NL4-3 carrying a YU2 envelope; HIV-1_{YU2})¹⁸. Viral load in plasma was determined by quantitative polymerase chain reaction with reverse transcription (qRT-PCR) with a limit of detection of 800 copies ml^{−1} (Supplementary Fig. 2). Viraemia was established (geometric mean of 1.06×10^5 copies ml^{−1}) by 14–20 days, and was stable for 60 days before decreasing to a geometric mean of 1.6×10^4 copies ml^{−1} at 120 days after infection (Fig. 1a). Persistent viraemia was associated with progressive reduction in CD4⁺ T cells as measured by decreasing CD4⁺ to CD8⁺ T-cell ratios (Supplementary Fig. 3).

To confirm that HIV-1_{YU2} infection in humanized mice is associated with viral diversification¹⁹, we cloned and sequenced 68 gp120 envelopes from 10 infected mice (Fig. 1a). After accounting for randomly introduced PCR errors (Supplementary Fig. 4a and b), we observed an average of 3.2 nucleotide substitutions per gp120 sequence, corresponding to a substitution rate of 2.2×10^{-3} bp^{−1} (Supplementary Fig. 4b). We conclude that HIV-1_{YU2} infection is well established by 14–20 days in humanized mice, it persists for several months, and the virus mutates generating viral swarms^{18,19}.

To examine the effects of broadly neutralizing antibodies on established HIV-1 infection, we treated groups of HIV-1_{YU2}-infected mice with antibody monotherapy using five different broadly neutralizing antibodies. The antibodies were selected based on their potency and breadth in *in vitro* neutralization assays and because they target different epitopes. 45-46^{G54W} is the most potent anti-CD4 binding site (CD4bs) antibody reported so far⁵, PG16 targets the V1/V2 loop region^{8,20}, PGT128 is a glycan-dependent anti-V3 loop antibody⁷, and 10-1074 is a more potent variant of PGT121 (refs 7, 30) that has no measurable affinity for protein-free complex-type N-glycans in microarrays³⁰. 3BC176 recognizes a conformational, yet-to-be-defined epitope, and neutralizes HIV-1 strains that are resistant to potent CD4bs antibodies²¹. Mice were treated subcutaneously with 0.5 mg of antibody per mouse (~ 20 mg kg^{−1}) either once or twice a week based on the antibodies' half-life in mice, which varied from 0.7 to 6.3 days (Supplementary Fig. 5).

At 6–7 days after the initiation of therapy, mice treated with PGT128 or 10-1074 showed an average decrease of 1.1 log₁₀ ($P \leq 0.05$) and 1.5 log₁₀ ($P \leq 0.01$) HIV-1 RNA copies ml^{−1}, respectively (Fig. 1b, c and Supplementary Table 1). The results for PG16 and 45-46^{G54W} were variable, with an average decrease of 0.23 log₁₀ and 0.56 log₁₀ copies ml^{−1} (Fig. 1b, c and Supplementary Table 1), whereas no effect was detected for 3BC176. However, with the exception of one mouse receiving 10-1074, viraemia rebounded after 14–16 days and no significant differences between treated and control groups were detected thereafter (Fig. 1b, c). We conclude that monotherapy with PG16, 45-46^{G54W}, PGT128 or 10-1074 results in an only transient decrease in the viral load in humanized mice infected with HIV-1_{YU2}.

To determine whether viral escape from monoclonal antibody therapy is linked to specific mutations, we cloned and sequenced gp120 from HIV-1_{YU2}-infected mice before (Supplementary Fig. 6) and after (Supplementary Fig. 7) viral rebound. In all cases, viral rebound was associated with recurring mutations (defined as substitutions within a range of 3 amino acids in a majority of gp120 clones in more than one

¹Laboratory of Molecular Immunology, The Rockefeller University, New York, New York 10065, USA. ²Medizinische Fakultät, Westfälische Wilhelms-Universität Münster, D-48149 Münster, Germany.

³Charité Universitätsmedizin, D-10117 Berlin, Germany. ⁴Laboratory of Molecular Genetics and Immunology, The Rockefeller University, New York, New York 10065, USA. ⁵Department of Microbiology and Immunology, Sophie Davis School of Biomedical Education, The City College of New York, New York, New York 10031, USA. ⁶Division of Biology, California Institute of Technology, Pasadena, California 91125, USA. ⁷Aaron Diamond AIDS Research Center, Laboratory of Retrovirology, The Rockefeller University, New York, New York 10065, USA. ⁸Laboratory of Virology and Infectious Diseases, The Rockefeller University, New York, New York 10065, USA. ⁹Faculty of Medicine Carl Gustav Carus, Technische Universität Dresden, D-01307 Dresden, Germany. ¹⁰Howard Hughes Medical Institute, The Rockefeller University, New York, New York 10065, USA. ¹¹Beth Israel Deaconess Medical Center, Boston, Massachusetts 02215, USA. ¹²Howard Hughes Medical Institute, California Institute of Technology, Pasadena, California 91125, USA.

*These authors contributed equally to this work.

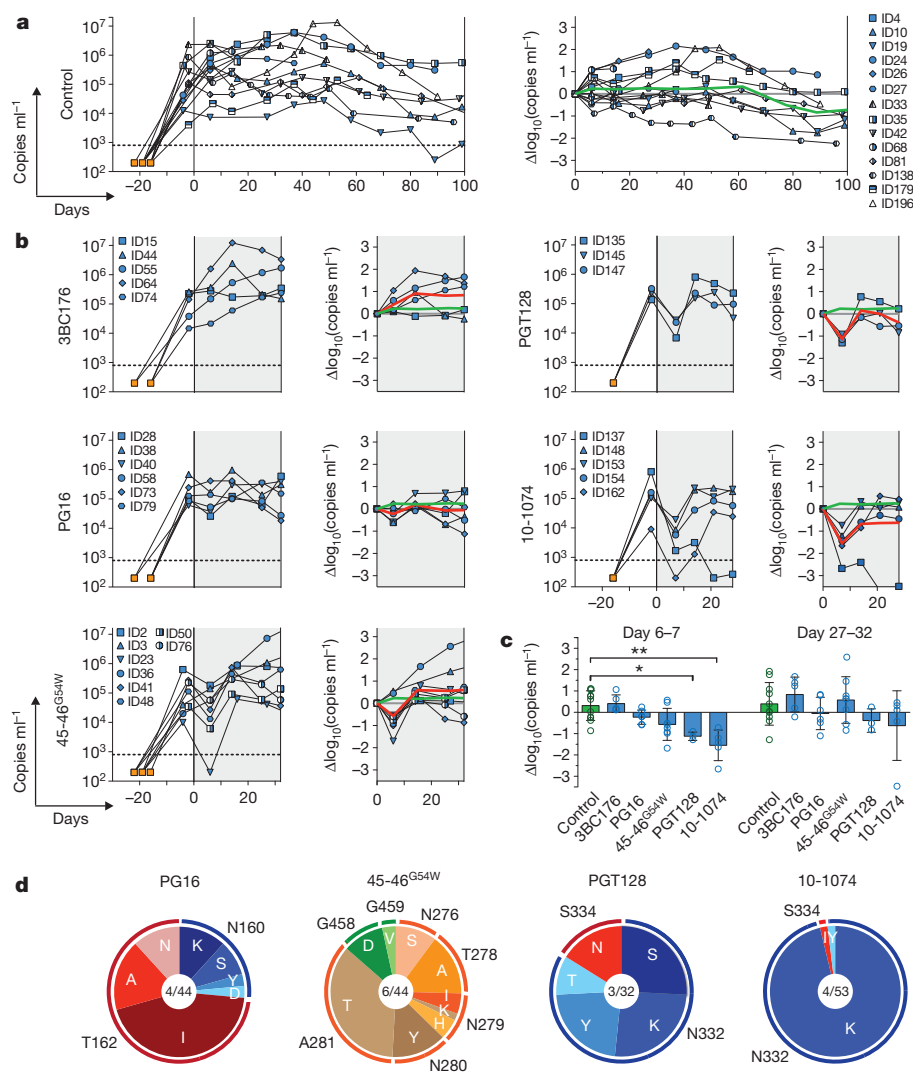


Figure 1 | Monotherapy using broadly neutralizing antibodies in HIV-1YU2-infected humanized mice. **a**, The left panel shows viral loads (RNA copies ml⁻¹, y axis) measured over time (days, x axis) in untreated HIV-1YU2-infected humanized mice (control group). Each line represents a single mouse and symbols reflect viral load measurements. Symbol characters correspond to individual mice as indicated (right). Humanized mice were infected with HIV-1YU2 (i.p.) between day -22 and -16 (orange square) and baseline viral loads were measured between day -4 and -2 (Supplementary Table 1). The dotted line represents the limit of detection for viral load determination (800 copies ml⁻¹). The right panel shows changes in log₁₀ (RNA copies ml⁻¹) from baseline (grey line) at day 0 with the green line representing the average in viral load changes. **b**, Illustration of HIV-1 viral loads as in **a** but with single antibody treatment (shaded in grey) starting at day 0. The red line represents the average in viral load changes superimposed with averages of the control group (green line, **a**). **c**, Changes in log₁₀ (RNA copies ml⁻¹) 6–7 days and

27–32 days after treatment initiation. Columns and error bars represent mean and standard deviation, respectively. Significant statistical differences among groups were determined by performing a Kruskal–Wallis test with Dunn multiple comparison post-hoc test using GraphPad Prism version 5.0b for Mac OS X, GraphPad software. Significant differences among groups were detected at day 6–7 but not at the later time point (27–32 days). Asterisks (**P* ≤ 0.05; ***P* ≤ 0.01) indicate a significant difference compared to the control group. **d**, Sequence analysis of HIV-1 gp120 after viral rebound while on therapy with single broadly neutralizing antibodies (Supplementary Fig. 7). Pie charts show the distribution of amino acid changes at recurrently mutated sites. A selection of amino acid substitutions was tested *in vitro* and confirmed antibody escape (Supplementary Fig. 8 and Supplementary Table 2b). Mutations are relative to HIV-1YU2 and numbered according to HXBc2. The total numbers of analysed mice/gp120 sequences are indicated in the centre of the charts (Supplementary Fig. 7 and Supplementary Table 2b).

mouse) in residues that map to the antibody target sites (Fig. 1d, Supplementary Fig. 7 and Supplementary Table 2b). For example, escape from 45-46^{G54W} was linked to mutations in residues 276–281, 458 or 459, which are located in or near the CD4bs²². Likewise, escape from PG16 was associated with mutations at residues 160 or 162, which correspond to the potential N-linked glycosylation site (PNGS) in the V1/V2 loop^{8,20}. Escape from PGT128 and 10-1074 was associated with mutations at residues 332 or 334, both of which abrogate the same PNGS (Fig. 1d, Supplementary Fig. 7 and Supplementary Table 2b).

To verify that the putative escape mutations rendered HIV-1YU2 resistant to the respective antibodies, we produced selected HIV-1YU2 pseudoviruses carrying the mutations and tested them in neutralization assays *in vitro*. Tested recurrent mutations associated with escape were

always associated with specific resistance to their respective antibodies (Supplementary Fig. 8). Passenger mutations, defined as occurring in only a single mouse, or in multiple mice but in fewer than 50% of gp120 sequences in those mice, had no apparent effect on viral sensitivity to the antibodies (Supplementary Fig. 8).

Although escape mutations were associated with antibody-targeted epitopes, some gp120 residues seemed to tolerate multiple alternative amino acid substitutions, whereas others were more restricted. For example, in humanized mice treated with 45-46^{G54W}, N279 mutated to H, K, or I, but A281 only became T (Fig. 1d and Supplementary Table 2b). Escape from PGT128 was associated with replacement of N332 with K, S, T or Y, whereas it became K in 51 out of 52 sequences from 4 humanized mice treated with 10-1074 (Fig. 1d,

and Supplementary Table 2b). Consistent with this observation, N332K is resistant to both PGT128 and 10-1074, whereas N332Y is resistant to PGT128 but remains sensitive to high concentrations of 10-1074 (Supplementary Fig. 8).

Because the selected broadly neutralizing antibodies target distinct epitopes on the HIV-1 spike, we investigated whether treatment with a combination of three (tri-mix: 3BC176, PG16 and 45-46^{G54W}) or five (penta-mix: 3BC176, PG16, 45-46^{G54W}, PGT128 and 10-1074) antibodies would alter the course of infection (Fig. 2 and Supplementary Table 1). These combinations neutralize all but 2 (tri-mix 98.3%) and 1 (penta-mix 99.2%) of 119 mostly tier 2 and 3 viruses from multiple clades with an IC₈₀ (geometric mean) of 0.121 $\mu\text{g ml}^{-1}$ and 0.046 $\mu\text{g ml}^{-1}$ for tri-mix and penta-mix, respectively (Supplementary Fig. 9).

A decline in the initial viral load was seen in 11 out of 12 tri-mix-treated mice, but 7 rebounded to pre-treatment levels (Fig. 2a, Supplementary Table 1c and Supplementary Fig. 10). In contrast to monotherapy where mice almost never controlled viraemia beyond 2 weeks of therapy, the tri-mix treatment led to prolonged and effective HIV-1 control in 3 of 12 animals. In 2 of these mice viral load rebounded 20–40 days after cessation of therapy at a time when the YU2 gp120-reactive antibody concentration in serum decreased to a level below detection (Fig. 3a). In the third mouse (ID21), viraemia was detected but remained low even in the absence of therapy for 60 days.

Sequences obtained from mice that experienced viral rebound while on tri-mix therapy showed a combination of the mutations found in the PG16 and 45-46^{G54W} monotherapy groups (Figs 1d and 2b, c and Supplementary Tables 2b and 3a). We verified that these mutations rendered HIV-1_{YU2} resistant to PG16 and 45-46^{G54W} by producing the corresponding mutant pseudoviruses and testing them in neutralization assays *in vitro* (Supplementary Fig. 8). The pseudoviruses were not resistant to 3BC176, confirming that this antibody did not exert selective pressure on HIV-1_{YU2} and therefore only 2 of the 3 antibodies in the tri-mix were efficacious.

In contrast, sequences obtained from the mice that exhibited sustained viral control and rebounded after cessation of therapy either lacked any broadly neutralizing antibody-associated mutation, or had a mutation mapped to the 45-46^{G54W} (K282R) or PG16 (N162P) target site, but not both (Fig. 3b and Supplementary Table 3a). In these mice, rebound viraemia only occurred after YU2 gp120-reactive antibody levels decreased to below detection, indicating that the viruses that emerged were latent and remained susceptible to the tri-mix.

All 14 mice treated with the penta-mix treatment showed a decrease in viral load 6–7 days after initiation of therapy (Fig. 2d and Supplementary Table 1d). However, in contrast to monotherapy and the tri-mix, all of the penta-mix-treated mice remained below baseline viral loads during the entire treatment course (Fig. 2d, Supplementary Table 1d and Supplementary Fig. 10). Of 13 mice (one died), 11 had viral loads below or near the limit of detection. The two mice with the slowest reduction in viral load during treatment showed signs of severe graft versus host disease. We conclude that penta-mix therapy reduces the viral load to levels below detection for up to 60 days in HIV-1_{YU2}-infected humanized mice.

Penta-mix therapy was discontinued after 31–60 days and the mice were monitored for an additional 100 days (Fig. 3c). In 7 out of 8 mice that survived, viraemia rebounded after an average of 60 days (Fig. 3c). In contrast, mice treated with antiretroviral therapy rebound after 10 days following discontinuation of therapy¹². Viral rebound in penta-mix-treated mice was always correlated with decreased levels of the administered antibodies (Fig. 3c). Only one tri-mix (ID21) and one penta-mix (ID129) mouse did not rebound. To determine their ability to support HIV-1 infection, these mice were re-infected with HIV-1_{YU2} (57.5 ng p24) and measured for viral load 2 weeks later. One of the two mice became infected but only at very low levels compared to the initial infection (Supplementary Fig. 11). Therefore, prolonged control was primarily due to the long half-life of the injected antibodies.

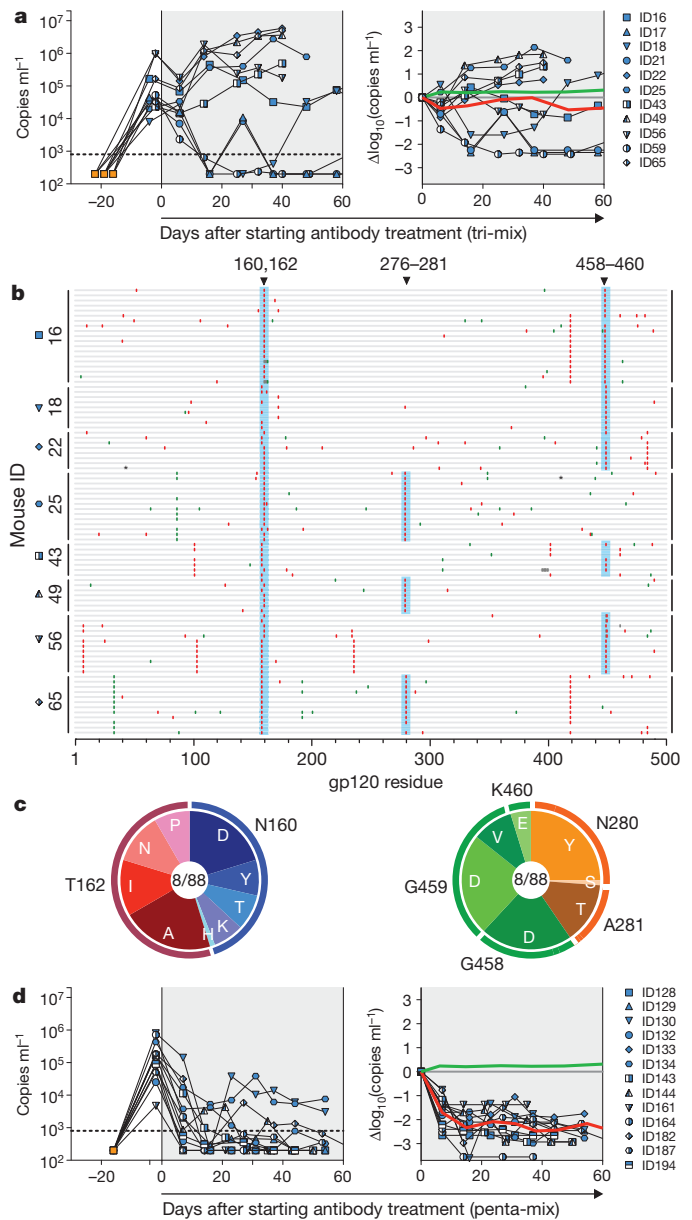


Figure 2 | HIV therapy by a combination of three (tri-mix) or five (penta-mix) broadly neutralizing antibodies in HIV-1_{YU2}-infected humanized mice. **a**, The left panel shows viral loads (RNA copies ml⁻¹, y axis) over time (days, x axis) in HIV-1_{YU2}-infected humanized mice treated with a combination of 3BC176, PG16 and 45-46^{G54W} (tri-mix; grey shading). Each line represents a single mouse and symbols indicate viral load measurements (Supplementary Table 1c). Infection and viral load determination was performed as in Fig. 1. The right panel shows changes in log₁₀ (RNA copies ml⁻¹) from baseline at day 0. Red and green lines represent the average values in viral load change of tri-mix and control group (Fig. 1a), respectively. **b**, Individual gp120 envelope sequences cloned from single mice (y axis) during tri-mix therapy after viral rebound. gp120 sequences are represented by horizontal grey bars with silent mutations indicated in green and amino acid replacements in red. Black asterisks represent mutations generating a stop codon and bold grey bars deletions. All mutations are relative to HIV-1_{YU2} and numbered according to HXBc2. Selected mutations at sites highlighted in blue can confer resistance to PG16- or 45-46^{G54W}-mediated neutralization *in vitro* (Supplementary Fig. 8 and Supplementary Table 3a). **c**, Pie charts as in Fig. 1d illustrate distribution of amino acid changes in gp120 (b) at PG16 (left) or 45-46^{G54W} (right) respective target sites (Supplementary Table 3a). **d**, As in **a**, for HIV-1_{YU2}-infected humanized mice treated with a combination of 3BC176, PG16, 45-46^{G54W}, PGT128 and 10-1074 (penta-mix; grey shading, Supplementary Table 1d). Mouse ID72 (tri-mix) and ID126 (penta-mix) died early and are not displayed.

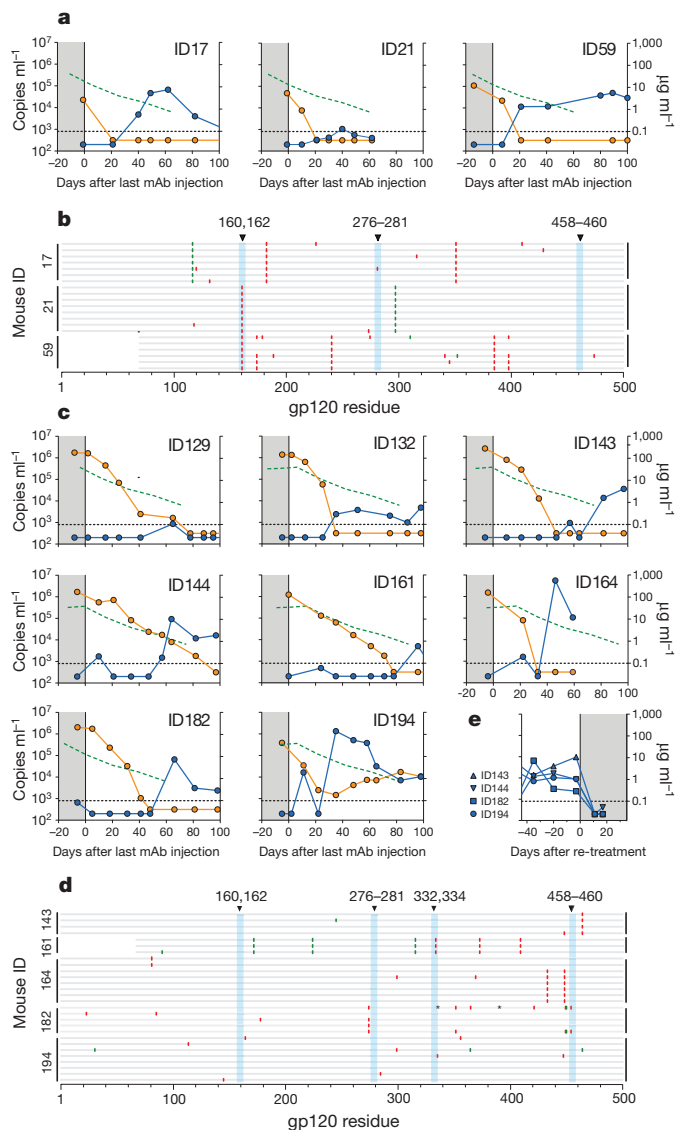


Figure 3 | Viral rebound in HIV-1_{YU2}-infected humanized mice after cessation of antibody therapy. Viral load in RNA copies ml⁻¹ (blue, left y axis) and antibody concentration reactive to YU2 gp120 in µg ml⁻¹ (orange, right y axis) over time (x axis) after the last antibody injection (day 0). The green dotted line indicates the viral load average of the control group (Fig. 1a). **a**, Viral load and YU2 gp120-reactive antibody concentration after stopping tri-mix therapy in mice that effectively controlled viraemia below the limit of detection. mAb, monoclonal antibody. **b**, gp120 sequences illustrated as in Fig. 2b for viruses obtained after viral rebound from mice previously treated with tri-mix therapy. Vertical blue bars highlight sites in which selected mutations are able to confer resistance (Supplementary Table 3a and Supplementary Fig. 8). **c**, Viral load and YU2 gp120-reactive antibody concentration after stopping penta-mix therapy. **d**, gp120 sequences for viruses obtained after rebound from mice previously treated with penta-mix therapy (Supplementary Table 3b). **e**, Viral load of four mice re-treated with penta-mix therapy after viral rebound (c). Treatment period is highlighted in grey. Mouse numbers correspond to the mice in c.

We attempted to clone gp120 sequences from the plasma and cell-associated RNA of all penta-mix mice. Although we succeeded in obtaining sequences from three mice during the treatment period, every sequenced clone had at least one in-frame stop codon, all of which were consistent with signature APOBEC3G/F mutations (Supplementary Fig. 12 and Supplementary Table 3b). In contrast, 27 out of 28 gp120 sequences from viruses cloned after therapy was stopped and viral load rebounded did not have stop codons (Fig. 3d and Supplementary Table 3b). Furthermore, viruses that rebounded carried no or only one signature resistance mutation and remained

susceptible to the penta-mix as viraemia was controlled by re-treatment (Fig. 3e). Therefore, humanized mice treated with the penta-mix were unable to escape antibody pressure by way of envelope mutations, but the virus remained latent throughout the treatment period in at least 7 out of 8 mice.

HIV-1 infection in humanized mice differs from HIV-1 infection in humans in a number of important respects including a lower total viral load and a near absence of antibody-mediated immune responses, and therefore there is no pre-existing selective pressure on the envelope¹⁸ (Supplementary Fig. 13).

Previous antibody therapy experiments in humanized mice and humans concluded that treatment with combinations of antibodies had only limited effects against established HIV-1 infection^{4,23,24}. However, the broadly neutralizing antibodies used in those experiments (that is, in mice b12, 2G12, 2F5; in humans 2G12, 4E10, 2F5) were orders of magnitude less potent than the ones used in this study. The difference in potency and the extended combination of broadly neutralizing antibodies probably account for the differences between our findings and earlier work.

Combination antibody therapy resembles antiretroviral, antimicrobial or anti-tumour combined therapy, in that escape requires the improbable appearance of multiple simultaneous mutations. However, antibodies differ from other therapeutic modalities for HIV in several respects. First, they can neutralize the pathogen directly; second, they have the potential to clear the virus and infected cells through engagement of innate effector responses²⁵; third, immune complexes produced by the passively transferred antibodies may enhance immunity to HIV-1²⁶; and fourth antibodies have far longer half-lives than currently used antiretroviral drugs. Finally, anti-HIV-1 antibodies can be stably expressed in mammalian hosts for many months using adeno-associated viruses and therefore the potential exists to prolong their bioavailability further^{27,28}. Although we have not combined antibodies and small molecule antiretroviral drugs, we speculate that such combinations may be particularly effective because antibodies add a new modality to existing therapies. In addition, a combination of highly potent antibodies may be effective in suppressing viraemia in individuals who do not tolerate anti-HIV medication.

This study establishes the principle that broadly neutralizing antibodies can suppress HIV-1 viraemia to levels that are below detection in humanized mice for prolonged periods of time. Their efficacy as therapeutics and their long-term effects on HIV-1 infection in humans can only be evaluated in clinical trials.

METHODS SUMMARY

Mice. Human fetal livers were procured from Advanced Bioscience Resources (ABR), Inc. NOD *Rag1*^{-/-} *Il2rg*^{null} mice (The Jackson Laboratory) were irradiated with 100 cGy and reconstituted by injecting 1.5–2 × 10⁵ human CD34⁺ haematopoietic stem cells (HSCs) intrahepatically. Eight or more weeks after CD34⁺ HSC injection, mice were infected intraperitoneally with HIV-1_{YU2} (57.5 ng p24). Viral load was determined 14–20 days after infection and mice with viral loads >4 × 10³ copies ml⁻¹ were subjected to experiments. All experiments were performed with authorization from the Institutional Review Board and the IACUC at The Rockefeller University.

Measuring HIV-1 viral load. Total RNA was extracted from 100 µl EDTA-plasma and samples were analysed for HIV-1 RNA by qRT-PCR. Primers and an amplicon-specific probe targeted a conserved region within the HIV-1 5' long terminal repeat. Forward and reverse primer sequences were 5'-GCCTC AATAAAGCTTGCCTTGA-3' and 5'-GGCGCCACTGCTAGAGATT-3', respectively²⁹. The internal probe (5'-AAGTAGTGTGTGCCGTCTGTTRT KTGACT-3')²⁹ contained a 5' 6-carboxyfluorescein reporter and an internal/3' ZEN-Iowa Black FQ double-quencher (Integrated DNA Technologies). The reaction mix was prepared using the TaqMan RNA-to-Ct 1-Step kit (Applied Biosystems). Cycle threshold (Ct) values were correlated to standard samples of known viral RNA copy number. The lower limit of detection was found at 800 HIV-1 RNA copies ml⁻¹.

Antibody treatment. Filtered (Ultrafree-CL 0.22 µm, Millipore) 0.5 mg of each antibody was injected subcutaneously once (3BC176) or twice (PG16, 45-46^{G54W}, PGT128, 10-1074) per week (Supplementary Fig. 5).

HIV-1 envelope sequence analysis. cDNA was generated from isolated RNA (Superscript III Reverse Transcriptase, Invitrogen) and amplified by nested PCR using gp120^{YU2}-specific primers. PCR amplicons were gel purified and cloned using a TOPO-TA cloning kit (Invitrogen). Sequence reads were assembled using Geneious Pro software version 5.5.6 (Biomatters Ltd.) and aligned to gp120^{YU2} (accession number M93258). All residues were numbered according to HXBc2 (<http://www.hiv.lanl.gov/content/sequence/LOCATE/locate.html>).

Full Methods and any associated references are available in the online version of the paper.

Received 21 May; accepted 20 September 2012.

Published online 24 October 2012.

- Hessell, A. J. *et al.* Effective, low-titer antibody protection against low-dose repeated mucosal SHIV challenge in macaques. *Nature Med.* **15**, 951–954 (2009).
- Mascola, J. R. *et al.* Protection of macaques against pathogenic simian/human immunodeficiency virus 89.6PD by passive transfer of neutralizing antibodies. *J. Virol.* **73**, 4009–4018 (1999).
- Wei, X. *et al.* Antibody neutralization and escape by HIV-1. *Nature* **422**, 307–312 (2003).
- Poignard, P. *et al.* Neutralizing antibodies have limited effects on the control of established HIV-1 infection *in vivo*. *Immunity* **10**, 431–438 (1999).
- Diskin, R. *et al.* Increasing the potency and breadth of an HIV antibody by using structure-based rational design. *Science* **334**, 1289–1293 (2011).
- Scheid, J. F. *et al.* Sequence and structural convergence of broad and potent HIV antibodies that mimic CD4 binding. *Science* **333**, 1633–1637 (2011).
- Walker, L. M. *et al.* Broad neutralization coverage of HIV by multiple highly potent antibodies. *Nature* **477**, 466–470 (2011).
- Walker, L. M. *et al.* Broad and potent neutralizing antibodies from an African donor reveal a new HIV-1 vaccine target. *Science* **326**, 285–289 (2009).
- Wu, X. *et al.* Rational design of envelope identifies broadly neutralizing human monoclonal antibodies to HIV-1. *Science* **329**, 856–861 (2010).
- Choudhary, S. K. *et al.* Suppression of human immunodeficiency virus type 1 (HIV-1) viremia with reverse transcriptase and integrase inhibitors, CD4⁺ T-cell recovery, and viral rebound upon interruption of therapy in a new model for HIV treatment in the humanized Rag2^{-/-}γC^{-/-} mouse. *J. Virol.* **83**, 8254–8258 (2009).
- Nischang, M. *et al.* Humanized mice recapitulate key features of HIV-1 infection: A novel concept using long-acting anti-retroviral drugs for treating HIV-1. *PLoS ONE* **7**, e38853 (2012).
- Denton, P. W. *et al.* Generation of HIV latency in humanized BLT mice. *J. Virol.* **86**, 630–634 (2012).
- Weiss, R. A. Special anniversary review: twenty-five years of human immunodeficiency virus research: successes and challenges. *Clin. Exp. Immunol.* **152**, 201–210 (2008).
- Finzi, D. & Siliciano, R. F. Viral dynamics in HIV-1 infection. *Cell* **93**, 665–671 (1998).
- Arts, E. J. & Hazuda, D. J. HIV-1 antiretroviral drug therapy. *Cold Spring Harb. Persp. Med.* **2**, a007161 (2012).
- Traggiai, E. *et al.* Development of a human adaptive immune system in cord blood cell-transplanted mice. *Science* **304**, 104–107 (2004).
- Brehm, M. A. *et al.* Parameters for establishing humanized mouse models to study human immunity: analysis of human hematopoietic stem cell engraftment in three immunodeficient strains of mice bearing the IL2r^{null} mutation. *Clin. Immunol.* **135**, 84–98 (2010).
- Baenziger, S. *et al.* Disseminated and sustained HIV infection in CD34⁺ cord blood cell-transplanted Rag2^{-/-}γC^{-/-} mice. *Proc. Natl Acad. Sci. USA* **103**, 15951–15956 (2006).
- Ince, W. L. *et al.* Evolution of the HIV-1 *env* gene in the Rag2^{-/-}γC^{-/-} humanized mouse model. *J. Virol.* **84**, 2740–2752 (2010).
- McLellan, J. S. *et al.* Structure of HIV-1 gp120 V1/V2 domain with broadly neutralizing antibody PG9. *Nature* **480**, 336–343 (2011).
- Klein, F. *et al.* Broad neutralization by a combination of antibodies recognizing the CD4 binding site and a new conformational epitope on the HIV-1 envelope protein. *J. Exp. Med.* **209**, 1469–1479 (2012).
- Kwong, P. D. *et al.* Structure of an HIV gp120 envelope glycoprotein in complex with the CD4 receptor and a neutralizing human antibody. *Nature* **393**, 648–659 (1998).
- Mehandru, S. *et al.* Adjunctive passive immunotherapy in human immunodeficiency virus type 1-infected individuals treated with antiviral therapy during acute and early infection. *J. Virol.* **81**, 11016–11031 (2007).
- Trkola, A. *et al.* Delay of HIV-1 rebound after cessation of antiretroviral therapy through passive transfer of human neutralizing antibodies. *Nature Med.* **11**, 615–622 (2005).
- Nimmerjahn, F. & Ravetch, J. V. Antibody-mediated modulation of immune responses. *Immunol. Rev.* **236**, 265–275 (2010).
- Ng, C. T. *et al.* Passive neutralizing antibody controls SHIV viremia and enhances B cell responses in infant macaques. *Nature Med.* **16**, 1117–1119 (2010).
- Johnson, P. R. *et al.* Vector-mediated gene transfer engenders long-lived neutralizing activity and protection against SIV infection in monkeys. *Nature Med.* **15**, 901–906 (2009).
- Balazs, A. B. *et al.* Antibody-based protection against HIV infection by vectored immunoprophylaxis. *Nature* **481**, 81–84 (2012).
- Rouet, F. *et al.* Transfer and evaluation of an automated, low-cost real-time reverse transcription-PCR test for diagnosis and monitoring of human immunodeficiency virus type 1 infection in a West African resource-limited setting. *J. Clin. Microbiol.* **43**, 2709–2717 (2005).
- Mouquet, H. Complex-type N-glycan recognition by potent broadly-neutralizing HIV antibodies. *Proc. Natl Acad. Sci. USA* (in the press).

Supplementary Information is available in the online version of the paper.

Acknowledgements We thank R. Kaiser for analysing viral loads of reference HIV-1 samples and N. N. Freund for producing YU2 gp120. We thank B. Flatley, T. Friling, H. Gao, S. Sell and S. Hinkley for assistance and technical support, M. Suarez-Farinas for advice on statistical analysis, and M. Babayeva for helping with antibody t_{1/2} estimation. M.C.N. and F.K. have a pending patent application for the antibody 3BC176 and M.C.N., P.J.B. and H.M. for the antibody 10-1074 with the United States Patent and Trademark Office. These reagents are available with a Material Transfer Agreement. F.K. (KL 2389/1-1), M.D. (DO 1450/1-1) and E.B. (BI 1422/1-1) were supported by the German Research Foundation (DFG). H.G., C.G. and R.-B.I. were supported by The German National Academic Foundation. M.S.S. was supported by the Bill and Melinda Gates Foundation's Comprehensive Antibody Vaccine Immune Monitoring Consortium, grant number 1032144. A.P. is a recipient of a Liver Scholar Award from the American Liver Foundation. This work was supported in part by CAVD grant OPP1033115 from the Bill and Melinda Gates Foundation to M.C.N., in part by NIAID 1UM1AI100663 to M.C.N. and NIH grant AI081677 to M.C.N., P.J.B. and P.D.B. are HHMI investigators.

Author Contributions F.K., A.H.-S. and J.A.H. planned and performed experiments and wrote the manuscript. H.G., J.F.H., S.B., H.M., L.A.S., R.D., A.A., T.Z., M.D., E.B., R.N.L., C.G., P.M.M., R.-B.I., T.R.E. and M.S.S. performed experiments. P.D.B., P.J.B., J.V.R. and A.P. provided reagents, advice and edited the manuscript. M.C.N. planned experiments and wrote the manuscript.

Author Information Reprints and permissions information is available at www.nature.com/reprints. The authors declare no competing financial interests. Readers are welcome to comment on the online version of the paper. Correspondence and requests for materials should be addressed to M.C.N. (nussen@rockefeller.edu).

METHODS

Mice. NOD *Rag1*^{-/-} *Il2rg*^{null} (NOD.Cg-*Rag1*^{tm1Mom} *Il2rg*^{tm1Wjl/SzJ}) mice were purchased from The Jackson Laboratory and bred and maintained at the Comparative Bioscience Center of The Rockefeller University according to guidelines established by the Institutional Animal Committee. All experiments were performed with authorization from the Institutional Review Board and the IACUC at The Rockefeller University.

Isolation of human HSCs and generation of humanized mice. Human fetal livers were procured from Advanced Bioscience Resources (ABR), Inc. (Alameda) or the Human Fetal Tissue Repository (HFTR). HSCs were isolated as previously described³¹. Briefly, human fetal liver was homogenized and incubated in digestion medium (HBSS with 0.1% collagenase IV (Sigma-Aldrich), 40 mM HEPES, 2 mM CaCl₂ and 2 U ml⁻¹ DNase I (Roche)) for 30 min at 37 °C. Human CD34⁺ HSCs were isolated using a CD34⁺ HSC isolation kit (Stem Cell Technologies, Inc.) according to the manufacturers' instructions. 1–5-day-old NOD *Rag1*^{-/-} *Il2rg*^{null} (NRG) mice were irradiated with 100 cGy and 1.5–2 × 10⁵ human CD34⁺ HSCs were injected intrahepatically 6 h after irradiation.

Flow cytometry. Flow cytometry was used to assess human haematopoietic engraftment in mouse xenorecipients and to determine CD4⁺ to CD8⁺ T-cell ratios. To this end, 200 µl of whole blood was collected from the superficial temporal vein of humanized mice and density gradient centrifugation (Ficoll-Paque) was performed. Isolated peripheral blood mononuclear cells (PBMCs) were stained with anti-mouse CD45-PEcy7 (BioLegend), anti-human CD3-Pacific-Blue (BD Pharmingen), CD4-PE (BD), CD8-FITC (BD), CD16-Alexa700 (BD Pharmingen), CD19-APC (BD Pharmingen) and CD45-Pacific-Orange (Invitrogen) for 25 min at 4 °C. Cells were washed and then fixed in 4% paraformaldehyde. To determine absolute numbers of CD4⁺ T cells in peripheral blood, AccuCheck Counting Beads (Molecular Probes) were added to the samples. FACS analysis was performed using a BD LSRFortessa cell analyser (BD Biosciences) and data was analysed using FlowJo software (Tree Star).

HIV-1YU2 virus production. HIV-1YU2 was produced as previously described³² and levels of p24 in viral supernatant were determined using Alliance HIV-1 p24 Antigen ELISA kit (PerkinElmer) according to the manufacturer's instructions.

Quantitative reverse-transcriptase PCR assay. Blood was obtained from the superficial temporal vein and collected into EDTA-Microtubes (Sarstedt). After centrifugation, RNA was extracted from 100 µl EDTA-plasma using a Qiagen MinElute Virus Spin kit (Qiagen) and eluted in 50 µl (2 × 25 µl elutions) RNase free water (Qiagen). RNA samples were analysed for HIV-1 RNA in a 50 µl reaction mix using the 1 × TaqMan RT-PCR mix, the 1 × TaqMan RT Enzyme mix (TaqMan RNA-to-Ct 1-Step kit, Applied Biosystems) and primers targeting a highly conserved region within the HIV-1 5' long terminal repeat (forward 5'-GCCTCAATAAAGCTTGCTTGA-3'; reverse 5'-GGCGCCACTGCTAGAGATT-3')²⁹. The internal probe (5'-AAGTAGTGTGTGCCGCTCTGTT RTKTAGACT-3')²⁹ contained a 5' 6-carboxyfluorescein reporter and an internal/3' ZEN-Iowa Black FQ double-quencher (Integrated DNA Technologies, Inc.). As standard references (standard no. 1 and no. 2) two different dilutions from a single HIV-1NL4-3/BaL preparation were generated and quantified in duplicates by the Roche COBAS TaqMan HIV-1 Test, v.2.0 (R. Kaiser). These reference aliquots were stored at -80 °C and always extracted in parallel with mouse plasma samples. To generate a reference curve standard no. 1 was fivefold serially diluted from 173,500,000 to 4 HIV-1 RNA copies ml⁻¹ (Supplementary Fig. 2). Standard no. 2 containing 2,600,000 copies ml⁻¹ was used as a control for experimental variation: all sample Ct values in a given experiment were adjusted by the difference between the experimental Ct value for standard no. 2 and its expected Ct value calculated using each experiment's standard curve (generated using standard no. 1). Final viral load values were calculated using the control-adjusted Ct for each sample.

qRT-PCR assay, limit of detection. The lower limit of detection (LOD) for the assay used in this study was found at 800 copies ml⁻¹. HIV-1 culture supernatant of known RNA copy number was serially diluted twofold to concentrations between 1,600 and 200 copies ml⁻¹ (corresponding to 64 to 8 copies per 20 µl RNA extract). Each dilution was independently extracted and assayed at *n* = 4 per experiment. The presence of a cycle threshold value for a given PCR reaction was scored as a detection event. Detection scores accumulated from five identical experiments were subjected to probit analysis, and the 85% LOD was found at 800 copies ml⁻¹ for undiluted RNA extract (corresponding to 32 copies per PCR reaction).

Antibody production, t_{1/2} estimation and administration. Antibodies were generated as previously described^{33,34}. Briefly, HEK 293T/17 or HEK 293-6E cells were transiently transfected with equal amounts of immunoglobulin heavy and light chain expression vectors. After supernatant was collected, purified IgG was obtained using HiTrap rProtein A FF columns (GE Healthcare) or Protein G sepharose 4 Fast Flow (GE Healthcare). Sterile filtration was performed for all

antibodies shortly before injection by using Ultrafree-CL Centrifugal Filters (0.22 µm, Millipore). Antibody t_{1/2} was calculated by ln(2)/*k* where *k* is 1st order reaction rate constant and calculated as a slope of ln(antibody concentration) versus time. On the basis of the t_{1/2} of broadly neutralizing antibodies, HIV-1YU2-infected humanized mice were treated with 0.5 mg of each antibody injected subcutaneously once (3BC176) or twice (PG16, 45-46^{G54W}, PGT128, 10-1074) per week. The tri-mix was composed of 3BC176, PG16 and 45-46^{G54W} whereas the penta-mix included all five given antibodies. To determine antibody t_{1/2}, 0.5 mg of antibody was administered intravenously by retro-orbital injection (Supplementary Fig. 5).

ELISA. Costar 96-Well EIA/RIA Stripwell plates were coated overnight with YU2 gp120 or goat anti-human IgG specific for Fcγ fragment at 250 and 150 ng well⁻¹, respectively. Plates were washed 3× with distilled water and blocked for 1 h with PBST (0.1% Tween-20) containing 2% BSA and 1 µM EDTA. Standard IgG1 κ (Sigma-Aldrich) and 10-1074 were used in duplicates as standard antibodies for quantifying total IgG and YU2 gp120-specific IgGs, respectively. After washing the plate, mouse plasma was applied in 1:3 serial dilutions with a 1:10 or 1:20 starting dilution and incubated for 2 h followed by washing the plate and 1 h incubation with peroxidase-conjugated goat anti-human IgG (Jackson ImmunoResearch). Plates were washed and developed using ABTS single solution (Invitrogen). Optical density was measured at 405 nm and IgG concentration determined by correlation to the standard curve of the reference antibodies. Of note, YU2 gp120 does not react with PG16 or 3BC176 and therefore these monoclonal antibodies are not detected by the YU2 gp120 ELISA.

Neutralization. Single antibodies and tri- and penta-mix were tested against a panel of HIV-1 envelope pseudoviruses as previously described^{6,35,36} or HIV-1YU2-mutant variants. Briefly, envelope pseudoviruses were incubated with fivefold serial dilutions of single antibodies or tri- and penta-mix samples and applied to TZM-bl cells that carry a luciferase-reporter gene. After 48 h cells were lysed and luminescence was measured. IC₅₀ and IC₈₀ reflect single antibody concentrations that caused a reduction in relative luminescence units (RLU) by 50% and 80%, respectively.

cDNA synthesis. Viral RNA was extracted as described above and subjected to first-strand cDNA synthesis using the SuperScript III reverse transcriptase kit (Invitrogen Life Technologies). For extraction of cellular RNA an RNA extraction kit was used (Qiagen). Sense and antisense primers used for cDNA synthesis were 5'-GGCTTAGGCATCTCCTATGGCAGGAAGAA-3' and 5'-GGTGTGTAGT TCTGCCAATCAGGGAAGWAGCCTTGTG-3', respectively.

PCR amplification and cloning. PCR amplifications were performed in Thermo-Grid 96-well plates (Denville Scientific) using either the Clontech Advantage 2 PCR System (BD) or the Expand High Fidelity PCR System (Roche). All PCR amplifications were performed in a 50 µl reaction mix. The primers used for the first round of PCR were 5'-GGCTTAGGCATCTCCTATGGCAGGAAGAA-3' and 5'-GGTGTGTAGT TCTGCCAATCAGGGAAGWAGCCTTGTG-3'. Primers for the second-round PCR were 5'-TAGAAAGAGCAGAAGACAGTGGC AATGA-3' and 5'-TCATCAATGGTGGTGTATGATGATGTTTCTCTCT GCACCACCTTCT-3'. Cycling parameters for first round PCR were 94 °C for 2 min followed by 40 cycles of 94 °C for 30 s, annealing temperature of 55–65 °C for 45 s, 68 °C for 4 min, and a final extension at 68 °C for 10 min, where the annealing temperature was 65 °C for the first 3 cycles, 60 °C for the next 11 cycles, and 55 °C for the final 26 cycles. 3 µl of product from the first round was used as the template for the second round of PCR. Cycling conditions for the second round PCR were 94 °C for 2 min followed by 40 cycles of 94 °C for 30 s, annealing temperature of 53–55 °C for 45 s, 68 °C for 2 min and 30 s, and a final extension at 68 °C for 10 min, where annealing temperature was 53 °C for the first 9 cycles and 55 °C for the next 31 cycles. After the second-round PCR amplification, 0.5 µl Taq polymerase was added to each 50 µl reaction and an additional 72 °C extension for 15 min was performed to add 3' A overhangs for use in cloning. Gel-purified PCR amplicons were ligated into pCR4-TOPO (Invitrogen) following the manufacturer's instructions and transformed into One Shot TOP10 (Invitrogen) cells. Individual colonies were sequenced using M13F and M13R primers.

Sequence alignments and mutation analysis. Forward and reverse sequence reads from individual samples were assembled using Geneious Pro software version 5.5.6 (Biomatters Ltd) and aligned to gp120^{YU2} (accession number M93258). *env* sequences containing frameshift mutations or large deletions were excluded from further analysis. All sequences were analysed for mutations relative to gp120^{YU2} using the Los Alamos Highlighter tool (http://www.hiv.lanl.gov/content/sequence/HIGHLIGHT/HIGHLIGHT_XYPLLOT/highlighter.html), and mutations were numbered using HXBc2 numbering as determined by the Los Alamos Sequence Locator tool (<http://www.hiv.lanl.gov/content/sequence/LOCATE/locate.html>). Mutations were considered recurrent when substitutions within a range of 3 amino acids occurred in the majority of gp120 clones in more

than one mouse. The fidelity of the combined reverse transcription and nested PCR reactions was determined by amplifying monoclonal wild-type HIV-1_{YU2} by the same amplification procedures and identifying RT- and PCR-induced mutations (Supplementary Fig. 4).

Generation of HIV-1_{YU2} envelope mutants. Single, double and triple mutations were introduced into wild-type HIV-1_{YU2} envelope by site-directed mutagenesis using the QuikChange (multi-) site-directed mutagenesis kit (Agilent Technologies) according to the manufacturer's specifications.

Statistical analysis. Kruskal–Wallis test with Dunn multiple comparison or Mann–Whitney *U* post-hoc tests were performed using GraphPad Prism version 5.0b for Mac OS X, GraphPad Software, for comparisons of the viral load levels among different antibody treatment groups and control group (Fig. 1c and Supplementary Fig. 10) and for comparing gp120 mutation rates (Supplementary Fig. 4). Levels of significance are indicated by asterisks (**P* ≤ 0.05; ***P* ≤ 0.01; ****P* ≤ 0.001). Correlation between viral load (RNA copies ml⁻¹) and absolute numbers of CD4⁺ T cells in peripheral blood (Supplementary Fig. 1b) was analysed by Spearman correlation coefficient (rho) using GraphPad Prism version 5.0b for Mac OS X. An unpaired student's *t*-test was used to compare

CD4⁺/CD8⁺ ratios of pre-infected mice in control and penta-mix group (Supplementary Fig. 3).

31. Billerbeck, E. *et al.* Development of human CD4⁺FoxP3⁺ regulatory T cells in human stem cell factor-, granulocyte-macrophage colony-stimulating factor-, and interleukin-3-expressing NOD-SCID IL2Rγ^{null} humanized mice. *Blood* **117**, 3076–3086 (2011).
32. Zhang, Y. J. *et al.* Envelope-dependent, cyclophilin-independent effects of glycosaminoglycans on human immunodeficiency virus type 1 attachment and infection. *J. Virol.* **76**, 6332–6343 (2002).
33. Scheid, J. F. *et al.* Broad diversity of neutralizing antibodies isolated from memory B cells in HIV-infected individuals. *Nature* **458**, 636–640 (2009).
34. Tiller, T. *et al.* Efficient generation of monoclonal antibodies from single human B cells by single cell RT-PCR and expression vector cloning. *J. Immunol. Methods* **329**, 112–124 (2008).
35. Montefiori, D. C. Evaluating neutralizing antibodies against HIV, SIV, and SHIV in luciferase reporter gene assays. *Curr. Protoc. Immunol.* Ch. 12, Unit 12 11 (2005).
36. Li, M. *et al.* Human immunodeficiency virus type 1 env clones from acute and early subtype B infections for standardized assessments of vaccine-elicited neutralizing antibodies. *J. Virol.* **79**, 10108–10125 (2005).

The calcium-sensing receptor regulates the NLRP3 inflammasome through Ca^{2+} and cAMP

Geun-Shik Lee^{1,2}, Naeha Subramanian³, Andrew I. Kim¹, Ivona Aksentijevich¹, Raphaela Goldbach-Mansky⁴, David B. Sacks⁵, Ronald N. Germain³, Daniel L. Kastner¹ & Jae Jin Chae¹

Mutations in the gene encoding NLRP3 cause a spectrum of auto-inflammatory diseases known as cryopyrin-associated periodic syndromes (CAPS)¹. NLRP3 is a key component of one of several distinct cytoplasmic multiprotein complexes (inflammasomes) that mediate the maturation of the proinflammatory cytokine interleukin-1 β (IL-1 β) by activating caspase-1. Although several models for inflammasome activation, such as K^{+} efflux², generation of reactive oxygen species³ and lysosomal destabilization⁴, have been proposed, the precise molecular mechanism of NLRP3 inflammasome activation, as well as the mechanism by which CAPS-associated mutations activate NLRP3, remain to be elucidated. Here we show that the murine calcium-sensing receptor (CASR) activates the NLRP3 inflammasome, mediated by increased intracellular Ca^{2+} and decreased cellular cyclic AMP (cAMP). Ca^{2+} or other CASR agonists activate the NLRP3 inflammasome in the absence of exogenous ATP, whereas knockdown of CASR reduces inflammasome activation in response to known NLRP3 activators. CASR activates the NLRP3 inflammasome through phospholipase C, which catalyses inositol-1,4,5-trisphosphate production and thereby induces release of Ca^{2+} from endoplasmic reticulum stores. The increased cytoplasmic Ca^{2+} promotes the assembly of inflammasome components, and intracellular Ca^{2+} is required for spontaneous inflammasome activity in cells from patients with CAPS. CASR stimulation also results in reduced intracellular cAMP, which independently activates the NLRP3 inflammasome. cAMP binds to NLRP3 directly to inhibit inflammasome assembly, and downregulation of cAMP relieves this inhibition. The binding affinity of cAMP for CAPS-associated mutant NLRP3 is substantially lower

than for wild-type NLRP3, and the uncontrolled mature IL-1 β production from CAPS patients' peripheral blood mononuclear cells is attenuated by increasing cAMP. Taken together, these findings indicate that Ca^{2+} and cAMP are two key molecular regulators of the NLRP3 inflammasome that have critical roles in the molecular pathogenesis of CAPS.

NLRP3 inflammasome activation by extracellular ATP is mediated through the purinergic receptor, P2X7R, and is inhibited by high concentrations of extracellular K^{+} , which may block K^{+} efflux⁵. However, ATP-driven NLRP3 inflammasome activation is also inhibited by other extracellular cations such as Ca^{2+} (ref. 6). Hence, we initially explored the role of extracellular cations in inflammasome activation to investigate the signalling pathway that links danger-associated molecular patterns to the NLRP3 inflammasome. As seen in previous reports, addition of K^{+} or Ca^{2+} with ATP to lipopolysaccharide (LPS)-primed mouse bone marrow-derived macrophages (BMDMs) suppressed bioactive IL-1 β secretion, and the same effect was also observed with Mg^{2+} (Fig. 1a). Surprisingly, we also found that in the absence of ATP, LPS-primed BMDMs secreted IL-1 β when cultured with Ca^{2+} alone but not with Mg^{2+} or K^{+} (Fig. 1a and Supplementary Fig. 1a). The Ca^{2+} -induced IL-1 β secretion was independent of P2X7R, or the AIM2 (absent in melanoma 2) or NLRC4 (IPAF, ICE protease-activating factor) inflammasomes, but dependent on the NLRP3 inflammasome (Fig. 1b and Supplementary Fig. 1b, c). NLRP3 inflammasome activation was also induced by gadolinium (Gd^{3+}), an agonist of CASR, or R-568, an allosteric agonist of CASR (Supplementary Fig. 1d). These results indicate that the recognition of extracellular Ca^{2+} through CASR activates the NLRP3 inflammasome.

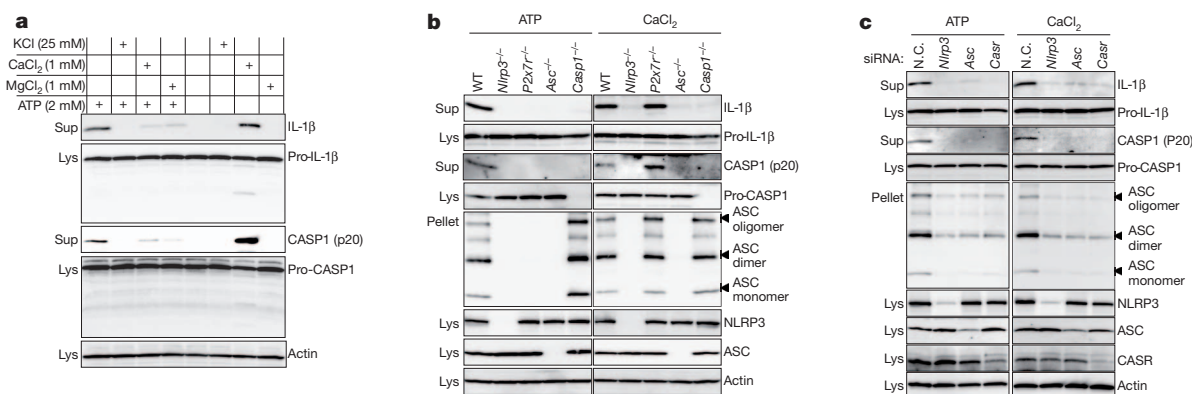


Figure 1 | Extracellular calcium and ATP activate the NLRP3 inflammasome through CASR. **a**, **b**, LPS-primed BMDMs from wild-type (WT) or designated knockout mice were stimulated in RPMI medium supplemented with the indicated reagents. **c**, BMDMs were transiently transfected with scrambled (N.C.), *Nlrp3*, *Asc*, or *Casr* siRNA, and then

stimulated with 2 mM ATP or 1 mM CaCl_2 after priming with LPS. Cell culture supernatants (Sup), cell lysates (Lys), and crosslinked pellets from whole-cell lysates were analysed by immunoblotting as indicated (**a–c**). All immunoblot data shown are representative of at least three independent experiments.

¹Inflammatory Disease Section, Medical Genetics Branch, National Human Genome Research Institute, National Institutes of Health, Bethesda, Maryland 20892, USA. ²College of Veterinary Medicine, Kangwon National University, Chuncheon, Gangwon 200-701, South Korea. ³Laboratory of Systems Biology, National Institute of Allergy and Infectious Diseases, National Institutes of Health, Bethesda, Maryland 20892, USA. ⁴Translational Autoinflammatory Disease Section, National Institute of Arthritis and Musculoskeletal and Skin Diseases, National Institutes of Health, Bethesda, Maryland 20892, USA. ⁵Department of Laboratory Medicine, Clinical Center, National Institutes of Health, Bethesda, Maryland 20892, USA.

It seemed paradoxical that high calcium buffers could inhibit ATP-induced IL-1 β secretion while stimulating IL-1 β secretion in the absence of ATP. The inhibitory effect of extracellular Ca²⁺ was confined to NLRP3 co-stimulation with ATP, as high calcium buffers did not inhibit inflammasome activation by other NLRP3 activators, double-stranded DNA (dsDNA), or flagellin (Supplementary Fig. 2a–c). In addition, although both high calcium and high magnesium buffers inhibited ATP-induced inflammasome activation, equivalent concentrations of the trivalent cation Gd³⁺ (which, like Ca²⁺ itself, is an agonist of CASR) did not inhibit ATP-induced inflammasome activation (Supplementary Fig. 2d). One possible explanation for these observations is the well-recognized interaction between divalent cations and ATP, in which unbound ATP acts as the agonist form^{7,8}. Indeed, when BMDMs were treated with a given stimulatory concentration of Ca²⁺, varying ATP concentrations, and vice versa, we observed first decreasing IL-1 β production as inactive Ca²⁺/ATP complexes form, and then eventually increasing IL-1 β activation as the ATP or Ca²⁺ exceeded the available free Ca²⁺ or ATP, respectively (Supplementary Fig. 2e, f).

Next, to examine the role of CASR in NLRP3 inflammasome activation further, the *Casr* gene was knocked down in mouse BMDMs by short interfering RNA (siRNA; Supplementary Fig. 3a, b). Similar to *Nlrp3* or *Asc* knockdowns, IL-1 β secretion from the BMDMs with *Casr* knockdown was substantially diminished in response to extracellular Ca²⁺ (Fig. 1c). Furthermore, we also observed that downregulation of *Casr* reduced IL-1 β secretion when BMDMs were stimulated with several other known NLRP3 inflammasome activators, but not with AIM2 or NLRC4 inflammasome activators (Fig. 1c and Supplementary Fig. 4). These findings suggest that CASR is an upstream gatekeeper of the NLRP3 inflammasome.

Intracellular Ca²⁺ signalling is important for NLRP3 inflammasome activation induced by extracellular ATP⁹. Elevation of extracellular Ca²⁺ concentrations or other CASR agonists commonly elicits intracellular Ca²⁺ signals through the interaction between CASR and phospholipase C (PLC)^{10,11}. We observed a correlation between PLC activity and the presence of active IL-1 β in the supernatant of LPS-primed BMDMs. Cells treated with 2,4,6-trimethyl-*N*-[3-(trifluoromethyl)phenyl]benzenesulphonamide (*m*-3M3FBS), a direct activator of PLC (Fig. 2a), secreted IL-1 β in the absence of any other exogenous stimulus, indicating a role for PLC-stimulated Ca²⁺ signals in inflammasome activation. In contrast, PLC inhibitors edelfosine or U73122 (but not

U73343, an inactive analogue of U73122) blocked IL-1 β secretion from cells treated with Ca²⁺ or ATP (Supplementary Fig. 5a and Fig. 2b). U73122 had no effect on AIM2 or NLRC4 inflammasome activation (Supplementary Fig. 5b), indicating that PLC activation is dispensable for triggering these inflammasomes.

PLC hydrolyses phosphatidylinositol-4,5-bisphosphate into diacylglycerol (DAG), which activates protein kinase C, and inositol trisphosphate (InsP₃), which causes the cytosolic concentration of Ca²⁺ to increase by binding to InsP₃ receptors (InsP₃R) in the endoplasmic reticulum (ER). Indeed, we observed generation of InsP₃ in BMDMs exposed to the NLRP3 inflammasome activators ATP or Ca²⁺ (Fig. 2c). When LPS-primed BMDMs were stimulated with ATP or Ca²⁺ in the presence of an InsP₃R inhibitor (2-APB), little or no IL-1 β was secreted (Fig. 2d), whereas IL-1 β secretion was not suppressed in the presence of protein kinase C inhibitors (Supplementary Fig. 5c). Moreover, in BMDMs in which the InsP₃ receptor (*Ip3r*; also called *Itpr1*) had been knocked down, IL-1 β secretion induced by extracellular Ca²⁺ or ATP was substantially reduced (Fig. 2e). In addition, when wild-type cells were stimulated with ATP, CaCl₂, or GdCl₃, we observed increased intracellular Ca²⁺ levels, which were blocked by 2-APB or BAPTA-AM (Supplementary Fig. 6a–c and Supplementary Videos 1–9), and IL-1 β secretion, but not IL-6 or TNF- α secretion, was markedly inhibited by chelating intracellular Ca²⁺ with BAPTA-AM but not the heavy metal chelator TPEN (Fig. 2f and Supplementary Fig. 7a, b). Conversely, inflammasome activation was observed in LPS-primed BMDMs by treatment with thapsigargin, which increases intracellular Ca²⁺ (Supplementary Fig. 7c). BAPTA-AM or 2-APB did not block IL-1 β secretion induced by dsDNA or flagellin (Fig. 2d, f), which do not induce intracellular Ca²⁺ increases (data not shown). Taken together, these data indicate that activation of the AIM2 and NLRC4 inflammasomes is independent of InsP₃R signalling and intracellular Ca²⁺, whereas signalling from CASR activates the NLRP3 inflammasome via InsP₃-mediated intracellular Ca²⁺ release. Indeed, the NLRP3–ASC association in cell-free lysates from BMDMs increased in the presence of Ca²⁺ (Fig. 2g), whereas Ca²⁺ had no direct effect on the activity of caspase 1 (Supplementary Fig. 7d). Nevertheless, it remains to be elucidated whether the role of Ca²⁺ on NLRP3 inflammasome activation is direct or indirect.

CASR interacts not only with PLC but also with adenylate cyclase (ADCY), which results in inhibition of ADCY and subsequent reduction

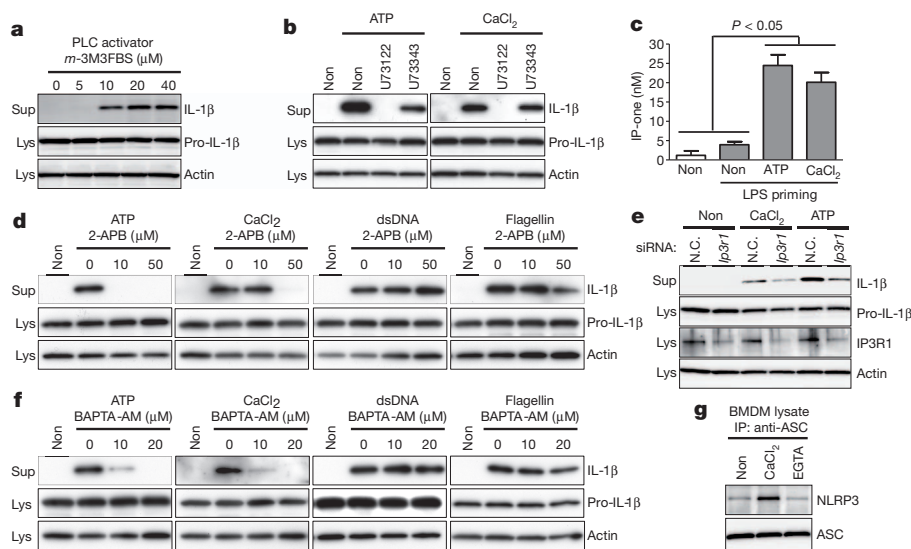


Figure 2 | PLC-InsP₃-mediated calcium release from the ER triggers NLRP3 inflammasome activation. **a–d, f**, LPS-primed BMDMs were treated as indicated. Intracellular inositol monophosphate (IP-one), a surrogate for InsP₃ levels, was measured (**c**). Data represent the mean \pm s.e.m. from three independent experiments. **e**, BMDMs transiently transfected with scrambled

(N.C.) or *Ip3r1* siRNA were primed with LPS and stimulated with 5 mM ATP or 1 mM CaCl₂. **g**, LPS-primed BMDMs were immunoprecipitated with anti-ASC antibody in buffer containing no additives (Non), 1 mM CaCl₂, or 1 mM EGTA. Supernatants and lysates were analysed by immunoblotting. Data are representative of three independent experiments.

of cellular cAMP levels¹⁰. Indeed, addition of ATP or Ca^{2+} reduced the LPS-mediated cAMP increase in BMDMs¹² (Fig. 3a). Thus, we also investigated a possible role for cAMP in inflammasome activation. Notably, an inverse correlation between the levels of cAMP and IL-1 β secretion was observed in LPS-primed BMDMs. The increase of cAMP synthesis by ADCY activators (NKH477 or forskolin) or the decrease of cAMP hydrolysis by phosphodiesterase (PDE) 4 inhibitors (Ro-20-1724, (R)-(-)-rolipram, or zardaverine) suppressed IL-1 β secretion, but not IL-6 or TNF- α secretion, and ASC oligomerization induced by ATP or Ca^{2+} , but did not inhibit cytokine secretion induced by dsDNA or flagellin (Fig. 3b, c and Supplementary Fig. 8a–e). In contrast, an ADCY inhibitor (KH7) alone induced dose-dependent secretion of IL-1 β and ASC oligomerization in wild-type BMDMs, but not in BMDMs from *Nlrp3*^{-/-}, *Asc*^{-/-} or *Casp1*^{-/-} mice (Supplementary Fig. 8f and Fig. 3d). Using knockdown experiments, we found that

ADCY and PLC are downstream of CASR in NLRP3 activation, and that these pathways are intact even after *Casr* knockdown (Supplementary Fig. 8g). We also observed that the NLRP3–ASC interaction in KH7-treated BMDM lysates increased, whereas the interaction in lysates from forskolin-treated cells decreased (Fig. 3e). Consistent with these data, spontaneous inflammasome activation was observed in BMDMs upon knockdown of the several adenylate cyclases (Fig. 3f) that are expressed in macrophages (ADCY3, ADCY6, ADCY7 and ADCY9; Supplementary Fig. 8h). Taken together, these results indicate that cAMP specifically suppresses NLRP3 inflammasome activation.

A major role of cAMP is activating protein kinase A (PKA), which could potentially suppress inflammasome activation. However, no IL-1 β secretion was observed in the supernatant of LPS-primed BMDMs treated with PKA inhibitors or after knockdown of *Prkaca* (also called *Pkax*) (Supplementary Fig. 9a, b). To understand how cAMP might suppress NLRP3 inflammasome activation, we tested whether cAMP interacts directly with NLRP3. In a pull-down assay, we found an interaction of endogenous NLRP3 from BMDMs with cAMP but not with cGMP (Fig. 3g). We also found that this interaction was mediated by the nucleotide-binding domain (NBD, also known as NACHT) of NLRP3 (Fig. 3h), which has previously been shown to bind and hydrolyse ATP¹³. However, cAMP does not inhibit binding of ATP to NLRP3 (Supplementary Fig. 8i).

Because cAMP suppresses NLRP3 inflammasome activation and binds to the NBD of NLRP3, which is the most common location of CAPS-associated mutations¹, we considered the possible effect of these mutations on binding to cAMP. The binding of cAMP to the disease-associated mutant NLRP3 (D303N, A352V and F523C) was substantially decreased relative to wild-type NLRP3 (Fig. 4a), which indicates that the spontaneous activation of the inflammasome in myeloid cells of patients with CAPS might be due to reduced suppression of NLRP3 activation by cAMP. Thus, we investigated the effect of cAMP on IL-1 β secretion from peripheral blood mononuclear cells (PBMCs) of CAPS (familial cold autoinflammatory syndrome, FCAS; Muckle-Wells syndrome, MWS; neonatal-onset multisystem inflammatory disease, NOMID) patients. As previously reported¹⁴, without any inflammasome activator, mutation-positive CAPS patients' PBMCs secreted IL-1 β in response to LPS priming alone, whereas healthy control PBMCs did not secrete IL-1 β (Supplementary Fig. 10a–c). However, IL-1 β secretion from CAPS PBMCs was substantially blocked by activating ADCY or inhibiting PDE4 (Fig. 4b, c and Supplementary Fig. 10b–d). In contrast, we observed no inhibitory effect of ADCY activator or PDE4 inhibitors on IL-1 β secretion from PBMCs of patients with familial Mediterranean fever (FMF) (Supplementary Fig. 10e), the prototypic autoinflammatory disease which is caused by mutations of pyrin that induce an NLRP3-independent inflammasome¹⁵. These results are consistent with the hypothesis that the inhibitory effect of cAMP on IL-1 β secretion is specific to the NLRP3 inflammasome.

In addition, we found that the constitutive IL-1 β secretion from CAPS PBMCs was also substantially reduced by blockers of InsP_3 -mediated intracellular Ca^{2+} signalling pathways, 2-APB and BAPTA-AM, (Fig. 4d, e and Supplementary Fig. 10f, g), which can also inhibit NLRP3 inflammasome activation induced by ATP or extracellular Ca^{2+} (Fig. 2d, f). These data indicate an essential role for intracellular Ca^{2+} signalling in CAPS-associated mutant NLRP3 activation.

Using a combination of genetic, pharmacological and biochemical approaches, we provide evidence that CASR has a major role in NLRP3 inflammasome activation through its effects on intracellular Ca^{2+} and cAMP (summarized in Supplementary Fig. 11 and modelled in Supplementary Fig. 12), which also suggests a possible role for extracellular Ca^{2+} as a danger signal. Indeed, extracellular fluid at sites of injury and inflammation has been reported to contain high concentrations of Ca^{2+} , attracting cells of the monocyte/macrophage lineage¹⁶. The CASR is a G-protein-coupled receptor that interacts directly not only with $\text{G}\alpha_q$ eliciting intracellular Ca^{2+} signals through PLC, but

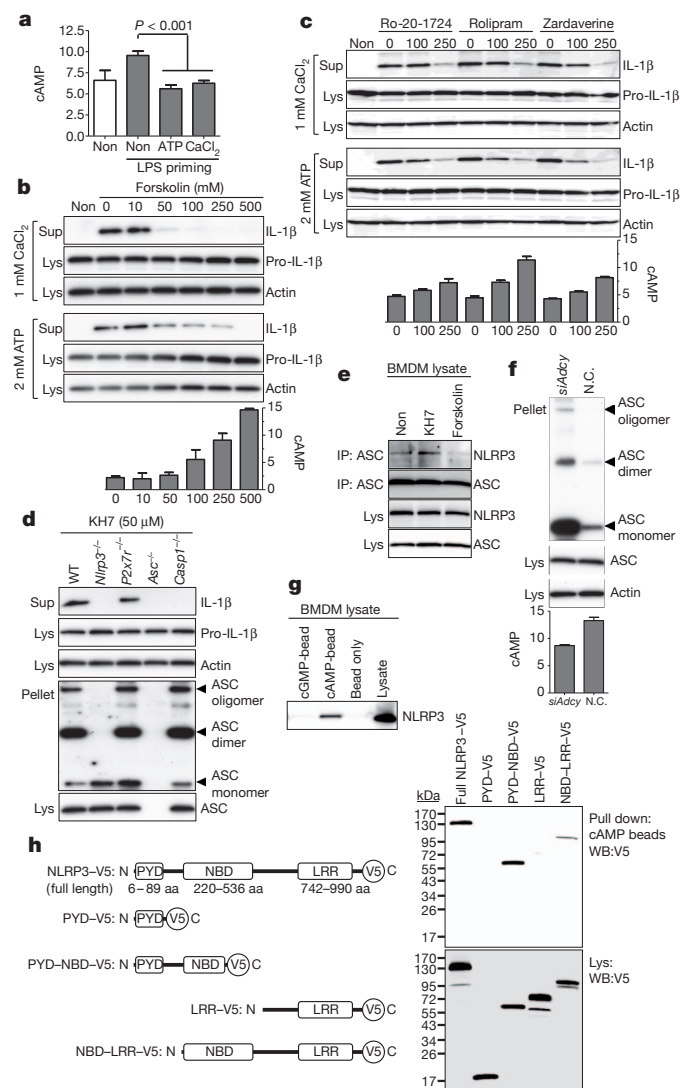


Figure 3 | cAMP binds to NLRP3 and suppresses inflammasome activation. **a–e**, LPS-primed BMDMs were treated as indicated. IL-1 β secretion (**b–d**), ASC–NLRP3 interaction (**e**), or intracellular cAMP levels (pmol per 1×10^6 cells) (**a–c**) were analysed. Data represent the mean \pm s.e.m. from five experiments. **f**, BMDMs transfected with scrambled or *Adcy3* + *Adcy6* + *Adcy7* + *Adcy9* siRNAs were analysed for ASC oligomerization after LPS priming. **g**, LPS-primed BMDMs were pulled down with indicated beads and analysed by immunoblot for NLRP3. **h**, Indicated NLRP3 proteins were expressed in 293T cells and pulled down with cAMP beads. LRR, leucine-rich repeats; NBD, nucleotide-binding domain; PYD, PYRIN domain. Data are representative of three independent experiments.

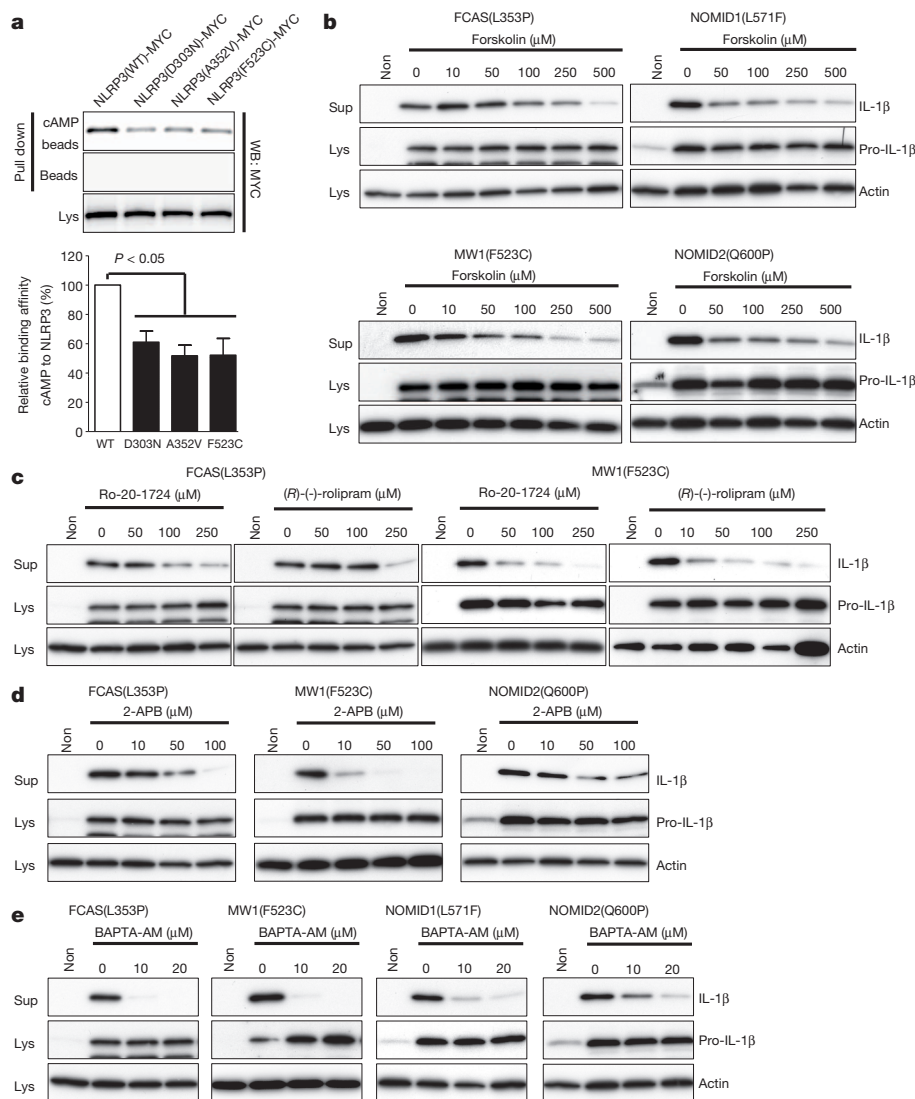


Figure 4 | The role of cAMP and calcium in the pathogenesis of CAPS. **a**, Wild-type or CAPS-associated mutant NLRP3 proteins were expressed in 293T cells and pulled down with cAMP beads. Densitometric analysis of cAMP-associated NLRP3 bands, normalized to the NLRP3 in lysates, is shown in the histogram. Data represent the mean \pm s.e.m. of the seven experiments.

also with $G_i\alpha$, which results in the inhibition of ADCY and a reduction in cellular cAMP levels¹⁰. It has been widely recognized that in inflammatory cells, cAMP acts as a negative regulator of immune and inflammatory responses^{17,18}. Our results clarify a molecular mechanism for how cAMP inhibits IL-1 β maturation in macrophages. As a second messenger, cAMP exerts its role by direct binding to the regulatory unit or domain of target proteins, thereby inducing conformational changes^{19,20}. The low binding affinity of cAMP with CAPS-associated mutant NLRP3 proteins and inhibition of IL-1 β secretion from CAPS PBMCs by activation of ADCY or the inhibition of PDE4 is also consistent with an inhibitory effect of cAMP on NLRP3 inflammasome activation. Although IL-1 inhibition is currently being used as an effective therapy for CAPS, our data indicate a broader spectrum of potential targets for therapy of CAPS as well as other inflammatory conditions involving the NLRP3 inflammasome, including gout²¹, type 2 diabetes mellitus^{3,22}, atherosclerosis²³ and Alzheimer's disease²⁴.

METHODS SUMMARY

Cell stimulation. BMDMs were obtained by differentiating bone marrow progenitors from tibial and femoral bone in Iscove's modified Dulbecco's medium (IMDM) containing 20 ng ml⁻¹ of M-CSF for 7 days. Blood specimens from

b–e, PBMCs from CAPS patients with the designated mutations in *NLRP3* were primed with LPS and treated with the indicated dose of forskolin (**b**), Ro-20-1724 or (R)-(-)-rolipram (**c**), 2-APB (**d**), or BAPTA-AM (**e**). Lysates and supernatants were analysed for IL-1 β secretion by immunoblot.

healthy controls, and patients with CAPS and FMF were drawn after obtaining informed consent under a protocol approved by the NIAMS/NIDDK Institutional Review Board. Human PBMCs were isolated by LSM-lymphocyte separation medium. Inflammasome activation experiments were performed in two stages: initial LPS priming for 3 h and then inflammasome activation for 30–50 min by replacing the medium with RPMI 1640 medium supplemented with activators (ATP, 2 mM; CaCl₂, 1 mM, resulting in a total [Ca²⁺] of 1.42 mM; GdCl₃, 1 mM; R-586, 10 μ M; nigericin, 20 μ M; KH7, 50 μ M; *m*-3M3FBS, 5–40 μ M; MSU, 200 μ g ml⁻¹; CPPD, 200 μ g ml⁻¹; thapsigargin, 50 nM; dsDNA, 1 μ g ml⁻¹ with 2.5 μ l ml⁻¹ of Lipofectamine 2000; flagellin, 0.5 μ g ml⁻¹ with 25 μ l ml⁻¹ DOTAP). For the inhibition of inflammasome activation, LPS-primed BMDMs were treated with inhibitors (U73122, 10 μ M; U73343, 10 μ M; edelfosine, 4–100 μ M; 2-APB, 10 or 50 μ M; BAPTA-AM, 10 or 20 μ M; forskolin, 10–500 μ M; NKH477, 10–500 μ M; Ro 20-1724, 50–250 μ M; (R)-(-)-rolipram, 50–250 μ M; zardaverine, 100 or 250 μ M; GF 109203X, 50 μ M; C-1, 50 μ M) in the presence of each activator.

Immunoprecipitation and pull-down assay. The lysates from BMDMs or 293T cells transiently co-transfected with expression constructs for the wild type, CAPS-associated mutant, or various deleted forms of NLRP3 were immunoprecipitated with anti-ASC antibody followed by protein A agarose, or pulled down with pre-conjugated cAMP, cGMP or ATP beads.

Biochemical assays. Mouse IL-1 β , IL-6 and TNF- α in cell culture supernatants and InsP₃ and cAMP in cell lysates were measured using ELISA.

Full Methods and any associated references are available in the online version of the paper.

Received 24 June 2011; accepted 14 September 2012.

Published online 11 November 2012.

1. Masters, S. L., Simon, A., Aksentijevich, I. & Kastner, D. L. Horror autoinflammaticus: the molecular pathophysiology of autoinflammatory disease. *Annu. Rev. Immunol.* **27**, 621–668 (2009).
2. Kahlenberg, J. M. & Dubyak, G. R. Mechanisms of caspase-1 activation by P2X7 receptor-mediated K⁺ release. *Am. J. Physiol. Cell Physiol.* **286**, C1100–C1108 (2004).
3. Zhou, R., Tardivel, A., Thorens, B., Choi, I. & Tschopp, J. Thioredoxin-interacting protein links oxidative stress to inflammasome activation. *Nature Immunol.* **11**, 136–140 (2010).
4. Hornung, V. *et al.* Silica crystals and aluminum salts activate the NALP3 inflammasome through phagosomal destabilization. *Nature Immunol.* **9**, 847–856 (2008).
5. Pétrilli, V. *et al.* Activation of the NALP3 inflammasome is triggered by low intracellular potassium concentration. *Cell Death Differ.* **14**, 1583–1589 (2007).
6. Brough, D. *et al.* Ca²⁺ stores and Ca²⁺ entry differentially contribute to the release of IL-1 β and IL-1 α from murine macrophages. *J. Immunol.* **170**, 3029–3036 (2003).
7. Cockcroft, S. & Gomperts, B. D. Activation and inhibition of calcium-dependent histamine secretion by ATP ions applied to rat mast cells. *J. Physiol. (Lond.)* **296**, 229–243 (1979).
8. Ross, P. E., Ehring, G. R. & Cahalan, M. D. Dynamics of ATP-induced calcium signaling in single mouse thymocytes. *J. Cell Biol.* **138**, 987–998 (1997).
9. Murakami, T. *et al.* Critical role for calcium mobilization in activation of the NLRP3 inflammasome. *Proc. Natl. Acad. Sci. USA* **109**, 11282–11287 (2012).
10. Hofer, A. M. & Brown, E. M. Extracellular calcium sensing and signalling. *Nature Rev. Mol. Cell Biol.* **4**, 530–538 (2003).
11. Xi, Y. H. *et al.* The functional expression of calcium-sensing receptor in the differentiated THP-1 cells. *Mol. Cell. Biochem.* **342**, 233–240 (2010).
12. Osawa, Y., Lee, H. T., Hirshman, C. A., Xu, D. & Emala, C. W. Lipopolysaccharide-induced sensitization of adenyl cyclase activity in murine macrophages. *Am. J. Physiol. Cell Physiol.* **290**, C143–C151 (2006).
13. Duncan, J. A. *et al.* Cryopyrin/NALP3 binds ATP/dATP, is an ATPase, and requires ATP binding to mediate inflammatory signaling. *Proc. Natl. Acad. Sci. USA* **104**, 8041–8046 (2007).
14. Gattorno, M. *et al.* Pattern of interleukin-1 β secretion in response to lipopolysaccharide and ATP before and after interleukin-1 blockade in patients with *CIAS1* mutations. *Arthritis Rheum.* **56**, 3138–3148 (2007).
15. Chae, J. J. *et al.* Gain-of-function pyrin mutations induce NLRP3 protein-independent interleukin-1 β activation and severe autoinflammation in mice. *Immunity* **34**, 755–768 (2011).
16. Menkin, V. *Biochemical Mechanisms in Inflammation* (Charles Thomas Publisher, 1981).
17. Peters-Golden, M. Putting on the brakes: cyclic AMP as a multipronged controller of macrophage function. *Sci. Signal.* **2**, pe37 (2009).
18. Torphy, T. J. Phosphodiesterase isozymes: molecular targets for novel antiasthma agents. *Am. J. Respir. Crit. Care Med.* **157**, 351–370 (1998).
19. Kim, C., Cheng, C. Y., Saldanha, S. A. & Taylor, S. S. PKA-I holoenzyme structure reveals a mechanism for cAMP-dependent activation. *Cell* **130**, 1032–1043 (2007).
20. Bos, J. L. Epac: a new cAMP target and new avenues in cAMP research. *Nature Rev. Mol. Cell Biol.* **4**, 733–738 (2003).
21. Martinon, F., Pétrilli, V., Mayor, A., Tardivel, A. & Tschopp, J. Gout-associated uric acid crystals activate the NALP3 inflammasome. *Nature* **440**, 237–241 (2006).
22. Vandanmagsar, B. *et al.* The NLRP3 inflammasome instigates obesity-induced inflammation and insulin resistance. *Nature Med.* **17**, 179–188 (2011).
23. Duweil, P. *et al.* NLRP3 inflammasomes are required for atherogenesis and activated by cholesterol crystals. *Nature* **464**, 1357–1361 (2010).
24. Halle, A. *et al.* The NALP3 inflammasome is involved in the innate immune response to amyloid- β . *Nature Immunol.* **9**, 857–865 (2008).

Supplementary Information is available in the online version of the paper.

Acknowledgements This work was supported by the Intramural Research Programs of the NIAMS, NHGRI, and NIAID, NIH. We thank E. Remmers for discussion and a thorough review of this manuscript.

Author Contributions G.-S.L., D.L.K. and J.J.C. designed the research; G.-S.L., N.S., A.I.K. and J.J.C. performed the experiments; G.-S.L., N.S., I.A., D.B.S., R.N.G., D.L.K. and J.J.C. analysed the results; R.G.-M., I.A. and D.L.K. provided patient samples; G.-S.L., J.J.C. and D.L.K. wrote the paper; N.S., I.A., R.G.-M., D.B.S. and R.N.G. edited and commented on the manuscript.

Author Information Reprints and permissions information is available at www.nature.com/reprints. The authors declare no competing financial interests. Readers are welcome to comment on the online version of the paper. Correspondence and requests for materials should be addressed to D.L.K. (kastnerd@mail.nih.gov) or J.J.C. (chaej@mail.nih.gov).

METHODS

Reagents. Nigericin (catalogue no. N7143), GdCl_3 (G7532), EGTA (E8145) and glyburide (G0639) were purchased from Sigma-Aldrich. Solutions of 2 M CaCl_2 (351-033-721) and 1 M MgCl_2 (351-130-721) were from Quality Biological, Inc. ATP (tlrl-atp), dsDNA (tlrl-patn), MSU (tlrl-msu), CPPD (tlrl-cppd), Z-VAD-FMK (tlrl-vad), ultra-pure flagellin (tlrl-pstfla), and ultra-pure LPS (tlrl-pelps) were obtained from InvivoGen. R-568 (3815), *m*-3M3FBS (1941), U73122 (1268), U73343 (4133), edelfosine (3022), 2-APB (1224), GF 109293X (0741), C-1 (0543), BAPTA-AM (2787), KH7 (3834), forskolin (1099), NKH477 (1603), KT5720 (1288), H89 (2910), Ro-20-1724 (0415), (R)-(-)-rolipram (1350) and zardaverine (1046) were from Tocris Bioscience.

Mice. *P2x7* deficient mice were purchased from the Jackson Laboratory. *Asc* and *Nlrp3* deficient mice were a gift from V. M. Dixit. *Casp1* deficient mice were from R. Flavell. All animal studies were performed according to National Institutes of Health guidelines and were approved by the Institutional Animal Care and Use Committee of National Human Genome Research Institute.

Cell preparation. Unless otherwise indicated, all cells were cultured at 37 °C. BMDMs were obtained by differentiating bone marrow progenitors from the tibia and femur in Iscove's modified Dulbecco's medium (IMDM) containing 20 ng ml⁻¹ of M-CSF (PeproTech), 10% heat-inactivated fetal bovine serum (FBS, Invitrogen), 1 mM sodium pyruvate, 100 U ml⁻¹ penicillin and 100 µg ml⁻¹ streptomycin (Invitrogen) for 7 days. BMDMs were then replated in 24-well plates 1 day before experiments. Blood specimens from healthy controls and patients with CAPS and FMF were drawn after obtaining informed consent under a protocol approved by the NIAMS/NIDDK Institutional Review Board. Human PBMCs were isolated by LSM-Lymphocyte Separation Medium (50494, MP Biomedicals) from freshly drawn peripheral venous blood from healthy controls or patients.

Inflammasome activation or inhibition. Inflammasome activation experiments were performed in two stages: LPS priming for 3 h and inflammasome activation (within 1 h), to avoid any chemical inducing interference on the LPS priming stage. The duration of the activation phase was minimized to exclude the effects of secondary protein translation. BMDMs (1.0×10^6 cells per well) or PBMCs (2.0×10^6 cells per well) were plated in 12-well plates and then primed with 1 µg ml⁻¹ LPS in RPMI 1640 (Invitrogen) containing 10% FBS, and antibiotics. For NLRP3 inflammasome activation, the medium was replaced with RPMI 1640 medium supplemented with ATP (2 mM), nigericin (20 µM), R-568 (10 µM), CaCl_2 (1 mM, resulting in a total Ca^{2+} concentration of 1.42 mM, which is still in the physiological range), GdCl_3 (1 mM), KH7 (50 µM), *m*-3M3FBS (5–40 µM), MSU (200 µg ml⁻¹), CPPD (200 µg ml⁻¹), or thapsigargin (50 nM). For AIM2 or NLRC4 inflammasome activation, 1 µg ml⁻¹ of dsDNA with 2.5 µl ml⁻¹ of Lipofectamine 2000 (Invitrogen) or 0.5 µg ml⁻¹ flagellin with 25 µl ml⁻¹ DOTAP (Roche), respectively, were mixed in RPMI 1640 medium and incubated for 10 min before treatment of the cells. For the inhibition of inflammasome activation, LPS-primed BMDMs were treated with U73122 (10 µM), U73343 (10 µM), edelfosine (4–100 µM), 2-APB (10 or 50 µM), BAPTA-AM (10 or 20 µM), forskolin (10–500 µM), NKH477 (10–500 µM), Ro-20-1724 (50–250 µM), (R)-(-)-rolipram (50–250 µM), zardaverine (100 or 250 µM), GF 109293X (50 µM), or C-1 (50 µM) in the presence of each activator (ATP, CaCl_2 , dsDNA, or flagellin).

After 30–50 min of treatment, supernatants and cell lysates were collected for immunoblot analysis. For the ASC pyroptosome, pellets from whole-cell lysates were crosslinked with disuccinimidyl suberate (DSS) and analysed by immunoblotting for ASC. None of the reagents in these experiments induced cytotoxicity as confirmed by LDH assay (K311-400, BioVision).

Gene knockdown assay. siRNAs targeting *Nlrp3*, *Asc*, *Aim2*, *Nlr4*, *Prkaca*, *Ip3r1*, *Adcy3*, *Adcy6*, *Adcy7* and *Adcy9*, and scrambled siRNA were purchased from Applied Biosystems, and siRNA targeting *Casr* was purchased from Invitrogen. The three siRNAs for *Nlrp3* knockdown were 5'-UCUCAAGUCUAAGC ACCAATT-3' (s103710), 5'-CAUCAAGUCUGCUUCGACATT-3' (s103711) and 5'-CAGUGACAAUACUCUGGGATT-3' (s103712), which were used in a mixture. The three siRNAs for *Asc* knockdown were 5'-GAGCAGCUGCAAAC GACUATT-3' (s205578), 5'-GCUACUAUCUGGAGUCGUATT-3' (s83918) and 5'-CCUGGAACCUGACCUGCAATT-3' (s83919), which were used in a mixture. The three siRNAs for *Casr* knockdown were 5'-CACGAGCUGGAA GACGAAUACAUCU-3' (MSS202652, *Casr* siRNA no. 1), 5'-GCGAUGGCUG ACAUUAUCGAGUAUU-3' (MSS202653, *Casr* siRNA no. 2) and 5'-CCA

UCCAGGAAGUCUGUCCACAAU-3' (MSS202654, *Casr* siRNA no. 3). *Aim2* siRNA is 5'-GAUAGAGUACUGUAUGGUATT-3' (s234106). *Nlr4* siRNA is 5'-GGGUGAAGAUUACGACAUATT-3' (s114184). *Prkaca* siRNA is 5'-GAAGCUCCCUCAUACCAATT-3' (s71681). *Ip3r1* siRNA is 5'-CCUUA GCGUUGGUUGAUGATT-3' (s68515). *Adcy3* siRNA is 5'-GCGCAUAGGCAU GAACAAATT-3' (s98221). *Adcy6* siRNA is 5'-GACUUUGACGAGAUA UCATT-3' (s61992). *Adcy7* siRNA is 5'-GCAUUGCGCUCAUCAGCAUTT-3' (s61993). *Adcy9* siRNA is 5'-GCACGGCAAAGAUCUGGAATT-3' (s62001). For siRNA gene knockdown experiments, BMDMs (0.5×10^6 cells per well) were replated in 12-well plates and transfected the next day with 60 pmol siRNA and 3 µl Lipofectamine 2000 according to the manufacturer's instructions. After 48 h, the siRNA-transfected cells were analysed for inflammasome activation.

Immunoprecipitation and pull-down assay. The lysates from BMDMs were immunoprecipitated with anti-ASC antibody (antibody sc-22514, Santa Cruz Biotechnology) followed by protein A plus agarose (Thermo Scientific). After washing, bound proteins were eluted from the beads and analysed by immunoblot for NLRP3 or ASC.

LPS-primed BMDMs or 293T cells transiently co-transfected with expression constructs for the wild type, CAPS-associated mutant, or various deleted forms of NLRP3 were lysed and incubated with pre-conjugated cAMP (AC-147 or AC-146, Jena Bioscience), cGMP (AC-148, Jena Bioscience), ATP (AC-127, Jena Bioscience), or empty/unconjugated beads for 90 min at room temperature. After washing, bound proteins were eluted by 2× SDS sample buffer and analysed by immunoblot for NLRP3 with anti-V5 or anti-MYC antibodies.

Immunoblots. Immunoblots were prepared with Novex Tris-Glycine Gel Systems (Invitrogen) and probed overnight at 4 °C with anti-human IL-1β antibody (AF-201-NA, R&D Systems); anti-mouse IL-1β antibody (AF-401-NA, R&D Systems); anti-caspase-1 p20 antibody (06-503, Millipore); anti-NLRP3 antibody (ALX-804-881, Enzo Life Sciences); anti-CASR antibody (ab18200, Abcam); anti-IP3R1 antibody (sc-28614, Santa Cruz Biotechnology); anti-ASC antibody (sc-22514, Santa Cruz Biotechnology); anti-caspase-1 antibody (sc-622, Santa Cruz Biotechnology); anti-actin antibody (sc-1615, Santa Cruz Biotechnology); anti-MYC antibody (sc-40, Santa Cruz Biotechnology); or anti-V5 antibody (Invitrogen).

Biochemical assays. Mouse IL-1β, IL-6 and TNF-α in cell culture supernatants were measured using mouse IL-1β /IL-1F2 Quantikine ELISA kit, mouse IL-6 Quantikine ELISA kit, and mouse TNF-α Quantikine ELISA kit (MLB00C, M6000B, MTA00B, R&D Systems), respectively. Intracellular cAMP was measured in cell lysates by an ELISA-based competitive immunoassay (K371-100, BioVision). PLC activity was tested by IP-one ELISA (72IP1PEA, Cisbio), in which BMDMs were stimulated with LPS and then cell culture medium was replaced by fresh medium without or with ATP (2 mM) or CaCl_2 (1 mM). Intracellular IP-one, a measure of the degradation products of InsP_3 and a surrogate for InsP_3 levels, was measured after LiCl (50 mM) treatment to prevent the degradation of IP-one into *myo*-inositol.

Calcium analysis by confocal microscopy. BMDMs were plated on 4-chambered coverglass dishes (155383, NUNC) at a density of 0.1×10^6 cells per well and incubated with fluo-4/AM. Cells were pre-treated with or without the InsP_3 receptor blocker 2-APB (50 µM) or intracellular calcium chelator BAPTA-AM (10 µM). Images of untreated cells were acquired ($t = 0$), then cells were treated with added 1 mM ATP, 1 mM CaCl_2 , or 1 mM GdCl_3 in RPMI 1640 (which already contains 0.42 mM Ca^{2+}). Cells were imaged for 30 min with acquisition at 15 s intervals. At the end of the imaging session (at 30 min), ionomycin was added to the medium to a final concentration of 5 µM and cells were further imaged for 10 min. Images were acquired on a Leica SP5 Confocal Imaging System using the 488-nm laser and emission in the range of 500–600. Images were analysed using Imares 7.3.1 software by creating surfaces to encompass the volume of each cell. Absolute intensity for all cells in a field at different time points was obtained, and normalized to time '0' to obtain the fold increase in intensity. Data are displayed as the relative intensity of all cells in a field (20–25 cells per field) and are representative of three independent fields.

Statistical analyses. Statistical analyses were performed with the *t*-test for two groups or one-way ANOVA for multiple groups using GraphPad Prism (GraphPad Software).

Structure of a force-conveying cadherin bond essential for inner-ear mechanotransduction

Marcos Sotomayor¹, Wilhelm A. Weihofen^{2†}, Rachele Gaudet² & David P. Corey¹

Hearing and balance use hair cells in the inner ear to transform mechanical stimuli into electrical signals¹. Mechanical force from sound waves or head movements is conveyed to hair-cell transduction channels by tip links^{2,3}, fine filaments formed by two atypical cadherins known as protocadherin 15 and cadherin 23 (refs 4, 5). These two proteins are involved in inherited deafness^{6–10} and feature long extracellular domains that interact tip-to-tip^{5,11} in a Ca^{2+} -dependent manner. However, the molecular architecture of this complex is unknown. Here we combine crystallography, molecular dynamics simulations and binding experiments to characterize the protocadherin 15–cadherin 23 bond. We find a unique cadherin interaction mechanism, in which the two most amino-terminal cadherin repeats (extracellular cadherin repeats 1 and 2) of each protein interact to form an overlapped, antiparallel heterodimer. Simulations predict that this tip-link bond is mechanically strong enough to resist forces in hair cells. In addition, the complex is shown to become unstable in response to Ca^{2+} removal owing to increased flexure of Ca^{2+} -free cadherin repeats. Finally, we use structures and biochemical measurements to study the molecular mechanisms by which deafness mutations disrupt tip-link function. Overall, our results shed light on the molecular mechanics of hair-cell sensory transduction and on new interaction mechanisms for cadherins, a large protein family implicated in tissue and organ morphogenesis^{12,13}, neural connectivity¹⁴ and cancer¹⁵.

Hair-cell mechanotransduction occurs within each bundle of stereocilia (Fig. 1a) that is deflected by mechanical stimulation¹. Deflection results in tension applied to tip links, protein filaments linking the tip of each stereocilium to its tallest neighbour^{2,3}. The tip links, acting in series with an elastic ‘gating spring’, pull open transduction channels¹. Recently, protocadherin 15 (Pcdh15) and cadherin 23 (Cdh23), which feature exceptionally long extracellular domains containing 11 and 27 extracellular cadherin (EC) repeats, respectively (Fig. 1b), were shown to form the tip link^{4,5}. To elucidate the tip-link heterophilic molecular bond between Pcdh15 and Cdh23, we determined the crystallographic structure of their interacting N termini (Fig. 1c; results summary in Supplementary Fig. 1). Size-exclusion chromatography (SEC) of co-refolded protein fragments comprising the EC1 and EC2 repeats of both Pcdh15 and Cdh23 (hereafter termed Pcdh15-EC1+2 and Cdh23-EC1+2, respectively) showed a monodisperse peak with the two protein fragments interacting in solution (Supplementary Fig. 2a). The complex crystallized in two packing arrangements and two independent models were fully refined (S1a–S1b and S2, respectively; Supplementary Fig. 3 and Supplementary Table 1).

The structures show that Pcdh15-EC1+2 and Cdh23-EC1+2 form an overlapping and antiparallel heterodimer (Fig. 1c, f, g). The interaction resembles an ‘extended handshake’ and involves repeats EC1 and EC2 from both proteins. The overall fold of the Pcdh15 and Cdh23 fragments matched the well-known Greek key motif of classical cadherins (Supplementary Fig. 4). As expected, three Ca^{2+} ions are found in a canonical arrangement (sites 1, 2 and 3) at the linker region between repeats EC1 and EC2 of each protein (Fig. 1c, e). However,

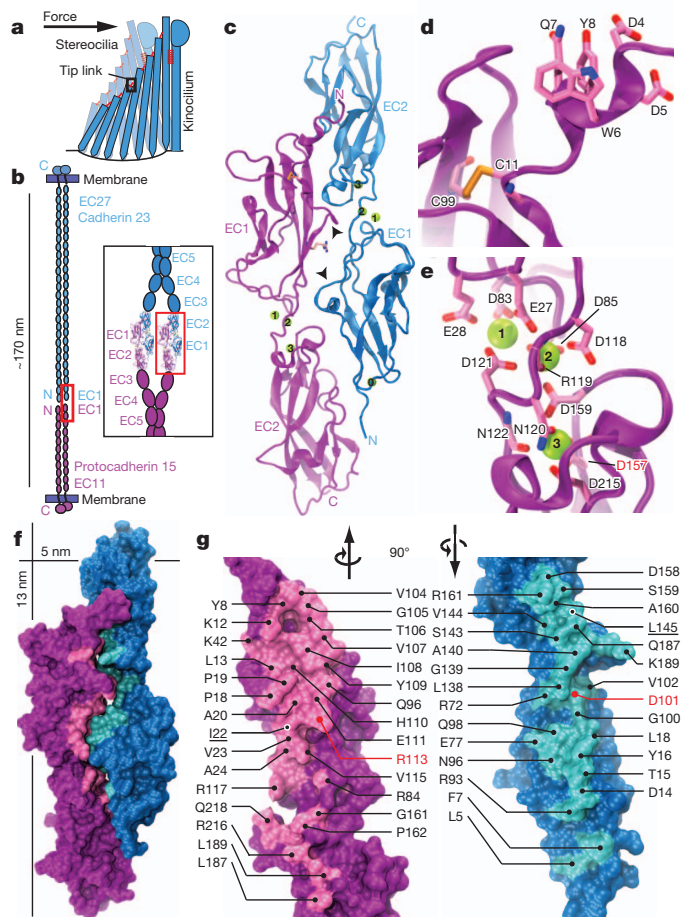


Figure 1 | Structure of tip-link protocadherin 15 bound to cadherin 23.

a, Hair-cell stereocilia bundle. A tip-link filament extends from the tip of each stereocilium to the side of its tallest neighbour. **b**, The tip link formed by a Pcdh15 parallel dimer interacting tip-to-tip with a Cdh23 parallel dimer⁵. These proteins feature 11 and 27 EC repeats, respectively. Inset shows possible arrangement at the junction. **c**, Ribbon diagram of Pcdh15-EC1+2 (purple) bound to Cdh23-EC1+2 (blue) with Ca^{2+} ions as green spheres. Arrowheads indicate the RGGPP loop of Pcdh15-EC1+2 and the 3_{10} helix of Cdh23-EC1+2. Residues Arg 113, Cys 11 and Cys 99 of Pcdh15 are shown in stick representation. **d**, Detail of disulphide bond Cys 11–Cys 99 and isoform-dependent residues Asp 4 to Tyr 8 at the Pcdh15 N terminus. **e**, Detail of Ca^{2+} -binding sites 1, 2 and 3 at the Pcdh15-EC1+2 linker. Protein backbone and side chains are in stick representations for labelled residues. **f**, Surface representation of Pcdh15-EC1+2 (purple and pink) and Cdh23-EC1+2 (blue and cyan) as in **c**. **g**, Pcdh15-EC1+2 and Cdh23-EC1+2 interaction surfaces exposed with interfacing residues labelled. Residues labelled in red are involved in inherited deafness; underlined residues were mutated to probe the interface.

¹Howard Hughes Medical Institute and Department of Neurobiology, Harvard Medical School, Boston, Massachusetts 02115, USA. ²Department of Molecular and Cellular Biology, Harvard University, Cambridge, Massachusetts 02138, USA. [†]Present address: Novartis Institutes for BioMedical Research, Cambridge, Massachusetts 02139, USA.

several novel structural features within Pcdh15-EC1+2 and Cdh23-EC1+2 enable the handshake interaction.

Pcdh15-EC1+2 has an elongated N terminus clamped by an intramolecular disulphide bond (Fig. 1d), which is followed by a conserved RXGPP (in which 'X' denotes glycine, threonine or serine) motif that forms a rigid and bulky loop (Supplementary Fig. 5a, b). This RXGPP loop, within strand A of Pcdh15-EC1, is tucked against the narrow wrist of the linker region of the adjacent Cdh23-EC1+2 (Fig. 1c). Similarly, Cdh23-EC1+2 has an elongated N terminus, stabilized at the tip by Ca^{2+} -binding site 0 (refs 16, 17), which is followed by a bulky 3_{10} helix within strand A that sits at the narrow wrist of the linker in the adjacent Pcdh15-EC1+2 (Fig. 1c). Thus, the Pcdh15-EC1+2–Cdh23-EC1+2 interface exploits unique structural protrusions within strand A of each EC1 repeat, which in turn are stabilized by a disulphide bond and a Ca^{2+} -binding site, and lead to the two main areas of interaction described below.

The Pcdh15-EC1+2–Cdh23-EC1+2 heterophilic interface differs from the strand-exchanged or X-dimer homophilic interfaces of classical cadherins^{18–20}. Furthermore, this interface is not directly mediated by Ca^{2+} as previously speculated^{16,17}. However, several factors indicate that this is a robust interface. The buried surface area is $\sim 1,000 \text{ \AA}^2$ per protomer (see Supplementary Tables 1 and 2), similar to that of classical cadherin interfaces (850 \AA^2 and $1,270 \text{ \AA}^2$ for type I and type II,

respectively). The interface is amphiphilic (Supplementary Fig. 6); all its residues are highly conserved in mouse, human and chicken homologues, and none are predicted to be glycosylated (Fig. 1g and Supplementary Fig. 7). Finally, the same interface was observed in two different crystal lattices, so it is unlikely to represent unphysiological crystal-packing interactions.

To further validate the Pcdh15-EC1+2–Cdh23-EC1+2 interface we used isothermal titration calorimetry (ITC) and site-directed mutagenesis. The stoichiometry of the wild-type complex was determined to be $N = 0.88 \pm 0.1$, consistent with the one-to-one crystallographic arrangement (Fig. 1). The measured dissociation constant was $K_d = 2.9 \pm 0.4 \mu\text{M}$ (temperature $T = 10^\circ\text{C}$, enthalpy change $\Delta H = 7.1 \pm 0.2 \text{ kcal mol}^{-1}$, entropy change $\Delta S = 50.4 \pm 1.1 \text{ cal mol}^{-1} \text{ deg}^{-1}$, two trials; Fig. 2a, b and Supplementary Discussion). The tip link is thought to be a heterotetramer of parallel Pcdh15 and Cdh23 dimers⁵ (Fig. 1b). However, our biochemical and crystallographic data do not show homophilic binding of Cdh23-EC1+2 or Pcdh15-EC1+2, suggesting that parallel dimerization is mediated by repeats other than EC1 and EC2. If so, the binding affinity for the heterotetramer is expected to be higher²¹.

The 'extended handshake' features two main areas of interaction. The first is located at and above the RXGPP loop of Pcdh15 and centres on Tyr 8, Pro 19 and Ile 108 in Pcdh15, and Leu 145 and Gln 187 in

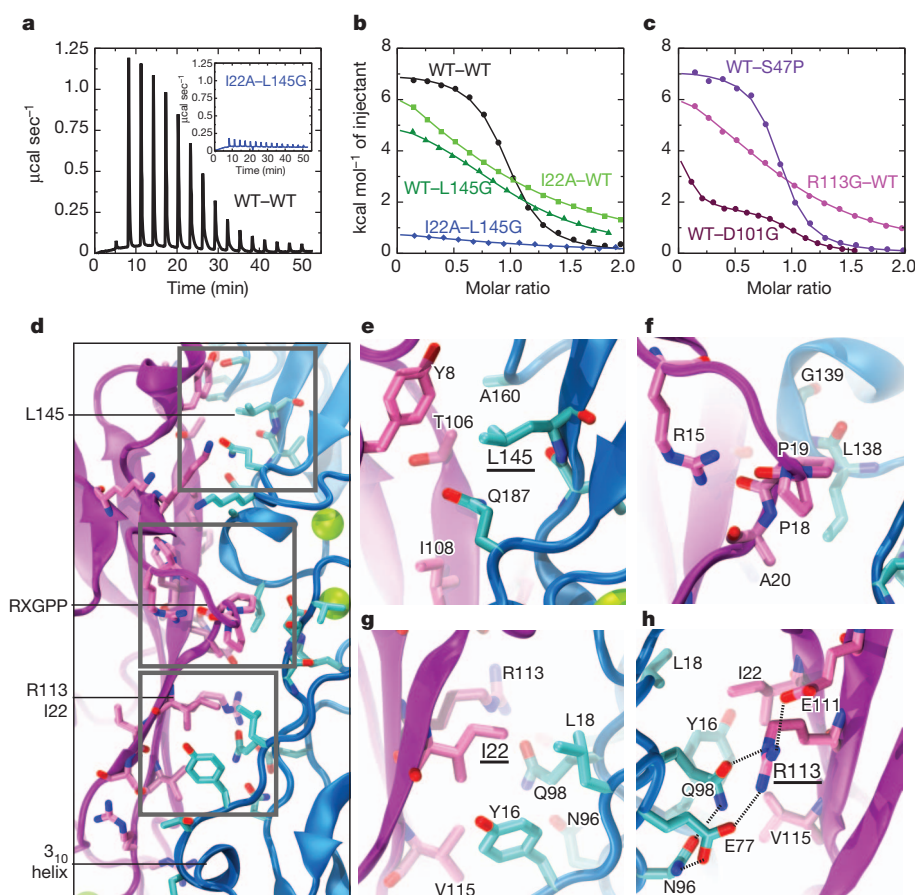


Figure 2 | Pcdh15-EC1+2–Cdh23-EC1+2 complex formation probed using ITC and site-directed mutagenesis. **a**, Raw power versus time data for Pcdh15-EC1+2 (111 μM) titrated with Cdh23-EC1+2 (1.1 mM) at 10°C (black, wild type–wild type (WT–WT)). Inset shows raw data (blue) for Pcdh15-EC1+2(I22A) (114 μM) titrated with Cdh23-EC1+2(L145G) (1.2 mM). **b**, **c**, Change in molar enthalpy for Pcdh15-EC1+2 titrated with Cdh23-EC1+2 (black, WT–WT); Pcdh15-EC1+2(I22A) with Cdh23-EC1+2 (light green); Pcdh15-EC1+2 with Cdh23-EC1+2(L145G) (dark green); and Pcdh15-EC1+2(I22A) with Cdh23-EC1+2(L145G) (blue) (**b**), and Pcdh15-EC1+2 with Cdh23-EC1+2(S47P) (violet); Pcdh15-EC1+2(R113G) with

Cdh23-EC1+2 (magenta); and Pcdh15-EC1+2 with Cdh23-EC1+2(D101G) (indigo) (concentrations in Supplementary Fig. 8) (**c**). Sigmoidal isotherms were observed only for Pcdh15-EC1+2–Cdh23-EC1+2 and Pcdh15-EC1+2–Cdh23-EC1+2(S47P). **d–h**, Details of the Pcdh15-EC1+2–Cdh23-EC1+2 interface, highlighting residue Leu 145 (**e**), the RXGPP loop (**f**) and residues Ile 22 (**g**) and Arg 113 (**h**). **h** is a 180° -rotated version of **g**. Protein backbone and interfacing residues (as identified by the Protein Interfaces, Surfaces and Assemblies (PISA) server) are in purple/pink for Pcdh15 and blue/cyan for Cdh23.

Cdh23 (Figs 1g and 2d–f). The second, located between the RXGPP loop and the 3_{10} helix of Cdh23, involves Ile 22, Arg 113 and Val 115 in Pcdh15 along with Tyr 16 and Gln 98 in Cdh23 (Figs 1g and 2d, g). To test the two interaction areas we introduced mutations predicted to disrupt them: I22A in Pcdh15 (Pcdh15-EC1+2(I22A)) and L145G in Cdh23 (Cdh23-EC1+2(L145G)); Fig. 2d, e, g). SEC confirmed proper folding and structural integrity of the mutant proteins. ITC experiments, testing binding with either one or both mutant partners, showed decreased affinity for each single-mutant complex (Pcdh15-EC1+2(I22A) and Cdh23-EC1+2, $K_d > 100 \mu\text{M}$; Pcdh15-EC1+2 and Cdh23-EC1+2(L145G), $K_d > 30 \mu\text{M}$), and complete lack of interaction for the double-mutant complex (Pcdh15-EC1+2(I22A) and Cdh23-EC1+2(L145G); Fig. 2a, b, d, e, g and Supplementary Figs 2, 8 and 9). Likewise, SEC of Pcdh15-EC1+2 and Cdh23-EC1 repeats alone did not show complex formation (Supplementary Fig. 2b). Taken together, these results indicate that the interface observed in the crystals is consistent with the interface observed in solution.

Next we wanted to know whether the interface has the properties expected for a tip-link bond. Tip links are regularly subjected to (and must withstand) forces ranging from 10 to 100 pN, both *in vivo* and in physiological experiments. Although SEC and ITC experiments provide a characterization of the bond in thermodynamic equilibrium, they do not probe its response to mechanical force. To determine whether the Pcdh15-EC1+2–Cdh23-EC1+2 interface is mechanically strong we used steered molecular dynamics (SMD) simulations (Methods and Supplementary Table 3). Force was applied to the carboxy terminus of each protomer to induce complex dissociation

(Fig. 3a). In all SMD simulations of Pcdh15-EC1+2–Cdh23-EC1+2 with Ca^{2+} , unbinding was observed without unfolding of repeats. Partial rupture of the binding interface at contacts formed by residues Pcdh15(T106)–Cdh23(L145) and Pcdh15(R84)–Cdh23(N96) was followed by sliding of the 3_{10} helix in strand A of Cdh23-EC1 over the Pcdh15 RXGPP loop, and simultaneous rupture of a salt bridge between Pcdh15 Arg 113 and Cdh23 Glu 77 (Fig. 3b, Supplementary Discussion, Supplementary Figs 10 and 11 and Supplementary Videos 1 and 2). Simulations performed using different stretching speeds, initial conditions, and thermodynamic ensembles revealed a similar scenario, with at least one force peak of >400 pN associated with complex unbinding (Fig. 3c, d and Supplementary Figs 10 and 11).

Unbinding forces followed the well-known dependence on stretching speed²², with less force required when the stretch was slower. The slowest speed used in our simulations matched the measured velocity of the basilar membrane induced by loud sound²³ as well as speeds of mechanical stimulators used in *ex vivo* electrophysiological experiments²⁴ (see Supplementary Discussion). In all our simulations the Pcdh15-EC1+2–Cdh23-EC1+2 interface was stronger than that of the classical C-cadherin interface pulled under identical conditions (Supplementary Fig. 12). Furthermore, the predicted force required to unbind parallel complexes was almost double that required to unbind a single Pcdh15-EC1+2–Cdh23-EC1+2 complex (Supplementary Figs 12b, c), which may correspond to the actual force that heterotetrameric tip links can withstand *in vivo* before rupture due to large mechanical stimuli, such as loud sound.

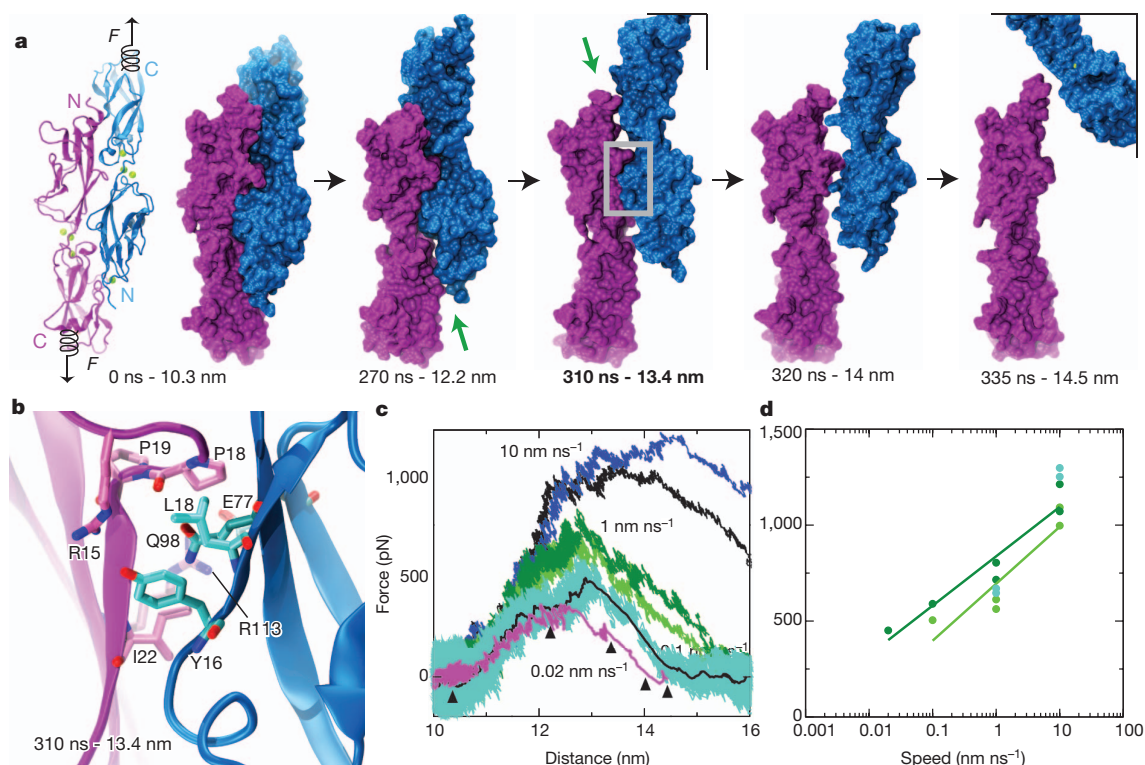


Figure 3 | Mechanical strength of the Pcdh15-EC1+2–Cdh23-EC1+2 complex probed by SMD simulations. **a**, Snapshots of Pcdh15-EC1+2 (purple) and Cdh23-EC1+2 (blue) unbinding during simulation SNA7 (Supplementary Table 3). The complex is shown in both cartoon and surface representations at the beginning, and in surface representation at indicated time points. Force (F) was applied to the C termini of both protomers (Supplementary Videos 1 and 2). Green arrows point to broken interfaces. **b**, Region of grey box in panel **a**, showing interacting residues during unbinding. **c**, Force applied to one C terminus versus distance between C-termini ends of Pcdh15-EC1+2 and Cdh23-EC1+2. Different traces

correspond to independent simulations performed at stretching speeds of 10 (blue and black), 1 (light and dark green), 0.1 (cyan, 1-ns running average shown in black) and 0.02 nm ns⁻¹ (magenta, 1-ns running average). Snapshots in **a** are indicated by arrowheads. **d**, Maximum-force peak values versus stretching speed for unbinding simulations of Pcdh15-EC1+2–Cdh23-EC1+2 started after a 1-ns or 1- μs equilibration (light green, SN2–SN6; dark green, SNA2–SNA7; cyan, SN10–SN13). Simulations SN2–SN6 and SNA2–SNA7 used the S1b structure and SN10–SN13 used S1a; unbinding forces for all three sets were equivalent.

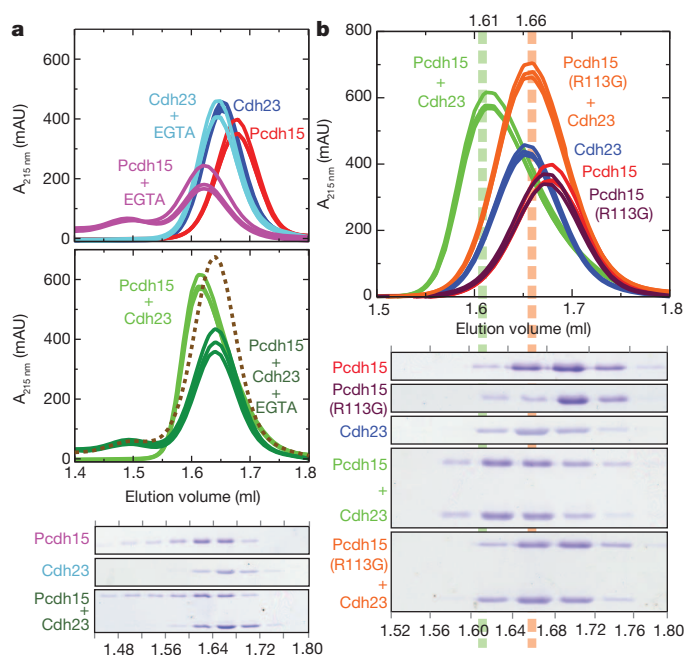


Figure 4 | Pcdh15-EC1+2-Cdh23-EC1+2 complex formation, its Ca^{2+} dependence and the role of the deafness mutation R113G, probed using analytical SEC. Individual traces represent independent experiments. **a**, Top, SEC traces for Pcdh15-EC1+2 and Cdh23-EC1+2 with Ca^{2+} (red and blue) or with 5 mM EGTA (purple and cyan). A shift in response to Ca^{2+} removal by EGTA was observed for Pcdh15-EC1+2 (purple versus red curves). Middle, SEC traces for Pcdh15-EC1+2-Cdh23-EC1+2 in the presence of Ca^{2+} (light green) or 5 mM EGTA (dark green). The summation of a purple and a cyan curve from above is shown as a dashed line. The EGTA-treated complex behaved as the sum of its EGTA-treated components, indicating Ca^{2+} -dependent complex formation. Bottom, Coomassie-stained SDS-polyacrylamide gel electrophoresis (SDS-PAGE) of eluted fractions from EGTA-treated proteins. **b**, Top, SEC traces for mutant Pcdh15-EC1+2(R113G) alone (maroon) and mixed with Cdh23-EC1+2 (orange). Wild-type proteins from **a** are shown for comparison. Bottom, Coomassie-stained SDS-PAGE of eluted fractions aligned to chromatogram. A reproducible shift in elution volume was observed for the wild-type (green) but not for the mutant mixture (Pcdh15-EC1+2(R113G)-Cdh23-EC1+2; orange). The shifted peak (1.61 ml) contained both proteins (1.56–1.64-ml fractions). mAU, milli-absorbance units.

The integrity of tip links in hair cells is Ca^{2+} dependent³, yet Ca^{2+} does not directly participate in the binding interface. We therefore determined whether the Pcdh15-EC1+2-Cdh23-EC1+2 complex is disrupted by Ca^{2+} removal using SEC experiments in the presence of ethylene glycol tetra-acetic acid (EGTA) (Fig. 4a). The Cdh23 fragment by itself did not show changes in its elution volume, whereas Pcdh15-EC1+2 in the presence of EGTA showed a shifted elution trace. Notably, the Pcdh15-EC1+2-Cdh23-EC1+2 complex was disrupted by addition of EGTA: its elution trace did not match that in the presence of Ca^{2+} , but rather corresponded to the summation of the traces of the individual components without the shift in elution volume that indicates interaction. The complex used for crystallization is thus Ca^{2+} dependent at equilibrium, in line with what is known about the full-length Pcdh15 and Cdh23 proteins and the tip link^{3,5}. To understand the basis of the Ca^{2+} dependence, we performed microsecond-long molecular dynamics simulations of the Ca^{2+} -free complex. These suggest a molecular mechanism: removal of Ca^{2+} is predicted to cause dissociation indirectly, through entropic stress (see Supplementary Discussion, Supplementary Figs 13 and 14 and Supplementary Videos 3, 4 and 5), as observed for other cadherins²⁵.

Over 40 missense mutations associated with deafness in humans or mice target the extracellular domains of Pcdh15 and Cdh23, and most modify Ca^{2+} -binding residues²⁶. Three human mutations causing

inherited deafness (PCDH15(D157G)²⁷, CDH23(D101G)²⁸ and PCDH15(R113G)²⁷), and one mouse mutation that accelerates progressive hearing loss (Cdh23(S47P)²⁹), are located within the crystallized Pcdh15-EC1+2-Cdh23-EC1+2 complex (Supplementary Figs 1c and 15). Our data provide a structural context to interpret their effect on tip-link function. We also constructed all four mutants to test formation of heterophilic complexes *in vitro* with ITC and SEC, finding that they each affect the Pcdh15-EC1+2-Cdh23-EC1+2 complex in different ways. Cdh23-EC1+2(D101G), Cdh23-EC1+2(S47P) and Pcdh15-EC1+2(R113G) refolded well, as assessed by SEC, whereas Pcdh15EC1+2(D157G) did not and its analysis was not possible. The D101G and S47P Cdh23-EC1+2 fragments crystallized in complex with Pcdh15-EC1+2 and show only minor changes in the interface and in binding (Fig. 2c, Supplementary Discussion and Supplementary Fig. 16). On the other hand, Pcdh15-EC1+2(R113G) showed impaired binding to Cdh23-EC1+2.

Residue Arg 113 of Pcdh15 is of particular interest because it is at the interface between Pcdh15-EC1+2 and Cdh23-EC1+2 (Fig. 2h). Mutation R113G, causing human non-syndromic deafness DFNB23 (ref. 27), eliminates the long arginine side chain that flanks the hydrophobic core of this interface and disrupts its integrated hydrogen-bond network. SEC of either co-refolded or independently refolded proteins showed no evidence of Pcdh15-EC1+2(R113G)-Cdh23-EC1+2 complex formation (Fig. 4b and Supplementary Fig. 2). Furthermore, ITC experiments show impaired binding and indicate an estimated K_d at least an order of magnitude larger than that measured for wild-type Pcdh15-EC1+2-Cdh23-EC1+2 ($>20 \mu\text{M}$, Fig. 2c and Supplementary Fig. 8). In other work, R113G impaired binding of full-length Pcdh15 and Cdh23 *in vitro*⁵, as well as binding of protein fragments to hair-cell tip links *ex vivo*¹¹. Together, these observations help to validate the interface observed in our crystal structure and indicate that this mutation causes deafness by directly interfering with binding between Pcdh15 and Cdh23. Residual interactions detected in ITC experiments may explain why vestibular function is not affected in human subjects carrying this mutation²⁷.

In summary (Supplementary Fig. 1), the Pcdh15-EC1+2-Cdh23-EC1+2 structure provides the first view of a heterophilic cadherin complex, revealing a novel extended-handshake interface that simulations predict to be mechanically stronger than required to resist forces produced by moderate sound. The structure helps explain the Ca^{2+} sensitivity of the tip link, and the aetiology of certain inherited deafness conditions. For other cadherins, both the existence of heterophilic cadherin bonds and the possibility of interdigitation have been debated²⁰. Although protocadherin 15 and cadherin 23 are rather specialized members of the cadherin family, the overlapping heterophilic complex formed by these molecules suggests structural determinants that could also favour these type of interactions in related members of the cadherin family, such as the Fat3 and Fat4 cadherins that control neuronal morphology and morphogenesis³⁰ (Supplementary Discussion and Supplementary Figs 18 and 19).

METHODS SUMMARY

Wild-type and mutant Cdh23 EC1 and EC1+EC2 repeats and Pcdh15 EC1+EC2 repeats were subcloned into a pET21a plasmid, expressed independently in BL21-CodonPlus (DE3)-RIPL *Escherichia coli* cells, purified under denaturing conditions with nickel-sepharose beads, and then mixed and co-refolded in six steps at 4 °C. Refolded proteins were further purified by SEC. Crystals were grown by vapour diffusion, cryoprotected and cryo-cooled in N_2 . X-ray diffraction data were collected as indicated in Supplementary Tables 1 and 2. Structures were determined by molecular replacement. ITC experiments were carried out using a MicroCal iTC₂₀₀ calorimeter with buffer-matched samples at 10 °C. Analytical SEC was performed on a Superdex200 PC 3.2/3.0 column on an AKTAmicro. Systems for molecular dynamics simulations were prepared with Visual Molecular Dynamics (VMD). Molecular dynamics simulations were performed using NAMD 2.7 or Anton with the CHARMM27 force field, the CMAP correction and the TIP3P water model. Interfaces of complexes were analysed with VMD and the Protein Interfaces, Surfaces and Assemblies (PISA) server.

Full Methods and any associated references are available in the online version of the paper.

Received 8 July 2011; accepted 13 September 2012.

Published online 7 November 2012.

- Gillespie, P. G. & Müller, U. Mechanotransduction by hair cells: models, molecules, and mechanisms. *Cell* **139**, 33–44 (2009).
- Pickles, J. O., Comis, S. D. & Osborne, M. P. Cross-links between stereocilia in the guinea pig organ of corti, and their possible relation to sensory transduction. *Hear. Res.* **15**, 103–112 (1984).
- Assad, J. A., Shepherd, G. & Corey, D. P. Tip-link integrity and mechanical transduction in vertebrate hair cells. *Neuron* **7**, 985–994 (1991).
- Ahmed, Z. M. *et al.* The tip-link antigen, a protein associated with the transduction complex of sensory hair cells, is protocadherin-15. *J. Neurosci.* **26**, 7022–7034 (2006).
- Kazmierczak, P. *et al.* Cadherin 23 and protocadherin 15 interact to form tip-link filaments in sensory hair cells. *Nature* **449**, 87–91 (2007).
- Alagramam, K. N. *et al.* The mouse Ames waltzer hearing-loss mutant is caused by mutation of *Pcdh15*, a novel protocadherin gene. *Nature Genet.* **27**, 99–102 (2001).
- Ahmed, Z. M. *et al.* Mutations of the protocadherin gene *PCDH15* cause Usher syndrome type 1F. *Am. J. Hum. Genet.* **69**, 25–34 (2001).
- Bolz, H. *et al.* Mutation of *CDH23*, encoding a new member of the cadherin gene family, causes Usher syndrome type 1D. *Nature Genet.* **27**, 108–112 (2001).
- Bork, J. M. *et al.* Usher syndrome 1D and nonsyndromic autosomal recessive deafness DFNB12 are caused by allelic mutations of the novel cadherin-like gene *CDH23*. *Am. J. Hum. Genet.* **68**, 26–37 (2001).
- Di Palma, F. *et al.* Mutations in *Cdh23*, encoding a new type of cadherin, cause stereocilia disorganization in waltzer, the mouse model for Usher syndrome type 1D. *Nature Genet.* **27**, 103–107 (2001).
- Lelli, A., Kazmierczak, P., Kawashima, Y., Muller, U. & Holt, J. R. Development and regeneration of sensory transduction in auditory hair cells requires functional interaction between cadherin-23 and protocadherin-15. *J. Neurosci.* **30**, 11259–11269 (2010).
- Takeichi, M. Cadherin cell adhesion receptors as a morphogenetic regulator. *Science* **251**, 1451–1455 (1991).
- Gumbiner, B. M. Regulation of cadherin-mediated adhesion in morphogenesis. *Nature Rev. Mol. Cell Biol.* **6**, 622–634 (2005).
- Shapiro, L., Love, J. & Colman, D. R. Adhesion molecules in the nervous system: structural insights into function and diversity. *Annu. Rev. Neurosci.* **30**, 451–474 (2007).
- Rouget-Quermalet, V. *et al.* Protocadherin 15 (PCDH15): a new secreted isoform and potential marker for NK/T cell lymphomas. *Oncogene* **25**, 2807–2811 (2006).
- Sotomayor, M., Weihofen, W. A., Gaudet, R. G. & Corey, D. P. Structural determinants of cadherin-23 function in hearing and deafness. *Neuron* **66**, 85–100 (2010).
- Elledge, H. M. *et al.* Structure of the N terminus of cadherin 23 reveals a new adhesion mechanism for a subset of cadherin superfamily members. *Proc. Natl Acad. Sci. USA* **107**, 10708–10712 (2010).
- Hulpiau, P. & van Roy, F. Molecular evolution of the cadherin superfamily. *Int. J. Biochem. Cell Biol.* **41**, 349–369 (2009).
- Brasch, J., Harrison, O. J., Honig, B. & Shapiro, L. Thinking outside the cell: how cadherins drive adhesion. *Trends Cell Biol.* **22**, 299–310 (2012).
- Leckband, D. & Prakasam, A. Mechanism and dynamics of cadherin adhesion. *Annu. Rev. Biomed. Eng.* **8**, 259–287 (2006).
- Kuriyan, J. & Eisenberg, D. The origin of protein interactions and allostery in colocalization. *Nature* **450**, 983–990 (2007).
- Evans, E. & Ritchie, K. Dynamic strength of molecular adhesion bonds. *Biophys. J.* **72**, 1541–1555 (1997).
- Robles, L. & Ruggero, M. A. Mechanics of mammalian cochlea. *Physiol. Rev.* **81**, 1305–1352 (2001).
- Stauffer, E. A. & Holt, J. R. Sensory transduction and adaptation in inner and outer hair cells of the mouse auditory system. *J. Neurophysiol.* **98**, 3360–3369 (2007).
- Häussinger, D. *et al.* Calcium-dependent homoassociation of E-cadherin by NMR spectroscopy: changes in mobility, conformation and mapping of contact regions. *J. Mol. Biol.* **324**, 823–839 (2002).
- de Brouwer, A. P. *et al.* Mutations in the calcium-binding motifs of *CDH23* and the 35delG mutation in *GJB2* cause hearing loss in one family. *Hum. Genet.* **112**, 156–163 (2003).
- Ahmed, Z. M. *et al.* Gene structure and mutant alleles of *PCDH15*: nonsyndromic deafness DFNB23 and type 1 Usher syndrome. *Hum. Genet.* **124**, 215–223 (2008).
- Astuto, L. M. *et al.* *CDH23* mutation and phenotype heterogeneity: a profile of 107 diverse families with Usher syndrome and nonsyndromic deafness. *Am. J. Hum. Genet.* **71**, 262–275 (2002).
- Han, F. *et al.* A new mouse mutant of the *Cdh23* gene with early-onset hearing loss facilitates evaluation of otoprotection drugs. *Pharmacogenomics J.* **12**, 30–44 (2012).
- Deans, M. R. *et al.* Control of neuronal morphology by the atypical cadherin fat3. *Neuron* **71**, 820–832 (2011).

Supplementary Information is available in the online version of the paper.

Acknowledgements We thank B. Derfler for assistance with mutagenesis, V. D'Souza and her laboratory for advice on calorimetry, and the Corey and Gaudet laboratories for discussions. Full-length complementary DNAs of *Cdh23* and *Pcdh15* used as template for some of our constructs were provided by U. Müller (The Scripps Research Institute) and T. B. Friedman (National Institutes of Health (NIH)). This work was supported by the NIH (R01 DC02281 to D.P.C.; RC2GM093307 to National Resource for Biomedical Supercomputing/Pittsburgh Supercomputing Center) and the National Science Foundation through TeraGrid/XSEDE (TRAC MCB080015). Simulations were performed at the NCSA-Abe, NICS-Kraken, TACC-Ranger and PSC-Anton supercomputers. Use of Advanced Photon Source beamlines was supported by NIH award RR-15301 and Department of Energy (DOE) contract no. DE-AC02-06CH11357. Use of Advanced Light Source beamline 4.2.2 was supported by DOE contract no. DE-AC02-05CH11231. M.S. was a Howard Hughes Medical Institute (HHMI) Fellow of the Helen Hay Whitney Foundation and D.P.C. is an HHMI Investigator.

Author Contributions All authors participated in all parts of this study. M.S. did all experiments and simulations.

Author Information Atomic coordinates and structure factors for the reported crystal structures have been deposited with the Protein Data Bank under accession codes 4apx (S1a), 4axw (S1b), 4aq8 (S2), 4aqa (S3) and 4aqe (S4). Reprints and permissions information is available at www.nature.com/reprints. The authors declare no competing financial interests. Readers are welcome to comment on the online version of the paper. Correspondence and requests for materials should be addressed to D.P.C. (dcorye@hms.harvard.edu) or R.G. (gaudet@mcb.harvard.edu).

METHODS

Cloning, expression and purification of Pcdh15 and Cdh23 repeats. Clones of mouse Cdh23 repeats EC1 and EC1+2 were previously described in ref. 16. Numbering corresponds to mouse cadherin-23 and protocadherin-15 without their signal sequences. Mouse protocadherin-15 EC1+2 comprising residues Q1–D233 (Q27–D259 in mouse NCBI reference sequence NP_001136218.1) was subcloned into the NdeI and XhoI sites of the vector pET21a (C-terminal His-tag). The signal sequence was replaced by a methionine at position 0. The R113G, D157G and I22A mutations in Pcdh15-EC1+2, as well as the L145G and S47P mutations in Cdh23-EC1+2 were generated using the QuikChange Lightning mutagenesis kit (Stratagene). All constructs were verified by DNA sequencing. Pcdh15-EC1+2, Pcdh15-EC1+2(R113G), Pcdh15-EC1+2(D157G), Pcdh15-EC1+2(I22A), Cdh23-EC1+2, Cdh23-EC1+2(D101G), Cdh23-EC1+2(S47P) and Cdh23-EC1 were expressed independently in BL21CodonPlus(DE3)-RIPL (Stratagene) cultured in Luria-Bertani medium and induced at OD₆₀₀ = 0.6 with 100 µM IPTG at 20 °C for ~16 h. Cells were lysed by sonication in denaturing buffer (20 mM HEPES at pH 7.5, 6 M guanidine hydrochloride (GuHCl), 10 mM CaCl₂, 20 mM imidazole at pH 7.0). The cleared lysates were loaded onto nickel-sepharose (GE Healthcare) and eluted with denaturing buffer supplemented with 500 mM imidazole. Wild-type and mutant Pcdh15-EC1+2 protein fragments were reduced by adding 1 mM dithiothreitol and incubating at 37 °C for ~30 min. Purified and denatured samples were mixed (Pcdh15-EC1+2 and Cdh23-EC1+2, Pcdh15-EC1+2(R113G) and Cdh23-EC1+2, Pcdh15-EC1+2(D157G) and Cdh23-EC1+2, Pcdh15-EC1+2 and Cdh23-EC1+2(D101G), Pcdh15-EC1+2 and Cdh23-EC1+2(S47P), Pcdh15-EC1+2 and Cdh23-EC1, Pcdh15-EC1+2(R113G) and Cdh23-EC1, and Pcdh15-EC1+2(I22A) and Cdh23-EC1) and co-refolded in six steps at 4 °C using membranes with a molecular weight cutoff of 2,000 (protocol adapted from ref. 31). First, the mixture was dialysed for 24 h against D buffer (20 mM Tris HCl, pH 8.0, 10 mM CaCl₂) with 6 M GuHCl, followed by two 24-h dialyses against D buffer with 3 M and 2 M GuHCl, respectively. The last three steps consisted of 12-h dialyses against D buffer with decreasing GuHCl concentration (1, 0.5 and 0 M) plus 400 mM L-Arg and 375 µM glutathione disulphide. Refolded protein used for crystallization was further purified in two consecutive SEC experiments with relevant fractions on a Superdex75 column (GE Healthcare) in 20 mM Tris HCl, pH 8.0, 200 mM KCl, with 10 and 1 mM CaCl₂, respectively. Predicted and apparent molecular weights (SDS-PAGE) for Pcdh15-EC1+2 and Cdh23-EC1+2 fragments were 27.5/37 kDa and 23.8/25 kDa, respectively. Identity of Pcdh15-EC1+2 was confirmed through N-terminal sequencing.

Crystallization, data collection and structure determination. Crystals were grown by vapour diffusion at 4 °C by mixing equal volumes of protein (5–10 mg ml⁻¹) and reservoir solution of 0.1 M MES, pH 6.5, 8% w/v PEG 8000 for S1a; 0.1 M MES, pH 6.5, 15% w/v PEG 550 MME for S1b; 0.1 M HEPES, pH 7.5, 10% w/v PEG 8000 for S2; 0.1 M MES, pH 6.5, 8% w/v PEG 20000 for S3; and 0.1 M MES, pH 6.5, 12% PEG 4000 for S4. All crystals were cryoprotected in reservoir solution plus 25% glycerol and cryo-cooled in N₂. X-ray diffraction data were collected as indicated in Supplementary Tables 1 and 2 and processed with HKL2000 (ref. 32). Structures were determined by molecular replacement using the Cdh23-EC1+2 structure (Protein Data Bank (PDB) code, 2wcp) and a Pcdh15-EC1+2 homology model (based on the same Cdh23-EC1+2 structure) as search models with Phaser³³. Model building was done using Coot³⁴ and restrained translation–libration–screw refinement using REFMAC5 (ref. 35). The final models include residues Met 0–Glu 207 (Cdh23) and Met 0–His 237 (Pcdh15) for S1a, Met 0–Glu 207 (Cdh23) and Gln 1–His 236 (Pcdh15) for S1b, Met 0 to Glu 207 (Cdh23 A and B) and Gln 1/Tyr 2 to His 237 (Pcdh15 C and D) for S2, Met 0 to Asp 205 (Cdh23(D101G) and Cdh23(S47P)) and Met 0 to His 236/His 237 (Pcdh15) for S3 and S4. Data collection and refinement statistics are provided in Supplementary Tables 1 and 2. Coordinates have been deposited in the PDB with entry codes 4apx (S1a), 4axw (S1b), 4aq8 (S2), 4aqa (S3) and 4aaq (S4).

Isothermal titration calorimetry. ITC experiments were carried out using a MicroCal iTC₂₀₀ calorimeter and designed following guidelines from ref. 36 and the manufacturer's manual. Wild type, I22A and R113G Pcdh15-EC1+2 fragments were co-refolded with Cdh23-EC1 as described above, and subsequent SEC was performed on a Superdex75 column with 20 mM Tris HCl, pH 8.0, 300 mM NaCl and 1 mM CaCl₂. Fractions with pure Pcdh15-EC1+2, Pcdh15-EC1+2(I22A), and Pcdh15-EC1+2(R113G) were collected, concentrated (to 100–150 µM) and placed in the sample cell of the calorimeter. Similarly, wild type, L145G, D101G and S47P Cdh23-EC1+2 fragments were refolded as previously described in ref. 16, concentrated (to 1–2 mM), buffer-matched through SEC and then used as titrants. Protein concentrations were measured using the absorbance of the samples at 280 nm and theoretical extinction coefficients. All experiments were performed at 10 °C, as no signal was detected and the protein tended to be unstable at room temperature. In a typical experiment, an initial

0.5-µl injection (disregarded in analyses) was followed by 15 2.44-µl injections of titrant ($\Delta t = 3$ min). Experiments and controls with each combination of fragments were repeated at least once (Supplementary Fig. 8). Fittings and binding constants were obtained using the MicroCal Software, a model with one set of sites, and blank-subtracted data. Fitting parameters are reported for saturating sigmoidal curves as the average \pm s.d. of two independent experiments. Attempts to obtain saturating sigmoidal curves and precise K_d for mutant proteins were hampered by aggregation of protein samples at the high concentration required (>2 mM).

Analytical SEC. SEC of co-refolded proteins (Pcdh15-EC1+2–Cdh23-EC1+2, Pcdh15-EC1+2(R113G)–Cdh23-EC1+2, Pcdh15-EC1+2(D157G)–Cdh23-EC1+2, Pcdh15-EC1+2–Cdh23-EC1+2(D101G), Pcdh15-EC1+2–Cdh23-EC1+2(S47P), Pcdh15-EC1+2–Cdh23-EC1, and Pcdh15-EC1+2(R113G)–Cdh23-EC1) was performed on a Superdex75 16/60 column with 20 mM Tris HCl pH 8.0, 300 mM NaCl and 1 mM CaCl₂ (Supplementary Fig. 2). Fractions with pure Cdh23-EC1+2 (excess from Pcdh15-EC1+2–Cdh23-EC1+2), Pcdh15-EC1+2 (from Pcdh15-EC1+2–Cdh23-EC1) and Pcdh15-EC1+2(R113G) (from Pcdh15-EC1+2(R113G)–Cdh23-EC1) were collected, concentrated (~0.5 mg ml⁻¹), and used for subsequent analytical SEC (Fig. 4a, b) on a Superdex200 PC 3.2/3.0 column equilibrated with the same buffer (plus 5 mM EGTA when indicated). Experiments were performed at 4 °C using a 10-µl loop and a 50 µl min⁻¹ flow rate on an AKTAmicro system equipped with a fused silica capillary tubing for collection of 40-µl fractions. EGTA was added to individual or pre-mixed concentrated samples followed by a 1 h mild shaking before SEC.

Simulated systems. The psfgen, solvate, and autoionize Visual Molecular Dynamics (VMD)³⁷ plugins were used to build all systems (Supplementary Table 3) as previously reported in ref. 16. Most of the Pcdh15-EC1+2–Cdh23-EC1+2 complex simulations used structure S1b (which we determined first), except simulations SN9 to SN13 (which used higher resolution structure S1a; Supplementary Tables 1 and 3). Structures with non-native N- and C-terminal tails were modified back to native sequences. Systems without bound Ca²⁺ were prepared by replacing Ca²⁺ atoms with K⁺.

Molecular dynamics simulations using NAMD. Molecular dynamics simulations were performed using NAMD 2.7 (ref. 38), the CHARMM27 force field for proteins with CMAP correction^{39,40}, and the TIP3P model for water. Simulation parameters were as in ref. 16, except for simulations SNA7 and SNC6, in which a multiple-time-step scheme was used with electrostatic interactions evaluated every other time step. Parameters for Ca²⁺ were from ref. 41. Each system was energy-minimized, then equilibrated in the constant number, pressure and temperature (NpT) ensemble, and the resulting state used to perform subsequent Anton or SMD simulations⁴². All simulations used $T = 310$ K. Coordinates of all atoms were saved for analysis every picosecond. Constant-velocity stretching simulations used the SMD method and NAMD Tcl Forces interface^{16,43}.

Molecular dynamics simulations using Anton. Anton is a massively parallel special-purpose machine for molecular dynamics simulations⁴⁴. Systems pre-equilibrated in NAMD (1.1 ns, $T = 310$ K) were converted to the Anton-compatible Maestro format using the convertNAMDtoMaestro.py script provided by NRBSC/PSC. Anton and NAMD simulations used the same force field. Hydrogen atoms were constrained with SHAKE. Restraints were applied to C $_{\alpha}$ atoms of residues 121, 173 and 205 of Cdh23-EC1+2 to avoid rotation of the complex and contact between periodic images. A multiple-time-step scheme was used with interactions evaluated every 2.5 fs, except for non-bonded interactions computed every other time step. A set of cutoff radii and parameters for evaluation of electrostatic forces was automatically generated for each simulated system using the guess_anton_config script. Simulations were performed in either the constant number, volume, and temperature (NVT) ensemble using the Nose-Hoover thermostat, or the NpT ensemble using the Berendsen thermostat/barostat. Centre of mass motion was removed. Coordinates of all atoms were saved for analysis every 50 (NpT) or 200 (NVT) picoseconds. Anton simulations are restricted in size (<120,000 atoms) and cannot incorporate SMD-like forces, hence the use of complementary NAMD simulations.

Analysis tools. The PISA server was used to analyse complex interfaces⁴⁵ and identify residues shown in Figs 1g and 2d. The VMD 'measure SASA' command was used to determine interface area throughout simulations with a probe radius of 1.4 Å. Interface area was defined as the difference in total solvent-accessible surface areas for each isolated protomer and for the complex divided by two. Glycosylation sites were predicted using OGPET (<http://ogpet.utep.edu/OGPET/>), NetNGlyc (<http://www.cbs.dtu.dk/services/NetNGlyc/>) and NetOGlyc (<http://www.cbs.dtu.dk/services/NetOGlyc/>). Intradomain r.m.s.d. and interdomain flexing were analysed using DynDom⁴⁶. Regression fits to data points of maximum force peaks versus stretching speeds were performed using a logarithmic expression of the form $y = a + b \log x$. Plots and curve fits were prepared using xmgrace. Molecular images in this paper were created with the molecular

graphics program VMD³⁷, except for Supplementary Fig. 5 which used PyMOL (Schrödinger, LLC).

31. Tsumoto, K. *et al.* Highly efficient recovery of functional single-chain Fv fragments from inclusion bodies overexpressed in *Escherichia coli* by controlled introduction of oxidizing reagent—application to a human single-chain Fv fragment. *J. Immunol. Methods* **219**, 119–129 (1998).
32. Otwinowski, Z. & Minor, W. Processing of X-ray diffraction data collected in oscillation mode. *Methods Enzymol.* **276**, 307–326 (1997).
33. McCoy, A. J. *et al.* Phaser crystallographic software. *J. Appl. Crystallogr.* **40**, 658–674 (2007).
34. Emsley, P. & Cowtan, K. Coot: model-building tools for molecular graphics. *Acta Crystallogr. D* **60**, 2126–2132 (2004).
35. Murshudov, G. N., Vagin, A. A. & Dodson, E. J. Refinement of macromolecular structures by the maximum-likelihood method. *Acta Crystallogr. D* **53**, 240–255 (1997).
36. Thomson, J. A. & Ladbury, J. E. in *Biocalorimetry 2: Applications of Calorimetry in the Biological Sciences* (eds Ladbury, J. E. & Doyle, M. L.) 37–58 (Wiley, 2004).
37. Humphrey, W., Dalke, A. & Schulten, K. VMD: visual molecular dynamics. *J. Mol. Graph.* **14**, 33–38 (1996).
38. Phillips, J. C. *et al.* Scalable molecular dynamics with NAMD. *J. Comput. Chem.* **26**, 1781–1802 (2005).
39. MacKerell, A. D. Jr *et al.* All-atom empirical potential for molecular modelling and dynamics studies of proteins. *J. Phys. Chem. B* **102**, 3586–3616 (1998).
40. MacKerell, A. D. Jr, Feig, M. & Brooks, C. L., III. Extending the treatment of backbone energetics in protein force fields: limitations of gas-phase quantum mechanics in reproducing protein conformational distributions in molecular dynamics simulations. *J. Comput. Chem.* **25**, 1400–1415 (2004).
41. Marchand, S. & Roux, B. Molecular dynamics study of calbindin D9k in the apo and singly and doubly calcium-loaded states. *Proteins Struct. Funct. Genet.* **33**, 265–284 (1998).
42. Sotomayor, M. & Schulten, K. Single-molecule experiments *in vitro* and *in silico*. *Science* **316**, 1144–1148 (2007).
43. Sotomayor, M. & Schulten, K. The allosteric role of the Ca⁺⁺ switch in adhesion and elasticity of C-cadherin. *Biophys. J.* **94**, 4621–4633 (2008).
44. Shaw, D. E. *et al.* Atomic-level characterization of the structural dynamics of proteins. *Science* **330**, 341–346 (2010).
45. Krissinel, E. & Henrick, K. Inference of macromolecular assemblies from crystalline state. *J. Mol. Biol.* **372**, 774–797 (2007).
46. Hayward, S. & Berendsen, H. J. Systematic analysis of domain motions in proteins from conformational change: new results on citrate synthase and T4 lysozyme. *Proteins* **30**, 144–154 (1998).

B₁₂ cofactors directly stabilize an mRNA regulatory switch

James E. Johnson Jr^{1*}, Francis E. Reyes^{1†*}, Jacob T. Polaski¹ & Robert T. Batey¹

Structures of riboswitch receptor domains bound to their effector have shown how messenger RNAs recognize diverse small molecules, but mechanistic details linking the structures to the regulation of gene expression remain elusive^{1,2}. To address this, here we solve crystal structures of two different classes of cobalamin (vitamin B₁₂)-binding riboswitches that include the structural switch of the downstream regulatory domain. These classes share a common cobalamin-binding core, but use distinct peripheral extensions to recognize different B₁₂ derivatives. In each case, recognition is accomplished through shape complementarity between the RNA and cobalamin, with relatively few hydrogen bonding interactions that typically govern RNA–small molecule recognition. We show that a composite cobalamin–RNA scaffold stabilizes an unusual long-range intramolecular kissing-loop interaction that controls mRNA expression. This is the first, to our knowledge, riboswitch crystal structure detailing how the receptor and regulatory domains communicate in a ligand-dependent fashion to regulate mRNA expression.

An mRNA leader identified as controlling expression of a cobalamin transport gene (*btuB*) in *Escherichia coli*^{3,4} was the first validated riboswitch shown to interact directly with cellular metabolites in the absence of proteins^{5,6}. Cobalamin riboswitches have since been found to regulate B₁₂ biosynthesis in bacteria widely^{7,8}, and they are one of the most broadly distributed riboswitches in biology^{9,10}. The cobalamin riboswitch family comprises two classes^{5,8} distinguished by peripheral extensions surrounding a common core. The secondary structure of both classes contains a central four-way junction (P3–P6 helices) forming the core receptor domain responsible for cobalamin binding (Fig. 1b and Supplementary Fig. 1). The other shared element is a kissing-loop (KL) interaction between loop L5 of the receptor and L13 of the regulatory domain that instructs the expression machinery. For cobalamin riboswitches that regulate translation, L13 typically contains the ribosome-binding site (RBS). Within the first cobalamin riboswitch class, the KL is generally linked to a downstream structural switch⁸ akin to that used by most riboswitches⁹. The classes are primarily differentiated by the presence of a large peripheral

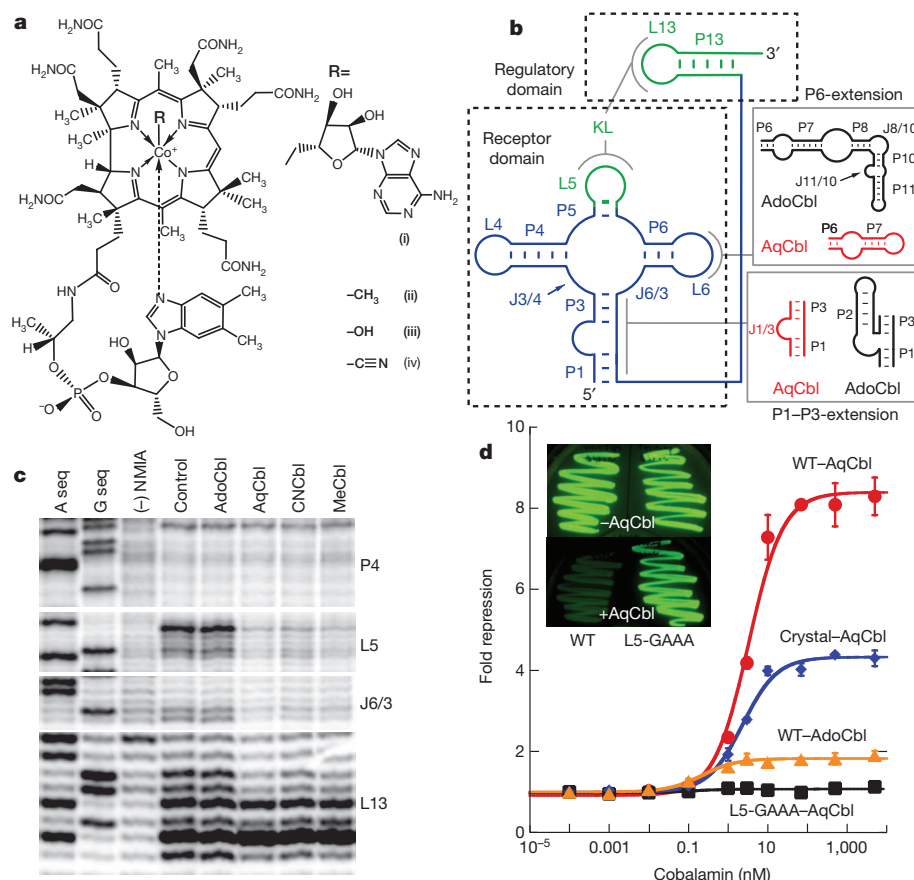


Figure 1 | Structures of cobalamins and cobalamin riboswitches. **a**, Cobalamins contain a corrin ring with a cobalt atom coordinated by an α -axial dimethylbenzimidazole (DMB) and a variable β -axial group. R denotes adenosylcobalamin (AdoCbl) (i), methylcobalamin (MeCbl) (ii), aquocobalamin (AqCbl) (iii) or cyanocobalamin (CNCbl) (iv). **b**, Secondary structure of the cobalamin riboswitch family. The conserved core is shown in blue, the KL interaction in green, and peripheral extensions distinguishing the two classes are shown in black (AdoCbl) and red (AqCbl). **c**, Chemical probing of the *env4AqCbl* riboswitch in the presence of cobalamins. The A and G sequencing lanes are shown to the left, followed by no probing reagent or ligand controls. NMIA, *N*-methylisatoic anhydride. **d**, Repression of GFPuv expression by the *env8AqCbl* riboswitch in *E. coli*. Red circles and orange triangles denote wild-type *env8AqCbl* riboswitch in the presence of AqCbl and AdoCbl, respectively; blue diamonds denote a leader sequence that spans the crystallized riboswitch sequence; and black squares denote an L5 mutant that cannot form the KL with L13. Error bars represent \pm s.d. The inset shows plates of the wild-type and L5 mutant grown in the absence (–) or presence (+) of AqCbl.

¹Department of Chemistry and Biochemistry, University of Colorado at Boulder, UCB 596, Boulder, Colorado 80309-0596, USA. [†]Present address: Physical Biosciences Division, Lawrence Berkeley National Laboratory, Berkeley, California 94720, USA.

*These authors contributed equally to this work.

extension of P6 in one class (representing approximately 95% of the sequences of the cobalamin family¹⁰) that is absent or severely truncated in the other class^{5,8} (Fig. 1b). Another peripheral extension between P1 and P3 further defines the classes. A unique feature of numerous cobalamin riboswitches, particularly those without the P6-extension, is that regulation seems to be achieved through tertiary structure formation (the KL interaction).

All cobalamin riboswitches are proposed to bind adenosylcobalamin (AdoCbl), despite experimental validation of only a few member sequences^{5,6,11}. Unexpectedly, we found some riboswitches recognize methylcobalamin (MeCbl) and aquocobalamin (AqCbl) with more than 500-fold higher affinity than AdoCbl (Supplementary Fig. 2 and Supplementary Table 1). Chemical probing¹² shows B₁₂-dependent reactivity changes in a riboswitch lacking the P6-extension only in the presence of derivatives with small β -axial moieties (Fig. 1a), unlike the *E. coli* *btuB* riboswitch that selectively binds adenosylcobalamin^{5,6} (Fig. 1c; Supplementary Fig. 3). Considerable reactivity changes are localized to three regions: the central junction (J6/3), L5 and L13, the latter two suggestive of KL formation. Cobalamin selectivity and the role of KL formation in gene regulation were validated by cell-based assays. Control of reporter gene expression by a riboswitch lacking the P6-extension was tested in a Δ *btuR* (cobalamin adenosyl transferase-deficient) strain of *E. coli* incapable of converting AqCbl to AdoCbl (ref. 13).

Expression of the green fluorescent protein variant GFPuv is repressed \sim 8.5-fold by AqCbl, but less than 2-fold by AdoCbl (Fig. 1d). A mutation of L5 in the mRNA (L5-GAAA) that retains cobalamin binding but eliminates KL formation abolishes repression, directly establishing the essential role of tertiary structure formation in regulating gene expression. Notably, similar sequences group on a branch of a cobalamin riboswitch phylogenetic tree highly populated by marine cyanobacterial⁸ and environmental (*env*) metagenomes of samples from the ocean surface¹⁴. The prevalence of these riboswitches in these bacteria suggests adaptation of the RNA to environments in which the free cobalamin pool is predominantly AqCbl owing to rapid photolysis of AdoCbl (ref. 15). Therefore, we refer to riboswitches containing the P6-extension as AdoCbl, and those lacking this extension as AqCbl, reflecting their probable biological effectors.

To determine the mechanistic basis for cobalamin-dependent regulation we solved structures of the *env8AqCbl* riboswitch in complex with AqCbl (Fig. 2a) and the *Thermoanaerobacter tengcongensis* (*Tte*) AdoCbl riboswitch bound to AdoCbl (Fig. 2b and Methods). AdoCbl riboswitches are the largest of the known riboswitches—at more than 200 nucleotides they are the size of the *Azoarcus* group I self-splicing intron¹⁶. The *env8AqCbl* riboswitch is the first structure containing both the receptor and regulatory domain. Insertion of the sequence spanning the crystal structure upstream of a GFPuv reporter confers cobalamin-dependent regulatory activity, albeit at lower efficiency than the wild-type riboswitch (Fig. 1d, crystal). Thus, the *env8AqCbl* structure corresponds to a completely functional riboswitch encompassing all of the sequence necessary and sufficient to impart biological activity.

The global architecture of both RNAs is defined by organization of their common secondary structure into two coaxial stacks, P1–P3–P6 and P4–P5–P13 (Fig. 2, blue and green, respectively), consistent with comparative analysis of known RNA structures¹⁷ and mutual information sequence analysis⁹. These stacks are joined by a T-loop–T-loop motif (L4–L6), a common module of RNA tertiary architecture^{18,19}. In *Tte*AdoCbl, the T-loop (L4) interacts with an internal loop between P6 and P7 that partially mimics the structure of the T-loop (Supplementary Fig. 4), rather than another T-loop as observed in the AqCbl and flavin mononucleotide riboswitches²⁰. Class-specific peripheral extensions flank the core (Fig. 2, magenta and cyan) that contact J6/3, a key element for cobalamin recognition.

Interactions between the RNA and cobalamin are mediated primarily through van der Waals shape complementarity with few direct hydrogen bonds. In both structures, cobalamin is sandwiched between

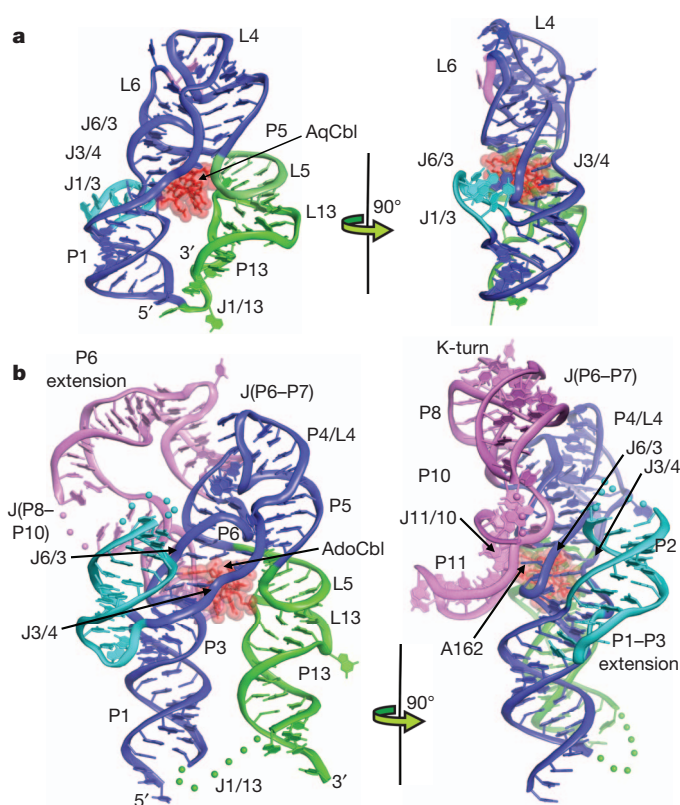


Figure 2 | Crystal structures of two distinct cobalamin riboswitches.

a, Structure of the *env8AqCbl* riboswitch from a 'front' and 'side' perspective. Coloured regions represent the core aptamer domain (blue), regulatory KL interaction (green), and peripheral subdomains (magenta and cyan). AqCbl is represented by van der Waals spheres (red). A secondary structural representation of *env8AqCbl* RNA reflecting the tertiary organization and non-canonical base pairing is shown in Supplementary Fig. 11. **b**, Cartoon representation of the structure of the *Tte*AdoCbl riboswitch complex. Colouring of the RNA and ligand is consistent with **a**. Disordered regions L2, J(P8–P10) and J1/13 are represented by spheres connecting the ends of the chain break.

the minor grooves of the P3–P6 coaxial stack and the helix created by base pairing of L5 and L13, forming the regulatory KL (Fig. 2). The J3/4 and J6/3 strands are central to the receptor side of the binding pocket; in *env8AqCbl*, stacking of four purines from these strands creates a relatively flat surface (G19, A20, A67 and A68; Fig. 3a). The β -axial face of cobalamin projects directly towards this surface, so the plane of the corrin ring is almost perpendicular to the bases of the purine stack. Despite numerous propionamide and acetamide groups surrounding the corrin ring, only one acetamide contacts the minor groove edge of G19 in *env8AqCbl* and its equivalent in *Tte*AdoCbl (G49) (Fig. 3b, c). A SELEX-generated aptamer uses a similar strategy to bind cyanocobalamin, although the molecular details of recognition are quite different²¹ (Supplementary Fig. 5).

Selectivity between cobalamin derivatives is achieved through conformational differences in J6/3 mediated by the peripheral extensions. In *env8AqCbl*, proximity of A20 and A68 to the corrin ring sterically occludes the 5'-deoxyadenosyl moiety of AdoCbl, establishing its selectivity for cobalamins with small β -axial moieties (Fig. 3b). The conformation of J6/3 that blocks AdoCbl binding is enforced through base pairing with the J1/3 peripheral extension (G10•U69 and C11–G70). In *Tte*AdoCbl, placement of J6/3 further from J3/4 allows the Hoogsteen face of A162, the equivalent of A68 in *env8AqCbl*, to base pair with the 5'-deoxyadenosyl moiety (Fig. 3c). Positioning of J6/3 is reinforced by two highly conserved adenosines (A130 and A131) in the internal loop between P10 and P11 of the P6-extension (Fig. 3c and Supplementary Fig. 6), in support of the finding that this extension is

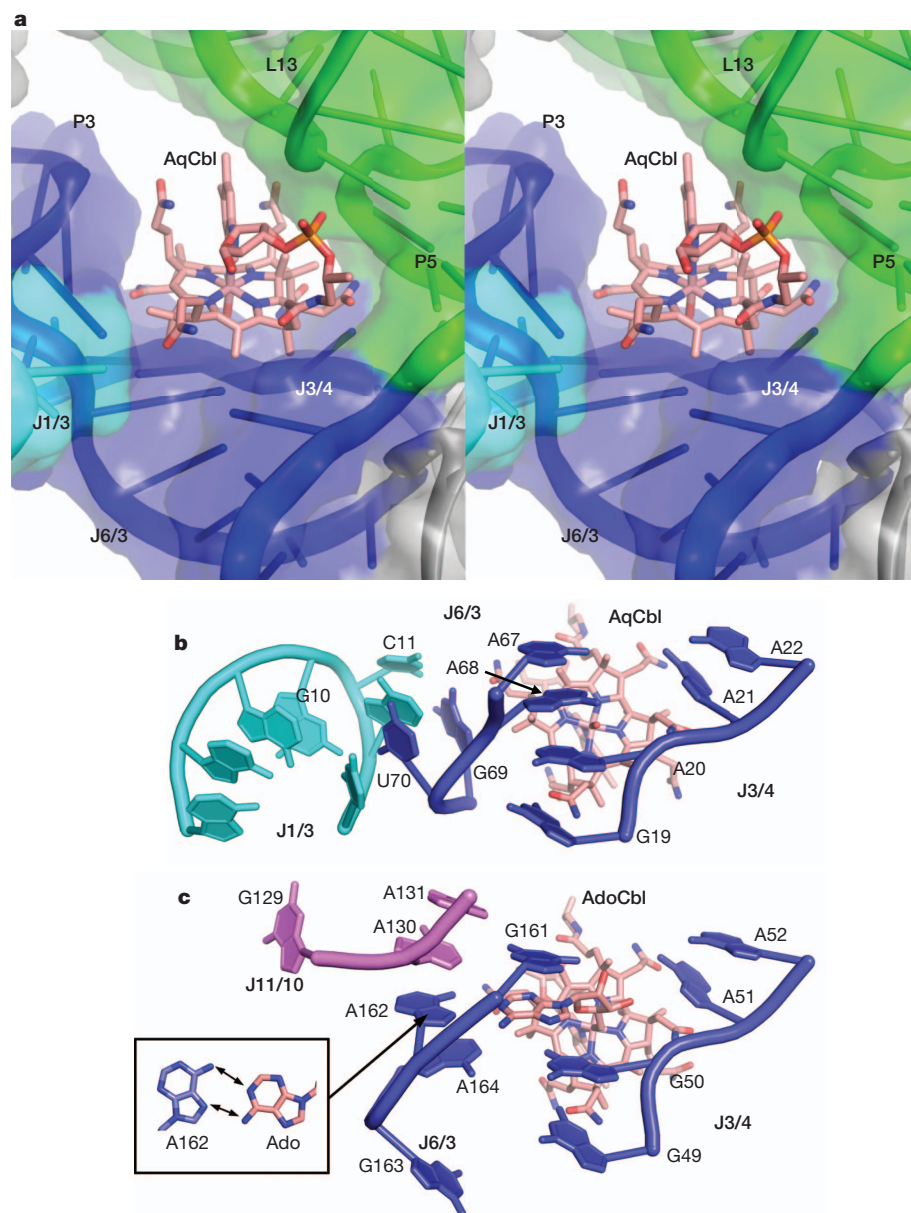


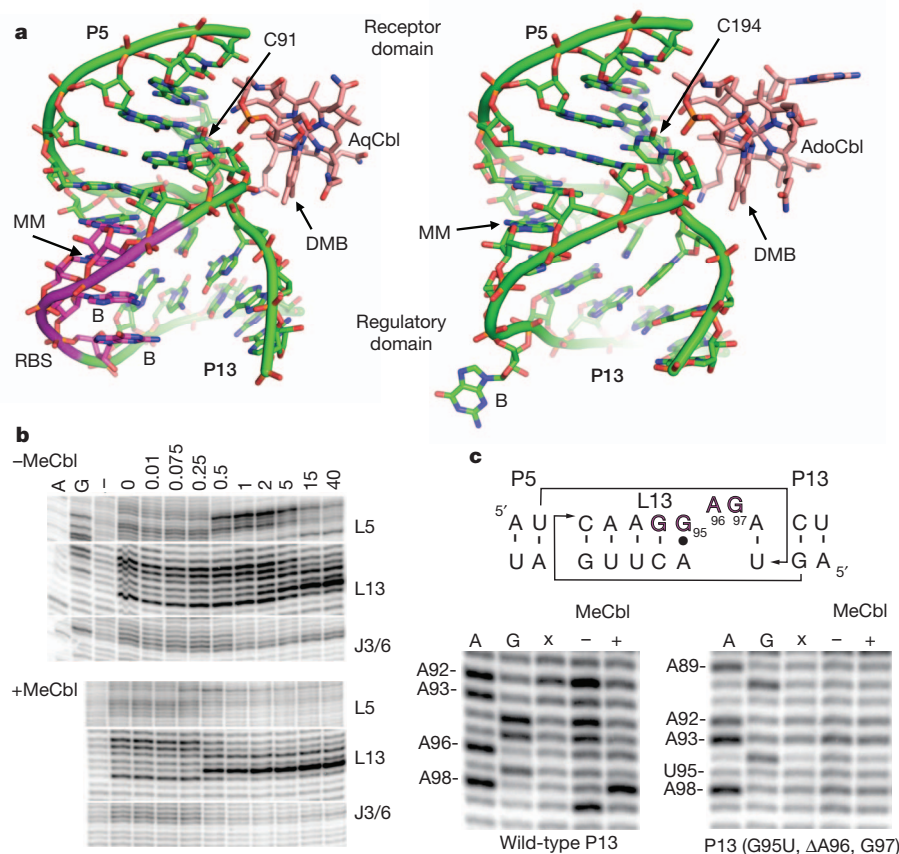
Figure 3 | Cobalamin recognition by the receptor domain. **a**, Stereo view of the surface representation of cobalamin binding to the receptor domain, emphasizing extensive shape complementarity between RNA and AqCbl. Colouring is consistent with Fig. 2. **b**, Recognition of AqCbl by the *env8AqCbl* riboswitch. A stack of four purines in J3/4 and J6/3 packs against the β -axial face of the corrin ring with J6/3 directly buttressed by J1/3 (cyan). **c**, Recognition of AdoCbl by the *TteAdoCbl* RNA. Although J3/4 is positioned identically to AqCbl, J6/3 adopts a different configuration that allows A162 to pair with the adenosyl base of AdoCbl (inset).

required for AdoCbl specificity (Supplementary Table 1). These adenosines are strongly protected from chemical modification only in the presence of AdoCbl (J11/10, Supplementary Fig. 3), suggesting that the peripheral domain docks with the core after initial cobalamin binding. Because other cobalamins can bind the AdoCbl riboswitch with ~ 80 -fold lower affinity (Supplementary Table 1), we propose that the P6-extension may allow these riboswitches to regulate gene expression differentially on the basis of whether the intracellular cobalamin pool is dominated by AdoCbl or its photolysed product AqCbl. Notably, a recently discovered repressor protein in *Myxococcus xanthus* uses B₁₂ to photoregulate carotenoid biosynthesis²². Use of peripheral extensions by a riboswitch to modulate its properties has not been previously observed, but is common with other large RNAs^{23,24}.

The receptor–cobalamin complex presents a composite surface composed of RNA and ligand that binds the regulatory domain. Superimposition of the full *env8AqCbl* riboswitch with a structure of the receptor domain alone indicates that the receptor–ligand complex provides a relatively rigid surface for docking of P13 (Supplementary Fig. 7). RNA–RNA interactions between the two domains are through base pairing of nucleotides in L5 and L13 to form the KL. In both structures, the α -axial face of B₁₂ interacts with the KL through structure-specific rather

than sequence-specific contacts. Dimethylbenzimidazole and the aminopropyl linker interact with the ribose–phosphate backbone of L5 and L13 primarily through van der Waals contacts; the only direct hydrogen bond is between the 2'-hydroxyl group of the cobalamin ribosyl moiety and the 2'-hydroxyl group of C91/C194 (Fig. 4a). Further contacts are made to the RNA by propionamide and acetamide groups with the only direct base contact being to the sugar edge of U44 (*env8AqCbl*) or its equivalent, G74 (*TteAdoCbl*), in L5. The KL–cobalamin interface is nearly identical between the two structures despite low sequence similarity in L5 and L13, indicating structure-specific recognition of the KL by B₁₂.

Kissing-loops are inherently stable structures widely used to promote tertiary architecture formation and RNA–RNA interactions^{25,26}. A unique feature of the KL in both structures is the presence of non-Watson–Crick pairs and bulged nucleotides in the helix formed by pairing of L5 and L13 (Fig. 4a, labelled MM and B). Mismatched pairs are strongly destabilizing to the KL²⁷, suggesting a mechanism for creating a cobalamin-dependent switch. To show bound cobalamin promotes KL formation, its structure was probed as a function of Mg²⁺, which promotes long-range tertiary interactions in RNA²⁸. Chemical probing of the unbound AqCbl riboswitch shows that at least 15 mM Mg²⁺ is required before reactivity protections consistent



with KL formation are observed, whereas bound ligand allows its formation under physiological Mg^{2+} concentrations (0.5–1 mM) (Fig. 4b and Supplementary Fig. 8). This same trend is observed for the *E. coli* *btuB* AdoCbl riboswitch (Supplementary Fig. 9). Stabilizing the KL with mutations in L13 that enable perfect Watson–Crick pairing with L5 (G95U, Δ A96 and Δ G97) results in cobalamin-independent KL formation, equivalent to a constitutively repressed mRNA due to sequestration of the RBS (Fig. 4c). Together, these data show that cobalamin riboswitches use ligand-dependent formation of a tertiary RNA module as the basis for gene regulation. This is a structurally distinct but functionally equivalent mechanism to most other RNA switches that use mutually exclusive secondary structures to achieve regulatory activity.

METHODS SUMMARY

RNAs were transcribed by T7 RNA polymerase, purified by denaturing methods and refolded before crystallization with either AqCbl or AdoCbl (ref. 29). Diffraction data was collected at the Advanced Light Source (beamlines 5.0.2, 8.2.1 and 8.2.2), and solved using a combination of multiwavelength anomalous dispersion and molecular replacement approaches. Data collection and refinement statistics are presented in Supplementary Tables 2 and 3. Biochemical analysis of an AdoCbl riboswitch was performed using a sequence that regulates the *E. coli* *btuB* gene; the *env4AqCbl* and *env8AqCbl* sequences were derived from the Pacific Ocean metagenome¹⁴ (85% identity shared between them). All experiments using AdoCbl or MeCbl were performed using a red safe light to minimize photolysis of this compound.

Full Methods and any associated references are available in the online version of the paper.

Received 2 April; accepted 25 September 2012.

Published online 14 October 2012.

- Garst, A. D., Edwards, A. L. & Batey, R. T. Riboswitches: structures and mechanisms. *Cold Spring Harb. Perspect. Biol.* **3**, a003533 (2011).
- Breaker, R. R. Riboswitches and the RNA world. *Cold Spring Harb. Perspect. Biol.* **4**, a003566 (2012).

- Lundrigan, M. D., Koster, W. & Kadner, R. J. Transcribed sequences of the *Escherichia coli* *btuB* gene control its expression and regulation by vitamin B₁₂. *Proc. Natl Acad. Sci. USA* **88**, 1479–1483 (1991).
- Franklund, C. V. & Kadner, R. J. Multiple transcribed elements control expression of the *Escherichia coli* *btuB* gene. *J. Bacteriol.* **179**, 4039–4042 (1997).
- Nahvi, A., Barrick, J. E. & Breaker, R. R. Coenzyme B₁₂ riboswitches are widespread genetic control elements in prokaryotes. *Nucleic Acids Res.* **32**, 143–150 (2004).
- Nahvi, A. *et al.* Genetic control by a metabolite binding mRNA. *Chem. Biol.* **9**, 1043 (2002).
- Rodionov, D. A., Vitreschak, A. G., Mironov, A. A. & Gelfand, M. S. Comparative genomics of the vitamin B₁₂ metabolism and regulation in prokaryotes. *J. Biol. Chem.* **278**, 41148–41159 (2003).
- Vitreschak, A. G., Rodionov, D. A., Mironov, A. A. & Gelfand, M. S. Regulation of the vitamin B₁₂ metabolism and transport in bacteria by a conserved RNA structural element. *RNA* **9**, 1084–1097 (2003).
- Barrick, J. E. & Breaker, R. R. The distributions, mechanisms, and structures of metabolite-binding riboswitches. *Genome Biol.* **8**, R239 (2007).
- Gardner, P. P. *et al.* Rfam: updates to the RNA families database. *Nucleic Acids Res.* **37**, D136–D140 (2009).
- Fox, K. *et al.* Multiple posttranscriptional regulatory mechanisms partner to control ethanolamine utilization in *Enterococcus faecalis*. *Proc. Natl Acad. Sci. USA* **106**, 4435–4440 (2009).
- Wilkinson, K. A., Merino, E. J. & Weeks, K. M. Selective 2'-hydroxyl acylation analyzed by primer extension (SHAPE): quantitative RNA structure analysis at single nucleotide resolution. *Nature Protocols* **1**, 1610–1616 (2006).
- Lundrigan, M. D. & Kadner, R. J. Altered cobalamin metabolism in *Escherichia coli* *btuB* mutants affects *btuB* gene regulation. *J. Bacteriol.* **171**, 154–161 (1989).
- Weinberg, Z. *et al.* Comparative genomics reveals 104 candidate structured RNAs from bacteria, archaea, and their metagenomes. *Genome Biol.* **11**, R31 (2010).
- Taylor, R. T., Smucker, L., Hanna, M. L. & Gill, J. Aerobic photolysis of alkylcobalamins: quantum yields and light-action spectra. *Arch. Biochem. Biophys.* **156**, 521–533 (1973).
- Adams, P. L., Stahley, M. R., Kosek, A. B., Wang, J. & Strobel, S. A. Crystal structure of a self-splicing group I intron with both exons. *Nature* **430**, 45–50 (2004).
- Jaeger, L., Verzemnieks, E. J. & Geary, C. The UA₄ handle: a versatile submotif in stable RNA architectures. *Nucleic Acids Res.* **37**, 215–230 (2009).
- Nagaswamy, U. & Fox, G. E. Frequent occurrence of the T-loop RNA folding motif in ribosomal RNAs. *RNA* **8**, 1112–1119 (2002).
- Krasilnikov, A. S. & Mondragon, A. On the occurrence of the T-loop RNA folding motif in large RNA molecules. *RNA* **9**, 640–643 (2003).
- Serganov, A., Huang, L. & Patel, D. J. Coenzyme recognition and gene regulation by a flavin mononucleotide riboswitch. *Nature* **458**, 233–237 (2009).

21. Sussman, D., Nix, J. C. & Wilson, C. The structural basis for molecular recognition by the vitamin B₁₂ RNA aptamer. *Nature Struct. Biol.* **7**, 53–57 (2000).
22. Ortiz-Guerrero, J. M., Polanco, M. C., Murillo, F. J., Padmanabhan, S. & Elias-Arnanz, M. Light-dependent gene regulation by a coenzyme B₁₂-based photoreceptor. *Proc. Natl Acad. Sci. USA* **108**, 7565–7570 (2011).
23. Vicens, Q. & Cech, T. R. Atomic level architecture of group I introns revealed. *Trends Biochem. Sci.* **31**, 41–51 (2006).
24. Melnikov, S. *et al.* One core, two shells: bacterial and eukaryotic ribosomes. *Nature Struct. Mol. Biol.* **19**, 560–567 (2012).
25. Xin, Y., Laing, C., Leontis, N. B. & Schlick, T. Annotation of tertiary interactions in RNA structures reveals variations and correlations. *RNA* **14**, 2465–2477 (2008).
26. Butcher, S. E. & Pyle, A. M. The molecular interactions that stabilize RNA tertiary structure: RNA motifs, patterns, and networks. *Acc. Chem. Res.* **44**, 1302–1311 (2011).
27. Gregorian, R. S. Jr & Crothers, D. M. Determinants of RNA hairpin loop-loop complex stability. *J. Mol. Biol.* **248**, 968–984 (1995).
28. Pyle, A. M. Metal ions in the structure and function of RNA. *J. Biol. Inorg. Chem.* **7**, 679–690 (2002).
29. Reyes, F. E., Garst, A. D. & Batey, R. T. Strategies in RNA crystallography. *Methods Enzymol.* **469**, 119–139 (2009).

Supplementary Information is available in the online version of the paper.

Acknowledgements This work was supported by grants from the National Institutes of Health (GM073850 and 1S10RR026516) to R.T.B. and by a Colorado Diversity Initiative Fellowship and NIH Ruth L. Kirschstein fellowship (F32GM095121) to J.E.J. The Advanced Light Source is supported by the Director, Office of Science, Office of Basic Energy Sciences, of the US Department of Energy under contract no. DE-AC02-05CH11231.

Author Contributions F.E.R. discovered the specificity of the AqCbl class and performed all aspects of the crystallography with assistance from J.T.P.; J.E.J. performed all biochemical experiments and fully characterized the specificities of the cobalamin family; J.T.P. obtained all *in vivo* data; and all authors contributed to the analysis of the data and the writing of this paper.

Author Information Atomic coordinates and structure factors have been deposited in the Protein Data Bank (PDB) under accession numbers 4FRG (*env8AqCbl*(ΔJ1/13,P13)), 4FRN (*env8AqCbl*) and 4GMA (*TteAdoCbl*). Reprints and permissions information is available at www.nature.com/reprints. The authors declare competing financial interests: details are available in the online version of the paper. Readers are welcome to comment on the online version of the paper. Correspondence and requests for materials should be addressed to R.T.B. (robert.batey@colorado.edu) or F.E.R. (francis.reyes@colorado.edu).

METHODS

RNA preparation. RNA constructs (full sequences are shown in Supplementary Fig. 1) were prepared using DNA templates generated from PCR amplification using established protocols^{29,30}. DNA templates for the *E. coli* *btuB* cobalamin riboswitch was amplified from *E. coli* genomic DNA, whereas the *env4*, *env8* and *T. tengcongensis* cobalamin riboswitches were amplified using a series of overlapping oligonucleotides. PCR products were used as a template for transcription reactions using T7 RNA polymerase³¹ and the RNA purified using denaturing PAGE (8% or 12%, 29:1 acrylamide:bisacrylamide). The RNA was buffer exchanged and concentrated into 0.5× TE buffer and frozen at −80 °C until use.

Isothermal titration calorimetry. RNA was dialysed overnight into a buffer containing 5 mM sodium-MES, pH 6.0, 100 mM KCl, and 5 mM MgCl₂. RNA was diluted up to a final concentration of 10 μM and titrated with AdoCbl, AqCbl or MeCbl dissolved in the dialysis buffer at concentrations tenfold in excess of the RNA. Titrations were all performed at 25 °C using a MicroCal iTC₂₀₀ microcalorimeter. Data analysis and fitting was performed with the Origin software suite as previously described³².

Chemical probing with NMIA. Chemical probing of RNAs were performed using slight modifications to established protocols¹². Purified RNA constructs were refolded by incubation at 70 °C for 3 min, room temperature for 5 min, and on ice for a minimum of 5 min. For ligand comparison experiments, 10 μl solutions were prepared to a final concentration of 0.1 μM RNA, 100 mM potassium-HEPES, pH 8.0, 100 mM NaCl, 6 mM MgCl₂, ligand and 6.5 mM NMIA. Final ligand concentrations for the *E. coli* *btuB* experiments were 0.5 mM AdoCbl, 2.5 mM AqCbl, CNCbl and MeCbl. For the *env4*AqCbl experiments, final ligand concentrations were 100 μM for all compounds. For magnesium titrations, the conditions were the same as the above mentioned conditions with the final concentrations of ligands as 500 μM AdoCbl or 100 μM MeCbl. Samples were reverse transcribed as previously described¹². Products were separated using 12% denaturing polyacrylamide gel and visualized using a Typhoon PhosphorImager (Molecular Dynamics).

In vivo reporter assay. For all *in vivo* assays, *E. coli* *ΔbtuR* (Keio collection³³ JW1262) cells were grown in a rich, chemically defined medium that was supplemented with (100 μg ml^{−1}) ampicillin and a varying amount of a cobalamin. For titration experiments, 5 μl of overnight culture was added to 5 ml of media and incubated for 6 h at 37 °C. Fluorescence and *A*_{600 nm} measurements were performed on 300 μl of cells from each replicate in clear-bottom 96-well plates. GFPuv fluorescence was read at an excitation wavelength of 395 nm and a 510 nm emission wavelength using an XfluoR SafireII fluorimeter (Tecan). All data shown represent average fluorescence values of three biological replicates that were normalized to the *A*_{600 nm} in each well. All fluorescence measurements were background corrected by taking identical fluorescence and *A*_{600 nm} measurements for *E. coli* *ΔbtuR* cells transformed with pBR322 vector that did not contain the reporter gene. Background fluorescence was subtracted from total fluorescence and the fold-repression was calculated by dividing the average normalized/background corrected fluorescence values for the unrepressed construct (−Cbl) by the average normalized/background corrected fluorescence value for each repressed construct (+Cbl). Titration data was fit to a two state equation to determine half-maximum effective concentration (EC₅₀) values, and error bars represent the standard deviation for each triplicate fluorescence measurement.

Structure solution of the *env8*AqCbl(ΔJ1/13,P13)–AqCbl complex. A representative sequence from the original sequence alignment (GenBank accession AAC021350931.1/557–442) was selected. The P13 stem was removed and the anti-RBS sequence in P5 was replaced with a stable GAAA tetraloop. The RNA was synthesized and refolded as described above. Diffraction quality crystals grew within 3 days at 30 °C in the presence of 100 mM magnesium acetate, 10% 2-methyl-1,3 propanediol and 5 mM iridium hexammine. Crystals were cryoprotected in Ficoll oil and flash frozen in liquid nitrogen. Complete data sets at the iridium and cobalt anomalous edges were collected and processed via autoPROC³⁴. The structure was solved using PHENIX³⁵. The density modified map showed excellent density for the entire RNA (Supplementary Fig. 10a, b). The model was built manually in COOT³⁶ and refined with BUSTER³⁷.

Structure solution of the *env8*AqCbl–AqCbl complex. The original *env8*AqCbl riboswitch (GenBank accession AAC021350931.1/557–442) was modified with the following mutations: G12A, A14G, A31U, G42C and C62G, and the replacement of the linker region with that of a sequence from the original alignment (GenBank accession AAC023653040/384–265). Each RNA synthesized was refolded as described earlier. Crystals grew within 3 months at 20 °C under 10% (v/v) 2-methyl-1,3 propanediol, 40 mM sodium cacodylate, pH 7.0, 12 mM spermine tetrahydrochloride, 80 mM KCl and 20 mM BaCl₂, by hanging drop vapour diffusion. A complete data set was collected on a crystal flash frozen in liquid nitrogen at the cobalt anomalous edge and reduced with autoPROC³⁴. The structure was solved via molecular replacement using *env8*AqCbl(ΔJ1/13,P13)–AqCbl. The solution was confirmed by anomalous difference fourier maps showing the location of aquocobalamin. BUSTER³⁷ refinement produced clear density for P5 and P13 (Supplementary Fig. 10c, d). Model building was assisted with RCRANE³⁸ within COOT³⁶. The final model was prepared using restrained refinement within BUSTER³⁷. Data collection, phasing and refinement statistics for the *env8*AqCbl–AqCbl and *env8*AqCbl(ΔJ1/13,P13)–AqCbl can be found in Supplementary Table 2.

Structure solution of the *Tte*AdoCbl–AdoCbl complex. The sequence of the original *Tte*AdoCbl riboswitch (GenBank accession AE008691.1/395133–395373) was modified to substitute the human U1A-binding protein RNA motif⁹ and a stable GAAA closing tetraloop for the non-conserved P2 and P10 helices, respectively. The RNA was synthesized and refolded as described earlier, to which 2 μl of a 4 mM solution of AdoCbl was added. Crystals grew over the course of 3 days at 30 °C by the hanging drop method in 10% isopropanol, 300 mM MgCl₂ and 100 mM sodium-HEPES, pH 7.5, in the absence of U1A and cryoprotected in 30% glycerol. Heavy atom derivatives were prepared by including 2–10 mM compound in the mother liquor during crystallization.

All data sets were collected at the cobalt anomalous edge for native data sets and the anomalous edges for TaBr and Ir derivatives. Molecular replacement in PHASER⁴⁰ using *env8*AqCbl RNA yielded a solution sufficient to locate heavy atoms in all data sets using anomalous difference data. Cross-crystal dispersive differences for cobalt were used to pair native data sets with heavy atom derivatives to create three sets of experimental phases (Supplementary Table 3). The phases were combined via DMULTI resulting in traceable density maps. Iterative cycles of model building, refinement in BUSTER and PHENIX, multiple crystal averaging and heavy atom phasing, allowed most of the RNA to be built; the U1A loop at the apex of P2, the junction between P8 and P10, and J1/13 remain unresolved in the electron density. Supporting electron density maps are shown in Supplementary Fig. 12. Data collection, phasing and refinement statistics can be found in Supplementary Table 3.

- Edwards, A. L., Garst, A. D. & Batey, R. T. Determining structures of RNA aptamers and riboswitches by X-ray crystallography. *Methods Mol. Biol.* **535**, 135–163 (2009).
- Milligan, J. F. & Uhlenbeck, O. C. Synthesis of small RNAs using T7 RNA polymerase. *Methods Enzymol.* **180**, 51–62 (1989).
- Gilbert, S. D. & Batey, R. T. Monitoring RNA–ligand interactions using isothermal titration calorimetry. *Methods Mol. Biol.* **540**, 97–114 (2009).
- Baba, T. *et al.* Construction of *Escherichia coli* K-12 in-frame, single-gene knockout mutants: the Keio collection. *Mol. Syst. Biol.* **2**, 2006.0008 (2006).
- Vonrhein, C. *et al.* Data processing and analysis with the autoPROC toolbox. *Acta Crystallogr. D* **67**, 293–302 (2011).
- Adams, P. D. *et al.* PHENIX: building new software for automated crystallographic structure determination. *Acta Crystallogr. D* **58**, 1948–1954 (2002).
- Emsley, P., Lohkamp, B., Scott, W. G. & Cowtan, K. Features and development of Coot. *Acta Crystallogr. D* **66**, 486–501 (2010).
- Blanc, E. *et al.* Refinement of severely incomplete structures with maximum likelihood in BUSTER-TNT. *Acta Crystallogr. D* **60**, 2210–2221 (2004).
- Keating, K. S. & Pyle, A. M. Semiautomated model building for RNA crystallography using a directed rotameric approach. *Proc. Natl Acad. Sci. USA* **107**, 8177–8182 (2010).
- Ferré-D'Amaré, A. R. Use of the spliceosomal protein U1A to facilitate crystallization and structure determination of complex RNAs. *Methods* **52**, 159–167 (2010).
- McCoy, A. J. *et al.* Phaser crystallographic software. *J. Appl. Crystallogr.* **40**, 658–674 (2007).

An alternative route to cyclic terpenes by reductive cyclization in iridoid biosynthesis

Fernando Geu-Flores¹, Nathaniel H. Sherden¹, Vincent Courdavault², Vincent Burlat^{3,4}, Weslee S. Glenn^{1,5}, Cen Wu⁶, Ezekiel Nims^{5,†}, Yuehua Cui⁶ & Sarah E. O'Connor^{1,7}

The iridoids comprise a large family of distinctive bicyclic monoterpenes that possess a wide range of pharmacological activities, including anticancer, anti-inflammatory, antifungal and antibacterial activities^{1–4}. Additionally, certain iridoids are used as sex pheromones in agriculturally important species of aphids, a fact that has underpinned innovative and integrated pest management strategies⁵. To harness the biotechnological potential of this natural product class, the enzymes involved in the biosynthetic pathway must be elucidated. Here we report the discovery of iridoid synthase, a plant-derived enzyme that generates the iridoid ring scaffold, as evidenced by biochemical assays, gene silencing, co-expression analysis and localization studies. In contrast to all known monoterpene cyclases, which use geranyl diphosphate as substrate and invoke a cationic intermediate, iridoid synthase uses the linear monoterpene 10-oxogeranial as substrate and probably couples an initial NAD(P)H-dependent reduction step with a subsequent cyclization

step via a Diels–Alder cycloaddition or a Michael addition. Our results illustrate how a short-chain reductase was recruited as cyclase for the production of iridoids in medicinal plants. Furthermore, we highlight the prospects of using unrelated reductases to generate artificial cyclic scaffolds. Beyond the recognition of an alternative biochemical mechanism for the biosynthesis of cyclic terpenes, we anticipate that our work will enable the large-scale heterologous production of iridoids in plants and microorganisms for agricultural^{5–8} and pharmaceutical^{1–4,9} applications.

The crucial step in the biosynthesis of all cyclic terpenes is the cyclization step that gives rise to the individual ring systems. In all kingdoms of life, this step has been shown to be catalysed by terpene cyclases, which are terpene synthases that use polyprenyl diphosphates such as geranyl diphosphate to produce a cationic species that is subsequently cyclized and rearranged to form one of hundreds of possible ring structures^{10,11}. However, the cyclization step that leads to the

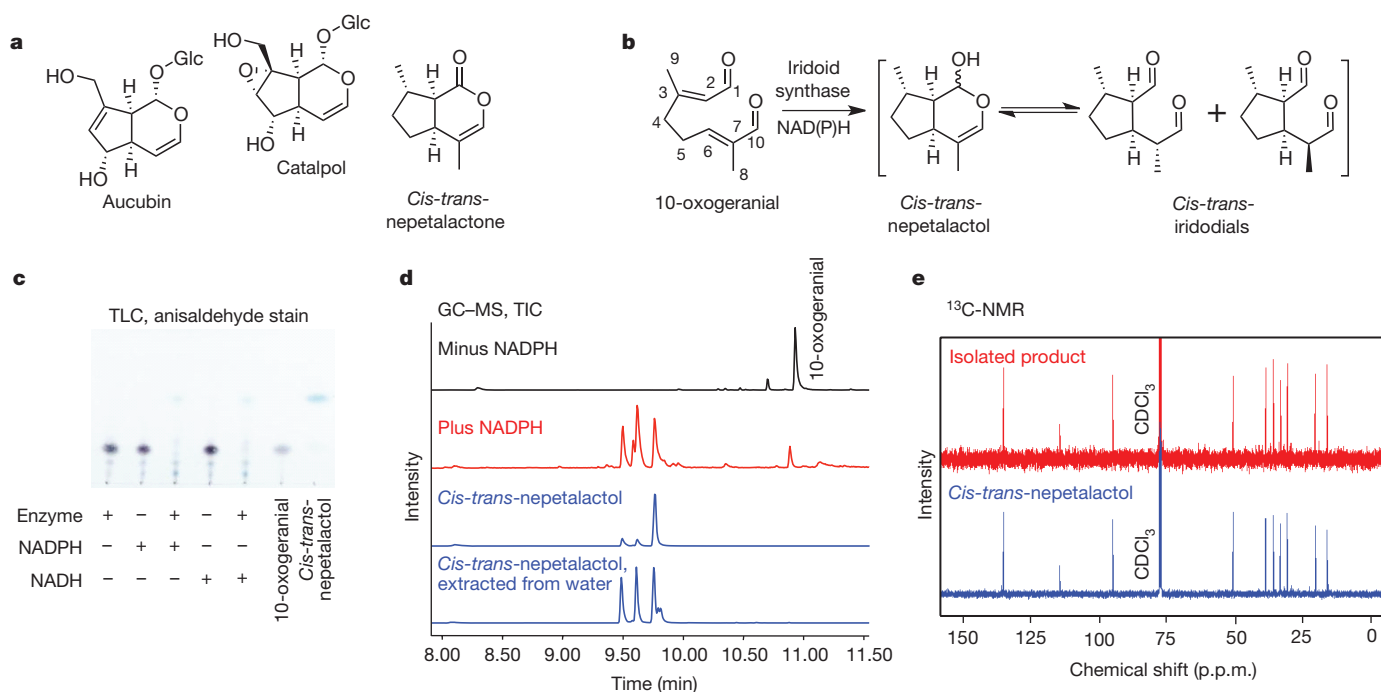


Figure 1 | Identification of the iridoid synthase from *C. roseus*. **a**, Chemical structure of three plant iridoids. Glc, β -glucopyranosyl. **b**, The iridoid synthase reaction in *C. roseus* (products may possess alternative stereochemistries in other organisms). **c**, Analysis of the reaction by TLC. CH_2Cl_2 extracts of different reaction mixtures were run in parallel with authentic samples of the substrate and expected product. **d**, Analysis of the reaction product by GC–MS. Total ion

chromatograms (TICs) of CH_2Cl_2 extracts of the iridoid synthase reaction ('plus NADPH') and of negative control ('minus NADPH') are compared to the TICs of freshly synthesized *cis-trans*-nepetalactol or *cis-trans*-nepetalactol that had been dissolved in water and subsequently extracted with CH_2Cl_2 . **e**, Comparison of the ¹³C-NMR spectra of the purified major product from a milligram-scale enzymatic reaction and the synthetic *cis-trans*-nepetalactol.

¹Department of Biological Chemistry, John Innes Centre, Norwich NR4 7UH, UK. ²Université François-Rabelais de Tours, EA2106, Biomolécules et Biotechnologies Végétales, 37200 Tours, France.

³Université de Toulouse, UPS, UMR 5546, Laboratoire de Recherche en Sciences Végétales, BP 42617 Auzeville, F-31326 Castanet-Tolosan, France. ⁴CNRS, UMR 5546, BP 42617, F-31326 Castanet-Tolosan, France. ⁵Department of Chemistry, Massachusetts Institute of Technology, Cambridge, Massachusetts 02139, USA. ⁶Department of Statistics and Probability, Michigan State University, East Lansing, Michigan 48824, USA. ⁷School of Chemistry, University of East Anglia, Norwich NR4 7TJ, UK. [†]Present address: Ra Pharmaceuticals, Inc., Cambridge, Massachusetts 02139, USA.

characteristic 5–6 bicyclic scaffold of iridoids (Fig. 1a) is markedly different. Feeding studies have suggested that the direct precursor of all iridoids in plants is not geranyl diphosphate, but the linear monoterpene 10-oxogeranial^{12–15}. These studies also suggest that the bicyclic compound nepetalactol is the general precursor of the more derivatized iridoids. Assays using crude plant extracts have indicated that 10-oxogeranial can be converted to nepetalactol in a NADH/NADPH-dependent manner (Fig. 1b)¹⁶. Nevertheless, the molecular identity of the enzyme catalysing this reaction, which we here call iridoid synthase, has hitherto remained unknown.

To identify iridoid synthase, we used recently available transcriptomic data from *Catharanthus roseus* (Apocynaceae)¹⁷, a medicinal plant that produces a variety of iridoid-derived monoterpene indole alkaloids (MIAs), including the anticancer alkaloid vinblastine. Because hundreds of NAD(P)H-dependent enzymes are encoded in the *C. roseus* transcriptome, we first applied a co-regulation criterion to reduce the number of candidates, reasoning that the iridoid synthase would probably have an expression profile similar to geraniol 10-hydroxylase (G10H), the closest characterized enzyme upstream of the cyclization step. In addition to a number of transcripts likely to be involved in the biosynthesis of MIAs, we observed two transcripts coding for NADPH-using enzymes among the 20 best co-regulated transcripts (Supplementary Table 1). The higher-ranking of these two

NADPH-using enzymes showed high similarity to progesterone-5 β -reductase (P5 β R) (67% amino acid identity compared to *Digitalis purpurea* P5 β R2) (Supplementary Fig. 1a–c), an enzyme that reduces the C–C double bond of the α,β -unsaturated carbonyl of progesterone in cardenolide biosynthesis¹⁸. Interestingly, many plant species, including *C. roseus*, possess P5 β R homologues but do not produce cardenolides, indicating that numerous genes annotated as P5 β R have some other physiological function¹⁹.

We expressed the iridoid synthase candidate in *Escherichia coli*, and although the heterologous enzyme did not metabolize progesterone, analysis by thin-layer chromatography (TLC) showed that it metabolized 10-oxogeranial in the presence of either NADH or NADPH (Fig. 1c). The identity of the product was confirmed by gas chromatography–mass spectrometry (GC–MS) analysis, which also evidenced the expected equilibrium between nepetalactol and its open dialdehyde forms (iridodials) in water (Fig. 1d). A milligram-scale enzyme reaction allowed the NMR-based assignment of the purified product as *cis-trans*-nepetalactol (Fig. 1e, see nomenclature in ref. 20), which is the expected isomer. The steady-state kinetic constants of the reaction

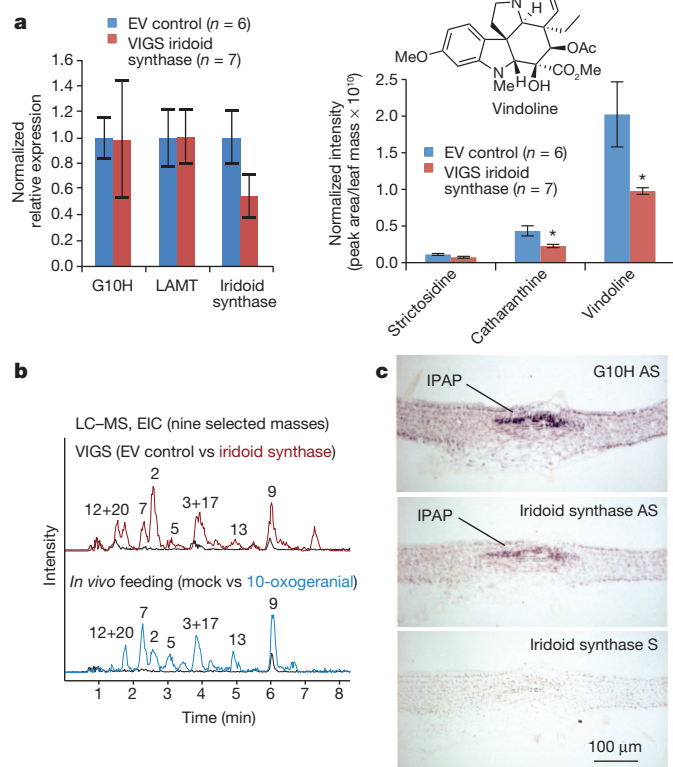


Figure 2 | In vivo studies of iridoid synthase. **a**, Transcript downregulation by VIGS. Left, relative transcript quantification by real-time PCR, including data for two known iridoid-related enzymes, G10H and loganic acid methyltransferase (LAMT). Right, quantification of the three major monoterpene indole alkaloids (MIAs) by LC–MS. EV, empty vector control. Asterisks denote statistical significance ($P < 0.05$ on unpaired Student's *t*-tests). Error bars represent standard errors. **b**, LC–MS analysis of compounds accumulating in both VIGS experiments (upper traces) and 10-oxogeranial feeding experiments (lower traces), including their respective controls (black traces). Traces are extracted ion chromatograms (EICs). Peak numbers refer to Supplementary Table 2. **c**, Cellular localization by RNA *in situ* hybridization on serial longitudinal sections of developing *C. roseus* leaves. Sense ('Iridoid synthase S'), antisense ('Iridoid synthase AS') and G10H probes ('G10H AS') are shown. IPAP, internal phloem-associated parenchyma cells.

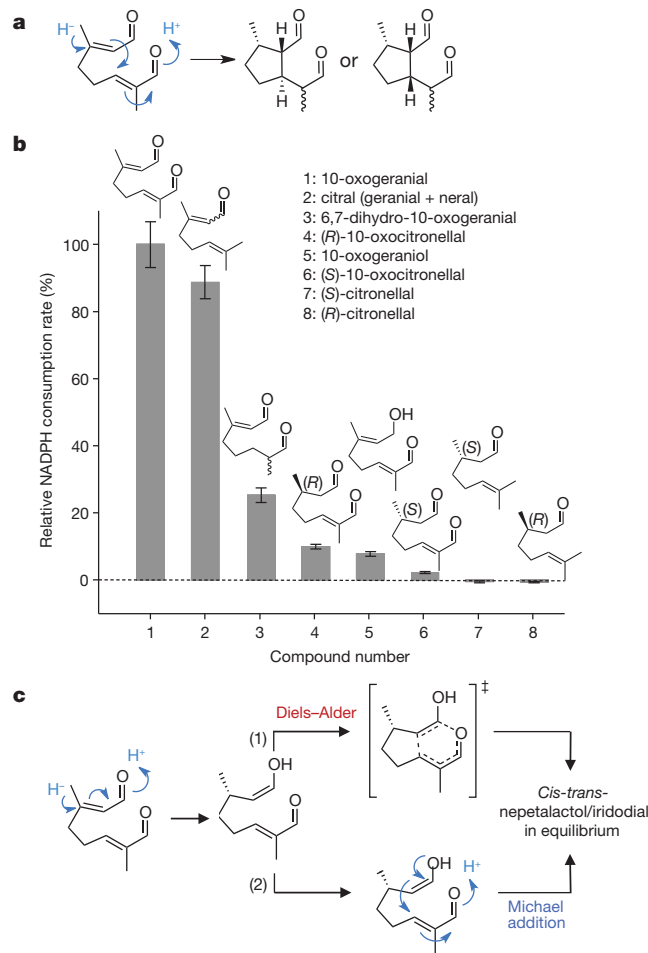


Figure 3 | Substrate specificity and mechanistic considerations.

a, Hypothetical fully concerted mechanism, which yields products with different stereochemistry than that of the *cis-trans* product observed experimentally (compare to Fig. 1a). Only one set of possible enantiomers is depicted. **b**, Substrate specificity. Relative activities for the different test substrates are expressed as percentages of the NADPH consumption rate for 10-oxogeranial. Product elucidation by GC–MS is presented in Supplementary Fig. 6 for substrates 2, 3, 4 and 6. Error bars represent standard errors. **c**, Two proposed mechanisms for the reductive cyclization of 10-oxogeranial. After 1,4-addition reduction, the enol intermediate can either undergo an inverse electron demand hetero-Diels–Alder (route (1)) or an intramolecular Michael addition (route (2)). The proposed reduction intermediate could also be an enolate.

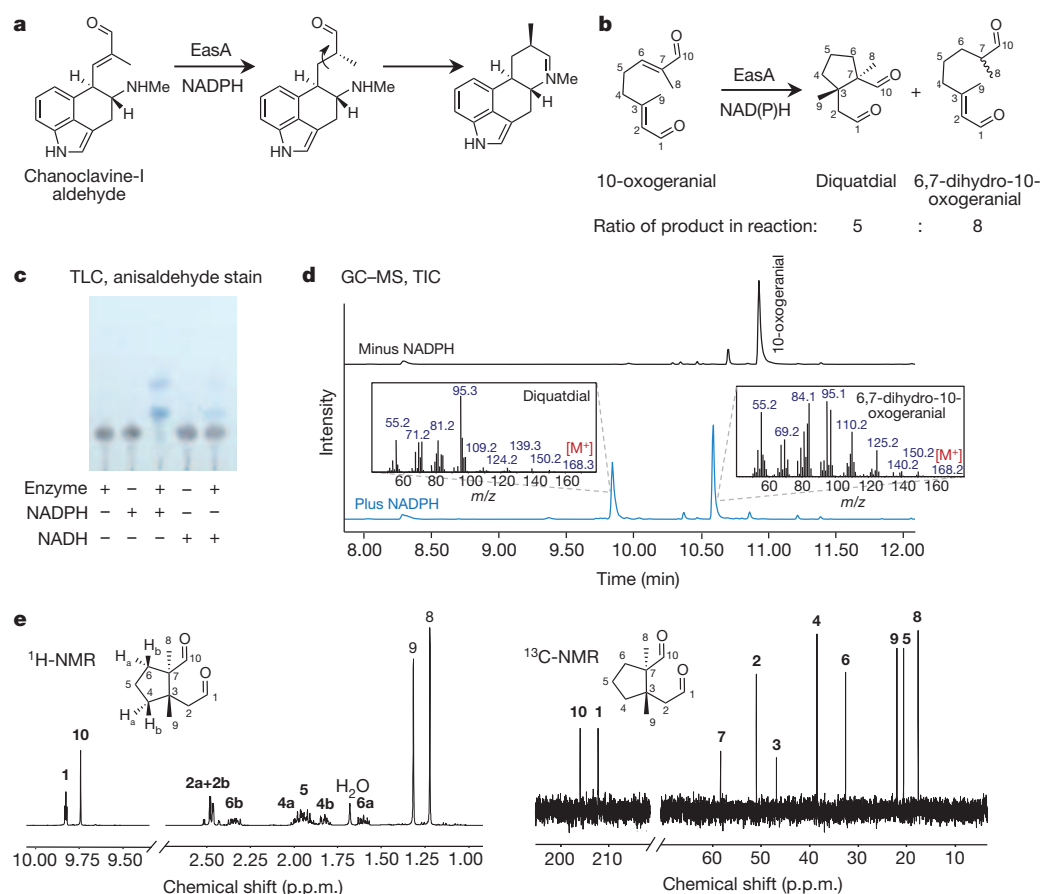


Figure 4 | An alternative cyclization catalysed by the fungal reductase EasA to generate the new artificial cyclopentanoid, named ‘diquatdial’ here. **a**, The physiological reaction carried out by EasA in *Aspergillus fumigatus*. **b**, The reaction catalysed by EasA when using 10-oxogeranial as substrate. **c**, Analysis of reaction mixtures by TLC (CH_2Cl_2 extracts). **d**, Analysis of the reaction by GC-MS. Total ion chromatograms (TICs) of CH_2Cl_2 extracts from the iridoid synthase reaction (‘plus NADPH’) are compared to a negative control (‘minus NADPH’). **e**, Assigned ^1H - and ^{13}C -NMR spectra of the purified cyclized product from a milligram-scale enzymatic reaction (absolute stereochemistry still uncharacterized).

were determined through spectrophotometric NADPH consumption assays (for 10-oxogeranial, $K_M = 4.5 \pm 0.2 \mu\text{M}$, $k_{\text{cat}} = 1.6 \pm 0.1 \text{ s}^{-1}$; for NADPH, $K_M = 4.7 \pm 0.7 \mu\text{M}$, $k_{\text{cat}} = 2.2 \pm 0.2 \text{ s}^{-1}$, all data mean \pm s.e.) (Supplementary Fig. 2).

To verify that iridoid synthase catalysed a similar reaction *in vivo*, we used virus-induced gene silencing (VIGS) to downregulate the iridoid synthase in young *C. roseus* leaves (Fig. 2a) and observed a decreased accumulation of the two major downstream MIA metabolites, vindoline and catharanthine (Fig. 2a). This decrease was not accompanied by a build-up of 10-oxogeranial, a reactive dialdehyde, but was accompanied instead by the accumulation of 22 unidentified compounds, as shown by untargeted liquid chromatography–mass spectrometry (LC–MS) analysis (Supplementary Table 2). Feeding millimolar amounts of 10-oxogeranial to young *C. roseus* leaves caused the accumulation of 10 out of the 22 compounds observed in the VIGS experiment, thus linking those 10 compounds to the presence of 10-oxogeranial in leaves (Fig. 2b and Supplementary Table 2).

Further *in vivo* evidence was obtained by studies on cellular and sub-cellular localization. The long MIA pathway in *C. roseus* is known for the disparate cellular localization of its constituent pathway branches²¹. Using RNA *in situ* hybridization in developing *C. roseus* leaves, we localized the iridoid synthase transcripts to internal phloem-associated parenchyma (IPAP) cells, which are the same cells to which G10H localizes²² (Fig. 2c). Four putative enzymes of the non-mevalonate pathway also localize in these cells^{22,23}, suggesting that in *C. roseus*, all of nepetalactol biosynthesis occurs in one cell type. To probe sub-cellular localization, we carried out analyses using fluorescent protein fusions as well as bimolecular fluorescence complementation assays, and these evidenced the formation of dimers or higher-order structures of exclusive cytosolic localization (Supplementary Figs 3 and 4). This is also consistent with the localization of G10H, which is an endoplasmic reticulum-anchored protein with a cytosolic active site²⁴.

We next examined the chemistry of this unusual reductive cyclization. A concerted mechanism would invoke hydride donation at carbon 3 of 10-oxogeranial, the concomitant generation of a C–C bond between carbons 2 and 6, and further π -electron translocation towards the terminal oxygen at carbon 10, where a proton could be donated to give iridodial/nepetalactol (Fig. 3a, leftmost structure). This mechanism is unlikely because, for steric reasons, the hydride delivery event and the creation of the new C–C bond must occur from opposite sides of the π nodal plane of carbons 2 and 3, thereby yielding iridodial/nepetalactol with incorrect stereochemistry (Fig. 3a and Supplementary Fig. 5). Instead, we propose a two-step mechanism in which iridoid synthase first catalyses a ‘stand-alone’ 1,4-reduction similar to the one catalysed by P5 β R, and then a cyclization step follows.

To test directly the ability of the iridoid synthase to perform stand-alone 1,4-reductions, we performed assays with a suite of 10-oxogeranial-related substrates that included two compounds—citral (mixture of geranial and neral) and 6,7-dihydro-10-oxogeranial—with intact α,β -unsaturated carbonyls at the desired position, but that were unlikely to cyclize upon reduction. Both citral and 6,7-dihydro-10-oxogeranial were converted efficiently to their respective 1,4-reduction products (Fig. 3b and Supplementary Fig. 6), thus supporting the feasibility of a multi-stage mechanism beginning with a 1,4-reduction.

The structures of three minor side-products isolated from the large-scale enzymatic reaction with 10-oxogeranial were also consistent with the ability of iridoid synthase to catalyse a stand-alone reduction reaction. Combined NMR and GC–MS analyses against authentic standards led to identification of these three compounds as (*S*)-10-oxocitronellal, 10-oxogeraniol and 10-oxolinalool (Supplementary Fig. 7). The (*S*)-10-oxocitronellal side-product probably resulted from a reaction similar to the reduction of progesterone by P5 β R, a 1,4-addition mechanism²⁵ (Supplementary Fig. 8). P5 β R itself belongs to a super-family of NAD(P)H-dependent reductases specialized in

1,2-addition reductions²⁵, and the 10-oxogeraniol product could have arisen via this mechanism. In turn, 10-oxolinalool may have been produced from 10-oxogeraniol by rearrangement after the 1,2-reduction. It seems that the three non-cyclic side-products are derived from vestigial 'reduction only' activities encompassing both 1,2- and 1,4-addition mechanisms.

Therefore, we propose that iridoid synthase first catalyses a reaction that parallels the 1,4-reduction of progesterone by P5 β R (Supplementary Fig. 8). The analogous 1,4-reduction of 10-oxogeraniol would yield an enol species that is poised for an inverse electron demand oxo-Diels–Alder reaction (Fig. 3c, route (1)), a rare occurrence in enzymology²⁶. One of the iridoid synthase by-products, (S)-10-oxocitronellal, could be formed when the enol tautomerizes to the aldehyde, preventing a Diels–Alder reaction. The inability of the iridoid synthase to cyclize (S)-10-oxocitronellal (Supplementary Fig. 6) is not at odds with the Diels–Alder proposal, because the cycloaddition would only be possible with the enol form, which is greatly disfavoured under the assay conditions and might only exist in the enzyme's active centre following 1,4-reduction. Alternatively, however, an intramolecular Michael addition of the enol reduction product could also lead to the expected product (Fig. 3c, route (2)). More detailed mechanistic, structural and modelling studies to definitively establish whether the concerted Diels–Alder reaction occurs are ongoing. Whatever the mechanistic details, this reaction is attributable to both the enzyme and the chemical structure of 10-oxogeraniol, which is primed for cyclization. Notably, after incubating 10-oxogeraniol with a fungal reductase²⁷ unrelated to iridoid synthase, a previously unreported cyclized compound was formed (Fig. 4). This implies that a wealth of structurally diverse products can be obtained by fine-tuning different reductases to act on 10-oxogeraniol.

The identification of the iridoid synthase highlights the power of unbiased bioinformatic strategies to rapidly mine the extraordinary chemistry harboured within medicinal plants. We anticipate that our molecular identification of this key enzyme will underpin ongoing efforts aimed at modifying and reconstituting iridoid and MIA pathways in crop plants or microbes for agricultural and pharmaceutical purposes.

METHODS SUMMARY

The iridoid synthase was identified from a transcriptome assembly of *C. roseus* complementary DNA through mutual-rank co-expression analysis using G10H as bait. The His-tagged protein was expressed in *E. coli* and purified by affinity chromatography. The substrate, 10-oxogeraniol, was synthesized from geraniol by protective acetylation, oxidation with SeO₂/tert-butyl hydroperoxide (TBHP), basic hydrolysis of the acetate ester, and Swern oxidation. The predicted product, *cis-trans*-nepetalactol, was synthesized from catnip oil as described²⁰. Reaction mixtures were qualitatively analysed by TLC (anisaldehyde stain) and GC–MS. The main reaction product and three minor by-products were purified from a large-scale enzymatic reaction (including an NADPH regeneration system) using flash chromatography and the purified compounds were analysed by NMR. The (S)-10-oxocitronellal by-product was further analysed by chiral GC–MS. Kinetic studies were performed by measuring NADPH consumption spectrophotometrically. To conduct substrate specificity assays, different 10-oxogeraniol-related compounds were synthesized using published techniques based on SeO₂/TBHP oxidations²². For the synthesis of 6,7-dihydro-10-oxogeraniol and 2,3,6,7-tetrahydro-10-oxogeraniol, large-scale enzymatic reactions with the fungal reductase EasA were used (instead of chemical synthesis). Relative activities towards different substrates were measured spectrophotometrically and products were identified by GC–MS analysis. The large-scale reaction producing 6,7-dihydro-10-oxogeraniol from 10-oxogeraniol also produced a new cyclopentanoid (diquatdial), which was purified and analysed by NMR. The iridoid synthase transcript was downregulated in young *C. roseus* leaves using TRV-based VIGS as described²⁸. Relative transcript quantification was carried out using real-time PCR, and untargeted metabolite analysis was performed by LC–MS. The results of the VIGS experiments were compared to the results of feeding millimolar amounts of 10-oxogeraniol to detached *C. roseus* leaves. The cellular localization of the iridoid synthase transcript was investigated in *C. roseus* leaves using RNA *in situ* hybridization with digoxigenin-labelled probes. The respective sub-cellular localization was probed in transformed *C. roseus* cells using fluorescent protein fusions.

Full Methods and any associated references are available in the online version of the paper.

Received 19 August; accepted 19 October 2012.

Published online 21 November; corrected online 5 December 2012 (see full-text HTML version for details).

- Dinda, B., Chowdhury, D. R. & Mohanta, B. C. Naturally occurring iridoids, secoiridoids and their bioactivity. An updated review, part 3. *Chem. Pharm. Bull. (Tokyo)* **57**, 765–796 (2009).
- Dinda, B., Debnath, S. & Banik, R. Naturally occurring iridoids and secoiridoids. An updated review, part 4. *Chem. Pharm. Bull. (Tokyo)* **59**, 803–833 (2011).
- Dinda, B., Debnath, S. & Harigaya, Y. Naturally occurring secoiridoids and bioactivity of naturally occurring iridoids and secoiridoids. A review, part 2. *Chem. Pharm. Bull. (Tokyo)* **55**, 689–728 (2007).
- Tundis, R., Loizzo, M. R., Menichini, F. & Statti, G. A. Biological and pharmacological activities of iridoids: recent developments. *Mini Rev. Med. Chem.* **8**, 399–420 (2008).
- Dewhirst, S. Y., Pickett, J. A. & Hardie, J. in *Vitamins and Hormones* Vol. 83 (ed. Litwack Gerald) 551–574 (Academic Press, 2010).
- Dobler, S., Petschenka, G. & Pankoke, H. Coping with toxic plant compounds—the insect's perspective on iridoid glycosides and cardenolides. *Phytochemistry* **72**, 1593–1604 (2011).
- McElvain, S. M., Walters, P. M. & Bright, R. D. The constituents of the volatile oil of catnip. II. The neutral components. Nepetalic anhydride. *J. Am. Chem. Soc.* **64**, 1828–1831 (1942).
- Søe, A. R. B., Bartram, S., Gatto, N. & Boland, W. Are iridoids in leaf beetle larvae synthesized de novo or derived from plant precursors? A methodological approach. *Isotopes Environ. Health Stud.* **40**, 175–180 (2004).
- van der Heijden, R., Jacobs, D. I., Snoeijs, W., Hallard, D. & Verpoorte, R. The *Catharanthus* alkaloids: pharmacognosy and biotechnology. *Curr. Med. Chem.* **11**, 607–628 (2004).
- Chen, F., Tholl, D., Bohlmann, J. & Pichersky, E. The family of terpene synthases in plants: a mid-size family of genes for specialized metabolism that is highly diversified throughout the kingdom. *Plant J.* **66**, 212–229 (2011).
- Degenhardt, J., Köllner, T. G. & Gershenzon, J. Monoterpene and sesquiterpene synthases and the origin of terpene skeletal diversity in plants. *Phytochemistry* **70**, 1621–1637 (2009).
- Inouye, H. Neuere Ergebnisse über die Biosynthese der Glucoside der Iridoidreihe. *Planta Med.* **33**, 193–216 (1978).
- Uesato, S., Matsuda, S., Iida, A., Inouye, H. & Zenk, M. H. Intermediacy of 10-hydroxygeraniol, 10-hydroxynerol and iridodial in the biosynthesis of ajmaline and vomilenine in *Rauwolfia serpentina* suspension cultures. *Chem. Pharm. Bull. (Tokyo)* **32**, 3764–3767 (1984).
- Uesato, S., Matsuda, S. & Inouye, H. Mechanism for iridane skeleton formation from acyclic monoterpenes in the biosynthesis of secologanin and vindoline in *Catharanthus roseus* and *Lonicera morrowii*. *Chem. Pharm. Bull. (Tokyo)* **32**, 1671–1674 (1984).
- Uesato, S., Ueda, S., Kobayashi, K. & Inouye, H. Mechanism of iridane skeleton formation in the biosynthesis of iridoid glucosides in *Gardenia jasminoides* cell cultures. *Chem. Pharm. Bull. (Tokyo)* **31**, 4185–4188 (1983).
- Uesato, S., Ikeda, H., Fujita, T., Inouye, H. & Zenk, M. H. Elucidation of iridodial formation mechanism - partial purification and characterization of the novel monoterpene cyclase from *Rauwolfia serpentina* cell suspension cultures. *Tetrahed. Lett.* **28**, 4431–4434 (1987).
- Giddings, L. A. et al. A stereoselective hydroxylation step of alkaloid biosynthesis by a unique cytochrome P450 in *Catharanthus roseus*. *J. Biol. Chem.* **286**, 16751–16757 (2011).
- Gavidia, I., Tarrio, R., Rodriguez-Trelles, F., Perez-Bermudez, P. & Seitz, H. U. Plant progesterone 5 β -reductase is not homologous to the animal enzyme. Molecular evolutionary characterization of P5 β R from *Digitalis purpurea*. *Phytochemistry* **68**, 853–864 (2007).
- Bauer, P. et al. Highly conserved progesterone 5 β -reductase genes (P5 β R) from 5 β -cardenolide-free and 5 β -cardenolide-producing angiosperms. *Phytochemistry* **71**, 1495–1505 (2010).
- Liblikas, I. et al. Simplified isolation procedure and interconversion of the diastereomers of nepetalactone and nepetalactol. *J. Nat. Prod.* **68**, 886–890 (2005).
- Ziegler, J. & Facchini, P. J. Alkaloid biosynthesis: metabolism and trafficking. *Annu. Rev. Plant Biol.* **59**, 735–769 (2008).
- Burlat, V., Oudin, A., Courtois, M., Rideau, M. & St-Pierre, B. Co-expression of three MEP pathway genes and geraniol 10-hydroxylase in internal phloem parenchyma of *Catharanthus roseus* implicates multicellular translocation of intermediates during the biosynthesis of monoterpene indole alkaloids and isoprenoid-derived primary metabolites. *Plant J.* **38**, 131–141 (2004).
- Oudin, A. et al. Spatial distribution and hormonal regulation of gene products from methyl erythritol phosphate and monoterpene-secoiridoid pathways in *Catharanthus roseus*. *Plant Mol. Biol.* **65**, 13–30 (2007).
- Guirimand, G. et al. Optimization of the transient transformation of *Catharanthus roseus* cells by particle bombardment and its application to the subcellular localization of hydroxymethylbutenyl 4-diphosphate synthase and geraniol 10-hydroxylase. *Plant Cell Rep.* **28**, 1215–1234 (2009).
- Thorn, A. et al. The crystal structure of progesterone 5 β -reductase from *Digitalis lanata* defines a novel class of short chain dehydrogenases/reductases. *J. Biol. Chem.* **283**, 17260–17269 (2008).

26. Kim, H. J., Ruszczycky, M. W. & Liu, H.-W. Current developments and challenges in the search for a naturally selected Diels-Alderase. *Curr. Opin. Chem. Biol.* **16**, 124–131 (2012).
27. Cheng, J. Z., Coyle, C. M., Panaccione, D. M. & O'Connor, S. E. A role for old yellow enzyme in ergot alkaloid biosynthesis. *J. Am. Chem. Soc.* **132**, 1776–1777 (2010).
28. Liscombe, D. K. & O'Connor, S. E. A virus-induced gene silencing approach to understanding alkaloid metabolism in *Catharanthus roseus*. *Phytochemistry* **72**, 1969–1977 (2011).

Supplementary Information is available in the online version of the paper.

Acknowledgements The present study was funded by the Danish Council for Independent Research (Natural Sciences) through Postdoctoral Fellowship 10-082858 granted to F.G.-F. Additional funding was received from the NIH (GM074820), the j004561SRC (BB/J004561/1 and BB/J009091/1) and the John Innes Foundation. This work was conducted under Defra Plant Health Licence PHSI 449/6612(07/2011). W.S.G. gratefully acknowledges a National Science Foundation Predoctoral Fellowship. Y.C. would like to thank the NSF for grant DMS-1209112. K. R. Chauhan is acknowledged for providing initial nepetalactol samples. We thank S. Fairhurst, L. Hill and A. Jones for NMR, LC–MS and GC–MS assistance, respectively. J. Ward and N. Hawkins are acknowledged for the GC–MS-based high-resolution mass

spectra (HRMS) of synthesized compounds. R. Buell and E. Góngora-Castillo provided many helpful discussions on the transcriptome data. The purified EasA protein was provided by J. Z. Cheng, to whom we are deeply indebted. S.E.O. receives salary support through a synergy initiative between the John Innes Centre and the University of East Anglia.

Author Contributions F.G.-F. and S.E.O. conceived the project; C.W., Y.C. and F.G.-F. constructed the G10H mutual ranking list; E.N. cloned the iridoid synthase from cDNA; F.G.-F. and W.S.G. expressed the recombinant protein; N.H.S. performed all chemical synthesis; F.G.-F. carried out all enzyme assays, enzyme-based synthesis, VIGS experiments, and feeding experiments; V.C. performed the sub-cellular localization studies; V.B. carried out the cellular localization studies; F.G.-F. and S.E.O. drafted the manuscript; and S.E.O. acted as overall study director.

Author Information The sequence of iridoid synthase has been deposited in GenBank/EMBL/DDJB with accession no. JX974564 and the short sequence reads are available in the NCBI SRA database under accession number SRP005953. Reprints and permissions information is available at www.nature.com/reprints. The authors declare no competing financial interests. Readers are welcome to comment on the online version of the paper. Correspondence and requests for materials should be addressed to Sarah E. O'Connor (sarah.o'connor@jic.ac.uk).

METHODS

Assembly of the *C. roseus* transcriptome and co-expression analysis. A *C. roseus* transcriptome assembly was generated using paired-end sequences (76 base pairs) from a normalized cDNA library constructed by pooling equimolar RNA isolated from mature leaf, immature leaf, flower, upper stem and entire roots of a single *C. roseus* reference plant as described previously²⁹. The assembly is composed of 41,875 total transcripts with an N50 size of 982 bp. Expression abundances for representative transcripts were determined as described²⁹ from single end-reads from RNA-seq libraries constructed from 17 development and elicitor treated tissues. The transcriptome assembly (cra_v1_33kmer_transcripts.fa.txt) and expression matrix (Catharanthus_matrix_v1_33kmer.xls) are available at ftp://ftp.plantbiology.msu.edu/pub/data/MPGR/Catharanthus_roseus/. The reads are available in the NCBI SRA under accession number SRP005953.

To reduce the transcriptomic data set to a workable size, we filtered out all genes exhibiting low expression in leaves (around 5,000 genes with fragments per kilobase of exon per million fragments mapped (FPKM) values of less than 2), and then filtered out genes that were not induced upon treatment with methyl jasmonate, a known elicitor of monoterpenoid indole alkaloids (around 13,000 genes with FPKM ratios of less than 0.9 when comparing uninduced with induced seedlings, 12 days after induction). All known MIA-related enzyme-coding transcripts remained in the data set after these filtering steps. The transcripts were then ordered by the mutual ranking analysis in terms of the similarity of their expression patterns to that of gene G10H. In step 1, we calculated the Pearson correlation coefficient (PCC) of G10H with respect to each of the rest of the contigs. The contigs were then ranked according to their corresponding PCC in descending order, where the contig with the highest correlation with gene G10H was ranked in the top. This is the rank for contig *i* in the rank list of G10H (denoted as 'Fwd rank' in Supplementary Table 1). In step 2, we picked the top 200 best-correlated contigs from the list, and computed the PCC of contig *i* (*i* = 1, 2, ..., 200) with respect to the rest of the contigs in the top 200 list. Following the same ranking procedure, we obtained a ranking list for each contig *i* (*i* = 1, 2, ..., 200), and recorded the rank of gene G10H in each contig's ranking list (denoted as 'Rev rank' in Supplementary Table 1). In step 3, the mutual rank value of contig *i* (*i* = 1, 2, ..., 200) was calculated by $\sqrt{\text{Fwd rank} \times \text{Rev rank}}$. We then ranked the 200 mutual rank values in ascending order to generate the final mutual rank list. The 20 best co-regulated transcripts on the mutual rank list are shown in Supplementary Table 1 of Supplementary Materials.

Cloning of the iridoid synthase from cDNA. The full-length sequence of iridoid synthase was assembled *in silico* using contig 729 from the *C. roseus* transcriptome assembly (see above) and EST 8191 from the Plant Genomic Database (<http://www.plantgdb.org/>). For the molecular cloning, total RNA was isolated from seedlings using an RNeasy Plant Mini Kit (Qiagen), and cDNA synthesis was performed using SuperScript III Reverse Transcriptase (Invitrogen) and oligo-dT primers. The entire coding sequence was amplified using primers ATGAG TTGGTGGTGAAGAGGT and CTAAGGAATAAACCTATAATCCCTCAT CTTATCAAT, and cloned into the Gateway compatible vector pCR8-GW-TOPO-T/A (Invitrogen) to give pCR8-*ISY*. Subcloning into the expression vector pDEST17 using Gateway cloning yielded the *E. coli* expression construct.

Heterologous protein expression and purification. Rosetta 2 cells (Merck Millipore) harbouring the desired plasmid were grown at 37 °C, induced with isopropyl β-D-1-thiogalactopyranoside (1 mM) at a $D_{600\text{ nm}}$ of 1, and then cultured at 15 °C for 12 h. The cells were lysed by sonication and the soluble portion was equilibrated with Ni-NTA agarose resin (Qiagen). The enzyme was then eluted via a stepwise imidazole gradient (25 mM, 50 mM, 100 mM, 150 mM and 300 mM), where the enzyme of interest eluted in the 100 mM, 150 mM and 300 mM imidazole fractions. These fractions were then pooled, concentrated and buffer-exchanged into a storage buffer of 20 mM MOPS.

Enzymatic assays. All enzyme assays were carried out using 20 mM MOPS pH 7.0 as buffer. Monoterpene substrates were kept as 50 mM stocks in tetrahydrofuran (THF) at −20 °C. During the preparation of master mixes, care was taken not to exceed TFH concentrations higher than 0.5% in the presence of enzyme, as concentrations above 1% TFH were found to affect activity adversely. The substrate, 10-oxogeranial, was synthesized from geraniol by protective acetylation, oxidation with SeO_2 /TBHP, basic hydrolysis of the acetate ester and Swern oxidation. The predicted product, *cis-trans*-nepetalactol, was synthesized from catnip oil as described²⁰. To conduct substrate specificity assays, different 10-oxogeraniol-related compounds were synthesized using published techniques based on SeO_2 /TBHP oxidations²². For the synthesis of 6,7-dihydro-10-oxogeranial and 2,3,6,7-tetrahydro-10-oxogeranial, large-scale enzymatic reactions with the fungal reductase EasA were used (instead of chemical synthesis). Detailed information on all synthetic procedures, including spectral characterization of novel chemical entities, can be found under Supplementary Materials. Individual characteristics of the different enzymatic assays performed are presented below.

TLC- and GC-MS-based assays (initial studies and substrate specificity studies). Reactions (100 μl) were set up in glass vials using 200 μM monoterpene, 400 μM NADH/NADPH and 2.2 μg of purified protein, and were terminated after 1 h by adding 400 μl CH_2Cl_2 . The organic phase was used directly for GC-MS analysis. For analysis by TLC, 300 μl of the organic phase was vacuum-concentrated to approximately 10 μl, spotted onto normal-phase TLC plates, run using 3:7 ethyl acetate:hexanes, and visualized with anisaldehyde stain.

Spectrophotometry-based assays (kinetic and substrate specificity studies). For kinetic studies, the absorbance at 340 nm of 200-μl assays with 80 ng of purified protein was measured using a 96-well plate reader. See the legend to Supplementary Fig. 2 for further experimental details. For substrate specificity studies, the absorbance at 340 nm of 200-μl assays with 200 μM monoterpene, 200 μM of NADPH and 0.41 μg of purified protein was measured in the same manner. Data were collected for 3–5 min, with individual measurements being taken for a single sample every 9 s when using full plate. The measured absorbances were plotted manually on Excel and the initial delta absorption/delta time values were calculated for the linear part of each reaction, with 12 data points having been the minimum number of data points considered for an individual slope calculation. NADPH consumption rates were calculated from these delta absorption/delta time values considering background NADPH decay and an extinction-coefficient-like value (dependent on assay volume) calculated separately.

Milligram-scale (large-scale) assays. Both milligram-scale assays (with the iridoid synthase and with EasA) were carried out using an NADPH-generation/regeneration system consisting of glucose-6-phosphate (G6P), glucose-6-phosphate dehydrogenase (G6PDH) and NADP^+ . The reaction with the iridoid synthase was set up in 447 ml of 50 mM MOPS pH 7.0 using 833 μg of purified enzyme, 15.7 mg of 10-oxogeranial, 85 mg of G6P, 211 U of G6PDH and 17.1 mg of NADP^+ . The reaction was monitored continuously by TLC using a short-wave ultraviolet lamp for detection, and went to completion after 1 h. The products were extracted twice with an equal volume of CH_2Cl_2 , 1 h later. The 13.2 mg of raw product mix were separated using silica-gel-based chromatography with ether/pentanes 3:7 in a Pasteur pipette. A final fraction was eluted in ethyl acetate, vacuum-concentrated, and used for a second flash chromatography column, this time with ether/pentanes 6:4. All products were characterized using a combination of GC-MS and NMR in comparison to synthesized standards as shown in Supplementary Fig. 7. The (S)-10-oxocitronellal by-product was further analysed by chiral GC-MS. The reaction with EasA was set up in 447 ml of 50 mM MOPS pH 7.0 using 491 μg of purified holoenzyme kindly provided by J. Cheng, 16.3 mg of 10-oxogeranial, 111 mg of G6P, 125 U of G6PDH and 17.1 mg of NADP^+ . The reaction was monitored continuously by TLC-UV, and the 10-oxogeranial substrate was nearly completely consumed after 6.75 h. The products were extracted twice with an equal volume of CH_2Cl_2 . The 12.9 mg of raw product mix were separated using silica-gel-based chromatography with ether/pentanes 3:7 on a Pasteur pipette. The first eluting product, diquatdial, was assigned by correlation spectroscopy (COSY), nuclear Overhauser effect spectroscopy (NOESY), edited heteronuclear single-quantum correlation spectroscopy (HSQC), and heteronuclear multiple-bond correlation spectroscopy (HMBC) two-dimensional NMR experiments. Given additional reaction time, EasA begins to reduce the 6,7-dihydro-10-oxogeranial to give the di-reduction product, which is difficult to separate from diquatdial by TLC. $^1\text{H-NMR}$ (diquatdial, CDCl_3): δ 1.06 (s, 3H, H_8), 1.16 (s, 3H, H_9), 1.43–1.52 (m, 1H, H_{6a}), 1.68–1.77 (m, 1H, H_{4b}), 1.77–1.95 (m, 3H, H_{4a} and H_5), 2.25–2.35 (m, 1H, H_{6b}), 2.42 (dd, $^3J_{2a,2b} = 15.3\text{ Hz}$, $^3J_{2a,1} = 2.3\text{ Hz}$, 1H, H_{2a}), 2.47 (dd, $^3J_{2b,2a} = 15.3\text{ Hz}$, $^3J_{2b,1} = 2.8\text{ Hz}$, 1H, H_{2b}), 9.71 (s, 1H, H_{10}), 9.80 (dd, $^3J_{1,2a} \approx 3.6\text{ Hz}$, 1H, H_1). $^{13}\text{C-NMR}$ (CDCl_3): δ 17.44 (C_8), 20.49 (C_5), 21.86 (C_3), 32.48 (C_6), 38.38 (C_4), 46.76 (C_3), 50.89 (C_2), 58.31 (C_7), 202.20 (C_1), 205.97 (C_{10}). HRMS (EI^+) m/z calculated for $\text{C}_{10}\text{H}_{16}\text{O}_2$ [$\text{M}]^+$: 168.1150, found 168.1150. The assignment of the product eluting second, 6,7-dihydro-10-oxogeranial, is presented under Supplementary Information (Synthesis of Chemicals), section E. Note: diquatdial underwent stepwise air oxidation in CDCl_3 at room temperature after 7 days. The resulting diacid was characterized spectroscopically using COSY and edited HSQC two-dimensional NMR experiments. $^1\text{H-NMR}$ (CDCl_3): δ 1.11 (s, 3H, H_9), 1.22 (s, 3H, H_8), 1.52–1.63 (m, 1H, $\text{H}_{6a/b}$), 1.62–1.84 (m, 2H, H_5), 1.71–1.94 (m, 2H, H_4), 2.42 (d, $^3J_{2a/b,2a/b} = 14.0\text{ Hz}$, 1H, $\text{H}_{2a/b}$), 2.39–2.54 (m, 1H, $\text{H}_{6a/b}$), 2.76 (d, $^3J_{2a/b,2a/b} = 13.9\text{ Hz}$, 1H, $\text{H}_{2a/b}$). $^{13}\text{C-NMR}$ (CDCl_3): δ 19.49 (C_5), 21.24 (C_8), 22.32 (C_9), 33.91 (C_6), 36.96 (C_4), 41.37 (C_2), 45.66 (C_3), 55.62 (C_7), 178.16 (C_1), 181.57 (C_{10}). HRMS (EI^+) m/z calculated for $\text{C}_{10}\text{H}_{12}\text{O}_2$ [$\text{M} - 2\text{H}_2\text{O}]^+$: 164.0837, found 164.0838.

Plant growth conditions. Plants were grown in a walk-in growth chamber at 25 °C under 12-h days using the John Innes compost mix No. 2 (peat-based).

Virus-induced gene silencing (VIGS). To expedite the assembly of VIGS constructs, we designed and constructed a USER-compatible VIGS vector based on pTRV2. A DNA cassette consisting of oligonucleotides ATTCGCTGAGGCGCGA TCGCAACCTCAGCG and AATTCGCTGAGGTTGCGATCGCGCCTCAGCG

was cloned into pTRV2-MCS (The *Arabidopsis* Biological Resource Center, ABRC) using EcoRI. The resulting vector, pTRV2u, was prepared for USER cloning by digesting with AsiSI and Nt.BbvCI. An approximately 500-nt fragment of the *C. roseus* iridoid synthase gene was USER-cloned³⁰ from pCR8-*ISY* (see earlier section on cloning of the iridoid synthase) into digested pTRV2u using primers GGC GCGAUGGTGGTGAAGAGGTCCATTG and GGTTCGAUCCTCGGTAAAGGCCAATCATGTG. The resulting pTRV2u-*ISY* construct was used to silence the iridoid synthase in *C. roseus* seedlings essentially as described in ref. 28. Briefly, 1-month-old plants were pinched once on their stems with fine forceps that had been dipped in a mixture of *Agrobacterium tumefaciens* strains harbouring the vector of interest and the pTRV1 vector (ABRC). The empty pTRV2u was used as a negative control, and pTRV2-ChlH²⁸ was used as visual marker for the timing of the silencing response. When pTRV2-ChlH infiltrated plants showed fully bleached leaves 1–3-cm long, a pair of leaves of similar size (equivalent leaves) was harvested from plants infiltrated with the constructs of interest. For each plant, one of these equivalent leaves was destined for LC-MS analysis and the other for quantitative real-time PCR. One out of the eight plants infiltrated with the pTRV2-*ISY* construct presented iridoid synthase expression levels above the empty vector control average and was therefore considered non-silenced and taken out of both final qPCR and LC-MS data pools.

In vivo feeding experiment of 10-oxogeraniol to *C. roseus*. Six 2–3-cm long *C. roseus* leaves were fed 100 µl of 5 mM 10-oxogeraniol in 1.5% THF through their cut petioles. Six equivalent leaves were fed 1.5% THF as a mock control. After uptake of the initial 100 µl of liquid, which took between 1 and 6 h, 300 µl of water was added, and the leaves were left overnight under constant light conditions. Twenty-four hours after the start of the experiment, the leaves were collected for analysis by LC-MS.

Subcellular localization studies. The subcellular localization of the iridoid synthase was studied by creating fluorescent fusion proteins using the pSCA-cassette YFPi plasmid²⁴. The full-length ORF of the iridoid synthase was amplified from pCR8-*ISY* (see section *Cloning of the iridoid synthase from cDNA*) using the specific primers CTGAGATCTAGAATGAGTTGGTGGTGAAGAGGTC and CTGAGATCTAGAAGGAATAAACCTATAATCCCTCATCTTACAATA, which were designed to introduce XbaI and SpeI restriction sites. The PCR product was cloned in-frame either at the 5' end of the yellow fluorescent protein (YFP) coding sequence to generate the iridoid synthase-YFP fusion or at the 3' end to generate the YFP-iridoid synthase fusion. The self-interaction ability of the iridoid synthase was characterized by bimolecular fluorescence complementation (BiFC) assays using the pSCA-SPYNE173 and pSCA-SPYCE(M) plasmids³¹, which allow expressing proteins fused to the amino-terminal extremity of the two split-YFP fragments (YFP^N, residues 1–173 and YFP^C, residues 156–239). The previously amplified PCR product was cloned via SpeI in pSCA-SPYNE173 for expression of ISY-YFP^N or in pSCA-SPYCE(M) to produce ISY-YFP^C. Transient transformation of *C. roseus* cells by particle bombardment and fluorescence imaging were performed following the procedures described in refs 24 and 31. Briefly, *C. roseus* plated cells were bombarded with DNA-coated gold particles (1 µm) and 1,100 p.s.i. rupture disc at a stopping-screen-to-target distance of 6 cm, using the Bio-Rad PDS1000/He system. Cells were cultivated for 14 h to 38 h before being collected, treated and observed. The subcellular localization was determined using an Olympus BX-51 epifluorescence microscope equipped with an Olympus DP-71 digital camera and a combination of YFP and cyan fluorescent protein (CFP) filters. The pattern of localization presented in this work is representative of approximately 50 observed cells. The cytosolic localization of the different fusion proteins was confirmed by co-transformation experiments using the cytosolic CFP-β-glucuronidase (GUS) marker³². Such plasmid co-transformations were performed using 400 ng of each plasmid or 100 ng for BiFC assays.

Cellular localization studies. The PCR product described earlier in section Subcellular localization studies) was cloned into the pGEM-T easy vector (Promega) and the resulting vector was used for the synthesis of sense and anti-sense RNA probes as previously described³³. For G10H, a previously described plasmid was used for the riboprobe transcription²². Paraffin-embedded serial longitudinal sections of young leaves were hybridized with digoxigenin-labelled transcripts and localized with anti-digoxigenin-alkaline phosphatase conjugates according to ref. 33.

Quantitative real-time PCR. Leaves collected were frozen in liquid nitrogen, powdered using a pre-chilled mortar and pestle, and subjected to RNA extraction using an RNeasy Plant Mini Kit (Qiagen). RNA (1 µg) was used to synthesize cDNA in 20-µl reactions using the iScript cDNA Synthesis Kit (Bio-Rad). The cDNA served as template for quantitative PCR performed using the CFX96 Real

Time PCR Detection System (Bio-Rad) and the SSO Advanced SYBR Green Supermix (Bio-Rad). As reference genes, we used both the *Elongation Factor 1 (EF1α)* and the *40S Ribosomal Protein S9 (rps9)*, with the respective primer pairs TCAGGAGGCTCTTCTGGTGA/AGCTCCCTTGGCAGGGTCAT and TTGAGCCGTATCAGAAATGC/CCCTCATCAAGCAGACCATA. For G10H, LAMT, and the iridoid synthase genes, the primer pairs used were CATTATTAGCGACCAACC/GAAGTTCTTTCGCCATTGTT, GAGTAATTGATGCAGC CAAG/TTGATTGGATCAAAGATTGG and CCTAGGCTAAATGTCCCAA/GTCTATGGACAGACCATGTT, respectively. All primer pair efficiencies were between 98% and 105%, and the individual efficiency values were considered in the calculation of normalized relative expression, which was performed using the Gene Study feature of CFX Manager Software. All biological samples were measured in technical duplicates.

GC-MS. GC-MS analyses were carried out in an Agilent 6890N GC system coupled to an Agilent 5973 MS detector. All non-chiral separations were performed with a Zebron ZB-5 HT column (30 m × 0.25 mm × 0.10 µm) using helium as carrier gas at a 1 ml min⁻¹ (linear velocity of 37 cm s⁻¹) and with an injector temperature of 220 °C. The program used was the following: 5 min isothermal at 60 °C, 20 °C min⁻¹ gradient up to 150 °C, 45 °C min⁻¹ gradient up to 280 °C, 4 min isothermal at 280 °C (run time = 16.39 min). The chiral analysis of 10-oxocitronellal was achieved with a Supelco β-DEX 225 column (30 m × 0.25 mm, 0.25 µm) using hydrogen as carrier gas at a 2.5 ml min⁻¹ flow (linear velocity of 86 cm s⁻¹) and an injector temperature of 220 °C. The program for this chiral separations was the following: 2 min isothermal at 60 °C, 30 °C min⁻¹ gradient up to 110 °C, 60 min isothermal at 110 °C, 0.5 °C min⁻¹ gradient up to 111 °C, 30 min isothermal at 111 °C, 0.5 °C min⁻¹ gradient up to 112 °C, 15 min isothermal at 112, 0.5 °C min⁻¹ gradient up to 113 °C, 7 min isothermal at 113 °C, 0.5 °C min⁻¹ gradient up to 114 °C, 3.5 min isothermal at 114 °C, 30 °C min⁻¹ gradient up to 180 °C, 4 min isothermal at 180 °C (run time = 133.97 min). The long program reflects the on-column instability of the compound above 115 °C and its high on-column retention below 110 °C. Although marginal, the separation of the 10-oxocitronellal isomers was reproducible under these conditions. The analysis presented in Supplementary Fig. 7i was repeated three times with similar results.

High-resolution mass spectra were obtained using a Waters GCT system consisting of an Agilent 6890 fitted with a cool-on-column injector and coupled to a Waters GCT Classic mass spectrometer. The column used was a Phenomenex Zebron HT-5ms (30 m × 0.25 mm, 0.25 µm) with a 5-m guard column, and helium was used as carrier gas at 1 ml min⁻¹ flow. To avoid thermal degradation of the diacid derived from diquadtal, a program with slower temperature gradient was used: 5 °C min⁻¹ gradient from 35 to 280 °C with initial and final hold times of 5 min. The mass axis was calibrated from *m/z* 49–285 using 2,4,6-tris(trifluoromethyl)-1,3,5-triazine at before the analysis of each sample. Data were acquired using background reference ions as lock masses—either column bleed ion 207.0329 (C₅H₁₅O₃Si₃) or 129.9144 (³⁵Cl isotope of trichloroethylene).

LC-MS. Leaves were weighed and collected into a fixed volume of methanol (200–600 µl) and incubated at 56 °C for 45 min. After a 30-min centrifugation step at 5,000g, an aliquot of the supernatant (50 µl) was mixed with an equal volume of water and analysed on a Thermo-Finnigan instrument equipped with a Deca XP ion trap detector. The column used was a Phenomenex Luna 3µ C18 (2) (100 × 2.00 mm, 3 µm), and the binary solvent system consisted of acetonitrile (ACN) and 0.1% formic acid in water. The elution program was the following: 1 min isocratic at 15% ACN, 5 min gradient up to 25% ACN, 2 min gradient up to 80%, 3 min isocratic at 80%, 1 min gradient down to 15%, and 4 min isocratic at 15%. Peak areas were calculated using the ICIS algorithm in Finnigan's Xcalibur software and normalized by leaf mass (fresh weight).

29. Góngora-Castillo, E. *et al.* Genomic approaches for interrogating the biochemistry of medicinal plant species. *Methods Enzymol.* **517**, 139–159 (2012).
30. Nour-Eldin, H. H., Geu-Flores, F. & Halkier, B. A. USER cloning and USER fusion: the ideal cloning techniques for small and big laboratories. *Methods Mol. Biol.* **643**, 185–200 (2010).
31. Guirimand, G. *et al.* Strictosidine activation in Apocynaceae: towards a “nuclear time bomb”? *BMC Plant Biol.* **10**, 182 (2010).
32. Guirimand, G. *et al.* Spatial organization of the vindoline biosynthetic pathway in *Catharanthus roseus*. *J. Plant Physiol.* **168**, 549–557 (2011).
33. Mahrour, S., Courdavault, V., Thiersault, M., St-Pierre, B. & Burlat, V. Epidermis is a pivotal site of at least four secondary metabolic pathways in *Catharanthus roseus* aerial organs. *Planta* **223**, 1191–1200 (2006).

CAREERS

CITATION Panel urges guidelines for data attribution and citation **p.145**

@NATUREJOBS Follow us on Twitter for the latest news and features go.nature.com/e492gf

NATUREJOBS For the latest career listings and advice www.naturejobs.com

IMAGES.COM/HELIX



DRUG DISCOVERY

A helping hand

The pharmaceutical industry is increasingly turning to academics to tackle the early stages of drug discovery.

BY TRISHA GURA

When neuroscientist Mark Zylka launched his laboratory at the University of North Carolina (UNC) in Chapel Hill six years ago, he was not thinking about synthesizing chemicals. He was focusing on trying to identify the molecules expressed by pain neurons and how they function. But then he discovered a pain-relieving pathway that might be targeted with a chemical: an adenosine receptor stimulator, or agonist. Unfortunately, drug developers had previously tested such agonists and found that they had serious cardiovascular side effects, such as slowed heart rate and blockages in the impulse that regulates heartbeat. Zylka had an idea about how to modify the agonist's structure to avoid these side effects. But to do that, he needed medicinal

chemistry experience, something his neuroscience training had not provided.

So he found a collaborator, Stephen Frye, who in 2007 had been recruited from the nearby research facility of drug firm Glaxo-SmithKline (GSK) in Research Triangle Park, North Carolina, to direct a new Center for Integrative Chemical Biology and Drug Discovery at UNC. Frye found a way to synthesize the modified agonist, which Zylka then used to gather preliminary data that showed that the agonist could mitigate pain without cardiovascular side effects. Together, the pair netted a grant from the US National Institutes of Health (NIH) in Bethesda, Maryland. Now Zylka, with Frye's help, is learning drug-discovery skills on the fly. "It is very different from academic research," he says.

Zylka is one of a new breed of researchers

who are staying in academia but moving into drug discovery, which has long been considered the domain of industry. "Before I die, I would love to directly identify something that would ultimately be used to treat a disease in humans," says Zylka. "But there is a big separation between what basic scientists do and what drug companies want. I felt it was important to try to bridge that gap."

It is a tall order — and a great opportunity. Industry has increasingly pulled out of the earliest stages of drug development, deeming them too risky and expensive. At the same time, "there has been an absolute deluge of new discoveries of the fundamental basis of disease," says Christopher Austin, director of the National Center for Advancing Translational Sciences (NCATS) at the NIH. "We are talking about the past 50 years of NIH-funded mechanistic science."

This accumulation of data that could be used to formulate new therapies has driven large-scale, national efforts to give academia a more industrial focus. For example, the NIH launched the US\$576-million NCATS less than a year ago to speed up the development of new therapeutics in academic settings (see *Nature* **481**, 128; 2012). At the same time, industry has stepped into academic territory, setting up drug-discovery collaborations with scientists working in basic research as well as joint industrial-academic fellowships for postdocs. These opportunities are blurring the lines between academia and industry, and, increasingly, ambitious academics can learn how to translate bench work into real-world applications by stepping into industry, at least temporarily. "This is something that is learned by doing," says Torsten Hoffmann, chair of the Roche Postdoc Fellowship (RPF) Program at the pharmaceutical company Roche in Basel, Switzerland.

NEW APPROACH

In the United States, the process of drug discovery typically occurs in three stages. First, researchers identify a biochemical pathway involved in the disease of interest. Second, cell and molecular biologists develop assays based on that pathway to screen libraries of small molecules for potential drugs. And third, geneticists create cell and animal models to validate drug targeting. Then, as the drug moves into development, teams of experts are assembled to run clinical trials and deal with regulatory agencies. The process also often entails other steps, such as formulating drug candidates to optimize delivery and doing ►

► toxicology studies. But for academics, the endpoint might be quite early in the process; identifying a molecule that biotechnology companies can develop further, for example, or, if a biotech partner cannot be found, launching a start-up company to take the work to early clinical trials.

Increasingly, scientists can learn these kinds of skills within academia. As a result of consolidation and programme cuts, “some very, very good people have left pharma to go to academic institutions”, says Austin. They are starting up translational medicine programmes to teach aspects of drug discovery.

Right now, says Austin, there is “a robust network” of more than 60 academic centres and programmes in the United States (<http://addconsortium.org>) with precisely this goal. The idea, says Austin, is not to replicate the work of industry, but rather to sort through the academic pile-up of ideas, to identify the most promising and make them attractive to potential industrial partners.

An academic who has discovered a disease-relevant target can contact one of these centres and apply to spend a year or more there, learning, for example, how to develop an assay that could be scaled up and used to identify promising drug compounds. “The kind of science that you use for drug discovery is a bit different from typical basic science,” says Marcie Glicksman, co-director of the Laboratory for Drug Discovery in Neurodegeneration at Harvard Medical School in Boston, Massachusetts, one of the 60 centres in the consortium.

Rather than making a breakthrough, publishing it and then moving on to the next project, as is typical in academic research, drug discovery involves creating procedures and assays that can be scaled up to high-throughput levels, with particular attention paid to reproducibility and standardization.

“You have a different level of quality control,” says Richard Boucher, co-principal investigator of translational research at UNC, “and also an element of documentation that you don’t have in a research lab. You are trying to continually make your measurement with better technology, more efficiently, faster.”

Garret FitzGerald, a pharmacologist and director of the Institute for Translational Medicine and Therapeutics at the University of Pennsylvania in Philadelphia, and his colleagues have formalized drug-discovery training with a three-year master’s programme for postdoctoral fellows or instructors at the early faculty stage. FitzGerald says that the idea is to recruit candidates with a PhD or medical doctorate in a specific discipline — for example, cell biology — and make them proficient

in drug discovery and development. A small percentage would then stay in the translational centres, working as the next generation of trainers.

As at conventional large ‘centres of clinical pharmacology’, the training is project-based and, at the end, the trainees go back to their disciplines “with value added”, FitzGerald says. “That should enhance their ability to be funded, and transform their departments.”

INDUSTRIAL STRENGTH

One possible criticism of these centres and of academia-focused translational science programmes is that some are run by academics without industrial drug-discovery expertise. “Everybody claims that they are doing translation,” says Rajesh Ranganathan, director of the Office of Translational Research at the US National Institute of Neurological Disorders and Stroke (NINDS) in Bethesda, Maryland. But he argues that only a small percentage of academics making that claim understand the process and have the resources to actually discover and develop a drug.

Thus, the best training involves establishing industry ties and working either in industry or with industrial scientists, says Ranganathan. “Get into a laboratory in an industrial setting and work on a project, take it forward. Do that for three, four years, whatever it might take,” he says. “Then you are in a position to move into situations where you can parlay that into a broader job in translation.”

One way to move into translational research is through postdoctoral fellowships sponsored by companies such as Roche, the Novartis Institute for Biomedical Research headquartered in Cambridge, Massachusetts, or Genentech, headquartered in South San Francisco, California. The fellowships pair academic postdocs with both industrial scientists and academic mentors to work on creative projects

“The kind of science that you use for drug discovery is a bit different from typical basic science.”



Erick Carreira says synthetic chemists need to include drug discovery in their skills repertoire.



Rajesh Ranganathan says that getting industrial experience in drug discovery is key for academics.

that would not normally be pursued by industry (see *Nature* **461**, 554–555; 2009).

The programmes aim to address one of the main concerns about industrial research, which was “getting more and more entangled in engineered research where everything was milestones and very short-sighted”, says Klaus Müller, a medicinal chemist at Roche. To keep from “drying out”, companies such as Roche recruit top scientists, promote cutting-edge science and encourage publication. At the same time, postdocs in company programmes have industry resources at their disposal, and gain experience in drug discovery.

But an element of caution is needed, says Ranganathan, who worked at Novartis and set up the company’s postdoctoral fellow programme before moving to the NINDS. “Make sure that such a programme is not a reward structure for internal scientists.” Otherwise academic postdocs act as a “pair of hands for those people who are already successful in the company”, he says, rather than as well-mentored trainees and achievers of scientific renown for themselves.

A PRODIGIOUS PARTNER

Academia–industry collaborations can be a way to both gain drug-discovery expertise and advance a project. Organic chemist Erick Carreira, at the Swiss Federal Institute of Technology in Zurich (ETHZ), followed that path when he began to collaborate with scientists at Roche. Before he came to Switzerland from the United States, his group was synthesizing new molecules and testing them through standard chemical means, such as measuring boiling and melting points or solubility. He never thought about designing drugs.

But shortly after joining the ETHZ 15 years ago, Carreira became a consultant with Roche; together, he and Roche scientists came up with a wild, “scribbled-on-a-napkin”

idea. What if they introduced a new kind of chemical unit into potential drugs to help them to work better?

The idea was to hunt outside the usual ‘chemical space’, searching for all the possible molecules of a given class, to look for structures with properties deemed ‘useful’ in the drug-discovery process. Müller identified a new class of synthetic chemicals called oxetanes as an under-explored area, and Carreira began modelling ways to substitute oxetanes for common functional groups already used in drug discovery. Normally, industrial scientists would consider such an idea too “odd, too risky and unlikely to succeed”, says Müller, who is secretary of the RPF Program. But for academics such as Carreira and his team, the project was perfect.

Roche backed the idea, supporting a synthetic-chemistry student, Georg Wuitschik, to work with Carreira, Müller and others to usher oxetanes into drug discovery. The results paid off, and the scientists published what became known as the oxetane concept (G. Wuitschik *et al.* *J. Med. Chem.* **53**, 3227–3246; 2010). It rapidly took hold in the drug-discovery community, offering potentially new ways to modify drugs. “This is really a gold mine,” says Müller.

Meanwhile, Carreira, in collaboration with Roche, is coaching chemistry students, postdocs and others who are interested in drug design. “The requirements of someone now coming out of graduate school in synthetic chemistry have changed,” he says. “Given the current job climate, a graduate student or postdoc needs to be fully conversant not only with the methods of chemical synthesis — how to make molecules — but also how to make novel chemicals with a pivotal role in the next generation of smart drugs.”

For Zylka, working with an industry veteran who had returned to academia was key. Before coming to UNC, Frye, as head of GSK’s discovery medicinal-chemistry group, had steered three drugs either to market or late-stage clinical trials. His team offers the best of both worlds, Zylka believes: the creativity and freedom of an academic lab and the wisdom and experience of an industrial mentor.

Those in academia who can take advantage of such industry ties and drug-discovery resources have a shot at a grand pay-off, and a new career path — if they dare to be bold, enterprising and an “expert at one discipline but knowledgeable about the other translational disciplines”, says Austin.

“The scientific ecosystem has evolved to a place where rapid advances will happen,” he adds. “And basic scientists can actually make that happen without going to a company. This is absolutely revolutionary.” ■

Trisha Gura is a science writer in Boston, Massachusetts.

CITATION

Data standards urged

The academic community needs better curation and authorship standards for data, according to a committee of the US National Academies. In *For Attribution — Developing Data Attribution and Citation Practices and Standards*, published on 19 November, the Board on Research Data and Information (BRDI) presents views from experts in data curation across all scientific disciplines. It says that scientific data — such as measurements and images — should be made available for scrutiny online or through an archive or repository, and that researchers should be given full credit for their efforts in creating those data. The report notes that some scientific associations, including the American Geophysical Union, endorse giving the same importance to the publication of scientific data as to the publication of papers.

Data citation, the committee says, gives authors proper credit, makes them accountable and helps to make science reproducible. Although it offers no formal recommendations, the report suggests that digital object identifiers similar to those used for research papers would provide a permanent online address for data sets and allow the data to be cited formally.

“People are using other people’s data more often, so they need a way to cite and attribute sources,” says Paul Uhlig, the committee rapporteur and director of the BRDI. “Up to now, there has been no convention for it. That’s really behind the whole rise in calls for data citation and attribution standards — it’s an infrastructure issue. Those people need credit.”

The report notes that questions remain regarding how to decide which data are curated, who would pay to maintain data in repositories or archives and who would peer review data and how.

Uhlig says that how often a researcher’s data are cited is likely to become an important career metric. The report suggests that it could be incorporated into tenure decisions, as paper citations and journal impact factors are now.

For Attribution is the first of several expected publications on the subject. The BRDI will contribute to a report to be released next year by the international Committee on Data for Science and Technology (CODATA), part of the International Council for Science in Paris on current practices in data curation and authorship. A final report from CODATA presenting best practices and recommendations is expected by 2014.



Rajesh Ranganathan says that getting industrial experience in drug discovery is key for academics.

that would not normally be pursued by industry (see *Nature* **461**, 554–555; 2009).

The programmes aim to address one of the main concerns about industrial research, which was “getting more and more entangled in engineered research where everything was milestones and very short-sighted”, says Klaus Müller, a medicinal chemist at Roche. To keep from “drying out”, companies such as Roche recruit top scientists, promote cutting-edge science and encourage publication. At the same time, postdocs in company programmes have industry resources at their disposal, and gain experience in drug discovery.

But an element of caution is needed, says Ranganathan, who worked at Novartis and set up the company’s postdoctoral fellow programme before moving to the NINDS. “Make sure that such a programme is not a reward structure for internal scientists.” Otherwise academic postdocs act as a “pair of hands for those people who are already successful in the company”, he says, rather than as well-mentored trainees and achievers of scientific renown for themselves.

A PRODIGIOUS PARTNER

Academia–industry collaborations can be a way to both gain drug-discovery expertise and advance a project. Organic chemist Erick Carreira, at the Swiss Federal Institute of Technology in Zurich (ETHZ), followed that path when he began to collaborate with scientists at Roche. Before he came to Switzerland from the United States, his group was synthesizing new molecules and testing them through standard chemical means, such as measuring boiling and melting points or solubility. He never thought about designing drugs.

But shortly after joining the ETHZ 15 years ago, Carreira became a consultant with Roche; together, he and Roche scientists came up with a wild, “scribbled-on-a-napkin”

idea. What if they introduced a new kind of chemical unit into potential drugs to help them to work better?

The idea was to hunt outside the usual ‘chemical space’, searching for all the possible molecules of a given class, to look for structures with properties deemed ‘useful’ in the drug-discovery process. Müller identified a new class of synthetic chemicals called oxetanes as an under-explored area, and Carreira began modelling ways to substitute oxetanes for common functional groups already used in drug discovery. Normally, industrial scientists would consider such an idea too “odd, too risky and unlikely to succeed”, says Müller, who is secretary of the RPF Program. But for academics such as Carreira and his team, the project was perfect.

Roche backed the idea, supporting a synthetic-chemistry student, Georg Wuitschik, to work with Carreira, Müller and others to usher oxetanes into drug discovery. The results paid off, and the scientists published what became known as the oxetane concept (G. Wuitschik *et al.* *J. Med. Chem.* **53**, 3227–3246; 2010). It rapidly took hold in the drug-discovery community, offering potentially new ways to modify drugs. “This is really a gold mine,” says Müller.

Meanwhile, Carreira, in collaboration with Roche, is coaching chemistry students, postdocs and others who are interested in drug design. “The requirements of someone now coming out of graduate school in synthetic chemistry have changed,” he says. “Given the current job climate, a graduate student or postdoc needs to be fully conversant not only with the methods of chemical synthesis — how to make molecules — but also how to make novel chemicals with a pivotal role in the next generation of smart drugs.”

For Zylka, working with an industry veteran who had returned to academia was key. Before coming to UNC, Frye, as head of GSK’s discovery medicinal-chemistry group, had steered three drugs either to market or late-stage clinical trials. His team offers the best of both worlds, Zylka believes: the creativity and freedom of an academic lab and the wisdom and experience of an industrial mentor.

Those in academia who can take advantage of such industry ties and drug-discovery resources have a shot at a grand pay-off, and a new career path — if they dare to be bold, enterprising and an “expert at one discipline but knowledgeable about the other translational disciplines”, says Austin.

“The scientific ecosystem has evolved to a place where rapid advances will happen,” he adds. “And basic scientists can actually make that happen without going to a company. This is absolutely revolutionary.” ■

Trisha Gura is a science writer in Boston, Massachusetts.

CITATION

Data standards urged

The academic community needs better curation and authorship standards for data, according to a committee of the US National Academies. In *For Attribution — Developing Data Attribution and Citation Practices and Standards*, published on 19 November, the Board on Research Data and Information (BRDI) presents views from experts in data curation across all scientific disciplines. It says that scientific data — such as measurements and images — should be made available for scrutiny online or through an archive or repository, and that researchers should be given full credit for their efforts in creating those data. The report notes that some scientific associations, including the American Geophysical Union, endorse giving the same importance to the publication of scientific data as to the publication of papers.

Data citation, the committee says, gives authors proper credit, makes them accountable and helps to make science reproducible. Although it offers no formal recommendations, the report suggests that digital object identifiers similar to those used for research papers would provide a permanent online address for data sets and allow the data to be cited formally.

“People are using other people’s data more often, so they need a way to cite and attribute sources,” says Paul Uhler, the committee rapporteur and director of the BRDI. “Up to now, there has been no convention for it. That’s really behind the whole rise in calls for data citation and attribution standards — it’s an infrastructure issue. Those people need credit.”

The report notes that questions remain regarding how to decide which data are curated, who would pay to maintain data in repositories or archives and who would peer review data and how.

Uhler says that how often a researcher’s data are cited is likely to become an important career metric. The report suggests that it could be incorporated into tenure decisions, as paper citations and journal impact factors are now.

For Attribution is the first of several expected publications on the subject. The BRDI will contribute to a report to be released next year by the international Committee on Data for Science and Technology (CODATA), part of the International Council for Science in Paris on current practices in data curation and authorship. A final report from CODATA presenting best practices and recommendations is expected by 2014.

TIME AND AGAIN

Reflections on the past.

BY MOSHE SIPPER

The thing I hated most was when people told me that I wasn't to blame, because, after all, I was only seven years old when the 'unpleasantness' began. I hated that too, the way they always used some kind of euphemism. It was not 'unpleasantness', nor 'troubles at home', nor 'sad period in life', nor any of those other phrases I've heard over the years. There are no words to describe what happened.

For what would you call a father who rapes his daughter daily from the time she is five years old until she's thirteen? What kind of 'unpleasantness' comes to a halt only when a thirteen-year-old kills herself? How 'sad' is it when the monster who committed these atrocities walks away a free man through some legal loophole? Our language was not invented to encompass such acts.

And, despite what everyone has said over the years, I do blame myself. Very much so. I was only seven years old when it all began, but I was fifteen by the time it ended. Had I done anything at any point in between, perhaps when I was twelve, or thirteen, or fourteen, then my sister would still be alive today. If only I could go back... I'd need just one instant, just a few seconds...

That's what drove me to major in physics, and later on to do graduate work on the nature of time. That was quite a while ago. I'm now a full professor of physics, with some well-known papers on the subject of time. But I only published those so that I could get tenure and promotion. So that people would leave me alone to do what I really wanted: find a way to travel back in time.

Of course, I didn't talk about that much, least of all with my colleagues. As a physicist it doesn't hurt if you're considered eccentric, it maybe even helps, but being labelled downright crazy can get you kicked out of your field — and your job. And I needed my job, I needed the time it afforded me to study time.

Fairly quickly I realized that the past could not be changed — at least not in my timeline. If I went back in time, my mere appearance, my very

first breath in the past, would create a new branch in time — a new universe. Years ago I'd mentioned this to a psychologist I'd been dating and she had eyed me askance and said: "So you want to create universes, huh? Sounds like a God complex to me."



I stopped dating psychologists after that. In fact, I hardly dated any women at all. I have no delusions of grandeur whatsoever, no God complex. And I don't wish to 'create universes', plural. I wish to create one single universe in which my sister grows up to become the wonderful person she could and should have been.

In that universe the monster is, of course, dead.

And now, after all those years of burning the midnight oil (and often the four-, five- and six-o'clock-in-the-morning oil too), I had it. The irony is that the solution turned out to be fairly simple, and the time-travelling device wasn't some large vehicle à la H. G. Wells, but a small, wrist-worn gadget.

There was absolutely no hesitation on my part, even though I knew this was a one-way trip: I would remain forever in the new universe I was about to create. I set the device to

the very day it had all begun, took one last unregretful look at my cluttered office — and vanished from this cursed universe.

Only to reappear, after a moment of disorientation, in a place I knew infamously well: our basement. A warm, fuzzy feeling filled my heart as I saw my old tricycle, the one I'd been given for my second birthday, rusting over in one corner. Success! I had travelled back in time. Then an icy hand seemed to grab my heart and twist it. I saw the thing on the floor next to the tricycle, looking for all the world like an innocent object but which to me was the epitome of evil: the dirty mattress.

In my shock I stumbled onto something and heard the sound of shattering glass. I looked down to find my mother's old make-up mirror lying there in pieces. Then I heard something that made my blood run cold.

"Hello cutie-pie, daddy's home."

The monster was in the house! And he would soon be taking my sister down here for the very first time. That dirty mattress was about to witness evil incarnate, and would do so for many years to come.

No, I shouted in my mind. *Not in this universe!* I thought I'd arrive with enough time to put my plan into action but apparently I had only moments to prepare. I scanned the basement quickly for something I could use as a weapon, perhaps a hammer, or maybe one of those bricks left over from when they'd redone the kitchen. *I'll kill him with my bare hands if I have to*, I thought, gazing down at my small hands.

Small?

Something clicked in my mind, a realization that should have come way back in that abandoned future. I quickly picked up a shard of broken mirror and looked into it.

Only to see my sister's face staring back at me.

I heard footsteps coming down the stairs. "Daddy's coming, cutie-pie."

I clenched my teeth as my small hands gripped the mirror shard tighter. ■

Moshe Sipper is a professor of computer science at Ben-Gurion University who also writes science fiction and fantasy stories. More of his work can be found at www.moshesipper.com.

JACEY

➤ NATURE.COM

Follow Futures:

@NatureFutures

go.nature.com/mtoodm



Cover art: Claudia Bentley

Editorial

Herb Brody,
Michelle Grayson,
Tony Scully,
Nick Haines,
Afsaneh Gray,
Rebecca Dargie

Art & Design

Wes Fernandes,
Alisdair Macdonald,
Andrea Duffy

Production

Donald McDonald,
Yvonne Strong, Kelly
Hopkins, Leonora
Dawson-Bowling

Sponsorship

Reya Silao, Yvette
Smith

Marketing

Elena Woodstock,
Hannah Phipps

Project Managers

Claudia Deasy,
Christian Manco

Art Director

Kelly Buckheit Krause

Chief Magazine Editor

Tim Appenzeller

Editor-in-Chief

Phil Campbell

Ageing is inevitable. Yet for centuries people have tried to slow or stop it, from bathing in the blood of virgin girls to concocting an elixir of life. These days, anti-ageing research is on a more scientific footing. And while we are no closer to finding the fountain of youth, humans — for a variety of reasons — are living longer than ever before (page S2).

Hitting the biologically arbitrary 100-year milestone used to be the preserve of the lucky few, who would often reach it in rude health. In theory, studying these centenarians might reveal the secrets of healthy ageing. But as life expectancy increases, more people are reaching their eleventh decade, muddying the gene pool. Might more valuable data be gleaned from the supercentenarians who reach 110 (S6)?

Scientific efforts to extend lifespan are progressing on several fronts. A short-lived species can evolve into a long-lived one, and researchers are keen to find out how (S10). Studies in other species have already shown that a severely restricted diet can add years of healthy living (S18). Diet affects ageing in humans too — how our food influences our gut microbes, and how they in turn affect our health and longevity, is under investigation (S14). Another line of enquiry focuses on harnessing the regenerative powers of stem cells (S12).

But what does healthy ageing mean? Sociologist Eva Kahana talks about this “slippery concept”, which she says is different for each individual (S9). With the threat of Alzheimer’s disease looming large, there is a lack of data on how the brain changes over time — a deficit that a new long-term study aims to correct (S4). In the meantime, for those of us who need a little help in our later years, new technologies can support, predict and possibly prevent some of the worst health problems associated with ageing (S16).

We are pleased to acknowledge the financial support of Nestlé Research Center in producing this Outlook. As always, Nature retains sole responsibility for all editorial content.

Michelle Grayson

Senior editor, supplements

CONTENTS

S2 DEMOGRAPHY

To the limit

The drive to increase life expectancy

S4 COGNITION

The brain’s decline

What happens to our cognitive functions when we get old?

S6 CENTENARIANS

Great expectations

The genetic link to a long, healthy life

S9 Q&A

Ageing proactively

Eva Kahana explores healthy ageing

S10 COMPARATIVE BIOLOGY

Looking for a master switch

Species with long lifespans might hold the key to extending our own

S12 STEM CELLS

Repeat to fade

The regeneration game

S14 MICROBIOME

Cultural differences

A gut reaction to our diet

S16 TECHNOLOGY

Dancing with robots

High-tech help for later life

S18 INTERVENTIONS

Live long and prosper

Eating less and the pathway to old age

COLLECTION

S21 Recruiting adaptive cellular stress responses for successful brain ageing
Alexis M. Stranahan and Mark P. Mattson

S29 Gut microbiota composition correlates with diet and health in the elderly
Marcus J. Claesson et al.

S36 Impact of caloric restriction on health and survival in rhesus monkeys from the NIA study
Julie A. Mattison et al.

S40 Shorter telomeres are associated with obesity and weight gain in the elderly
OT Njajou et al.

Nature Outlooks are sponsored supplements that aim to stimulate interest and debate around a subject of interest to the sponsor, while satisfying the editorial values of Nature and our readers’ expectations. The boundaries of sponsor involvement are clearly delineated in the Nature Outlook Editorial guidelines available at http://www.nature.com/advertising/resources/pdf/outlook_guidelines.pdf

CITING THE OUTLOOK

Cite as a supplement to Nature, for example, Nature Vol XXX, No. XXXX Suppl. Sxx–Sxx (2012). To cite previously published articles from the collection, please use the original citation, which can be found at the start of each article.

VISIT THE OUTLOOK ONLINE

The Nature Outlook Ageing supplement can be found at <http://www.nature.com/nature/outlook/ageing>

All featured articles will be freely available for 6 months.

SUBSCRIPTIONS AND CUSTOMER SERVICES

For UK/Europe (excluding Japan): Nature Publishing Group, Subscriptions, Brunel Road, Basingstoke, Hants, RG21 6XS, UK. Tel: +44 (0) 1256 329242. Subscriptions and customer services for Americas – including Canada, Latin America and the Caribbean: Nature Publishing Group, 75 Varick St, 9th floor, New York, NY 10013-1917, USA. Tel: +1 866 363 7860 (US/Canada) or +1 212 726 9223 (outside US/Canada). Japan/China/Korea: Nature Publishing Group — Asia-Pacific, Chiyoda Building 5-6th Floor, 2-37 Ichigaya Tamachi, Shinjuku-ku, Tokyo, 162-0843, Japan. Tel: +81 3 3267 8751.

CUSTOMER SERVICES

Feedback@nature.com
Copyright © 2012 Nature Publishing Group

TO THE LIMIT

More people are surviving to older ages than ever before, pushing life expectancy from birth to unprecedented highs. Further gains will require tackling age-related conditions, across the world, with ramifications for society as a whole. By **Tony Scully**.

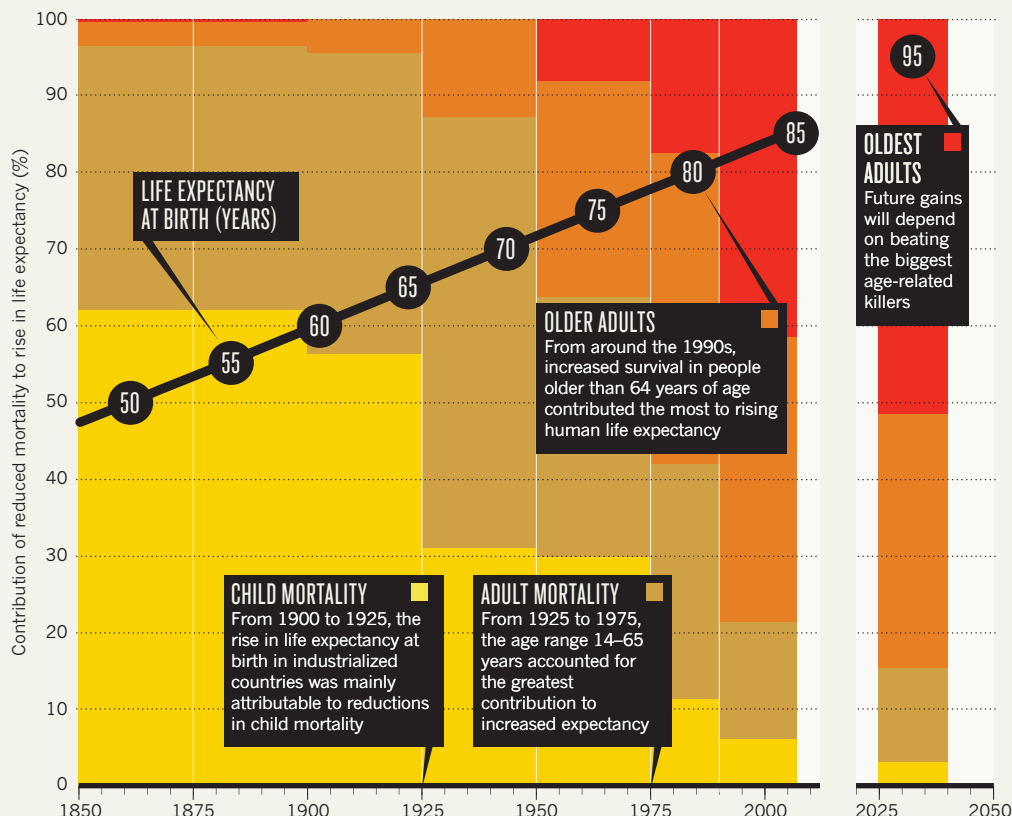
BORN SURVIVORS

Over the past 150 years, modern medicine and improved standards of living have increased life expectancy at birth by roughly 3 months per year. This graph plots women in several industrialized countries, but this trend is also true for men, and most of the world is following behind.

For humanity to continue to extend life expectancy, the rates of mortality in the oldest age groups must decline the most. This will only be achieved if the biggest killers — cancer, heart disease, stroke and Alzheimer's disease — are consigned to the past. But this will be tough given the rising levels of obesity and diabetes.

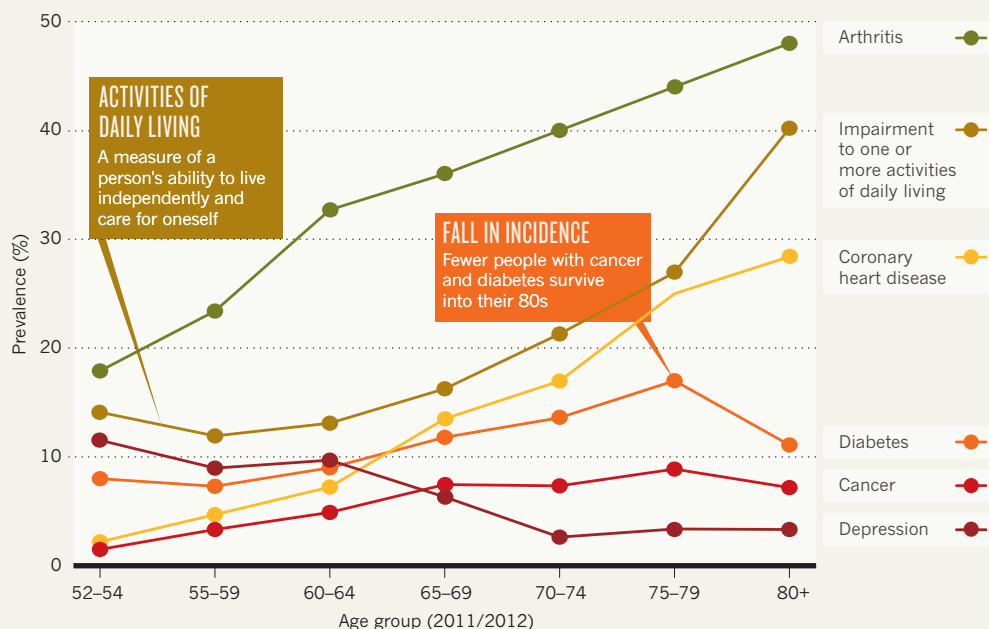
Another strategy to prolong life might be to slow the ageing process itself (see 'Live long and prosper', page S18).

CONTRIBUTION TO RISE IN LIFE EXPECTANCY AT BIRTH



THE COMING OF AGE

A survey in England asked over 10,000 people aged 50 years and older to report their health status and any limitations with independent living. The survey found that the prevalence of health problems increases with age while people become increasingly dependent on healthcare and community support to survive.



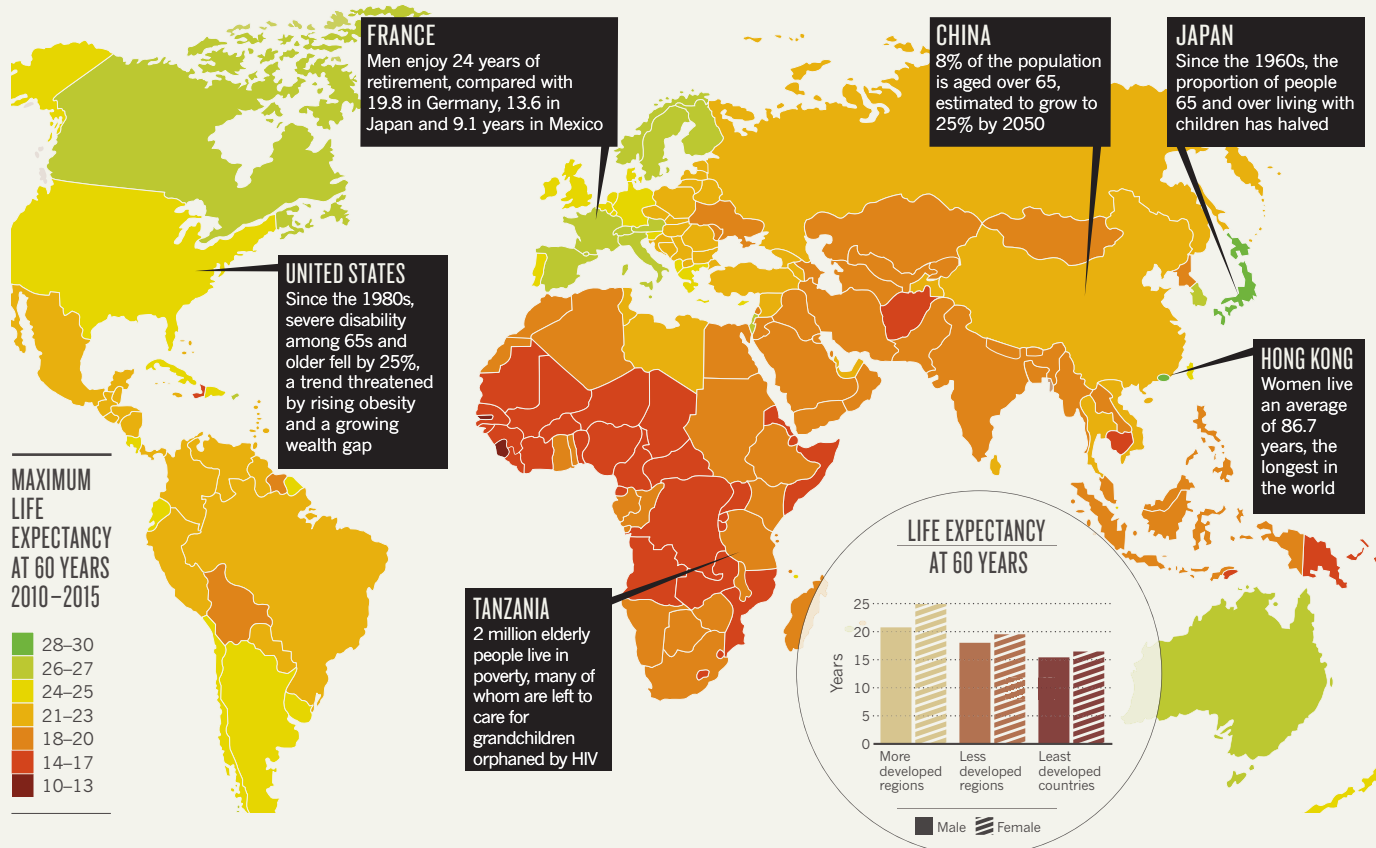
60+

LIFE EXPECTANCY AT 60 YEARS OF AGE

A better indicator of the prospects of elderly people than life expectancy from birth, a 60-year-old person living in one of the least developed regions is still expected to reach 70 years of age and a person living in a developed country has a fair chance of reaching 90 years. The global population of people aged 60 years and older will more than double, from 542 million in 1995 to about 1.2 billion in 2025.

25.2

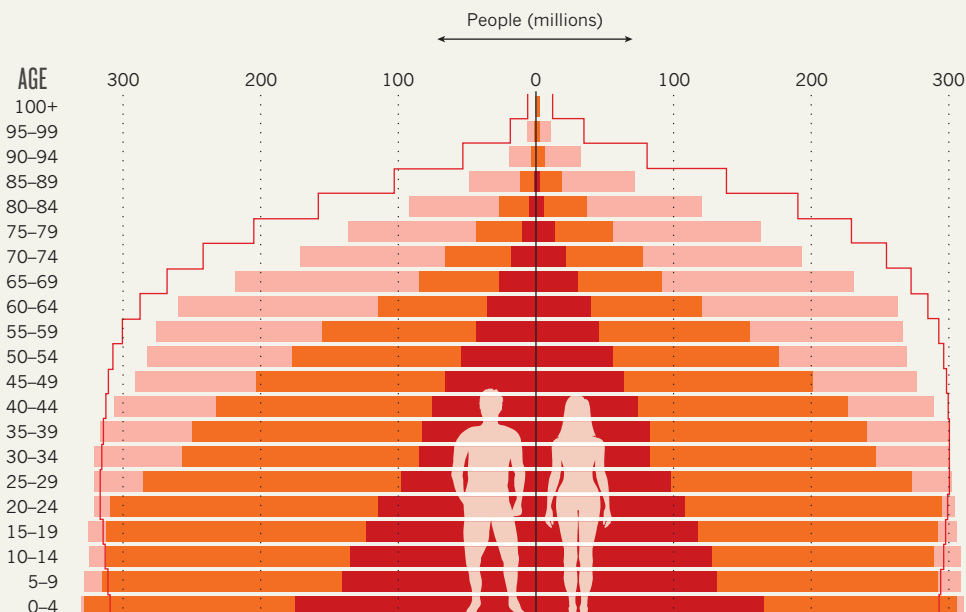
years added to life expectancy for people living in less developed countries since 1950



CHANGING SHAPE OF GLOBAL SOCIETY

Throughout history, most human populations have formed a sort of pyramid structure: a wide base of children and economically productive adults supporting relatively few and more socially dependent elders. As the world develops, people have fewer children and live longer. The traditional pyramid is morphing into a rectangle; society's structure is changing and people will need to adapt.

YEAR





Elderly people often retain existing memories but may need help remembering new things.

COGNITION

The brain's decline

Treating cognitive problems common in elderly people requires a deeper understanding of how a healthy brain ages.

BY ALISON ABBOTT

Swedish brothers Jonas and Robert af Joch-nick became wealthy philanthropists after their direct-selling company, Oriflame Cosmetics, found success peddling dreams of ever-youthful complexions to post-communist Eastern Europe.

The brothers are now in their 70s, an age where dreams of youthful skin have morphed

nervously into hopes of a youthful brain. They recently donated SKr50 million (US\$7.6 million) to the Karolinska Institute in Stockholm to support its research into the healthy ageing of the brain.

Neuroscientist Lars Bäckman won the entire endowment for his proposal to launch a large-scale, multimodal imaging study called COBRA (for Cognition, Brain and Ageing), which this year began recruiting its 180 participants. This

ambitious study is unusual in providing a wide range of tests on the same subjects over the coming years, with the aim of understanding how cognition declines as the brain ages — and whether we can do anything about it.

Bäckman's goal is to understand ordinary, non-disease-influenced ageing. "We all want to know what's normal," says Cheryl Grady, who studies ageing brains at the Rotman Research Institute in Toronto, Canada, "both as a reference for dementia research, and as a guide for any future interventions."

Given the concern in most developed countries about their ageing populations and the problem of dementia, it is surprising how little we know about healthy brain ageing. There are only a few things that researchers can agree on. First, after the age of 60, nearly everyone will start to experience some decline in cognitive skills, most noticeably in memory, and this decline will be accompanied by a change in brain structure. Second, aerobic exercise slows or delays this mental slippage.

The realm of uncertainty is much larger. Researchers still don't understand the mechanisms underlying the decline or the order of events. They can't explain why some people manage to stay cogent and alert well into their 80s, whereas others become slow-witted and forgetful in their 60s. They don't even know whether Alzheimer's disease is an abnormal pathological condition or simply an acceleration of normal ageing. And no one knows of any drugs that can help those who lose cognitive function as they age, or whether brain training programmes really help.

MEMORY FAILURE

The COBRA study is recruiting healthy subjects aged 63–65 and aims to follow them for at least a decade. It will carry out various tests, including structural and functional imaging to see which parts of the brain are active on any given task, and how its volume changes over time. Diffusion tensor imaging will visualize the integrity of white matter — the long bands of neuronal axons that transmit signals between different brain regions. And positron-emission tomography (PET) will assess dopamine levels — this is rarely used, says Bäckman, because a single PET scan can cost several thousand dollars. In addition, subjects will carry out a wide range of cognitive tests to measure attributes such as working memory. Participants will also provide information about their health and lifestyle, and provide blood samples for extensive analyses, including genetic testing.

There have been many studies into these topics but, unlike COBRA, they have typically compared young adults with older ones, and study cohorts have been small. Probably for these reasons, the results have been contradictory. "These cross-sectional studies have led to discrepancies in the literature," says Bäckman. "Individuals vary massively in how their brains function and the speed of their age-related

ANNE DE HAAS/GETTY IMAGES

decline.” In addition, he points out, comparing a cohort born in the 1930s with one born in the 1980s introduces confounding factors: variables other than age, such as early experiences, environment and education, will be different between the two groups.

Even so, cross-sectional studies have provided some reliable pointers. They have shown that as the brain ages, the grey matter shrinks and the white matter starts to break up. Shrinkage is particularly evident in the prefrontal cortex, where high-level thinking and reasoning takes place, and the hippocampus, which plays a central role in memory. There are fewer receptors and other proteins too, but the most dramatic fall is in the amount of dopamine (see ‘Ages of dopamine’) — a neurotransmitter whose many functions include movement control, general motivation and learning. From early adulthood onwards, dopamine levels drop by about 10% per decade, making it a powerful marker for brain ageing.

Some cognitive functions seem to be more sensitive to the ageing process than others. Semantic long-term memory — general knowledge not linked to personal experience — is typically well preserved as we age, but many other attributes start to decline. Reaction speed deteriorates rapidly, for example. Episodic memory, which allows us to reflect on past events, and working memory, which allows distinct pieces of information to be held transiently in the mind, both deteriorate with the advancing years. As a result, as people age they are more easily distracted and find it more difficult to switch quickly between cognitive tasks. They also tend to forget names. And they complain that by the time they open the fridge door they can no longer remember what they wanted — but they still know what a fridge is for.

Not everyone is convinced that some cognitive functions fade faster than others, however. Ulman Lindenberger, a COBRA collaborator and director of the Centre for Lifespan Psychology at the Max Planck Institute for Human Development in Berlin, suspects that all functions fade together within an individual, but that previous studies have been too simple to capture this effect. He hopes that COBRA’s approach of using different cognitive tests to measure the same function will help clarify such questions.

A HEALTHY INTEREST

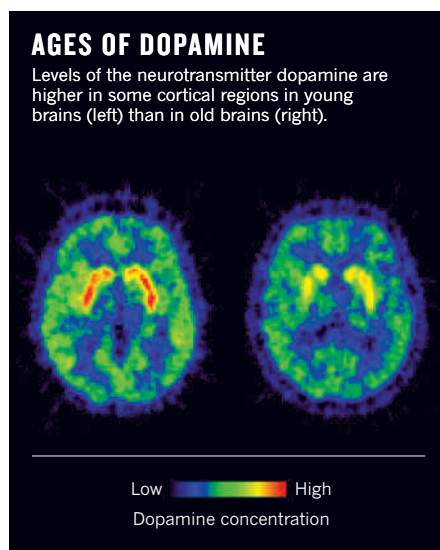
Long-term, prospective studies such as COBRA tend to be expensive to run and take many years to gather data. Yet they provide the best opportunity to address many important questions about ageing. For example, which structural changes in an individual’s brain affect the different cognitive skills? What genetic or environmental factors will be protective? What is the best way to develop treatment strategies?

Most longitudinal studies into ageing focus on dementias such as Alzheimer’s disease, which is associated with deposits of amyloid

plaque and tangles of tau protein in the brain. Politicians find it easier to support research on such burdensome diseases than on healthy cognitive ageing, says Bäckman. One of the largest studies of this sort is the Alzheimer’s Disease Neuroimaging Initiative (ADNI), based at the University of California, San Francisco (UCSF), and funded by the US National

Some cognitive functions seem to be more sensitive to the ageing process than others.

Institutes of Health and several pharmaceutical companies. It studies 200 people with Alzheimer’s disease, 400 subjects with mild cognitive impairment, and 200 elderly controls with no diagnosed mental deterioration. Its primary aim is to find markers that can predict the onset or progression of Alzheimer’s, although data from subjects with mild cognitive impairment and controls without dementia will provide leads for understanding non-pathologic ageing.



Understanding how Alzheimer’s disease begins will also help studies on healthy ageing screen out those with pathologies to ensure that researchers are not detecting the wrong thing. “We are never sure if the cognitive declines we are measuring are actually the otherwise-invisible beginnings of a dementia that does not become overt during the study,” says behavioural neuroscientist Susan Resnick of the US National Institute on Aging in Baltimore, Maryland. Detection of abnormal levels of protein is not a specific enough test. “Nearly a third of old people who are cognitively normal have enough amyloid and tau in their brains to meet the criteria for Alzheimer’s disease.”

Another problem with longitudinal studies is that it can be hard to convince people to keep returning — a particular problem for ageing studies. “As subjects decline, their families become overstressed and the study seems lower priority,” says ADNI director Michael

Weiner at UCSF. In an attempt to avoid this issue, COBRA is recruiting subjects in the northern Swedish town of Umeå, where the population is settled and has strong trust in health authorities.

EXERCISE FOR THE BRAIN

Describing the process of normal cognitive ageing is a necessary prelude to helping people achieve it. Bäckman believes that successful cognitive ageing depends on maintaining brain integrity — the fewer signs of pathology or brain shrinkage, the better the cognitive function. This corresponds with the widely held view that if we lived long enough, we would all eventually accumulate enough physical damage in the brain to develop dementia. Damage is caused by the accumulation of amyloid plaques or tau tangles, or leakages from small blood vessels in the brain, which occur at different speeds in different individuals. The brain maintenance theory is consistent with evidence that aerobic exercise can slow cognitive decline by stimulating production of brain-derived neurotrophic factor, which helps the growth of new blood vessels, not only in the muscles being exercised but in the brain as well.

But it’s a rare octogenarian who can take a long run or play a heart-pounding game of squash, so scientists hope that studies such as COBRA will lead to alternative strategies. One idea is to develop drugs that improve particular types of neurotransmission, but this might have limited value against a background of brain tissue shrinkage. Another strategy could be to use computer-based cognitive training programmes designed to sharpen mental processing speed or working memory. Several studies have shown that people of all ages can improve their performance on specific computer tasks in which they train. Neuroscientist Adam Gazzaley at UCSF is so confident in the potential of this approach that he is developing commercial software for use at home. But even he admits there is no evidence that the improvements seen in computer-based tasks can help with life-related activities — such as helping you remember why you went to the fridge.

As is perhaps appropriate for ageing research, answers will come only with time. “Once we have a tighter link between neurochemistry and structural changes in the brain in relation to cognitive outcome, we’ll know what are the main pacemakers of change at this level,” says Lindenberger. “Then we’ll know how to think about interventions.”

The af Jochnick brothers, meanwhile, are learning from the science they support. Both work out in the gym and play tennis. “Our cosmetics helped keep skin young,” says 72-year-old Robert. “Hopefully this research will eventually help keep brains young.” ■

Alison Abbott is *Nature’s* senior European correspondent based in Munich.



CHRISTOPHER LANE/CONTOUR BY GETTY IMAGES

Irving Kahn, the oldest trader on Wall Street, is remarkably active despite being over 100 years of age — and scientists hope many more will match him.

CENTENARIANS

Great expectations

Scientists are searching for a genetic blueprint that will enable humans to stay healthy and vital well into their old age.

BY MICHAEL EISENSTEIN

On any weekday morning, you might catch Irving Kahn heading into his office in Manhattan, where he works as an investor and financial analyst — seemingly unremarkable, except for the fact that he has been in the business more or less continuously since 1928.

The 106-year-old Kahn is one of many who have managed to live well into their eleventh decade with mental faculties intact and in surprisingly good health — and researchers into ageing have taken notice. Thomas Perls, a gerontologist at Boston University in Massachusetts and director of the New England Centenarian study, recalls an early encounter with two centenarians that challenged his expectation that the remarkably old would be remarkably unhealthy. While he was training at a rehabilitation centre, Perls saw one centenarian “out and about playing piano for everybody”, while another — a retired tailor — “was in occupational therapy mending people’s

clothes and teaching other people how to sew”.

But the data increasingly suggest that people who reach such ripe old ages are getting a biological helping hand (see ‘Disease delay and genetics’). For example, recent research from Perls supports a hypothesis known as ‘compression of morbidity’, in which individuals whose lifespan is considerably longer than average (at least 100 years old) tend to stay healthy for longer, with delayed onset of age-associated diseases such as cancer and cardiovascular disease¹. “These diseases don’t appear until roughly the last 5% of their lives,” says Perls. If this is the case, exploring extreme longevity could provide insights into the foundations of many common diseases — and into new weapons with which to fight them.

ARMOUR AGAINST AGEING

Much of the seminal work in assessing genetic contributions to healthy ageing in the general population has been done in Scandinavia, where political peace and a strong societal infrastructure have minimized the external

forces that prematurely shorten life elsewhere. “Over the past 100 years, we’ve basically had ‘laboratory conditions’ for humans,” jokes Kaare Christensen, a genetic epidemiologist specializing in human ageing at the University of Southern Denmark in Odense. From studies of fraternal and identical twins, Christensen has found that roughly 25% of longevity is attributable to hereditary factors². Furthermore, he suspects there is a clear age dependency for this genetic contribution. “Before age 60, genetic factors are not that important in the cohorts that we have studied,” says Christensen, “but after age 60 their impact increases, and seems to get strongest at the very highest ages.” In other words, a healthy lifestyle and environment are the key determinants of whether most people will reach their seventh decade, but after that it’s increasingly down to their genes.

However, a healthy lifestyle might not be mandatory for everybody. Many specialists in ageing now believe that the extremely old possess beneficial genetic variants that protect

them against the vicissitudes of ageing throughout life. It is only beyond a certain age — as the health of less-fortunate people begins to decline — that these variants become apparent.

Gerontologist Nir Barzilai of the Albert Einstein College of Medicine in New York is among the leading researchers in this field. He has been tracking a large cohort of Ashkenazi Jews for many years in an effort to understand what sets the extremely old apart from their peers. “We have 2,500 people between the ages of 60 and 112, including nearly 600 people over 95,” says Barzilai. His aim is to identify genomic variants that are more common in the oldest cohort than in those who achieve only an average lifespan. “Most genotypes do not change in frequency because they’re not involved in lifespan,” he says. “Therefore, those genotypes that do change are either going down in frequency because they’re killing people or going up because they are promoting longevity.”

One might expect these ‘longevity genotypes’ to be perfectly attuned for health — devoid of variants associated with increased disease risk. But several studies have shown that this is not the case. For example, the Leiden Longevity Study found that the genomes of nonagenarians were as likely to contain common risk factors for cancer, diabetes and other diseases as were the genomes of a young, control population³. This suggests that other variants in the longevity genome are somehow insulating their possessors against the effects of these potentially harmful genes — an effect that Christensen has also observed in family studies. “In Denmark, we have seen that children of the long-lived have about 25% lower cancer risk compared with other people.” For Barzilai, patterns like this suggest that the genomes of the extremely old might provide clinical researchers with a guide for understanding how health deteriorates over time. “What really controls our ageing rate,” he says, “are protective mechanisms and protective genes.”

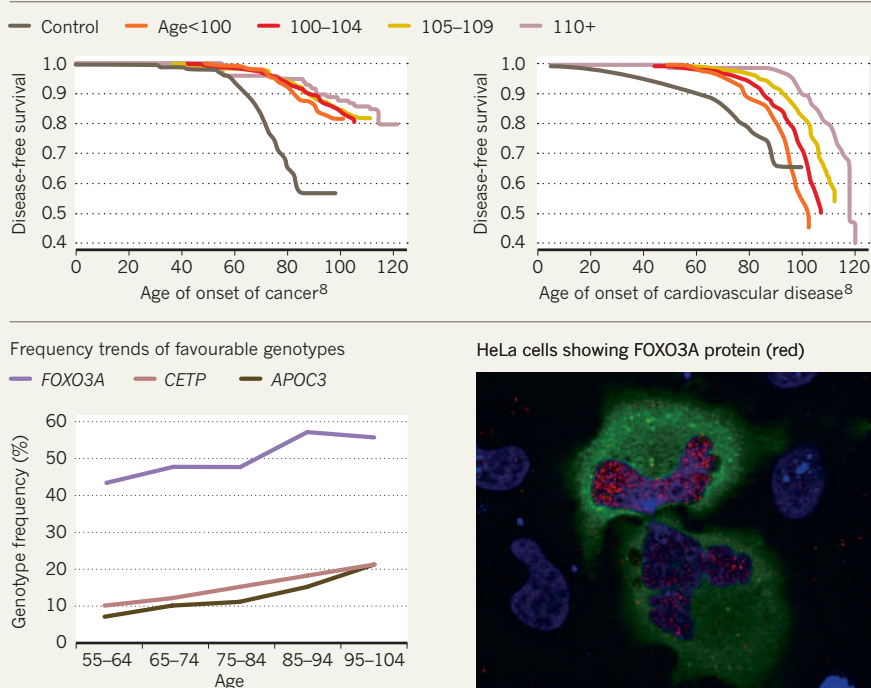
THE HUNT IS ON

For most diseases with a heritable component, the search for contributory genes takes the form of a genome-wide association study (GWAS). This is essentially a fishing expedition for individual variations — single nucleotide polymorphisms (SNPs) — that are statistically more or less common in individuals with a trait of interest than in a control population. However, to avoid overloading researchers with false-positive results, a high bar is set for designating hits. Furthermore, it can be nearly impossible to discover factors that are rare or exert only a modest effect on their own, as these might appear as noise in a large study population. “It’s highly unlikely that there’s a single genetic variant or even a handful of genetic variants that have a powerful enough influence to pop up in a GWAS and be independently associated with longevity,” says Perls.

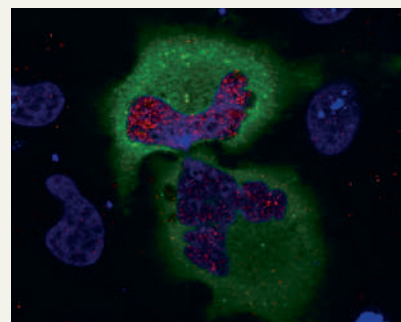
To sidestep this problem, Perls and his

DISEASE DELAY AND GENETICS

Long-lived individuals show apparent compression of morbidity, with delayed onset of age-related diseases.



HeLa cells showing FOXO3A protein (red)



colleague at Boston University, Paola Sebastiani, performed a different kind of GWAS. They focused not on individual SNPs but on groups of SNPs, seeking variants with weak individual effects that seem to act synergistically in long-lived individuals. These SNP groups might then reveal dependencies in the genome — clusters of variants that must occur together — that establish a protective biological environment that favours an extended lifespan. Perls and Sebastiani uncovered a number of such ‘fingerprints’, but their 2010 paper was retracted from *Science* a year later owing to technical mistakes that called their analysis into question. The team partnered with genetic epidemiologists at Yale University in New Haven, Connecticut, to address these issues, and re-published their research in *PLoS ONE*⁴ in

“Genotypes that change in frequency are either going down because they kill people or up because they promote longevity.”

2012. Perls concedes that the retraction cast an unfortunate cloud over the study, but he stands by his team’s discovery: a collection of 281 SNPs linked to at least 130 genes that seem to be notably enriched in centenarians. “Here’s a bunch of variants that together are probably influencing one another and interacting with the environment to have an important impact on living to these most extreme ages,” says Perls, adding that “the accuracy of the model became greater and greater with subjects of older and older ages”.

Several genes identified in this study have also cropped up in research in animal models. Indeed, data from animal studies have generally been more effective in uncovering human genetic variations associated with healthy ageing than GWAS. One of the associations that has been most heavily replicated in humans is a variant of the apolipoprotein E (APOE) gene known as *E4*, which is linked not with longevity but with frailty⁵ — understandable given that this variant greatly increases the risk of both Alzheimer’s disease and cardiovascular problems. However, some see it purely as a risk factor for disease and are reluctant to call it a true ‘ageing gene’. With regards to the latter, variations in a gene encoding a regulatory factor called forkhead box O3A (FOXO3A) — the human counterpart of *daf-16*, a gene that modulates lifespan in worms — have been repeatedly linked to longevity in diverse populations of humans⁶. “It has been replicated in Han Chinese, Japanese, Ashkenazi Jews, southern Europeans and Germans,” says Stefan Schreiber, director of the Research Group for Healthy Ageing at Christian Albrechts University in Kiel, Germany. “This means that the origin of the genetic variant must be very old.” FOXO3A is part of a set of signalling pathways that govern growth and metabolic activity. In research that further supports the importance of metabolic pathways in ageing, Barzilai has found similar results in his Ashkenazi cohort. In particular, he has identified variants in genes encoding two proteins involved in lipid metabolism that reduce the levels of functional cholesterol esterase transport protein (CETP) and apolipoprotein C3

(APOC3)⁷. “They seem to behave like longevity genes — these variants go from 8–10% frequency in a population of 60-year-olds to about 20% in centenarians,” says Barzilai.

Studies of centenarians are fraught with difficulties, however. For example, there is the issue of control groups: centenarians have experienced environmental and lifestyle changes that will not necessarily be matched in modern-day populations. “If you’re studying centenarians born in 1910, ideally you’d want a cohort of individuals who were also born in 1910 and died at age 50, and there’s little or no DNA available to do those studies,” says Nicholas Schork, a bioinformatician at the Scripps Research Institute in San Diego, California. On the other hand, dramatic improvements in contemporary medical care and diet mean that would-be control cohorts might harbour secret centenarians — lucky individuals with ‘normal’ genotypes who reach a ripe old age today, but who would have probably died younger in harder times. “The bet is that only a small number of control individuals will live to a very old age,” says Perls, “but there may be more people than were once thought who can live to 100.”

SUPER-OLD, SUPER-HEALTHY

Researchers are devising craftier strategies for tracking down biological factors that support very long life. Schreiber’s team is among those beginning to focus on ‘supercentenarians’ — those rare individuals who reach 110 years of age. “We’re starting with the most extreme and deploying all of our genomic and genetic tools to really dive deep,” says Schreiber. He notes that he has successfully used this type of approach for Crohn’s disease: by focusing on children who developed the disease at an unusually early age he has uncovered several causative genetic factors.

Another approach is to bank on the compression of morbidity model and focus on individuals in their 80s or 90s who are ‘biologically young’. Schork is involved with the Welllderly study at Scripps, which works along these lines. “If somebody is 80 years old and as fit as a 50-year-old, studying them could shed light on what allows people to live to old age,” he says.

As with GWAS, the difficulty in finding longevity gene candidates across populations might in part be a result of scientists casting their nets too wide. Given that most of the benefits of longevity genes are likely to kick in well after our child-rearing days, these variants probably lack the evolutionary momentum to spread, existing only as ‘family heirlooms’ that are passed from parent to child. There is certainly anecdotal evidence of this — all three of Kahn’s siblings, for example, also lived past the age of 100. Accordingly, several research groups and collaborative efforts such as the multinational Long Life Family Study, backed by the US National Institute on Aging (NIA) in Bethesda, Maryland, are attempting to get a better handle on this relationship. “We’re



People who enjoy good health in old age may have a genetic advantage.

looking at longevity-enriched families; for control persons we are using their spouses,” says Christensen, one of the study’s investigators. “We’ve performed GWAS on these individuals, and now we are moving on to sequencing.”

As sequencing technology becomes cheaper and more powerful, it is likely to become an essential tool in the field. “I don’t think there will be major progress until we can analyse and interpret the whole-genome sequences of our centenarians,” says Schork. Barzilai has long been interested in this approach: a grant proposal from his group to perform whole-genome sequencing on centenarians didn’t find traction with the US National Institutes of Health (NIH) but ultimately became the foundation for the Archon Genomics X PRIZE. This competition will award US\$10 million to the genome-sequencing team that can deliver the fastest, best and cheapest sequences for Archon’s cohort of centenarian volunteers, termed the ‘100 over 100’. This effort has continued to benefit from input from both Barzilai and Perls, and both scientists see it as a good start. “One hundred people is not a large enough sample size,” says Perls, “but it is a fantastic step in the right direction.”

Still, Barzilai cautions against thinking of genetic analysis as an end in itself. He would

like to see how genetic variants translate into physiological effects, such as shifts in a person’s metabolic profile that directly reflect the state of their health. “Measure something in the blood, and then tell us if it’s relevant,” he says. He notes that although there might be numerous variations in different genes, they could all lead to the same life-extending result. “All our findings have had a relationship to a phenotype,” says Barzilai. “With CETP, the CETP levels were low. With APOC3, the APOC3 levels were low. And with both of them there were changes in cholesterol levels.” He further notes that although *FOXO3* variations have been linked to longevity in several genetic studies, their physiological impact has yet to be demonstrated.

Fortunately, there are a handful of other prospective, longitudinal studies of ageing-related health that can provide phenotypic data with which to compare genotypic findings. These include two osteoporosis studies that have been running at the University of California, San Francisco, since 2000, one focusing on men and the other on women. “Large numbers of those cohorts have passed away because they’ve reached their 70s and 80s,” says Perls. “But they happen to be about the same birth cohort as the children of our centenarians, the vast majority of whom are still alive.”

Despite all these leads, researchers in both Europe and the United States are hampered by a lack of funding for longevity research. For example, the NIA-backed Longevity Consortium, which has supported many genetic studies of human ageing, is running on a limited and dwindling budget, says Schork. On the other hand, the field has strong support from NIH director Francis Collins. Collins is a driving force behind the NIH’s new Geroscience Interest Group, which envisages ageing as a primary link between many diseases. According to this perspective, understanding ageing might indicate a point of attack for treating or preventing conditions that have otherwise proven difficult to conquer, such as Alzheimer’s and cardiovascular disease (see ‘Live long and prosper’, page S18). “You have many more genetic susceptibilities within you than you will have diseases — and the mechanisms that either make a disease manifest or protect you are therefore of extreme importance,” says Schreiber. “Studying longevity is one way into this.” ■

Michael Eisenstein is a freelance science writer based in Philadelphia, Pennsylvania.

1. Andersen, S. L. *et al.* *J. Gerontol. A Biol. Sci. Med. Sci.* **67**, 395–405 (2012).
2. Herskind, A. M. *et al.* *Hum. Genet.* **97**, 319–323 (1996).
3. Beekman, M. *et al.* *Proc. Natl Acad. Sci. USA* **107**, 18046–18049 (2010).
4. Sebastiani, P. *et al.* *PLoS ONE* **7**, e29848 (2012).
5. Nebel, A. *et al.* *Mech. Ageing. Dev.* **132**, 324–330 (2011).
6. Kenyon, C. J. *Nature* **464**, 504–512 (2010).
7. Bergman, A. *PLoS Comp. Biol.* **3**, e170 (2007).



Eva Kahana with her husband and collaborator Boaz.

Q&A Eva Kahana

Ageing proactively

Why do some people cope better than others with getting old? Sociologist Eva Kahana, director of the Elderly Care Research Center at Case Western Reserve University, offers some clues.

Is there a secret to ageing well?

There are a few. I've been studying how older people cope with the stressors of later life — the physical decline and loss of friends and relatives that often result in adverse psychological and social outcomes. It turns out that the people who age best engage in two kinds of adaptation. The first is preventive behaviours, such as physical exercise and healthy diet. Helping others and holding altruistic attitudes also seem to improve happiness in late life — that's a phenomenon I'm investigating now with my collaborator on all this work — my husband Boaz Kahana, a psychologist at Cleveland State University.

The other type of adaptation comes into play after the stressors have arisen. In a study published in May 2012, we found that actively asking for help and planning ahead for purchases or trips are important predictors of maintaining psychological well-being and social connectedness¹. In other words, the people who do best still try to make the most of their future.

Your observations have led to your theory of 'successful ageing'. Isn't that a loaded term?

Successful ageing is a slippery concept, but most gerontologists use it. A lot of early models assumed that you have to be healthy, wealthy and wise to age successfully. Today, the term

is in flux. Some people say it's subjective — if you think you're ageing successfully, then you are. Others say that if you're sick and depressed with no social support then you are not ageing very successfully — and self-perception is neither here nor there.

Our view is that people are dealt different hands in life. As long as they do the best they can to make their lives better they can have a place at the table of successful ageing.

On what research do you base these ideas?

Much of it comes from a long-term project, the Florida Retirement Study. It started in 1989 with 1,000 people who had relocated to a large retirement community in Florida. We hypothesized that if you're far from your previous social supports, such as your children, you will have more problems facing the stressors of old age.

Every year, we interviewed each resident about their lives, leisure pursuits, aspirations, health, well-being and social relationships. We followed the same group for 20 years, by which time we were down to fewer than 100 people. It's one of the longest studies of its kind.

We found that the progression of frailty identified by many studies did occur, but slowly. These people led active, leisure-oriented lives, and maintained good health and functioning

for a long time. We also found that they enjoyed living among older people, which many gerontologists thought was not beneficial. On average they scored high² on measures of happiness and life satisfaction, despite being far from their families. Many of them said: "Our grandchildren visit at Christmas. We're happy to see them come, and we're even happier to see them go."

Did that surprise you?

I wouldn't want to live in an age-segregated retirement community, far away from my children and grandchildren, so I presumed these people would not be very happy or healthy. But, much to our surprise, they were flourishing. That's the wonderful thing about science — you don't always find what you expected.

There are great differences among individuals, and people who choose to enter age-segregated communities or move away from the younger generation can do just fine.

Has your own ageing changed your approach to this research?

I'm 71. Studying ageing while ageing is wonderful because I find that many of my ideas come from my experience. For instance, as my husband and I have encountered our own health challenges, I have become acutely aware of the importance of advocacy in obtaining good healthcare. We now have a study teaching disadvantaged older people at senior centres to communicate with their doctors, for example, to prepare questions in advance of an appointment, or to take somebody along who can listen in case they don't catch something. That way, they can advocate for themselves and not just be passive healthcare consumers.

Has life informed your research in other ways?

When my late mother, who was a Holocaust survivor, was admitted to the hospital, I fought unsuccessfully to get her a private room. But then she told me she didn't want a private room. She said: "If there's another person in the room, then nobody will mistreat me." I was shocked, and I began to think about it. Why do we assume that everybody wants the same thing? That led to my theory of person-environment fit³, a model for understanding how living environments affect older people's well-being.

Gerontologists tend to look for universal solutions and say something is good or harmful for everybody. But as we found with the Florida study, that's not always the case. Even though it's been 30 years, this theory of person-environment fit remains my most cited work. ■

Interview by Rebecca Kessler, a freelance science journalist in Providence, Rhode Island.

1. Kahana, E. et al. *Aging Mental Health* **16**, 438–451 (2012).
2. Kahana, E. et al. *Psychosomat. Med.* **64**, 382–394 (2002).
3. Kahana, E. A. in *Theory Development in Environment and Aging* (eds Windley, P. G., Byerts, T. O. & F.G. Ernst, F. G.) 181–217 (Wiley, New York, 1975).

Looking for a master switch

Evolution can extend a species' lifespan by an order of magnitude. Can we learn the same tricks?

BY SARAH DEWEERDT

Lonesome George, the Galapagos tortoise famous for being the last of his subspecies, was thought to be about 100 years old when he died on 24 June 2012. That's a lifespan that fewer than 1 in 10,000 humans attain. But for his species, it was nothing special — giant tortoises can live for about 180 years, proving that slow and steady really can win the race.

To humans, contemplating a mortality that rushes up all too quickly, such long-lived creatures are fascinating. How do they last for so long — and could we learn to do the same?

So far, most research on the mechanisms of ageing has involved model organisms such as mice, roundworms and yeast. These studies have helped scientists uncover various ageing-related genes and biochemical pathways (see 'Live long and prosper', page S18).

But these species have become model organisms precisely because they don't live very long. They mature quickly, reproduce prolifically and soon die — all qualities that make scientific studies feasible. "We may be overlooking a whole category of tricks for long life that you're never going to see in short-lived animals," says Steven Austad, interim director of the Barshop Center for Longevity and Aging Studies at the University of Texas Health Science Center in San Antonio.

So researchers are looking for clues in other animals, including some with impressive lifespans in absolute terms and others that outlive related species.

The first strategy is to study animals that exhibit what Caleb Finch, director of the Gerontology Research Institute at the University of Southern California in Los Angeles, has dubbed 'negligible senescence'. Examples include deep-sea rockfish, which still produce a normal number of eggs at the age of 100; long-lived species of turtles and tortoises; and certain clams and oysters that live for nearly half a millennium (see 'Maximum lifespans').

Long-lived animals tend to have one attribute in common: protection. Oysters and clams have tough outer shells, whereas bowhead whales, which can reach 200 years old, are protected by their size — larger species tend to live longer than smaller species. "There's no point building a mouse that can live 40 or 50 years, because they're all going to get eaten in the first year of life," says Richard Miller, who studies the biology of ageing in mammals at the University of Michigan in Ann Arbor. But that's not such a problem for a bat that can fly out of harm's way, a sea urchin that can deter enemies with its spines, or an elephant that is too powerful to be taken down by predators. "Nature makes long-lived species whenever there's an opportunity in the form of a low-hazard niche," Miller says.

And that opportunity has arisen over and over again. "Every kind of animal in every phylum has species that are short lived and species that are long lived," says Finch. "So lifespans can go in either direction, depending on the evolutionary pressures." In other words, evolution can extend the lifespan while keeping the same basic body plan and genetic heritage.

LEARNING TO LIVE LONGER

One result of surveying long-lived species is the realization that we are already members of that select group. "Humans are really sort of outliers," says Vera Gorbunova, professor of biology at the University of Rochester in New York. We have the longest lifespan of any primate, and live four times longer than similar-sized animals such as deer and cougars.

Even so, some researchers think we can still glean useful insights from species with even greater feats of longevity. Austad is studying hydras, small freshwater polyps related to jellyfish. "So far as we can tell, those things never age," Austad says. But hydras only achieve an indefinite lifespan if they reproduce asexually, budding off daughters from the mother's body wall. If environmental conditions turn harsh, the change can trigger each hydra to begin

producing either sperm or eggs — and then it lives only as long as a fruitfly.

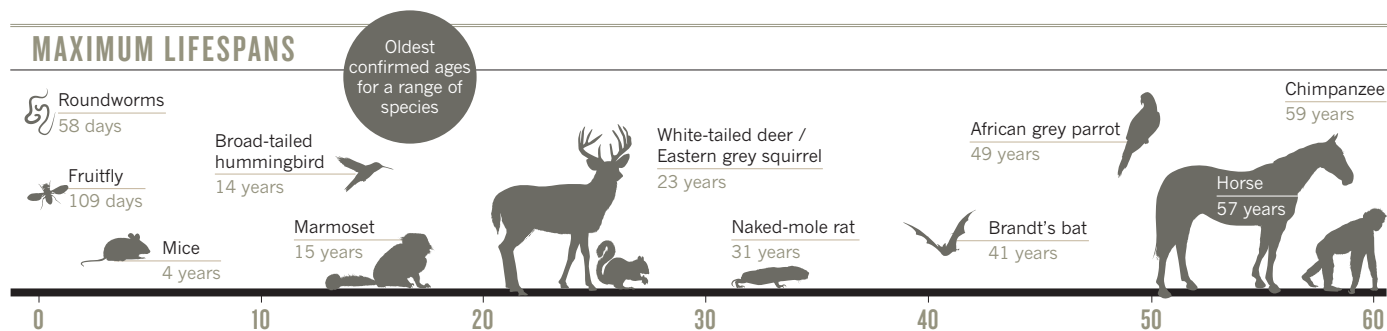
It's not clear how the hydra's genome is tuned to produce either extremely slow or extremely rapid ageing. But investigating this creature has great benefits: Austad points out that the hydra shares many genes with humans that have been lost in worms and fruitflies. "There's a universe of genes that we haven't been able to investigate in the traditional invertebrate models that may lead us to some new genetic pathways" involved in human ageing, he says.

Others are more cautious about extrapolating from long-lived species to humans. Many of these species are only distantly related to us and have very different lifestyles. Turtles, for example, have a low metabolic rate and live a slow, sluggish existence. They are "close to being dead most of the time, physiologically," says George Zug, curator emeritus of amphibians and reptiles at the Smithsonian Institution's National Museum of Natural History in Washington DC. Zug adds that evolution doesn't select for longevity directly, but for how long an organism takes to become reproductively mature, and for the length of its reproductive lifespan. So looking to evolution for insights on how to extend our post-reproductive lifespan might be a non-starter.

It might be better to compare species in the same taxonomic group with similar genetic material. For example, laboratory mice live for 4 years at most, but the longest-lived rodent, the naked mole-rat — a buck-toothed, wrinkly creature that dwells in colonies underground — can survive for nearly 30 years. Moreover, longevity has evolved in four different rodent lineages: porcupines, beavers and squirrels can also live for more than 20 years.

Even though none of these species lives as long as humans, we can learn a lot from them. Gorbunova points out that by manipulating single genes in a mouse, scientists have been able to extend their lives by 10–20%. "But compared to a mouse, a naked mole-rat lives ten

SOURCE: THE ANAGE DATABASE





Lonesome George lived to about 100, which is merely middle-aged for a Galapagos tortoise.

times longer," she says. Clearly evolution is the superior experimentalist here.

MECHANICS OF AGEING

Comparative studies are beginning to give clues to the cellular and molecular mechanisms that enable some species to live longer than related species. Miller's team, for example, cultured skin cells from nine rodent species and exposed them to various stresses, including cadmium, hydrogen peroxide and heat¹. Similar experiments² involved skin cells from 35 different bird species. Both studies showed that cells from long-lived animals are more resistant to stresses than those of short-lived species, says Miller.

Similar research also suggests one possible reason why birds tend to live longer than mammals of similar size, Miller adds. "Bird cells tend to be three- to ten-fold more resistant to many

of these stresses than cells from rodents of the same size. We can't prove that's why birds live a long time, but it's a good guess."

Another possible mechanism of longevity comes from Austad's studies of protein stability³ — the ability of proteins to remain properly folded when researchers try to disrupt them with chemicals or heat. "We've looked at protein stability in a number of long-lived organisms, and it seems to be the one thing that reliably associates with long life" in creatures as diverse as bats, naked mole-rats and clams, he reports.

Miller's and Austad's results don't necessarily contradict each other. "When an organism ages, so many things go wrong," Gorbunova says. To build an organism that lives substantially longer than related species, "you need to improve multiple maintenance mechanisms". Long-lived species might have better mechanisms of DNA

repair, for example, something Gorbunova is currently investigating in cells from 20 different rodent species. Her team has shown⁴ that naked mole-rat cells are hypersensitive to contact inhibition, the tendency to stop growing and dividing when they touch other cells. This characteristic makes the species extraordinarily resistant to cancer.

The naked mole-rat seems to have several potential protective mechanisms at its disposal. For example, a team of Israeli and US researchers recently reported⁵ that the animals also have an unusually high level of NRG-1, a protein that protects nerve cells in the brain.

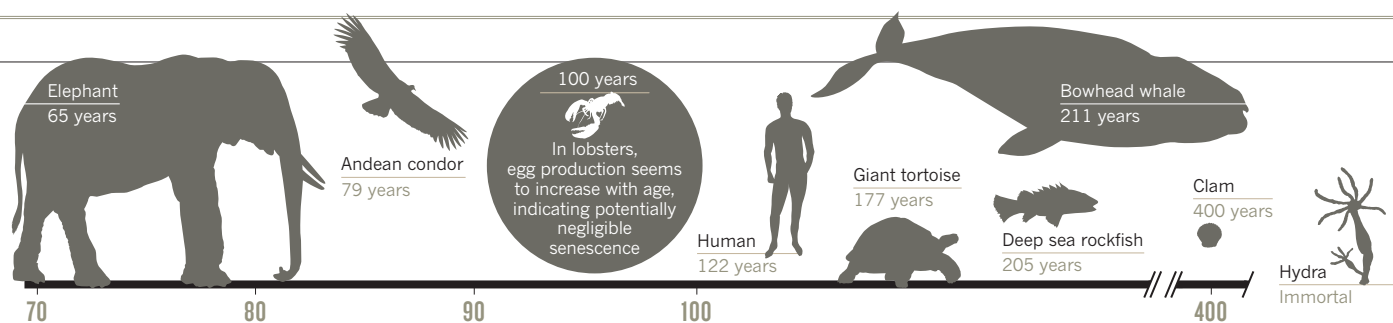
A more comprehensive approach to investigating the mechanics of ageing is provided by metabolomics, which attempts to identify the small molecules that comprise the metabolic profiles of cells. Daniel Promislow, a geneticist at the University of Georgia in Athens, investigated⁶ the levels of about 2,500 different molecules in the bloodstream of young and old marmosets. This small monkey, native to South America, is becoming a popular model for studying ageing in primates because it is relatively short-lived and easy to keep in captivity. "All these metabolites and their interactions paint a portrait of the state of that individual," explains Promislow. "And that portrait changes with age."

Promislow's group is carrying out an even larger metabolomics study that will track the levels of more than 20,000 molecules over five years, charting differences between young and old marmosets, and in individual monkeys over time. He has also just finished collecting a similar data set in fruitflies.

So researchers are not short of anti-ageing mechanisms to investigate. For Miller the bigger question is whether these mechanisms are all separate or derived from a common 'master switch' for longevity. As he puts it: "When Nature wants to build a long-lived species, does she have more than one trick to do it?" ■

Sarah Deweerdt is a freelance science writer based in Seattle, Washington.

1. Harper, J. M. *et al.* *Ageing Cell* **6**, 1–13 (2007).
2. Harper, J. M. *et al.* *J. Exp. Biol.* **214**, 1902–1910 (2011).
3. Austad, S. N. *J. Comp. Pathol.* **142**, S10–S21 (2010).
4. Seluanov, A. *et al.* *Proc. Natl Acad. Sci. USA* **106**, 19352–19357 (2009).
5. Edrey, Y. H. *et al.* *Ageing Cell* **11**, 213–222 (2012).
6. Soltow, Q. A., Jones, D. P. & Promislow, D. E. L. *Integr. Comp. Biol.* **50**, 844–854 (2010).





Helping stem cells to replicate over and over again could hold back the signs of ageing.

STEM CELLS

Repeat to fade

Stem cells rejuvenate our tissues but are not resistant to ageing themselves. How can they retain their effectiveness?

BY PETER WEHRWEIN

Stem cells are the cells that keep on giving. They resupply the body with new cells as the old ones wear out from DNA damage, the accumulation of malformed proteins, or shortening of the telomeres (DNA caps on the tips of the chromosomes). They also make copies of themselves, replenishing their own ranks in the process.

ERIK DREYER/GETTY IMAGES

Little wonder that harnessing stem cells is seen as a possible way to fix or maintain failing organs and tissues, and maybe slow the general physical decline of old age. With a ready supply of active stem cells, older muscles might be made stronger, failing brains could become less prone to cognitive lapses, and aged bone marrow could be better able to produce the infection-fighting T and B cells.

If only it were that simple. As with so much else, stem cells in an older person are not the same as those in someone younger. They tend to be less productive and less reliable, and become slower and less predictable when it comes to replenishing cells affected by injury, illness or senescence — and the tissues they serve become less healthy and vital. In other words, stem cells are prominent in the fundamental biology of ageing. If stem cells in older people could be made to retain their effectiveness, perhaps broken bones and skin wounds could be made to heal faster and, with time, we might be able to treat the conditions of old age, such as dementia and heart disease.

Thomas Rando, a stem-cell researcher at Stanford University in California, points out that we already transplant bone marrow and perform skin grafts. Stem-cell transplantation of certain types of cells — those that mature into pancreatic cells, for example, to treat diabetes — could become a reality in five years, he says. “It’s not so futuristic.”

STEM-CELL HIERARCHY

There are different categories of stem cells with varying degrees of potency — the potential to differentiate into other cell types. Totipotent stem cells — found only in embryos — can become any type of cell in the body. As these stem cells differentiate, they become more specific to certain tissue types. Examples of these multipotent stem cells include neural stem cells, which develop only into neurons, astrocytes and oligodendrocytes. Muscle stem cells are even more specialized — these unipotent cells produce only muscle cells.

Ageing affects various stem-cell types in different ways. Blood-forming (haematopoietic) stem cells in the bone marrow, for example, shift towards making more myeloid cells and fewer of the lymphoid cells that generate T and B cells. This change might help explain why older people are more likely to develop myeloid-related cancers and are more vulnerable to infections. Similarly, according to a study¹ by Mark

➔ **NATURE.COM**

For some of the latest research on stem cells:

go.nature.com/bLxt1n

LaBarge, a cell biologist at Lawrence Berkeley National Laboratory in California, older stem cells in human breast tissue tend to produce fewer tumour-suppressing myoepithelial cells than younger stem cells in the breast. In both cases, the number of stem cells may remain the same, or even increase, with age.

With the brain and hair, it seems to be a different story. The pool of available stem cells starts to deplete. Indeed, the cognitive and sensory decline of old age has been associated with a reduction in the number of neural stem cells and hence the production of new brain cells. And fewer melanin-producing melanocyte stem cells leads to greying hair, one of the most obvious signs of senior status.

NICHE EFFECTS

Stem cells don't live in splendid isolation. Their behaviour is heavily influenced by their surroundings, and it has become apparent that the ageing stem cell is as much a product of its environment as of its intrinsic make-up.

In 2005, Rando and Irina Conboy, a bioengineer who was then working in Rando's Stanford lab, conducted a landmark experiment² showing the dramatic effect that external factors can have on stem cells. Working from what Rando says was a hunch, the researchers surgically attached the circulatory systems of pairs of mice — one young, one old — so that the two shared the same blood. They found that a minor muscle injury inflicted on the older mouse healed much better when the animal was attached to a younger mouse. Furthermore, tests showed that this improved healing was the result of the activity of the older mouse's stem cells, not those of its younger, conjoined companion. Clearly, something in the blood of the younger animal was rejuvenating the stem cells in the older one. This finding opened up the possibility of arresting, or even reversing, the decline of older stem cells by manipulating their environment. Or, as Rando puts it, "enhancing the niche may be just as important as finding the best stem cells".

Using similar studies, other researchers have extended Rando and Conboy's findings to different types of stem cell. Conboy, now at the University of California, Berkeley, offers a hypothesis to explain this effect. She notes that stem cells are typically quiescent. "They have a talent for sitting quietly and waiting," she says. In old tissue, signals to stem cells might not get through "so they continue to sit quietly and do nothing". But enliven their environment and the signal can carry.

Now comes the hard work: working out precisely what it is that affects the stem-cell niche. As Conboy points out, it's likely to involve many factors, including some that reduce stem-cell activity as well as those that rev it up. As an example of a debilitating factor, Rando's team reported³ that eotaxin — a chemokine, or immune-system chemical messenger — seems to contribute to

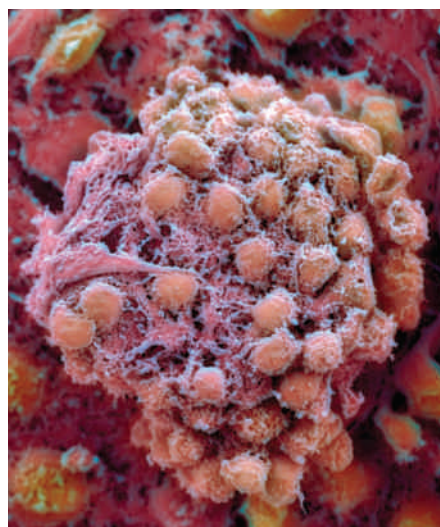
age-related cognitive impairment by inhibiting adult neural stem cells.

Another aspect of the stem-cell environment is the ageing of normal cells. Senescent cells secrete a variety of signalling molecules such as cytokines and chemokines; proteins such as growth factors; and enzymes such as proteases. According to Judith Campisi, who studies senescence at the Buck Institute for Research on Aging in Novato, California, cytokines can act directly on stem cells to restrict proliferation and versatility, and proteases can degrade the extracellular environment. Transplanting young stem cells into a neighbourhood full of

"Stem cells have a talent for sitting quietly and waiting."

older cells, some of which are senescent, is probably not going to work very well, she says. "There's mounting evidence that senescent cells in the niche are going to be an important part of the stem-cell transplant story."

How does a change in the niche alter a stem cell's behaviour? The cell's genes don't change, but epigenetic factors might cause them to be expressed in different quantities. So, both genes and environment play a role. "A cell's behaviour is always dictated by the micro-environment it is in," says LaBarge. "But the array of potential responses within those contexts is probably dictated by the genetic state of the cell."



Embryonic stem cells can replenish any type of cell, but that potency is lost during ageing.

One way stem cells are connected to their niches is through signalling pathways, whose complexities are slowly coming into focus. Research has shown^{4,5}, for example, that an active Notch signalling pathway turns on the regenerative power of muscle stem cells, whereas firing up the Wnt signalling pathway leads to fibrosis. These pathways aren't isolated from one another. The strength of the Notch pathway depends in part on another pathway,

known as MAP/ERK6. The Wnt pathway has a role in regulating telomerase, an enzyme that restores the chromosomal DNA caps, or telomeres, that otherwise shorten each time the chromosome is copied.

THE FLIP-SIDE OF THE COIN

Researchers studying stem-cell rejuvenation see an array of potential clinical applications. Bioengineered polymers could deliver drug packages that ramp up signalling pathways such as Notch. Agents that tweak DNA-reading RNA could alter which genes are expressed in an effort to return youthful vigour to decrepit stem cells. Investigation of agents already known to have anti-ageing effects, such as rapamycin (see 'Live long and prosper', page S18), might reveal pathways that alter older stem cells or their niches, or both.

However, says Rando, any treatment needs to be targeted, both in duration and specific location, to avoid the potential harm of systemically and chronically stimulating stem-cell function. The most worrying of the potential side effects is cancer. Many of the factors and mechanisms that reduce the efficacy of stem cells also keep cancer in check.

For example, when dividing cells are damaged or stressed, cell senescence keeps them from becoming cancerous. But once cells are senescent, they secrete cytokines and other molecules that might tip their neighbours — and possibly more distal cells — into a proliferative, cancerous state. Campisi says that some adult stem cells — for example, mesenchymal stem cells in connective tissue, and blood-forming haematopoietic stem cells — also undergo senescence. These cells are particularly disruptive and can activate nearby dormant cancer stem cells.

The p16 tumour-suppressor gene is another good example of the ageing-cancer trade-off⁷. Increased expression of p16 has been observed in a number of older tissues — so much so that active p16 seems to be an overall marker for ageing. But p16 is a tumour-suppressor gene that might limit age-related diseases, so targeting it is a high-risk strategy. "Tumour suppression and ageing are two sides of the same coin," notes Rando.

So, as enthusiastic as researchers are about making old stem cells young again, they are well aware that this is new territory where the best of intentions could easily have unintended consequences. ■

Peter Wehrwein is a freelance science writer based in Newton, Massachusetts.

1. Garbe, J. C. *et al. Cancer Res.* **72**, 3687–3701 (2012).
2. Conboy, I. M. *et al. Nature* **433**, 760–764 (2005).
3. Villeda, S. A. *et al. Nature* **477**, 90–94 (2011).
4. Brack, A. S. *et al. Science* **317**, 807–810 (2007).
5. Naito, A. T. *et al. Cell* **149**, 1298–1313 (2012).
6. Conboy, I. M. *et al. Aging* **3**, 555–563 (2011).
7. Jones, D. L. & Rando, T. A. *Nature Cell Biol.* **13**, 506–512 (2011).



DAVID SUTHERLAND/GETTY IMAGES

Could a Mediterranean diet, rich in olive oil, fish and fresh fruit, lead to a healthy microbiome in old age?

MICROBIOME

Cultural differences

Studies of gut bacteria are beginning to untangle how diet affects health in old age — but determining cause and effect is tricky.

BY VIRGINIA HUGHES

Almost everything about eating gets more difficult with age. Elderly people typically cannot taste or smell as well as they used to, decreasing the appeal of some foods. Dental issues or a dry mouth can impede chewing; loss of muscle tone in the pharynx can make swallowing difficult; constipation and the side effects of medication can make digestion uncomfortable; and decreased mobility makes a chore of grocery shopping or cooking complex meals. Little wonder that older people eat an increasingly narrow range of foods. But can this, in itself, adversely affect health?

Recent research shows that diet influences the composition of the gut microbiome — the bacterial community in our intestines — in the elderly. In July, a group of researchers, mostly based in Ireland, published¹ the largest study so far of the microbiome in an elderly population. The data indicate that the frailest older people tend to harbour similar intestinal microbial communities. More provocatively, the study also suggests that this

microbial make-up is driven by a diet high in fat and lacking in fibre, and that a decline in our microbial community underlies ill health as we grow old.

The conclusion is controversial, as many scientists say these associations can go the other way. An individual's health, and thus the state of his or her immune system, can also affect the gut microbiota and drive eating habits.

One thing on which everyone agrees, however, is the value of finding out how to alter the microbiome in our favour. "The potential is enormous, especially the idea of figuring out what diet is right for individuals," says Rob Knight, a microbiome expert at the University of Colorado in Boulder, who was not involved in the new study. "We just don't have a very good idea yet of the specific parameters that could set the microbiota in a good direction versus a bad direction."

THOUSANDS OF HITCHHIKERS

The microbiome has received a lot of scientific attention of late. By sequencing the DNA of our microscopic stowaways, researchers have

discovered², for instance, that more than 1,000 bacterial species can live in the human gut, helping us break down food and boosting the immune system. Microbial profiles vary among individuals, with the average person harbouring about 160 different species. The intestinal microbiome is stable for most of our lives. But "at the extremes of life, both in babies and old people, it's chaotic", notes Paul O'Toole, a geneticist at University College Cork in Ireland, and leader of the new study.

There are no microorganisms in the womb; infants get their first exposure in the birth canal. Over the next few months, as babies drink milk and interact with the environment, additional species move in. The microscopic community does not settle down until about 12 months of age. But the changes that take place in the microbiome towards the end of life are less well understood.

O'Toole's interest in the subject started in 2007, when Ireland's Department of Agriculture, Food

➔ NATURE.COM

For some of the latest research on the microbiome: go.nature.com/zrvrut



A nursing-home diet has a marked effect on an individual's gut microbiome.

and the Marine in Dublin started an initiative to fund research to promote the food industry. The government was particularly interested in the diets of older consumers, a group whose numbers will rise dramatically in the next couple of decades.

O'Toole received a €5-million (US\$7-million), five-year grant to study the gut microbiota of the elderly. Results from research since the 1970s suggested that he would find certain patterns. For example, several studies showed that stool samples from older people contain fewer species in the genus *Bifidobacterium* — which are thought to have beneficial health effects — than samples from middle-aged controls.

These earlier studies, however, analysed only those microorganisms that could be cultured in the laboratory, which make up about one-third of the total number of species in the gut, says O'Toole. So he set out to sequence the genes of all the organisms found in faecal samples from hundreds of people aged 65 or older, and to mine this massive data set for links between microbes and health.

CAUSE OR EFFECT?

In 2011, O'Toole's team published³ the first significant batch of data from the project, dubbed ELDERMET. Echoing previous studies, the scientists found that the diversity of species living in an individual declines with age. They also showed that the type of species lost varies greatly from person to person, meaning that the gut microbiota of two older people look more different from each other than do those

of two middle-aged people.

The latest ELDERMET study¹ aimed to find out what was driving this variability. O'Toole categorized 178 participants into four groups based on where they lived: in the general community, day hospitals, short-term hospital care or long-term nursing homes. He found that the microbial profiles of the first two groups were similar to those of 13 younger adult controls. But the profiles of the older people in institutional care were notably different: they carried a higher proportion of bacteria from the phylum Bacteroidetes, and a lower proportion from the phylum Firmicutes.

Importantly, these links correlated with diet. Residents of nursing homes often eat high-fat, low-fibre diets, heavy with starchy foods such as porridge and potatoes, fried meats, puddings and sugary juices. Outside nursing homes, older people tend to have a much more balanced diet, with more fibre, less red meat and more oily fish.

The study also found that certain microbial profiles were associated with specific health measures. For example, a gut high in Bacteroidetes correlated with several markers of inflammation, high blood pressure and small calf circumference (a measure of frailty).

The researchers also looked at the timing of these dietary and health changes. When individuals move into a nursing home, their diets change within a couple of weeks. Their microbial profiles took up to one year to change completely, whereas their health took several years to deteriorate. "The microbiota appear to be driven by what people eat," O'Toole says. And this microbial profile, in turn, "correlates with whether or not the subject is healthy or frail, inflamed or not inflamed, has lots of muscle tone or poor muscle tone."

Tracking the nursing-home residents over time adds weight to O'Toole's argument, "but there probably were other things happening to those people over the course of the year," notes James

"The microbiota appear to be driven by what people eat."

Lewis, a specialist in epidemiology and gastroenterology at the University of Pennsylvania in Philadelphia. "We have to be cautious about trying to extrapolate too far in terms of what came first."

Lewis and several other scientists argue that there are probably many non-dietary factors influencing the microbiota of the elderly in O'Toole's study. After all, they say, some amount of weakness or frailty is generally what puts someone in a nursing home in the first place. And studies of younger adults who have acute gastroenteritis or Crohn's disease, for example, show a similar loss of microbial diversity to that seen in the elderly. "An already compromised health status could be among the major driving forces that differentiates the microbiomes of the free-living elderly from those of the long-term-care residents," says

Elena Biagi, a molecular microbiologist at the University of Bologna in Italy, who has studied the gut microbiota of centenarians.

Other factors, such as constipation and dental hygiene, could also explain part of the association. As Knight notes, when it comes to microbiome studies, "there are very few cases where cause and effect are known".

MEDITERRANEAN MODELS

There have been some short-term studies of how dietary patterns influence the microbiome. Last year, Lewis and colleagues showed⁴ that changing an individual's diet for ten days has little effect on the gut microbiome. Only long-term dietary patterns were associated with specific and stable microbial profiles.

Investigating the latter in more detail requires a more rigorous — and time-consuming — approach. That is what O'Toole and Claudio Franceschi, an immunologist at the University of Bologna, plan to use to investigate whether the so-called Mediterranean diet can help people age well.

Franceschi has been studying the elderly for more than 25 years. Several of his studies centre on the Italian island of Sardinia, which has an unusually high number of male centenarians⁵. He attributes this preponderance at least in part to the men's regular physical exercise and simple Mediterranean diet — rich in olive oil, fish, fresh vegetables and fruits. Intriguingly, this diet is also broadly similar — low in fat, high in fibre — to the diets of the healthiest elderly people in O'Toole's recent study.

Franceschi, O'Toole and two dozen other academic and industry groups are now part of a €9 million project called NU-AGE, which includes 1,250 older individuals from France, Italy, Poland, the Netherlands and the United Kingdom. For one year, half will be given the Mediterranean diet, half will remain on their normal diet, and the NU-AGE researchers will measure how their health changes. O'Toole's team will sequence the participants' gut microbiota before and after the dietary intervention, while other researchers will look at genetic, epigenetic and metabolic signatures in their blood. Each of these biological levels might give insight on how the diet changes the microbiome.

NU-AGE is exactly the kind of large, longitudinal study that scientists the world over are clamouring for. The hope is that interrogating the link between diet and the microbiome will show how some of our trillions of microbial hitchhikers can steer us to long and healthy lives — and how we can entice them to stay. ■

Virginia Hughes is a freelance science journalist based in Brooklyn, New York.

1. Claesson, M. J. *et al. Nature* **488**, 178–184 (2012).
2. Qin, J. *et al. Nature* **464**, 59–65 (2010).
3. Claesson, M. J. *et al. Proc. Natl. Acad. Sci. USA* **108**, 4586–4591 (2011).
4. Wu, G. D. *et al. Science* **334**, 105–108 (2011).
5. Poulain, M. *et al. Exp. Gerontol.* **39**, 1423–1429 (2004).

Dancing with robots

High-tech gadgets such as sensors that detect falls and robots that can fetch items are helping people stay independent and safe into their later years.

BY NEIL SAVAGE

Marilyn Rantz knows only too well how vulnerable old age can make us. Her mother fell one day, badly fracturing her shoulder. She owned a wearable device that would summon help at the press of a button, but had left it just out of reach from where she fell. After eight hours on the floor, she was able to crawl to the device and call for help, but the stress of those hours bearing untreated injuries took its toll — within six months she was dead.

To circumvent the limitations of such devices, Rantz, a gerontologist and associate director of the Interdisciplinary Center on Aging at the University of Missouri in Columbia, prefers systems that people don't have to carry with them. "It's one of the reasons we've moved to environment-based sensors instead of wearable sensors," she says, "because people don't wear them."

Rantz and Marjorie Skubic, an electrical and computer engineer and director of the university's Center for Eldercare and Rehabilitation Technology, are developing systems to monitor the health and well-being of older adults.

Research into this type of technology is burgeoning in line with the growing proportion of elderly people. Sensors are being developed that can not only detect falls, but also monitor changes in gait or daily routine that could flag concerns and alert caregivers before physical problems become acute. Other technologies, such as robotics, could prolong independence and help people stay active.

NOT SO TECHNOPHOBIC

Although elderly people can be reluctant to embrace new gadgets, they are happy to adopt technology if it's easy to use and will help them retain their independence, says Wendy Rogers, an engineering psychologist at the Georgia Institute of Technology in Atlanta. Over-65s have a wide spectrum of abilities and conditions, says Rogers, and range from people who are still working to those in the late stages of dementia. Their needs require a wide variety of technologies from smartphone fitness apps for the active to vital-sign monitors for the bed-ridden.

To study how technology can best help older adults, the University of Missouri, in collaboration with private company Americare, developed Tiger Place — an active retirement

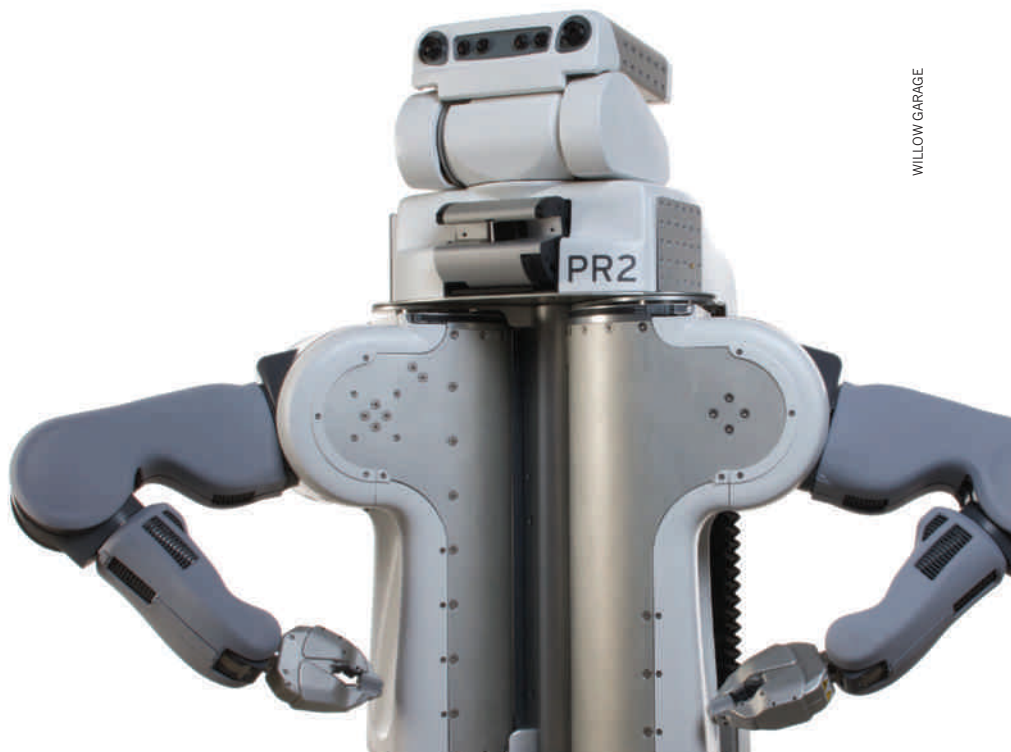
community. The aim is to allow people to stay in their apartments until the end of their lives without moving into nursing homes — a trend known as ageing in place. Rantz is executive director of the Aging in Place programme at Tiger Place, and she says that most people prefer not to move frequently; the stress of transition can contribute to health problems and earlier death. "Just the process of moving is enough to kick some people over — people who might have had many years ahead of them," she says. And for most people, going into a nursing home lessens the incentive to help themselves, leading to reduced activity and a loss of physical capability.

Tiger Place provides an environment for researchers to test their sensors. Some measures installed in its apartments are simply infrared motion detectors, the kind developed for security systems. The detectors help researchers discern individuals' personal patterns of activity: how much they move around, when and how often they leave their home, and how long they're gone for. Changed activity levels can be early warnings of problems — they can be more telling than a questionnaire in a doctor's office, and can highlight problems a lot sooner, Rantz says. A one-bedroom apartment in Tiger Place might be discreetly equipped with 10 motion sensors, a

gait-monitoring system, and bed sensors that can measure restlessness, heart rate and breathing.

One of the main hazards being monitored is falling. According to the US Centers for Disease Control and Prevention, a third of Americans aged over 65 fall each year; in 2009, this resulted in 20,000 fatalities. And the longer people lie injured, the poorer their prospects for healing. One Tiger Place project uses an array of microphones to detect the sound of a fall. Computers using statistical techniques can differentiate the distinctive acoustic characteristics of a body falling from, for example, a book being dropped or noise from a television. Preliminary work used stuntmen simulating falls, and microphones have now been installed in apartments to get more real-world data and make the system more accurate.

It is, of course, better to prevent falls occurring in the first place. Skubic is monitoring how people walk, gathering information about speed, stride length and sway to discover whether they have balance or other problems that increase the risk of falling. One of the sensors she's investigating is the Microsoft Kinect, a three-dimensional camera system designed as a hands-free controller for video games. Off-the-shelf sensors would hasten the adoption of these systems — the Kinect provides



WILLOW GARAGE



Robots such as the PR2 can help elderly people with limited mobility by fetching items and reminding them to take medication.

sophisticated 3D imaging for less than US\$150. The challenge lies in developing software that can make sense of the data. Skubic says that although she gets near-perfect results for gait measurement in a laboratory setting, it's more difficult to sort out relevant information from noise in a person's home, where lighting conditions vary, different people walk around, furniture gets moved, and so on.

More personal types of sensor system are under development. "When someone gets depressed, they physically slow down — and we would be able to detect that," says Tanzeem Choudhury, a computer scientist at Cornell University in Ithaca, New York. She adds that people under stress speak more loudly, with less tonal variation and more jitter in their voice; stress is a risk factor for poor health.

To test these ideas, Choudhury has developed a smartphone app, BeWell. The app listens to the sound of conversation — without keeping a recording of actual words spoken — to estimate a person's level of social interaction. The phone's accelerometer measures how much the person moves, and its GPS can tell if they're leaving the house, indicating physical activity and a higher chance of social contact. The app even attempts to monitor sleep by noting a lack of activity, although Choudhury says that's mostly a best-guess approximation. Among the unresolved issues are the willingness of older people to adopt monitoring software (or even the phones themselves) and technical considerations such as the effect on battery life.

THE RISE OF THE ROBOTS

Sensors can provide important health information, but older people often need physical assistance — and here robotic technology

could fill the gap. Toyota, for instance, plans to launch four devices next year it calls Nursing and Healthcare Partner Robots, designed to assist people who have trouble walking. They range in size: the smallest is a sort of knee brace attached to a footpad, worn on a paralysed leg. An accelerometer and gyroscope attached to the thigh and a load sensor in the footpad determine when a person tries to walk and how fast, and bend the knee joint accordingly. The largest of Toyota's robots assists in actually moving an immobile person to walk between, say, the bed and the toilet.

For intensive support with independence, Yoshiyuki Sankai, an engineer at the University of Tsukuba in Japan, has designed the Hybrid Assistive Limb (HAL) suit — a wearable robot that provides joint strength and limb support for people with diminished function. Sensors on the skin read weak

Machines that buzz around the house doing laundry and preparing dinner are still in the realm of science fiction.

electrical signals involved in muscle movement and trigger the suit to move appropriately. A spin-off company from the Tsukuba lab, Cyberdyne, produces HAL suits that health-care facilities can hire.

Charles Kemp, director of the Healthcare Robotics Lab at Georgia Tech, thinks mobile robots for the home could become a reality within the decade. Kemp has been conducting research on the PR2, a robot built by Willow Garage in Menlo Park, California, that has helped a quadriplegic man shave himself. Kemp says that older adults he has worked with are surprisingly willing to have a robot

help out: telling a machine to perform tasks rather than asking a relative or hiring an aide helps preserve privacy and a sense of control, he says. Kemp sees other benefits too. "Robots may enhance people's lives in surprising ways," he says. "Dancing with robots might be fun, healthy and even therapeutic."

Unlike industrial robots that perform tasks such as moving objects from one fixed location to another, personal robots will have to deal with the more variable and unstructured environment of a home. Such variation presents a challenge for their designers. "You can't completely predict where the coffee mug is going to be in the kitchen," says Kemp. The other major hurdle, he says, is the cost — a robot arm alone can cost \$100,000. Kemp is optimistic that robotics will follow the same path as computers, which went from rare and expensive to ubiquitous and cheap. There are signs this is already happening: Rethink Robotics, a Boston company, recently released a robotic arm costing \$22,000.

"It's going to be a while before we have robots that are fully intelligent and have human movement capabilities," Kemp says. Machines that buzz around the house doing laundry and preparing dinner are still in the realm of science fiction, but smaller devices that can pick up a dropped remote control, remind people to take medication or help with personal hygiene are possible in the next five years.

Older people may not be the digital natives of the young generation, says Rogers, but they are open to new technology if the benefit to them is clear. "They don't want novelty for novelty's sake." ■

Neil Savage is a freelance science and technology writer based in Lowell, Massachusetts.



Will it be possible to stop the clock and prevent the effects of ageing?

ANTI-AGEING

Live long and prosper

Researchers are learning about the molecular basis of ageing — and finding clues about how to treat diseases in the process.

BY KATHERINE BOURZAC

The Ames mice in Andrzej Bartke's lab look alike at birth. In every litter, however, some mice will have a genetic mutation that inhibits or prevents the production of growth hormone or insulin-like growth factor (IGF). These hormone-free mice will grow to a third of the size of their siblings without the mutation. But around middle age, their fortunes change: the tiny mice age differently.

As Bartke first observed in the early 1990s, when the normal mice started to appear hunched and grey, the dwarf mice stood apart. "They stay healthy and they look young," says Bartke, a gerontologist at the Southern Illinois School of Medicine in Springfield. To test whether they really did live longer, Bartke started a lifespan study. In 1996 he reported his results¹: normal Ames mice typically live about 720 days; male dwarf mice got an extra 350 days, and females lived another 470. Two of the dwarf females in the study lived for four years. This was the first solid evidence that a single genetic mutation could extend lifespan in a mammal.

By studying models such as the Ames mice, researchers like Bartke are learning that ageing is not an uncontrollable, entropic process. Using clues from studies of diets and other interventions, researchers are delving into underlying molecular mechanisms in the hope of developing drugs that thwart the process of ageing. Such therapies will protect against "potentially every age-related disease," says Felipe Sierra, a gerontologist at the US National Institute on Aging (NIA) in Bethesda, Maryland. "If we can get it to work in humans we will make a big impact on quality of life."

EAT LESS, LIVE LONGER

Much of the research into the mechanisms of ageing can be traced back to work in the 1930s by nutritionist and gerontologist Clive McCay at Columbia University in New York. McCay devised the caloric restriction diet, which involves reducing calories by about 30% without causing malnutrition. He pioneered the technique in mice and rats. Since then, caloric restriction has been found to extend lifespan in every species studied, including yeast, worms, flies and dogs.

In mice, caloric restriction extends life by 30–40%. It also broadly protects against age-related diseases, including cancer, diabetes and autoimmune disease. "Caloric restriction is the most powerful known intervention in ageing," says Luigi Fontana, a gerontologist at the Washington University School of Medicine in St Louis, Missouri. For this reason, researchers are using the diet to explore the mechanisms of ageing with a view to extending the work to humans.

Two major long-term studies are testing caloric restriction in non-human primates. Although both have demonstrated major

➔ **NATURE.COM**

For some of the latest research on anti-ageing:
go.nature.com/ixmhin

ASIASELECTS/GETTY IMAGES

JEFF MILLER

health benefits, they are far less conclusive about the effect on lifespan.

At the Wisconsin National Primate Research Center, the average lifespan of a male rhesus monkey is about 27 years. By this age, a normal monkey is stooped, with grey fur on its face and sagging skin on its torso. In contrast, a monkey the same age on a calorie-restricted diet has a lively look in its eyes, a full brown coat, and holds its tail up. These monkeys also have a threefold increase in resistance to age-associated diseases, says geriatrics researcher Richard Weindruch, who heads the Wisconsin study. Rates of cancer, diabetes, brain atrophy and cardiovascular disease are all much lower in these animals.

The second study, also in rhesus monkeys, is being conducted by the NIA at its Poolesville site in Maryland. In August 2012, the NIA group reported² that monkeys on a calorie-restricted diet not only had lower cancer rates, but also delayed onset of age-related diseases. Calorie restriction did not, however, seem to provide cardiovascular benefits or reduce the incidence of diabetes.

The biggest divergence in the two studies relates to lifespan extension. In 2009, the Wisconsin group published³ preliminary evidence that fewer calorie-restricted monkeys died of age-related diseases than the control group. Equivalent results from the NIA don't show this effect.

Researchers on both teams say this difference is probably the result of their study designs — the control diet, in particular. Julie Mattison, an experimental gerontologist and one of the leaders of the NIA study, says that their control monkeys have an especially healthy diet. “We didn't want to stack the deck with the diet,” she explains. In contrast, the control monkeys in the Wisconsin group are able to eat as much as they want. “This is more like what you see in the human population,” says Ricki Colman, a senior scientist at the Wisconsin Center. It makes sense that a diet providing minimal yet balanced nutrition will appear to be better in comparison with an unhealthy diet than with a healthy one.

The Wisconsin and NIA teams plan to pool their data to come up with more definitive results, say Mattison and Colman. The two groups have been collecting microarray data about genes that are up- or downregulated in monkeys on the diet. This should help them to understand the mechanisms underlying ageing, and the beneficial health effects of the diet. However, conclusive results will not be available until after all the monkeys have died, which won't be for another decade at least. “As a guy who's done lots of mouse lifespan studies, I can say this requires patience,” says Weindruch.

HUMAN GUINEA-PIGS

While researchers wait for statistical proof of the diet's effects in primates, some people have elected to go on the diet anyway. CRONies — the label adopted by those on a diet of



A hunger for life: an elderly rhesus monkey fed a calorie-restricted diet (left) appears younger and has better health than normal monkeys of a similar age (right).

Caloric Restriction with Optimal Nutrition — voluntarily eat 30% fewer calories than recommended by the US Department of Agriculture. That can be as low as 1,400 calories a day for men, and 1,120 for women.

Fontana, who studies the CRONies, says most of the health benefits seen in animals on the caloric restriction diet also appear in humans. He says that people who started caloric restriction in middle age and stayed with the regimen for eight years have a “fantastic” cardio-metabolic profile. He adds that he has seen subjects in their late 70s with the blood pressure of teenagers.

Fontana's group has published data showing that caloric restriction protects against atherosclerosis⁴ and leads to greater heart elasticity and heart-rate variability⁵ — a marker of cardiac health. “These studies are proving, in humans, that it's possible to completely prevent obesity, diabetes and cardiovascular diseases,” Fontana says. “This is the most powerful thing I've seen in my life as a physician.”

Fontana is compiling some of the first molecular data from humans on the diet. Using biopsies from fat and muscle tissue, he will examine patterns of gene expression and hormone levels to see if they correlate with those found in animals on the diet.

It's unlikely, however, that large numbers of people will ever sign up to such a curtailed diet. After all, it's hard enough getting people to limit themselves to only the recommended amount of calories. Fontana says in his experience, US men who are not dieting tend to eat more than

the recommended upper limit of 3,000 calories a day. Even researchers who study caloric restriction rarely practise it — none of those interviewed for this report do.

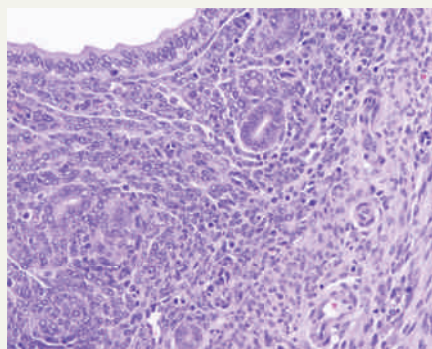
Instead, the value of caloric restriction is that it demonstrates that in principle it is possible to prevent many age-related diseases with one intervention. “We've spent the last 80 years trying to treat one disease at a time,” says Rafael de Cabo, an experimental gerontologist at the NIA and the principle investigator of its monkey calorie-restriction study. Learning about the processes underlying ageing, he says, may make it possible to tackle multiple age-related diseases at once.

Caloric restriction also provides a useful tool to study the genetics of the ageing process in animal models. Previous studies into the genetics of longevity have focused on breeding short-lived invertebrates such as worms or flies that lack or can't express certain genes. Comparing the life-spans of these model animals with normal ones reveals whether the missing genes are important in ageing. To figure out which genes are important in caloric restriction researchers put established animal models on the diet; if the diet doesn't extend lifespan, the missing gene is probably vital to the process.

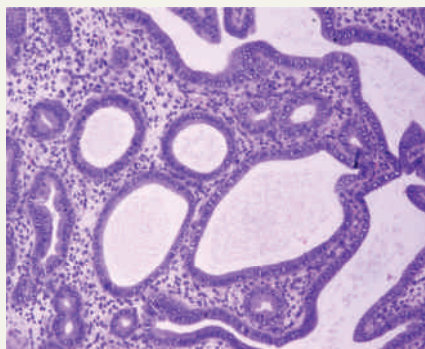
There is one fundamental unknown factor about caloric restriction: how does eating less lead to such drastic longevity and health benefits? Most researchers believe that two pathways are central to the process. One is IGF — the same pathway Bartke found was key to the long life of the Ames dwarf mice. The second is TOR (target of rapamycin), which is involved in both protein translation and intracellular clean-up. A third possible pathway involves the sirtuins — a group of seven

RISKY RAPAMYCIN

Rapamycin has been shown to increase lifespan in mice, perhaps by slowing the progression of cancer. But potential immune-related side effects have driven the search for safer alternatives with a similar mechanism of action.



A slice of uterus from a mouse given rapamycin appears perfectly healthy.



A similar slice from a control mouse shows signs of cystic endometrial hyperplasia, a risk factor for cancer.

related proteins that caused a lot of excitement after their discovery in 1999. In mice that can't make the proteins SIRT1 or SIRT3, the effects of caloric restriction are blocked. Some researchers, including Harvard University's David Sinclair, say this means that these proteins are critical to the diet's effects, and play an important role in ageing.

But the proposed connection between sirtuins and ageing is contentious. The disagreement came to a head in 2010, when a review of the field in *Science* by Fontana, Valter Longo at the University of Southern California, and Linda Partridge at University College London excluded sirtuins from the molecular mechanisms behind caloric restriction. The review prompted a flood of correspondence to the journal. Researchers including Sinclair and biologist Leonard Guarente at the Massachusetts Institute of Technology in Cambridge were adamant that sirtuins are connected with lifespan extension in mice on caloric restriction — only to have the review's authors reply that they were not convinced by the data for mammals. Sirtuins are likely to be connected to health and disease, but not ageing, they wrote.

Sirtuins are still controversial. "The field is polarized, and that's OK," says Brian Kennedy, president of the Buck Institute for Research on Aging in Novato, California. While at MIT, working under Guarente, Kennedy helped to establish the role of sirtuins in ageing. Now, however, he focuses mostly on TOR.

AN ANTI-AGEING PILL?

To mimic the beneficial effects of caloric restriction in a drug, it's not necessary to know exactly how it works. Large-scale studies can test promising compounds in mammals, looking for any evidence of lifespan extension. Several are already underway, including the NIA's rigorous Interventions Testing Program (ITP).

Started in 2004, the ITP encompasses three study sites where five compounds are screened each year in genetically heterogeneous mice eating food from the same supplier and sleeping on the same bedding. These studies are designed to be able to detect a 10% change in average lifespan with high confidence, even if data from one of the sites proves to be unusable.

The greatest recent success is rapamycin, which targets TOR. (The 'target of rapamycin' pathway is named after the drug that shuts it down.) A 2009 study⁶ showed that adding rapamycin to a mouse's food starting at 600 days old — roughly equivalent to a human age of 60 years — increases lifespan by 14% in females and 9% in males.

These numbers have convinced many researchers who study ageing. Arlan Richardson, a biologist at the University of Texas Health Sciences Center in San Antonio, has been doing ageing research for 40 years. He has seen many supposed anti-ageing drugs come and go, including vitamins E and C and melatonin. "I never thought we'd have the potential for an anti-ageing pill," he says. "Rapamycin is a breakthrough." His group is testing rapamycin in marmosets.

It isn't clear whether rapamycin extends lifespan by slowing cancer growth, by intervening in the mechanisms of ageing, or both, says Richard Miller, a pathologist at the University of Michigan in Ann Arbor who heads the ITP. He says his Michigan group has been looking into this question, and has unpublished data showing that the drug slows down ageing in multiple normal cell types, suggesting a broad anti-ageing effect.

However, rapamycin has several negative side effects that are likely to keep it out of the

running as a potential anti-ageing drug. It is known to cause cataracts in mice, and in humans it is used as an immunosuppressant to prevent organ-transplant rejection. This suggests that it might have serious immune-related consequences. "I don't view the studies we're doing as a precursor to clinical trials," says Miller.

The next step is to figure out which mechanisms in the TOR pathway are responsible for the positive effects of rapamycin, and then develop a more targeted drug. Understanding mechanisms "helps in terms of scoping out potential side effects", says David Glass, a specialist in muscle diseases at the Novartis Institutes for Biomedical Research in Cambridge, Massachusetts.

Miller's group is trying to discern these effects by studying rapamycin in various different tissue types in the mice. Other researchers are testing derivatives that may have more targeted effects. Kennedy's team, for example, is currently working with Biotica Technology, a drug development company in Cambridge, UK, that makes rapamycin derivatives, in the hope of finding a version that works without the side effects.

Not all compounds screened by the ITP show as much promise as rapamycin. Resveratrol, a compound found in red wine that targets sirtuins, had been shown to extend lifespan in obese mice fed a high-fat diet — but it failed to produce results in the ITP studies at any dose, says Miller. Many researchers still hope that resveratrol has positive effects. Sirtris Pharmaceuticals, a Cambridge, Massachusetts-based biotechnology company owned by GlaxoSmithKline, is testing resveratrol derivatives in ulcerative colitis and psoriasis. Meanwhile, the ITP will soon publish data on two new life-extending compounds, says Miller.

Ageing isn't a disease, and lifespan extension will be almost impossible to prove in humans. Instead, Glass, Sierra and others hope that research on ageing interventions will change the way we think about disease and drug development, and lead to treatments that tackle multiple age-related diseases at once. Major causes of death worldwide, including cancer and cardiovascular disease, share a common risk factor: age. Tackling one disease at a time isn't working, says the NIA's de Cabo. "Ageing is the leading risk factor for all chronic diseases," he says. "Postpone ageing, and you postpone these diseases." ■

Katherine Bourzac is a freelance journalist based in San Francisco.

1. Brown-Borg, H. M. et al. *Nature* **384**, 33 (1996).
2. Mattison, J. A. et al. *Nature* **489**, 318–321 (2012).
3. Colman, R. J. et al. *Science* **325**, 201–204 (2009).
4. Fontana, L. et al. *Proc. Natl Acad. Sci. USA* **101**, 6659–6663 (2004).
5. Stein, P. K. et al. *Ageing Cell* **11**, 644–650 (2012).
6. Harrison, D. E. et al. *Nature* **460**, 392–395 (2009).